Lucas Center Annual Report 2010

Lucas Center Annual Report 2010

Stanford University School of Medicine
Department of Radiology

Stanford University School of Medicine
Department of Radiology

Richard M. Lucas Center for Imaging

Annual Report 2010

Stanford University School of Medicine
Department of Radiology

Richard M. Lucas Center for Imaging

Annual Report 2010

Cover Image:

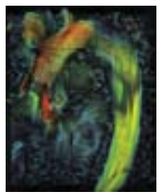

A single frame of a 4D MRI study that displays streamlines of velocity vectors in the heart and the aorta in a patient who has had a surgical repair of the aortic valve and root. Note the complex spiral in the ascending aorta and acceleration across the aortic valve.

2010 Lucas Report Team:

Editor: Susan Kopiwoda
Design: Amy Morris
Production: Joe Hubbard, Amy Morris
Photography: Mark Riesenberger
Archiving: Amy Morris
Printing: Lahlouh, Inc.

Stanford University
School of Medicine
Department of Radiology

Contents

in Medical Imaging

It is hard to believe that it has been over 20 years since the Richard M. Lucas Center for Imaging was conceptualized and its construction initiated. The pace of discovery and innovation continues to be extremely rapid so that each year we reinvent the Center and its programs.

This year, we are reinventing the Center by renovating its interior and by siting the most up-to-date instrumentation in our building. Our renovations will begin in May of 2011 and represent a $7.1M investment on the part of the Department. Over the years, we have maintained all of our MRI scanners at their latest software/hardware releases. However, one 1.5T and one 3.0T scanner can no longer be upgraded, and we plan to replace them with the latest whole body 3.0T instruments. We will also add equipment to hyperpolarize MRI signal, a technology that allows us to chemically modify compounds to increase the MRI signal by many orders of magnitude thereby markedly increasing signal detection. In addition, we will upgrade our 7.0T whole body scanner with new hardware and electronics; renovate an office area to provide additional space; and modernize an animal surgery lab.

In preparation for a new program in PET/MR, our renovations will also allow the siting of one of the earliest PET/MRI hybrid scanners in the world by 2012. Combining the superior soft-tissue contrast and high spatial resolution of MRI with the high sensitivity of positron emission tomography (PET), our PET/MR Program will advance the diagnosis of disease and the monitoring of treatment. There are currently no integrated whole body PET/MR systems in the United States.

The people and programs of the Lucas Center continue to be highly recognized throughout the imaging world. I am delighted that a new program has been established: “Modeling the Role of Differentiation in Cancer Progression,” which is one of the National Cancer Institute’s 11 new Centers for Cancer Systems Biology (CCSB). Our new Center complements our other 3 existing NIH-funded Centers of Excellence: the Center for Advanced Magnetic Resonance Technology at Stanford (CAMRT); the In Vivo Cellular and Molecular Imaging Center at Stanford (ICMIC); and the Center for Cancer Nanotechnology Excellence Focused on Therapy Response (CCNE-TR). We are the only U.S. radiology department with 4 large multidisciplinary NIH-funded centers.

CCSB research focuses on uncovering the disruption of normal processes underlying cellular differentiation in cancer for the development of novel molecular therapies. Research from the CCNE-TR includes a new magnetic cell sorter to isolate very rare cells from blood. ICMIC scientists are combining PET imaging with in vitro diagnostics to analyze patient response to anti-cancer therapies. Recent CAMRT innovations include the application of hyperpolarized 13C MRSI acquisition methods to measure treatment response in prostate and liver cancers; the improvement of cerebral blood flow techniques; the integration of imaging techniques to quantify fat, tissue perfusion, and blood flow; and the application of real-time fMRI for controlling brain regions associated with depression.

In this golden age of medical imaging, we are grateful for your support, which has helped us become leaders in biomedical imaging. You have made the Lucas Center synonymous with excellence in the development of world-leading technology and imaging programs.

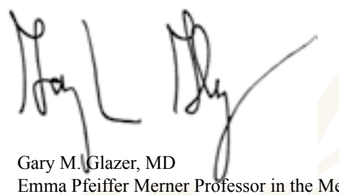

Gary M. Glazer, MD
Emma Pfeiffer Merner Professor in the Medical Sciences
Professor and Chairman
Department of Radiology
Stanford University School of Medicine

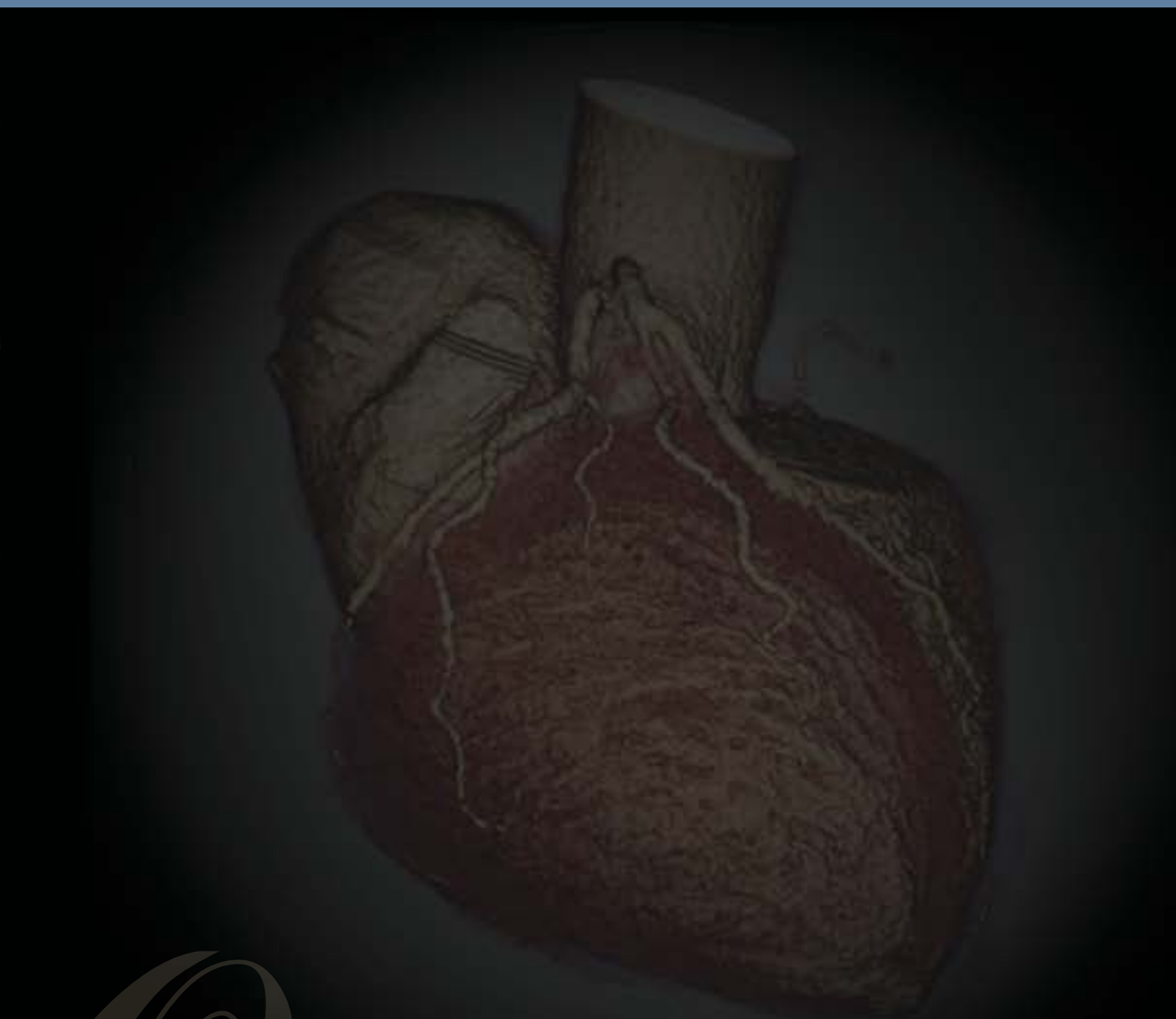

Overvie

Centers of Excellence

The Stanford Department of Radiology now leads four NIH-funded Centers of Excellence and is the only academic radiology department in the country with four NIH funded Centers of Excellence under the leadership of a single department. Our four Centers have contributed significant advances to improve health care, diagnosis, treatment, and monitoring for patients worldwide. In addition to technological, biochemical, and biological innovation in the imaging sciences, we have formally trained more than 500 individuals (including residents, fellows, postdocs, and graduate students) since our first center, the Center for Advanced MR Technology, was established in 1995.

In 2009, all four of our Centers of Excellence completed the competing renewal process; all four of these Centers did remarkably well and are in various stages of initiating new funding cylces. The following text gives a brief summary of each of these programs.

The National Center for Advanced Magnetic Resonance Technology at Stanford (CAMRT - P41)

The CAMRT, now in its sixteenth year of operation as a National Research Resource and directed by Gary Glover, PhD, is funded by a grant from the NIH National Center for Research Resources. This Resource has five core technology development areas that include reconstruction methods (Dwight Nishimura and John Pauly, EE Department, core directors), hardware development (Brian Rutt, core director), neuro imaging methods (Gary Glover, core director and PI, Mike Moseley, Roland Bammer), diffusion and perfusion +weighted imaging methods (Mike Moseley, core director), Body imaging (Brian Hargreaves, core director), spectroscopic and multinuclear imaging development (Dan Spielman, core director). In addition to development of technology projects, the CAMRT provides support for collaborations and service use of the facilities, with users in the Radiology department as well as more than 75 faculty and more than 200 other users from at least 14 departments. For further details, please see http://rsl.stanford.edu/research/camrt.html and the CAMRT/RSL Overview (page 6-7).

The In Vivo Cellular and Molecular Imaging Center at Stanford (ICMIC@Stanford - P50)

The ICMIC, directed by Sam Gambhir, MD, PhD, and initially funded in 2005, brings together more than 50 faculty across the Stanford campus from more than 15 different departments, including the Department of Radiology. As one of a small number of in vivo cellular and molecular imaging centers (ICMIC) in the country, the ICMIC@Stanford studies disease by connecting preclinical models with clinical management through advances in multimodality molecular imaging. The goals of the program are to fundamentally change how biological research is performed with cells in their intact environment in living subjects and to develop new ways to diagnose diseases and monitor therapies in patients. Areas of active investigation are cancer research, microbiology/immunology, developmental biology and pharmacology. The ICMIC benefits from the highly regarded infrastructure provided by the Department of Radiology, the CAMRT, and the RSL in the Richard M. Lucas Center for Imaging. For further details, please see http://mips.stanford.edu/public/grants/icmic/ and the MIPS Overview (page 10).

The Center for Cancer Nanotechnology Excellence (CCNE - U54)

Stanford Radiology is one of only a few (less than 10) institutions in the nation supported by the NIH to develop a major nanotechnology center: the Center for Cancer Nanotechnology Excellence Focused on Therapy Response (CCNE-TR). This center, established in 2006 and led by Sam Gambhir, MD, PhD, includes scientists from Stanford and five other sites across the country. The goal of this center is to use nanotechnology for the benefit of cancer patient management. Our new Center for Cancer Nanotechnology Excellence and Translation (CCNE-T), approved for funding in 2010, builds on the success of the CCNE-TR and brings together scientists and physicians from Stanford University, University of California Berkeley/Lawrence Berkeley National Lab, University of California Los Angeles, University of Southern California and the Massachusetts Institute of Technology. Our goals with the new CCNE-T build on our vision that in vitro diagnostics, used in conjunction with in vivo diagnostics, can markedly impact cancer patient management. It is through the use of nanotechnology that we will be able to significantly advance both in vitro diagnostics through proteomic nanosensors and in vivo diagnostics through nanoparticles for molecular imaging. Both the CCNE-TR and the CCNE-T will run simultaneously for ~1 year as we begin ramping up the CCNE-T to focus markedly on bringing nanotechnology into clinical use. For further details of the CCNE, please see http://mips.stanford.edu/public/grants/ccne/ and the CCNE Overview (page 12).

Center for Cancer Systems Biology (CCSB - U54)

The Stanford Center for Cancer Systems Biology (CCSB), led by Sylvia Plevritis PhD, promotes the discovery of molecular mechanisms underlying cancer progression by studying cancer as a complex biological system that is driven, in part, by impaired differentiation. Our CCSB's overarching goal is to better understand the self-renewing properties of cancer and its cellular hierarchy for the purposes of identifying effective therapeutic strategies. Our approach integrates a variety of high-throughput experimental datasets at the genomic, transcriptomic and proteomic levels, with novel computational techniques, in order to reveal critical molecular networks that drive cancer progression. This multidisciplinary Center brings together 10 Stanford faculty from the Schools of Medicine, Engineering, and Human Sciences, with expertise ranging from molecular biology and oncology to mathematics, statistics, and computer science. It is one of twelve centers, nation-wide, newly funded by the NIH/NCI Integrative Cancer Biology Program (http://icbp.nci.nih.gov/icbp) to promote the analysis of cancer as a complex system by merging experimental and computational methods. For further details of the CCSB, please see http://icbp.stanford.edu/ and the ISIS Overview (page 8-9).

Research Overview

Norbert Pelc, ScD, Associate Chair for Research
Susan Kopiwoda, MS, MPH, Director, Strategic Research Development

Once again, we have had a very successful year. Our research productivity and extramural funding (see abstract pages 61-133; funded projects pages 209-214) ranks with the best and most productive radiology departments anywhere. In addition to typical funding mechanisms, we received an additional $4M in 2009-10 (with $3M for 2010-11) through the 2009 American Recovery and Reinvestment Act (ARRA). These funds have allowed us to retain or hire research scientists and establish new projects as the ARRA funding tapers off and comes to an end.

2010 Success: During 2010, we have enjoyed remarkable progress. Our faculty secured funding for 23 New (or Competing Renewal) sponsored projects. These newly funded projects include the following: 3 Center Grants (Gambhir, Glover, Plevritis); 8 new or renewed R01s (Bammer, Butts Pauly, Fahrig, Gold, Rubin, Spielman, Vasanawala, Wu); 1 RC Grant (Wu); 3 R21s (Daniel, Butts Pauly, Fahrig); 2 S10s (Fahrig, Moseley); 1 Training Grant (Pelc); 2 DoD projects (Cheng, Levin); 2 foundation grants (Gambhir, Gold); and 4 industry grants (Gambhir, Levin, Marks, Hofmann). While most of these projects are led by experienced faculty with long standing research programs, we note that 2 faculty (Rubin, Vasanawala) were awarded their first NIH-supported R01. Congratulations to all Radiology researchers, including faculty, postdocs, students, and staff members – all of whom contribute to the success of our phenomenal Department.

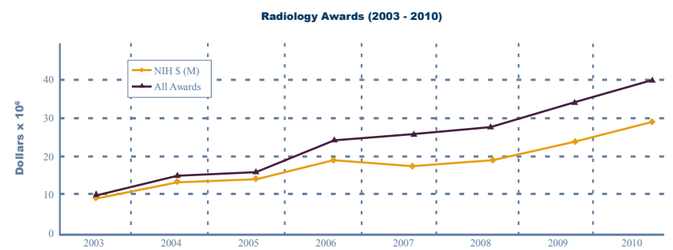

Figure 1: Shows Stanford Radiology awards history. Total 2010 awards equals $37M (purple line). Of that $37M, $26M (75%) is due to NIH funded projects (yellow line).

Figure 1 presents a history of the Stanford Radiology awards from 2003 to 2010. It is worth noting that from 2003 to 2005 NIH represented approximately 95% of sponsored project funding. Since 2007, this profile has shifted such that NIH funded projects, while still our largest source of funding, now represents 75% of total funding. Industry makes up the next largest group, representing 14% of all awards received. In the current economic environment, including concerns about NIH funding and due to an increase in our overall research activity, we will likely observe changes in these patterns.

Figure 2 gives an overview of proposal activity from the Department. If we removed the flurry of ARRA related activity ($40M and 47 projects), we would see a modest increase in proposal activity from 2009 to 2010 of about 10% instead of a 24% decrease as shown in Figure 2. Because there is a direct relationship between the number of proposals and the amount of research funding procured, we focus significant effort on proposal activity with an effort toward making the submission process as transparent as possible.

Personnel: During 2010, 5 new faculty with combined research and clinical responsibilities, joined the Department. Drs. Gloria Hwang, Heike Daldrup-Link, Andre Iagaru, Jafi Lipson, and Michael Zeineh will establish their research labs in the coming months and will contribute significantly to the Department's research efforts. (See page 22-23 for a brief introduction to each of our new faculty). Generally, each new research faculty joining our program recruits 2-5 scientists as they establish their labs and acquire funding to support their research; we can anticipate growth in personnel to continue at least through the next two years while these new labs are being settled.

Space: On campus, the Richard M. Lucas Center for Imaging will shortly undergo a third remodel to accommodate new and upgraded facilities, office space for new faculty, additional space for research, and space for the students and staff associated with new faculty. At our off-campus research site on California Avenue, the Canary Center at Stanford, which opened in June 2009, is nearing capacity after one short year. As we hire new faculty and expand our research, we continue an active dialogue with the University and Hospital leadership for facilities to support our programs

We are pleased to present the Lucas Family Foundation Trustees with the 2010 Lucas Annual Report. In the next few pages, you will read about our 4 NIH-supported Centers of Excellence (Page 4), and the three Stanford Radiology sections that make up our research effort: 1) the Radiological Sciences Lab (RSL), led by Gary Glover, PhD; 2) the Molecular Imaging Program at Stanford (MIPS), led by Sanjiv (Sam) Gambhir, MD, PhD; and 3) Information Sciences in Imaging @ Stanford (ISIS), co-led by Sandy Napel, PhD and Sylvia Plevritis, PhD. You will also find a complete listing of all of our sponsored projects on pages 209-214).

It is with continued support of the Lucas Family Foundation and the Canary Foundation that we are able to maintain leadership in research, train the next generation of imaging clinicians and scientists, and, above all, deliver the most advanced diagnostic and therapeutic techniques to benefit our patients and patients worldwide.

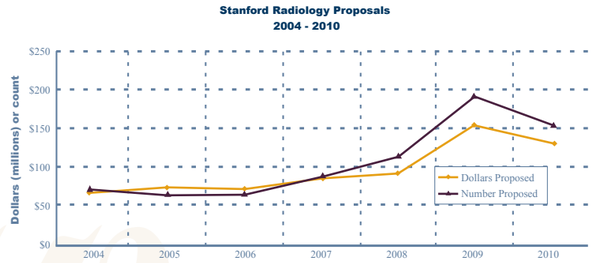

Figure 2: A summary of proposals submitted from 2008 - 2010. The 2009 increase is due to $40M/47 proposals due to stimulus/ARRA opportunities.

RSL Overview

Radiological Sciences Laboratory and The Center for Advanced MR Technology (CAMRT)
Gary H. Glover, PhD, Director, Radiological Sciences Laboratory

The Lucas Center has been home to the Radiological Sciences Laboratory (RSL), a section of the Radiology Department since the building's dedication in 1992, and in conjunction with the Electrical Engineering Department has hosted the Center for Advanced MR Technology, an NIH-funded National Research Resource since 1995. The Center also houses a cyclotron and radiochemistry labs as well as other wet labs for the Molecular Imaging Program under Dr. Sanjiv Gambhir. The Center's state of the art imaging facilities support research of the RSL and others in the Radiology department as well as hundreds of on-campus and extramural researchers as a core facility. The Center has always been, and remains, an exciting and lively nexus for fundamental imaging research.

THE RADIOLOGICAL SCIENCES LABORATORY

The RSL comprises 9 faculty, approximately 35 graduate and postdoctoral students, approximately 30 scientific staff and 7 administrative assistants, as well as the Lucas Center/RSL Administrative Services Director, Donna Cronister.

The faculty serve in a wide variety of advisory roles to government and foundation agencies such as the NIH and in policy-making positions for international scientific societies such as the ISMRM and RSNA. Many of our faculty, scientific staff and students have garnered prestigious awards for their exceptional research achievements.

THE NATIONAL CENTER FOR ADVANCED MR TECHNOLOGY AT STANFORD (CAMRT)

The CAMRT is a National Biotechnology Research Resource, sponsored by the NIH's National Center for Research Resources (NCRR) with Dr. Glover as PI. The Center was initiated in 1995 with the broad goal of developing and making available a spectrum of cutting edge MR imaging research tools for scientists who would otherwise not have access, as well as to train students and others in MRI. Over the years that goal has remained as research projects have been introduced, matured and been replaced with new developments and opportunities.

The five-year grant was up for its third renewal last year as was reported in the 2009 Annual Report. The review was conducted with a site visit by an NIH review panel in October 2009, and we were gratified to receive a score of 10, which, on a scale of 10-90, is Perfect! This recognition by our peer reviewers/colleagues is a testament to CAMRT's continuing international excellence and prominence in MRI physics development and collaborations. The grant was restructured somewhat in consultation with our National Advisory Board's recommendations to include a new Hardware Core headed by Brian Rutt, which will be described next year (the new funding cycle started in July 2010 and so is not included here). We therefore have now entered our sixteenth year of continuous support of the National Center.

Outstanding progress has been made in all six of the core technology development areas that include reconstruction methods (John Pauly, EE Department, core director), imaging of brain activation (Gary Glover), diffusion and perfusion weighted imaging methods (Mike Moseley), imaging of cardiovascular structure and function (Brian Hargreaves), spectroscopic imaging development (Dan Spielman) and interventional MRI technique development (Kim Butts). Much of this exciting research is chronicled in the scientific reports that follow. These reports are acknowledged with funding from P41 RR009784.

Faculty and their Students' Activities

Roland Bammer:

- Promoted to Associate Professor. Congratulations, Roland!
- Awarded the John Caffey Award for Best Basic Science Research Paper at the 2010 Society for Pediatric Radiology (SPR), "T1-Weighted 3D SAP-EPI for Use in Pediatric Imaging"
- Continues as a reviewer on NIH study sections
- Is a full member of ISMRM editorial board
- Hired 1st Stanford ARRA funded postdoc (Rafael O'Halloran)

Kim Butts Pauly:

- Elected to the board of ISTU (International Society for Therapeutic Ultrasound)
- Performed NIH study section service.
- Appointed Director of CBIS (Center for Biomedical Imaging at Stanford).
- Received two NIH grants in 2009.
- Postdoc Will Grissom is now employed at GE's research labs, Munich.
- Grad student Kelly Townsend received a Master's and is now employed by a local company.
- Postdoc Rachelle Bitton received an award from the California Breast Cancer Research Program.
- Research Associate Viola Rieke received a K99 award in 2009.

Brian Hargreaves:

- Anderson Nnewihe, MS, graduate student in Brian's lab received the First Place Best Poster Award for "High Resolution Breast MRI," at the 2nd Annual CBIS Symposium.
- Brian: GE Thought Leadership award for "Reducing Metal Artifacts" in April. This award recognized the SEMAC project.
- Kristin Granlund and Caroline Jordan both served on the CBIS organizing committee.

Rebecca Fahrig:

- Breathe California Columbo Award, $10,000 directed research award in the area of early detection of lung cancer.
- Media Coverage: Front Page, San Francisco Chronicle, Friday August 21, 2009, "Mummies and Medicine: Scanner sees past Veil of Time" and other news outlets.
- Award for "Best Paper in Navigation", 12th Annual MICCAI for "Towards Guidance of Electrophysiological Procedures with Real-time 3D Intracardiac Echocardiography Fusion to C-arm CT".
- Received R01 (Dual kV/MV Imaging For Metal Artifact Reduction), R21 (Ultrafast Tomosynthesis for Guidance of Transbronchial Needle Biopsy) and S10 (Axiom zeego instrument) grants from the NIH

Gary Glover:

- Continues as a member, NIH NIBIB National Scientific Advisory Council
- Will receive, Oct. 2010: University of Minnesota's Outstanding Achievement Award, 2nd highest UoM honor given.
- MD/PhD student Rebecca Rakow Penner received PhD in Biophysics, and was a finalist in the ISMRM Moore Young Investigator Award competition. She was also honored with the department's Norman Blank Award.
- Postdoc Priti Balchandani was selected as one of five ISMRM Junior Fellows for 2010. In a letter from ISMRM President David Norris, "The review committee was impressed with your commitment to the ISMRM through membership and attendance at ISMRM-sponsored events, your publication history, as well as your selection as a presenter at our upcoming meeting in Stockholm".

Michael Moseley:

- Editorial Boards:
  - Journal of Magnetic Resonance Imaging (JMRI); Cerebrovascular Diseases (CD); Journal of Cerebral Blood Flow and Metabolism (JCBFM); International Journal of Stroke (IJS)
- Advisory Boards:
  - AHA. American Heart Association
  - AHA/ASA Stroke Council Writing Committee (Definition of Stroke)
- Study section service
  - NIH CSR - Service on 6 study sections
  - NIH CSR. NIBIB ARRA P30 Review. Wellcome Trust. October 2009, Reviewer.
  - Israeli Science Foundation. January 2010. Reviewer.
  - ISMRM "Seed Grant" Grant Review Committee, 2010.
    - Grants Funded: NIH 1 S10 RR026917-01 "Upgrade of the Stanford GE-Varian Experimental MRI scanner to the Current Model".

Norbert Pelc:

- Postdoc Sam Mazin won a Kauffman Entrepreneur Postdoctoral Fellowship
- Chair, AAPM Science Council
- Awarded NIH T32 Training Grant: "Predoctoral Training in Biomedical Imaging at Stanford University".

Brian Rutt:

- Named Fellow of the American Institute for Medical and Biological Engineering
- Permanent study section member: Cancer Prevention and Research Institute of Texas, Interfaces Review Committee (IRC)
- New Funding:
  - BioX: Equipment grant for small animal MRI
  - SINTN: Equipment grant for small animal MRI
  - GE: Seed funding for high field parallel transmit hardware & GE-funded new faculty fellowship
- Postdoc Prachi Pandit: awarded Stanford Molecular Imaging Scholars postdoctoral fellowship.

Daniel Spielman:

- Promoted to full Professor. Congratulations, Dan!
- Continues to serve on NIH Study Sections
- Leads his course "In vivo Magnetic Resonance Spectroscopy and Imaging"
- Awarded a new NIH R01 "Metabolic Imaging of the Cardioprotective Effects of Alcohol and ALDH2 Activators"
- Priti Balchandani awarded 2010 International Society for Magnetic Resonance in Medicine (ISMRM) Junior Fellow award

ISIS Overview

Information Sciences in Imaging at Stanford
Sandy Napel, PhD and Sylvia Plevritis, PhD, Co-Directors

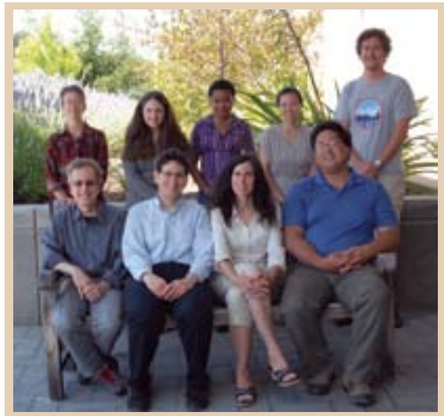

ISIS (Information Sciences in Imaging at Stanford), the newest section of the Radiology Department, is committed to harnessing new knowledge from imaging examinations by integrating and analyzing them with related clinical and molecular data. ISIS is working toward this goal by exploring the full spectrum of information-intensive activities in imaging (e.g., image management, storage, retrieval, processing, analysis, understanding, visualization, navigation, interpretation, reporting, and communications) and in non-imaging domains (e.g., pathology, molecular and genetic markers, family history, prior medical reports, and clinical outcomes).

The expertise of the ISIS faculty spans image quantization, imaging informatics, molecular imaging bioinformatics, and systems biology. The ISIS core faculty includes Sandy Napel, Professor of Radiology and co-Director of the Radiology 3D Laboratory, Sylvia K. Plevritis, Associate Professor of Radiology, David S. Paik, Assistant Professor of Radiology, and Daniel L. Rubin, Assistant Professor of Radiology. ISIS is co-led by Drs. Napel and Plevritis. ISIS also has an affiliate faculty member Professor Robert J. Herfkens whose expertise helps ISIS bridge between clinical imaging and information systems. Over the past year, ISIS has recruited an Administrative Program Manager Danae Barnes, and is in the process of finalizing its search for a Clinical Research Coordinator.

Critical to the ISIS mission is the development of core capability to collect annotated imaging, clinical and molecular data, and to integrate them by creating databases and novel computational models that identify relationships among these data. Advancements in critical resources over the past year include:

- Image Physician Annotation Device (iPAD): iPAD (not to be confused with the recently introduced tablet device by Apple Inc.), led by Dr. Rubin, is an open source tool enabling researchers and clinicians to create "semantic annotations" on radiological images in a standards-based syntax created by the cancer Biomedical Informatics Grid (caBIG) project. Semantic annotations enforce standardized terminologies such as RadLex and SNOMED. Currently, iPAD is being used in many ISIS projects.
- Content Based Image Retrieval (CBIR) for Decision Support: CBIR, led by Drs. Rubin, Beaulieu and Napel, is being created to search databases of radiological images based on image features, which include detailed information about lesions: (1) feature descriptors coded by radiologists using iPAD (described above), (2) computer-generated quantitative features derived from the image, and (3) clinical information about the patient.
- RadBank Data Warehouse: RadBank, led by Dr. Rubin, is an integrated data warehouse that brings together radiology reports with pathology and clinical information (and in the future molecular data) to enable researchers, clinicians, and educators to find cases of particular imaging findings, diagnoses, modalities, and other information. To date, RadBank has been used to identify teaching cases, to perform retrospective research, and to identify cohorts for new research.
- Imaging Biomarker Ontology (IBO): The Paik Lab has developed an initial draft of the Imaging Biomarker Ontology and is working to refine and expand it to cover the domain of how quantitative measurements are captured from imaging data, with an emphasis on molecular imaging. IBO aims to enable intelligent and semantically-searchable warehousing of quantitative measurements from molecular imaging analogous to the way in which microarray data is currently captured in public databases, thereby enabling imaging to realize its potential in translational bioinformatics research.
- Standards for Interchange of Nanoparticle Data: As part of a national working group, the Paik Lab has been developing standards for the computational representation of data about nanoparticles that are used for diagnostic imaging and/or therapeutic delivery. These efforts have helped guide development of caNanoLab, the NCI's repository of nanoparticle characterization data, the adoption of the NanoParticle Ontology (NPO) as a standard and the development of Nano-TAB, a data exchange format for nanomaterial composition and characterization.

Four key grants have been awarded to ISIS over the past year:

Modeling the Role of Differentiation in Cancer Progression: In one of twelve national Centers for Cancer Systems Biology funded by the NIH, Dr. Sylvia Plevritis will direct a $12.8 million dollar multidisciplinary program over the next 5-year period to study the role of differentiation in hematologic malignancies. This program integrates a diversity of high-throughput data, including genomic, transcriptomic, and proteomic, to elucidate molecular networks driving cancer progression.

Computerized Quantitative Imaging Assessment of Tumor Burden: Dr. Rubin is Principal Investigator of one of the centers in the newly established Quantitative Imaging Network (QIN), composed of researchers who will develop approaches to validate and standardize imaging data and related imaging metadata for quantitative measurements of responses to cancer therapies. Stanford's part of the QIN will be to create computer algorithms to measure tumor burden in patients, and to identify and quantify novel imaging biomarkers that can provide earlier indications of treatment response to cancer therapies.

Cancer Intervention and Surveillance Network (CISNET): Sylvia Plevritis' CISNET programs over the past ten years have received an additional 5 years of funding to mathematically model the impact the early detection strategies on population trends in cancer incidence and mortality. Dr. Plevritis had two grants funded by CISNET: one to evaluate the role of CT in screening for lung cancer; and the other to evaluate risk-stratified screening strategies for breast cancer.

Integration of Imaging and Molecular Phenotypes for Improved Management and Understanding of Lung Cancer: In a pilot project supported, in part, with a grant from General Electric Medical Systems and led by Drs. Sandy Napel and Sylvia Plevritis, ISIS has effectively launched its first effort to integrate imaging and molecular features from lung cancer patients who undergo surgical resection. The imaging features are obtained from CT and annotated using much of the technology from our CBIR project (see above). In addition, PET data has been collected and annotated. Illumina gene expression microarray expression was generated on the human tissue specimens. Currently, an association map between the CT and PET image features and the tissue molecular profile is being created.

Finally, ISIS has acquired a Discovery Lab that will enable experimental validation of computationally derived results; this lab is located in LUCAS P169 and is under the supervision of Dr. Plevritis.

Through these efforts, we believe that ISIS has made progress that will enable the realization of its three main goals: (1) an evidenced-based diagnostic decision support system, whereby patient-specific image, clinical and, if available, molecular data, can be compared to the database to suggest the most likely diagnoses, prognoses, and most relevant treatments, (2) biological discovery, i.e., synthesis and potential testing of hypotheses regarding the underlying biology in the development, progression and hopeful eradication of specific diseases, and (3) the translation of these developments into clinical practice using computers and image storage systems that are ubiquitous in healthcare enterprises today.

IPAD 1 Use of our iPAD tool to annotate a lung tumor on a CT scan. In addition to the controlled terminology selected using the interface, computer algorithms will characterize image features within the region of interest.

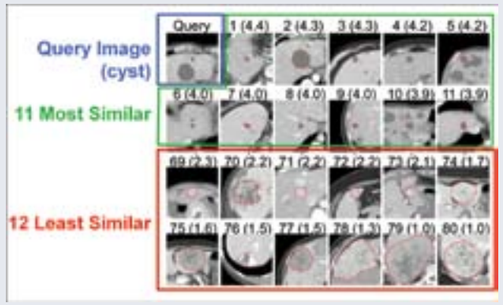

CBIR 1 Example of using images features within a region of interest defining a lesion (red) in a query image (blue) to return the most (green) and least (red) visually similar images of other lesions in a large database

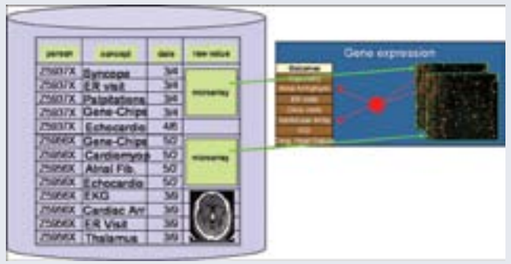

RadBank 1 Example of integrating patient data to discover genes that are associated with patient symptoms.

IBO 1 A tag cloud representation of the quantitative molecular imaging concepts extracted from approximately 30 scientific articles, where the size of each term is proportional to its frequency of occurrence in these articles in order to provide an overview of their content from which 176 imaging biomarkers were defined.

MIPS Overview

Molecular Imaging Program at Stanford
Sanjiv S. Gambhir, MD, PhD, Director, Molecular Imaging Program at Stanford

The Molecular Imaging Program at Stanford (MIPS) (http://mips.stanford.edu) continues to experience significant growth. Many faculty within the Department of Radiology and from other Departments continue to help build the program. The faculty received several new grants from the NIH as well as other agencies over the last year. We were fortunate to have our NCI-funded In vivo Cellular Molecular Imaging Center (ICMIC) P50 grant renewed which is now starting its 6th year. We are in the fifth year of the NCI Center for Cancer Nanotechnology Excellence (CCNE) U54 grant. We had another major NCI U54 Center grant awarded focused on Cancer Nanotechnology that will start its first year in a few months. We are also in the fifth year of the NIH R25T training grant, Stanford Molecular Imaging Scholars (SMIS), to train the next generation of cancer molecular imaging post-doctoral scholars. This grant has been submitted for a renewal. An NIH post-doctoral training grant (T32) for cardiovascular molecular imaging is in its second year. In addition, all labs continue to grow with many new students, post-doctoral fellows, and outstanding research staff joining the program. In addition, many visiting scientists from all around the world are coming to our program to learn more about molecular imaging.

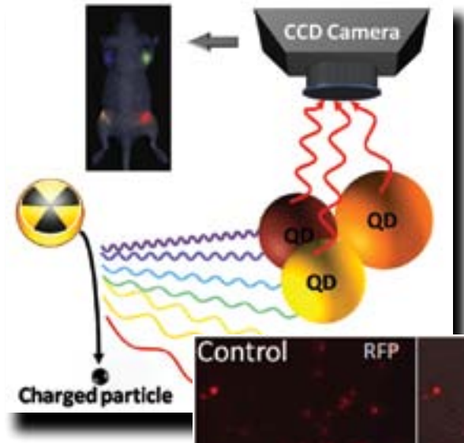

Schematic illustration of radiation luminescence excited QDs for optical imaging (see Cheng abstract, page 135).

Funding from the Canary Foundation to develop a new center for early cancer detection in the previous year is helping build bridges with many investigators on campus. Significantly increased funding from the Canary Foundation is expected with continued growth of the program. New off-campus space on California Avenue is facilitating the effort in early cancer detection including facilities for blood/tissue based detection of disease. We are convinced that more investments are needed in the earlier detection of all disease, including cancer. The ability to detect disease earlier will allow much better potential for cure. This center will work on novel in vitro diagnostics (e.g., using patient blood samples) as well as new imaging strategies with high sensitivity to detect very low burden disease. It is hoped that in the next 3-5 years Stanford can become a world-leader in the important field of early cancer detection.

We continue to have several seminar series on campus to help educate scientists about molecular imaging. The molecular imaging seminar series (http://mips.stanford.edu/public/mi_seminar.adp) is now in its fifth year and has a large collection of videos available on-line of speakers from the last few years. This year we also initiated students presenting from different MIPS labs. The Nanobiotechnology seminar series (http://mips.stanford.edu/public/nanobiotech_seminar.adp) which focuses on new applications of nanotechnology to cancer continues to draw attendance for faculty from all over campus. Several speakers from around the country have already presented in the series and all lectures are available on-line.

There are now 21 MIPS faculty that are full members of the program with many more associate members from all over campus. Many of the full members are from the Department of Radiology. The number of graduate students, MSTP students, post-doctoral fellows, research scientists, technicians, and administrative staff continues to grow and is currently approximately 150. We expect significant growth over the next 2-3 years with the new center on early cancer detection and occupancy of the space on California Avenue.

Construction of a new Molecular Imaging/Nuclear Medicine clinic is about to finish with a grand opening expected in September 2010. This new facility will consolidate all of the PET-CT and SPECT equipment and new radiochemistry facilities will be added. Newer cardiac and optical imaging equipment is also expected to be placed into this new clinic. We have also designed the clinic so that large animal imaging can be performed there. Research trials that combine state-of-art imaging with in vitro diagnostics (e.g., blood proteomics) should also be possible in this new facility.

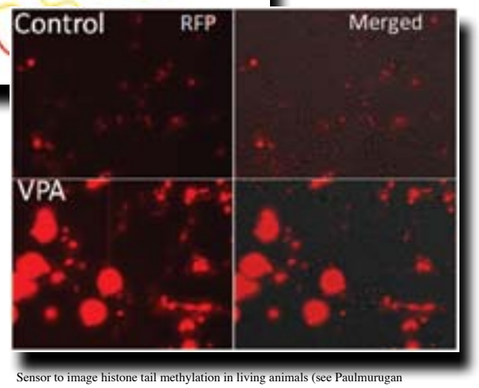

Sensor to image histone tail methylation in living animals (see Paulmurugan abstract, page 160).

We also continue to grow our industrial partnerships with key leaders in the molecular imaging community. Several projects to develop new imaging agents/strategies are underway with General Electric Global Research, General Electric Healthcare, Schering-Plough as well as Bayer-Schering. A new relationship with GlaxoSmithKline has just started. It is likely that additional industrial partners will enter into collaborative research relationships over the next several years. These will be key to help translate discoveries at Stanford to the patient bedside. Several faculty are also involved in new startup-company efforts with intellectual property from their laboratories at Stanford. These include new efforts in diagnostics, small animal imaging and clinical imaging.

Canary Center Overview

Sanjiv Sam Gambhir, MD, PhD, Director
Daniela Starcevic, PhD, Deputy Director

The Canary Center at Stanford for Cancer Early Detection celebrated its first year anniversary in June 2010. The mission of the Canary Center, which occupies ~30,000 square feet of the building at 1501 S. California Ave, is to house and foster research programs leading to the development of blood and imaging tests for the early detection of lethal types of cancer. The center represents a novel alliance between the Canary Foundation, the Department of Radiology, the Cancer Center, and the School of Medicine. The Center also actively fosters intellectual and programmatic alliances with the Schools of Engineering & Humanities and Sciences.

The Center mission is based on the striking association between early cancer diagnosis and improved survival rates. Chances of survival are far greater when cancer is detected in its earliest stages while still localized to the organ of origin and amenable to treatment. To optimize the detection of cancer at this stage, the Center is taking a binary approach including 1) identifying blood biomarkers that can be detected by simple blood screening tests and developing clinically translatable screens for these biomarkers, and 2) developing molecular imaging tests to confirm and localize early cancerous lesions. The extraordinary technical challenges associated with this dual strategy include the refinement of molecular imaging agents to specifically detect pre-invasive malignant tumors the size of a blueberry (< 5 mm). They also include the development of proteomic approaches that can reliably detect minute (< 0.1 ng/ml) quantities of cancer-specific proteins released into the bloodstream by these small lesions. Cost-effective solutions are expected by applying a relatively cheap blood test followed by a more expensive imaging study, although in some cases the blood test and the imaging test will be performed concurrently. Having both approaches will also likely lead to a greater overall accuracy.

To accomplish these goals, the Center was specifically designed to house state-of-the-art core facilities and collaborative research programs in molecular imaging, proteomics, chemistry, and bioinformatics. The Proteomics Core facility houses cutting-edge mass spectrometry platforms dedicated to the discovery and validation of blood and tissue protein biomarkers. Dr. Mark Stolowitz has been recruited as Core Director. The Chemistry Core is engaged in the specific design and refinement of molecular imaging agents for early detection, which then undergo preclinical testing using in vivo and ex vivo model systems, including patient blood and tissue samples. Dr. Jelena Levi has been recruited to direct the Chemistry Core. The Molecular and Cell Biology Core works closely with both the Proteomics and Chemistry Cores to screen and refine agents that can bind cancer-specific targets in tissues and thus complements the efforts of the Chemistry and Proteomics Cores to develop blood and imaging tests for cancer early detection. Dr. Richard Kimura has been recruited to head the Molecular Cell Biology Core. A significant effort has been put forward over the past year to equip the Center cores and laboratories with state-of-the-art instrumentation to promote and facilitate innovative research efforts. Two new mass spectrometers are already in place and the acquisition of 1-2 more is planned.

Collaborative research efforts fostered at the Center are made possible by creating a truly multidisciplinary team of faculty members. Current faculty members focus on imaging technologies, chemistry and disease mechanisms/cell biology. Two new faculty members have been recruited and are anticipated to join the Center in the fall of 2010. These two new faculty members will bring in complementary proteomics expertise. Additionally, Canary Center research programs are actively interfacing with other facilities and programs on campus, including MIPS and CCNE-TR in order to leverage the latest developments in molecular imaging and nanotechnology into the early detection effort.

Collectively, these initiatives form a direct pipeline for the translation of early cancer detection into clinical trials and practice. A specific example of a novel molecular imaging strategy that is expected to help the goal of early cancer detection is ultrasound with targeted microbubbles. These gas filled microbubbles can be chemically coupled to targeting ligands that allow the bubbles to bind to tumor vasculature. This will allow molecular imaging using a conventional anatomical imaging strategy (ultrasound). This is expected to allow detection of tumors in the 3-5 mm range. A specific example of a novel strategy being pursued for blood biomarker detection is based on magneto-nanoarrays being developed as part of the Stanford CCNE-TR. This novel technology is allowing the detection of many different biomarkers at levels that are 10-100 fold better than the most sensitive ELISA tests currently available.

The National Cancer Institute (NCI) Early Cancer Detection Network (EDRN) has recently awarded a major U01 grant to the Canary Center team – under the leadership of Drs. Sam Gambhir and James Brooks (Department of Urology) - to further examine the microbubble and magneto-nanoarray techonologies as they apply to prostate cancer early detection and to enable the first clinical trial using this technology. Many exciting new developments for early cancer detection are on the horizon and will be pioneered by the Canary Center. The past year was marked by an aggressive effort to bring additional funding into the Center through both private foundations and government funding. Decisions regarding the outcome of several pending grant proposals are expected in the coming months.

As we head into 2011, our goals include recruiting several new faculty members in the area of bioinformatics and in vitro and in vivo diagnostics, building up the Biorepository Core which will store and organize human samples for research efforts headed by the Center, and pursuing a number of other funding opportunities. More information about the Canary Center can be found at http://canarycenter.stanford.edu.

CCNE Overview

Sanjiv Sam Gambhir, MD, PhD, Director
Demir Akin, DVM, PhD, Deputy Director

The original Center for Cancer Nanotechnology Excellence focused on Therapy Response (CCNE-TR), based in the Radiology Department, was established in May 2006 with funding from the NCI Alliance for Nanotechnology in Cancer. The Stanford CCNE-TR is a consortium of private and public universities, non-profit institutions, foundations, and for-profit corporations. It brings together scientists from different disciplines including chemistry, materials science, engineering, radiology, molecular biology, cancer biology, and oncology. Most of our CCNE-TR members had never previously collaborated. These new collaborations have resulted in a remarkable scientific team that has come together to help fuel the center and its relatively rapid progress. In its fourth year of funding, the CCNE-TR continues as a highly interactive and successful center that develops novel diagnostic cancer nanotechnologies and has made significant advancements in moving the center's nano-medical discoveries towards clinical translation. Figure 1 signifies the strength of these collaborations as measured by our scientific output. All involved in this CCNE are highly committed to the success of this program. The level of productivity as shown in Figure 1 is a strong testament to the dedication of our faculty, staff, students, and post-doctoral fellows. Our center is constantly growing both in its research scope and also in its physical boundaries thanks to the significant investment in our center from Stanford University, the School of Medicine, the Stanford Cancer Center, the Radiology Department, the Lucas Foundation, and the National Cancer Institute (NCI).

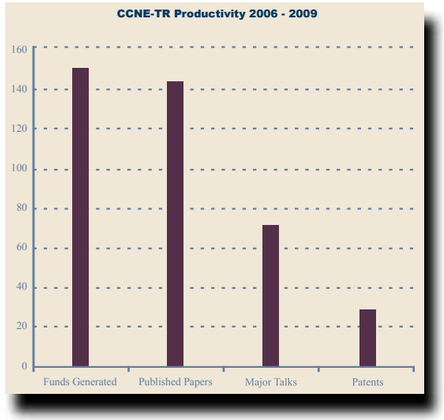

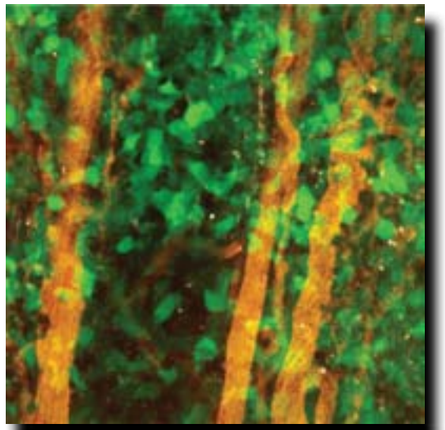

Image 1: In the image above, the white spots are single-walled carbon nanotubes that have been chemically linked to molecules that selectively target the cancer cells (green). These nanotubes can be used to diagnose and kill tumors (Bryan R. Smith, Ph.D. and Sanjiv Sam Gambhir, MD, PhD)

We believe that nanoscience applied to cancer research is a critical approach for the elimination of cancer and, thus, are convinced that nanotechnology will make a significant impact on cancer diagnosis and management in potentially revolutionary ways. In vitro diagnostics used in conjunction with in vivo molecular imaging can markedly impact future cancer patient management by providing a synergy that neither strategy alone can offer. Nanotechnology can significantly advance both in vitro diagnostics through proteomic and circulating tumor cell nanosensors and in vivo diagnostics through nanoparticles for molecular imaging. The areas of earlier cancer detection and the prediction and monitoring of response to anti-cancer therapies are both very important applications of nanotechnology with near-term clinical translational potential. Through an integrated, cohesive five-year plan that builds on our first four years of significant progress, we are pursuing the use of in vitro protein nanosensors and in vivo nanoparticles for next generation molecular imaging.

The CCNE-TR is committed to clinical translation of our nanotechnologies by leveraging our large network of clinical trials and patient samples at USC, FHCRC, UCLA, Cedars Sinai Medical Center, and Stanford. Towards this, we are working on clinical translation of our technologies via our research and developments for in vitro proteomic nanosensors and in vivo molecular imaging.

Very recently, we received news that our new Center for Cancer Nanotechnology Excellence and Translation (CCNE-T) will also be supported by NCI. This program will continue expanding the work of the CCNE-TR with a concerted focus to move our nanotechnology successes into clinical use. For approximately two years both centers will continue while the CCNE-TR phases out and the CCNE-T becomes firmly established. In this highly interdisciplinary center, faculty from radiology, bioengineering, materials science, oncology, and numerous other departments collaborate in an effort to use nanotechnology to improve cancer-patient management. For the new CCNE (CCNE-T) we engage faculty from UCLA, UC Berkley, USC, and MIT to collaborate with our Stanford faculty. Key investigators on this U54 include Drs. David Agus, Demir Akin, Paul Alivisatos, Jonathan Berek, Alice Fan, Dean Felsher, Sanjiv Sam Gambhir (PI), Luke Lee, Parag Mallick, Scott Manalis, Ed Myers, David Paik, Steve Quake, Jianghong Rao, Brian Rutt, Robert Sinclair, Mark Stolowitz, Mary Tang, Shan Wang (Co-PI), Irv Weissman, Robert Wilson and Anna Wu.

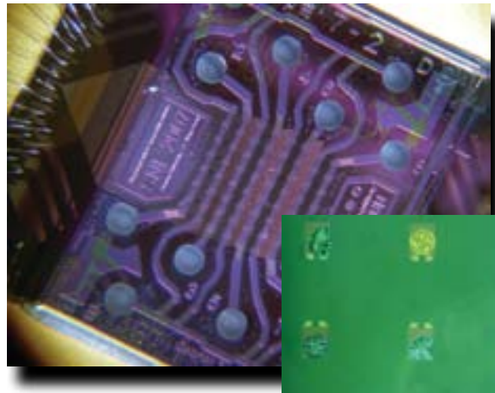

Image 2: The image to the left is microfluidic magneto-nano chip with 8 by 8 sensors arrays and 8 microfluidic channels (Sebastian J. Osterfeld, PhD and Shan X. Wang, PhD).

Image 3: The image below results from work in the CCNE program, which is developing magnetic-nanoparticle detecting sensors to improve cancer diagnosis. Each of the tiny squares in the above image is a sensor (Sebastian J. Osterfeld, PhD and Shan X. Wang, PhD).

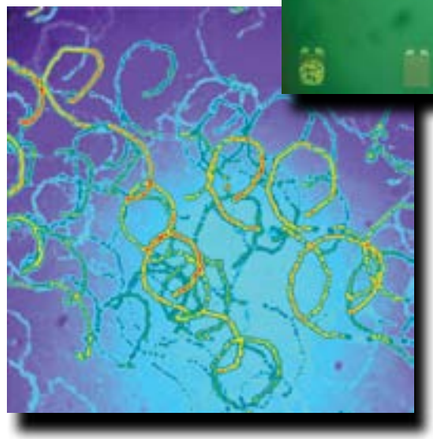

Image 4: This image reveals the trajectories of flurophore labeled magnetic naoparticles under a rotating magnetic field gradient (Aihua Fu, PhD and Shan X. Wang, PhD)

The primary focus of the CCNE-T is to develop and use nanotechnology for earlier cancer detection and to monitor response to anti-cancer therapy. This NCI-funded center supports projects focused on nanoparticle technology including: i) the production of next generation smart nanoparticles; ii) magnetonanotechnology for blood proteomics and cell sorting; iii) multiple nano-platforms to interrogate single circulating tumor cells; iv) molecular imaging with photoacoustics and nanoparticles and monitoring response to therapy using imaging and magneto-nanosensors.

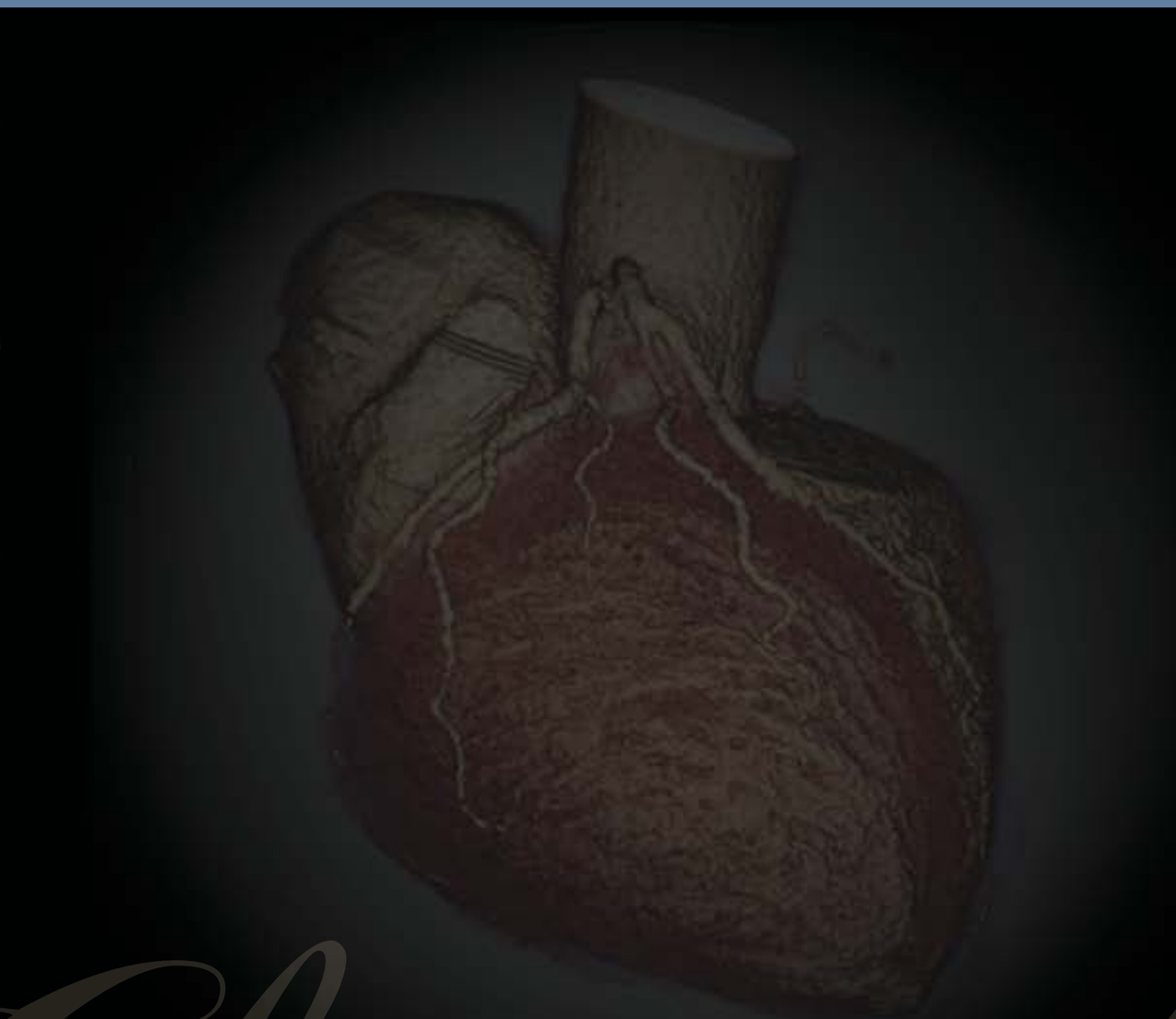

Clinical

Clinical Collaborations Foster Translational Research

Susan Kopiwoda, Director, Strategic Research Development

In this new section for the Lucas Report, we highlight clinicians who lead their own research programs and who have developed strong collaborations with basic scientists in the Lucas Center. It is through these collaborations that we are able to influence change in the clinical environment and present advanced imaging solutions for the benefit of our patients and patients worldwide. It is also through such clinical collaborations that our trainees begin to undertand the needs and limitations of clinical imaging. We encourage our trainees to enhance their training experience through mentoring opportunities with clinical scientists. Each year we will highlight clinical faculty in this section to recognize our commitment to translating research concepts into clinical use.

Bruce Daniel, MD, Associate Professor of Radiology

Chief of Breast MRI Service

Dr. Daniel is interested in new MRI techniques for imaging the breast. He is also interested in MR-guided interventions for breast and for prostate cancer. Through his research interests, Dr. Daniel has developed collaborations with several of our Lucas Center scientists and has been instrumental in introducing new imaging techniques into everyday clinical use. Techniques spawned from this research have been used over the last 12 years to image thousands of patients with known or potential breast cancer. These advanced breast imaging techniques continue to be used everyday at Stanford. These include 3D spiral MRI with dual slab excitation, temporal sensitivity encoding acceleration, and independent slab phase modulation for ultra-fast 3 dimensional dynamic contrast-enhanced MRI, as well as high resolution 3D MRI with water-selective spectro-spatial excitation. Ongoing research into ultra-high resolution MR imaging and methods to image breast cancer without injecting contrast material hold great promise for clinical translation in the future. In interventional MRI, Dr. Daniel has performed several hundred MR-guided procedures and MR-guided cryoablation, all of which use pulse sequences and other techniques developed at the Lucas center. Other translational research areas include the development of miniaturized MR-compatible robotics.

Nancy Fischbein, MD, Associate Professor of Radiology

Neuroradiology Section

Dr. Fischbein, a neuroradiologist with a particular focus on head and neck imaging as well as imaging of patients with acute neurological problems such as ischemic stroke and brain hemorrhage, has developed numerous collaborations with basic science faculty in the Lucas Center. Dr. Fischbein has collaborated with faculty and post-doctoral scholars at the Lucas Center to improve the diffusion-weighted imaging (DWI) assessment of cholesteatoma with PROPELLER and RS-EPI techniques. She has also assisted in the investigation of new techniques for diffusion and perfusion, such as SENSE/GRAPPA and ASL, and their applications to acute neurological illness. These collaborations provide a critical link that allows us to translate advanced MR imaging protocols into daily clinical use.

Garry Gold, MD, Associate Professor of Radiology

Musculoskeletal Section

Dr. Gold, who is PI on an NIH-funded R01 for the study of osteoarthritis, an Arthritis Foundation grant, and a multi-investigator industry funded project to develop advanced MR applications, collaborates daily through his research with Lucas Center faculty. Through his research and basic science collaborations, Dr. Gold has been able to introduce a number of new solutions for musculoskeletal imaging into clinical use. These include improved MR imaging around metallic implants, isotropic 3D imaging, and sodium MRI for detection and characterization of osteoarthritis. Dr. Gold's background and training in Electrical Engineering and as a practicing radiologist makes him an ideal collaborator for faculty, postdocs, and graduate students who are interested in discussing and understanding biomedical imaging limitations and requirements for clinical applications.

Robert Herfkens, MD, Professor of Radiology

Associate Chair for Clinical Technology, and Director of MRI; Destination Digital (PACS); Co-director of PET/CT

Dr. Herfkens combines his strong technology interests with his clinical skills and leadership in MRI and CT. Through Dr. Herfken's efforts as Associate Chair for Clinical Technology, the Department of Radiology has transformed its analog film environment to a paperless digital department. In addition to his technology interests, Dr. Herfkens' research interests include cardiovascular imaging with CT and MRI, utilizing fast imaging techniques for physiologically based evaluation. He works closely with cardiovascular surgery and cardiology to provide innovative tools for improved clinical evaluation of patients with cardiovascular disease.

Andrew Quon, MD, Assistant Professor of Radiology

Nuclear Medicine Section (MIPS)

Dr. Quon, with expertise in multimodality fusion imaging, has given presentations and received awards at major Radiology and Nuclear Medicine conferences for his work on PET/CT imaging. His research with molecular imaging scientists in the Lucas and Clark centers provides opportunity to introduce new imaging probes into clinical use. Dr. Quon's current projects include: i) evaluation of the radiotracer NaF for orthopedic disease; ii) evaluation of 18F-FLT, a thymidine analog, for post-therapy monitoring of diffuse large B cell lymphoma; iii) a pilot study using the novel radiotracer 18F-5FU to assess modulation of 5FU receptors by bevacizumab; and iv) comparison of the effects of regadenoson and adenosine on myocardial blood flow using 13NH3 PET.

Graham Sommer, MD, Professor of Radiology

Body Imaging Section

Dr. Sommer has worked closely with a number of Lucas Center faculty over the past 20 years, pursuing advanced processing techniques for CT and MR data. He has also collaborated on NIH-funded studies involving the evaluation of renal function and structure with MRI, and studies of prostate and pancreatic tumor ablation under MRI guidance. These collaborations have lead to several important areas of clinical translation. Advanced 3D processing of CT data developed in conjunction with Lucas faculty has led to the development of 3D CT urography, an advanced GU imaging technique developed at Stanford, which has been adapted throughout the world. MRI renal functional research has led to entirely new MRI applications in renal MRI and in the evaluation of renal transplants and pediatric kidneys. Collaborative work on prostate ablation has led to the development of devices ideally suited for prostate tumor (BPH, cancer) ablation under MRI guidance. Clinical studies using these technologies are now in progress.

Shreyas Vasanawala, MD, PhD, Assistant Professor of Radiology

Pediatric Radiology Section (Lucile Packard Children's Hospital)

Dr. Vasanawala is PI on an NIH-funded research program that focuses on reducing exam time in pediatric MR imaging. As children cannot tolerate long exams, they are often scanned under anesthesia or subjected to the ionizing radiation of CT scans. Dr. Vasanawala works closely with Lucas Center physicists and engineers and, through his funded research and collaborations, has begun to realize MR imaging solutions that address his goal of improving imaging for children. These efforts, in collaboration with Dr. Brian Hargreaves, include developing novel pediatric-specific hardware to speed image acquisition. In collaboration with Dr. Marcus Alley, Dr. Vasanawala also develops novel MRI pulse sequence and image reconstruction approaches for faster motion-insensitive MRI to image congenital heart disease. When the hardware and software approaches are combined in synergistic fashion, comprehensive cardiac MRI examination times may be reduced from over one hour to less than ten minutes.

Gregory Zaharchuk, MD, PhD, Assistant Professor of Radiology

Neuroradiology Section

Dr. Zaharchuk is PI on two projects: an NIH-funded R01 evaluating arterial spin labeling (ASL) to detect and quantify blood flow delivered through collateral networks and a Neuroradiology Education and Research Foundation (NERF) project that utilizes ASL to study Moyamoya disease. Dr. Zaharchuk has an office in the Lucas Center, facilitating the translation of advanced imaging research into the daily routine of the clinical neuroradiology service, and has resulted in collaborations with many Lucas Center basic scientists. These projects include novel imaging approaches for acute ischemic stroke, transient ischemic attack, Moyamoya disease, and venous imaging of multiple sclerosis.

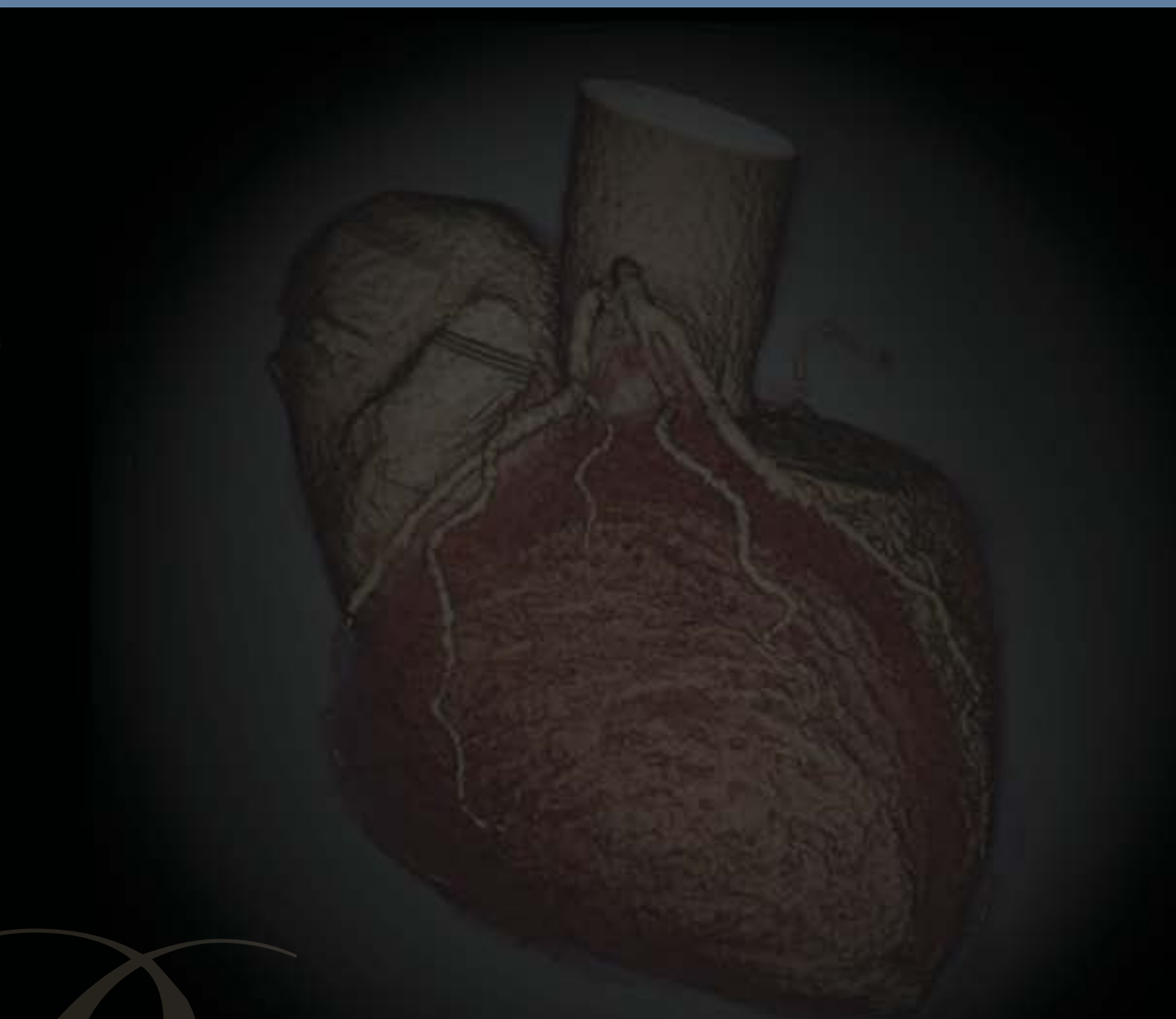

Personnel

Radiology Research Faculty, Staff, and Students

Faculty & Staff

Faculty

Roland Bammer, PhD
Sandip Biswal, MD
Kim Butts Pauly, PhD
Zhen Cheng, PhD
Bruce Daniel, MD
Rebecca Fahrig, PhD
Sanjiv Sam Gambhir, MD, PhD
Gary M. Glazer, MD
Gary H. Glover, PhD
Garry Gold, MD
Brian Hargreaves, PhD
Robert J. Herfkens, MD
Andrei Iagaru, MD
Craig Levin, PhD
Michael E. Moseley, PhD
Sandy Napel, PhD
David Paik, PhD
Norbert J. Pelc, ScD
Sylvia K. Plevritis, PhD
Andrew Quon, MD
Paulmurugan Ramasamy, PhD
Jianghong Rao, PhD
Daniel Rubin, MD
Brian Rutt, PhD
Daniel M. Spielman, PhD
Shreyas Vasanawala, MD, PhD
Juergen Willmann, MD
Joseph Wu, MD, PhD
Greg Zaharchuk, MD, PhD

Administrative & Support Staff

Karen Aguilar
Danae Barnes, MS
Mary Bobel, MA, MBA
Maggie Bos
Janet Checchi-Acosta
Michelle Christierson
Bonita Crabbe
Donna Cronister
Lin Davis
Debra Frank
Elizabeth Gill
Sofia Gonzales, MS
Sondra Horn
Joe Hubbard, BS
Mandeep Kaur, BA
Susan Kopiwoda, MS, MPH
Marlys Lesene
John Mendoza
Amy Morris, BA
Teresa Newton, BA
Donna Nierberger, RN
Kala Raman, MS
John Reuling
Patricia Riley
Lanzie Rivera
Billie Robles, BS
Julie Ruiz, PhD
David Russel
Monique Schareck, MHA
Judy Schwimmer, MBA, MA
Susan Singh
Jean Stevens
Wei Xiong

Scientific Staff

Demir Akin, DVM, PhD
Marcus Alley, PhD
Sanjiv Bandhari
Wendy Baumgardner, RVT, LATg
Rhona Berganos, BS
Nicole Brandon, MS
Thomas Brosnan, PhD
Carmel Chan, PhD
Edwin Chang, PhD
Danye Cheng, MS
Frederick Chin, PhD
Garry Chinn, PhD
Aradhana Dhanabalan, MS
David Dick, PhD
Aloma D'Souza, PhD
Aihua Fu, PhD
Arundhuti Ganguly, PhD
Xuwen Gao, MS
Andrew Gentles, PhD
Gayatri Gowrishankar, PhD
Frezghi Habte, PhD
Frezghi Habte, PhD
Pam Hertz, RVT
Samantha Holdsworth, PhD
Linda Horst RT
Fangjun Jia, PhD
William Johnsen, RT, CV
Richard Kimura, PhD
Moritz Kircher, PhD
Keshni Kumar, CRT
Ken Lau
Jelena Levi, PhD
Amelie Lutz, MD
Dirk Mayer, PhD
Sam Mazin, PhD
Erik Mittra, MD, PhD
Mohammed Namavari, PhD
Kazim Narsinh, MD
Arutselvan Natarajan, PhD, DVM
Laura Pierce, MPA, RT
Laura Pisani, PhD
Sam Quezada, MBA
Robert Reeves, MA
Viola Rieke, PhD
Sandra Rodriguez, RT (R)(MR)
Jarrett Rosenberg, PhD
Ataya Sathirachinda
Anne Marie Sawyer, BS, RT (R)(MR)
Cathy Shachaf, PhD
Stefan Skare, PhD
Marc Sofilos, RT
Daniela Starcevic, PhD
Mark Stolowitz, PhD
Matus Straka, PhD
Murugesan Subbarayan, PhD
Martin Tall, PhD
Sen Wang, PhD
Ron Watkins
Lingyun Xu, PhD
Yingding(Bryan) Xu
Xinrui Yan, PhD
David Yerushalmi, PhD
Sung-Won Yoon, PhD

Our group photo represents approximately half of the Radiology research personnel found in various locations on the medical school campus.

Trainees

Post-Doctoral Fellows

Priti Balchandani, PhD
Deepak Behera, PhD
Stephanie Chan, PhD
Qiang Chen, PhD
Kai Chen, PhD
Kai Cheng, PhD
Dragos Constantin, PhD
Ben Cosgrove, PhD
Bao Dao, MD
Adam de la Zerda, PhD
Moses Darpolor, PhD
Nirupama Deshpande, PhD
Ihsan Djomehri, PhD
Anca Dragulescu-Andrasi, PhD
Hua Fan-Minogue, MD, PhD
Kira Foygel, PhD
Hewei Gao, PhD
Jinhao Gao, PhD
Olivier Gavaert, PhD
Sarah Geneser, PhD
Zhumur Ghosh, PhD
Meng Gu, PhD
Benjamin Hackel, PhD
Aileen Hoehne, Phd
Sharon Hori, PhD
Shijun Hu, PhD
Mei Huang, PhD
Nicholas Hughes, PhD
Ken Ito, PhD
Michelle James, PhD
Jesse Jokerst, PhD
Sonal Josan, PhD
Sri-Rajasekhar Kothapali, PhD
Feng Lan, PhD
Joo Hyun Lee, PhD
Zongjin Li, PhD
Zhe Liu, PhD
Zheng Miao, PhD
Gang Niu, PhD
Natesh Parashurama, MD, PhD
Kyeongsoon Park, PhD
Hao Peng, PhD
Guillem Pratx, PhD
MaryBeth Pysz, PhD.
Peng Qiu, PhD
Gang Ren, PhD, MD
Hongjun Ren, PhD
Ying Ren, PhD
John Ronald, PhD
Debashis Sahoo, PhD
Bryan Smith, PhD
Virginia Spanoudaki, PhD
Ning Sun, PhD
Kyung Sung, PhD
Alessia Tognolini, MD
Grace Tye, MD
Domonique Van de Sompel, PhD
Arne Vandenbroucke, PhD
Thillai Sekar Veerapazham, PhD
Hui Wang, PhD
Pauline Worters, PhD
Song Wu, PhD
Yun Wu, PhD
Zuyong Xia, PhD
Yung Xing, PhD
Cristina Zavaleta, Ph.D.
Keren Ziv, PhD

Graduate Students

Neeraj Agrawal
Murat Aksoy, PhD
Aravind Babu, MS
Jongduk Baek, PhD
Catie Chang, MS
Jessica Faruque, MS
Erin Girard-Hughes, MS
Kristin Granlund, MS
Alex Grant, MS
Yi Gu, MS
Misung Han, MS
Andrew Holbrook, MS
Scott Hsish, MS
Caroline Jordan, MS
Elena Kaye, MS
Hojin Kim
Kranthi Kode, BS
Danny Korenblum, MS
Frances Lau, MS
Christine Law, MS
Andrew Lee, BS
Prasheel Lillaney, MS
Ray Lin, MS
Tiffany Ting Liu
Diego Munoz, BS
Chinyere Nwabugwu
Peter Olcott, MS
Jeremy Pearl, BS
Rebecca Rakow-Penner, MD, PhD
Julia Rasooly, BS
Paul Reynolds, MS
Witi Sachchamarga
Laura Sasportas, MS
Erica Savig
Heiko Schmiedeskamp, MS
Harpeet Singh
Jared Starman, MS
Ernesto Staroswiecki. MS
Emily Tsai, BS
Adam Wang, MS
Kitch Wilson, MD
Jung Ho Won, MS
Jiajing Xu
Tao Xu, PhD
Jinjian Zhai, MS
Jian Zheng, MS

Undergraduate & High School Students

Sunil Bodapati
Victor Em
Katie Hsih
Brett Lullo
Jithun Nair
Danielle Rasooly
Allika Walvekar

Visitors

Visiting Researchers & Scholars

Cheol-Hee Ahn, PhD
Byeong-Cheol Ben Ahn, MD, PhD
Colin Carpenter, PhD
Andreas Fieselmann, MSc
Hayit Greenspan, PhD
Han Jiang
Barris Kandemir
Daniel Kopenigg, PhD
Hongguang Liu, PhD
Tarik Massoud, PhD
Christine Niebler, PhD
Carsten Nielsen, MSc
Chang-Hyun Oh, MD
Catherine Planey
Shibo Qi, PhD
Si Yeol Song, PhD
Zhengming Xiong, MD, PhD
Zianzhong Zhang, PhD

New Research Faculty

Heike Daldrup-Link, MD, Acting Associate Professor of Radiology, Lucile Packard Children's Hospital

Dr. Daldrup-Link, who was previously an Associate Professor of Radiology and Pediatrics at the University of California, San Francisco, (UCSF) and joined the Stanford Department of Radiology September 1, 2010. She earned her medical degree from the University of Munster, Germany, in 1992 and completed a radiology residency and fellowship in pediatric radiology and molecular imaging at the Technical University of Munich, Germany, in 2004. While at UCSF as a research fellow, Dr. Daldrup-Link studied uses of contrast media for image enhancement. She currently leads several projects including "Monitoring of Stem Cell Engraftment in Arthritic Joints with MR Imaging" (R01); and "Novel Imaging Approach to Monitor Chondrogenic Differentiation of IPS Cells" (R21). Dr. Daldrup-Link is also a practicing radiologist with an interest in pediatric oncology, molecular imaging, general pediatric radiology, and teaching. Along with other professional memberships, Dr. Daldrup-Link is also a member of the board of directors of the Society for Pediatric Radiology (SPR) and a permanent member of the NIH Cancer Immunology and Immunotherapy Study Section. Her recently published textbook, Essentials of Pediatric Radiology: A Multimodality Approach, provides a concise overview of both basic and complex topics encountered by pediatric radiologists in their daily practice.

Jafi Lipson, MD, Assistant Professor of Radiology, Breast Imaging Section

Dr. Jafi Lipson joined the Department August 1, 2010, as an Assistant Professor in the Breast Imaging Section. A graduate of Harvard College, UCSF School of Medicine, and UCSF Radiology Residency, Dr. Lipson completed her medical training as a Stanford Breast Imaging Fellow in June, 2010. Her research interests include medical informatics applications in breast imaging and breast radiologic-pathologic correlation. Her prior research activities focused on CT radiation dose and the associated risk of cancer. As a T32 research fellow and mentored by Dr. Rebecca Smith-Bindman, Dr. Lipson conducted a study of four Bay Area hospitals in which she reviewed 1,200 CT examinations and dose reports; estimated the effective dose from each examination; and calculated the associated risk of cancer attributable to that effective dose. Her study culminated in an article entitled "Radiation Dose Associated with Common Computed Tomography Examinations and the Associated Lifetime Attributable Risk of Cancer" (Arch Intern Med. 2009 Dec 14;169(22):2078-86), which is one of only a few articles that have raised national attention regarding the issue of medical radiation and the need for clinical practice guidelines to track and reduce dose. Dr. Lipson's current projects include the creation and evaluation of an Annotated Breast Map, which is an automated, WIKI-form summary of a patient's breast history; integration of the BI-RADS lexicon for mammography, ultrasound, and MRI into the RSNA RadLex lexicon; and classification and quantification of dynamic contrast enhanced breast MRI patterns of response to poly (ADP-ribose) polymerase (PARP) inhibitor therapy in the neoadjuvant treatment of triple-negative and BRCA-associated breast cancer.

Michael Zeineh, MD, PhD, Assistant Professor of Radiology, Neuroradiology Section

Dr. Michael Zeineh joined the Department as an Assistant Professor in the Neuroradiology Section on September 1, 2010. After completing his undergraduate training at California Institute of Technology, Dr. Zeineh completed an MD & PhD program at the University of California, Los Angeles (UCLA). His PhD work focused on using high-resolution structural and functional MRI to investigate the neural underpinnings of memory formation and retrieval. While a radiology resident at Stanford, he received a two-year Radiological Society of North America (RSNA) Research Fellowship to pursue high-field imaging in neuroradiology. Dr. Zeineh was also awarded General Electric (GE) seed funding to support his ongoing research as a neuroradiology fellow. His research is driven by the challenge to noninvasively characterize the microscopic pathology underlying neurologic disease, particularly those with a significant component of pathology invisible to conventional imaging methods. Dr. Zeineh utilizes high-field MRI, advanced susceptibility based processing, and diffusion tensor imaging with the following applications: 1) MR imaging and characterization of amyloid plaques in the brains of Alzheimer's patients; 2) early in vivo biomarker imaging for Alzheimer's disease; 3) improved imaging of seizure foci in localization-related epilepsy; 4) identifying network derangements and microstructural alterations in Parkinson's disease; 5) imaging biomarkers for multiple sclerosis with quantitative imaging (measurement of myelin content); and 6) general applications of ultra-high field MRI for neurologic disease.

Gloria Hwang, MD, Assistant Professor of Radiology, Interventional Radiology Section

Dr. Hwang joined our Department as Assistant Professor of Interventional Radiology on May 1, 2010, after an appointment as clinical instructor that began July 1, 2008. Dr. Hwang came to Stanford for her medical training after graduating magna cum laude from Harvard College with a Bachelor's degree in the Biochemical Sciences. After completing her residency in radiology at Stanford, where she was Chief Resident, she then joined the laboratory of Lawrence Hofmann, MD, for a year. She completed her clinical fellowship in Interventional Radiology at Stanford in 2008. While an undergraduate, Dr. Hwang studied signal transduction proteins, and as a medical student she studied the immunological basis of Type I diabetes. In Dr. Hofmann's lab, she studied the use of molecular imaging techniques to track delivery of angiogenesis promoters for the treatment of limb ischemia and helped develop a non-viral vector for gene therapy in primary liver cancer. Her current research interests include interventional oncology and image-guided gene therapy, in particular, image-guided techniques to treat or palliate pancreatic cancer. Dr. Hwang is also interested in improving the localization and safety profile of gene therapy through minimally invasive image-guided techniques.

Andrei Iagaru, MD, Assistant Professor of Radiology, Nuclear Medicine Section and MIPS

Dr. Iagaru joined our Department as an Assistant Professor of Radiology on September 1, 2010, with a subspecialty in Nuclear Medicine. Dr. Iagaru completed medical school at Carol Davila University of Medicine, Bucharest, Romania, and a medical internship at Drexel University College of Medicine. He began his residency at the University of Southern California (USC) Keck School of Medicine, Los Angeles, in the Division of Nuclear Medicine, where he was the chief resident. He finished his residency and completed a PET/CT fellowship at Stanford in the Division of Nuclear Medicine. His research interests include whole-body MRI and PET/CT for early cancer detection; clinical translation of novel PET radiopharmaceuticals; radioimmunotherapy; optical imaging of breast cancer; and PET/CT imaging for thyroid, breast, cervical and ovarian cancers, melanoma, lymphoma, and sarcomas. As a clinical instructor in Nuclear Medicine, Dr. Iagaru received several awards including the Society of Nuclear Medicine (SNM) 2009 Image of the Year Award, SNM/American College of Nuclear Medicine (ACNM) Mid-Winter Conference 2010 Best Essay Award, 2009 Western Regional SNM Scientist Award, and a Stanford Cancer Center 2009 Developmental Cancer Research Award in Translational Science. With his interests, background, and training, Dr. Iagaru will find many opportunities for collaboration, teaching, and introducing his successful research into the clinical practice of Nuclear Medicine.

New Clinical Instructors

We also welcome six new Clinical Instructors whose primary and critical role is to provide excellence in radiological clinical care, teaching, and institutional service appropriate to their training and clinical interest areas. Please welcome our new clinical instructors whose commitment and dedication to patient care are highly valued and provide critical service and discipline in all clinical areas of the Department of Radiology.

Bo Yoon Ha, MD, Neuroradiology
Medical Education: Seoul National Univ., South Korea

John Chang, MD, PhD, Body Imaging
Medical Education: Univ. of Illinois at Urbana-Champaign, IL

Arvind Sonik, MD, Pediatric Imaging
Medical Education: Univ. of California, Davis

Hedieh Eslamy, MD, Pediatric Imaging
Medical Education: Tehran Univ. of Medical Sciences, Iran

Payam Massaband, MD, VA Radiology
Medical Education: Univ. of Southern California, Keck School of Medicine

Martin Laufik, MD, VA Radiology
Medical Education: Univ. of California, San Diego School of Medicine

Welcome

Faculty Awards

Recipient	Award
Scott Atlas, MD	Sociedade de Radiologia de Pernambuco in Recife, Brazil awards Dr. Atlas for his "important contributions to radiology and to education in Brazil"
Roland Bammer, PhD	John Caffey Award for Best Basic Science Research Paper at the 2010 Society for Pediatric Radiology (SPR), "3D SAP-EPI in Motion-Corrected Fast Susceptibility Weighted Imaging (SWI)" (Roland Bammer, PhD, Samantha J Holdsworth, PhD; Stefan Skare, PhD; Kristen Yeom, MD; Patrick D Barnes, MD)
Roland Bammer, PhD	2010 John Caffey Award for Best Basic Science Research Paper at the 2010 Society for Pediatric Radiology (SPR), "T1-Weighted 3D SAP-EPI for Use in Pediatric Imaging" (Roland Bammer, PhD, Samantha J Holdsworth, PhD; Stefan Skare, PhD; Kristen Yeom, MD; Patrick D Barnes, MD)
Kim Butts Pauly, PhD	Elected to the Board of the International Society for Therapeutic Ultrasound
Bao Do, MD	RSNA Certificate of Merit: "RadTF: An NLP-generated Teaching File" (Bao Do, MD, Aya Kamaya, MD, Andrew Wu, MD, Sandip Biswal, MD)
Bao Do, MD	RSNA Certificate of Merit and Selected for Radiographics: "XRAYHEAD MSK ONLINE: A Radiology Teaching File Based on RSNA's RadLex" (Andrew Wu, MD, Kate Stevens, MD, Sandip Biswal, MD, Christopher Beaulieu, MD, PhD, Garry Gold, MD, Daniel Rubin, MD)
Rebecca Fahrig, PhD	Media Coverage: "Mummies and Medicine: Scanner sees past Veil of Time" Front Page, San Francisco Chronicle, August 21, 2009
Rebecca Fahrig, PhD	Best Paper in Navigation award: "Towards Guidance of Electrophysiological Procedures with Real-time 3D Intracardiac Echocardiography Fusion to C-arm CT," 12th International MICCAI Conference (W. Wein, E. Camus, M. John, C. Duong, M. Diallo, A. Al-Ahmad, R. Fahrig, A. Khamene, and C. Xu)
Michael Federle, MD	2010 Society of Gastrointestinal Radiologists (SGR) Walter B. Cannon Medal Award
Sanjiv Sam Gambhir, MD, PhD	American College of Cardiology Foundations Parmley Prize
Sanjiv Sam Gambhir, MD, PhD	Endowed Professorship - Virginia and D. K. Ludwig Professor for Clinical Investigation in Cancer Research
Sanjiv Sam Gambhir, MD, PhD	Radiological Society of North America (RSNA) Outstanding Researcher Award
Gary Glover, PhD	University of Minnesota's Oustanding Achievement Alumnus Award given for his "outstanding contributions in refining medical magnetic resonance technologies to improve patients' lives while substantially expanding our knowledge of biomedical imaging"
Garry Gold, MD	American Society of Biomechanics 2009 Clinical Biomechanics Young Investigator Award (Senior Author), "Using real-time MRI to quantify altered joint kinematics in subjects with patellofemoral pain and to evaluate the effects of a patellar brace or sleeve on joint motion"
Garry Gold, MD	GE Healthcare Thought Leadership Award
C Chen, B Hargreaves, W Chen, S Vasanawala, S Godman, K Koch, A Brau, G Gold.	SCBT/MR 2010 Young Investigator Award: "Improved Methods for MR Imaging around Metallic Implants: Artifact Assessment and Clinical Impact"
Andrei Iagaru, MD	2009 Alavi-Mandell Award for the Journal of Nuclear Medicine publication: "A Novel Strategy for a Cocktail 18F Fluoride and 18F FDG PET/CT Scan for Evaluation of Malignancy: Results of the Pilot Phase Study"
Andrei Iagaru, MD	2010 Society of Nuclear Medicine (SNM)/American College of Nuclear Medicine (ACNM) Best Essay Award: "Combined 18F NaF and 18F FDG PET/CT Scan for Evaluation of Malignancy: Beyond the Pilot Study"

Faculty Awards

Recipient	Award
Andrei Iagaru, MD	Norman D. Poe Memorial Scholarship Award, presented at the 34th Western Regional SNM annual meeting
Debra Ikeda, MD	Visiting Professorship, Kansas City Radiological Society
Aya Kamaya, MD	Certificate of Merit & Power Hour Presentation: "Color Doppler Evaluation of Retained Products of Conception: Potential Guide to Clinical Management". American Roentgen Ray Society
Aya Kamaya, MD	Certificate of Merit award: "Recurrence in the Thyroidectomy Bed: Sonographic Findings" American Roentgen Ray Society, 2010
Aya Kamaya, MD	Finalist, New Investigator Award, American Institute of Ultrasound in Medicine, San Diego, CA March 25, 2010. 2010
Nishita Kothary, MD	Invited member of 6 US interventional radiologists to create the interventional radiology component of the new American Board of Radiology certifying examination for diagnostic radiology
William Kuo, MD	Featured Manuscript - SIR National Press Release, Society of Interventional Radiology (SIR), "Reporting Standards for Endovascular Treatment of Pulmonary Embolism"
Craig Levin, PhD	2nd Place, Paper Award, 2010 IEEE Medical Imaging Conference, Featured Manuscript - SIR National Press Release, Society of Interventional Radiology (SIR), "Reporting Standards for Endovascular Treatment of Pulmonary Embolism"Fully 3-D Time-of-Flight Positron Emission Tomography Image Reconstruction from List-mode Data Using GPUs and CUDA"
Craig Levin, PhD	Physics in Medicine and Biology Featured Article by Editors of Institute of Physics: "Bayesian reconstruction of photon interaction sequences for high-resolution PET detectors"
Margaret Lin, MD	Clinican Educator of the Year - awarded by Stanford Radiology graduating Residents
Sandy Napel, PhD	Elected to the College of Fellows of the American Institute for Medical and Biological Engineering (AIMBE)
Norbert Pelc, ScD	Elected to the position of Third Vice President of the Radiological Society of North America (RSNA)
Peter Poullos, MD	Association of University Radiologists (AUR)-Philips Academic Faculty Development Program
Daniel Rubin, MD	RSNA Certificate of Merit: "J-Viewer: A Free Javascript Library for Creating Web (and iPhone) Teaching Files with Simple PACS Functionality" (Bao Do, MD, Nishant Parekh, Andrew Wu, MD, Sandip Biswal, MD, Daniel Rubin, MD)
Brian Rutt, PhD	Named a Fellow of the American Institute for Medical and Biological Engineering
Daniel Sze, MD, PhD	Western Angiographic and Interventional Society, President 2010
Shreyas Vasanawala, MD, PhD	ISMRM-GE Healthcare 2010 Thought Leader Award: innovation in pediatric MRI
Juergen Willmann, MD	2009 Radiology Editor's Recognition Award with Distinction
Juergen Willmann, MD	2009 Walter Friedrich Award of the German Society of Radiology for oustanding research in Radiology
Juergen Willmann, MD	2010 Roscoe E. Miller Award for best paper presentation at the Annual Meeting of the Society of Gastrointestinal Radiology: "Monitoring Anti-Angiogenic Therapy in Colon Cancer with Molecular Ultrasound and a Novel Clinically Translatable Ultrasound Contrast Agent"

Trainee Awards

Recipient	Award
Priti Balchandani, PhD	2010 International Society for Magnetic Resonance in Medicine (ISMRM) Junior Fellow award
Pat Basu, MD	National Finalist for the 2010-11 White House Fellowship Program
Rachel Bitton, PhD	2010 International Society of Magnetic Resonance in Medicine (ISMRM) Student Stipend
Rachel Bitton, PhD	California Breast Cancer Research Program Grant: "MRI-guided Focused Ultrasound in Breast Cancer Treatment"
Abdelkader Bousselham, PhD	Trainee Award: Postdoctoral Fellowship from the Swedish Research Council
Stephanie Carr, MD	Society of Interventional Radiology (SIR) Foundation Dr. Constantin Cope Medical Student Annual Scientific Meeting Research Award: "Common Iliac Vein Diameter and Risk of Deep Venous Thrombosis"
Bao Do, MD	RSNA Trainee Research Prize for mentored resident: “A Natural Language Processor to Detect Uncertainty and Recommendations in Radiology Reports”
Christine Draper, PhD	Society of Nuclear Medicine's Correlative Imaging Council/Walter Wolf award: "Correlation between MRI and and NaF PET/CT in Patients with Patellofemoral Knee Pain"
Hua Fan-Minogue, MD, PhD	American Association for Cancer Research (AACR)-Merck Scholar-in-Training Award
Fan-Minogue, Hua	Travel Fellowship award from the Helena Anna Henzl Gabor Young Women in Science Fund to attend the American Association for Cancer Research (AACR) 101st Annual Meeting 2010
Pejman Ghanouni, MD, PhD	2009 Radiological Society of North America Research Trainee Awards: "Minocycline Prevents Development of Neuropathic Pain by Mitigating Macrophage Recruitment to Site of Nerve Injury as Shown with USPIO-MRI"
Alex Grant, MS	Stanford Bio-X Graduate Student Fellowship to support his research in molecular imaging
Yi Gu, PhD	Trainee Award: Attend the 2009 IEEE Medical Imaging Conference, Orlando FL, October 25-31
Benjamin Hackel, PhD	American Cancer Society/Canary Foundation Early Detection of Cancer Postdoctoral Fellowship: "Novel High Affinity Protein Scaffolds for Molecular Imaging of Tumors"
Albert Hsiao, MD, PhD	Society of Computed Body Tomography and Magnetic Resonance Cum Laude Award: “Quantitative assessment of pediatric pulmonary arterial flow dynamics with time-resolved volumetric phase-contrast”
Albert Hsiao, MD, PhD	John Kirkpatrick Young Investigator Award: "Volumetric Flow Assessment in Congenital Heart Disease with 4D Flow MRI"
Shijun Hu, PhD	American Heart Association Postdoctoral Fellowship Award: "Transplantation and Imaging of Novel Cardiac Stem Cell Therapy"
Ealgoo Kim, PhD	Trainee Award: 2-year Postdoctoral Scholarship from TLI, Inc., Seoul, South Korea
Frances Lau, PhD	California Breast Cancer Research Program (CBCRP) Award: "Electronics for High Resolution Breast-Dedicated PET"
Andrew Lee	RSNA Research & Education Foundation's Research Medical Student Grant, "Noninvasive Imaging of Cardiac Stem Cells in a Large Animal Model"
Andrew Lee	Bio-X Graduate Student Fellowship Award
Hongguang Liu, MD, PhD	Molecular Imaging Center of Excellence (MICoE) Young Investigator Award: "Noninvasive molecular imaging of radioactive tracers using optical imaging techniques"

Trainee Awards

Recipient	Award
Anderson Nnewihe	1st Place Best Poster award: "High Resolution Breast MRI" at the 2nd annual Center for Biomedical Imaging at Stanford (CBIS) Symposium
Peter Olcott	2009 IEEE Nuclear Science Symposium and Medical Imaging Conference (NSS/MIC) Best Student Paper Award: "Cross-strip capacitive multiplexing and electro-optical coupling for silicon photomultiplier arrays for PET detectors"
Peter Olcott	Trainee Travel Award: 2009 Society of Nuclear Medicine Meeting
Peter Olcott	2009 Bio-X Stanford Interdisciplinary Graduate Fellowship
Hao Peng, PhD	Trainee Travel Award: 2009 IEEE Medical Imaging Conference. Trainee Travel Award: 2009 World Molecular Imaging Conference.
Guillem Pratx, PhD	American Association of Physicists in Medicine (AAPM) Research Seed Grant: "Using X-ray activatable nanophosphors for anatomical and molecular imaging"
Guillem Pratx, PhD	Trainee Travel Award: 2009 Society of Nuclear Medicine Meeting
Guillem Pratx, PhD	Dean's Postdoctoral Fellowship at Stanford University School of Medicine: "X-ray Luminecescence Computed Tomography"
Rebecca Rakow-Penner, MD, PhD	2010 Norman Blank Award for the oustanding medical student in radiology
Rebecca Rakow-Penner, MD, PhD	Finalist for the Young Investigators' W.S. Moore Award in clinical sciences
Vijay Rao, PhD	2009 Radiological Society of North America Research Trainee Awards: "[18F]Fluoride Ion PET-CT Predicts Painful Metastatic Bone Lesions in the Thoracolumbar Spine"
Gang Ren, PhD	"Journal of Nuclear Medicine’s Top 3 Basic Science Papers of 2009: “A 2-Helix Small Protein Labeled with 68Ga for PET Imaging of HER2 Expression”
Ying Ren, PhD	2010 Stanford Dean's Fellowship Award: "Evaluation of Activity and Remission of Inflammatory Bowel Disease by Molecular Targeted Microbubble-Enhanced Ultrasound in a Mouse Colitis Model"
Virginia Spanoudaki, PhD	Axa Group Postdoctoral Fellowship: "1mm Resolution Position Emission Tomography for Enhanced Molecular Breast Cancer Imaging"
Virginia Spanoudaki, PhD	Trainee Travel Award: 2009 IEEE Medical Imaging Conference Trainee Travel Award: 2009 Society of Nuclear Medicine Meeting
Stefan T Skare, PhD	John Caffey Award for Best Basic Science Research Paper at the 2010 Society for Pediatric Radiology (SPR) "High-Resolution Motion-Corrected Diffusion-Tensor Imaging (DTI) in Infants" (Stefan T Skare, PhD, Samantha J Holdsworth, PhD; Kirsten Yeom, MD; Patrick D Barnes, MD; Roland Bammer, PhD)
Daniel Sze, MD, PhD	Featured abstract, Society of Interventional Radiology Annual Meeting 2010
Arne Vandenbrouke, PhD	Postdoctoral Fellowship from the DoD Breast Cancer Research Program (BCRP): "Commissioning and characterization of the world's first 1 mm^3 resolution clinical PET camera"
Arne Vandenbrouke, PhD	Trainee Award: 2009 IEEE Medical Imaging Conference
David Wang, MD	Travel Award: Radiological Sciences of North America (RSNA) Young Investigators in Molecular Imaging. Travel Award: World Molecular Imaging Conference
Andrew Quon, MD	Awarded the SNM 2010 Walter Wolf Young Investigator Award
Maurice Zissen, MD	Awarded a Medical Scholars Scholarship for "Monitoring Anti-VEGF Therapy Using [18F]-5-Fluorouracil PET/CT Imaging

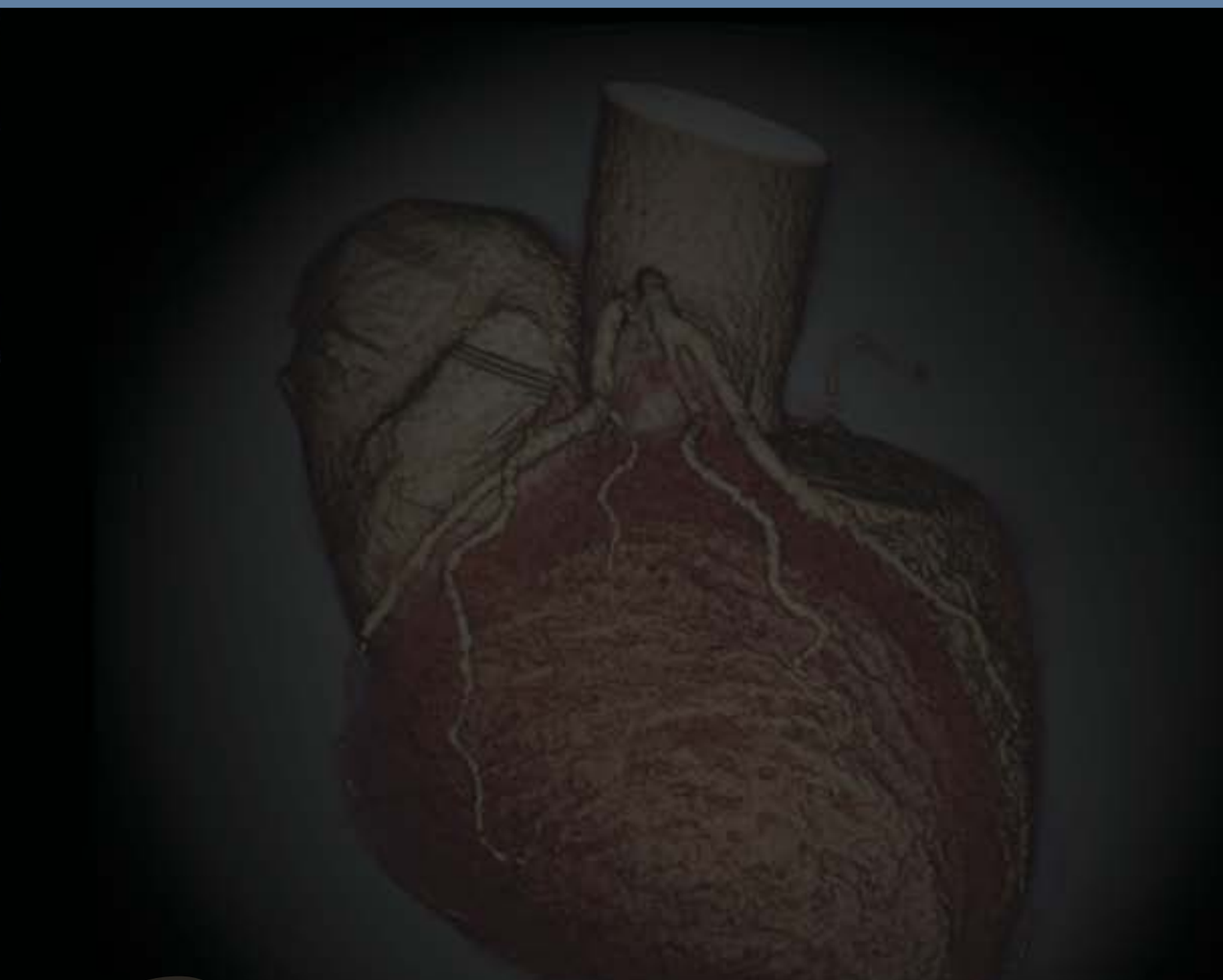

Educat

NIH/NCI T32 CA 09695

Advanced Techniques for Cancer Imaging and Detection - T32

PI: Gary M. Glazer, MD
Program Manager: Lanzie Rivera

The Department of Radiology at Stanford University offers qualified individuals a unique research opportunity through our Advanced Techniques for Cancer Imaging and Detection Program, which began its 18th year of training on March 1, 2010. The goal of our program is to provide MD and PhD research fellows training in cancer-related imaging research. Fellows have the opportunity to work with our world-renowned faculty who are committed to sharing their knowledge and mentoring future leaders in radiology. Our program allows basic scientists in medical imaging (PhD) and clinical scientists (MD post-residency) to collaborate in an unparalleled environment that combines medical imaging sciences, clinical sciences, a strong cancer focus, and an institutional commitment to training academic radiologists and basic scientists in imaging science. We are currently advertising in major radiology venues to fill two open positions before February 28, 2011.

A specific aim of our training program is to position our trainees for a career in academic radiology. To date, we have graduated 30 trainees from our program. Our trainees continue to be extremely productive. We often collaborate with them in their new positions both locally and throughout the country. We are grateful to the National Institutes of Health for its recognition of the strength and success of our training program

Current trainees are Dragos Constantin, PhD, Grace Tye, MD, and Pejman Ghanouni, MD, PhD. Their research interests are shown in the table below. Of our most recent graduates, Rachel Bitton, PhD, and Moses Darpolor, PhD, have remained at Stanford working with faculty within the Department of Radiology and Radiation Oncology.

Rachel Bitton, PhD, joined the Radiological Sciences Lab as an NCI fellow in March, 2008. Her research interests include photoacoustic imaging of micro-vasculature using high frequency ultrasonic transducers, MR temperature guidance for interventional high intensity focused ultrasound therapy (HIFU), and targeted contrast agents for photoacoustic imaging and therapy. In March, Rachel was reappointed as a postdoctoral fellow working with Dr. Kim Butts-Pauly and her focused ultrasound project. Dr. Bitton was recently awarded a two year breast cancer research award from the University of California. Her award "MRI Guided Focused Ultrasound in Breast Cancer Treatment" began on July 1, 2010 through June 30, 2011.

Moses Darpolor, PhD, joined the RSL group as an NCI fellow June, 2008. He is interested in applying multi-parametric MR and multi-modality imaging in oncology. His previous and ongoing projects include DSC-MRI in conjunction with micro-CT imaging of vascular function and morphology of brain tumor with antiangiogenic treatment; 1H decoupled 31P CSI of tumor bioenergetics to detect early response of subsequent CPT11 and flavopiridol treatment; and hyperpolarized 13C imaging to detect early tumor response to radiation therapy. Moses' two-year appointment ended on May 31, 2010. He is now working with Professors Daniel Spielman and Lei Xing in the Department of Radiation Oncology.

Dragos Constantin, PhD, joined RSL as an NCI fellow in 2009. His research interests involve theoretical and experimental investigation of the magnetic resonance imaging integration with a medical linear accelerator to provide real-time image guidance to target temporally changing tumor anatomy, particularly for cancers in the thorax and abdomen. Dr. Constatin began his second year of training with Dr. Rebecca Fahrig in February, 2010, and is working closely with faculty in the Department of Radiation Oncology.

Grace Tye, MD, joined the RSL group in July, 2009. Grace has been very active working on several cancer-related projects with faculty in the Radiological Sciences Laboratory (RSL), Molecular Imaging Program (MIPS and the newly formed Information Sciences in Imaging at Stanford (ISIS) and has attended several conferences and workshops designed to further her academic radiology career interests.

Pejman Ghanouni, MD, PhD, joined the NCI program on July 1, 2010 after graduating from the Stanford Radiology Residency Program. Pejman has a very keen interest in research and has submitted a project entitled "In Vivo MRI-Guided High Intensity Focused Ultrasound Thermal Ablation of Porcine Liver" to the Radiological Society of North America Research Resident/Fellow Program. We are waiting to hear from the sponsor regarding his proposal. His mentor for this project is Dr. F. Graham Sommer who has received several NIH awards to study pancreatic and prostate cancers.

T32 Program Graduates

NCI Fellow	Completed	Current Position	Current Institution	Primary Mentor
John Strang, MD	1995	Assistant Professor	University of Rochester, Rochester, NY	Herfkens
Susan Lemieux, PhD	1996	Assistant Professor	Diagnostic Imaging Western Virginia Univ., Morgantown, WV	Glover
Ian Chen, MD	1996	Radiologist	Southwest Washington Medical Center, Vancouver, WA	Li
Yi-Fen Yen, PhD	1997	Research Scientist	GE Advanced Health Care	Glover
Garry Gold, MD	1997	Associate Professor	Radiology, Stanford University, Stanford, CA	Macovski
Bruce Daniel, MD	1997	Associate Professor	Radiology, Stanford University, Stanford, CA	Herfkens
Roger Shifrin, MD	1998	Assistant Professor	University of Florida, FL	Pelc & Herfkens
Esther Yuh, PhD	1998	Clinical Fellow	Radiology (Neuroradiology), UCSF, CA	Li & Napel
Steven Heiss, MD	1999	Radiologist	Radiology Imaging Associates, Denver, CO	Li
Martin Blum, MD	2000	Researcher	PET/Nuclear Medicine, Palo Alto VA, CA	Jeffrey
Curtis Coulam, MD	2001	Radiologist	Gem State Radiology Group, Boise, ID	Sommer
Lawrence Chow, MD	2002	Assistant Professor	University of Oregon, Eugene, OR	Sommer
Yishan Yang, PhD	2002	Research Associate	Radiology, Stanford University, Stanford, CA	Bednarski
Samira Guccione, PhD	2002	Assistant Professor	Radiology, Stanford University, Stanford, CA	Bednarski
Charles Liu, MD	2003	Radiologist	La Jolla Radiology, La Jolla, CA	Herfkens & Sommer
Susan Hobbs, MD, PhD	2003	Radiologist	CT Section Chief, Kaiser Permanente, Walnut Creek, CA	Bednarski
Karl Vigen, PhD	2003	Research Scientist	University of Wisconsin-Madison, Madison, WI	Butts Pauly
Laura Pisani, PhD	2004	Postdoctoral Fellow	Radiology, Stanford University, Stanford, CA	Glover
John Levin, MD	2004	Radiologist	St. Luke's Medical Center & Clinic, Minneapolis, MN	Herfkens & Sommer
Daniel Margolis, MD	2005	Assistant Professor	Dept. of Radiology, UCLA, Los Angeles, CA	Jeffrey
Daniel Ennis, PhD	2006	Postdoctoral Fellow	University of Washington, Seattle, WA	Pelc
Michael McDonald, PhD	2007	Research Scientist	NIH, Washington, DC	Guccione
Anthony Faranesh, PhD	2007	Research Scientist	NIH, Washington, DC	Pelc & Hargreaves
Lewis Shin, MD	2007	Assistant Professor	Radiology, Stanford University, Stanford, CA	Herfkens
Jinha Park, MD, PhD	2008	Assistant Professor	University of Southern California, Los Angeles, CA	Gambhir
Byard Edwards, MD, PhD	2008	Scientific Researcher	Vanderbilt University	Jeffrey
Cristina Zavaleta, PhD	2008	Scientific Researcher	MIPS, Radiology, Stanford University, Stanford, CA	Gambhir
Stephanie Bailey, PhD	2009	Scientific Researcher	Comprehensive San Diego State Univsity/UCSD Cancer Center Partnership	Plevritis
Rachel Bitton, PhD	2010	Postdoctoral Fellow	RSL, Stanford University, Stanford, CA	Butts-Pauly
Moses Darpolor, PhD	2010	Postdoctoral Fellow	Radiation Oncology, Stanford University, Stanford, CA	Spielman

NIH/NCI R25 CA 118681

Stanford Molecular Imaging Scholars - SMIS R25

PI: Sanjiv Sam Gambhir, MD, PhD
Program Manager: Sofia Gonzales, MS

The Stanford Molecular Imaging Scholars (SMIS) program is a cross-disciplinary post-doctoral training program at Stanford University that brings together 45 faculty mentors from 15 departments in the Schools of Medicine, Engineering, and Humanities and Sciences. Faculty mentors provide a diverse training environment spanning biology, physics, mathematics/biocomputation/biomedical informatics, engineering, chemistry, biochemistry, cancer biology, immunology, and medical sciences. The centerpiece of the SMIS program is the opportunity for trainees (PhD or MD with an emphasis on PhD) to conduct innovative molecular imaging research that is co-mentored by faculty in complementary disciplines. SMIS trainees also engage in specialized coursework, seminars, national conferences, clinical rounds, ethics training, and the responsible conduct of research. The three-year program culminates with the preparation and review of a mock grant in support of trainee transition to an independent career in cancer molecular imaging with the ultimate goal of training them to become leaders in the field. Thus far, 14 trainees have entered the SMIS program and 8 have completed the program.

The following summarizes our trainees and their progress since the program began in 2006.

SMIS Trainee Research Interests

Benjamin Cosgrove, PhD, joined SMIS in 2008 and is interested in developing novel molecular imaging technologies to investigate stem cell signaling-phenotype relationships. These molecular imaging technologies will be employed to generate multivariate dynamic stem cell signaling-response data collected under a wide variety of micro environmental stimuli, including tethered and soluble growth factors, in a multi-well three-dimensional hydrogel system, which will then be used to identify key intracellular signaling activities that govern specific stem cell differentiation programs. This work will be conducted under the joint supervision of Drs. Jianghong Rao and Helen Blau.

Sharon Hori, PhD, began her appointment in September 2008. Her research interests include: 1) data-driven mechanistic biomodeling in relation to cancer and other diseases; 2) math modeling, and parameter estimation methods; 3) the development of imaging probes and optimization of their delivery to molecular targets via an integrative imaging/experimental and kinetic modeling approach. She is working with Drs. Plevritis, Paik, and Gambhir.

Marybeth Pysz, PhD, joined Dr. Juergen Willmann's lab in October, 2008. She is interested in multi-modality imaging of pancreatic cancer and identifying new molecular targets for early detection using molecular ultrasound and/or PET-CT imaging. She also investigates other methods for sensitive quantitation of vascular map profiles of microbubble contrast agent signals with real-time ultrasound imaging in mice using a clinical ultrasound scanner and a high-resolution ultrasound scanner for small animals. Mentors for Dr. Pysz include Drs. Willmann and Cochran.

Nicholas Conley, PhD, joined the SMIS program in 2009 after completing his PhD in Chemistry at Stanford. He is working with Drs. Matthew Scott and Jennifer Cochran on projects related to the Hedgehog signaling pathway. Hedgehog (Hh) signaling is responsible for controlling cell fates in most developing tissues and organs, as well as during many regeneration events. Unregulated activation of the Hh signaling pathway leads to birth defects and cancer.

Eric Gonzalez, PhD, began his SMIS fellowship in 2009 after completing a PhD in physics at Texas Christian University in Fort Worth, Texas. His research interests include the development of algorithms for Positron Emission Tomography (PET). He works with Dr. Craig Levin as his primary mentor to develop a methodology of detecting and processing multiple-photon events that are typically discarded in standard PET imaging.

Jesse Jokerst, PhD, who also joined the SMIS program in 2009 after completing his PhD in chemistry at University of Texas at Austin. With a background in graduate school that emphasized Raman fluorescent nanoparticles for biomarker measurement in vitro, Dr. Jokerst has found the SMIS program and opportunity to expand his experience in nanotechnology a perfect fit. His primary mentor in the program is Dr. Jianghong Rao.

R25 Program Graduates

SMIS Fellow	Completed	Current Position	Institution	Primary Mentor
Jill Lin, PhD	2009	Consultant	Beghou Consulting, Emeryville, CA	Gambhir
Keith Hartman, PhD	2009	Senior Analyst	Boston Consulting Group, Washington, DC	Gambhir
Henry Haeberle, PhD	2010	Sr Scientific Officer	Univ of New South Wales, Australia	Contag
Jennifer Prescher, PhD	2010	Assistant Professor, Chemistry	UC Irvine	Contag
Richard Kimura, PhD	2010	Sr. Research Scientist	The Canary Center, Palo Alto CA	Cochran
Bryan Smith, PhD	2010	Post Doctoral Scholar	Stanford University (MIPS)	Gambhir
Hua Fan Minogue, MD, PhD	2010	Post Doctoral Scholar	Stanford University (MIPS)	Felsher

NIH/NCI P50 CA 114747

In Vivo Cellular and Molecular Imaging - ICMIC P50

PI: Sanjiv Sam Gambhir, MD, PhD
Program Manager: Billie Robles, BS

ICMIC - P50 GRADUATES (NCI P50CA114747)

The following trainees completed postdoctoral training with support from the ICMIC@Stanford program. This program was initiated and maintained until the SMIS R25 program stabilized; we currently recruit all molecular imaging postdoctoral trainees to the SMIS R25.

ICMIC Fellow	Completed	Current Position	Institution	Primary Mentor
Sheen-Woo Lee, PhD	2005	Musculoskeletal Imaging Fellow	Asian Medical Center, Seoul, Korea	Sandip Biswal, MD
Erhan Yenilmez, PhD	2007	Post Doctoral Scholar	Materials Science & Engineering, Stanford University	Nicholas Melosh, PhD
Frank Cochran, PhD	2008	Post Doctoral Fellow	Bioengineering, Stanford University	Jennifer Cochran, PhD
Mike Helms, PhD	2008	Post Doctoral Fellow	Pediatrics, Stanford University	Christopher Contag, PhD
Mike Benoit, PhD	2009	Post Doctoral Fellow	Microbiology & Immunology	A.C. Matin, PhD
Priti Balchandani, PhD	2009	Post Doctoral Fellow	Radiology	Dan Spielman, PhD

Introducing a new Training Program: NIH NIBIB T32 EB009653-01

Predoctoral Training in Biomedical Imaging at Stanford – T32

PI: Norbert Pelc, ScD
Program Manager: Teresa Newton

This is a new multidisciplinary pre-doctoral training program at Stanford University in biomedical imaging technologies. Our mission is to train the next generation of researchers in and inventors of biomedical imaging technology. Imaging technology continues to evolve at a rapid pace generating new techniques in research today that will become the standard of care for tomorrow. There is a high need for trained researchers in this field to fill positions in academia, industry, and government. Stanford University has a unique multidisciplinary research effort in biomedical imaging, spanning magnetic resonance, computed tomography and radiography, radionuclide and optical methods for molecular imaging, ultrasound, and hybrid imaging such as Xray/ MR and PET/MR, as well as image processing and analysis for diagnosis, radiation therapy, and science.

Our new training program will draw and fund students from six different degree granting programs to train in biomedical imaging technology with faculty from 8 different departments and Interdepartmental Programs. Two students would be recruited the first year and three new students would be recruited in each subsequent year. Each trainee will be funded for the initial two years of their considerably longer PhD programs, therefore, two students would be funded in the first year, five in the second year, and six in each subsequent year of the program. We are currently recruiting students to our program.

Postgraduate Education

Continuing Medical Education Program

Susie Spielman, Director, Strategic Initiatives and Program Management

Over the past 19 years, Stanford University, Department of Radiology has constructed a world class CME program targeted to practicing physicians, academic scientists, radiology technologists, and industry-based engineers and scientists. Stanford Radiology is distinguished by an international reputation for excellence and innovation in postgraduate medical education. The Department was motivated to create such a program to fulfill the educational mission and to disseminate radiological advances. Further the benefits of the effort included an increase in reputation for the Department overall and for the individual faculty, as well as an opportunity to foster relationships globally with academic institutions and societies. The program was especially important to building the reputation and careers of our junior faculty.

The fostering of international relationships has been critical to our educational efforts. We developed courses co-hosted by strategic academic partners and societies in Japan, China and Europe. In 2009 we held our 12th annual collaborative CME course with the leading universities in Japan. These courses are co-directed by the chairmen of Stanford Radiology, Keio University, University of Tokyo and Osaka University and include speakers from all the institutions. We have held biennial courses in Europe in collaboration with Universities of Munich and Erasmus, which again bring together faculty from all participating institutions. In 2007 and 2009, Stanford presented symposia in China with the Chinese Society of Radiology and in 2010 welcomed academic radiology leaders from China for a symposium on campus at Stanford. Finally, for the past five years we have educated technologists from throughout Japan with our annual summer course offered in collaboration with the Japanese Society of Radiologic Technology. Our goal is to continue to build upon these important relationships, which have already led to vital scientific collaborations.

In 2008, the Stanford School of Medicine instituted new policies regarding CME. It was determined that Stanford Radiology's vision to conduct large, off-site and global CME courses was no longer financially or strategically viable under the new policies. Our CME team will be disbanding in 2011 and moving forward we are developing a strategy for the next generation of education programs that are viable under the SOM policies.

Stanford Radiology CME Attendees

Stanford Radiology's CME program reached over 3,000 attendees per year at its peak. Due to University policy changes, our CME effort is winding down with only two courses planned for 2011. We are currently developing a strategy for the next phase of our educational efforts.

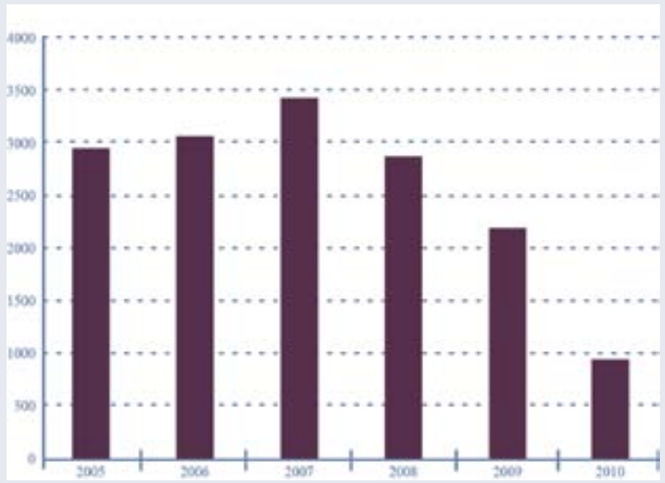

Lucas Center MR Systems Training and Support

1.5T, 3T1, 3T2, and 7T Whole Body Magnets

Anne Marie Sawyer, BS, RT (R)(MR), FSMRT
Sandra Rodriguez, BS, RT (R)(MR)

MRI SAFETY TRAINING AND SYSTEM OPERATION INSTRUCTION 2009 - 2010

MRI safety training and system instruction have been provided to 167 new researchers conducting experimental MR studies at the Lucas Center over the last twelve months. Initial magnet safety training and the annual refresher course are required for all researchers assisting or conducting studies on any of the magnet systems at the Lucas Center. The annual magnet safety refresher course has recently been developed as an on-line tutorial and will provide instruction to 358 researchers during 2010. This ensures that all users and assistants are qualified to operate the MR systems and satisfies Lucas Center and University requirements for safety. System and safety support is provided to the researchers 7 days a week, 24 hours a day to ensure that research endeavors are successful, generate valuable data, and, above all, are safe for the researchers, the human subjects and the MR systems and components (Figures 1, 2 and 3). Magnet safety is an on-going concern as the MR environment is a potentially lethal setting without continuing education and persevering support.

Figure 1. Researchers from the Department of Psychiatry prepare a young scan subject at 3T1 for a functional MRI study of the brain complete with response box seen in the subject's right hand, and physiological monitoring of heart rate, respiratory rate, and GSR (galvanic skin response).

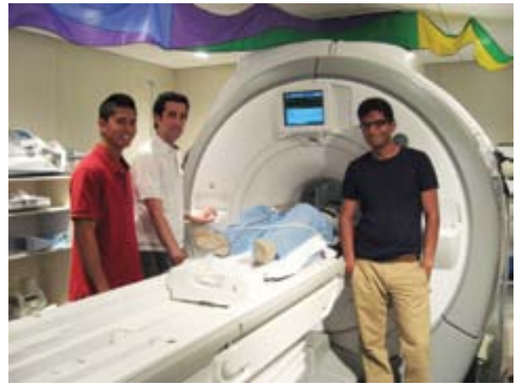

Figure 2. Researchers from the Department of Psychology prepare to conduct a functional MRI scan at the 3T2 at the Lucas Center.

The research environment generates many new yet prototype designs in RF imaging coils, imaging equipment, monitoring and response devices such as button boxes, eye trackers, and electroencephalogram (EEG) recorders, and sensory devices. Evaluation of these new devices is on-going to ensure that neither the image data, the safety of the human subject, nor the integrity of the MR system is compromised by the presence of these devices in the magnet room, in the bore of the magnet, or in the presence of an RF coil.

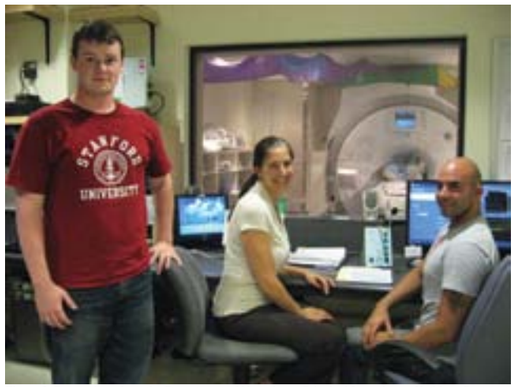

Figure 3. Researchers from the Department of Neurology (Principal Investigator Kathleen Poston, MD) conduct a functional MRI scan at 3T2 on a patient enrolled in a study of Parkinson's Disease.

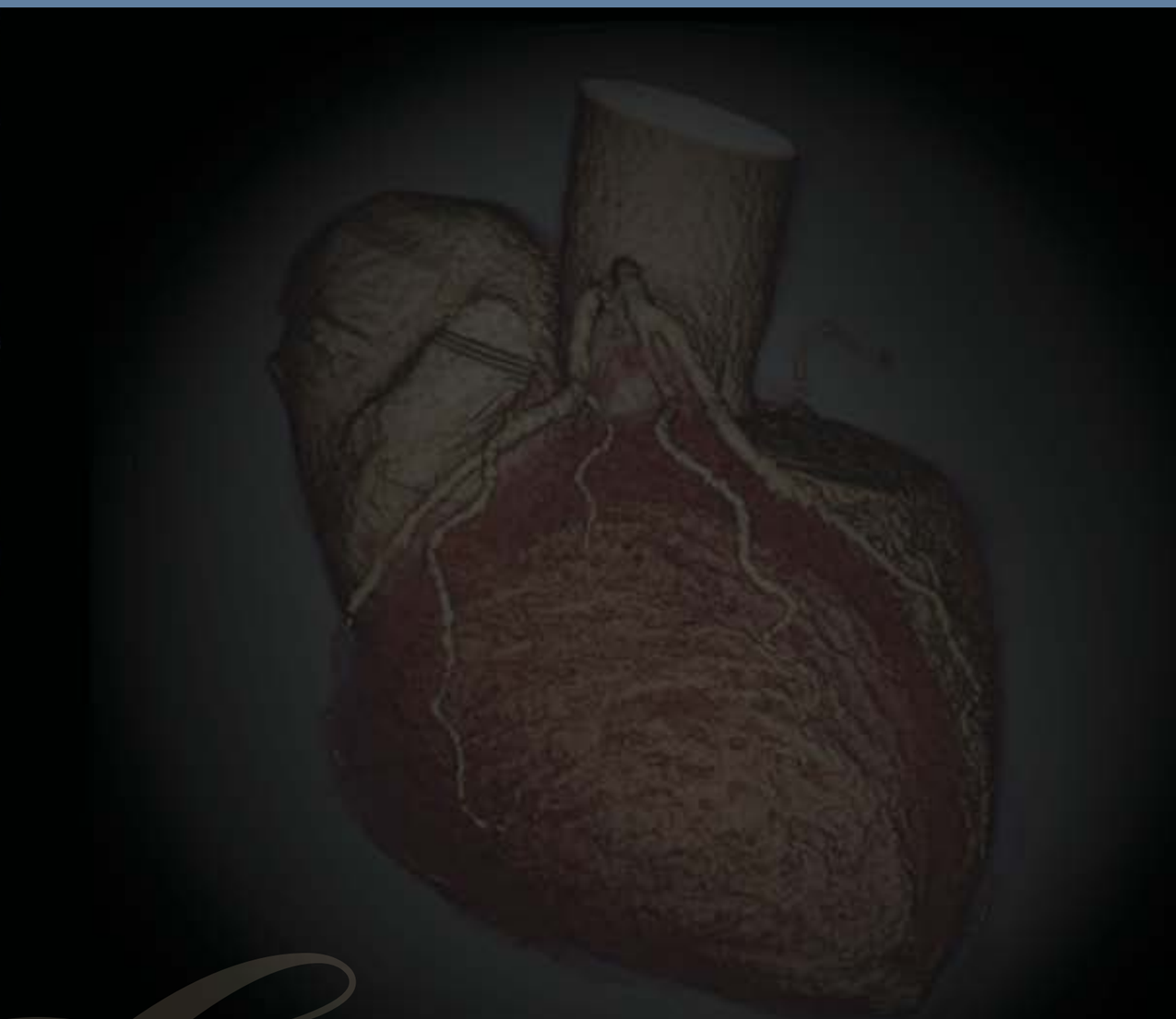

Groups

Inverse Geometry CT and Conventional CT

Norbert Pelc, ScD

Our research efforts concentrate on the development of technology and applications of computed tomography (CT). The long-term aim of this work is to push the limits of CT performance and to aid in the development of new applications. Intrinsic in this aim is the need to understand the basic limitations in current systems and, when physically possible, to develop solutions to effectively address them.

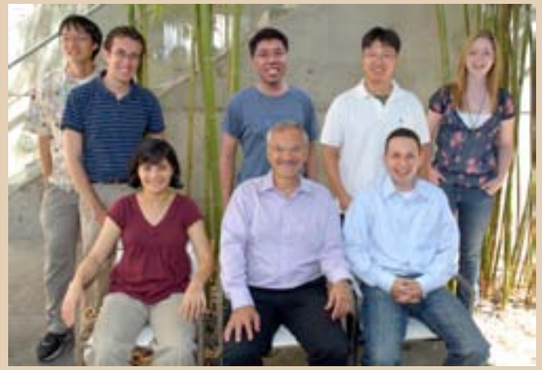

left to right, top row: Scott Hsieh, Juan Plata, Adam Wang, Jongduk Baek, Caroline Golden, bottom row: Arun Ganguly, Norbert Pelc, Sam Mazin

For many years, we have been working on a project to develop a system that can image an arbitrarily thick section of anatomy (e.g. an entire organ) in a single fast rotation while producing uncompromised image quality and outstanding dose efficiency using an inverted geometry (therefore the term Inverse Geometry CT). Recently we saw the culmination of 4 years of NIH-funded work with the initial testing of a first-ever, gantry-based IGCT system (Pelc abstract). The distributed source provides the IGCT system with the possibility to carefully control not just the overall intensity but also the distribution of x-rays incident on the patient, a concept called "virtual bowtie". Construction of a wider source array, funded by an ARRA grant from NIH, is underway and will allow us to test this concept.

We are also working on a number of problems relevant to all CT configurations. Continuing his work on "spectral" CT, Adam Wang developed a technique that can use dual energy CT data from a patient, acquired with two specific spectra, to simulate single and dual energy protocols at arbitrary kVp and filtration. Subject to certain constraints, the method can be used to demonstrate the image quality that would be obtained at a particular technique and dose (Wang abstract). Jongduk Baek continued his work on noise power spectra (NPS) and their eventual use for system evaluation. We derived and evaluated the impact of detector lag on the NPS (Baek abstract). We also continued our work on algorithms to mitigate the artifacts caused by metal implants in the patient (e.g. dental work or artificial joints). Caroline Golden, a visiting undergraduate student from Ireland, conducted a comparison of four correction methods and showed that the technique developed by one of our residents outperformed the other techniques (Golden abstract).

Finally, Sam Mazin, a postdoctoral fellow funded by the Kauffman conducted an initial demonstration of a concept for PET guided radiation therapy (Mazin abstract). See pages 62-65 for these abstracts.

X-Ray Guidance of Interventional Procedures

Rebecca Fahrig, PhD

Our group conducts research with the broad goal of improving the x-ray guidance of minimally invasive procedures, including guidance of radiation therapy. The Axiom Lab (C-arm CT system) is used for in vivo investigations and the Advanced X-Ray Imaging Lab is used for hardware and software development (table-top digital x-ray imaging, cone beam CT, new detector development and X-ray/MR system development).

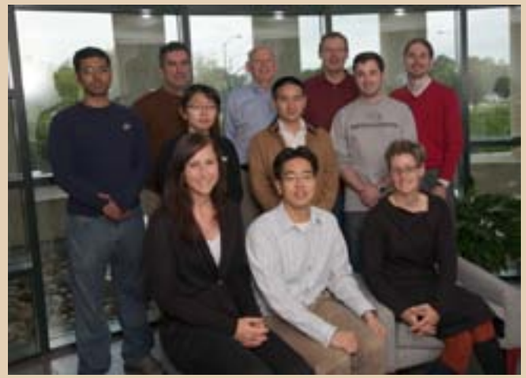

(back row) Prasheel Lillaney, Dragos Constatin, Waldo Hinshaw, Andreas Maier, Chris Schwemmer, (middle row) Mihye Shin, Hewei Gao, Jared Starman, (front row) Erin Girard-Hughes, Sungwon Yoon, Rebecca Fahrig, (missing) Arun Ganguly, Andreas Keil, Jang-hwan Choi

Software investigations have the primary goal of improving the image quality of C-arm CT reconstructions. Our modulator approach for scatter correction (abstract by Gao, NIH R21 Scatter) is now moving into clinical testing. A new lag correction approach for amorphous silicon flat-panel detectors provides close-to-CT image quality (abstract by Starman, collaboration with Varian GTC). We are also building a flexible, open-source JAVA-based framework for C-arm CT reconstruction including CUDA-accelerated forward and back-projection that provides the ability to test our new algorithms against industry standards for the first time (abstract by Maier and Keil and by Schwemmer, NIH R01 Cardiac ARRA, collaboration with University of Erlangen-Nurnberg).

In hardware developments, design and optimization of an MR-compatible rotating anode x-ray tube continues (abstracts by Lillaney and Shin, NIH R01 X-ray Tube), as does our simulations of new designs for an MR-compatible linear accelerator (abstract by Constantin, NIH NCI fellow). We also now have two projects on x-ray detector development. The first project is optimizing a new CMOS detector with direct converter HgI2 for faster high-resolution fluoroscopic imaging (abstract by Ganguly, NIH K99 CMOS, collaboration with RTR Inc.). The second project is a newly-funded NIH R01 academic-industry collaboration with Varian GTC to develop a combined kV-MV detector for CT imaging around dense metal objects such as hip implants or fillings.

We continue to develop new clinical imaging protocols using ECG-gated C-arm CT, and are now looking at the ability to image fresh myocardial infarct in the cardiac interventional suite (abstract by Girard-Hughes, collaboration with Siemens AX). We have also completed our study demonstrating the ability to make quantitative measures of brain perfusion using the C-arm system (abstract by Ganguly and Fieselman, collaboration with Siemens AX). The next area for C-arm CT development is imaging in a weight-bearing geometry, which we hope to use for patellar motion tracking and perhaps spinal imaging (abstract by Choi). Finally, we recently received funding to optimize the inverse geometry scanning beam digital x-ray system for use during magnetically-guided lung nodule biopsy (abstract by Yoon, NIH R21 Lung Biopsy). See pages 65-71 for these abstracts.

Laboratory of Imaging Informatics

Daniel L. Rubin, MD

Left to right: Neeraj Agrawal, Jafi Lipson, Daniel Rubin, Allika Walvekar, Katie Hsih, Irene Liu

Our research group uses computational methods to leverage the information in images to enable biomedical discovery and to guide physicians in personalized care. Just as biology has been revolutionized by online genetic data, our goal is to advance radiology by developing computational methods to extract quantitative and semantic content from images ("image biomarkers") and to electronically correlate images with other clinical data such as pathology and molecular data to discover image-based predictors of disease and treatment response. Our work develops and translates basic biomedical informatics methods to improve radiology practice and decision making in several areas: tools to efficiently and thoroughly capture the semantic terms radiologists use to describe lesions (structured reporting, ontologies, and next-generation PACS); standardized terminologies to enable radiologists to describe lesions comprehensively and consistently; image processing methods to extract quantitative features from images that are informative of the underlying biology of lesions; content-based image retrieval; quantitative imagine—methods to enable physicians to objectively and reproducibly assess lesions in images and to more effectively monitor the response to treatment; natural language techniques to enable uniform indexing, searching, and retrieval of radiology information resources such as radiology reports; and decision support applications that relate radiology findings to diagnoses to improve diagnostic accuracy.

This year our laboratory become one of the sites in the Quantitative Imaging Network (QIN), a newly established national research consortium by NCI who will advance the science of quantitative methods of imaging to understand cancer. We are developing a national informatics infrastructure to define a new paradigm for acquiring, mining, and using a broad range of quantitative imaging data in cancer research, and to provide decision support to oncologists based on quantitative imaging assessments of patients with cancer. We are also establishing a large database of annotated quantitative imaging cancer studies as a resource for discovering new biomarkers that will improve the sensitivity of detecting cancer treatment response.

We collaborate with a variety of investigators at Stanford both in Radiology and Oncology as well as with investigators outside Stanford. We also participate in a national working group that is developing imaging informatics infrastructure for the cancer Biomedical Informatics Grid program at NCI. Our ultimate goal is to bridge the divide between radiological knowledge and practice - for all radiological knowledge and research data to be structured, accessed, and processed by computers so that we can create and deploy decision support applications in image workstations to improve radiologist clinical effectiveness.

Cancer Systems Biology Laboratory (CSBL)

Sylvia K. Plevritis, PhD

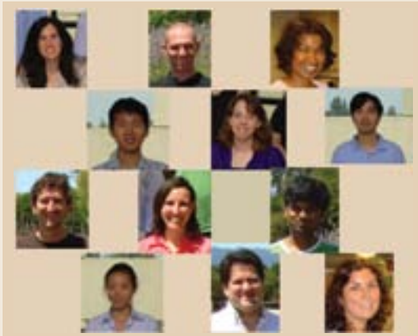

Sylvia Plevritis, Andrew Gentles, Cathy Shachaf, Peng Qiu, Allison Kurian, Ray Lin, Olivier Gevaert, Sarah Geneser, Aravind Babu, Emily Tsai, Diego Munoz, Nicole Brandon

The Cancer Systems Biology Lab (CSBL) views cancer as a complex system whose components can be reverse-engineered for the purposes of understanding the underlying mechanisms of cancer progression and identifying approaches for more effective cancer control strategies. Currently, our laboratory infers complex features of cancer progression through a variety of approaches that include: (1) reconstructing molecular networks of cancer, (2) integrating a diversity of molecular, pathological, imaging and clinical cancer data, and (3) mathematically modeling the progression of primary disease to metastatic stages in patients. Ultimately, our goal is to develop a comprehensive, multiscale view of cancer progression that merges these various approaches.

(1) Reconstructing molecular networks: We apply a wide range of computational and statistical techniques to infer molecular networks underlying cancer using genomic, transcriptomic and proteomic data. These networks often represent interactions between genes or sets of genes, mediated by a diversity of transcriptional regulators. Typically, we use these networks to generate new hypotheses about the stem-cell-like and self-renewing properties of cancer progression. Recently, we have been funded by the NCI Integrative Cancer Biology Program as a national Center for Cancer Systems Biology to promote this research with a grant entitled "Modeling the Role of Differentiation in Cancer Progression," focusing on hematologic malignancies with a multi-disciplinary team across the Stanford campus. In addition, we have established a "wet-lab" in LUCAS P169 to experimentally validate our computationally-derived findings. With the new "wet-lab" we are now expanding our molecular-network-based research to the analysis of solid tumors, specifically breast cancer.

(2) Integrating a diversity of molecular, imaging and clinical data: We have embarked on numerous projects that involve the integration of multi-platform cancer datasets through probabilistic modeling. In a recent collaborative effort through ISIS, with investigators from the Stanford Departments of Radiology and Surgery, we are creating an association map between CT and PET image features and gene expression microarrays of human non-small cell lung carcinoma. This map should provide a molecular characterization of imaging features of lung cancer. It should also enable us to infer the prognostic significance of CT lung imaging features by leveraging on a vast amount of clinically annotated, publically available lung cancer gene expression microarray. This effort has pilot funds from GE Medical Systems.

(3) Mathematically modeling the progression of primary disease to metastatic stages in cancer patients: We develop multi-scale models of the natural history of cancer that describe the stochastic behavior of tumor growth and metastatic spread. We have used these models to address important health policy questions related to early detection, such as: how does screening mammography and MRI impact breast cancer mortality; and how would CT screening for lung cancer impact lung cancer mortality rates? This effort has been funded for over 10 years and has been renewed for an additional 5 years of funding through the NCI Cancer Intervention and Surveillance Network (CISNET).

In CSBL, computational and biomathematical scientists and engineers work side-by-side with biological experimentalists and clinical researchers to ensure the biological and clinical relevance and translation of our work. By developing new computational methods to integrate complex experimental cancer data, we aim to contribute to a more comprehensive, multi-scale understanding of cancer progression that will identify new approaches to eliminate deadly aspects of this disease.

Research Group Updates

Image Analysis, Bioinformatics, and Computational Modeling

Imaging Bioinformatics

David Paik, PhD

Our group is primarily interested in how biological information is extracted and quantified from both anatomic and molecular imaging, how it is represented, how it is modeled and how it is disseminated with an outlook toward combining imaging-derived information with other sources of biological and clinical information. We are particularly interested in applying computational techniques toward a better understanding of cancer. While most computational models and analyses focus on a single source or modality of data, it is becoming increasingly clear that models must integrate across a wide variety of data types as well as spatial and temporal scales. Our focus is on developing these types of models.

Bottom row (left to right): Kranthi Kode, Tiffany Ting Liu, Erica Savig. Back row (left to right): Frezghi Habte, David Paik, Danielle Rasooly, Chinyere Nwabugwu.

Beginning with information extraction, we are working to investigate how radiologists visually interpret images in collaboration with Geoff Rubin, Sandy Napel and Justus Roos. We are continuing work on computational methods to maximize the multiplexing capabilities of hyperspectral imaging with Raman labeled nanoparticles. In the area of modeling, we have an ongoing collaboration with Dean Felsher's laboratory in mathematically modeling oncogene addiction through quantitative imaging. This has led to new areas of investigation including using rate kinetics equations of the apoptosis caspase cascade in order to better predict the effect on overall tumor growth kinetics. In the area of knowledge representation and dissemination, we have several related projects in nanoparticle agent knowledgebases in collaboration with the NCI's CCNE Program, the National Center for Biomedical Ontology and the NCI's caBIG initiative.

Our long-term goal is to enable and simplify the problem of information extraction and information flow from medical/molecular imaging to be on par with that of genomic and proteomic profiling technologies so that these very different types of information may be treated as siblings computationally. Our philosophy is that for an integrative approach to imaging and non-imaging information to come to fruition, a major pre-requisite is to be able to maximally extract and represent information from imaging, with emphasis on the specificity of molecular imaging.

Radiology 3D Visualization and Analysis Laboratory

Sandy Napel, PhD

Our group addresses the field of medical image analysis, focusing on volumetric visualization, structure segmentation, quantitative analysis, computer-aided detection of lesions, and the capture and use of imaging phenotype for decision support and integration with other clinical data, including those from high throughput technologies such as gene arrays.

left to right: Allika Walvekar (high school intern), Hayit Greenspan (Visiting Professor), Martin Tall, Danny Korenblum, Jiajing Xu, Jessica Faruque, Front: Sandy Napel, Missing: Neeraj Agrawal, Dominik Fleischmann, Barris Kandemir (Turkish undergrad exchange student), Jithun Nair, Daniel L. Rubin, Geoffrey D. Rubin, Grace Tye
Group Members who have left – Jingyu Cui, Yongjun Ma (Visiting Professor), Ronald Summers (Visiting Professor) Justus Roos, Cesar Rodriguez, Florian Schmitzberger

Advances here have impact in many technical and clinical areas. Examples are: automated visualization and quantitation of vascular image data, virtual colonoscopy, intra-procedural registration of 2D fluoroscopic images of instruments with 3D volume data, automated computation of peak flow velocity using a novel ultrasound transducer for reproducible determinations of carotid stenosis, automatic generation of curved-planar images through blood vessels, determination of likely neuronal connections of the visual tracts in the brain. More recent work includes visualization of dual energy CT data from the head and neck, and cardiac CT segmentation and visualization. Our group is highly collaborative, working with many radiology department investigators (including Chris Beaulieu, Dominik Fleischmann, Lawrence Hoffmann, Brooke Jeffrey, David Paik, Justus Roos, Daniel L. Rubin, and Geoffrey D. Rubin) as well as many other Stanford faculty (including Pierre Khuri-Yakub, electrical engineering). This year we have focused on automated feature extraction from liver CT images, correlation of image features to molecular profiles of excised tissue in lung cancer, evaluation of CAD of lung nodule data, evaluation methods for CAD in the absence of ground truth, and gaze tracking for improving interpretations. Based on our work this past year, 8 new manuscripts have been accepted for publication, 8 presentations were given at international meetings, and 5 grant proposals, all related to our ISIS initiative, were submitted to the NIH.

Research Group Updates

Magnetic Resonance Research

Interventional and Open MRI

Kim Butts Pauly, PhD

This year, our group focused primarily on MR-guided focused ultrasound for the treatment of diseases in the liver, prostate, breast, heart, and brain. Ultrasound energy can be focused to a point deep within the body without damage to overlying tissues. MRI provides a means to target the treatment, monitor the temperature during treatment, and evaluate the tissue after the treatment.

In body applications, our major projects include the development of an MR-guided focused ultrasound treatment for the liver. This includes developing the MR temperature imaging during free breathing, as well as developing therapeutic capacitive micromachined ultrasonic transducers. We also have a project for MR-guided high intensity ultrasound ablation in the prostate with transurethral ultrasound applicators. This year, we have been developing feedback and control of the treatment. Our cardiac project has been focused on generating good quality temperature images in the heart based on a hybrid multibaseline-referenceless processing approach. In the breast, we have looked at the effect of focused ultrasound on the appearance of the tissue, its visibility and stiffness.

left to right, row 1: Pejman Ghanouni, Viola Rieke, Valentina Giannini, Rachelle Bitton, row 2: Juan Plata, Hyo-Seon Yoon, Kim Butts-Pauly, row 3: Ron Watkins, Elena Kaye, Randy King, top row: Andrew Holbrook

In the brain, we have been developing a method for MR-guided focusing in the presence of phase aberrations. This depends on imaging the focus with acoustic radiation force imaging. We are analyzing the effect of nearby calcifications on tissue heating. We have also been investigating neuromodulation with focused ultrasound. Lastly, we have investigated the opening of the blood brain barrier with ultrasound. You should see all of this in the following abstracts.

Magnetic In Vivo Spectroscopy and Multinuclear Imaging

Daniel Spielman, PhD

Our investigations continue to focus along three distinct lines. Research on the technical development of ultra-high field (7T) proton spectroscopy of the brain continues from last year with an added emphasis on the design and evaluation of novel RF excitation pulses for addressing the magnetic field inhomogeneities encountered at 7T. The development of 7T neuroimaging sequences using a self-refocused adiabatic pulse for spin echo imaging and an adiabatic magnetization preparation pulse for T2-contrast are highlights of this year's work. Under an ongoing program in the development of volumetric 1H MRSI at 1.5 T and 3.0 T, funded through an NIBIB Bioengineering Partnership grant (EB000822), we have successfully implemented a volumetric echo-planar spectroscopic imaging sequence and developed associated conversion software so that the data can be processed using a general purpose MRSI software package, MIDAS. Furthermore we have extended our 1H spectroscopic imaging tools to include the robust measurement of the neurotransmitters glutamine and glutamate throughout the brain. Finally, our efforts in the area of hyperpolarized 13C MRS and MRSI continues to move rapidly forward. Hyperpolarized 13C is a highly promising technology capable of directly probing key metabolic pathways by providing unprecedented increases in signal-to-noise ratio for these in vivo measurements. Over the past year we have successfully developed several novel MRSI protocols and associated metabolic modeling tools including single-shot brain MRSI, non-CPMG spectroscopic imaging, and an adiabatic double spin echo method. We are currently applying these techniques to the study of a number of pathologies including liver metabolic disorders, hepatocellular carcinoma, prostate cancer, alcoholism, and pediatric arthritis. This work is now funded under NIH grants EB009070 "Dynamic Metabolic Imaging of Hyperpolarized Substrates", AA018681 "Metabolic Imaging of the Cardioprotective Effects of Alcohol and ALDH2 Activators", and RR09784 "Center for Advanced Magnetic Resonance Technology at Stanford".

left to right: Sonal Josan, Moses Darpolor, Daniel Spielman, Tao Xu, Dirk Mayer, Meng Gu, Jae Mo Park, Lasitha Senadheera, Priti Balchandani

Research Group Updates

Magnetic Resonance Research

Body MR Imaging

Brian A. Hargreaves, PhD

The Body MR imaging group addresses applications of MRI to clinical body imaging, including abdominal imaging, musculoskeletal imaging, breast imaging and cardiovascular imaging. We collaborate with clinicians as well as scientists at GE Healthcare and in Electrical Engineering. More information is available at http://bmr.group.stanford.edu.

From right to left: Pauline Worters, Misung Han, Caroline Jordan, Manojkumar Saranathan, Kristin Granlund, Ernesto Staroswiecki, Anderson Nnewihe, Kyung Sung, Ho Jin Kim, and Brian Hargreaves

This year the group welcomes Dr. Manoj Saranathan as a senior research associate, most recently from GE Healthcare's Applied Science Lab. Manoj is working on breast MRI and vascular imaging, as well as 7T technology with Brian Rutt's group. Dr. Catherine (Kitty) Moran has also joined us as a post-doctoral fellow, following her PhD at University of Wisconsin. Kitty is primarily working on breast MRI. This year Misung Han successfully defended her thesis, entitled "Dynamic Contrast-Enhanced Breast MRI" and will soon begin a post-doctoral fellowship at UCSF. Ernesto Staroswiecki and Kristin Granlund are studying a new 3D diffusion and T2-measurement method in the knee and breast, and Marc Alley has enabled this method for routine clinical use. Anderson Nnewihe continues to work on high-resolution breast imaging, and completed his 16-channel breast receive coil, which offers some of the highest resolution MR images of the whole breast seen to date. Caroline Jordan successfully completed her Bioengineering qualifying examination, and has been working on non-contrast vascular imaging, as well as modeling susceptibility effects. Kyung Sung has developed a new method based on Compressed Sensing to exploit the varying information content at different sharpness levels in images. Pauline Worters has made significant contributions to vascular imaging, and more recently to imaging near metallic implants. Both Pauline and Kyung were recently promoted to research associate positions. Marcus Alley continues to support new applications in the clinic, including vascular, musculoskeletal and breast imaging, and has made substantial improvements to imaging abdominal blood flow in collaboration with Dr. Shreyas Vasanawala. Our group continues strong collaborations with numerous radiologists including Bruce Daniel, Bob Herfkens, Garry Gold, and Shreyas Vasanawala.

High Field MR

Brian Rutt, PhD

Michael Zeineh, Priti Balchandani, Jonathan Lu, Jason Su, Prachi Pandit, Manoj Sananathan, Mohammad Khaligi, Brian Rutt.

The long-term objective of the High Field MR Group is to develop a next-generation 7 Tesla whole-body magnetic resonance imaging (MRI) facility at Stanford, to serve as a platform for cutting-edge imaging research and development, as well as for radiological and neuroscience research. The scientific scope of the projects that will use this new facility will span the range from fundamental biology to patient-based clinical imaging research. The group approach will be interdisciplinary, bringing together researchers from the specialties of physics, engineering, bioengineering, biology, physiology, radiology, neurology, psychiatry, and psychology. The 7T MR facility will act as a catalyst and common platform for these broad groups to create, refine, implement, validate and utilize the most advanced forms of magnetic resonance imaging. Major patient-based imaging research applications of the next-generation 7T MRI platform will include studies of brain development, psychopathology, drug dependence, alcohol-induced brain damage and its functional consequences, neurodegenerative processes, brain injury, musculoskeletal disorders, and therapeutic interventions associated with some or all of the above.

Major technology development directions that will be enabled by this next-generation 7T MRI platform include MR spectroscopic imaging (MRSI) of the proton (1H) nucleus as well as non-proton nuclei, in both brain and musculoskeletal systems, advanced perfusion and diffusion tensor imaging in brain, and, importantly, parallel transmit technology for mitigating B1 inhomogeneities that limit the use of high magnetic field MRI in any organ system. The initial goals of the High Field MR Group are to develop software and hardware methods to allow 7T MRI to have a much greater impact on clinical research than has ever been possible, as well as to extend the capabilities of high field MRI to unprecedented levels of spatial resolution, metabolite and iron sensitivity, and tissue characterization. Major users are expected to come from interdisciplinary laboratories directed by international leaders in imaging research. Projects and research foci have already been established in the following areas: high field and high sensitivity MRI methodology development, developmental disorders and clinical neuroscience, DTI methodology development, musculoskeletal and breast MRI methodology development, parallel transmit and RF pulse technology development, psychiatric disorders and neuroimaging, MR spectroscopic imaging methodology development, psychiatric disorders and clinical neuroscience, cognitive neuroscience and neuroimaging and neurovascular imaging.

Research Group Updates

Magnetic Resonance Research

Functional Imaging

Gary Glover, PhD

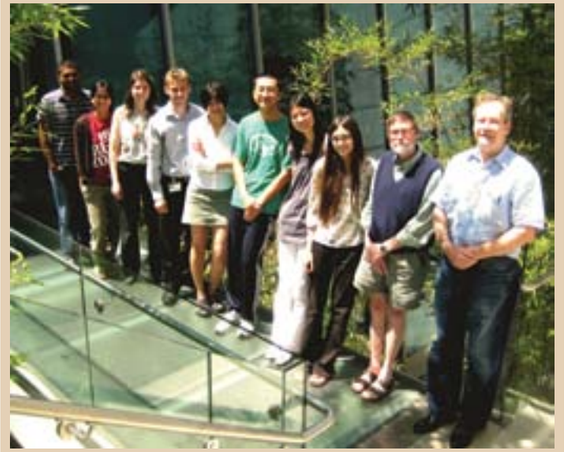

Left to right: Thomas John, Mai Le, Allyson Rosen, Jeffrey Stephens, Prachi Pandit, Xingping Shen, Jingyuan Chen, Cattie Chang, Gary Glover, Paul Mazaika. Not shown: Justin Brown, Fumiko Hoeft, Sean Mackey.

The Functional MRI Group continues to develop and optimize methods for the acquisition of functional MR imaging data. Projects include the development of fMRI methods that reduce signal dropout and/or improve efficiency, real-time biofeedback for training brains and reduction of physiological noise in fMRI signals and investigation of brain network dynamics. In addition, we continue to play an active role in the NCRR-funded FIRST BIRN schizophrenia test bed project, with Gary Glover as the chair of the calibration working group.

The following are only a few of the highlights of scientific progress; see abstracts for further details.

Graduate/PGY4-MD student Rebecca Rakow-Penner defended her PhD thesis in Biophysics and is finalizing the writeup on the use of BOLD contrast for detecting and characterizing breast tumors. She was nominated as a finalist in the prestigious ISMRM's Moore Young Investigator Award competition. She was honored with the Norman Blank Award from the Radiology Department, and received her hood at graduation this June, with family from near and far in attendance. She is in final stages of publishing her work on artifact reduction in breast imaging using an innovative saturation method that reduces confounding signal from the heart.

Postdoc Moriah Thomason Caires has continued work on genetic influences on brain development in children and is now considering choices for several faculty appointments.

Grad student Catie Chang discovered that the brain's resting state networks are highly variable in their inter-region activity, and has published her methods of investigation of this unexpected phenomenon. She collaborates with many investigators at Stanford on real-time fMRI, and internationally with scientists who use her denoising algorithms and her dynamic network methods.

Anesthesia Faculty and group member Sean Mackey was featured in a 3-page article in Nature (Vol 461:T194, 29 October 2009), discussing his research studies on mitigation of pain using the real-time biofeedback methods developed by our group. Dr. Mackey cautioned that the techniques are still in research phase but show promising results in training patients to reduce their chronic and episodal pain.

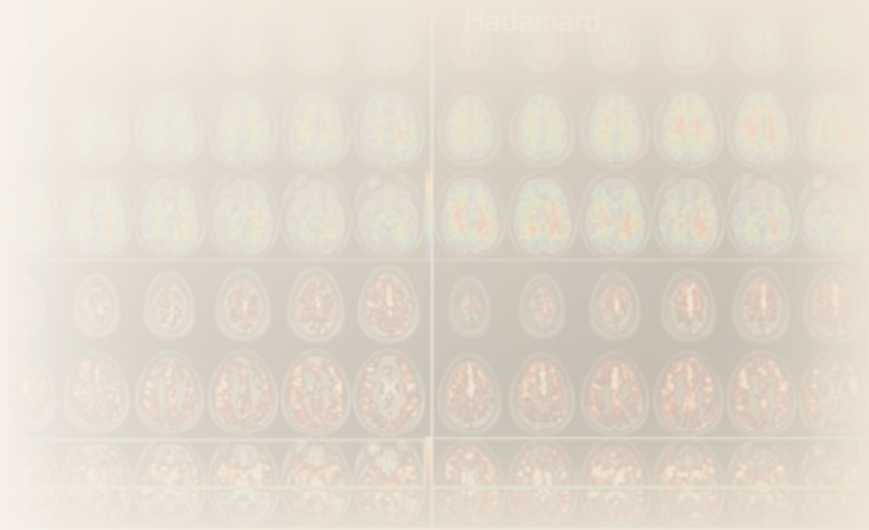

Research Group Updates

Magnetic Resonance Research

Clinical Center for Advanced Neuroimaging (CFAN)

Advances in magnetic resonance imaging (MRI) continue to revolutionize neuroimaging. We now routinely map and measure brain tissue water movement, blood flow, and the brain's ability to develop and maintain functional-structural integrity in adult and pediatric patients. To apply our clinical excellence in advanced neuroimaging, the Clinical Center for Advanced Neuro Imaging (CFAN) is built upon the large framework of a number of funded NIH grants from the RSL, Lucas Center, Stanford Stroke Center, and the Pediatric Radiology faculty dedicated to providing the best MRI techniques to help clinicians do their job more effectively.

The research program behind CFAN brings over $2.2M per year to Stanford, which has been augmented in part by stimulus grants. These grants focus exclusively on clinical neuroimaging from a team of MD and PhD clinicians and researchers across several departments in the Stanford School of Medicine and the Lucille Packard Children's Hospital. CFAN brings a wide and growing array of funded efforts together and is disease as well as method oriented.

We continue to make significant progress in developing advanced imaging technologies in several key adult and pediatric clinical areas. These include diffusion and perfusion techniques to image acute stroke and to image white matter structure and integrity. We are now funded to use the whole body 7 Tesla MRI scanner and research parallel RF transmit methods to improve higher-resolution tools of high-field and high-speed MRI, focusing on disease processes in "brain attacks" (cerebral stroke) in both adults and in children, cerebral palsy, and pediatric tumors using diffusion MRI (DWI), tissue perfusion mapping (PWI), as well as the new field of mapping the brain connectivity, DTI, and susceptibility-weighted MRI (SWI). Clinical imaging of Moyamoya and transient ischemic attacks (TIA) of the brain have also been recently added.

CFAN also maps high-resolution diffusion images to explore and map hippocampus structure and function in active mental tasking, which will reveal new key findings in developing and aging brain function to separate short-term from long-term structural changes in the brain. Similar high resolution methods are also used in cholesteatomas to isolate recurrent/residual abnormalities to assess nerve viability. Recently, we have expanded our portfolio of sequences to include rapid 3D relaxometry, which accurately measures T1, T2, proton-density and transmit fields simultaneously without the use of prohibitively (especially important in children) high RF energy deposition. These tools offer great potential for pre-clinical contrast agent studies and in an advanced assessment of patients suffering from demyelinating diseases, such as MS.

CFAN also focuses on improving angiographic methods by inventing innovative MR pulse sequences and optimizing the timing and amount of contrast delivery. Efforts are also underway to improve analysis and mapping of complex flow patterns by blood flow streamline analysis and comparing those results to computational fluid dynamic models.

CFAN is also interested in reducing image blur and artifacts by developing both hardware and software for real-time motion correction of MRI scans with a special focus on children. This prospective approach is a major paradigm change and promises to reduce sedation needed to image children.

Roland Bammer was recently promoted to Associate Professor of Radiology and Neurology, and Neurological Sciences (by courtesy), and is the key imaging physicist for Pediatric Radiology. He is also a visiting professor at Bosporus University, Istanbul, a university Docent at the Medical University of Graz, Austria, and a Senior Fellow of the Freiburg Institute for Advanced Studies (FRIAS). Roland also serves as a reviewer on NIH study sections; is a full member of the editorial board of Magnetic Resonance in Medicine and the Journal of Magnetic Resonance Imaging; and was recently elected to Chair of the ISMRM publication committee. He also directs the year-long Physics course for Radiology residents. This year Roland also received the prestigious Caffey research award from the Society of Pediatric Radiology (SPR).

Greg Zaharchuk is an Associate Professor in Neuroradiology. He has several funded projects and works with Neurology and Neurosurgery to clinically evaluate CFAN methods in patients with altered CNS blood flow in MS, Moyamoya, TIA, stroke, and cerebral vascular diseases of the aging brain. Dr. Zaharchuk is our expert on diffusible tracers to study brain perfusion and has revamped the research in arterial spin labeling (ASL) and dynamic Xe-enhanced CT. For his work on ASL, he received the ASNR award. His mentee, Albert Hsiao, received the SPR poster award. Greg's research has also helped optimize our CT perfusion methods, bringing them to a competitive level. His efforts also directly benefit patients. This year, Greg also received his first NIH R01, which supports him and his team to study blood flow in Moyamoya patients. He also leads a Tiger-team neuro project, part of a multi-disciplinary joint effort with GE Healthcare to advance MR applications development.

Mike Moseley is a past President and Gold Medal winner of the International Society of Magnetic Resonance in Medicine (ISMRM) and was elected as a Lifetime Member of the Society of Magnetic Resonance Technologists (SMRT). As a leading expert and pioneer of stroke imaging, he also sits on many NIH study sections and journal editorial boards. This year Mike was successful in receiving a highly competitive NIH S10 award, which allows for a major hardware upgrade for the 7T animal system, the work horse for preclinical studies in the small animal imaging suite.

One of CFAN's goals is to actively engage and collaborate with new faculty, such as Dr. Kristen Yeom at Stanford and Lucille Packard to develop key approaches to imaging children. Kristen recently received a research grant from the LPCH research council to study pediatric tumors pre- and post-therapy using CFAN methods. Another example of CFAN guidance involves Dr. Michael Zeineh, who with the support and mentorship of Scott Atlas and working with Samantha Holdsworth, has developed a high-resolution DTI sequence to trace white matter fiber tracts in the hippocampus, an anatomical structure that could not be visualized before.

Thomas Christen, Ryan Spilker, and Greg Zaharchuk have developed a battery of clinical imaging methods mapping brain oxygenation utilization and reserve for patients with compromised vascular systems. This work is being added to the clinical stroke workup protocol in an effort to predict whether acute stroke therapy can be extended to patients receiving early MRI scans.

Roland Bammer, PhD, Greg Zaharchuk, PhD, MD, Michael Moseley, PhD

First Row (Left to Right): Murat Aksoy, Samantha Holdsworth, Tom Brosnan, Florian Schneider, Heiko Schmiedeskamp. Second Row: Deqiang Qiu, Lanzie Rivera, Roland Bammer, Greg Zaharchuk, Raphael O'Halloran. Third Row: Thomas Christen, Mike Moseley, Shanging Feng, Matus Straka, Jordan Michael Nechvatal. Bottom Row: Eyun Soo Choi, Christoph Forman, Ryan Spilker, Didem Aksoy, and Daniel Kopeinigg.

Patient motion has been one of the unsolved problems in MRI. Children and patients who suffer from certain diseases are often unable to remain still during an exam. Murat Aksoy, a postdoctoral scholar works with Roland Bammer on MRI motion correction. Murat has developed a method to eliminate motion artifacts from infant scanning protocols. Murat's work is critical for making CFAN tools work on routine acute infant and adolescent MRI. Stefan Skare, a senior research associate, focuses on multi-shot MR sequences for high-resolution diffusion in the presence of patient motion. Stefan and Samantha Holdsworth, research associate, lead a team of physicists to develop high-resolution diffusion sequences at 3T. Matus Straka, research associate, is focused on parallel computing issues for image reconstruction and quantitative parameter mapping.

Heiko Schmiedeskamp, a Bioengineering graduate student, is adapting his novel imaging sequences for imaging blood flow and functional changes in stroke. Daniel Kopeinigg, a graduate student in Electrical Engineering, works with Roland, Marcus Alley, and Dominik Fleischmann on contrast-enhanced angiography with a special focus on improving contrast injection profiles to achieve desired enhancement profiles in the arterial system. Raphael O'Halloran, a new research associate, uses novel 3D volume diffusion spiral methods for clinical imaging. Eyun Soo Choi and Shangping Feng are both second year graduate students in Electrical Engineering. Eun Soo has already made major strides in writing software to perform coherence path analysis and Bloch simulations for complex MR sequences.

Thomas Brosnan, who is a senior research scientist, directs the RSL and Lucas IT infrastructure. His work is key in adapting the novel MR sequences to the clinics where imaging data is fed in real-time to the RSL servers for rapid processing and feedback to the clinicians. Where companies employ a whole battalion of computer engineers and specialists, Tom single-handedly provides superb infrastructure that CFAN could not do without. Last but not least, Lanzie Rivera is the CFAN administrator and grants manager. She provides administrative support for us and is a critical resource for institutional review boards, grants management, and financial matters.

Research Group Updates

Molecular Imaging

Multimodality Molecular Imaging Lab (MMIL)

Sanjiv Sam Gambhir, MD, PhD

We are developing imaging assays to monitor fundamental cellular events in living subjects. We are actively investigating technologies such as micro-positron emission tomography (micro-PET); bioluminescence optical imaging with a charge coupled-device (CCD) camera; fluorescence optical imaging; micro-computerized axial tomography (microCAT); ultrasound; photoacoustics; intravital microscopy; and Raman spectroscopy in small animal models. Our goals are to marry fundamental advances in molecular/cell biology with those in biomedical imaging to advance the field of molecular imaging. We have a particular focus on cancer biology. We have developed several reporter genes/reporter probes compatible with all of the above imaging modalities. These reporter genes are being used in cell trafficking models, gene therapy models, as well as in transgenic models for studying cancer biology. Assays to interrogate cells for mRNA levels, cell surface antigens, protein-protein interactions, protein phosphorylation, and intramolecular folding are also under active development. We are also extending many of these approaches for human clinical applications. New patient trials for PET imaging of T-cell trafficking in patients are being performed with our reporter gene strategies. We are also developing several new PET agents for cell surface targets based on new protein scaffolds.

Multimodality Molecular Imaging Lab

Cancer Molecular Imaging Chemistry Lab (CMICL)

Zhen Cheng, PhD

The main research of our group is to develop novel multimodality imaging probes and techniques for cancer early detection. Our multidisciplinary team is composed of members with expertise in organic chemistry, radiochemistry, bionanotechnology, biochemistry, molecular and cell biology, radiological science, medicine, and molecular imaging.

Currently, we are actively studying several important problems in the molecular imaging field. First, we are investigating a variety of novel platform molecules (peptides, proteins, nanoparticles) as universal strategies for cancer imaging. Second, we are establishing new methodologies for site-specific labeling these platform molecules for multimodality imaging. Third, by applying the knowledge obtained from the above research, we are optimizing PET and optical imaging probes for imaging of melanoma, breast cancer, prostate cancer, and ovarian cancer. We hope to quickly translate two molecular probes into clinical PET imaging in the very near future.

(l-r), front: Gang Ren, Jinhao Gao, Song Wu, Shibo Qi, Edwin Chang; back: Qizhen Cao, Kai Chen, Zhen Cheng, Eue-Soon Jang, Shuanglong Liu, Zhang Miao, Susan Hoppmann

Our research is supported by National Institute of Health, Department of Defense, the Melanoma Research Alliance and the Radiology Department at Stanford.

Research Group Updates

Molecular Imaging

Cellular and Molecular Imaging Lab (CMIL)

Jianghong Rao, PhD

The general research interest in the Rao lab is to develop novel molecular probes and imaging strategies for in vivo imaging by combining chemical synthesis and macromolecular engineering with imaging technology. Current projects are broadly defined in three areas: 1) imaging enzyme activity in vivo. As a unique class of protein molecules, enzymes catalyze biochemical transformations and are widely implicated in biological processes and diseases. We are developing "smart" activatable probes for imaging and detection of beta-lactamase activity from Mycobacterium tuberculosis (TB) in vivo to study TB biology and to evaluate the efficacy of therapeutics in preclinical animal models. The second class of enzyme target we are interested in is proteases, many of which display aberrant activity in diseases such as cancers and arthritis. We are employing both small molecule probes and nanoparticles-based nanosensors to in vitro detection and in vivo imaging of the activity of proteases such as matrix metalloproteinase-2 (MMP-2) and furin in cancer cells. Toward imaging these enzyme targets, different imaging modalities have been employed from optical imaging, to magnetic resonance imaging, to positron emission tomography. 2) A second major area of interest is developing general strategies to label proteins and RNAs in living cells for in vivo imaging. Our approach is to design small organic dye molecules that are not fluorescent initially but that become fluorescent after binding to a receptor or tag fused to either a protein or RNA molecule of interest. We are combining rational design and library selection methods, such as SELEX and phage display, to discover such novel molecular tags for super high resolution single-molecule imaging in living cells. 3) The third research focus is to develop novel sensing and imaging technologies. We mimicked the naturally occurring bioluminescence resonance energy transfer (BRET) system in the sea pansy, Renilla reniformis, and developed a QD-BRET technology widely applicable for in vitro biosensing and in vivo imaging. We are applying both protein engineering and nano engineering to create novel nanoparticles for imaging and sensing applications.

Nan Ma, Jocelyn Barker, Jianghong Rao, Jongho Jeon, Liqin Xiong, Jessica Gall, Young-Pil Kim, Zuyong Xia, Hexin Xie, Deju Ye, Kyung Hyun Lee, Yi Lin, Ke Zhan,

Molecular Imaging Instrumentation Laboratory (MIIL)

Craig Levin, PhD

Our research interests are to advance instrumentation and algorithms for the non-invasive imaging of basic cellular and molecular signatures associated with disease. These new "cameras" image photon emissions from molecular probes designed to target specific molecular processes associated with disease in cells located deep within the tissues of living subjects. The technical goals of the instrumentation projects are to advance the photon detection efficiency and spatial, spectral, and temporal resolutions. The algorithmic goals are to understand the physical system comprising the subject tissues, photon transport, and camera, and to realize the best available reconstructed image quality and quantitative accuracy. The work involves the design, development, and testing of novel position sensitive photon sensors and systems; low-noise readout electronics; data acquisition electronics; computer modeling; computer graphics; tomographic image reconstruction algorithms; signal/image processing algorithms; and data/image analysis. Key goals of our research are to incorporate these innovations into practical imaging devices and introduce new in vivo imaging tools to advance studies of molecular mechanisms and aid discovery of novel treatments of disease in the clinic as well as in preclinical research. If successful, these novel system will substantially enhance the visualization and quantification of subtle molecular signatures associated with disease with the hope that molecular imaging can play a role in earlier disease management.

Bottom row, left to right: Jinjian Zhai, Virginia Spanoudaki, Craig Levin, Garry Chinn, and Abdelkader Bousselham, Second Row from bottom, left to right: Faron Addison, Jing-Yu Cui, Eric Gonzalez, Frances Lau, and Ealgoo Kim, Third Row from Bottom: Yi Gu, Arne Vandenbrouke, Marie Feng, Jang-Hwan Choi, Four Row from bottom (Top Row): Derek Innes, Peter Olcott, Alex Grant, Zhiguang Wang, Hao Peng, Paul Reynolds, and Guillem Pratx.

The research is supported by grants from the National Cancer Institute, National Institute of Biomedical Imaging and Bioengineering, Department of Energy, GE Healthcare and Philips Healthcare. Trainee fellowships are supported by Stanford's Bio-X Program, School of Medicine Deans Fellowship Program, Stanford Molecular Imaging Scholars Program, Stanford REU Program, US Department of Defense, Society of Nuclear Medicine, Swedish Research Council, National Science and Engineering Research Council of Canada, China Scholarship Council, AXA Research Fund, and TLI Inc.

Cardiovascular and Molecular Imaging Lab (CMIL)

Joseph Wu, MD, PhD

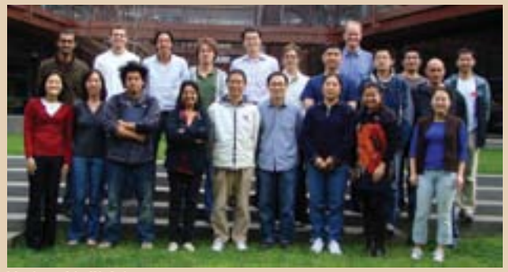
Members of the Wu Lab.

Ischemic heart disease is the number one cause of morbidity and mortality in the United States. The repeated ischemic insults can lead to congestive heart failure, which is the leading cause of hospital admissions for people aged 65 years and over. In the next decade, cardiovascular diseases will likely be targeted at the basic cellular and molecular levels. The Cardiovascular Cellular & Molecular Imaging lab (http://wulab.stanford.edu) combines expertise in molecular and cell biology, cardiovascular physiology, and molecular imaging. We work on the biological mechanisms of adult stem cells, embryonic stem cells, and induced pluripotent stem cells. We use a combination of gene profiling, tissue engineering, physiological testing, and molecular imaging technologies to better understand stem cell biology in vitro and in vivo. For adult stem cells, we are interested in monitoring stem cell survival, proliferation, and differentiation. For ESC, we are currently studying their tumorigenicity, immunogenicity, and differentiation. For iPSC, we are working on novel derivation techniques. We also work on development of novel vectors and therapeutic genes for cardiovascular gene therapy applications. The eventual goal is to establish molecular imaging as a platform for translational research in cellular and gene therapies for ischemic heart disease in the 21st century.

Molecular Imaging of Nocieption and Inflammation Lab (MINIL)

Sandip Biswal, MD


left to right: Deepak Behera, Archana Prabhakar, Sandip Biswal, Pejman Ghanouni, Bao Do. Not pictured: Kathleen Jacobs, Vijay Rao.

Chronic pain sufferers are unfortunately limited by poor diagnostic tests and therapies. The lab is interested in using multimodality molecular imaging techniques to study nocieption and neuronal inflammation as a means of improving objective, image-guided diagnosis and treatment of chronic pain generators. The past couple of years welcomed a number of exciting members and collaborations to the group. Justin Du Bois, PhD, William Parsons, BS, Frederick Chin, PhD, Aileen Hoehne, PhD, David Yeomans, PhD and the Biswal lab have formed a unique alliance to radiolabel guanidinium toxins, which are neurotoxins with nanomolar affinity for the tetrodotoxin-sensitive members of the voltage-gated sodium channels. Deepak Behera, DNB, the Biswal lab leader, has been playing an important role in this unique interdisciplinary collaboration fostered by Bio-X. In subjects suffering from neuropathic pain, Dr. Behera has preliminarily shown radiolabeled toxin localized to the site of nerve injury using PET-MRI. Kathleen Jacobs, BS, a Stanford medical student has determined whether manganese, a MR contrast agent and surrogate marker for calcium flux, can be administered orally to identify hypersensitive pain-sensing nerves using MRI. Her work has resulted in a Travel Award to the 2010 ISMRM. Pejman Ghanouni, MD, PhD, previously a Radiology Resident and currently an NCI Fellow, has used ultrasmall paramagnetic iron oxide particles to track circulating macrophages. He found macrophages would traffic to the site of nerve injury in subjects suffering from neuropathic pain. In subjects with neuropathic pain but treated with minocycline, an agent known to 'deactivate' macrophages, not only would the macrophages be inhibited from trafficking to the site of nerve injury, but also the subjects would experience less pain, suggesting an important relationship between macrophages, neurons and the pain experience. This work won Dr. Ghanouni a 2009 RSNA Research Scholar Award. Vijay Rao MD, a Radiology Resident from SCVMC, used his spare time to determine that [18F]NaF PET-CT could more accurately determine painful metastatic bone lesions than [18F]FDG PET-CT. This work won him a 2009 RSNA Research Scholar Award. Subrat Behera, MBBS, joined the lab recently to help with the lab projects and to initiate collaboration with Dr. Jyotsna Rao, a nuclear medicine physician in Hyderbad, India. Drs. Archana Prabhakar and Sumit Singh have also recently joined the lab and will be studying the role of various neuronal mediators in chronic pain models using PET-MRI. Important collaborations with the Stuart Goodman Lab continue to thrive as we have been examining the role of mesenchymal stem cells and macrophages in the prosthetic-induced osteolysis and in fracture models. A new collaboration with Pankaj Jay Pasricha MD, Chief of the Division of Gastroenterology and Hepatology, has formed in hopes of finding better PET-based methods to study abdominal pain syndromes.

Cellular Pathway Imaging Laboratory (CPIL)

Ramasamy Paulmurugan, PhD


l to r: Thillai V. Sekar, Ramasamy Paulmurugan, Aradhana Dhanabalan

Breast cancer is a highly heterogeneous disease, and there is a growing body of evidence that this heterogeneity arises at both genetic and phenotypic levels. The heterogeneous nature of breast cancer complicates the issue of developing a general therapeutic scheme that can be used to treat breast cancers of different sub-types. Although breast cancer researchers have improved the efficacy of therapies, especially for a sub-type of breast cancer that is estrogen receptor positive (endocrine therapy), the increase in the incidence of receptor negative phenotype, and the presence of receptor positive anti-estrogen non-responsive (tamoxifen resistant) phenotype, have contributed to the increase in the mortality rate of breast cancer. Our lab focuses on developing new therapeutic strategies for treating receptor negative and tamoxifen resistant breast cancers as well as imaging estrogen receptor (α and β) ligand interactions to elucidate the basic mechanisms involved in the development of tamoxifen resistance by the receptor positive sub-type. Endocrine therapy is mainly designed to target ERα, and is considered to be negative in receptor negative breast cancers. The discovery of ERβ thus raises the concern of its status in receptor negative breast cancers, but also opens the option to use ERβ specific ligands for endocrine therapy. Specifically, we are interested in developing a combinatorial therapeutic approach in which we will use ERβ- specific ligands in combination with the down-regulation of some specific microRNAs (miR21, miR10b, miR335, miR155, miR373 and miR520c) that are over-expressed in receptor negative breast cancers. As ERβ currently is not explored in these sub-types of breast cancers, this strategy, if successful, has enormous potential as a new anti-estrogen therapy (β-specific) for receptor negative breast cancers. The anti-sense microRNAs will be explored to block the functions of microRNAs that are over-expressed. In addition, our lab is also developing new in vivo imaging assays for monitoring different epigenetic processes (DNA-methylation, histone methylation, and histone acetylation) that are critical for maintaining cellular homeostasis, and are considered to be a potential therapeutic target for treating many diseases arising from altered cellular homeostasis such as different types of cancers.

Translational Molecular Imaging Lab (TMIL)

Jürgen K. Willmann, MD


left to right: Juergen K. Willmann, MD; David Wang, MD; Nirupama Deshpande, PhD; Alice Gardner; Ying Ren, MD; Marybeth Pysz, PhD; Sunitha Bachawal, PhD

In the United States, cancer continues to be the leading cause of death in patients between 25 and 64 years of age, and the second leading cause of death in patients both above 65 years and between 1 and 14 years. Prognosis and survival of patients with cancer very much depends on what tumor stage the cancer is at the time of diagnosis, and therefore early cancer detection is showing great promise in prolonging survival and improving quality of life for cancer patients. Consequently, novel imaging strategies that allow detection of cancer at early, still curable stages are highly desirable. With the advent of novel therapeutic options for cancer patients, there is an increasing demand for non-invasive imaging biomarkers to identify those patients early on who benefit most from a given treatment or to modify/terminate treatment for those patients not responding to treatment.

In our lab, we focus on the development and clinical translation of novel molecular and functional imaging biomarkers. We have a special focus on imaging abdominal and pelvic cancer including pancreatic, liver, renal, ovarian, and prostate cancers. We further advance clinically available radiological imaging modalities such as ultrasound, magnetic resonance imaging (MRI), and positron emission tomography (PET) as promising imaging tools for early detection and treatment monitoring of abdominal and pelvic cancer.

Our mission is to translate these novel molecular and functional imaging strategies into clinical protocols for improved patient care in the shortest possible time frame.

Facilities

Radiology Imaging Facilities

Department of Radiology Clinical Imaging and Research Locations

In order to accommodate the Department of Radiology's expanding clinical services and research needs, we now occupy space in several areas on campus and off campus. The following gives a sense of how broadly situated our Department has become, including facilities on the Stanford campus, Palo Alto, and in Redwood City.

Clinical Imaging Facilities

- Medical School Campus
- Stanford University Hospital
- Lucile Packard Children's Hospital
- The Stanford Cancer Center
- Blake Wilbur Imaging
- Diagnostic Radiology Center, VA Palo Alto
- Stanford Medicine Outpatient Center, Redwood City
- Stanford Medicine Imaging Center, Sherman Avenue, Palo Alto

Research Facilities

- The Richard M. Lucas Center for Imaging
- The James H. Clark Center
- Edwards Building
- Grant Building
- Alway Building
- 1501 California Avenue, Palo Alto
- 480 California, Palo Alto

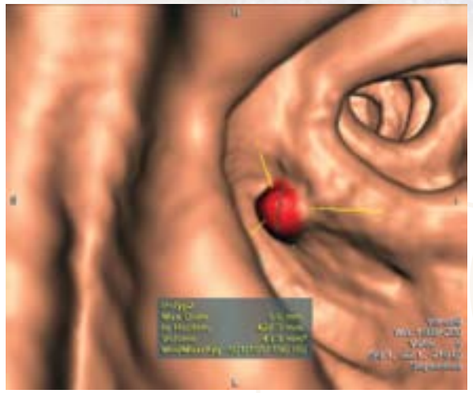

Figure1. Endoscopic view of a colon polyp discovered and documented in the 3D Laboratory utilizing Vital Images 3D Imaging software.

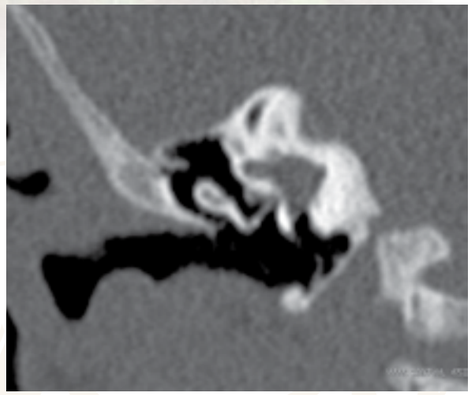

Figure 2. Volume Rendered view of the bones in the inner ear, created in the 3D Laboratory with Vital Images Vitrea FX 3D software.

Stanford 3D Medical Imaging Laboratory

Geoffrey Rubin, MD
Sandy Napel, PhD
Laura Pierce, MPA, RT(CT), Lab Manager

The Stanford 3D Medical Imaging Laboratory is guided by the mission of developing and applying innovative techniques for efficient analysis and display of medical imaging data through interdisciplinary collaboration. Since 1996, our clinical goal has been to deliver 3D imaging advances as rapidly as possible for the swift and accurate diagnosis and treatment of disease; our educational goal is to disseminate knowledge and duplicate our 3D services at other institutions; and we continue to facilitate cutting edge research through our collaborations with faculty in Radiology sand other Departments. To facilitate the bridge between innovation and other clinical use of technology, we also offer services as an imaging core lab for medical device developers.

Back row, left to right: William Johnsen, RT (CV) (RCIS), Lakeesha Winston BA, Linda Novello, RT (MRI), Kala Raman MS, Kristen Bogart, RT, Nancy Ware, RT, Shannon Walters, BA, RT (MRI), Debra Frank, John William Weidenger, RT, Marc Sofilos, RT. Front row, left to right: Geoffrey Rubin, MD, Laura Pierce, MPA, RT (CT), Sandy Napel, PhD. Missing, pictured on monitor: Keshni Kumar, CRT.

Progress

Clinical: Over the past year, the 3D Laboratory has continued its operations simultaneously in the Lucas Center as well as the James H. Clark Center, a building dedicated to interdisciplinary science. Our average monthly 3D volume has increased to approximately 950 examinations, and we have processed over 78,000 examinations overall since our inception. The majority of our referrals continue to come from vascular surgery, cardiothoracic surgery, gastroenterology, cardiology, urology, reconstructive surgery, orthopedics, neurology and neurosurgery. 3D clinical procedures now offered by the Lab include CT Virtual Colonoscopy for both diagnostic and screening evaluation of polyps (fig 1), CT Temporal Bones for visualization of tiny structures in the inner ear (fig 2), and MR Heart for quantification of muscle mass, ejection fractions, and flow velocity (fig 3).

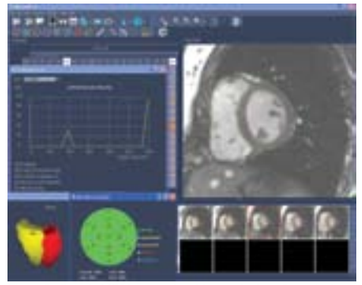

Figure 3. Sample MRI heart study with quantitation of ventricular ejection fractions and myocardial mass.

Education: This year the 3D Laboratory has been attended by international visiting scholars from Japan, as well as Stanford Radiology fellows, residents, and medical students who acquire skills in 3D interpretation as part of their medical training. Stanford researchers from engineering and medical departments have also been trained in acquiring 3D images and data for research projects, including measurements of craniofacial deformities for reconstructive surgery, pulmonary vasculature volumes for 3D model fluid flow simulations for vascular surgery, and 3D modeling for multimodality small animal imagers. The 3D Laboratory has also hosted several visiting radiology managers and technologists from domestic and international medical centers through our 3D clinical fellowship program.

Infrastructure

3D imaging specialists include: Laura Pierce, 3D Laboratory manager; senior 3D technologists Marc Sofilos and Linda Novello; 3D technologists Keshni Kumar; William Johnsen, Nancy Ware and Shannon Walters. Technologists John William Weidinger and Kristen Bogart provide per diem 3D services to maintain up-to-date workflow (image 1). Our technologists offer not only expertise in 3D imaging, but also experience in CT and MRI scanning techniques as well. Support staff includes administrative assistants Lakeesha Winston and Debra Frank, and database administrator, Kala Raman. The research arm of the lab retains an annual average of 12 engineering graduate students and post-doctoral scholars as well as 2 clinical MD researchers. In the Clark Center, a central area table invites professional collaboration, and student desks with moveable workspaces provide areas for independent research. The Lucas Center 3D Laboratory also houses equipment on a central area table, surrounded by student carrels. The lab equipment comprises a total of 13 advanced 3D workstations, three TeraRecon servers, which also provide remote 3D rendering to the Stanford medical community, and two research and development servers for image and data storage. Three remote PACS workstations allow access to all Stanford medical imaging and reporting.

We continue our excellent relationships with corporate developers of 3D workstations (e.g., GE Healthcare, TeraRecon, and Vital Images) who site their hardware and software in the 3D lab in anticipation of our feedback. These relationships ensure that we maintain the most advanced multi-dimensional analytical technologies available. To expedite workflow and allow for flexible workspaces, we are upgrading the infrastructure of the 3D Laboratory to access all 3D software applications on centrally located vendor-supplied servers, to allow for processing and sharing of image data throughout our enterprise on generic PC workstations. We have already begun this transition by utilizing the TeraRecon Intuition® server from multiple locations for real-time interactive 3D rendering, and the MEDIS QMass® and QFlow® analysis software which allows for enterprise collaboration when measuring cardiac output and analyzing muscle mass.

Conclusion

The 3D Medical Imaging Laboratory continues to function as an international leader in clinical care, teaching, and research in medical imaging analysis. The confluence of talented, medical and engineering expertise as well as the most up-to-date equipment has been a consistent source of innovative developments in diagnostic and treatment planning approaches.

Animal Model Management

Wendy Baumgardner, RVT, LATg
Pam Hertz, RVT

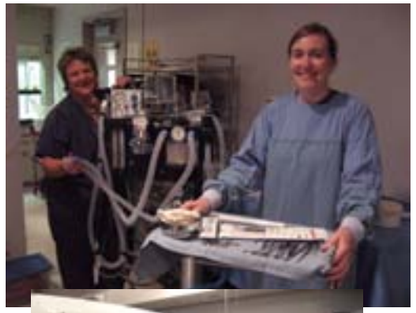

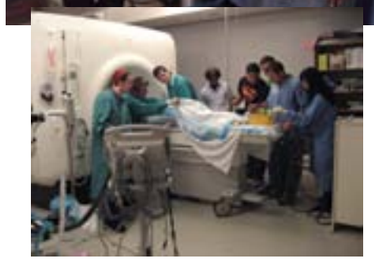

In our continuing efforts to provide support to the Radiology investigative staff, we are entrusted with the responsibility of overseeing all animal model protocols within our department and all other departments carrying on research studies at the Lucas Center. Two-experienced California Licensed Veterinary Nurses (RVT), with over 32 years in the field, support all animal model studies and ensure the health and welfare of the animal is always our most important priority. Diligent care is taken during all procedures involving animal subjects; they are treated with the utmost respect, compassion, and professional care. Animal studies at the Lucas Center enhance both treatment and diagnostic abilities for human patients, and are considered equal to our compassion for clinical patient medical imaging and examinations.

All personnel working with animal models under approved Institutional Animal Care and Use Committee (IACUC) protocols have completed required training from Stanford University Department of Comparative Medicine. In addition, specifically tailored "one on one" training for more advanced techniques are taught by the veterinary technicians at the Lucas Center.

We realize that living subjects are needed to advance our knowledge, and to that end we ensure that proper respect for life is part of all research studies. Research conducted at the Lucas Center improves and develops new invasive and non-invasive procedures that utilize magnetic resonance imaging (MRI), high intensity focused ultrasound (HIFU), computed tomography (CT), CT/fluoroscopy, and positron emission tomography (PET) to guide them. Clinical studies currently conducted include the study of cardiac and liver radio frequency (RF) ablation, myocardial infarction, liver and prostate cancers, neuromodulation with ultrasound, and structural neuroimaging of the brain. The techniques currently being explored at the Lucas Center contribute to more efficient and effective medical treatment for human illness and disease.

Small Animal Imaging Center - SCi3

Tim Doyle, PhD, Head, Small Animal Imaging Facility, MIPS

The Stanford Center for Innovation in In Vivo Imaging (SCi3) has seen another successful year as a shared core facility, both in terms of instruments available and time used on the equipment. Demand for instrument time has increased by about ten percent, and we have purchased new instruments, which are now available to the research community at Stanford. Oversight of the core has been transferred from the Department of Pediatrics (Neonatology) to the School of Medicine. The Dean of the SoM, along with the University President and the Department of Radiation Oncology, generously provided unrestricted funds to the core, thanks to the efforts of Professor Gambhir. These were used earlier in the year to purchase a second small animal ultrasound scanner, which provides improved functionality as well as increasing the capacity to image animals with this popular modality. We will use the remainder of these funds to replace our aging MicroPET R4 scanner, which has been the workhorse PET scanner of the facility, and have just placed an order for the latest Inveon MicroPET-CT scanner. This system will permit automated co-registration of PET and CT scans of mice and rats, in addition to providing CT-based attenuation correction of the MicroPET data.

Professor Michael Moseley recently received notice that his NIH small instrument grant to upgrade our small animal 7 Tesla MRI was funded. This will provide funds to replace the gradient coil with a pair of "nested" coils, along with other upgrades that will hopefully provide greater utility of the MRI. Dr. Brian Rutt also secured funds from the Department of Neurosciences, with matching funds from the Bio-X program to help with these upgrades, and we hope that the hardware will be installed before the end of the year.

Finally, the planning of a second Small Animal Imaging Facility to be located in the basement of the new Lorry I. Lokey Stem Cell Research Building (lokey.stanford.edu) were finalized this year, and will be occupied in September. This new core will serve animals housed in a clean "barrier" facility, which is also located in the basement of this building. The new core will run in parallel with the current facility, serving the two populations of mice housed at Stanford (those in the new barrier, as well as those in current housing facilities). The core will initially be equipped with an Inveon MicroPET-CT scanner, funded by the CIRM, as well as an IVIS Optical Imaging system that was purchased by Prof. Irving Weissman, and has space to expand to the other modalities already in place in the SCi3, such as SPECT, ultrasound, MRI and MicroCT. This extra imaging capacity will ensure that Stanford remains a leader in Molecular Imaging.

Lucas Center MR Systems

Anne Marie Sawyer, BS, RT (R)(MR), FSMRT
Sandra Rodriguez, BS, RT (R)(MR)

1.5T, 3T1, 3T2 AND 7T Whole Body Magnets

Research Support 2009 - 2010

The 1.5 Tesla (Figures 1 and 2) and 3.0 Tesla #1 GE Healthcare MR systems are currently operating at 15.x systems revision; the 3.0 Tesla #2 "750" (Figure 3) at 20.x software; and the 7.0 Tesla (Figure 4) at 12.x. The systems operate at a maximum slew rate of 150 Tesla per meter per second and maximum gradient amplitudes of 50 milliTesla per meter (1.5T and 3T2) and 40 milliTesla per meter (3T1 and 7T). The hardware currently allows the use of 8-channel phased array coils at 1.5T; 16 channels at 3T1 and 7T; and 32 channels at 3T2.

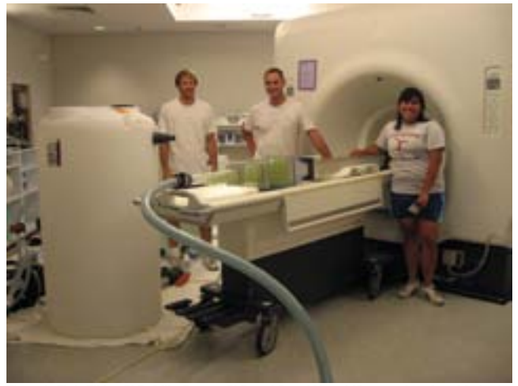

Figure 1. Chris Elkins, PhD, Mike Benson, PhD, and Sayuri Yapa, MS, researchers from Mechanical Engineering prepare for MR scans using a mechanical flow phantom at the 1.5T whole body magnet.

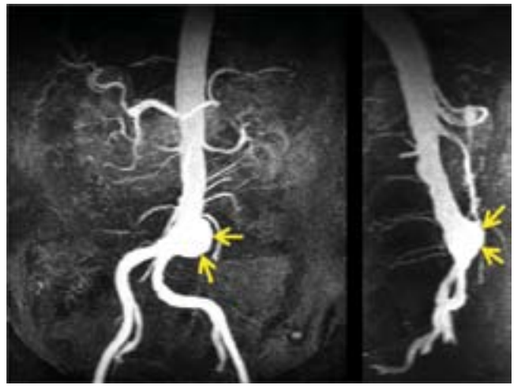

Figure 2. MR image of the abdominal vessels acquired at 1.5T using an 8-channel abdominal phased array coil demonstrating an aneurysm in the aorta (arrows) seen in an 3D coronal image (left) and in a reformatted sagittal image (right).

Figure 3. Anja Brau, PhD, GE Healthcare and Rafael O'Halloran, PhD, collaborate on high speed imaging of brain function at the 3T2 GE Healthcare '750' MRI system.

Figure 4. At the 7.0T whole body magnet, researchers Tom Brosnan, PhD and Murat Aksoy, PhD, review a prototype head coil with GE Healthcare scientist Mohammad Khalighi, PhD and GE Healthcare engineer Mina Makram, B.S.

Daily support in MR system operation and screening and safety is provided to all researchers including faculty, post-doctoral fellows, graduate students, and visiting scholars in the Lucas Center and Department of Radiology; researchers from other University departments such as Psychology, Psychiatry, Neurology, Neurosurgery, and Nephrology; and service center users from outside of the University.

Cyclotron Suite Update

Frederick Chin, PhD
David Dick, PhD

The Radiochemistry Facility (RF) develops and offers radiotracers for early detection and therapeutic monitoring of disease in both preclinical and clinical imaging settings. Radiochemistry personnel (faculty, staff, and postdocs) numbers around 30 people. New instruments that were recently installed include an Eckert & Ziegler Radiosynthesis Modular Lab with autosyringe and two high-pressure liquid chromatography systems with autosamplers. The facility is expanding to include radiochemistry space for making clinical-grade radiopharmaceuticals in the new Molecular Imaging Clinic that is scheduled to open in October. The additional space will meet essential clinical radiochemistry demands as well as comply with current regulatory policies. The existing radiochemistry labs continue to provide tracers for pre-clinical investigations and maintains our [C-11]carbon dioxide and [F-18]fluorine gas radiochemistries for all our research needs.

From Left to Right: Bin Shen, Aileen Hoehne, Rhona Berganos, Fred Chin, Michelle James, George Montoya, and David Dick

Our staff provides routine clinical tracers for use at the Stanford Hospital. Fluorine-18 labeled fluorodeoxyglucose (FDG) is still produced daily (now 6-days/week) and can also be made using the new FASTlab FDG system with much higher yields relative to the current MX-FDG module. Nitrogen-13 ammonia (myocardial perfusion assessment) and Fluorine-18 sodium fluoride (bone imaging) are also synthesized for the clinic as needed.

GE TRACERlab modules are the workhorses in the lab and perform the syntheses of our ^{18}F and ^{11}C-labeled radiotracers for collaborative researchers at Stanford and pharma. These modules have enabled us to perform new radiochemistries, providing [^{18}F]EF-5 (imaging tumor hypoxia) and [^{18}F]FPPRGD2 (imaging tumor angiogenesis) for human studies. Additional PET radiotracers that study the mechanisms and treatment of cancer as well as neurological disorders will soon become available to meet the increasing needs for performing preclinical ([^{11}C]raclopride, [^{18}F]saxitoxin, [^{18}F]FBR, [^{18}F]FTC-146) and clinical ([^{64}Cu]rituximab, [^{18}F]Avid/Bayer compounds) research studies with PET.

Radiolabeled Compounds

The following table summarizes an updated list of requested radiolabeled compounds that are made in the research radiochemistry lab, excluding research compounds protected under confidentiality agreements (**Bolded tracers** = preclinical and clinical use).

Tracer	Use	Application
[^{11}C]Raclopride	Imaging dopamine-2 receptors (D2R)	Monitoring D2R-related neurological disorders (i.e. Parkinson's Disease)
[^{11}C]PIB	**Imaging αβ amyloid in brain**	**Monitoring progression of Alzheimer disease in brain**
[^{18}F] FAZA	Hypoxia imaging agent	Evaluating clinical-relevant hypoxia-directed cancer therapies
[^{18}F]MISO	Hypoxia imaging agent	Evaluating clinical-relevant hypoxia-directed cancer therapies
[^{18}F]EF-5	**Hypoxia imaging agent**	**Evaluating clinical-relevant hypoxia-directed cancer therapies**
[^{18}F]Fluorouracil	**Tumor imaging agent**	**Evaluating clinical-relevant cancer therapies**
[^{18}F]CBT	Prosthetic labeling group	Radiolabeling peptides with specific cysteine moiety
[^{18}F]fluorobenzaldehyde	Prosthetic labeling group	1) Radiolabeling peptides for potential clinical use 2) Radiolabeled affibody for imaging of NER2neu
[^{18}F]fluorobenzoic acid	Prosthetic labeling group	Radiolabeling peptides for potential clinical use
[^{18}F]Fluoropropionic Acid	Prosthetic labeling group	Radiolabeling peptides for potential clinical use
[^{18}F]SFB	Prosthetic labeling group	Radiolabeling peptides for clinical use
[^{18}F]FBR	Imaging agent for TSPO receptors (formerly known as peripheral benzodiazepine receptors)	Monitoring neuroinflammation induced by stroke or radiotherapy
[^{18}F]FEAU	Imaging substrates expressing mutant HSV1-sr39tk	1) Monitoring gene therapies targeting cancer 2) Monitoring cell therapies
[^{18}F]FHBG	**Imaging agent for tumors expressing HSV1-tk**	**Monitoring various cancer therapies**
[^{18}F]FLT	**Imaging agent for tumor cell proliferation**	**Monitoring various cancer therapies**
[^{18}F]FPPRGD2	**$\alpha_v\beta_3$ integrin imaging agent**	**Imaging tumor integrin expression**
[^{18}F]FTC-146	imaging agent for sigma-1 receptor	Imaging agent for studying depression, Scizophrenia, Alzheimer's Disease, drug addiction, and certain cancers (e.g., prostate, breast)
[^{18}F]Saxitoxin	imaging agent for sodium channels	Imaging agent for sodium channels linked to pain
Other ^{18}F-labeled RGD peptides	$\alpha_v\beta_3$ integrin imaging agent	Imaging tumor integrin expression

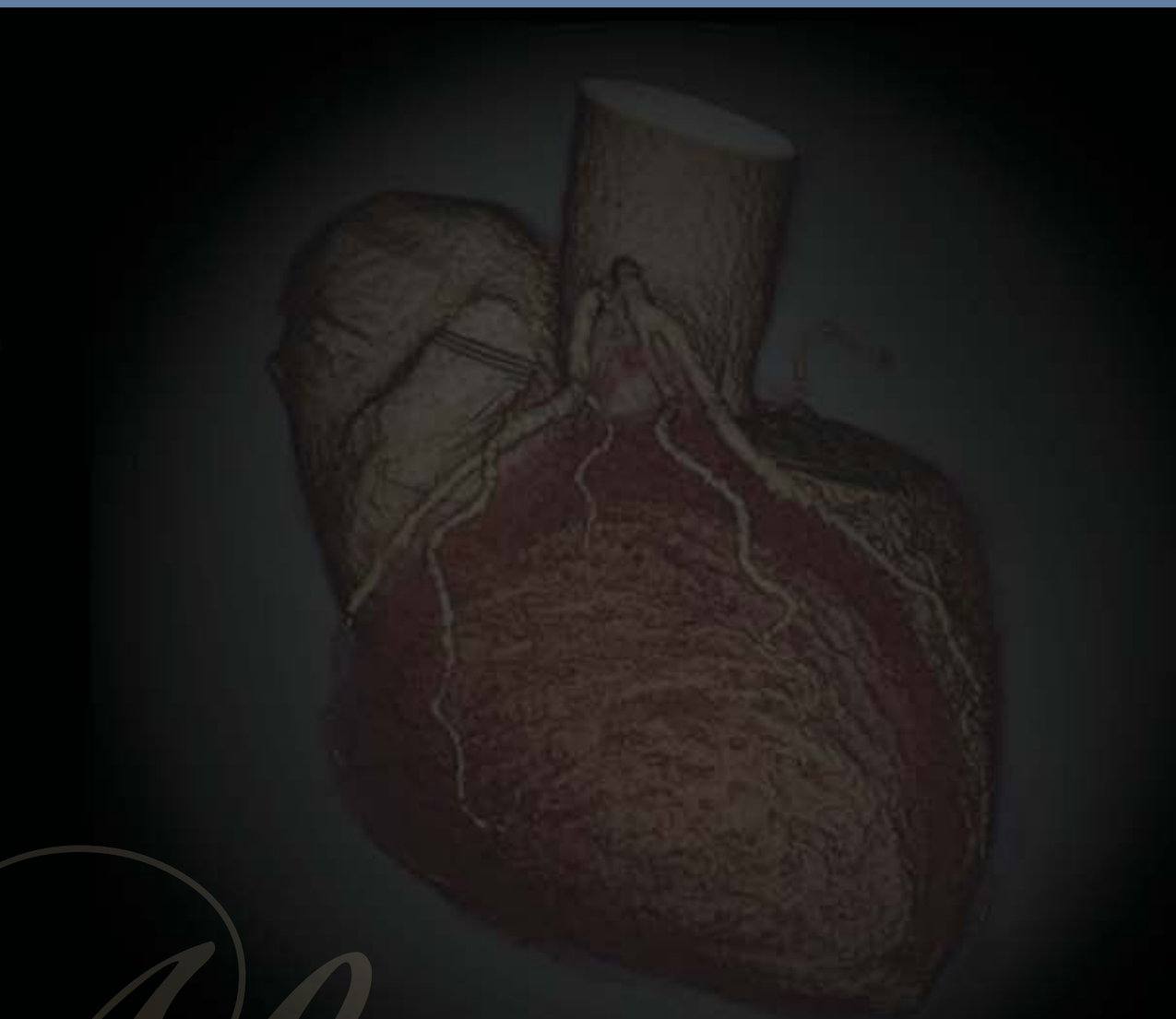

Abstracts

Advanced X-Ray and Computed Tomography (CT) Techniques

Advanced X-Ray and Computed Tomography (CT) Techniques

Abstracts in this section describe research that is conducted using sophisticated x-ray and Computed Tomography (CT) techniques to improve image quality, decrease the amount of radiation exposure, or reduce the amount of time required to complete an exam. The overall goal of these projects is to improve our ability to detect and monitor disease using these x-ray based methods.

Emission Guided Radiation Therapy (EGRT) System: A Feasibility Study

S Mazin[1,3], A Nanduri[3], NJ Pelc[1,2]
Departments of [1]Radiology and [2]Bioengineering, Stanford University, CA; [3]RefleXion Medical Inc., Menlo Park, CA

Purpose: We are developing a combined PET-radiotherapy system that will perform real-time adaptive radiation therapy to account for tumor motion due to respiration. This will enable biological targeting and will obviate the need for implanted fiducial markers for stereotactic treatments.

Methods: One method to compensate for respiratory motion is to deliver radiation beam-lets along individual PET emission paths as they are detected. The system involves rotating a radiation therapy source and PET detectors on a gantry while dynamically controlling a binary multi-leaf collimator to deliver the beam-let responses in a helical mode. Simulations were conducted using GATE to model 300 seconds of PET list-mode acquisition of a 'hot' 3 cm diameter tumor exhibiting 3.7 second periodic 2 cm peak-to-peak motion in a 'warm' background. A 5 cm planning target volume (PTV) was used as a filter to reject emissions that did not intersect this volume. Emissions that intersected the PTV and whose time-stamps were within a 500 ms cutoff window were responded to. A voxel-based Monte Carlo simulation package was used to model the resultant dose distributions comparing the emission guided (EGRT) method with uniform coverage of the PTV. Composite dose volume histograms were calculated using 12 phases of the motion cycle. Dose to the non-tumor volume was normalized to the same mean value for both scenarios.

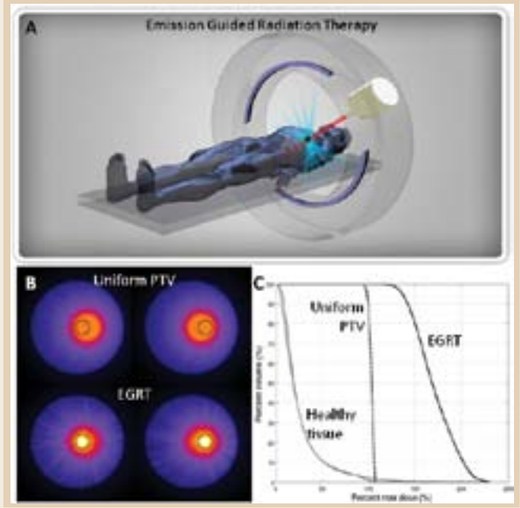

Results: The EGRT approach exhibited a non-uniform dose distribution to the tumor compared to uniform PTV coverage. However, even with the non-uniformity, there was a 30% relative increase in minimum dose to the tumor volume for the EGRT approach.

Conclusion: Although this basic EGRT method results in inhomogenous dose to the tumor, the feasibility of using PET to guide radiation delivery in real-time has been demonstrated.

A Comparison of Four Algorithms for Metal Artifact Reduction in CT Imaging

CT Golden[1], SR Mazin[1], FE Boas[2], G Tye[1], P Ghanouni[1], GE Gold[3], M Sofilos[1], NJ Pelc[1]
Departments of [1]Radiology, RSL, [2]Radiology, [3]Radiology, Neuromuscular and Biomechanics Laboratory, Bioengineering, Stanford University, CA.

Streak artifacts caused by the presence of metal have been a significant problem in CT imaging since its inception in 1972. With the fast evolving industry of medical devices, the level of metal objects implanted in patients is increasing annually. This correlates directly with an increased likelihood of encountering metal in a patient CT scan, thus necessitating the need for an effective and reproducible metal artifact reduction (MAR) algorithm. Comparisons between MAR algorithms have been limited by the range of metal implants evaluated and the scope of anatomical regions from which patient data was taken. Although, the results of many methods are promising [1-4], the reproducibility of these results is key to providing more tangible evidence of their effectiveness. This study presents a direct comparison between the performances of four MAR algorithms: 3 non-iterative and one iterative method, all applied and compared to the original clinical DICOM images. The resulting data was subdivided into near region of interest (ROI) (Use 1), far ROI (Use 2), 'small' metal (Use 3) and 'large' metal (Use 4). The average radiologist score for each algorithm was calculated, and the data was also subdivided into 25th and 75th percentiles, and standard deviation of the radiologists' scores in the four sets of results. The individual scores for each use can be seen in Figure 2(a-d).The results of the evaluation indicated a negative mean score in almost all uses for two of the non-iterative methods, Rubout and Wei, signifying an overall decrease in the diagnostic quality of the images, generally due to perceived loss of detail. One non-iterative algorithm, Rubout Plus showed a slight improvement. The iterative algorithm, Metal Deletion Technique (MDT) was superior in all studies by producing a considerable improvement in all uses.

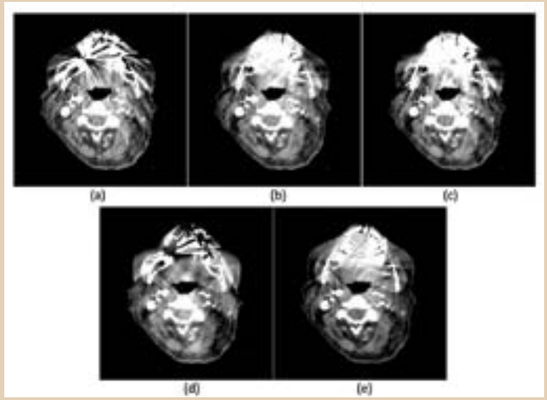

One of the 80 CT slices evaluated in the study. (a) Original image, (b)-(e) corrected image using Rubout, Rubout Plus, Wei, and MDT, respectively.

References/Funding Source The Lucas Foundation. CT Golden, SJ Mazin, FE Boas, G Tye, P Ghanouni, GE Gold, M Sofilos, NJ Pelc, "A comparison of four algorithms for metal artifact reduction in CT imaging", Proc. SPIE: Medical Imaging 2011, submitted.

Synthetic CT: Simulating arbitrary low dose single and dual energy protocols

AS Wang[1,2], NJ Pelc[1,2,3]
Departments of [1]Electrical Engineering, [2]Radiology, [3]Bioengineering, Stanford University, CA

While imaging protocol is a critical determinant of radiation dose and image quality, it is difficult to find the protocol (kVp, mAs, filtration) that offers the lowest dose for images of appropriate diagnostic quality. Therefore, we developed a method for retrospectively synthesizing CT scans of arbitrary kVp and filtration for low dose single and dual energy protocols using a previously acquired dual energy scan.

Axial scans of a phantom were acquired on a GE CT750 HD system at 80 kVp and separately at 140 kVp. Additional scans at 100 and 120 kVp and at different exposures were made to compare with synthesized results. Material decomposition is performed in projection space, and the desired spectrum is transmitted through the material decomposition. However, to synthesize realistic single energy scans and dual energy decompositions, the noise must have the correct statistics. The original data has an inherent noise that can be found from the covariance of the decomposition. Noise is then added so that the total noise matches the expected noise of the simulated protocol.

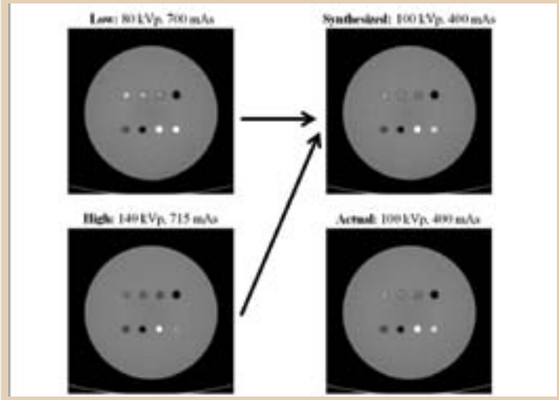

A low and high energy scan (left) are used to synthesize a 100 kVp, 400 mAs image of the same object (top right). The synthesized image has identical properties to the actual scan (bottom right). Other kVp and mAs combinations can be synthesized – for instance, 100 kVp at exposures 900 mAs and below (down to the electronic noise limit) or 120 kVp at exposures 1000 mAs and below.

The resulting synthesized 100 kVp scans are indistinguishable from the actual 100 kVp scans. Similarly, a synthesized 100/120 kVp dual energy decomposition is equivalent to the actual decomposition. In conclusion, synthetic CT enables users to see the impact of protocol changes on the contrast and noise of single and dual energy scans by providing realistic feedback that can be used to develop lower dose protocols for future scans by demonstrating dose/noise/protocol trade-offs and source filtration effects.

References/Funding Source GE Healthcare and the Lucas Foundation. NJ Pelc, "Simulation of Single and Dual Energy Protocols Based on Clinical Data," International Society for Computed Tomography: MDCT Symposia in San Francisco, 2010. AS Wang and NJ Pelc, Synthetic CT: Simulating arbitrary low dose single and dual energy protocols from a dual energy scan (in preparation).

Effect of Image Lag on Noise Power Spectrum

J Baek[1], NJ Pelc[1,2,3]
Departments of [1]Radiology, RSL, [2]Bioengineering, [3]Electrical Enginnering, Stanford University, CA

Purpose: We examined the effect of detector lag on CT image noise and quantified it with noise power spectrum (NPS). Methods: We first derived an analytical expression of the NPS with image lag, and then verified it using computer simulations. The dependence of the NPS on image lag coefficients (i.e., "High lag" and "Nominal lag"), location and size of the ROI, and the number of views used in the reconstruction (i.e., 500 and 1,000 views) was investigated with uniform and view dependent non-uniform noise profile. For image reconstruction, we chose a parallel beam geometry since it otherwise would have stationary noise behavior, to show the effect of image lag most clearly. Results: The NPS with "High lag" coefficients showed more noise correlation in the azimuthal direction and reduced the amplitude of the NPS. The azimuthal blurring increased with increasing radial distance, and therefore the local ROI images centered at the larger radial distance had lower noise power. In addition, the NPS of a smaller ROI image showed lower noise power due to increased noise correlation. With constant lag per sample, compared to a noise image reconstructed with 1,000 views, a noise image reconstructed with 500 views showed more noise correlation which decreased the amplitude of the NPS. Conclusions: The shape of the NPS showed the dependence on image lag coefficients, location and size of the ROI, and the number of views used in the reconstruction. In general, the noise correlation caused by image lag decreased the amplitude of the NPS.

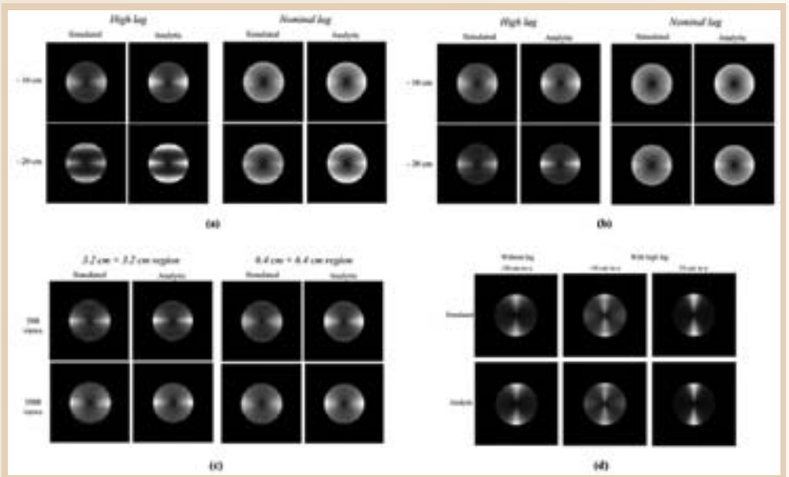

(a) NPS with 500 views. (b) NPS with 1000 views. (c) NPS dependence on ROI size. (d) NPS with view dependent nonuniform noise.

References/Funding Source GE Healthcare, Lucas Foundation, and NIH grant EB006837

Multi-spot Inverse Geometry CT (IGCT) System

NJ Pelc[1,2,3], J Baek[1], RJ Herfkens[1], D Fleischmann[1]
Departments of [1]Radiology, RSL, [2]Bioengineering, [3]Electrical Engineering, Stanford University, CA

Purpose: The aim of this NIH-funded collaboration with GE's Global Research Center is to build the first-ever gantry-mounted IGCT system. Methods: In contrast to conventional CT scanners which have one or perhaps two x-ray sources, the IGCT architecture uses a wide distributed source array and a detector that is narrower in the lateral direction. Each source only illuminates a portion of the object, allowing customization of the radiation field and significant dose reduction. We completed construction of a 2x4 (z*x) source module (left image) in which each source can be independently addressed and energized. The source array, along with a custom 256x64 (z*x) detector array were integrated into a rotatable gantry (center image). After careful dynamic balancing, we demonstrated the ability to rotate the system at rotation times as fast as 1 sec and to collect x-ray transmission data. The measured data are rebinned into full FOV and reconstructed. With one source module we can image a ~7.2 cm (lateral) by ~15 cm (axial) field of view. Results: The sources demonstrate operation with switching times of ~1 μs. Initial images of small phantoms and an ex-vivo rat were recently acquired (right image). Conclusions: We were successful in the development and very preliminary testing of a gantry-based IGCT system. Three additional source modules are under construction that will increase the lateral field of view by a factor of ~4. The system is expected to demonstrate significant dose reduction compared to conventional systems at the same image quality.

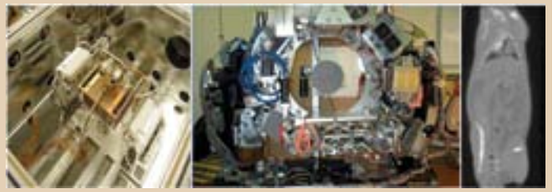

(left) photograph of the 2x4 module in its vacuum vessel (center) IGCT gantry (right) sagittal rat image

References/Funding Source NIH grant EB006837, and the Lucas Foundation

An Inverse Geometry CT System with Scanned Stationary Source Arrays

SS Hsieh, NJ Pelc
Department of Radiology and Electrical Engineering, Stanford University, CA

Traditional CT systems face a tradeoff between temporal resolution, volumetric coverage and cone beam artifacts. Inverse geometry CT (IGCT) enhances volumetric coverage while suppressing cone beam artifacts by placing a small, agile detector opposite a large, rotating scanned source array. However, like traditional CT systems, its temporal resolution is ultimately limited by the gantry rotation speed, which in turn is limited by mechanical constraints introduced by the heavy, and possibly fragile x-ray source. By replacing this rotating source with a series of stationary scanned sources we can greatly accelerate gantry rotation speeds and hence temporal resolution. We investigate the feasibility of this design. We anticipate that it will be necessary to have a physical separation between the separate source arrays, gaps in the sinogram will appear which in most cases prohibit reconstruction with standard techniques. However, in the case of three source arrays, a triangular field of view emerges where the gaps can be filled in using symmetry. A timing and collimation scheme was developed that efficiently uses the source array and small detector to virtually build up fan-beam sources with large detector except within the gaps. In simulations, the two-dimensional MTF and noise characteristics are comparable to a parallel-beam scan. We anticipate that under this scheme, a complete volumetric scan can be completed within 100 milliseconds.

Reconstruction of a Shepp-Logan phantom with the proposed system (left) and with a reference parallel beam system (right).

References/Funding Source National Defense Science and Engineering Graduate Fellowship, NIH grant R01EB006837

Real-Time Scanning Beam Digital X-ray Image Guidance System for Transbronchial Needle Biopsy

S Yoon[1], BP Wilfley[2], K Jasperson[3], G Krishna[4], R Fahrig[1]
Department of [1]Radiology, Stanford University, CA; [2]Triple Ring Technologies, Inc., Newark, CA; [3]superDimension, Inc., Minneapolis, MN;
[4]Palo Alto Medical Foundation, Palo Alto, CA

We investigate a real-time digital tomosynthesis (DTS) imaging modality that provides improved image guidance for transbronchial needle biopsy (TBNbx), a minimally invasive lung nodule biopsy procedure. Specifically, we investigate an alternative DTS approach based on the scanning beam digital x-ray (SBDX) hardware used in conjunction with an electromagnetic navigation bronchoscopy (ENB). Because the SBDX system source uses electron beams, steered by electromagnets, to generate x-rays, and the ENB system generates an electromagnetic field to localize and track locatable guides, the two systems will affect each other when used in close proximity in an interventional setting. Therefore, we investigate the compatibility of the real-time SBDX DTS system and an ENB system. Additionally, SBDX system DTS images provide depth information, which is not available in the currently used fluoroscopic imaging. Because the SBDX system has a limited tomographic angle, we investigate the improvement in lung nodule visualization when using the current SBDX system configuration.

There exist a well-defined interference-free region, where the volume-of-interest (VOI) is at least 50cm away from the SBDX system source and detector. Inside this region, tomographic angle ranges from 3° to 10° depending on the VOI location. Improved lung nodule (<20mm) contrast is achieved by imaging the VOI near the SBDX system detector, where the tomographic angle is maximized.

The combination of the SBDX image guidance with an ENB system would enable a real-time visualization with improved localization of the target and needle/biopsy instrument, thereby increasing the average and lowering the variance of the yield for TBNbx.

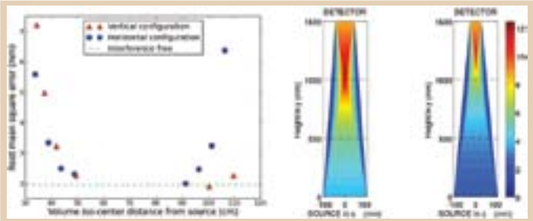

(left) ENB system localization root mean square error as a function of the distance of the volume iso-center from the SBDX system source plane. (right) Analytical tomographic angle per pixel on the central x-y and z-y planes. Source size of 23cmx23cm and detector size of 10cmx6cm were assumed. The dotted lines denote the interference-free region.

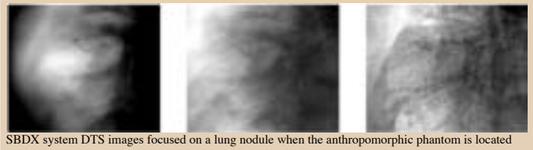

SBDX system DTS images focused on a lung nodule when the anthropomorphic phantom is located at (left) y=100cm (larger tomographic angle) and (middle) y=50cm. (right) Projection image with the lung nodule centered. Window and level have been adjusted (for all images) to maximize lung nodule visualization.

References/Funding Source NIH NHLBI R21 HL098683-01 and the Lucas Foundation

Advanced X-Ray and Computed Tomography (CT) Techniques

Simultaneous Segmentation and Reconstruction for Limited View Computed Tomography

S Yoon[1], AR Pineda[2], R Fahrig[§]
Departments of [1]Radiology, Stanford University, CA; [2]Mathematics, California State University, CA

An iterative tomographic reconstruction algorithm that simultaneously segments and reconstructs the reconstruction domain is proposed and is applied to tomographic reconstructions from a sparse number of projection images. The proposed algorithm uses a 2-phase level set method segmentation in conjunction with an iterative tomographic reconstruction to achieve simultaneous segmentation and reconstruction. The simultaneous segmentation and reconstruction is achieved by alternating between level set function evolutions and per-region intensity value updates. To deal with the limited number of projections, a priori information about the reconstruction is enforced via penalized likelihood function. Specifically, smooth function within each region (piecewise smooth function) and bounded function intensity values for each region are assumed. Such a priori information is formulated into a quadratic objective function with linear bound constraints. The level set function evolutions are achieved by artificially time-evolving the level set function in the negative gradient direction; the intensity value updates are achieved by using the gradient projection conjugate gradient algorithm.

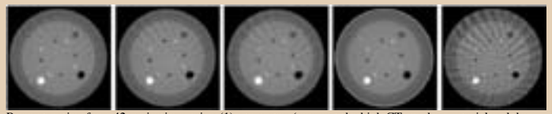

Reconstruction from 42 projections using (1) a two-step (segment the high CT number material and the low CT number material separately, and combine) of the proposed algorithm, (2) the propose algorithm (high CT number material segmentation), (3) a penalized likelihood algorithm, (4) a penalized likelihood algorithm followed by segmentation, (5) filtered back-projection. All images shown in [-400, 400]HU window and level.

The proposed simultaneous segmentation and reconstruction results were compared to "conventional" iterative reconstruction (with no segmentation), iterative reconstruction followed by segmentation, and filtered back-projection. Improvements of 6-13% in normalized root mean square error were observed when the proposed algorithm was applied to real fan-beam projections (42 projections to reconstruct 512^2 image) of the Catphan phantom, which did not satisfy the a priori assumptions. The proposed simultaneous segmentation and reconstruction resulted in improved reconstruction image quality. The algorithm correctly segments the reconstruction space into regions, preserves sharp edges between different regions, and smooths the noise within each region. The proposed algorithm framework has the flexibility to be adapted to different a priori constraints while maintaining the benefits achieved by the simultaneous segmentation and reconstruction.

References/Funding Source Baxter Foundation, NIH grants R01 EB003524 and R01 HL087917, and the Lucas Foundation. S Yoon, AR Pineda, R Fahrig. "Simultaneous segmentation and reconstruction: A level set method approach for limited view computed tomography," Medical Physics, 2010, vol. 37, pp. 2329-2340.

Mechanical Modal Analysis of an MR Compatible X-ray Tube

M Shin[1,2]
Departments of [1]Radiology, RSL and [2]Mechanical Engineering, Stanford University, CA

We are developing a new x-ray tube for an MR compatible x-ray system. One of the design constraints is that the system cannot operate continuously at or near the mechanical resonant frequency of the x-ray tube assembly. It is important to determine the resonant frequency in order to avoid passing through it during the spin-up of the anode. Mechanical modal analysis of the x-ray tube has been done by means of both a finite element software program and an analytical approach.

Based on a 3D structural mechanics simulation using the commercial software COMSOL and a simplified x-ray tube model, the first modal frequency is 85.5 Hz (5130 rpm). Since this frequency is higher than the expected rotational frequency of 60 Hz (3600 rpm), our tube design satisfies our constraint.

Modal analysis for an x-ray tube. (a) COMSOL 3D model of actual x-ray tube, (b) mechanical response for simplified model at the first modal frequency of 85.5 Hz, (c) resonant frequency trend according to mass distribution

Based on the analytical method, the first modal frequency is 82.8 Hz (4970 rpm), which is within about 3% of the solution from finite element method. This agreement means we can analytically investigate the dependence of the first modal frequencies of the x-ray tube upon the mass distribution between anode disk and rotor body. We find that the lighter the disk and rotor, the higher the first resonant frequency. Thus it is better to utilize light materials for high resonant frequencies and reduced spin-up torque. Since the anode is made out of tungsten and other heavy metals, its influence on the frequency is greater than that of the rotor body. We are investigating what materials and geometries are best for our application.

References/Funding Source NIHR01 EB 007627 and the Lucas Foundation

A New Method for Lag Reduction in Flat-Panel X-ray Detectors

J Starman[1,2], J Star-Lack[3], R Fahrig[1]
Departments of [1]Radiology, Bioengineering, [2]Electrical Engineering, Stanford University, CA; [3]Varian Medical Systems, Mountain View, CA

Detector lag, or residual signal, in a-Si flat-panel (FP) detectors can cause significant shading artifacts in cone-beam CT reconstructions. Most correction models have assumed a linear time-invariant (LTI) model and correct lag by deconvolution with an impulse response function (IRF). However, many ways to determine the IRF exist. Specifically, the lag correction is sensitive to the exposure intensity used for measuring the step-response. Even when the LTI correction that produces the minimum error is found, residual artifacts remain. A non-LTI method that is calibrated for individual pixels has been developed to take into account the exposure dependencies.

We collected step-response data (rising and falling edge) on a Varian 4030CB a-Si FP operating in dynamic gain mode at 15 fps at ten incident exposures (0.5% - 84% of a-Si FP saturation exposure). We implemented multi-exponential (N=4) LTI and non-LTI models for lag. For the non-LTI method, the coefficients of the IRF become functions of exposure intensity. The resulting corrections were applied to CT acquisitions of a large (42 cm x 26 cm) pelvic phantom. Five pairs of ROIs were defined and the maximum and mean error for each pair calculated. The ROI pairs are indicated in Figure (a).

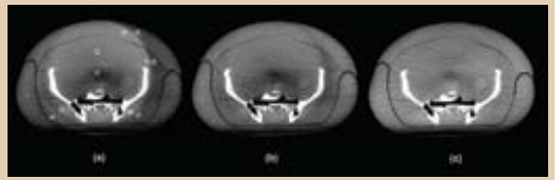

CT reconstructions for three cases. (a) No lag correction with an average error of 43 HU, (b) an LTI correction from the optimal exposure with 17 HU error, and (c) the non-LTI correction with 11 HU average ROI error.

The figure shows CT reconstructions for three cases. (a) No lag correction with an average error of 43 HU, (b) an LTI correction from the optimal exposure with 17 HU error, and (c) the non-LTI correction with 11 HU average ROI error. The non-LTI provides superior image uniformity, especially in the center of the image. This appears to be due to uncorrected lag artifact from the bone in (b) that is corrected in (c).

The non-LTI method decreased the average ROI error for a pelvic phantom by 35% and provided superior image uniformity, as compared to an LTI method calibrated at the optimal exposure.

References/Funding Source Varian Medical Systems, the Stanford-NIH Biotechnology Traineeship, NIH Grants EB003524 and HL087917, and the Lucas Foundation

High-Density Object Removal from X-ray Projection Images

C Schwemmer[1,2], M Prümmer[1], R Fahrig[2]
[1]Pattern Recognition Lab, Department of Computer Science, University of Erlangen-Nuremberg, Germany; [2]Radiology RSL, Stanford University, CA

Artifacts from dense objects in CT imaging are a well-known problem. In interventional C-arm CT, catheters or wires produce artifacts that reduce image quality and hinder motion-estimation algorithms.

In this work, we compared established interpolation algorithms and introduced a novel technique called Subtract-and-Shift (SaS). Both 1-D (linear interpolation and cubic B-splines) and 2-D methods (interpolation in frequency space, inpainting and the Healing Brush) were evaluated. In-vitro datasets from a plastic phantom and in vivo data were used for this.

SaS is based on the observation that most dense objects do not absorb all incident radiation, allowing the extraction of remaining structure information from within the "shadow" of the object. We subtract a Gaussian model of the object from the projection images, and shift the remaining structure inside back to the intensity level of its surroundings. The shifting is achieved by linear interpolation. Therefore, if no information could be retained after subtraction, the method gracefully degrades to linear interpolation.

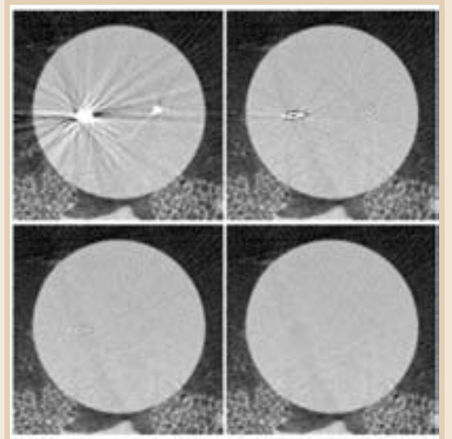

A slice of an in-vitro dataset processed with SaS using different parameters. Top left is original.

The quantitative evaluation showed that SaS performed best among the tested methods, followed by linear interpolation and then inpainting. Qualitative evaluation of the projection images confirmed this (structures underneath dense objects were correctly continued by SaS), although no difference between SaS and linear interpolation could be seen in the reconstructed 3-D images.

Another benefit of SaS was discovered during the evaluation. By changing the parameters of the Gaussian model, the visibility of the dense object in the 3-D reconstruction can be arbitrarily controlled from fully visible to fully removed, while artifacts are already greatly reduced when the object is still visible. This is beneficial in situations where the location of the dense object is of interest to the user. Also, spurious structure created by the interpolation algorithm can be differentiated from actual pathologies if the location of the object is clear.

References/Funding Source DAAD D/09/48916, NIH grant R01HL087917. C. Schwemmer: High-density Object Removal from X-ray Projection Images, diploma (master) thesis, Technical Faculty, University of Erlangen-Nuremberg, DE, 2010.

KONRAD - A Kardiac-Optimized Numerical Reconstruction Algorithm Database

A Maier, R Fahrig
Department of Radiology, RSL, Stanford University, CA

KONRAD is a C-arm CT image processing and reconstruction framework. It is implemented in Java and allows us to implement highly parallelized algorithms platform-independently to meet interventional time constraints. Futhermore, KONRAD supports JCuda for processing algorithms on graphics cards using Nvidia's Compute Unified Device Architecture (CUDA).

All algorithms in KONRAD support parallel processing. As many correction and filtering steps only require access to a single projection or slice during their computation, KONRAD provides wrapper classes to compute these steps in parallel. Projection-based processing can hence be executed in parallel without any additional programming efforts. KONRAD also offers classes to compute algorithms which require full or partial access to the projection or slice stack in a parallel manner at an increased cost of memory consumption.

The architecture also employs JCuda [1] to run algorithms with a high computational demand on a CUDA-compatible graphics card. Code to be executed on the graphics card is written in C and loaded using the Java Native Interface. Memory and processing management is performed by KONRAD automatically in the background. During the execution of a custom-made pipeline KONRAD analyzes its configuration on-the-fly and distributes work packages automatically.

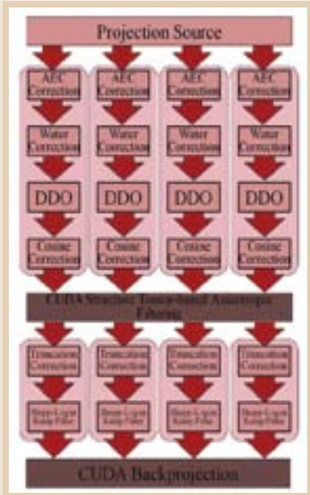

Example for the pipeline processing in KONRAD with 4 CPUs and two CUDA algorithms. The planning of the pipeline is performed automatically in the background by KONRAD without additional user interaction.

Using the JCUDA interface, the reconstruction time is reduced from 57 seconds (Manufacturer's Reconstruction Pipeline) to 15 seconds using our parallel implementation (speed-up factor 3.8). Hence, reconstruction is sped up considerably with an off-the-shelf CUDA-compatible graphics card.

Furthermore, computationally highly expensive adaptive noise filters can be computed within the interventional time constraints. With a complete implementation of an adaptive noise filter in CUDA, we can reduce the computation time further from 1,336 seconds on the CPU to 168 seconds on the graphics card. This corresponds to an 8.9-fold speed-up.

References/Funding Source National Institute of Health (NIH, grant 1R01HL087917), by Siemens Health Care, and by the Lucas Foundation

Electrostatic Focal Spot Correction Methods for X-Ray Tubes in Magnetic Fields

P Lillaney[1,2], R Fahrig[1]
Departments of [1]Radiology and [2]Bioengineering, Stanford University, CA

A challenge in the development of hybrid X-Ray/MRI imaging systems is the close proximity of the x-ray source to the MR magnet. The fringe field of the magnet affects the electron optics of the x-ray source causing focal spot defocusing and deflection. Previous work from our group focused on correcting for these effects using an active magnetic shielding approach [1,2]. However, problems with heating of the active shield arise when correcting for magnetic field strengths on the order of 0.1 T. It is proposed that the focal spot deflection can be corrected by applying a static electric field ($\mathbf{E_{EXT}}$) in the direction parallel to the deflection (fig 1a).

The analytical solution for the electron trajectories in this combined electric and magnetic field environment can be solved for using the appropriate coordinate transformation, and subsequent Lorentz boost to an inertial frame K', which moves with velocity **u** in the $\mathbf{E_{EFF}} \times \mathbf{B_{MR}}$ direction with respect to the laboratory frame K (here $\mathbf{E_{EFF}}$ is the vector addition of $\mathbf{E_{EXT}}$ and the electric field of the X-Ray tube, $\mathbf{E_{TUBE}}$). In the boosted inertial frame K' there exists only a magnetic field **B'** (assuming $|\mathbf{B_{MR}}| > |\mathbf{E_{EFF}}|/c$, c = speed of light), yielding a simple solution to the relativistic equations of motion [3]. Trajectories in the laboratory frame K are found by applying an inverse Lorentz transform followed by an inverse coordinate transform.

The method described above was solved and plotted for a tube potential of 70 kVp, an anode-cathode separation of ~1.5 cm, $\mathbf{B_{MR}} = 0.1$T, and $\mathbf{E_{EXT}} = 6$ MV/m (120 kV separated by 2.0 cm). The electron trajectory with no $\mathbf{E_{EXT}}$ applied curves drastically and the electron never reaches the anode (fig 1b). However, with $\mathbf{E_{EXT}}$ applied the electron reaches the anode with an insignificant amount of deflection (fig 1c).

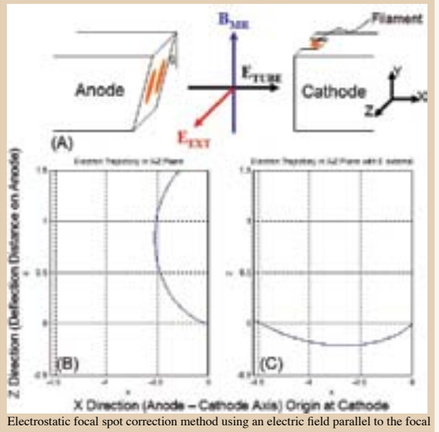

Electrostatic focal spot correction method using an electric field parallel to the focal spot deflection. (a) X-Ray tube schematic demonstrating orientation of combined electric and magnetic fields (b) Electron trajectory from center of cathode filament with $\mathbf{E_{EXT}}$ not applied. Anode is located at X ~ -1.5 cm. (c) Electron trajectory with $\mathbf{E_{EXT}} = 6$MV / m. Electron reaches anode with insignificant deflection.

References/Funding Source Stanford School of Medicine Bio-X Fellowship, NIH Grant EB007626, and the Lucas Foundation. [1] P Lillaney, J Bracken, A Ganguly, J Rowlands, R Fahrig, Development of an MR Compatible Rotating Anode X-Ray Tube. Proc. of SPIE Vol. 6913, Medical Imaging 2008: Physics of Medical Imaging. [2] J Bracken, G DeCrescenzo, P Komljenovic, P Lillaney, R Fahrig, J Rowlands, Closed-bore XMR (CBXMR) systems for aortic valve replacement: Active magnetic shielding of x-ray tubes. Med. Phys. 2009 May; 36(5):1717-26. [3] J. J. Jackson, Classical Electrodynamics, 3rd ed. Wiley, New York,1998.

Adapted Iterative Methods for Specialized Cone Beam Reconstructions

A Keil[1], J Star-Lack[2], R Fahrig[1]
Departments of [1]Radiology, Bioengineering, Stanford University, CA; [2]Varian Medical Systems, Mountain View, CA

Modern radiotherapy systems rely on the accurate delineation of lesions and critical structures in diagnostic CT images for generating an optimized treatment plan. Segmentation of anatomical structures, however, is hampered by reconstruction artifacts. One of the currently most severe artifacts is streaking caused by metal implants blocking the photons completely. This is especially relevant in the pelvic region in the case of hip implants or in neurology applications in the presence of tooth fillings. Since this highly nonlinear physical fact is not modeled in standard algorithms, the resulting images are reconstructed based on false assumptions. Methods have been proposed to iteratively cope with these streak artifacts (mostly by interpolating the missing data). But the underlying problem of not having any measureable data along rays intersecting high-density material cannot be solved without additional means for obtaining true measurements.

Luckily, such means are available in modern radiotherapy systems since images can be captured from the high-voltage treatment beams. The mega-voltage treatment photons can penetrate high-density objects and thus provide valuable measurement data where the low-voltage diagnostic photons are blocked. The downside of reconstructions purely based on MV photon data is the lower soft tissue contrast resolution. A combination of both input data therefore has the potential to yield reconstructions with improved, artifact-less reconstructions. This should result in better treatment plans with a better effective dose rate and thus improved treatment outcomes for cancer patients with metal implants.

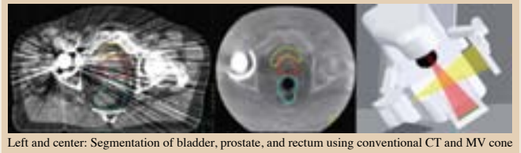

Left and center: Segmentation of bladder, prostate, and rectum using conventional CT and MV cone beam CT showing discrepancy in delineated prostate size due to streak artifacts in the kV image (images from Aubin et al., The use of megavoltage cone-beam CT to complement CT for target definition in pelvic radiotherapy in the presence of hip replacement. Br J Radiol, 79(947):918-921, 2006). Right: Illustration of the proposed hybrid kV-MV system.

Although the mechanical setup of current radiotherapy systems already offers some desirable properties like the mechanical stability of the system and the fixed alignment of the diagnostic and treatment beam, numerous questions have to be addressed over the course of this new project. Optimization of the MV detector, new approaches for combining the two input data sets, and better modeling of the physical processes involved in the attenuation of both kV and MV photons are just a few of the research directions.

References/Funding Source NIH Grant 1R01CA138426-01A1

Contrast-enhanced Cardiac C-arm CT Evaluation of Radiofrequency Ablation Lesions in the Left Ventricle

E Girard-Hughes[1], A Al-Ahmad[2], J Rosenberg[3], R Luong[4], T Moore[5], G Lauritsch[2], J Boese[2], R Fahrig[3]
Departments of [1]Bioengineering, [2]Cardiovascular Medicine, and [3]Radiology, and [4]Comparative Medicine, Stanford University, CA, USA; [5]Siemens Medical Solutions Incorporation, Malvern, PA, USA; [6]Siemens AG Healthcare Sector, Forchheim, Germany

Radiofrequency ablation (RFA) is an important non-pharmacological strategy in the treatment of ventricular arrhythmias. Currently, during RF lesion creation, only surrogates of lesion quality are assessed (e.g. temperature at the catheter tip, power delivered) and despite monitoring these parameters, failure to deliver an adequate lesion remains one cause of failed catheter ablation procedures. 3D cardiac images may be obtained during an interventional procedure using C-arm CT, an imaging modality that uses a standard C-arm fluoroscopy system rotating around the patient. Cardiac C-arm CT has high spatial resolution, does not alter the fundamental clinical workflow, and accurately represents the anatomic and hemodynamic state of the patient during the RFA procedure.

We visualized RFA lesions using an ECG-gated C-arm CT im¬aging protocol and acquired images during iodine contrast injection and every 5 minutes for up to 30 minutes, with no additional contrast. We correlated C-arm CT lesion dimensions and area with pathology measurements, and described the contrast kinetics of ablated myocardial tissue using a time series of C-arm CT images. All ablation lesions (n=29) were visualized and lesion dimensions, as measured on C-arm CT, correlated well with postmortem tissue measurements (1D dimensions : r = 0.87; area : r = 0.90). Lesions were visualized as a perfusion defect on first-pass C-arm CT images with a signal intensity 95 HU lower than normal myocardium (95% confidence interval: -111 to -79 HU). Images acquired at 1 and 5 minutes more clearly showed the peripheral enhancement as a ring surrounding the perfusion defect and 24 (83%) of the lesions had peripheral enhancement.

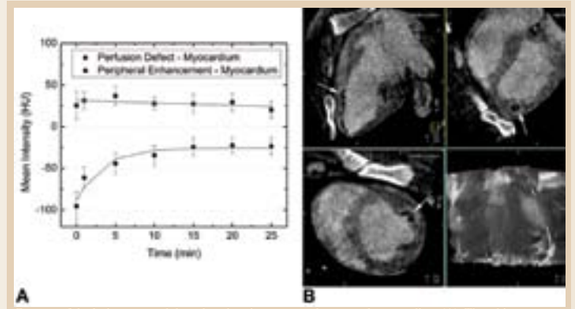

Contrast of the lesion core and the enhancing ring compared to normal myocardium (A). The white arrows (B) point to the same lesion in three perpendicular slices in an image acquired at 1 min post-contrast. Gray-scale window W = 290 HU, C = 165 HU.

RFA lesion size, including transmurality, can be assessed using ECG-gated cardiac C-arm CT in the interventional suite. Visualization of RFA lesions using cardiac C-arm CT may facilitate the assessment of adequate lesion delivery and provide valuable feedback during cardiac ablation procedures.

References/Funding Source NIH grant R01 HL087917, Siemens Medical Solutions (Malvern, PA), Medtron AG (Saarbruecken, Germany). Oral presentation at Heart Rhythm 2010, May 12-15, 2010, Denver, CO.

Optimization of Modulator Parameters for X-ray Scatter Correction Using Primary Modulation

H Gao[1], L Zhu[2], R Fahrig[1]
Department of [1]Radiology, Stanford University, CA; [2]Nuclear and Radiological Engineering and Medical Physics Programs, The George W. Woodruff School of Mechanical Engineering, Georgia Institute of Technology, Atlanta, GA

Recently, a promising scatter measurement and correction method for x-ray computed tomography (CT) has been developed and experimentally verified. The method uses a primary modulator, a checkerboard pattern of attenuating blockers, placed between the x-ray source and the object. We have studied the effects of the system parameters of the modulator on the x-ray scatter correction. An optimization of the modulator design is presented. The blocker size, d, and the blocker transmission factor, α, are critical to the performance of the method. In this work, an error caused by the primary aliasing (whose magnitude depends on the choices of d and α, and the scanned object) is set as the object function to be minimized. The constraints include the x-ray focal spot, the physical size of the detector element, and the noise level. The optimization is carried out by two steps. In the first step, d is chosen as small as possible subject to a lower-bound condition. In the second step, α is selected to balance the error level in the scatter estimation and the noise level in the reconstructed image. The lower bound of d on our tabletop CT system is 0.83 mm. Numerical simulations suggest 0.6 <α< 0.8 is appropriate. Using a Catphan@600 phantom, a copper modulator (d = 0.89 mm, α= 0.70) expectedly outperforms an aluminum modulator (d = 2.83 mm, α= 0.90), reducing the error of CT number from 371.4 to 21.9 Hounsfield units, and increasing the contrast to noise ratio from 10.9 to 19.2.

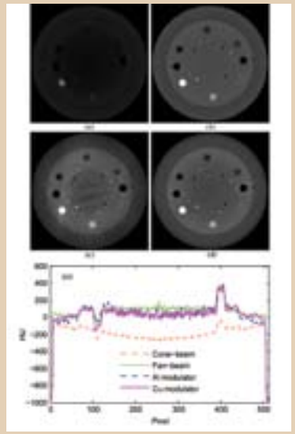

Image reconstructions of the CatPhan@600 phantom from cone-beam scans with and without scatter correction. Display window: [–300, 630] Hounsfield units. (a) The cone-beam image without scatter correction; (b) the fan-beam image (reference); (c) the cone-beam image with scatter corrected using an aluminum modulator; (d) the cone-beam image with scatter corrected using a copper modulator; and (e) the corresponding vertical profiles.

References/Funding Source NIH R21 EB008186 and the Lucas Foundation. This work was presented at SPIE Medical Imaging 2010.

C-arm Cone-Beam CT for Cerebral Perfusion Imaging

A Ganguly[1], A Fielselmann[2,3,4], M Marks[1], J Rosenberg[1], J Boese[4], Y Deuerling-Zheng[4], M Straka[1], G Zaharchuk[1], R Bammer[1], R Fahrig[1]
[1]Dept of Radiology, Stanford University, CA, [2]Dept of Computer Science, [3]Erlangen Graduate School in Advanced Optical Technologies (SAOT), Friedrich-Alexander University Erlangen-Nuremberg, Germany, [4]Siemens AG, Healthcare Sector, Forchheim, Germany

Perfusion CT (PCT) imaging is commonly used in identifying salvageable tissue in cases of ischemic stroke. Based on a CT diagnosis, a stroke patient may be a candidate for endovascular treatment. Such procedures are guided by angiographic/fluoroscopic systems on a C-arm. However delays between the CT diagnosis and the start of the interventions have a median value of 5.3h1. Enabling C-arm systems to perform perfusion CT could alleviate the problem and permit intra and post procedural PCT. However, rotation speeds of C-arms are slow compared to CT. We have developed a PCT protocol for C-arm cone-beam CT (C-arm CBCT) that overcomes this problem and have evaluated it in an animal study.

Five anesthetized pigs (54.1±4.7kg) were imaged using a C-arm CBCT system (Axiom Artis dTA and DynaCT, Siemens AG) and a conventional CT scanner (Sensation 64, Siemens AG). The C-arm rotates in 4.3s with 1.25s for turnaround, vs. 0.5s on a clinical CT.

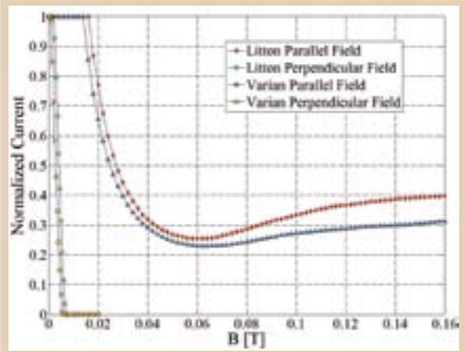

Cerebral perfusion map comparison between CT (left) and C-arm CBCT (right)

One C-arm scan consists of 6 continuous bi-directional sweeps. Multiple scans with different delays between starts of scans and intra-arterial injection of iodine were used to increase temporal resolution. Scan combinations (6 scans, 3 scans or 2 scans) and different injection protocols (3ml/s at 100%, 3ml/s at 67% and 6ml/s at 50% contrast concentration) were studied. Cerebral blood flow (CBF) maps from C-arm CBCT and CT were calculated in 2 slices and compared.

A linear fit correction to the CBF data resulted in the 6ml/s 50% contrast injection having the best intra-modality match and highest concordance correlation coefficient (CCC) (mean difference 0.00±6.88 ml/100g/min of tissue, CCC=0.894). Some of the more clinically relevant 3- and 2-scan sets have performance similar to the 6-scan dataset. This animal study demonstrates that C-arm CBCT can produce accurate cerebral blood flow perfusion maps.

References/Funding Source [1]1 A Furlan, R Higashida, L. W. Intra-arterial Prourokinase for Acute Ischemic Stroke:The PROACT II Study: A Randomized Controlled Trial. JAMA 1999;282(21):2003-2011. K99 EB007676-01A2 and research grant from Siemens AG, Healthcare, Germany.

C-arm CT Development for Imaging in a Weight-bearing Geometry

A Maier[1], J-H Choi[3], A Keil[1], C Niebler[6], M Sarmiento[7], A Fieselmann[6], S Pal[5], T Besier[4], GE Gold[1], S Delp[2,3,4], R Fahrig[1,2]
Departments of [1]Radiology, [2]Bioengineering, [3]Mechanical Engineering, [4]Orthopaedic Surgery, [5]Computational Biomechanics Lab, Stanford University, CA, USA; [6]University of Erlangen-Nuremberg, [7]Siemens AG, Healthcare Division, Forchheim, Germany

C-arm angiography systems offer great flexibility in the acquisition of trajectories for computed tomography. Theoretically, these systems are able to scan patients while standing in an upright position. This would allow novel insights into structural changes of human anatomy in weight-bearing position. However, a scan on a horizontal trajectory parallel to the ground floor is required to do so which is not supported by standard C-arm CT acquisition protocols.

With access to hardware sub-system controls on a C-Arm system, we were able to acquire data in a horizontal scan for the first time. In theory, reconstruction of a horizontal and a vertical scan are exactly the same. In practice, however, a horizontal scan may introduce additional challenges to the reconstruction as external forces such as gravity may have substantial influence on the properties of the C-arm system. Hence, it is not guaranteed that a horizontal scan will be of the same quality as the well-known vertical trajectories.

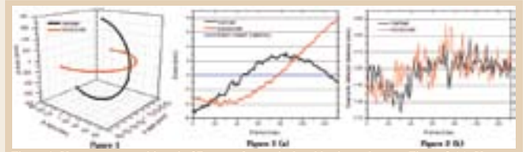

Figure 1. X-ray source positions in 3D space for vertical and horizontal scans. Figure 2 (a). X-ray source positions in Z-axis. The source position of the horizontal exhibits a significant sag in the beginning of the scan. Figure 2 (b). Variance of the source to detector distance along frame indices.

X-ray source position and the source to detector distance are considered as important parameters to describe the scan geometry. The two parameters are larger in horizontal scan mode than in vertical scan mode. Based on the assessment of the reconstructed image error of the deviation in the x, y, and z coordinates between the reconstructed calibration bead positions and their positions as defined in the PDS-2 calibration phantom specification, the two parameters do not have an impact on the image quality. The reconstruction image accuracy is similar in vertical and horizontal scan modes (RMSE 0.26, 0.12 mm respectively). Compared to the detector resolution, both errors are negligible. In summary, the image data acquired with the horizontal scan trajectory is of very good quality and will be used to generate weight-bearing volume images for clinical assessment of joint stresses in the future.

References/Funding Source National Institute of Health (NIH, grant 1R01HL087917), by Siemens Health Care, and by the Lucas Foundation.

Image Analysis, Bioinformatics, and Computational Modeling

In this section, you will read about innovations in display and interaction, feature extraction, and computer simulation and modeling techniques. These projects aim to improve the accuracy and efficiency of human interpretation of medical imagery, as well as predict patient prognosis, the molecular subtypes of their disease, and their response to treatment options in a way that is highly personalized for each patient. These efforts share the common goal of developing decision-making tools that assist with patient diagnosis, treatment, and disease monitoring.

An Approach to Structured Reporting in Clinical Research

D Rubin[1], V Kleper[2], A Flanders[3], D Channin[2], P Mongkolwat[2]
Department of [1]Radiology, Stanford University, CA; [2]Northwestern University, Evanston, IL; [3]Thomas Jefferson University, Philadelphia PA

Background: Clinical radiology research depends on robust collection of complete information, quantitative and qualitative, about each case. Our goal was to develop an approach to structured reporting of comprehensive image information that can be introduced into the clinical workflow.

Evaluation: We reviewed the existing information models for structured capture of image interpretation from the RSNA structured reporting initiative, from imaging case report forms for tumor response in cancer clinical trials, and from the Annotation and Image Markup (AIM) standard of caBIG. We created an information model to harmonize these approaches, and we implemented that model in an open source image annotation plug-in (called "ClearCapture") to the ClearCanvas open source workstation. The plug-in provides a graphical structured reporting form that captures comprehensive description of quantitative and qualitative information in images and saves it in the standard AIM format. ClearCapture enforces use of controlled terminology and alerts the user if invalid or incomplete information is reported. A neuroradiologist used ClearCapture to report the findings in 10 MRI cases of brain glioma and evaluated the usability of the tool.

ClearCapture structured reporting tool. An image being interpreted by the radiologist (left) is reported using a form-driven structured reporting template (right) which records radiologist observations using controlled terminology. Annotations on the image (left) are automatically included in the structured report.

Discussion: We have developed a tool integrated into an image viewing workstation that enables structured reporting of cases in a comprehensive manner. In addition, the structured report is stored in compliance with the emerging AIM standard. The tool was reported by the radiologist to be intuitive to use, though it was more time-consuming to record the report data using the menu-driven tool than using unconstrained dictation. On the other hand, ClearCapture ensured complete reports, cuing the radiologist if any necessary information was omitted.

References/Funding Source caBIG Imaging Workspace, NCI. DL Rubin, V Kleper, AE Flanders, DS Channin, P Mongkolwat: An Approach to Structured Reporting in Clinical Research. Annual Meeting of the Radiological Society of North America, Chicago, IL, 2010.

XRAYHEAD MSK : A Musculoskeletal Radiology Web-Reference Based on Radlex

B Do, S Biswal, K Stevens, GE Gold, C Beaulieu, A Lutz, D Rubin
Department of Radiology, Stanford University, CA

Introduction: Despite the fact that the primary work product by Radiologists are reports and image annotations which are an electronic format and therefore can be copied and shared, Radiology domain data systems (picture archiving and communications systems (PACS), Radiology information systems (RIS), and Radiology teaching files) do not use standard terminology which limits inter-operability and data sharing. For example, although numerous Radiology teaching resources exist on the internet, their data are fragmented, and users must search sites independently, even using different terms to find the same cases and concepts. Radiology domain data systems can benefit from standardization of nomenclature and terms.

Method: RSNA's RadLex is a lexicon for uniform indexing and retrieval of Radiology information resources. A web-based database (xrayhead msk = XM) was developed to store interesting Radiology teaching cases using a PHP-configured MySQL database on an Apache web server. An AJAX based auto-suggest function was implemented. The auto-suggest function suggests RadLex terms and ID's in real-time as the user enters a diagnosis to describe and index an interesting case.

XM is a web application which leverages the RSNA's RadLex lexicion and terms relationship to automatically generate disease "synonyms" and "subtypes" based on user queries. For example, if the user is learning about osteonecrosis, XM automatically lists Keinbock and Panner's disease (lower right-hand corner), subtypes of osteonecrosis. These "suggestions" are automatically generated in real-time.

Result: The RadLex lexicon was successfully integrated into the teaching file database. An AJAX based auto-suggest function allowed users to retrieve RadLex terms and IDs in real-time as users entered the diagnosis field for each interesting case, facilitating the linking of case diagnosis with standard RadLex IDs (RIDs).

Conclusion: We have developed a novel RadLex-based, online database of interesting Radiology cases called XM. XM uses standard RadLex terms which can be used to share information with other web services with improved precision compared to existing systems which use terms depending on the Radiologist training and background. RSNA's RadLex is a lexicon for uniform indexing and retrieval of Radiology information resources and can be implemented in teaching resources to promote the exchange of radiology data and empower radiologists' collaborative clinical and scholarly activities.

References/Funding Source Electronic Exhibit and CME presentation, Radiological Society of North America Meeting, Chicago, Illinois. November 28-December 3, 2010.

Reinventing Radiology Reporting: Combining Structured Capture and Radiology Image Annotation

D Rubin[1], C Beaulieu[1], C Rodriguez[1], C Baldassano[2], S Napel[1]
Departments of [1]Radiology and [2]Computer Science, Stanford University, CA

Background: Capturing quantitative and qualitative aspects of images is an essential activity of radiology research. Our goal was to develop a tool to capture this information as the radiologist records observations about images. Our tool can be customized and applied to any particular study, making all quantitative and qualitative image content explicit as part of the radiology report.

Evaluation: We previously developed a semantic image annotation tool, the image Physician Annotation Device (iPAD), a plugin to OsiriX. iPAD provides a structured reporting template for quantitative and semantic information in images, and stores this in the Annotation and Image Markup format for interoperability. We developed an application for defining and editing custom templates, permitting iPAD's data capture capabilities to generalize to a diversity of radiology studies. To evaluate this tool, we used it to create structured data capture templates for three radiology studies for describing characteristics of (1) liver lesions, and (2) brain tumors, and (3) for assessing the RECIST criteria in cancer patients. These templates were used and evaluated by three users for sufficiency and efficiency in conducting the respective studies.

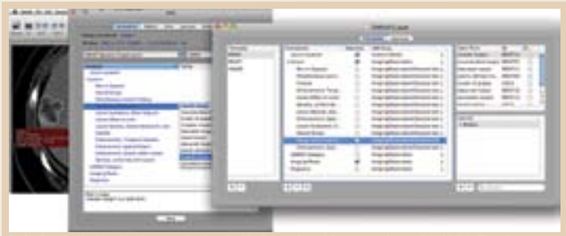

Left: Image displayed and reported using the iPAD template-driven reporting tool (middle). Templates are created and updated using the Template Editor (right) which allows users to specify templates (left panel), data entry items (middle panel) and valid terms and terminologies (right panel).

Discussion: The template editor application provides a menu-driven interface permitting users to define the data capture fields desired for a given study, the applicable controlled terminologies, whether or not an item is required, and nesting of items. Templates can then be imported into iPAD and used for structured reporting of quantitative and semantic aspects of studies. The users reported that the templates created for the three studies were sufficient for the data collection tasks and that the workflow in using the templates in the research studies was more efficient than it would have been without the tool because data collection is integrated with image viewing.

References/Funding Source caBIG Imaging Workspace, NCI. DL Rubin, CF Beaulieu, C Rodriguez, C Baldassano, S Napel: Reinventing Radiology Reporting: Combining Structured Capture and Radiology Image Annotation, Annual Meeting of the Radiological Society of North America, Chicago, IL, 2010.

Semantic Annotation and Image Markup in a Commercial PACS Workstation

D Rubin[1], D Korenblum[1], V Yeluri[2], P Frederick[2], R Herfkens[1]
Department of [1]Radiology, Stanford University, CA; [2]GE Medical Systems

Background: The NCI caBIG project recently developed standards in image annotation and markup (AIM) for capturing and sharing quantitative and qualitative information in images. To date AIM is not implemented in the clinical PACS. Our goal was to implement AIM in a commercial PACS to demonstrate the feasibility and utility of broad adoption of this important standard in clinical imaging workstations.

Annotation and Image Markup (AIM) in a commercial PACS. LEFT: An image has been annotated using the workstation's existing annotation tools (the maximum dimension of a mass in the left lung has been measured). RIGHT: The workstation records the annotation information in the structured XML-based AIM format which is machine-accessible. This records the coordinates of the annotation, measurements, and other quantitative and semantic information.

Evaluation: We implemented the AIM image metadata standard in the GE RA1000 PACS workstation (GE Medical Systems, Milwaukee, WI). We extended the pre-existing annotation tools to save the annotation information in the AIM format. Text annotations created after drawing an ROI provide the label for the ROI. AIM objects are stored in a database separate from the images to facilitate image query and to reduce any performance impact on the operational PACS database. We evaluated our implementation by annotating images containing cancer lesions in serial CT studies and by validating the resulting AIM. We also created a software module to analyze AIM annotations to produce automated quantitative summaries of lesion measurements for tracking tumor burden.

Discussion: Our implementation is transparent to the user; while annotating images in the workstation, an AIM document is produced simultaneously, without interfering with the speed of image annotation or workflow. AIM objects contain all pertinent image metadata, and they are interoperable with those obtained from other AIM-compliant systems. Our tumor burden tracking application consumes image annotations to summarize the lesion status in cancer patients. To our knowledge, ours is the first implementation of AIM in a commercial PACS workstation demonstrating collection of image annotations and their implementation in a clinically-useful application.

References/Funding Source Grant from GE Medical Systems. DL Rubin, D Korenblum, V Yeluri, P Frederick, RJ Herfkens: Semantic Annotation and Image Markup in a Commercial PACS Workstation, Annual Meeting of the Radiological Society of North America, Chicago, IL, 2010.

The Annotated Breast Map: A Novel Paradigm to Improve Interpretation in Breast Imaging

J Lipson, D Nwamuo, D Rubin
Department of Radiology, Stanford University, CA

Purpose: Accurate interpretation of breast imaging studies depends on adequate preparation, which in turn depends on the radiologist's ability to integrate a myriad of data: clinical history, pathology, and results from prior imaging. This complex task is time-consuming and error-prone. We developed and evaluated an informatics tool to provide a visual summary of pertinent clinical information and tested the hypothesis that our tool will improve efficiency and completeness of preparation for breast imaging interpretation.

Method and Materials: We developed an Annotated Breast Map (ABM), a tool providing visual display of data pertinent to comprehensive assessment of breast imaging studies. A patient-centric temporal data model populated by extracting data from electronic medical record and radiology information systems, the tool integrates demographics, breast cancer risk factors, and exam indication, providing annotated images of both breasts, summarizing breast findings graphically, including location of prior breast procedures, pathologic diagnoses at each location, and correlates other imaging modalities. Images are annotated using the caBIG Annotation and Image Markup (AIM) standard, enabling automated summarization of lesion identities and locations. We evaluated the ABM and tested our hypothesis by comparing preparation time and completeness of a breast imaging specialist who evaluated 10 breast imaging studies.

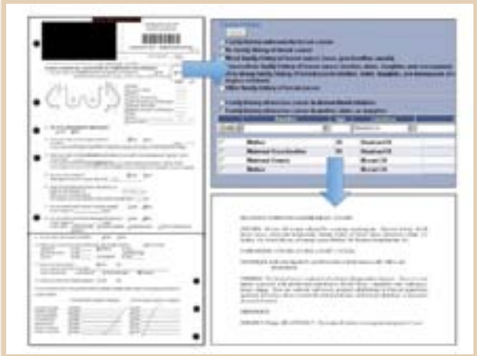

Diagrammatic overview of information flow to populate the Annotated Breast Map (ABM). Patient history form (left) is completed by patient, and the information entered into the electronic record system (right, top). Other pertinent data from the medical record systems populate the ABM, including the report of the other imaging studies (right, bottom).

Results: Preparation for interpretation required synthesizing 1) exam indication, 2) pathologic diagnoses, 3) prior exam findings, 4) clinical context, and 5) history provided by the patient. The baseline preparation time of the radiologist without using ABM was 25 minutes/case on average (stdev 5 minutes; range 15-35 minutes). The baseline preparation completeness was 100% (5/5 pieces of pertinent data reported). Performance significantly improved by using the ABM, with preparation time decreasing to an average of 15 minutes/case (stdev 5 minutes; range 10-20 minutes; $p < 0.05$; CI 5.30 – 14.70) and completeness in preparation maintained at 100% (5/5 pieces of pertinent data reported; $p < 0.05$).

Conclusion: Our visual approach to information integration improved efficiency and maintained the accuracy of preparation for breast imaging interpretation.

References/Funding Source JA Lipson, DC Nwamuo, DL Rubin: The Annotated Breast Map: A Novel Paradigm to Improve Interpretation in Breast Imaging, Radiological Society of North America (RSNA) Annual Meeting, Chicago IL, 2010.

Semantic Reasoning with Image Annotations for Tumor Assessment

M Levy[1], D Rubin[2]
Departments of [1]Biomedical Informatics, Vanderbilt University, TN; [1]Radiology, Stanford University, CA

Purpose: Identifying, tracking and reasoning about cancer lesions is a key task for assessing cancer treatment response, but currently this is a laborious, error-prone process. Our goal was to develop methods to enable computerized reasoning about tumor lesions to automate and reduce variation in imaging assessment of treatment response.

Method and Materials: We adapted the Annotation and Image Markup (AIM) caBIG information model to encode the semantic information related to cancer imaging findings, and we implemented AIM as a plugin to the Osirix image viewing workstation. We developed a methodology and a suite of tools for transforming AIM image annotations in XML into Web Ontology Language (OWL), and an OWL ontology for computer reasoning with AIM annotations for tumor lesion assessment. We also defined and implemented two computer processing procedures that perform image-based reasoning on OWL instances derived from images: 1) calculation of the length of each lesion, and 2) classification of lesions as measurable and non-measurable based on semantic information about the location, type, and calculated length of each lesion. To evaluate our system, we used our tool to annotate 116 images from 10 cancer patients who had serial imaging studies and to infer response characteristics of cancer lesions.

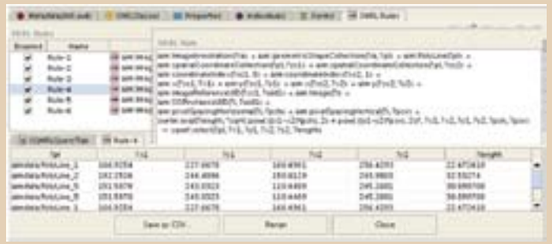

Screen shot of the Protégé application for semantic reasoning. The rule shown calculates the length of a line from pixel information in the image using the Pythagorean theorem.

Results: The inferences produced by our system were reviewed by an oncologist who confirmed that they were correct based on the raw image annotation information. The image annotations could be acquired as part of routine clinical workflow, and automated assessment of lesions to calculate tumor response took a fraction of time as when it was done without support. In qualitative terms, the oncologist believed our system will streamline image-based evaluation of cancer patients.

Conclusion: Our system enables automated inference of semantic information about cancer lesions in images. This approach could improve the accuracy and reproducibility of image-based cancer treatment response assessment.

References/Funding Source caBIG Imaging Workspace, NCI

Automated Computational Assessment of Tumor Burden

D Rubin[1], C Baldassano[1], C Rodriguez[1], M Levy[2]
Departments of [1]Radiology, Stanford University; [2]Biomedical Informatics, Vanderbilt University

Background: Radiological imaging provides rich information for evaluating the response of cancer patients to treatment. A challenge however is that there are many images, many studies, and no systematic way to identify the tumor burden being tracked nor to consistently capture quantitative aspects of each lesion. Different lesions may be measured on each exam which is interpreted by different radiologists, and applying response criteria such as RECIST is time-consuming and error-prone. We sought to develop an open source tool to automate assessment of tumor burden.

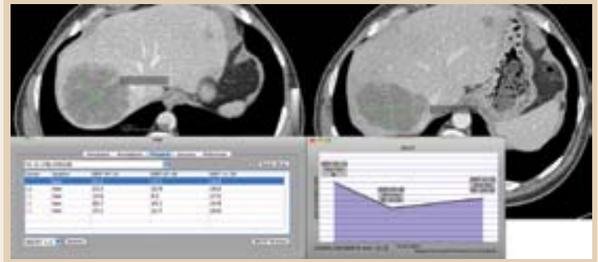

Screen Shot of iPAD image annotation tool showing lesion flow sheet and a liver cancer lesion annotated at two time points. Within the lesion flow sheet (lower left), RECIST target lesions are shown in blue ("L1" and "L2"), and RECIST non-target lesions are shown in brown ("L3," "L4," "L5"). The flow sheet is used to open the hanging protocol to display the images where that lesion has been annotated. Also shown is a graphic (lower right) showing RECIST sum of diameters across the serial imaging studies and percent change from baseline and from the minimum sum of diameters for the first and second follow-up time point, respectively.

Evaluation: We previously built a semantically-aware image annotation tool called iPAD, an open source plugin to the Osirix image viewing workstation. iPAD extracts and saves quantitative and semantic image metadata in the caBIG AIM standard format. We extended iPAD with analytic routines to process each annotated lesion, classify it as target or non-target lesions, and calculate quantitative features needed to assess the RECIST response criteria. We evaluated our tool by using it to annotate lesions seen in serial imaging studies from patients in a cancer research study. The tool automatically generated target lesion treatment response assessments (categories of response) directly from the image annotations. An oncologist validated the treatment response assessments automatically derived from our tool.

Discussion: Our tool produced RECIST target lesion response category assessments that agreed with those determined by the oncologist. The advantage of our tool is that all the information needed to derive automated assessment of tumor burden is directly derived from image annotations; all the user need do is identify (with linear or circumscribed ROI) each lesion.

Conclusion: We developed and evaluated a tool to automatically apply RECIST response criteria directly from image annotations, eliminating the need to perform calculations and apply criteria by hand. This approach may improve the ability of oncologists and radiologists to use quantitative information in images to evaluate tumor burden.

RADTF: A Semantic Search Enabled, Natural Language Processor (NLP) Generated Radiology Teaching File

B Do[1], A Wu[2], S Biswal[1], A Kamaya[1], D Rubin[1]
Departments of [1]Radiology, Stanford University, CA; [2]Radiology, Kaiser Permanente Downey Medical Center

Background: Storing and retrieving radiology cases is an important activity for education and clinical research, but this process can be time consuming. Organizing structured teaching files can also omit incidental pathologies not pertinent to the primary teaching point such as when a user saves images of the aortic dissection but disregards the incidental osteoid osteoma. An alternate strategy of identifying teaching cases is text search of reports in radiology information systems (RIS), but retrieved reports are unstructured, teaching-related content is not highlighted, and patient identifying information is not removed. Furthermore, searching unstructured reports requires sophisticated retrieval methodologies for useful results. We developed RADTF, an open source, RadLex-compatible teaching file solution that uses natural language processing (NLP) methods to processes radiology reports to create a searchable teaching resource from the RIS/PACS.

Example search result from the RADTF MRI database. A query for "ACL tear" yields 89 results which are ranked by relevancy based on semantic context. For example, RADTF retrieves all reports containing the exact search string, "ACL tear" (results # 1, 3, and 6), but also reports that contain the concepts "ACL" and "tear." Thus, more matches are retrieved (results # 2, 4, 5, and 7).

Method: We developed RADTF using a PHP-configured MySQL database server running on Apache Linux. The NLP system extracts and de-identifies teaching relevant statements from full reports to generate a radiology database of case material, converting existing RIS archives into an on-demand source of teaching material.

Results: Using RADTF, we generated a semantic search-enabled, web-based radiology archive containing over 700,000 "cases" with millions of images in less than 1 day. For comparison, the commercial, web-based teaching file, MyPACS.net contains ~21,000 cases contributed from 8,952 hospitals.

Conclusion: RADTF combines a compact representation of the teaching-relevant content in reports and a versatile search engine with the scale of the entire RIS/PACS collection of case material. NLP enables more precise semantic-based search.

References/Funding Source B Do, A Wu, S Biswal, A Kamaya, DL Rubin: RADTF: A semantic search enabled natural language processor generated radiology teaching file, Radiographics (in press), 2010.

Biomedical Image Metadata Management for Similar Image Retrieval

D Korenblum, D Rubin, S Napel, C Rodriguez, C Beaulieu
Department of Radiology, Stanford University, CA

Metadata, such as imaging observations ("semantic" metadata) describing radiology images, are usually described in text reports that are not directly linked to the images; this disconnect hinders basic research and the development of new medical systems and educational training tools. We developed a system, the Biomedical Image Metadata Manager (BIMM), (1) to address the problem of managing biomedical image metadata, and (2) to facilitate the retrieval of similar images using semantic feature metadata. Our approach allows radiologists, researchers, and students to take advantage of the vast and growing repositories of medical image data by explicitly linking images to their associated metadata in a relational database that is globally accessible through a Web application. BIMM receives input in the form of standards-based metadata files using a Web service, parses, and stores the metadata in a relational database allowing efficient data query and maintenance capabilities. BIMM image search results display twodimensional regions of interest (ROIs) stored as metadata that are automatically rendered onto preview images. The system's "match observations" function retrieves images with similar ROIs based on specific semantic features that describe imaging observation characteristics (IOCs). Using IOCs alone, BIMM accurately retrieves images with diagnoses matching the query images; we evaluate its performance on a set of annotated liver lesion images. Future work will focus on increasing the size of our dataset and adding and improving the imaging features included; e.g., incorporating pixel features to improve similar image retrieval results. As our reference dataset grows, we will obtain more clinically relevant evaluation results than those obtained from our single type of images (liver CT), compared to searching an entire PACS database containing multiple modalities and lesion types. BIMM is also poised to interface with emerging semantic web projects with overlapping interests to allow automated information sharing across broader areas of knowledge.

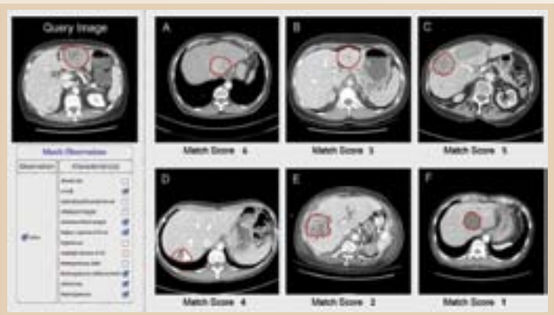

Query has 6 of 12 IOCs selected (checked boxes) for matching. Clicking on "Match Observations" sorted the cases in the reference library according to number of features matched; scores indicate matching of 1 to 6 features. Images A-F are returned images from a database of 90 annotated images. The query image was a metastasis from colorectal carcinoma. Returned images were (A) hepatocellular carcinoma, (B) focal nodular hyperplasia, (C) metastasis from transitional cell carcinoma of the bladder, (D) hemangioma, (E) bacterial abscess, and (F) simple cyst.

References/Funding Source NIH CA72023 and the caBIG Imaging Workspace, NCI

Toward Real-time Monitoring for Patient Safety: Recording, Extracting, and Reporting CT Radiation Dose Using New DICOM Standards

D Rubin[1], D Fleischmann[1], V Yeluri[2], P Frederick[2], R Herfkens[1]
Department of [1]Radiology, Stanford University, CA; [2]GE Medical Systems

Background: Given the recent high-profile cases of excessive radiation exposure to patients undergoing diagnostic imaging, it is crucial that institutions begin monitoring the radiation dose from their imaging equipment. We developed an approach to real-time monitoring and reporting of CT radiation dose.

Evaluation: Our CT scanner (Discovery CT 750 HD; GE medical systems) was adapted to output patient dose information as DICOM SR objects ("Dose SR"). We developed a utility in Java that extracts the dose values, the exam procedure, and patient information from the SR objects and stores them in a local database. We set up a Linux server to receive, store, and generate reports from the dose information extracted from Dose SR. We developed a utility to query the dose database to mine it for trends in dose in populations and in individual patients. We confirmed the accuracy of dose recording and reporting using a sample data that we obtained from the vendor.

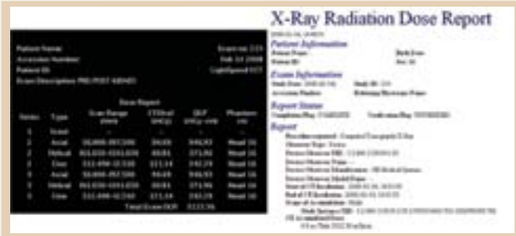

Automated dose reporting. Left: DICOM Dose SR object generated by the CT scanner which records dose exposure dose information. Right: DICOM "Dose Report" that is automatically generated by processing data in the Dose SR object.

Discussion: Our system permits continuous monitoring of our CT equipment and is crucial to our patient safety program. Our system will also facilitate data sharing with national dose registries. It is our hope that similar approaches will be deployed nationally. One limitation is that our approach requires that the scanner outputs the information in Dose SR objects. Many older scanners only output dose information on secondary capture images, requiring optical character recognition (OCR) to extract dose information. This may not be completely reliable and should be validated before being adopted.

References/Funding Source GE Medical Systems. DL Rubin, D Fleischmann, V Yeluri, P Frederick, RJ Herfkens: Toward Real-time Monitoring for Patient Safety: Recording, Extracting, and Reporting CT Radiation Dose Using New DICOM Standards, Annual Meeting of the Radiological Society of North America, Chicago IL, 2010.

Automatic Quantification of Margin Sharpness of Liver Lesions at CT: Application to CBIR

N Agrawal[1], S Napel[2], J Xu[3], D Rubin[2]
Departments of [1]Computer Science, [2]Radiology, [3]Electrical Engineering, Stanford University, CA

Purpose: Margin sharpness of liver lesions is related to invasiveness; thus we sought to develop a method to characterize margin sharpness, and evaluate it for similar image retrieval.

Method: We defined 2 attributes to characterize margin sharpness: difference in intensities between the lesion and its surroundings ("intensity difference"), and the abruptness of transition across the lesion boundary ("blur"). We calculated these attributes by fitting sigmoid functions along radial lines automatically drawn across the margin and observing parameters obtained for each fitted curve. We represent each lesion by a histogram of these parameters. We created 100 simulated CT reconstructions of circular liver lesions with varying intensity and blur to evaluate our feature in images with known margin characteristics, and noise. We used the correlation coefficient between the known parameters and corresponding computed features as a measure of performance. We also evaluated this feature using 79 lesions (25 cysts, 14 hemangiomas, 24 metastases, 6 HCCs, 3 abscesses, 5 FNHs, 1 fat deposit, and 1 laceration) in portal venous liver CT images from 44 patients. For these images, we created an independent reference standard for pairwise image similarity, and evaluated our feature using each image for query and rank ordering the remaining images by Euclidean distance between feature vectors. We then computed Mean Normalized Discounted Cumulative Gain (NDCG) over all 79 query images to compare this ordering with the expected ordering from the reference standard.

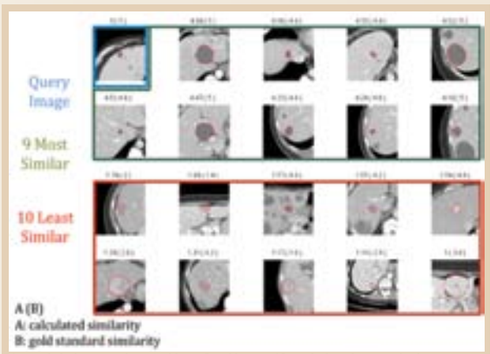

A sample lesion query image with top 9 and bottom 10 results based on margin sharpness similarity

Results: The correlation coefficient for blur and intensity difference attributes in simulated images was 0.983 and 0.998 respectively. The mean; standard deviation; worst case NDCG score for clinical images for the retrieval of K images, K = 10, 20 and 30, were 0.84;0.07;0.63, 0.85;0.06;0.61 and 0.86;0.05;0.65, respectively.

Discussion: Our quantitative feature is highly correlated with known margin attributes and accurately predicts reference standard rankings in clinical CT images of liver lesions.

Toward Best-Practice Reporting: A Natural Language Processor to Identify Semantic Content and Automatically Generate Standardized Knee MRI Reports

B Do, S Biswal, K Stevens, D Rubin
Department of Radiology, Stanford University, CA

Introduction: Structured reporting can distract radiologists and be cumbersome compared with conventional unconstrained dictation. The purpose of this work is to develop and validate an NLP to identify semantic content in knee MRI statements from unstructured text and automatically generates full, structured knee MRI reports.

Method: We designed an NLP using the Apache/PHP/MySql platform. The NLP processes whole knee MRI reports. Using a lexicon of "signals" or regular expressions that specify anatomy, findings, or disease terms, the NLP assigns each sentence to 1 of 8 categories of a standardized knee MRI template: (1) joint/effusion/synovitis/loose bodies, (2) menisci, (3) cruciate ligaments, (4) collateral ligaments, (5) extensor mechanism, (6) cartilage, (7) bone and marrow, and (8) miscellaneous (muscle, tendon, Baker's cyst, etc). Approximately 2,000 sentences from 125 knee MRI reports at our institution between 2005-2009 were reviewed to generate 59 signals determined by 2 musculoskeletal subspecialists to be specific for the 8 semantic categories. For validation, 25 knee MRI reports between 2005-2009 were randomly selected. Reports were pre-processed and converted to a single paragraph of sentences by removing all section headers. Accuracy in semantic assignment was assessed. Sentences containing 2 semantic concepts were assigned to at least 1 of the 2 categories.

Unstructured (LEFT) and post processed, structured (RIGHT) knee MRI reports. The NLP processes a block of unstructured knee MRI statements, identifies semantic content, and generates a structured report. Note the first sentence in the original report (LEFT) describing osteophytosis is correctly placed under the "BONE" category in the final, unstructured report.

Results: The NLP classified 381 sentences to the 8 categories. 10 sentences in 9 reports were inaccurately categorized for an overall accuracy of 97% and 64% accuracy per sentence and per report, respectively. The most common sources of classification error include absent lexicon and signal non-specificity.

Conclusion: We have developed a simple rules-based NLP to extract semantic concepts from knee MRI statements to automatically create structured reports. The extensible infrastructure has potential for integration with future RadLex-based best-practice templates. NLP systems that can stratify semantic content can potentially provide transparent, real-time feedback ("missing content"), decision support, QA, and data mining.

References/Funding Source Scientific presentation, Radiological Society of North America Meeting, Chicago, Illinois. November 28-December 3, 2010.

Extension of the Imaging Biomarker Ontology for In Vivo Microscopy Imaging

ES Savig[1,3], D Rubin[1,2], D Paik[1,2]
Departments of [1]Radiology, [2]Molecular Imaging Program at Stanford (MIPS), [3]Cancer Biology Program, Stanford University, CA

Purpose: There is a need for more reliable standardization and documentation of and access to quantitative imaging data in order to facilitate further comparative research studies utilizing imaging and deeper understanding of published research. The lack of standards for quantifying imaging data is a major factor due to the complexity and diversity of image quantitation techniques. To resolve these issues, we are designing an ontology of imaging biomarkers – a hierarchical infrastructure of terminology, with definitions, attributes, and relationships, that represent the intersection of the domains of imaging physics, image analysis, and biomedical investigations. This ontology provides a reference framework from which future imaging databases can be built and from which researchers can directly access image quantitation data.

Methods: This research project looks at the field of microscopy in particular with an emphasis on in vivo methods, where a massive amount of a wide variety of imaging data is being produced with very few quantitation methods available. The ontology is being built within the Protégé-Frames ontology editor, and contains categories (classes) that cover the types of microscopy, the types of measurements that can be taken from images, the contrast agents used to visualize processes within specimen, and the biology under investigation.

A portion of the Imaging Biomarker Ontology class hierarchy shown in the Protégé editor environment.

Results: By merging the domains of microscopy, image analysis, and biological experimentation into an ontology, knowledge surrounding imaging data becomes intricately networked through shared attributes such as a particular disease, a molecular target, a quantitation algorithm, or a measured parameter.

Conclusion: On one level, the ontology promotes the standardization of imaging data, making knowledge on how to quantify images readily available to researchers. On another level, by supporting the structure of imaging databases, it enables the dissemination of useful quantitative imaging data across disciplinary fields and from research to medicine, similar to what is currently available for microarray data. Such accessibility would facilitate large-scale image-based research studies. On yet another level, the ontology provides a networked infrastructure that allows for discoveries of unforeseen links between information. A search through a database built from the ontology will reveal new potential biomarker measurements for a disease simply because of a common target molecule with another disease.

Evaluation of ROI Methods for High Throughput Molecular Image Quantification

F Habte[1], S Budhiraja[1], T Doyle[3], C Levin[1], D Paik[1,2]
Departments of [1]Radiology, [2]Bioengineering, [3]Pediatrics, Stanford University, CA.

Purpose: Previous studies showed that there is a significant variability on molecular image quantification depending heavily on the definition of region of interest (ROI). To address this issue, several semi-automatic segmentation tools have been developed. For molecular images, these tools usually perform poorly due to lack of clear boundaries of a specific region of interest. This is especially a challenge in high throughput image quantification such as in pre-clinical animal imaging. The goal of this study is to evaluate and compare the performance of different ROI delineation methods.

Materials and Methods: For this study, we used five dynamic datasets obtained from microPET system. We also performed a phantom study. In the first part of our study, we used a large volumetric ellipsoid ROI to completely define region of interest. The normalized and adjusted ROI mean statistic value at each time point of the dynamic data is computed and compared with different threshold level, which is applied to remove low-level pixels from considering on the computation of ROI statistics. In subsequent study, we compared mean ROI statistics of most commonly used manual ROIs (rectangular, elliptic cylinder and ellipsoid) with the semi-automatic region grow method. The result indicates that the variability when using manual ROIs with different threshold value are comparable across different randomly selected data sets.

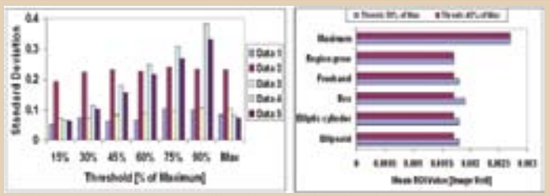

Left: Comparison of variability across different time point of five dynamic images of microPET selected randomly. Right: Comparison of ROI statistic value of different manual ROI definitions to the semi-automatic region grow method.

Results: Slightly higher variability (s.d. > 0.25) is shown when threshed is applied at greater than 60% of the maximum pixel value. On the other hand, all manual ROI methods with 40-50% threshed setting provided equivalent result compared to semi-automatic region-grow method seeded with a peak pixel at 50% tolerance level. These suggest that for high throughput quantification studies, a manually defined ROI that completely enclose a region of interest can be used when an appropriate threshold level is used.

Conclusion: This will eliminated the subjective variability while significantly speeding analysis of data for high throughput.

Software Only Method for QC of Monitor Quality and Reading Conditions in Multisite Image Reading Trials

D Rasooly, F Schmitzberger, TJ Kim, M Tall, J Roos, S Napel, G Rubin, D Paik
Department of Radiology, Stanford University, CA

Purpose: Quality control of display monitors and reading environment in a multisite image reading trial is difficult to maintain. We have validated a simple psychoperceptual software-only test that eliminates the need to send a photometer to each site for QC.

Methods: Characteristic luminance curves were measured using a photometer on 24 displays (18 LCD, 6 CRT). 6 readers incremented grayscale intensity differences (ΔI) until able to correctly read a 4-digit code in an 8-bit image on a white background. Tests were done with indoor lighting both on and off, with the controls done in a closed office (no windows) and the experimental measurements in a non-clinical reading environment (windows). As a gold standard of reader contrast detectability, just noticeable difference in contrast (C_JND) was calculated. Acceptable performance under the various lighting conditions was set at C_JND<7.5%.

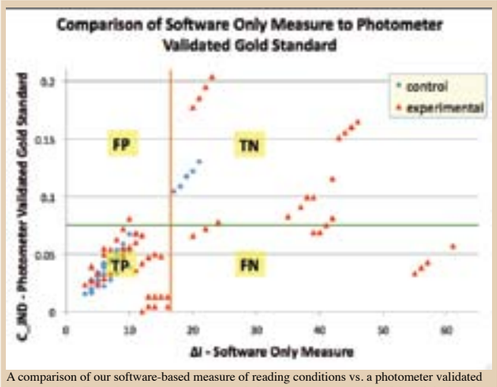

A comparison of our software-based measure of reading conditions vs. a photometer validated gold standard. Control measurements were made in a room representative of the clinical reading environment while experimental measurements were made in a typical research laboratory setting with higher ambient light. For both groups, thresholding the software measure matched the gold standard measurement.

Results: Using a threshold of ΔI≤16, our software-only test achieved a sensitivity of 92.1%, a specificity of 97.5% in classifying acceptable gold standard reader contrast detectability (N=204). While the DICOM GSDF corrects Weber's law at very low luminance, C_JND calculated using GSDF would vary minimally (0.6%-0.9%) for our experimental conditions (luminance of 20-482 cd/m^2). We set the 7.5% contrast threshold higher than the GSDF perceptual limits due to the added task of reading the 4-digit code. C_JND was significantly lower in the control group than the experimental group ($p<0.0002$) as was ΔI ($p<10^{-13}$). Many experimental group monitors were in the range of the control group monitors in both monitors but there more unacceptable outliers in the experimental group.

Conclusion: As image reading trials are likely to increase, controlling for confounding variables such as differences in monitors and reading conditions is vital. We can validate monitor quality in a distributed reading trial without needing to send a photometer and technician to each site.

Image Analysis, Bioinformatics, and Computational Modeling

Quantitative Unmixing of Surface-Enhanced Raman Scattering Spectra

C Nwabugwu[2], K Kode[3], D Van de Sompel[1], C Zavaleta[1], SS Gambhir[1], D.Paik[1]
Departments of [1]Radiology, [2]Electrical Engineering, [3]iCME, Stanford University, CA

Purpose: Surface-enhanced Raman scattering (SERS) microscopy is a light scattering technique of vibrational microspectroscopy for the selective detection of specific biomolecules. This technique combines the advantages of Raman imaging and biofunctionalized gold nanoparticles for visualizing and quantifying the distribution of target molecules. It is a useful tool to analyze the molecular composition and structure of a sample on the basis of unique Raman signatures characterized by a series of Stokes shifts with narrow peak widths, which form a unique pattern for different organic molecules. This project involves developing and validating an algorithm to quantitatively unmix the spectra of multiplexed Raman nanoparticles in living subjects.

Materials and Methods: Surface-enhanced Raman scattering nanoparticles were used to demonstrate whole-body Raman imaging, nanoparticle pharmacokinetics, multiplexing, and in vivo tumor targeting, using an optical microscope adapted for small-animal Raman imaging. Three female 8-week-old nude mice were used for all Raman spectroscope studies. The unmixing process was carried out on Raman spectra of 4 nanoparticles injected simultaneously using unmixing algorithm that parameterizes individual Raman peaks and uses Nelder-Mead optimization, accounting for changes in peak position and width.

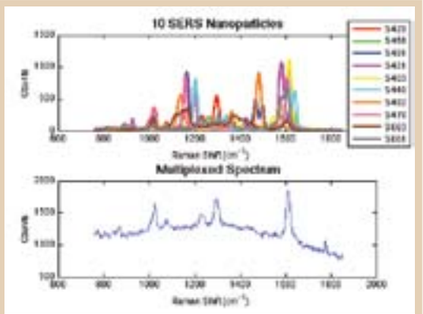

Top. Graph depicts unique Raman spectra associated with each of the 10 SERS Nanoparticles used for in vivo multiplexed imaging, each spectra has been assigned a color corresponding to its unique Raman active layer.
Bottom. Graph shows multiplexed Raman Spectra, represents a mix of individual spectra from Fig. 1.

Results: Distorting effects such as fluorescence background, peak location and width heterogeneity break the assumptions of linear and instantaneous generative model needed by typical source separation methods. Individual Raman peaks have been modeled to accurately depict the Raman spectra of nanoparticles. Simulated data based upon empirical measurements of peak location, width and height statistics was used to test the accuracy of our previously developed algorithm. Other constrained optimization methods have been explored and tested.

Discussion: The initial results of this project have shown that many of the similar issues in other Raman spectral unmixing apply to this data where the relatively lower signal-to-noise-ratio in vivo presents an even greater challenge. We are currently working toward optimizing the performance of this quantitative technique for Raman spectra unmixing in living subjects thereby resulting in significant potential for application of Raman spectroscopy in the analysis of nanoparticles.

References/Funding Source S. Schlücker, SERS Microscopy: Nanoparticle Probes and Biomedical Applications, ChemPhysChem 2009, 10, 1344 – 1354 C. Zavaleta et. Al, Noninvasive Raman Spectroscopy in Living Mice for Evaluation of Tumor Targeting with Carbon Nanotubes, Nano Lett., Vol. 8, No. 9, 2008

Raman Labeled Nanoparticles for In-vivo Imaging: Characterization of Variability and Improved Method for Unmixing

K Kode[1], C Shachaf[1,2], S Elchuri[2], G Nolan[2], D Paik[1]
Department of [1]Radiology and [2]Microbiology and Immunology, Stanford University, CA.

Raman spectroscopy can differentiate the spectral fingerprint of many molecules, resulting in potentially high multiplexing capabilities. However, accurate quantitative unmixing of Raman spectra is challenging because of overlaps of the Raman peaks from each molecule as well sensitivity to variation across spectra of a given molecule. If not accounted for, these inconsistencies in the spectra produce significant error which will ultimately result in poor unmixing accuracy. The objective of our study was to develop and validate mathematical techniques using parametric models of the Raman spectra of nanoparticles to unmix the contributions from each nanoparticle to allow for simultaneous multiplexed quantitation of nanoparticle concentrations for tumor cell characterization with applications in in-vivo imaging. This study consists of two parts: 1) statistical characterization of the variations in individual spectra, and 2) an algorithm for quantitative unmixing of the spectra. The variation in the heights of individual peaks of spectra for Raman labeled composite organic inorganic nanoparticles (COINs) is upto 20% and the location of peaks shifted by up to 10 cm-1 which was as much as 50% of full width half max. These variations between the peaks are uncorrelated with R2 ranging from 0.08 to 0.16. We modeled individual Raman peaks to accurately represent the Raman spectra of COINs and successfully unmixed up to 6 COINS after accounting for the spectral variations, achieving considerable improvement over the results obtained using direct linear least squares. The errors in estimation of the individual contributions of each nanoparticle using classical least squares were in the range of 20-70% while the error based on results from our model-based algorithm are in the range of 10-20% for unmixing of 6 COINS. To the best of our knowledge, we are reporting here for the first time, the quantitative unmixing up to 6 nanoparticles with maximum error less than 20%.

Imaging Biomarker Ontology (IBO)

T Liu[1,2], D Rubin[1,2], D Paik[1,2]
Departments of [1]Biomedical Informatics, [2]Radiology, Stanford University, CA

Purpose: With the advancement of pre-clinical molecular imaging techniques, a wide array of novel imaging biomarkers have been developed and demonstrated effectiveness in quantifying biological processes and in early prediction of therapeutic outcomes. However, integration and re-use of imaging biomarker data and knowledge is incomplete because most of the quantitative measurements are only available in the text-based literature that requires expertise and time to synthesize. The goal of this work was to develop an ontology of imaging biomarkers to enable storage and retrieval of desired imaging biomarker measurements, mining new information from the expanding imaging biomarker literature, and translation of novel imaging biomarkers to laboratory and clinical research.

Method: We have begun a bottom-up approach to constructing the ontology by conducting a literature review of the Journal of Molecular Imaging and Biology (2006-present) to identify and catalog imaging biomarkers. To resolve ambiguity, we decompose a quantitative imaging biomarker into three components: quantitative measurement and combination of data (single point, serial, etc.), measurement modality and contrast agent/tracer, and biological target. This approach enables capture of meaningful features of a biomarker, including imaging data acquisition and analysis as well as biological application. In addition, we curate the disease, biological process and experimental subject that are associated with each biomarker.

The Imaging Biomarker Ontology shown in Protégé, which is a widely used ontology editor and knowledge-modeling tool. The entity imaging biomarker is in expanded-view, where its subclasses are shown.

Progress: We currently identified 143 quantitative imaging biomarkers from 19 primary research articles across 14 types of diseases. The associated imaging modalities range from PET, CT, MRI to molecular microscopy and bioluminescent imaging. Principal biomarker characteristics were distinguished from the biomarker catalog and defined as entities in the ontology.

Conclusion: This is our initial effort towards creating a comprehensive database of imaging biomarkers and iteratively building the ontology using the curation for the ultimate goal of accelerating the translation of imaging biomarker development to scientific and clinical research.

A Scalable Method for Developing A Similarity Reference Standard for Content-Based Image Retrieval

J Faruque[1], DL Rubin[2], CF Beaulieu[2], R Summers[3], A Kamaya[2], G Tye[2], S Napel[2]
Departments of [1]Electrical Engineering, [2]Radiology, Stanford University, CA; [3]Radiology, National Institutes of Health, Bethesda, MD

Purpose: This project creates a reference standard for visual similarity of liver lesions seen at CT for training and validating a Content-Based Image Retrieval (CBIR) system by computing image similarity from subjective ratings of attributes on single images.

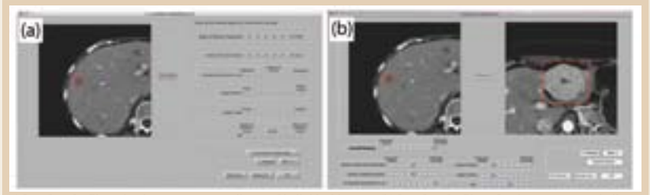

a) Interface for Phase 1, where users rate attributes of individual images, (b) Interface for Phase 2, where users rate similarity in attributes and overall similarity in pairs of images.

Method and Materials: We displayed 19 portal venous CT images containing liver lesions individually (phase 1) and in all 171 pair-wise combinations (phase 2) to 3 radiologists in random order. For phase 1, each image was rated for 6 visual attributes (number of different compartments and densities, average density, margin definition and contour, and rim density) on a 9-point scale. For phase 2, each pair of images was rated for similarity in the same 6 attributes as well as for overall similarity. We averaged readers' ratings and performed (1) a linear fit between pair-wise attribute and overall similarity ratings, (2) a linear fit between the absolute values of rating differences for each attribute between lesion pairs and overall pair-wise similarity, and (3) linear fits between the absolute values of rating differences for each attribute between lesion pairs and each pair-wise attribute similarity.

Results: The correlation coefficients between pair-wise attribute similarity and overall similarity ratings, and between the absolute values of rating differences between lesion pairs for each attribute to overall pair-wise similarity, were 0.81 and 0.67, respectively. The best and worst correlation coefficients between individual and pair-wise attribute ratings were 0.83 (average density) and 0.41 (number of different compartments), respectively. For overall similarity ratings, pairs of readers agreed to within 2 points in 64-84% of all ratings.

Conclusion: There were clear positive linear trends between the 3 sets of ratings. The best predictor of overall similarity was average density, and there was reasonable agreement between readers. Hence, this scalable method is feasible for creating a visual similarity reference standard for training and evaluating CBIR systems.

References/Funding Source NIH NIGMS Training Grant in Biomedical Computation, Stanford Bio-X Program

Image Analysis, Bioinformatics, and Computational Modeling

Prototype Software for Content-based Image Retrieval of Similar Appearing Lesions in Medical Images

J Xu[1], CF Beaulieu[2], DL Rubin[2], S Napel[2]
Departments of [1]Electrical Engineering, [2]Radiology, Stanford University, CA

Purpose: To develop a software platform for retrieving medical images containing similar appearing lesions.

Materials and Methods: We included a combination of semantic features described by radiologists (using iPAD — see separate report), and pixel-based features derived by computer algorithms, to create rich feature vectors describing each image in our database. Similarity between any pair of images was computed as the negation of a weighted sum of differences between corresponding elements of two feature vectors. Weights were derived using a machine-learning method that maximizes the retrieval performance, as measured by Normalized Discounted Cumulative Gain (NDCG). The software was tested using a database of 79 portal venous liver CT images containing various types of lesions and several reference standards created by radiologists. Performance was evaluated using NDCG and Precision-Recall Metrics.

Results: The system performed well, ranking images in the database appropriately with respect to the query and the reference standard. See Figure for details.

Conclusions: Content-based retrieval of lesions seen in radiological images is feasible. This warranted continued development of a larger more comprehensive database, and extension to other diseases and modalities.

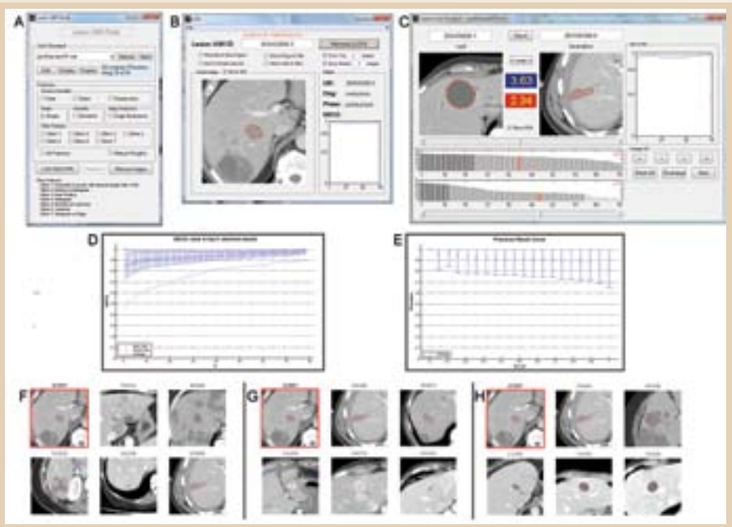

(A) Lesion CBIR Portal main window, allowing (i) choice of reference standard (ii) exploration/modification of the reference standard (see C) (iii) leave-one-out analysis to compare rankings of similarity to each query image with the expected ranking based on the reference standard (iv) retrieval from the database images containing lesions that are similar to the one in query image (see B) (v) selection of the weightings of the features to be used.

(B) Image Retrieval Window. Allows performance evaluation via NDCG and image ranking for query lesion in database or, for unseen images, ranking only.

(C) Reference Standard Explorer. Two images are shown side-by-side, with lesion circled in red. The blue score indicates the similarity score in the reference standard on a scale of 1 to 5; the red score indicates the computed similarity score from the machine learning analysis. Similar to (B), a NDCG plot is shown to display the performance of retrieval using the query image (on the left). Two bar plots in the bottom show the distributions of reference standard (top) and computed (bottom) similarity scores with the query image.

(D) NDCG plot showing average gain (circles; error bars indicate 1 s.d.) as a function of the number, K, of top-ranked retrieved images using the database using all features and weights trained to best match an overall similarity standard set by radiologists.

(E) Precision-recall plot, showing average performance (circles; error bars indicate 1 s.d.) for the same experiment as (D).

(F) Ranking based on shape feature only; query image is in upper left of each panel of 6 images, with the 2 highest rankings in the top half of each panel and the 3 lowest rankings of 78 images in the bottom half. Numbers above each image, x (y), show x = computed similarity score and y = similarity from the reference standard, both on a scale of 1 to 5 with 5 best. This retrieval is done using shape feature (the smoothness of boundary) only. Examples show similar shapes to query image in top half and quite different shapes in lower half, as expected.

(G) Similar to (F), except the ranking is done with the texture features only. Notice similar texture to query image in top half and quite different textures in lower half, as expected.

(H) Similar to (F), except the ranking is done with the edge-sharpness feature only. Notice show edge sharpness to query image in top half and quite different edge sharpness in lower half, as expected.

A Quantitative Shape Descriptor for Content-Based Retrieval of Similar Appearing Lesions in Medical Images

J Xu[1], J Faruque[1], CF Beaulieu[2], DL Rubin[2], S Napel[2]
Departments of [1]Electrical Engineering and [2]Radiology, Stanford University, CA

Purpose: To develop a quantitative descriptor of shape for use in content-based image retrieval of similar appearing lesions in medical images.

Materials and Methods: We used three distinct contour-based shape features: compactness, centroid distance signal, and multi-scale local area integral invariant (LAII). Compactness gives a rough measure of circularity. Centroid distance signal is obtained by sampling the shape boundary in a polar coordinate system centered at the centroid of the shape. LAII entails the notion of curvature in a scale-space. Together these features comprise a 14-element feature vector invariant to translation, rotation, and scale. We defined the similarity between two images as the inverse of a weighted sum of the absolute difference between each element. We tested our feature with simulated images using several reference standards, and with clinical images (lesions from 79 portal-venous-phase liver CT scans) using a reference standard for similarity derived from five readers who rated the smoothness of each lesion boundary on a 5 point scale. We used a leave one out analysis and Normalized Discounted Cumulative Gain (NDCG) to compare rankings of similarity to each query image with the expected ranking based on the reference standard, and averaged over all query images.

Results: In simulated images, the feature combining weights were trained to get excellent results for all reference standards, with average NDCG >90% for all queries. Quite good results were also obtained with clinical images.

Conclusions: Experiments in a simulated lesion database show that our computational shape descriptor is trainable to a wide variation of notions of similarity and, in each case, ranks similarity in close agreement with the reference standard. Results in clinical images were visually excellent, but mean NDCG scores were not as favorable owing to difficulties in setting the reference standard.

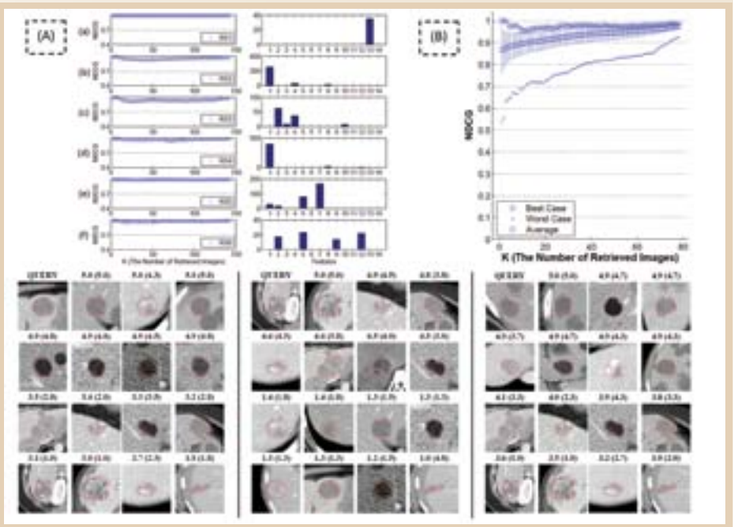

(Top, A) (a-f) Left column: NDCG(K) plots show average performance in a simulated dataset containing 144 shapes, using optimal weights learned using the following reference standards:
(a) the inverse of the absolute difference of compactness for both shapes
(b-e) the inverse of a weighted sum of squared differences between the corresponding parameters (lobulation amplitude, lobulation frequency, and eccentricity) that were used to generate each shape: (b) all weights=1, (c) the weights were 3, 1, and 1, (d) the weights were 1, 3, and 1, and (e) the weights were 1, 1, and 3, for eccentricity, lobulation amplitude, and lobulation frequency, respectively.
(f) the inverse of the absolute difference in the axis ratios between ellipses fitted to each shape.
The mean NDCGs over K for (a)-(f) were 100%, 96%, 91%, 98%, 100%, and 98%, respectively.
(a-f) Right Column: Optimal weights learned in the training using corresponding reference standards. Note: In row (a) where we have used compactness differences as the reference standard, the training process resulted in the assignment of a heavier weight to the compactness feature (element #13) and much lower weights to all other weights.
(Top, B) Best, worst and average NDCG plotted for the dataset containing 79 lesions, using the optimal weights trained using the human-derived similarity standard. For K=5, 10, and 15, the combined distance achieved an average score of 89%, 90%, and 91%, respectively.
(Bottom) Examples of rankings for 3 liver lesions from a database of 79 portal venous CT scans. Query image is in upper left of each panel of 16 images, within which rankings go from highest on upper left to lowest on lower right. Due to space limitations, we only show the 7 highest rankings in the top half of each panel and the 8 lowest rankings in the bottom half. Examples show similar shapes to query image in top half and quite different shapes in lower half, as expected. Numbers above each image, x (y), show x = computed similarity score and y = similarity from the reference standard, both on a scale of 1 to 5 with 5 best.

Lung Nodule Detection in the Peripheral Visual Field: Impact of Size, Distance and Local Lung Complexity

M Tall, D Ly, K Roychoudhury, J Roos, D Paik, S Napel, G Rubin
Department of Radiology, Stanford University, CA

Purpose: To determine the factors that attract or distract observer attention when searching for lung nodules in volumetric CT data.

Method: A 3x3x5 cm lung mass was simulated and imbedded into 5-cm thick subvolumes (SV) extracted from 3 unenhanced lung MDCT scans (64-row, 1.25 mm thickness, 0.7 mm increment). The mass was visible on all transverse sections in the SV. Two collections of 30 solid secondary nodules were simulated with 4-6 mm and 7-8 mm diameters, respectively. A total of 207 SVs were created containing one secondary nodule imbedded at a random depth at a distance from the edge of the mass of 2.5, 5, 7.5, or 10 cm, and along rays cast every 45° from the center of the mass. For each SV, we created a movie of the sections from superior to inferior at 3 sections/s. Six radiologists observed each movie once. Eye tracking hardware assured that vision was centered on the 3 cm mass throughout playback. Upon completion of each viewing the radiologist assigned a confidence rating (0-5) to the detection of a secondary nodule and indicated its location on the screen.

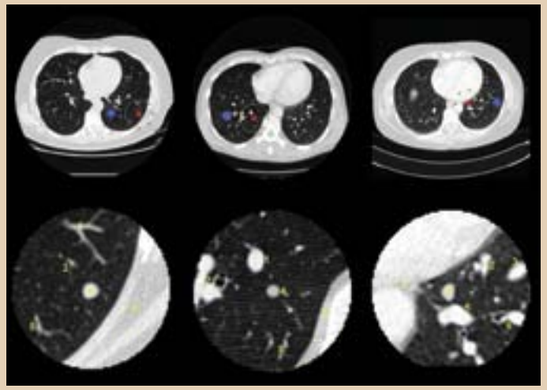

Illustration of localized visual complexity. The upper row illustrates the test cases, primary lesions (fixation points, colored blue) and secondary nodules (periphery detection, colored red). Yellow circle indicates the localized complexity region centered on the secondary nodule. Detection scores; Left, detected by 6/6 readers. Middle, detected by 4/6 readers. Right, undetected by all readers. Note: the chest wall and mediastinum were excluded from analysis (objects 2, 3, 1 in left, middle, and right, respectively).

Detection sensitivity was analyzed relative to the secondary nodule size, and radial position and distance from the mass, and local lung complexity (LLC) of the secondary nodule based upon the number and combined area of discrete lung opacities (e.g., vessel cross-sections) within 3cm and > -500 HU.

Results: Using a proportional odds logistic regression model and eliminating redundant predictors, models fit individually to each reader resulted in the following decreasing order of association based on greatest reduction in Akaike Information Criterion (AIC): seconday nodule diameter (6/6 readers, max p-value <0.001), distance from central mass (6/6 readers, max p-value<0.001), LLC:number (5/6 readers, max p-value=0.05), and LLC:area (3/6 readers, max p-value=0.03).

Conclusion: When searching for lung nodules in CT scans, detection sensitivity varies depending upon the size of the nodule and the complexity of the lung background.

References/Funding Source G Rubin, M Tall, D Ly, K Roychoudhury, J Roos, D Paik, S Napel. (2010). Perception of Lesions in the Gaze Cone Periphery: Impact of Lesion Size, Distance, and Background Lung Complexity on Detection. Submitted to RSNA2010.

Correlating Imaging and Molecular Phenotypes in Lung Cancer

S Napel[1], DL Rubin[1], C Hoang[2], AN Leung[1], A Quon[1], J Xu[1,3], SK Plevritis[1]
Departments of [1]Radiology, ISIS, [2]Cardiothoracic Surgery, [2]Electrical Engineering, Stanford University, CA

Purpose: This is a work in progress to discover relationships between imaging features of lung cancer and molecular profiles derived using gene arrays. This relationship may be used to predict the molecular profiles from the imaging data, and/or to enhance the contributions of each.

Approach: We have been identifying preoperative thin slice CT and PET datasets from patients who have had tissue from resected lung tumors stored in the Stanford Cancer Center Tissue Bank. From these datasets we are deriving several types of features: CT: (1) semantic features as entered by a thoracic radiologist using our iPAD tool, which enforces a complete description using a controlled vocabulary (Figure), (2) features (texture, margin sharpness, etc.) directly computed from the regions of interest containing the tumors. PET: (1) quantitative descriptors such as standard uptake values, (2) annotations describing morphological characteristics of high metabolic activity distribution. RNA samples will be extracted from the tissue samples and processed by the microarray services of the Functional Genomics Facility using Illumina Whole Genome Bead Chips.

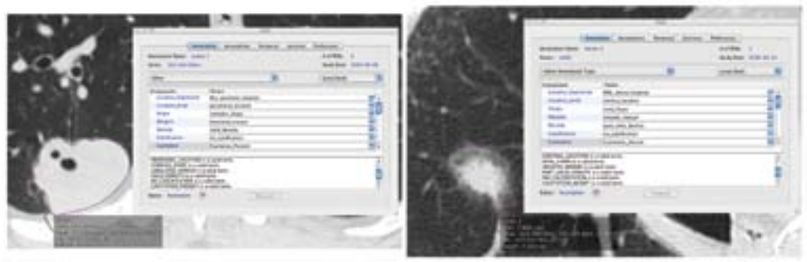

Examples of two lung cancer tumors visible on CT scans, outlined and annotated for entry into our database. The outline not only provides a reference for the semantic annotation, shown being collected by the iPAD windows, but will also drive computer algorithms to extract reproducible computational features.

Finally we will employ bioinformatics methods to compute a radiogenomic map relating the image to the molecular features.

Progress: We have adapted our computational tools, originally developed for computation of features from CT scans of the liver, to the lung cancer domain, and have been collecting the image data for preliminary annotation and feature extraction. We have identified approximately 20 cases and are beginning to prepare the corresponding samples for molecular analysis. We are looking forward to analyzing data for 30 samples in support of an NIH proposal submission this fall.

References/Funding Source General Electric Medical Systems

Content-Based Image Retrieval of Similar Appearing Lesions: Application to Liver CT and Pilot Study

S Napel[1], DL Rubin[1], J Xu[1,2], G Tye[1], J Faruque[1,2], CF Beaulieu[1,3]
Departments of [1]Radiology, ISIS, [2]Electrical Engineering, [3]Radiology, MSK, Stanford University, CA

Purpose: To improve radiological decision support, we developed a CBIR system and performed a preliminary evaluation of it using a database of CT images of the liver and an external standard of image similarity.

Method and Materials: Under IRB approval for retrospective analysis of de-identified patient images, we selected 79 lesions (25 cysts, 14 hemangiomas, 24 metastases, 6 HCCs, 3 abscesses, 5 FNHs, 1 fat deposit, and 1 laceration) in portal venous liver CT images from 44 patients. Using a tool we developed for complete and standardized description of lesions, a radiologist identified and annotated each lesion with semantic features using a controlled terminology; additionally, our software automatically computed image features based on image texture, boundary sharpness, lesion shape, and other pixel-based features. All features were combined into a feature vector, and similarity between pairs of images was defined as a function of the weighted sum of absolute differences between the corresponding feature vector elements. We created an independent reference standard for pair-wise image similarity, which we used in a leave-one-out cross-validation to train weights that optimized the rankings of images in the database in terms of similarity to query images. Performance was evaluated for all withheld lesions using both precision-recall curves, and normalized discounted cumulative gain (NDCG), a common measure for information retrieval utility.

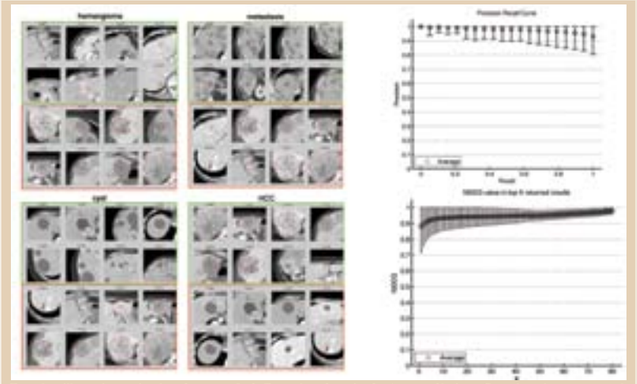

Two plots illustrating retrieval performance. Left: Examples of queries for 4 types of lesions: Green box shows query and 7 top ranked images, and red box shows 8 lowest ranked images of 78. Numbers show computed similarity score and, in parentheses, similarity score in reference standard, on a 1 to 5 scale, 5 being most similar. Top Right: Mean and standard deviation of precision (fraction of similar images in retrieved images) over all 79 queries as a function of recall (fraction of similar images in entire database retrieved). Bottom Right: Mean and standard deviation of a measure NDCG, a measure of information retrieval quality, as a function of K, the number of images retrieved. Both plots indicate excellent performance.

Results: Considering all 79 possible query images, mean precision was >90% at all values of recall. Mean, best, and worst case retrieval accuracy was >98%, 100%, and >52%, respectively, using NDCG, when ranking 3 or more images in the database.

Conclusion: Preliminary assessment of our system shows excellent retrieval results for most types of liver lesions visible in portal venous CT scans. Poorer performance for some lesions is most likely due to small numbers of certain lesion types, and imperfections in the reference standard.

References/Funding Source General Electric Medical Systems. SA Napel, CF Beaulieu, C Rodriguez, J Cui, J Xu, A Gupta, D Korenblum, H Greenspan, Y Ma, DL Rubin. Radiology. 2010; 256 (1): 243-52.

Developing a Similarity Reference Standard for Content Based Image Retrieval Using Matrix Completion

J Faruque[1], DL Rubin[2], CF Beaulieu[2], R Summers[3], A Kamaya[2], G Tye[2], S Napel[2]
Departments of [1]Electrical Engineering, [2]Radiology, Stanford University, CA; [3]Radiology, National Institutes of Health, Bethesda, MD

Purpose: To investigate scalable matrix completion techniques for creation of a reference standard for pair-wise visual similarity of liver lesions seen at CT, for training and validating a Content Based Image Retrieval (CBIR) system.

Method and Materials: We displayed 19 portal venous CT images containing liver lesions in all 171 pair-wise combinations in random order to 3 radiologists, and asked them to rate each pair for overall visual similarity on a scale of 0 to 8 (8=most similar). To investigate if the overall similarity matrix, averaged over the readers, could be predicted from a subset of the entries, we removed a random subset, and predicted the remaining ones by minimizing the maximum sum of the singular values of the matrix. We created 180 subsets containing between 8% and 99% of the matrix, computed the RMS error between the predicted and actual entries for each subset, binned the results into bins of width 10% of the actual entries included in the matrix, and computed the means and standard deviations of RMS error in each bin. We compared its performance to that when using an "ideal similarity matrix," created by randomly assigning each image a score on the same scale and calculating the pair-wise image similarity from the difference between scores of the individual images.

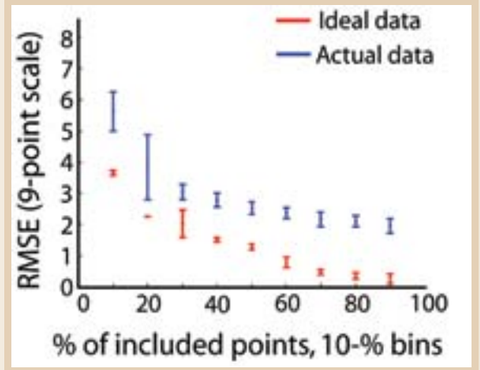

Binned mean RMS error as a function of percentages of entries included, shown for actual radiologist-determined similarity ratings and ideal ratings.

Results: Using the ideal similarity matrix, when retaining 20% or more of the original matrix entries, the mean RMS error was below 3 points. With radiologist-established similarity ratings, this accuracy can be achieved when 30% or more of the original matrix is present (Figure).

Conclusion: These very preliminary results show that we can establish pair-wise similarity ratings with a small fraction of actual ratings. We are investigating how these results scale as the matrix size increases, and are continuing to evaluate this method for establishing similarity in large databases.

References/Funding Source NIH NIGMS Training Grant in Biomedical Computation, Stanford Bio-X Program

Quantifying and Comparing the Disease Progression Characteristics of Lung Cancer and Breast Cancer

R S Lin[1], and S K Plevritis[2]
Departments of [1]Biomedical Informatics and [2]Radiology, Stanford University, CA

Cancer screening programs are currently recommended for only certain types of cancer, such as breast cancer, but not for others, such as lung cancer. The goal of this project is to develop progression models for lung cancer and breast cancer in order to address two critical issues in cancer screening: how early we need to detect cancer (i.e., the ideal detection threshold) and how often we need to screen asymptomatic individuals, so that we can capture the tumor before it progresses beyond cure (i.e., the ideal screening interval).

We develop a stochastic model for cancer progression, which enables us to estimate the cure fraction from cancer and the tumor volume doubling time. The estimate about cure fraction allows us to address the ideal detection threshold of a screening technology whereas the doubling time allows us to estimate the ideal screening interval. The model is applied to data on lung cancer and breast cancer separately. The study population was identified from the Surveillance, Epidemiology and End Results (SEER) cancer registry and included patients diagnosed with non-small cell lung carcinoma from 1988 to 2003 and patients diagnosed with invasive ductal carcinoma from 1975 to 1979. Model parameters were estimated based on the SEER data using the maximum likelihood estimates. The model reproduces SEER, validates against two external clinical trials and produces estimates of tumor volume doubling times that are consistent with empirical data.

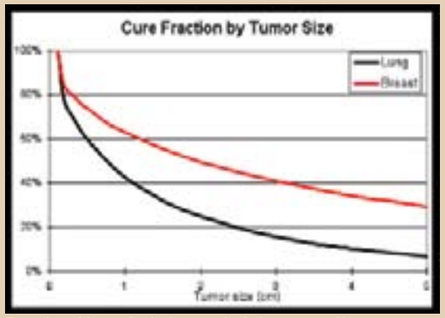

Comparison of the cure fraction by tumor size for lung cancer and breast cancer.

Our results demonstrate that breast cancer has a much higher cure fraction than lung cancer if the tumors are detected at the same size. In the absence of screening, we predict that the likelihood of cure due to clinical detection is 44% for breast cancer whereas 6% for lung cancer. In order to achieve a cure fraction of 50% by screening, breast cancer needs to be detected and treated when it is 1.9 cm in size whereas lung cancer needs to be detected and treated when it is 0.7 cm. Our estimates also show that lung cancer grows more rapidly than breast cancer: the estimated median tumor volume doubling time 134 days for lung cancer versus 252 days for breast cancer. These findings suggest that when compared to breast cancer screening, an effective screening program for lung cancer needs to use a technology with smaller detection threshold and a shorter screening interval.

References/Funding Source U01CA88248 and Canary Foundation

Estimating the Likelihood of Cure from Breast Cancer

R S Lin[1], and S K Plevritis[2]
Departments of [1]Biomedical Informatics and [2]Radiology, Stanford University, CA

Breast cancer is the leading cancer for women in the United States. Patients' outcomes have been improved since the 1980's due to cancer interventions, such as mammography screening and adjuvant therapy. The goal of this study is to quantify the effects of mammography screening and adjuvant therapy on likelihood of cure from breast cancer

We developed a mathematical model of the natural history of cancer to estimate the relationship between the size of the primary tumor and the likelihood of cure. The model is applied to breast cancer, separately to patients who were diagnosed from 1975 to 1979 and those diagnosed from 1991 to 1993. Model parameters were estimated using data from the Surveillance, Epidemiology and End Results (SEER) cancer registry. The model reproduces SEER, validates against an external clinical trial and produces estimates of tumor volume doubling times that are consistent with empirical data.

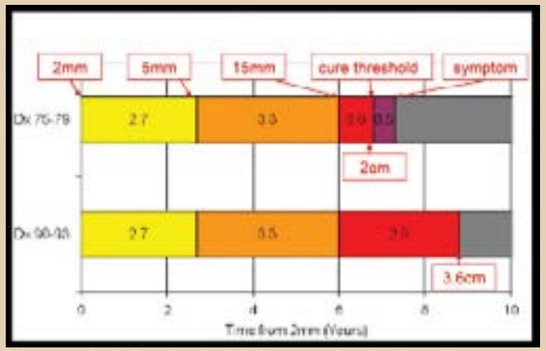

Disease progression timeline and cure threshold of breast cancer for patients diagnosed between years 1975 and 1979 versus those diagnosed between years 1990 and 1993

Our results suggest that the likelihood of cure from breast cancer has been substantially improved (from 44% to 67%) from 1975 to 1993 due to the advances in adjuvant therapies and screening mammography. The median tumor size at which the disease progresses to non-curable state has increased from 2 cm to 3.6 cm, primarily due to advances in adjuvant therapy. Consequently, the median time for screening mammography (with detection threshold 1.5 cm) to detect a tumor while the disease is curable increased from 0.8 years to 2.8 years, indicating screening has become more effective due to the advances in treatment. Our results suggest that given the efficacy of current treatments, the benefit of biannual versus annual screening has increased significantly.

We plan to further develop natural history model for breast cancer patients with different hormone receptor statuses and use the model to understand the cancer progression patterns of these cancer.

References/Funding Source U01CA88248

Cancer Incidence, and Survival with Risk-Reducting Strategies for BRCA1/2 Mutation Carriers

A W Kurian[1,2], D F Munoz[3], S Plevritis[3]
Departments of [1]Medicine, [2]Health Research and Policy and [3]Radiology, Stanford University, CA

Women with BRCA1/2 mutations must choose between prophylactic surgeries and screening to manage their high risks of breast and ovarian cancer; the outcomes of these alternatives have not been compared directly. We simulated multiple different risk-reducing strategies, and compared resulting cancer incidence, tumor prognostic features, and overall survival.

We built a Monte Carlo model of breast screening with annual mammography plus magnetic resonance imaging (MRI) from ages 25-69, prophylactic mastectomy (PM) and/or prophylactic oophorectomy (PO) performed at various ages in 25-year old BRCA1/2 mutation carriers.

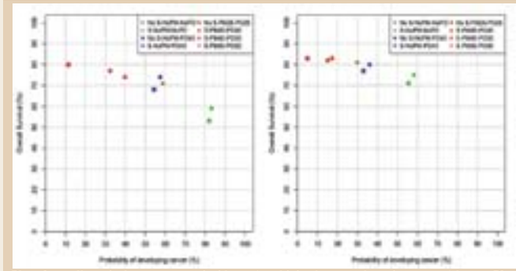
Plot of overall survival versus cancer incidence (combining breast and ovarian cancers) by age 70 for 25 year-old BRCA1 (left panel) and BRCA2 (right panel) mutation carriers choosing different cancer risk-reducing strategies, including prophylactic mastectomy (PM), prophylactic oophorectomy (PO) and/or annual breast screening with mammography and magnetic resonance imaging (S), performed at various ages (age in years at time of surgery indicated by number following PM or PO).

For BRCA1 and BRCA2 mutation carriers, PM plus PO at age 25 minimizes cancer incidence (4-11%) and maximizes overall survival (80-83%) to age 70, whereas MRI-based breast screening plus PO at age 40 results in higher cancer incidence (36-57%), yet similar overall survival (74-80%). Without intervention, BRCA1/2 mutation carriers most often develop Stage II-III breast cancers (72-74%); with MRI-based screening, 67-68% are diagnosed with Stage I cancers, mostly estrogen receptor (ER)-negative with BRCA1 (63%) and ER-positive with BRCA2 mutations (81%). Although prophylactic surgeries prevent cancer most effectively, MRI-based breast screening can offer comparable survival to PM by diagnosing mostly Stage I breast tumors; ER expression by BRCA1- (34%) versus BRCA2-associated (79%) cancers may prompt different therapy recommendations. This study of the factors that influence cancer treatment experiences may guide risk-reduction decisions for BRCA1/2 mutation carriers.

References/Funding Source Robert Johnson Foundation; U01 CA88248

The Effect of Mammography Screening Schedules on Age-Specific Mortality and Survival

S. Geneser[1], S. Plevritis[1]
Departments of [1]Radiology, RSL, Stanford University, CA

Background: The recent changes in U.S. Preventive Services Task Force (USPSTF) breast cancer screening recommendations have generated significant confusion and controversy. Indeed, the suggestion that women from 40-49 years of age make individualized decisions to screen based on their medical history and values pushes the burden of information regarding the complex interplay of mammography screening benefits and harms to clinicians.

Objective: Our goal is to simulate and examine the benefits of various mammography screening schedules among various age groups and provide additional metrics to better elucidate the impact of screening.

Methods: We simulated screening and treatment among a large population of women to determine the effects of screening women aged 40-49 on age-specific breast cancer survival, mortality, and life years saved.

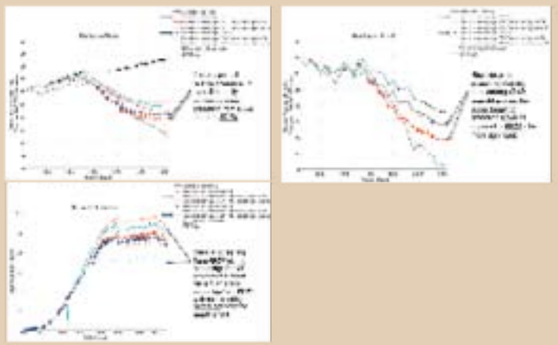
The upper left and upper right images depict mortality rates for various screening schedules for women aged 40+ and 40-49, respectively. The lower left image shows the life years saved for various screening schedules normalized over the number of women screened.

Results: Though there is little relative difference between the overall population mortality levels, there is a significant improvement in mortality rates among women who die in their 40s and 50s when the population is regularly screened from 40-74 as opposed to 50-74. Moreover, our preliminary analysis indicates that regular screening among women aged 40-74 with no screening after age 74 to be the most efficient screening schedule in terms of life years saved per woman screened.

Conclusion: An age-based analysis of mammography screening schedules provides additional information about the benefits of screening that may well be useful in deliberations regarding the benefit of screening women between the ages of 40 and 50.

References/Funding Source U01 CA88248, Dean's Postdoctoral Fellowship School of Medicine, Stanford University (2010-2011). S.E. Geneser, S.L. Rutledge, S.K. Plevritis. "Identifying Effective Age-Based Mammogram Screening Schedules Using a Stochastic Population Model of Breast Cancer". Joint Mathematics Meeting (AMA/MAA), San Francisco, CA, 01/15/10.

Magnetic Resonance Research

This MRI section will explore and highlight new and novel accomplishments made over the last year in the critical areas of MRI instrumentation and applications. These new advances provide improved capabilities to detect pathologies in clinical applications as well as to inform basic science understanding of the human body's physiology, function, and biology.

Body MR Imaging

Distortion Reduction of Metal Artifacts in MRI using Shear Correction

PW Worters, K Butts-Pauly, BA Hargreaves
Department of Radiology, RSL, Stanford University, CA

Imaging around metal in MRI is known to be challenging due to susceptibility effects [1]. Susceptibility differences give rise to arbitrary frequency shifts which is the primary reason for distortion and image artifacts. Our method Slice Encoding for Metal Artifact Correction (SEMAC [2] correct for slice distortion by using extra slice phase-encoding, and correct for readout distortion by using view-angle tilting (VAT) [3].

VAT is a simple modification that comprises playing the same slice gradient used for excitation during the readout window. This essentially tilts the voxels in such a way that off-resonance spins appear to be located in the correct position with respect to on-resonance spins.

There are, however, limitations associated with this method: (a) the readout window is limited to the length of the slice gradient, which leads to restrictions of the readout duty cycle and thus signal-to-noise (SNR) efficiency; (b) the readout k-space is effectively modulated by the shape of the RF pulse profile which results in reduced spatial resolution.

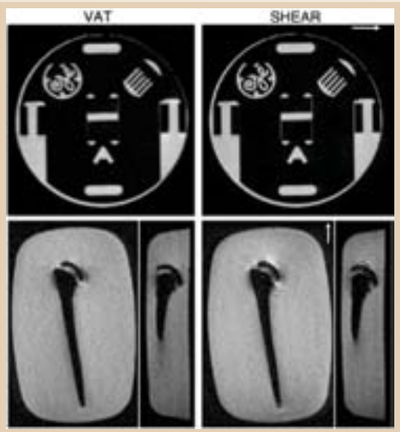

Top row: Images from a resolution phantom demonstrating the spatial resolution effects of VAT and shear. Significant blurring in the readout direction (white arrows) was observed in the VAT image on the left, which is not apparent in shear-corrected image on the right. Bottom row: Coronal and reformatted sagittal images from a phantom with a metallic shoulder implant. The shear method has the same distortion correction capability as VAT.

Butts-Pauly has shown that this blurring can be mitigated with the use of a quadratic phase RF and/or restricting the readout window to the main lobe of the RF pulse [4].

This work proposes the use of a processing method, called shear correction, to resolve readout distortion instead of using VAT. In SEMAC, slice distortion is resolved by performing extra phase-encoding in the slice direction. Therefore, the exact amount of off-resonance is known as it is linear with z-distance from the center on-resonance slice. Instead of using VAT, slice distortion can be corrected by shifting the slices in the readout direction. Thus, the readout window is no longer limited to the length of the RF pulse width, allowing longer readout windows (e.g., lower receive bandwidth), increased SNR and/or higher spatial resolution images.

References/Funding Source NIH: R01 EB009055, NIH: R21 EB008190, NIH: P41 RR009784. [1] JF Schenck. The role of magnetic susceptibility in magnetic resonance imaging: MRI magnetic compatibility of the first and second kinds. Med Phys 1996; 23:815–50.[2] Lu W, Pauly KB, Gold GE, Pauly JM, Hargreaves BA. SEMAC: Slice encoding for metal artifact correction in MRI. Magn Reson Med 2009; 62:66–76. [3] Cho Z, Kim D, Kim Y. Total inhomogeneity correction including chemical shifts and susceptibility by view angle tilting. Med Phys 1988; 15:7. [4] Butts K, Pauly JM, Gold GE. Reduction of blurring in view angle tilting MRI. Magn Reson Med 2005; 53:418–24.

In Vivo Metabolic Imaging of Hyperpolarized [1-^{13}C]-Pyruvate in Orthotopic Hepatocellular Carcinoma

MM Darpolor[1], Y-F Yen[2], W Shi[3], L Xing[4], RH Clarke-Katzenberg[1], M-S Chua[3], D Mayer[1,5], S Jason[5], RE Hurd[2], A Pfefferbaum[5], L Senadheera[4], S So[3], L Hofmann[1], GM Glazer[1], DM Spielman[1]
Departments of [1]Radiology, [3]Surgery, [4]Radiation Oncology-Physics, Stanford University, Stanford, CA; [2]Global Applied Science Laboratory, GE Healthcare, Menlo Park, CA; [5]SRI International, Neuroscience Program, Menlo Park, CA

A primary liver cancer, hepatocellular carcinoma (HCC), is a highly malignant tumor type with average survival rates that are currently less than a year following diagnosis. Most patients with HCC are diagnosed at an advanced stage, and no efficient marker exists for determining prognosis and/or predicting response(s) to therapy. In the present study, we implemented a three-dimensional double-spin-echo echo-planar spectroscopic imaging (3D DSE-EPSI) pulse sequence to investigate potential hallmarks of cellular carbon metabolism in rat liver bearing orthotopic HCC. In addition, gene expression analysis was performed for lactate dehydrogenase-alpha (LDH-α), NADH quinone oxidoreductase-1 (NQO1), and alanine aminotransferase (ALT) using quantitative real-time PCR. We show that differentially expressed genes and proteins in pyruvate metabolism could be exploited to distinguish HCC tissues from normal liver tissues.

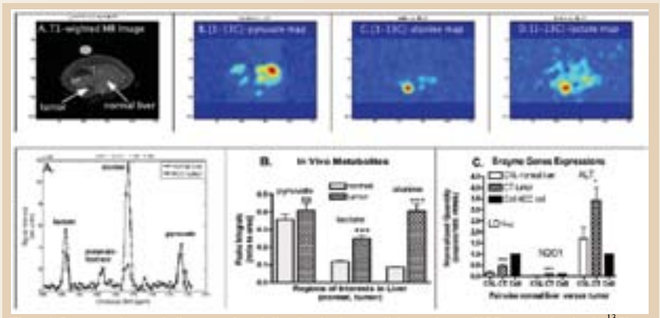

Figure 1: Representative metabolite maps of a rat's liver bearing hepatocellular carcinoma (HCC) tumors showing [1-^{13}C]-lactate and [1-^{13}C]-alanine production after a bolus injection of hyperpolarized [1-^{13}C]-pyruvate. Metabolite maps were computed as integral of metabolite peak for each voxel's spectrum from 3D DSE-EPSI data. [A] T1-weighted image of rat's abdomen with HCC tumors (arrows) in the liver, [B] [1-^{13}C]-pyruvate metabolic map, [C] [1-^{13}C]-lactate metabolic map, and [D] [1-^{13}C]-alanine metabolic map. Figure 2: [A] Representations of *in vivo* hyperpolarized 13C MRS spectra of normal liver and HCC tumor obtained within the same rat. [B] Quantitative measures of ^{13}C-metabolites peaks intregrals plotted as bar graphs for control rats. [C] Pairwise bar graphs of enzyme gene expression from normal liver and tumor tissues of lactate dehydrogenase-α (LDH-α), NADH quinone oxidoreductase-1 (NQO1), and alanine aminotransferase (ALT) gene expressions. All bar graphs are displayed as mean±SEM, and the p-values were evaluated by unpaired t-test (*p-value ≤ 0.05, ** p-value ≤ 0.01, *** p-value ≤ 0.001).

A total of 7 buffalo rats were surgically implanted with hepatocellular carcinoma cells into the medial lobe of the liver. A 3 ml bolus injection of hyperpolarized [1-^{13}C]-pyruvate was administered via the tail vein, resulting in a peak blood concentration of approximately 8 mmol/L. Acquisition of MRSI data began 20 s after the start of bolus injection.

Computed sets of metabolic maps are display along with a T1-weighted proton image from a representative 3D volume of a rat liver (Fig 1, top). Spectra from tumor voxel and normal liver voxel displayed elevated Lac and Ala (Fig. 2a-b), with corresponding gene expressions for LDH and ALT shown in Fig 2c. The data herein suggest that the conversion of exogenous [1-^{13}C]-pyruvate to [1-^{13}C]-lactate and [1-^{13}C]-alanine is a characteristic marker of HCC *in vivo*. Such molecular signatures of HCC should serve as an impetus to developing novel enzyme inhibitors as therapeutic agents with hyperpolarized ^{13}C 3D MRSI serving as a diagnostic tool for early detection a surrogate marker or endpoint for drug activity targeting these specific enzymatic pathways.

References/Funding Source NIH/NCI 2 T32 CA-09695-16 (Glazer), NIBIB R01 EB009070, NIAAA R01 AA018681, RR P41 RR009784, T.S. Kwok Foundation, H.M. Lui Foundation. M Darpolor, YF Yen, W Shi, L Xing, R Clarke-Katzenberg, M Chua, D Mayer, S Jason, R Hurd, A Pfefferbaum, L Senadheera, S So, L Hofmann, G Glazer, and D Spielman, In Vivo Magnetic Resonance Spectroscopic Imaging of Hyperpolarized [1-13C]Pyruvate Metabolism in Rat Hepatocellular Carcinoma, NMR in Biomedicine, in press.

Parallel Transmit Enabled Pulse Sequence Development for High Field MRI

R Watkins, B Rutt
Department of Radiology, RSL, Stanford University, CA

We are developing multi-channel RF transmit systems hardware and methods for improving B1 uniformity for 7-Tesla human MRI imaging. Due to the RF wavelength becoming comparable to human body dimensions at 7T, image quality can be seriously degraded as a result of propagation delays through conductive/dielectric tissue, leading to destructive interference of the transmitted B1 field and serious inhomogeneity. By implementing multiple transmit sources and coil elements, we will create the ability to transmit independently to each coil element. A major application of this new technology will be to improve B1 uniformity. Two specific methods will be investigated. The first is referred to as "B1 shimming", and is a scalable method which replaces a single large RF power amplifier with an array of smaller amplifiers, permitting independent control of the phase and amplitude of the RF pulse transmitted from each coil element. A second method known as "parallel transmit", will allow the transmission of multiple RF waveforms simultaneously, one from each coil element, which enables the acceleration of 2D and 3D RF pulses, thereby allowing geometrically tailored excitation volumes. In addition we are developing hardware and methods to explore the use of multiple spatial modes associated with volumetric transmit array coils and variations of the Butler Matrix beam forming networks. This will allow us to control many field patterns with only one or two transmit waveform sources and RF power amplifiers. By interleaving multiple B1 field distributions we have the potential to improve overall RF transmit uniformity and image quality over larger fields of view.

References/Funding Source GE Healthcare

High-Frequency Subband Compressed Sensing MRI

K Sung, BA Hargreaves
Departments of Radiology, RSL, Stanford University, CA

Compressed sensing (CS) is an acquisition and reconstruction technique that can dramatically reduce the measurement size [1,2]. Its promise to improve imaging speed of magnetic resonance imaging (MRI) has been successfully demonstrated with the wavelet transform [3]. CS MRI assumes that MR images are sparse (or compressive) typically in the wavelet domain, meaning many wavelet coefficients are close to or equal to zero. Conventional CS MRI, however, is limited by complicated integration with existing acceleration methods as well as by possible reconstruction failure, which manifests as residual incoherent artifacts.

We present a novel method, called Hi-Sub CS (High-Frequency Subband Compressed Sensing), to better exploit the increased sparsity of the high frequency information in images compared with that of the lower frequency information. The idea of this method is to undersample the outer k-space region (high-frequency subband) much more than the central k-space region. Wavelet subbands typically contain different sparsities due to the wavelet-tree structure; high-frequency subbands are exceptionally sparse whereas low-frequency subbands are less sparse. Separate Fourier sampling of each wavelet subband exploits this uneven sparsity property [4], and allows improved reconstruction accuracy. Our new scheme capitalizes on the link between k-space and the wavelet space used in the CS reconstruction, and permits undersampling of outer k-space by factors of 16-24 with very little loss in high-resolution features.

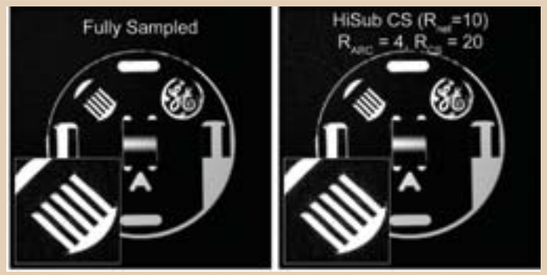

Hi-Sub CS in a resolution phantom, beginning with a 512 X 512 fully-sampled image (LEFT), and the corresponding image created with 10x less data using Hi-Sub CS (RIGHT). In Hi-Sub CS, the use of parallel imaging (GE's ARC method with 4x reduction) and outer k-space reduction of 20 leads to 10x net acceleration with very little loss of high resolution edges. This is highlighted in the zoomed regions around the comb-shaped structure.

In Hi-Sub CS, the k-space sampling uses a small fully-sampled region for coil calibration, an intermediate region sampled to exploit parallel imaging, and a much larger outer area that is highly undersampled with randomized sample positions. A demonstration of Hi-Sub CS in a GE resolution phantom is shown in the figure. Despite a net acceleration of 10 (R_{ARC} = 4 and R_{CS} = 20), the high-resolution features in the phantom are very well depicted due to a better sparsifying transform for CS.

References/Funding Source NIH R01-EB009055 and Supplement to R01-EB009055. [1] Donoho, IEEE TIT, 2006;52(4):1289, [2] Candes et al., IEEE TIT, 2006;52(2):489, [3] Lustig et al., MRM, 2007;58:1182, [4] Candes et al., Inverse Problems, 2007;23:969. K Sung, BA Hargreaves. High-Frequency Subband Compressed Sensing MRI, Proceedings ISMRM Eighteenth Scientific Sessions, May 2010, p4848

Non-contrast Breath-held Renal MR Angiography

M Saranathan[1], P Worters[1], E Bayram[2], S Vasanawala[1]
Department of [1]Radiology, RSL, Stanford University, CA; [2]GE Healthcare, Waukesha, WI.

While contrast-enhanced MR Angiography (CEMRA) is widely used for evaluation of vascular pathology, recent nephrogenic systemic fibrosis (NSF) concerns following administration of Gadolinium based contrast agents have spurred interest in non-contrast MRA methods. Balanced steady state free precession (b-SSFP) imaging [1] has shown great promise due to its high SNR and short scan times and has been successful in coronary and renal artery imaging. Robust fat suppression remains challenging at high field strengths due to B0 and B1 inhomogeneities. Conventional fat saturation compromises the SSFP steady state, causing ghosting artifacts. We propose GUINNESS (**G**roup-encoded **U**ngated **I**nversion **N**ulling for **N**on-contrast **E**nhancement in the **S**teady **S**tate) a balanced SSFP-Dixon 3D technique with a novel group-encoded k-space segmentation scheme for **breath-held** non-contrast MRA.

A new group-encoded view ordering scheme was developed to a) minimize eddy currents b) retain sequential and centric view ordering properties for contrast manipulation and immunity to breath-hold loss c) enable use of non-separable sampling patterns such as 2D self-calibrated parallel imaging as well as k-space corner removal. The new flexible view ordering helped restrict scan times to breath-holding limits. A 3D dual-echo bipolar readout balanced SSFP pulse sequence with a robust two-point Dixon reconstruction algorithm [5] was used for fat-water separation, eliminating the need for conventional fat suppression pulses. A slab-selective hyperbolic secant inversion pulse offset in the inferior direction relative to the acquisition slab was used to simultaneously effect venous and background suppression. The inversion time was set to 1300ms at 3T. This enabled us to acquire the 3D volume in a single breath-hold, eliminating the need for respiratory triggering which could be unreliable or prolong scan times, especially in sick and elderly patients. Additionally, free-breathing scans were acquired to assess the motion robustness of the group-encoded k-space segmentation scheme.

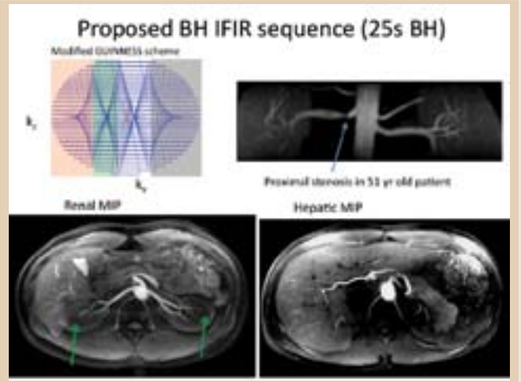

Proposed k-space ordering scheme (GUINNESS) is shown top left. Bottom panel shows MIPs of GUINNESS slabs obtained in 2 volunteers of renal and hepatic arteries depicting branching vessels with excellent contrast and SNR. Top right panel shows a patient with proximal right renal artery stenosis nicely depicted in the GUINNESS MIP

References/Funding Source M Saranathan, E Bayram, J Glockner. Group-encoded Ungated Inversion Nulling for Non-contrast Enhancement in the Steady State (GUINNESS): a balanced SSFP-Dixon technique for breath-held non-contrast MRA. Proceedings ISMRM Eighteenth Scientific Sessions, May 2010. Saranathan M, Worters P, and Vasanawala S. Breath-held non-contrast enhanced MR angiography with a novel group- encoded k-space segmentation scheme. Accepted for presentation at the MR Angio Club 2010 (Oct 6-9th 2010), Seoul Korea

T2 Maps and Diffusion-Weighted Imaging of Knee Cartilage with a DESS Sequence at 3T

E Staroswiecki[1,2], KL Granlund[1,2], MT Alley[1], GE Gold[1], BA Hargreaves[1]
Departments of [1]Radiology, RSL, [2]Electrical Engineering, Stanford University, CA

INTRODUCTION: In order to follow the changes related to early osteoarthritis and cartilage repair, we require the capability to show the morphological and biochemical properties of cartilage. Two promising techniques are T2 mapping and diffusion-weighted imaging (DWI).

The Dual-Echo Steady-State (DESS) sequence has been used for morphological imaging and T2 mapping. In this work, we improve the accuracy of T2 measurement using DESS by simultaneously solving for diffusion characteristics (ADC).

THEORY: The DESS sequence acquires two echoes per repetition of the RF pulse. The echoes are separated by a spoiler gradient, which provides diffusion sensitivity. The echoes have signal contributions from different pathways and therefore exhibit different diffusion and T2 weightings depending on sequence parameters like flip angle, spoiler gradient area, and timing. While the dependence of the signal on sequence and tissue parameters is complex, two different acquisitions, resulting in four images, can be fitted to the signal equations to estimate T2 and ADC.

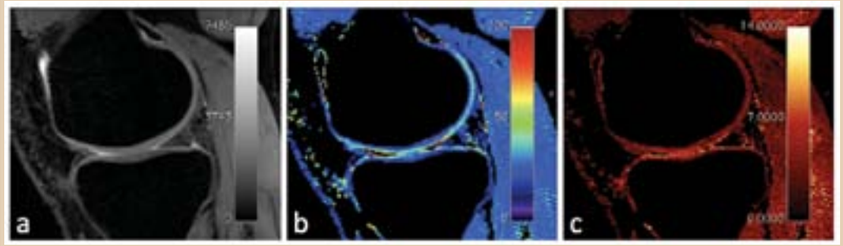

Figure shows: a) morphological DESS image, b) T2 map of knee cartilage generated with two DESS acquisitions, c) ADC map of knee generated simultaneously with T2 map.

METHODS AND RESULTS: We scanned 5 subjects using a 3D DESS sequence at 3T. We obtained fat-suppressed images from two acquisitions: one with a gradient amplitude of 4.0G/cm and an 18° flip angle, and a second with a gradient amplitude of 0.5G/cm and a 35° flip angle. From the four acquired images, we calculated T2 and ADC maps. The T2 values were compared to those generated with the gold standard sequence (a spin-echo series of acquisitions with varying echo times). In all cases, the T2 values estimated simultaneously with ADC were closer to the gold standard than when estimating T2 independently of these effects.

References/Funding Source Richard M Lucas Foundation, R01 NIH EB009055. E Staroswiecki, KL Granlund, MT Alley, GE Gold, BA Hargreaves, "T2 Maps and Diffusion-Weighted Imaging of Knee Cartilage with a DESS Sequence at 3T", Proc. of the 18th Meeting of the ISMRM, Stockholm, Sweeden. p. 824, 2010

Variable Voxel-Size Intensity Correction

A Nnewihe[1,2], K Sung[1], BA Hargreaves[1,3]
Departments of [1]Radiology, RSL [2]Bioengineering, [3]Electrical Engineering, Stanford University, CA

High-density surface coil arrays have been used for attaining highly-accelerated, high resolution images for brain, breast and cardiac MRI studies [1,2]. Due to the layout and size of the coil elements, these arrays usually exhibit sensitivity variations across the field of view. Several intensity correction schemes have been investigated in literature, and many of these algorithms significantly change the spatial noise profile during the process, which is undesirable [3,4]. In this study, we present a variable voxel-size intensity correction method that maintains the original noise profile while reducing intensity variations across the image.

The principle idea consists of averaging voxels in regions of low sensitivity and properly scaling the result, thereby boosting the SNR in these regions. We present the results of this variable voxel-size algorithm for an ultrahigh resolution, 3D breast patient scan using a 16-channel surface coil array. We assumed that the coil intensity profile is a slowly varying spatial function and approximated this bias field using a low pass filter on the original data. We normalized this bias field and created a "voxel volume" map where larger voxel sizes correspond to regions of low intensity of the bias field. We passed the original dataset individually through scaled low pass filters of varying bandwidths to achieve the desired resolution in the voxel volume map. In the final corrected dataset, we chose the appropriate dataset for each voxel based on the voxel volume map.

The results show better visualization of the glandular tissue near the chest well using the variable voxel correction. Additionally, the correction algorithm is conservative in terms of increase in voxel volume, so there is no noticeable loss of detail in the breast. Further studies need to be performed to evaluate the utility of this algorithm in a clinical setting.

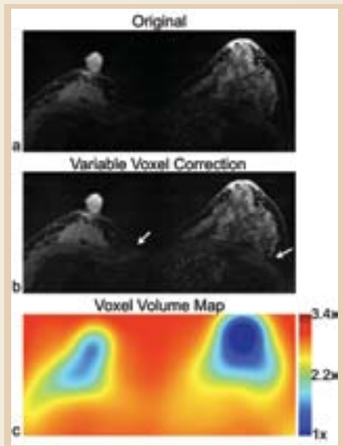

The variable voxel-size intensity correction image shows better visualization of anatomy near the chest wall (see arrows) when compared with the original image. The voxel-volume map shows the increase in voxel volume across the image.

References/Funding Source [1] Wiggens, et al. MRM 2006; 16:216. [2] Wintersperger, et al. JMRI 2006; 23:222. [3] Brey, et al. Med. Phys. 1987; 15:241. [4] Lin, et al. Human Brain Mapping 2003; 19:96. / P41RR009784, R01-EB009055, and General Electric Healthcare.

B1 Mapping Near Metallic Implants

U Monu[1], P Worters[2], K Sung[2], GE Gold[2], BA Hargreaves[2]
Departments of [1]Electrical Engineering and [2]Radiology, Stanford University, CA

Power or specific absorption rate (SAR) estimations are important when testing the MR compatibility of implanted metallic objects. B1 mapping through flip angle maps, is a tool often used to determine SAR experimentally. As the number of metallic implants used during orthopedic surgeries increases [1], there is a need for an accurate and safe imaging technique. Recent developments in pulse sequences such as SEMAC [2], has enabled MRI near metallic implants by correcting image artifacts present and allows for improved image quality. Despite these advancements, more experiments need to be carried out to make sure that the new sequences comply with SAR limits [3] and do not cause overheating of tissues.

In MRI, the measurement of RF excitation fields is challenging. Futhermore, B0 inhomogeneities make B1 mapping near metallic implants especially difficult. Currently available B1 mapping methods that are based on gradient echo and spin echo techniques [4,5] have not been successfully used around metallic implants. This is mostly due to signal loss from increased susceptibility and imaging artifacts near metal.

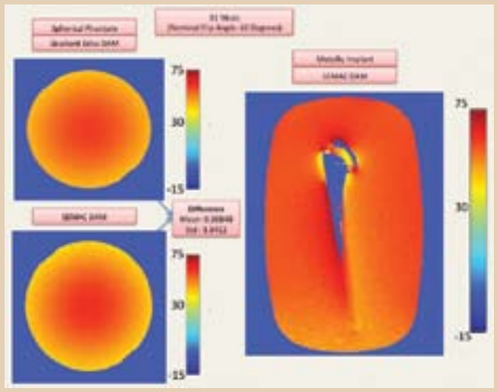

B1 maps acquired from a spherical phantom (diameter ~30 cm) using the gradient echo and SEMAC double angle methods (left). A nominal flip angle of 60° is applied. The maps show that the B1 is highest in the middle. The difference between the double angle methods is 0.51 ± 1.8 (s.d.). A B1 map of the shoulder implant using the SEMAC double angle method is shown (right).

In this work, B1 maps of phantoms were obtained using the standard gradient echo double angle method (DAM) and using the SEMAC DAM [4,5] on a 1.5T whole-body MR scanner. A comparison of these maps shows an insignificant difference of 0.85% between both techniques, validating the accuracy of the SEMAC DAM technique. We have applied the SEMAC DAM technique to a shoulder implant phantom as shown in the figure. Our work has validated the use of the SEMAC double angle spin echo method for B1 mapping around metal. Further experiments need to be carried out on different metallic implants, in different orientations. The results obtained will help determine locations that may suffer from increased local SAR.

References/Funding Source NIH EB 002524, EB 008190, P41 RR009784-11 and General Electric Healthcare. [1] S Kurtz, F Mowat, K Ong, N Chan, E Lau, M Halpern. Prevalence of primary and revision total hip and knee arthroplasty in the united states from 1990 through 2002. J Bone Joint Surg Am 2005;87:1487-1497. [2] W Lu, K Butts-Pauly, GE Gold, JM Pauly, BA Hargreaves. SEMAC: slice encoding for metal artifact correction in MRI. Magn Reson Med 2009;62:66-76. [3] FG Shellock, TO Woods, JV Crues III. MR labeling Information for Implants and Devices: Explanation of Terminology. Radiology 2009; 253:26-30. [4] CH Cunnungham, JM Pauly, KS Nayak. Saturated double-angle method for rapid B1+ mapping. Magn Reson Med 2006;55:1326-1333. [5] EK Insko, L Bolinger. Mapping of the Radiofrequency Field. J. Magn. Reson. 103,82-85 (1993).

High-resolution T2- and Diffusion-weighted Breast Imaging using FADE

KL Granlund[1,2], E Staroswiecki[1,2], MT Alley[1], BL Daniel[1], BA Hargreaves[1]
Departments of [1]Radiology, RSL and [2]Electrical Engineering, Stanford University, CA

Dynamic contrast-enhanced MRI is commonly used to detect breast tumors. However, its use is limited by the fact that it requires intravenous contrast injection, which is expensive and requires a physician to be present for the study. Reducing the cost and invasiveness of breast MRI improve the feasibility of using MRI for breast cancer screening.

We are using a fast acquisition double echo (FADE) sequence [1] to image breast lesions without injecting contrast. The FADE sequence is a steady-state imaging sequence that acquires two images with spoiler gradients played between the two acquisitions. The first echo has T1/T2 weighting and the second echo has strong T2 weighting. We are able to modify the image contrast by changing the flip angle, the echo times, and the spoiler gradient areas; for our current studies, we are modifying the diffusion weighting by changing the spoiler gradient areas.

We have scanned 7 patients with suspected lesions using the standard clinical breast MRI protocol and the FADE sequence. In all seven patients, the lesions that are visible on dynamic contrast-enhanced images are also visible in the FADE images. In the patient shown in the figure, the FADE sequence highlights a lesion that is only visible on contrast-enhanced T1-weighted images and not with any other non-contrast method (including mammography and ultrasound).

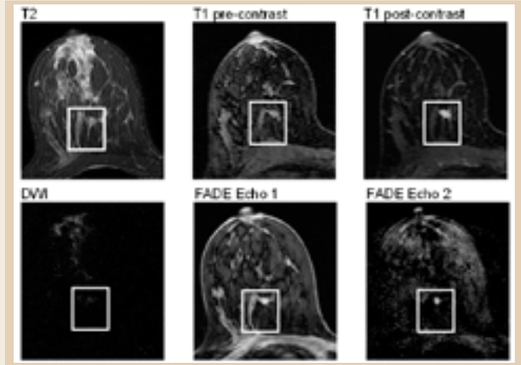

Images from a patient with an invasive ductal carcinoma. The boxed region shows the lesion and nearby glandular tissue. The lesion and glandular tissue are isointense on the T2-weighted, T1-weighted pre-contrast, and diffusion-weighted images. The tumor is highlighted in both the T1-weighted post-contrast image (gold standard) and Echo 2 of the FADE sequence. The FADE images were acquired with the same resolution as the T2-weighted image, but in one-third the scan time.

Echo 1 of the FADE sequence provides a high-SNR anatomical reference image and Echo 2 highlights lesions with restricted diffusion or long T2. Together, these images provide comparable image contrast to the sequences of a standard breast MRI protocol. By using a steady-state sequence, we are able to rapidly acquire high-resolution, 3D images with T2 and diffusion weighting and image lesions without administering an exogenous contrast agent.

References/Funding Source NIH Grant RR009784, NIH Grant EB009055, Richard M. Lucas Foundation, GE Healthcare. [1] TW Redpath, RA Jones. FADE – a new fast imaging sequence. Magnetic Resonance in Medicine, 6(2):224-34, 1988. KL Granlund, E Staroswiecki, MT Alley, BL Daniel, BA Hargreaves. High resolution T2 breast imaging using FADE. Proc. of 18th ISMRM, Stockholm, 2010. p. 366. M Saranathan, P Worters, S Vasanawala. Breath-held non-contrast enhanced MR angiography with a novel group- encoded k-space segmentation scheme. Accepted for presentation at the MR Angio Club 2010 (Oct 6-9th 2010), Seoul Korea.

Comparison of Non-Contrast-Enhanced IFIR bSSFP for Renal and Mesenteric MRA at 1.5T and 3T

CD Jordan[1,2], PW Worters[1], SS Vasanawala[1], BL Daniel[1], MT Alley[1], MF Kircher[1], RJ Herfkens[1], BA Hargreaves[1]
Departments of [1]Radiology, RSL, [2]Bioengineering, Stanford University, CA

Patients with kidney disease are most likely to need renal imaging, yet the standard technique of contrast-enhanced MR angiography with gadolinium may be contraindicated in these patients. This and other disadvantages demonstrate a need to explore non-contrast-enhanced MRA methods [1]. We evaluated one non-contrast-enhanced MRI technique, which has shown promising results: respiratory-gated In-Flow Inversion Recovery (IFIR) bSSFP2. The purpose of this study was to optimize the inversion time (TI) of the images at both 1.5T and 3T, and then compare the images quantitatively and qualitatively. The inversion time is critical because it affects the signal of the inflowing arterial blood, the extent of the imaging volume and the background suppression. Fig. 1 shows IFIR images of the same volunteer at 1.5T and 3T, demonstrating the increased contrast in the renal and mesenteric arteries at 3T in comparison to 1.5T. Four radiologists rated the images of 5 healthy volunteers scanned at 1.5T and 3T for visualization at 2 different TI times. The radiologists consistently gave higher visualization ratings for the 3T images of the renal, superior mesenteric and segmental intrarenal arteries with significant p-values for all categories except the superior mesenteric artery with a TI of 800ms. Considering acquisitions at both 1.5T and 3T, the relative contrast was highest using TI = 800ms, followed by TI =1000ms, then TI = 1200ms, and lastly TI = 1400ms. When the 1.5T and 3T images were then compared side-by-side, the radiologists rated improved artery delineation in the 3T images in 37 of 40 times, and the same in the other 3 times. This study demonstrated that IFIR at 3T may provide a means of avoiding contrast injection, and possible advantages of imaging at higher magnetic field strength include better resolution and more flexibility.

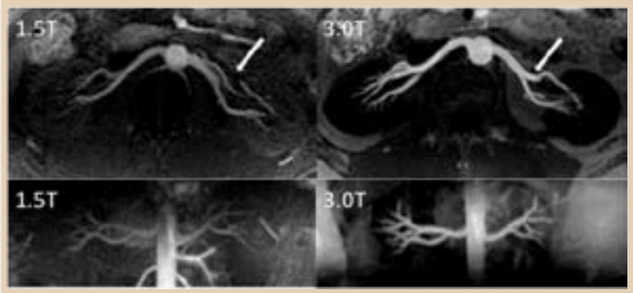

Figure 1. Axial (top) and coronal (bottom) maximum intensity projection (MIP) reformats acquired at1.5T and 3T. Arrows highlight higher contrast of renal artery at 3T than at 1.5T. Both have a TI of 800ms.

References/Funding Source NIH P41RR009784, Richard M. Lucas Foundation, NSF Graduate Research Fellowship Program, GE Healthcare. 1. M. Miyazaki and V. S. Lee. Radiol, 248(1):20–43, 2008. 2. P Young, et al. ISMRM, p.1870 (2009). CD Jordan, PW Worters, S Vasanawala, BL Daniel, MT Alley, MF Kircher, RJ Herfkens, BA Hargreaves. "Optimization and Comparison of Non-Contrast-Enhanced Inflow-Sensitive Inversion Recovery bSSFP for Renal and Mesenteric MRA at 1.5T and 3.0T." Published in Proceedings of the International Society for Magnetic Resonance in Medicine, Stockholm, Sweden, 2010.

Reducing the Scan Time of Time-Resolved, 3D Phase Contrast Imaging with 2D Autocalibrated Parallel Imaging

MT Alley[1], PJ Beatty[2], A Hsiao[1], SS Vasanawala[1]
Department of [1]Radiology, Stanford University, Stanford CA; [2]MR Applied Science Lab, GE Healthcare, Menlo Park, CA

Time-resolved 3-dimensional phase-contrast MR imaging (3D-PC MRI) has developed as an active area of research for vascular imaging because of its ability to acquire directional flow information along all three principle axes. While 3D-PC MRI shows potential in a wide range of applications, in general the clinical adoption of this approach for routine vascular imaging has been hampered by the long acquisition times inherent in the technique. Several groups have addressed this issue by using parallel imaging to accelerate data acquisition in one dimension. In this work we demonstrate the ability to perform auto-calibrated parallel imaging in both the in-plane and slice directions to significantly reduce the overall scan time.

All imaging was done using Signa scanners (GE Healthcare, Milwaukee, WI, USA). The sequence used for the time-resolved flow measurements was a 3D spoiled gradient-recalled echo (SPGR) phase contrast sequence modified to collect k-space data suitable for an auto-calibrated parallel imaging reconstruction. Parallel imaging was performed in the phase and slice direction using an outer reduction factor of 2×2. In addition, the corners of (ky,kz) space were not acquired. To provide autocalibration data for the reconstruction, a region of 24×20 central phase encodes in the ky×kz direction was fully sampled. This prescription reduces the total number of (ky,kz) pairs necessary for a complete study from 9648 to 2208. After the accelerated data were interpolated into the different temporal phases, unaliasing was performed using the Autocalibrating Reconstruction for Cartesian sampling (ARC) [1] method using a 3-dimensional reconstruction kernel.

We have shown that using parallel imaging in both phase encode directions reduces the scan time by approximately 77% (compared to 59% with 1D acceleration alone). This reduction can be used to improve patient compliance without sacrificing the coverage needed for a comprehensive vascular imaging protocol.

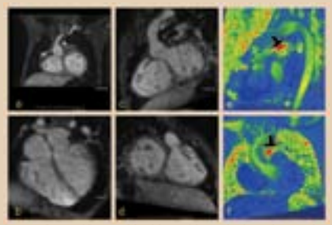

Images from a 10 year old subject with repaired tetralogy and pulmonary artery stents. This protocol consisted of 60 slices and an in-plane matrix of 256 x 192 for a final resolution of 1 x 1.4 x 3 mm3. A Poisson disc sampling pattern was used with a reduction factor of 2 in both directions, leading to an overall scan time of 9 minutes. The ARC algorithm was used to reconstruct the images. Gadofosveset was given intravenously as a blood-pool contrast agent and the subject was under general anesthesia. Figs. 2a-2d show coronal, 4 chamber, ascending aortic, and short axis reformats, respectively, from the data set. The arrows in Figs. 2e and 2f show the presence of a jet in the pulmonary artery

References/Funding Source NIH P41RR009784 and GE Healthcare. M Alley, P Beatty, A Hsiao, S Vasanawala, Reducing the Scan Time of Time-Resolved, 3D Phase Contrast Imaging with 2D Autocalibrated Parallel Imaging, in Proc., ISMRM, 18th Annual Meeting, Stockholm, page 1343, 2010.

Adaptive Slice Encoding for Metal Artifact Correction

BA Hargreaves[1], PW Worters[1] , GE Gold[1], JM Pauly[2], K Butts-Pauly[1]
Department of [1]Radiology, RSL and [2]Electrical Engineering, Stanford University, CA

Metallic implants are routinely used for joint replacements, bone reconstructions, spinal fixation and dental fillings. In MRI, metallic implants cause severe susceptibility variations that result in static magnetic field variations on the order of +/-10 kHz at 1.5T. These cause severe imaging artifacts in normal imaging, often rendering MRI non-diagnostic. However, by acquiring a limited 4D (x,y,z,f) space, where f=frequency, image distortions can be dramatically reduced at a cost of increased scan time. We recently developed a method called slice-encoding for metal artifact correction (SEMAC), which is used fairly routine at Stanford Hospital [1].

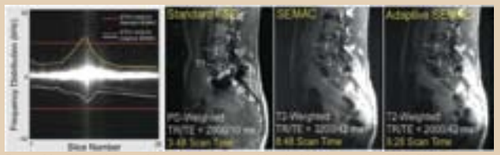

Spectral localizer (right) and image in a subject with spinal hardware using FSE, SEMAC and Adaptive SEMAC with 320x192 matrix over 28 cm FOV, 4mm slices, ETL=8. Adaptive SEMAC reduces scan time by 38% with similar artifact correction, and ability to visualize nerve roots (arrows) near metal, unlike FSE.

The main limitation of SEMAC is the increased scan times, often around 8-10 minutes. Because the pattern of magnetic field distortion varies considerably based on the metal device shape, composition, size and orientation, it is desirable to tailor the scan to the specific device, often enabling reduced scan times.

For each slice a "spectral localizer" scan is obtained by turning off the readout gradients in a standard 2D multislice scan (about 30 seconds), to detect the frequency range for each slice. A modified SEMAC acquisition and reconstruction uses a variable z-FOV for each slice, and the slice interleaving is modified to efficiently support variable numbers of phase encode lines per slice. We have compared standard spin echo, SEMAC, and adaptive SEMAC images phantoms and human subjects with metal implants. A sample result, (Figure 1) shows that adaptive SEMAC images show similar ability to correct distortions near metallic implants (arrows in images). There is some SNR loss and contrast change due to reduced repetition time.

Overall, adaptive SEMAC is a promising approach to tailor scans to the specific implant characteristics, in the same way that MRI scans routinely use a localizer to tailor scan parameters to the subject size.

References/Funding Source NIH: R21 EB008190, NIH: P41 RR009784. [1] W Lu, K Butts-Pauly, GE Gold, JM Pauly, BA Hargreaves. SEMAC: Slice encoding for metal artifact correction in MRI. Magn Reson Med 2009; 62:66–76.

Combined Excitation and Partial Saturation to Reduce Inflow Enhancement

M Han[1,2], BA Hargreaves[1]
Departments of [1]Radiology and [2]Electrical Engineering, Stanford University, CA

Partial saturation of an outer slab can reduce inflow enhancement and pulsatile ghost artifacts by preparing flowing spins to a steady state before entering the imaging slab, while dephasing their signal [1]. However, the partial saturation requires an additional RF pulse and spoilers, increasing TR. Here, we present a short RF pulse that simultaneously excites the imaging slab while partially saturating the outer slab [2].

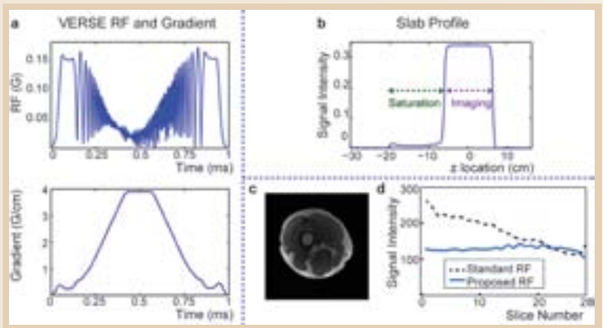

(a) Proposed VERSE RF pulse and gradient waveform with a constraint of the peak RF 0.17 gauss and maximum gradient strength of 3.9 gauss/cm. (b) Simulated slab profile from the proposed RF excitation. (c) Axial leg imaging was conducted to see signal changes along the femoral artery, shown by an ROI. (d) Signal intensity changes from the superior to inferior direction are compared between the standard RF pulse and the proposed RF pulse.

The new RF pulse combined a maximum-phase RF pulse for the partial saturation slab and a minimum-phase RF pulse for the imaging slab [3]. By using the maximum-phase RF pulse for the partial saturation slab, gradient spoiling for this slab can be achieved by the slab-select gradient itself. To provide sufficient spoiling, the time-bandwidth product of RF pulses was 96. The composite RF pulse was designed by an inverse SLR transform [4] and then the variable-rate selective excitation algorithm (VERSE) [5] was applied to reduce the pulse duration. Figure a shows the final 1 ms VERSE RF pulse with a 20° flip angle and the slab-select gradient, which can excite a 12.8 cm-thick imaging slab and partially saturate an outer slab with 13.8 cm-thickness. Figure b shows the simulated slab profile from this RF pulse.

The new RF pulse and gradient were incorporated into a standard 3D RF-spoiled gradient sequence and tested at the 1.5T scanner. Figure d shows signal intensity changes along the femoral artery (Fig. c) across the whole slab from one healthy volunteer. The proposed RF pulse reduced inflow enhancement significantly and provided an almost uniform signal profile across the slab.

Without increasing scan time, this pulse can reduce flow artifacts and provide T1 contrast, thus it can be useful in measuring arterial input function with high temporal resolution. Since VERSE excitation is sensitive to timing errors, the gradient timing delay should be properly compensated to generate the slab profile as designed.

References/Funding Source NIH P41RR009784. [1] Pang et al., 16th ISMRM, P2775, 2008.[2] Cunningham et al., 11th ISMRM, P699, 2004.[3] Staroswiecki et al., 17th ISMRM, P4506, 2009. [4] Pauly et al., IEEE TMI 10:53-65, 1991. [5] Conolly et al., MRM 78: 440-458, 1988. M Han, BA Hargreaves. Combined Excitation and Partial Saturation to Reduce Inflow Enhancement. Proceedings 18th Scientific Meeting, International Society for Magnetic Resonance in Medicine, Stockholm, Sweden, 2010, pp. 4947.

Ultra-High Field Microscopic Magnetic Resonance Imaging of Alzheimer's Pathology

M Zeineh[1], B Rutt[2]
Department of [1]Radiology, Neuroradiology and [2]Radiology, RSL, Stanford University, CA

The impact of Alzheimer's disease (AD) on the aging population of the world is growing. While there is an extensive literature on the importance and pathological evolution of amyloid plaques in AD, imaging this pathogenesis remains elusive. In vivo imaging of human amyloid plaques is only currently possible using PET tracers. However, PET suffers from poor spatial resolution, limiting the ability to specifically characterize and quantify plaques. With the advent of high-field MRI, there exists the potential for more direct plaque visualization. Using 7T ultra-high resolution MRI on human Alzheimer specimens, we have identified small round hypointense foci that may correspond to amyloid plaques. Our primary goal is to validate that these hypointense foci correspond with amyloid plaques as identified on pathological staining. Another question we would like to answer is whether iron is responsible for the degree of MR hypointensity of amyloid plaques.

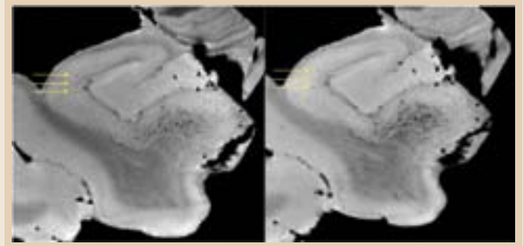

Amyloid Plaques Identified at 3T (left) and 7T (right)

References/Funding Source RSNA. M Zeineh, H Kitzler, S Atlas, B Rutt. Increased Detectability of Alzheimer Plaques at 7T vs. 3T using High Resolution bSSFP. Proc. ISMRM 18:4438 (2010).

Development of Enzyme-Activated MRI Probes for Cancer Imaging

P Pandit[1], J Rao[2], B Rutt[1]
Departments of [1]Radiology, RSL, MIPS and [2]Radiology, MIPS, Stanford University, CA

Our goal is to develop magnetic resonance imaging based molecular imaging systems to image cancer-specific enzymatic activity of protease in vivo. The platform is based on the protease activity triggered polymerization between two chemical moieties (the amino and the thiol groups of cysteine and 2-cyanobenothiozole) incorporated into a small-molecule imaging probe. This polymerization process converts the small-molecule probe into larger molecules (or even nanoparticles) to achieve probe concentration and retention at the target site and to generate amplified readout signals. Within the overall objective to develop and test enzyme-activatable MRI probes for in vivo imaging of furin activity, the following specific aims are defined

1. Design and synthesize furin-activatable MRI probes, and validate furin-specific activation of the MRI probes in vitro and in cells
2. Develop the theoretical models for these probes (using NMRD profiles and MR imaging at 0.5T, 1.5T, 3T and 7T) to better understand the underlying contrast mechanism.
3. Validate the in vivo MR imaging of furin activity in tumor xenografts.

References/Funding Source Stanford Molecular Imaging Scholars (SMIS) Program, NIH U54 CA119367 (CCNE-T)

Finite Element Simulation of RF Coils for High Field MRI

J Lu[1], B Rutt[2]
Departments of [1]Electrical Engineering and Computer Science, UC Berkeley, CA; [2]Radiology, RSL, MIPS, Stanford University, CA

We are using finite element method simulation tools for studying different radio frequency (RF) coils for 7T MRI. Various geometries and loading conditions are being modeled, and electric and magnetic field distributions being calculated. Such studies may enable us to achieve larger image uniformity and to determine local power deposition effects that may help to deal with issues of patient safety. We hope to use these tools to better understand and extend novel concepts for parallel RF transmission at 7T. Our group is currently working on building and modeling other RF hardware components: for example the Butler matrix, which allows for the generation of various modes of a birdcage coil. Currently, our group has created a low power Butler matrix and will be beginning construction of a high-power Butler matrix. Using a Butler matrix linked with a degenerate birdcage, it will be possible to take advantage of these orthogonal circularly polarized modes to maximize RF excitation uniformity. We plan to use numerical modeling tools to simulate all components of the RF transmission front end, including Butler matrix and multi-element coil, to study the effectiveness of these method in real world applications. Computational methods such as cluster computing are being examined to determine their potential benefits for more complicated and time-consuming simulations.

References/Funding Source GE Healthcare.

Multi-Component T1 and T2 Mapping to Study Myelination in Multiple Sclerosis

J Su[1], B Rutt[2]
Departments of [1]Electrical Engineering and [2]Radiology, RSL, MIPS, Stanford University, CA

Multiple sclerosis is a disease characterized by demyelination of the spinal cord and brain tissue. Traditionally, quantitative MR imaging has been hampered by long scan times. However, the mcDESPOT (multi-component driven equilibrium single pulse observation of T1/T2) technique allows for not only fast and accurate mapping of T1 and T2 relaxation times in the whole brain, but also the characterization of two water pools within a voxel. The faster pool is thought to represent water trapped inside a myelin sheath. The myelin water fraction (MWF) map describes the balance of these pools. MWF is well estimated by mcDESPOT and may directly show the effects of MS as the loss of myelin releases trapped water. With a non-linear warp, subject brains can be registered to a standard brain so that their MWF maps can be compared at every individual voxel. Using voxel-based analysis, voxels with very low MWF compared to the control group are identified as demyelinated and summed to produce the new measure: demyelinated volume. This metric has been found to correlate with disability scores as well as to discriminate between normals and early MS clinically-isolated syndrome patients, which is something traditional measures cannot do. New efforts are being made to bring mcDESPOT to higher field strengths to further study the invisible burden of MS.

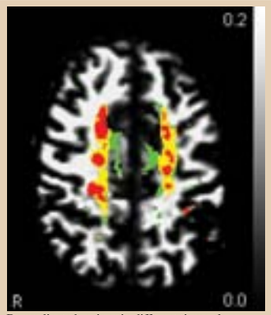

Demyelinated regions in different tissue classes shown on top of a quantitative MWF map. Red: in lesions; yellow: in dirty-appearing WM; green: in normal-appearing white matter, the invisible burden of disease.

References/Funding Source Canadian Institutes of Health Research. HH Kitzler, J Su, M Zeineh, SC Deoni, C Harper-Little, A Leung, M Kremenchutzky, BK Rutt. mcDESPOT-Derived Demyelination Volume in Multiple Sclerosis Patients Correlates with Clinical Disability and Senses Early Myelin Loss. Proc. ISMRM 18:382 (2010).

Quantitation of In-Vivo Rat Kidney Metabolic Kinetics of Pyruvate using Hyperpolarized ^{13}C MRSI

T Xu[1], D Mayer[2], M Gu[2], Y-F Yen[3], E Johansson[4], J Tropp[5], R Hurd[3], D Spielman[1,2]
Departments of [1]Electrical Engineering, [2]Radiology, Stanford University, CA, USA; [3]Global Applied Sciences Laboratory, GE Healthcare, Menlo Park, CA, USA; [4]Medical Diagnostics R&D, GE Healthcare, Oslo, Norway, [5]Global Applied Sciences Laboratory, GE Healthcare, Fremont, CA, USA

With signal-to-noise ratio enhancements on the order of 10,000-fold, hyperpolarized MR spectroscopic imaging (MRSI) of metabolically active substrates allows the study of both the injected substrate and downstream metabolic products in vivo. Although hyperpolarized [1-13C]-pyruvate, in particular, has been used to demonstrate metabolic activities in various animal models, robust quantitation and metabolic modeling remain important areas of investigation. Enzyme saturation effects are routinely seen with commonly used doses of hyperpolarized [1-13C]-pyruvate, however most metrics proposed to date, including metabolite ratios, time-to-peak of metabolic products, or estimated exchange rate constants fail to capture these saturation effects. In addition, the widely used small flip-angle excitation approach doesn't correctly model the inflow of fresh downstream metabolites generated distal to the targeted slice, which is often a significant factor in vivo. In this work, we developed an efficient quantitation framework employing a spiral-based dynamic spectroscopic imaging approach that can overcome the aforementioned limitations, and demonstrated that the in-vivo ^{13}C label conversion of a bolus injection of pyruvate to its downstream metabolic products of lactate and alanine was well approximated by a saturatable kinetics, which can be mathematically modeled using a Michaelis-Menten-like formulation with the resulting estimated apparent maximal reaction velocity Vmax and apparent Michaelis constant K_M parameters being unbiased with respect to critical experimental parameters including the substrate dose, bolus shape, and duration.

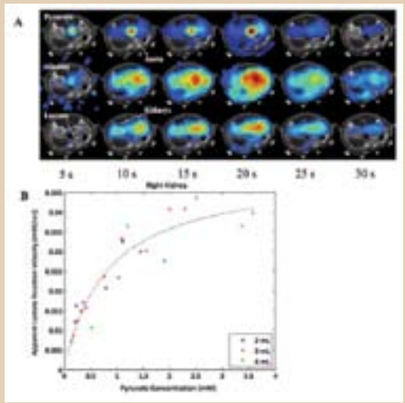

Figure: (A) Temporal dynamics of metabolites acquired using a Multi-interleave spiral-based pulse sequence. Time is from 5 sec to 30 sec after injection (TR=5 sec). BC) Lac reaction velocity versus Pyr concentration. We experimented with three different Pyr doses (2mL, 3mL, and 4mL) and similar kinetics was observed in each case.

References/Funding Source NIH grants: RR09784, AA05965, AA13521-INIA, EB009070, Lucas Foundation. [1] JH Ardenkjaer-Larsen, et al. Proc. of the National Academy of Sciences 2003; 100(18):10158-10163. [2] ML Zierhut, et al. Proc. ISMRM 2008, 891. [3] Xu, T., et al. Proc. ISMRM 2009, 6115. [4] Z.L, et al. JMR 1996. Presented at ISMRM 2010 Annual Meeting

Parallel Transmit Enabled Pulse Sequence Development for High-Field MRI

M Saranathan[1], M Khalighi[2], B Rutt[1]
Department of [1]Radiology, RSL, Stanford University, CA; [2]GE Healtchare, Applied Science Laboratory West, Menlo Park, CA

High-field MRI systems have the potential to enable ultra high spatial resolution imaging, provide enhanced susceptibility contrast and improved chemical species discrimination in spectroscopy. However, high-field MRI also poses challenges in the form of decreased radio frequency (RF) excitation homogeneity. This manifests as shading artifacts in the images, making quantitative imaging challenging. Recent developments in multi-transmit radiofrequency pulse design offer a possibility of combating this by using multiple parallel transmitters to excite a complex pattern in excitation k-space using RF and gradient pulses in multiple channels that results in a net uniform excitation field across the region of interest. One of the key inputs to such an RF pulse design is the so-called B1 map, a spatial mapping of the excitation field, which is a time consuming step. Accurate but fast B1 mapping is hence key in generating shading-free images at high fields.

We have been using "spokes" RF pulses [1] for optimizing the B1 excitation across the ROI as well as investigating the optimal behavior of these pulses in 2D and 3D gradient echo pulse sequences. We have also implemented and tested a few B1 mapping methods such as Bloch-Siegert [2], Actual Flip Angle [3] and Double Angle Look-Locker [4] mapping methods, and are evaluating and quantifying the sources of error in these methods and their effect on overall image quality. Lastly, we have also modified several MRI pulse sequences to enable multi-slice acquisition using the optimized spokes pulses with real-time switching of RF and gradient waveforms.

References/Funding Source GE Healthcare. MM Khalighi [1], LI Sacolick [2], WT Dixon [3], RD Watkins [4], S Josan [4], BK Rutt. Fast and Robust B1 Mapping at 7T by the Bloch-Siegert Method. Proc. ISMRM 18:2831 (2010). [1] Grissom et al. Magn Reson Med. 56(3):620-9 (2006); [2] Sacolick et al. Magn Reson Med. 63(5):1315-22 (2010); [3] Yarnykh et al. Magn Reson Med. 57(1):192-200. (2007); [4] Wade et al. PISMRM. 16:200 (2007)

Multi-excitation non-CPMG with Low Flip Angles (MENLO) for Hyperpolarized ^{13}C MRS

YF Yen[1], P Le Roux[2,3], D Mayer[4,5], A Takahashi[1], J Tropp[1], D Spielman[4], A Pfefferbaum[4,5], R Hurd[1]
[1]Global Applied Science Laboratory, GE Healthcare, Menlo Park, CA, USA; [2]Global Applied Science Laboratory, GE Healthcare, Palaiseau, France; [3]SHFJ, CEA, Orsay, France; [4]Department of Radiology, Stanford University, CA, USA; [5]SRI International, Neuroscience Program, Menlo Park, CA

We report a new MR spectroscopic imaging sequence that utilizes non-CPMG[1,2] FSE echo trains with quadratic phase modulation of the refocusing pulses to catalyze the stability of longitudinal magnetization while keeping the transverse magnetization refocused during the echo train. Other alternative phase modulation schemes (XY, MLEV…) are useful only over a very restricted range, close to π, of the refocusing pulse rotation angle (nutation)[1]. The non-CPMG phase scheme performs well for nutations as low as 160° and with a proper design of RF pulses of wide bandwidth, this technique can be quite suitable for fast spectroscopic imaging. Because non-CPMG allows us to obtain a full magnitude signal even in the presence of initial phase variation, we can perform multiple low flip-angle excitations with FSE readouts without waiting for the longitudinal signal to recover via T_1 relaxation, a condition ideal for spectroscopic imaging of hyperpolarized nuclei. In this report, we show preliminary test results of multi-excitation non-CPMG with low flip angles (MENLO) and one of its potential applications for mapping T_2 relaxation time. The tests were performed on a ^{13}C-enriched phantom, with imaging parameters suitable for future hyperpolarized ^{13}C applications.

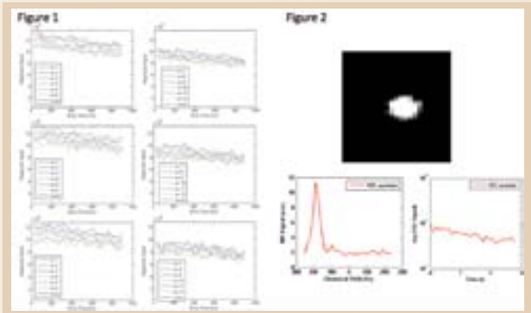

Figure 1: On-resonance (top pair), -375Hz off-resonance (middle pair), and +408Hz (bottom pair) from the first experiment. Figure 2: ^{13}C-acetate image (left), spectrum (center), and T_2 curve (right).

Consistent and stable FSE signals were obtained for a range of 780Hz chemical shift frequencies (Fig.1) and the longitudinal signal sustained for multiple excitations. Figure 2 shows the ^{13}C-acetate image acquired at 180Hz off-resonance frequency. A T_2 curve was obtained for every pixel and the average T_2 curve of an ROI covering most of the ^{13}C-acetate sphere is shown on the right. T_2 of 3.7s was obtained from curve fitting. This preliminary result shows the MENLO technique works well for a wide range of CS frequencies and is promising for T_2 mapping. Its feasibility in hyperpolarized ^{13}C applications will be explored in the future.

References/Funding Source NIH grants RR09784 and EB009070. 1) P Le Roux. J Magn Reson 2002; 155:278. 2) M Bastin and P Le Roux. Magn Reson Med 2002; 48:6. 3) J Pauly, et al. IEEE Trans Med Imaging 1991; 10:53. 4) K Derby, et al. J Magn Reson 1990; 86:645. 5) Y Levin, et al. Magn Reson Med 2007; 58:245. 6) S Reeder, et al. J Magn Reson Imaging 2007; 26:1145. Presented at ENC 2009.

Magnetic Resonance Spectroscopy

Adiabatic Magnetization Preparation Pulse for T2-contrast at 7-Tesla

P Balchandani[1], J Pauly[2], D Spielman[1]
Departments of [1]Radiology and [2]Electrical Engineering, Stanford University, CA

High-resolution MRI at 7T has the potential to provide tremendous improvement in the diagnosis and treatment of a wide range of neurological diseases. High-resolution T_2-weighted sequences are sensitive for assessing subtle structural abnormalities associated with many of these diseases [1]. Unfortunately, conventional T_2-weighted sequences, such as Fast Spin Echo (FSE), utilize a train of high flip-angle Shinnar Le-Roux (SLR) [2] refocusing pulses that are very susceptible to the severe B_1 inhomogeneity and SAR limitations observed at 7T. We propose an alternative adiabatic magnetization preparation (AMP) technique to obtain B1-insensitive T_2-contrast at 7T. A BIR-4 pulse [3,4] with a flip angle of 0° with delays inserted between segments is used to introduce T_2 decay. An AMP pulse was designed for use at 7T and validated with phantom and *in vivo* experiments.

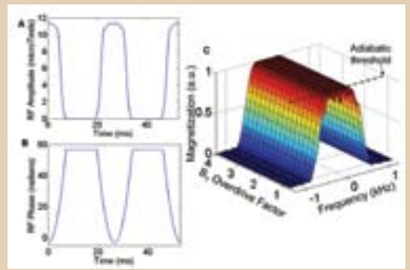

Figure 1: (A) Amplitude and (B) phase of AMP pulse. (C) The spectral profile of AMP pulse followed by a 90° excitation pulse plotted for the AMP pulse scaled to a range of B_1 overdrive factors.

Amplitude and phase waveforms for the AMP pulse are shown in Figs. 1 A and B. Simulations were performed to test the B_1-insensitivity of the AMP pulse. The profile of the AMP pulse followed by a 90° linear-phase excitation pulse was simulated for a range of AMP pulse amplitudes above the adiabatic threshold. Figure 1 C shows the simulated spectral profile for a range of B_1 overdrive factors (i.e. percentage by which B_1 was increased above the adiabatic threshold for the AMP pulse). Phantom and *in vivo* results show that the AMP pulse achieves more uniform T_2-contrast and SNR over the entire FOV. Some B_1-sensitivity still exists due to the linear phase excitation pulse.

References/Funding Source Lucas Foundation, NIH R01 MH080913 and GE Healthcare. [1] S Atlas, MRI of the Brain and Spine, Lippincott Williams & Wilkins, 1996. [2] J Pauly, et al. IEEE TMI 1991; 10(1):53–65. [3] Staewen RS, et al. Invest Radiol 1990; 25:559–567. [4] M Garwood, Y Ke. J Magn Reson 1991; 94:511–525. Priti Balchandani and Daniel Spielman. "Adiabatic Magnetization Preparation Pulse for T2-contrast at 7 Tesla" poster presentation at ISMRM Annual Meeting, Stockholm, April 2010.

Dynamic and High-Resolution Metabolic Imaging of Hyperpolarized [1-^{13}C]-Pyruvate in the Rat Brain

D Mayer[1,2], Y-F Yen[3], A Takahashi[3], S Josan[1,2], J Tropp[3], BK Rutt[2], RE Hurd[3], DM Spielman[2], A Pfefferbaum[2,4]
Departments of [2]Radiology, [4]Psychiatry & Behavioral Sciences, Stanford University, CA; [1]Neuroscience Program, SRI International, Menlo Park, CA; [3]GE Healthcare ASL-West, Menlo Park, CA

Fast chemical shift imaging techniques are advantageous in metabolic imaging of hyperpolarized compounds due to the limited duration of the signal amplification. At the same time, reducing the acquisition time in hyperpolarized imaging does not necessarily lead to the conventional penalty in signal-to-noise ratio that occurs in imaging at thermal equilibrium polarization levels. Here a high-performance gradient insert was used in combination with undersampled spiral chemical shift imaging to increase either the imaging speed or the spatial resolution of hyperpolarized ^{13}C metabolic imaging on a clinical 3T MR scanner. Both a single-shot sequence with a total acquisition time of 125 ms and a 3-shot sequence with a nominal in-plane resolution of 1.5 mm were implemented. The *k*-space trajectories were measured and then used during image reconstruction. The technique was applied to metabolic imaging of the rat brain *in vivo* after the injection of hyperpolarized [1-^{13}C]-pyruvate. Dynamic imaging afforded the measurement of region-of-interest-specific time courses of pyruvate and its metabolic products, while imaging at high spatial resolution was used to better characterize the spatial distribution of the metabolite signals.

Fig.1: Time-resolved metabolic images of a rat brain after injection of hyperpolarized pyruvate: the substrate (a) and its metabolic products lactate (b), alanine (c), and bicarbonate (d).

References/Funding Source R01 EB009070 "Dynamic Metabolic Imaging of Hyperpolarized Substrates", Dirk Mayer. R37 AA005965, "CNS DEFICITS: INTERACTION OF AGE AND ALCOHOLISM", Adolf Pfefferbaum. U01 AA013521, "INIA: Imaging Core", Adolf Pfefferbaum. P41 RR009784, "Center for advanced MR Technology at Stanford", Gary H. Glover. R01 AA018681, "Metabolic Imaging of the Cardioprotective Effects of Alcohol & ALDH2 Activators", Daniel M. Spielman. D Mayer, Y-F Yen, A Takahashi, S Josan, J Tropp, A Pfefferbaum, RE Hurd, DM Spielman "Dynamic and High-Resolution Metabolic Imaging of the Rat Brain *In Vivo* Using Hyperpolarized [1-^{13}C]-Pyruvate", Proc ISMRM, 18th Annual Meeting, Stockholm, 2010, 1019. RE Hurd, Y-F Yen, J Tropp, A Pfefferbaum, DM Spielman, D Mayer "Cerebral Dynamics and Metabolism of Hyperpolarized [1-^{13}C] Pyruvate using Time Resolved MR Spectroscopic Imaging", J. Cereb. Blood Flow Metab., in press.

Glutamate and Glutamine Changes with Ethanol Treatment in the Rat Brain Detectable using 3T CT-PRESS

NM Zahr[1,2], M Gu[3], D Mayer[2,3], D Spielman[3], EV Sullivan[1], A Pfefferbaum[1,2]
Departments of [1]Psychiatry & Behavioral Sciences, [3]Radiology, Stanford University, CA; [2]Neuroscience Program, SRI International, Menlo Park, CA;

A variety of psychiatric disorders are associated with brain elevations in the combined resonances of glutamate (Glu)+glutamine (Gln)+glutathione (GSH) (i.e., Glx) [1]. However, Glx measurements blur the complex relationship between Glu and Gln. The current analysis was conducted to determine whether the signal from Gln could be quantified separately from that of Glu.

The study group comprised 10 pairs of healthy Wistar rats. After the pre-EtOH baseline scanning session (MRS1), one rat from each sibling pair was exposed to a mixture of EtOH and air, and the other to air using a rodent alcohol inhalation system. Animals received intermittent exposure to vaporized EtOH (14h at night) for 24 weeks. MRS was performed at week 16 (MRS2) when blood EtOH concentrations (BECs) averaged ~293mg/100ml and week 24 (MRS3) when BECs averaged ~445mg/100ml in the EtOH group. MRS spectra were acquired with CT-PRESS from a 10x5x5 mm3 voxel in the basal ganglia. The novel finding presented here is the observation of higher levels of Gln in the EtOH group compared with the Con group after 16 weeks of EtOH exposure (MRS2; Figure 1).

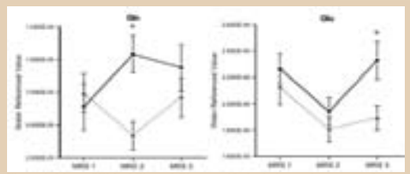

Figure 1. Mean±SEM of Glu and Gln quantified relative to tissue water for each of the 3 MRS acquisitions for control (open triangles) and EtOH-exposed (closed circles) rats. *p≤.05.

Increases in brain Gln are reported in patients with hepatic encephalopathy upon postmortem examination [5]. Evidence for mild liver damage in the EtOH group [1] and for elevations in blood ammonia with EtOH exposure [6] suggests an explanation for elevated Gln. The mechanism of brain ammonia detoxification is the formation of Gln from Glu by the enzyme Gln synthetase [7]. With prolonged EtOH exposure, however, the levels of Gln synthetase may be compromised [8], leading instead to a build-up in the levels of Glu as observed after 24 weeks of EtOH exposure. Given the decline in NAA, the current results may imply that elevated Glu levels mediate brain EtOH toxicity [e.g., 9].

References/Funding Source NIH grants AA013521-INIA; AA005965; AA012388; RR09784. [1] NM Zahr, et al., Neuropsychopharmacology 2009;6:1427. [2] W Dreher, et al., Magn Reson Imag 1999;17:141. [3] D Mayer, et al., Psychiatry Res 2007;154:267. [4] Masuo Electrophoresis 2009;30:1259. [5] Jalan, et al. Gut 2000;46:546. [6] Mohanachari, Toxic Lett 84;20:225. [7] Cooper & Plum, Phys Rev 1987;67:440. [8] Bondy & Guo, Biochem Pharm 1995;49:69. [9] Hoffman et al., ACER 1995;19:721. Presented at ISMRM 2010 Annual Meeting.

Quantification of Glutamate and Glutamine using CT-PRESS at 3T

M Gu[1], NM Zahr [2,3], D Spielman[1], EV Sullivan[2], A Pfefferbaum[2,3], D Mayer [1,3]
Departments of [1]Radiology, [2]Psychiatry & Behavioral Sciences, Stanford, CA; [3]Neuroscience Program, SRI International, Menlo Park, CA

Glutamate (Glu) and glutamine (Gln) are two major neurochemicals in the central nervous system. Quantifying Glu and Gln *in vivo* using magnetic resonance spectroscopy (MRS) has been of particular interest to basic science for understanding the Glu/Gln component of the Krebs cycle and its alteration by neuropsychiatric disorders such as Alzheimer's disease, epilepsy and alcoholism. However, quantification of Glu and Gln using conventional *in vivo* MRS techniques is difficult because of the multiplet structure of the coupled resonances and signal overlap.

Constant time point resolved spectroscopy (CT-PRESS) [1] has been developed to reduce signal overlap by applying effective homonuclear decoupling, and the method has been optimized to detect the Glu C4 resonance at 2.35 ppm [2]. However, the Gln C4 resonance is not well resolved as it overlaps with the resonance from the aspartate moiety of NAA at 2.5 ppm. Because the decoupled CT-PRESS spectra are generated by integrating the 2D spectra along the diagonal in magnitude mode for the purpose of SNR, linear least square fitting techniques with prior knowledge [3], are not directly applicable. In this work, we developed a method that achieves quantification of both Glu and Gln using CT-PRESS, validated it in phantom experiments, and applied it to data from an *in vivo* study on the effects of ethanol (EtOH) on rat brain chemistry.

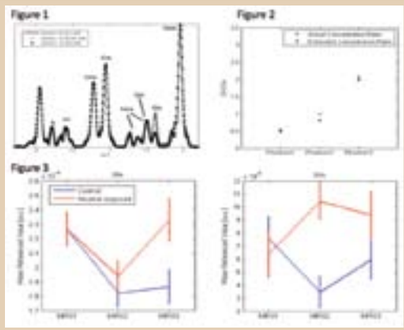

Fig. 1. CT-PRESS spectra of 3 phantoms. Fig. 2. Actual and estimated Gln/Glu ratios. Fig. 3. Quantified Glu and Gln from control and EtOH exposed rat brain.

To validate the method, CT-PRESS sequence was performed on custom-built spherical phantoms with different Glu/Gln concentrations using a GE 3T whole-body MR scanner. The method was then used to reanalyze data from a study with 10 wild-type Wistar rats were exposed to EtOH vapor over a period of 24 weeks [6]. Analysis with the proposed method confirmed the finding for Glu concentration, but also revealed significantly higher Gln concentration in the EtOH group at MRS2 compared to controls (Figure. 3).

References/Funding Source Lucas foundation, GE Healthcare, NIH grants RR 09784, AA005965, AA012388 and AA013521-INIA. [1] W. Dreher, et al, MRI 17 :141-150, 1999. [2] D Mayer, et al, MRM 54:439-442, 2005. [3] S Provencher, et al, MRM 30:672-679, 1993. [4] SA Smith et al, JMR A 106 :75-105, 1994. [5] V Govindaraju, et al, NMR Biomed. 13 :129-153, 2000. [6] NM Zahr et al., Neuropsychopharmacology 34(6) : 1427-42, 2009. [7] R Schulte et al, NMR Biomed 19(2) :255-263, 2006. Presented at ISMRM 2010 Annual Meeting.

Self-Refocused Adiabatic Pulse for Spin Echo Imaging at 7T

P Balchandani[1], J Pauly[2], D Spielman[1]
Departments of [1]Radiology and [2]Electrical Engineering, Stanford University, CA

7T MR scanners offer the advantages of higher spatial resolution, increased spectral separation as well as enhanced contrast. Unfortunately, several technical issues at 7T, such as B_1 inhomogeneity and increased SAR, result in signal loss and limit the spatial coverage when using conventional imaging sequences. Apparent T_2 values are also effectively reduced for single echo sequences at ultrahigh field strengths [1,2]. Conventional Shinnar Le-Roux (SLR) [3] 180° pulses used in spin-echo sequences are highly susceptible to B_1 inhomogeneity. Adiabatic 180° pulses may be used instead of SLR pulses in spin echo sequences to provide B_1-insensitive refocusing. However, due to the quadratic phase across the slice profile generated by adiabatic pulses, adiabatic pulses must be used in pairs to refocus the phase of the resultant spin echo. This results in increased SAR and longer minimum echo times (TE's). It is possible to design a matched-phase 90° pulse for an adiabatic 180° pulse so that a linear-phase spin echo may be produced without the use of a second 180° pulse. Similarly, a self-refocused adiabatic (SRA) 90°-180° pulse may be designed using the method described in [5]. Such pulse pairs provide the advantages of B_1-insensitive refocusing, reduced SAR when compared to pairs of refocusing pulses and shorter minimum TE values. An SRA pulse was designed, implemented and validated with phantom and in vivo experiments. Figures 3 A and B show images of the brain obtained at 7T using a conventional spin echo sequence and the SRA pulse sequence, respectively. The corresponding B_1 map is shown in Fig. 3 C. The SRA pulse achieves greater signal both at the center and edges of the brain where the B_1 field reaches its highest and lowest values, respectively. The SRA pulse offers greater immunity to the B1-insensitivity and reduced RF power deposition while enabling shorter echo times.

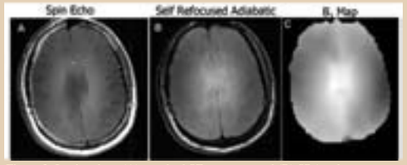

Figure 3: In vivo data: (A) standard SE sequence and (B) SRA pulse sequence. (C)Corresponding B1 map. Scan parameters: 7T, TE/TR = 16.5/200 ms, 4 mm slice, 256x256 matrix, 23x23 cm FOV.

References/Funding Source Lucas Foundation, NIH R01 MH080913 and GE Healthcare. [1] WT Yuh, et al. Top Magn Reson Imaging. 2006 Apr;17(2):53-61. Review. [2] R Bartha, et al. Magn Reson Med. 2002;47:742-750. [3] Pauly J, et al. IEEE TMI 1991; 10(1):53–65. [4] P Balchandani, et al. Proc. ISMRM 17. Honolulu, 2009; 178. [5] P Balchandani, et al. Magn Reson Med. 2009 Jul; 62(1):183-92. Priti Balchandani, Daniel Spielman and John Pauly. "Self-Refocused Adiabatic Pulse for Spin Echo Imaging at 7T" oral presentation at ISMRM Annual Meeting, Stockholm, April 2010.

Hyperpolarized 13C MRSI for Therapeutic Response Monitoring of Prostate Cancer to Radiotherapy

L Senadheera[1], D Mayer[2,3], M Darpolor[2], Y-F Yen[4], L Xing[1], D Spielman[2]
Departments of [1]Radiation Oncology, [2]Radiology, Stanford University, Stanford, CA; [3]Neuroscience Program, SRI International, Menlo Park, CA; [4]Global Applied Science Laboratory, GE Healthcare, Menlo Park, CA

Early detection of prostate cancer therapeutic response is necessary to choose the most appropriate treatment plan. Taking the advantage of cancer specific aerobic glycolysis, known as the 'Warberg effect', metabolic imaging with hyperpolarized ^{13}C-labeled pyruvate (pyr) has demonstrated potential of early detecting prostate cancer; a potentially better alternative to conventional therapeutic response monitoring taking months to become apparent. In this technique, the transient fate of pyr and its downstream metabolites lactate (lac), alanine, and bicarbonate is measured with ^{13}C Magnetic Resonance Spectroscopy Imaging (MRSI) following an injection of hyperpolarized pyr. Our aim is to investigate the efficacy of this technique in order to monitor the therapeutic response of prostate cancer to radiotherapy.

A cross-sectional study was designed to assess metabolic response of prostate cancer to radiotherapy in transgenic mouse model of prostatic adenocarcinoma (TRAMP), a model that closely resembles human prostate cancer.

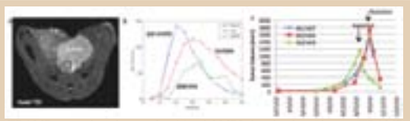

TRAMP mouse imaging results: (a) axial MRI showing hyperintense TRAMP tumor, (b) representative time courses from a tumor ROI as measured using bolus injection of hyperpolarized ^{13}C-Pyr and dynamic 3D spiral MRSI (5 mm isotropic resolution, 5 s TR, 5.6 deg flip angle, 8 cm FOV, 12 time points), (c) measurements of tumor volumes (as determined by 3D MRI) showing TRAMP tumor growth followed by tumor volume reduction following 20 Gy doses (two daily fractions of 10 Gy each) of radiation.

The tumor volume of three experimental groups, containing ≥4 mice in each for statistical significance, was followed biweekly by T2-weighted MRI at 7T. When tumors reached ~1.5 cm, Group-1 was subjected to ^{13}C MRSI at 3T to set the baseline. Group-2 with the same lesion size as Group-1 was given radiation (~20 Gy at 200 kVp) before 13C MRSI. Group-3, which received no treatment, was subjected to ^{13}C MRSI at the same post-irradiation as Group-2. Histopathology was performed MRSI. A fast 3D dynamic spectroscopy sequence was employed to acquire hyperpolarized ^{13}C spectra of the prostate following the injection. Metabolic maps of each metabolite were obtained by peak integration.

The ratio pf Pyr/Lac was found to be higher in malignant tissues than normal. Our initial experience suggests capability of ^{13}C MRSI for detecting therapeutic response of prostate cancer to radiation in TRAMP mice. Further investigations are underway for assessing the best metabolic metrics correlating with histopathology of prostate.

References/Funding Source To be presented at ASTRO 2010 Annual Meeting

In Vivo Detection of Radiation-Induced Metabolic Response in Rat Kidneys by 13C Hyperpolarized MRSI

L Senadheera[1], D Mayer[2,3], M Darpolor[2], Y-F Yen[4], L Xing[1], D Spielman[2]
Departments of [1]Radiation Oncology, [2]Radiology, Stanford University, CA; [3]Neuroscience Program, SRI International, Menlo Park, CA; [4]Global Applied Science Laboratory, GE Healthcare, Menlo Park, CA

The safe delivery of an ionization radiation dose to a tumor is often limited by the irradiation of the adjacent normal tissues. In total body irradiation, for instance, unintended radiation dose to the kidneys can result in the loss of renal function and radiation-induced nephropathy[1]. Radiation injuries in radiosensitive late responding critical organs, such as the kidneys, can take months or years to become apparent as structural changes[2]. Early detection of radiation-induced tissue damage is beneficial to manage the risk of late complications and to better design radiation therapy. Changes of lactate dehydrogenase (LDH) and lactate levels have been observed in various ex vivo animal tissues within few days following x-ray irradiation[3, 4]. Therefore, it may be suggested that metabolic response may reflect early signs of radiation-induced tissue alterations when measured in vivo. 13C hyperpolarized MRI/MR spectroscopic imaging (MRSI) is an emerging technique that can be utilized to measure in vivo metabolic response [5, 6]. The purpose of this study was to explore the potential of using currently available hyperpolarized 13C MRSI techniques to detect radiation-induced metabolic alterations in rat kidneys at clinically relevant radiation doses.

The localized x-ray irradiation was delivered to the right kidney of 11 male Wistar rats. Surface radiation doses of 15-26 Gy were administered targeting the right kidney in 3 – 4 fractions. 13C MRSI was performed 2-28 days postirradiation with hyperpolarized pyruvate solution injected into the rat via tail vain catheter. A 3-shot spiral spectroscopic pulse sequence[7] was employed to obtain dynamic chemical shift spectra of 13C metabolites at every 6th sec, starting 10 sec post-injection. Overall, no trend in Lactate/pyruvate ratios was observed between irradiated and normal kidneys of the same animal. Metabolic response of irradiated kidneys might not be strong enough to become visible in 13C MRSI, within our experimental errors and conditions.

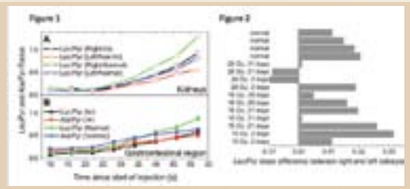

Figure 1: A and B are representative data of two rats (normal and irradiated – 18 Gy/28 days) showing dynamic MRCSI time points of Lac/Pyr and Ala/Pyr ratios in kidney ROIs (open symbols) and the gastrointestinel region ROIs ventral to the right kidney (closed symbols) following the tail vein injection of [1-13C]pyruvate. respectively. Figure 2: Difference of Lac/Pyr slopes between right and left kidneys versus radiation dose and postirradiation time of each rat.

References/Funding Source NIH grants RR09784, and EB009070. [1] EP Cohen, et al. Semin Nephrol 23, 486 (2003). [2] F Stewart, et al. in Radiopathology of organs and tissues, edtd by E. Scherer (Springer, 1991), pp. 405. [3] J Mishra, et al. Indian J Exp Biol 40, 1310 (2002). [4] A Khan, et al., in Proc ISMRM Hawaii, (2009), p. 4306. [5] K Golman, et al., Cancer Res 66, 10855 (2006). [6] MJ Albers, et al., Cancer Res 68, 8607 (2008). [7] D Mayer, et al., Magn Reson Med 62, 557 (2009). Presented at ISMRM 2010 Annual Meeting.

Dynamic and High-Resolution Metabolic Imaging of Hyperpolarized [1-^{13}C]-Pyruvate in the Rat Brain

S Josan[1,2], Y-F Yen[3], RE Hurd[3], A Pfefferbaum[2,4], DM Spielman[2], D Mayer[1,2]
Departments of [1]Neuroscience Program, SRI International, Menlo Park, CA, [2]Radiology, [4]Psychiatry & Behavioral Sciences, Stanford University, CA; [3]GE Healthcare ASL-West, Menlo Park, CA,

Rapid chemical shift imaging (CSI) techniques are of considerable interest for dynamic metabolic imaging in vivo with hyperpolarized ^{13}C-labeled substrates. Undersampled spiral CSI (spCSI) with free induction decay (FID) acquisition allows sub-second metabolic imaging of hyperpolarized ^{13}C [1]. Phase correction of the FID acquisition can be challenging, especially with contributions from aliased out-of-phase peaks. This work extends the spCSI sequence to incorporate a double spin echo (DSE) using a pair of adiabatic refocusing pulses, to eliminate the need for phase correction and provide high quality spectra in magnitude mode. The DSE-spCSI sequence was compared to FID-spCSI in single time-point and dynamic imaging of hyperpolarized ^{13}C-pyruvate and its metabolic products lactate, alanine and bicarbonate.

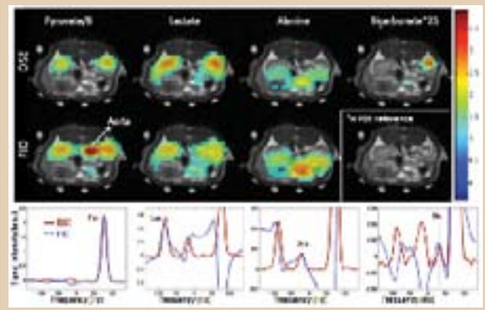

Fig.1: Metabolic images and spectra from a voxel in a rat kidney. DSE-spCSI magnitude mode yields similar linewidth as FID-spCSI absorption mode spectra, eliminating the need for phase correction.

Figure 1 shows metabolic images superimposed on MR anatomical images, along with spectra from a voxel in a rat kidney. The DSE-spCSI magnitude mode spectra yield similar linewidth as FID-spCSI absorption mode spectra, eliminating the need for phase correction. The Bic signal is obscured in the FID acquisition as phase-correction failed due to its proximity to the Pyr peak, but can be easily distinguished in the DSE.

The DSE sequence provides an added benefit of attenuating signal from flowing spins, which can otherwise contaminate signal in the organ of interest. The refocusing pulses can potentially lead to a loss of hyperpolarized magnetization in dynamic imaging due to flow of spins through the fringe field of the RF coil, where the refocusing pulses fail to provide complete refocusing. Care must be taken for dynamic imaging to ensure that the spins remain within the RF coil volume with reasonably homogeneous B_1.

References/Funding Source R01 EB009070 "Dynamic Metabolic Imaging of Hyperpolarized Substrates", Dirk Mayer, R37 AA005965, "CNS DEFICITS: INTERACTION OF AGE AND ALCOHOLISM", Adolf Pfefferbaum, U01 AA013521, "INIA: Imaging Core", Adolf Pfefferbaum, P41 RR009784, "Center for advanced MR Technology at Stanford", Gary H. Glover, R01 AA018681, "Metabolic Imaging of the Cardioprotective Effects of Alcohol & ALDH2 Activators", DM Spielman. S Josan, Y-F Yen, R Hurd, A Pfefferbaum, DM Spielman, D Mayer "Double Spin-Echo Spiral Chemical Shift Imaging for Rapid Metabolic Imaging of Hyperpolarized [1-13C]-Pyruvate", Proc ISMRM, 18th Annual Meeting, Stockholm, 2010, 1017.

Cerebral Dynamics and Metabolism of Hyperpolarized [1-13C] Pyruvate using Time Resolved Spiral-MRSI

RE Hurd[1], D Mayer[2,3], Y-F Yen[1], J Tropp[1], A Pfefferbaum[3,4], D Spielman[2]
Departments of [2]Radiology, [4]Psychiatry and Behavioral Sciences, Stanford University, CA; [1]Global Applied Science Laboratory, GE Healthcare, CA; [3]SRI International, Neuroscience Program, Menlo Park, CA

MR metabolic imaging of hyperpolarized [1-^{13}C]-pyruvate is a useful tool in the study of oncology and cardiology (1,2). Dynamic and tissue level changes in [1-^{13}C]-pyruvate and its metabolic products, [1-^{13}C]-lactate, [1-^{13}C]-alanine and [^{13}C] bicarbonate, have been shown to correlate with metabolic states of interest including disease progression (3) and response to therapy (4,5). However, because of the limited lifetime of hyperpolarized signal, brain metabolism has been largely ignored as an application for this method. Although the kinetics of blood-brain transport of pyruvate (6-8), does limit the in-brain pyruvate concentration, single time point images have been reported showing pyruvate uptake, along with lactate and bicarbonate labeling in normal anesthetized rat brain (9). Hyperpolarized pyruvate, delivered as an 80 m*M* bolus, was reported to result in between100-700 nmol g^{-1} brain tissue levels of hyperpolarized ^{13}C label. This is substantially less than blood levels, but it is sufficient to map lactate levels. In this study, fast 125 msec dynamic imaging (10) is used to better characterize the bolus, transport and metabolic effects, separating the metabolites in the cerebral blood volume from the metabolites in brain tissue.

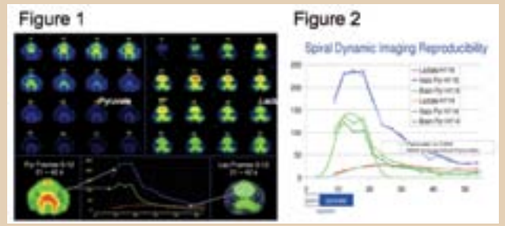

Figure 1. Dynamic metabolic images of lactate and pyruvate. Figure 2. Dynamic metabolic responses of lactate and pyruvate with CBV/transport kinetics overlay.

In all 14 individual runs the lactate response was very consistent and represents the bulk of the ^{13}C label in brain. Based on calculations using the ^{13}C urea reference and intravascular T_1 of pyruvate (13), the blood-to-brain transport of pyruvate is sufficient to label ~400nmol g^{-1} of the lactate pool. There appears to be sufficient LDH activity in the anesthetized rat brain to maintain ^{13}C-labeled lactate/pyruvate levels >1 once pyruvate contributions from the cerebral blood volume are removed. The cerebral ^{13}C-lactate also appears to remain in the brain for the duration of the hyperpolarized observation window. This is consistent with other measurements, which estimate 14% min-1 lactate exchange across the blood brain barrier (14).

References/Funding Source NIH grants R01 EB009070, R37 AA005965, U01 AA013521, P41 RR009784, and R01 AA018681. 1. Golman et al.(2006) Cancer Res 66:10855, 2. Golman et al.(2008) Magn Reson Med. 59:1005, 3. Albers et al.(2008) Cancer Res 68:8607, 4. Chen et al.(2008) Proc 16th Annual ISMRM, p. 888, 5. Day et al.(2007) Nature Medicine 13:1382 6. Cremer et al.(1979) J. Neurochem 33:439, 7. Miller and Oldendorf (1986) J. Neurochem. 46:1412, 8. Pardridge (1983) American Physiol. Soc. 63:1481, 9. Hurd et al (2009) Proc 17th Annual ISMRM p. 222, 10. Mayer et al.(2009) MRM, 11. Kohler et al.(2007) MRM. 58:65, 12. Julien-Dolbec et al.(2002) Br J. Anaest 89:287, 13. Leung et al.(2009) Proc 17th Annual ISMRM p. 2432, 14 Leegsma-Vogt et al.(2004) JCBFM 24:1071. RE Hurd, Y-F Yen, J Tropp, A Pfefferbaum, DM Spielman, D Mayer. Cerebral dynamics and metabolism of hyperpolarized [1-(13)C]pyruvate using time-resolved MR spectroscopic imaging. J Cereb Blood Flow Metab. 2010 Jun 30. [Epub ahead of print] PubMed PMID: 20588318.

Positive Contrast MRI of Magnetotactic Bacteria

S Josan[1,2], A Hamilton[3], M Benoit[3], CH Cunningham[4], A Matin[3], D Mayer[1,2]
Departments of [2]Radiology, [3]Microbiology and Immunology, Stanford University, CA; [1]Neuroscience Program, SRI International, Menlo Park, CA; [4]Sunnybrook Health Sciences Centre, University of Toronto, Canada

The objective of this work is to explore techniques for improvements in imaging cancer with genetically encoded magnetite using magnetic resonance imaging. Magnetotactic bacteria AMB-1 produce magnetite particles and colonize tumors in mice following systemic delivery [1]. Several techniques exist for visualization of the magnetite particles, but accurate quantitation in vivo remains challenging. In this work, two methods were implemented for positive contrast imaging and quantitative detection of the magnetite particles on the 7T animal scanner.

Fig.1: MR images of a phantom containing four spots of AMB-1 cells with varying iron concentration. The positive contrast images visualize the AMB-1 spots and show linear correlation of signal with iron concentration.

Off-resonance excitation: This method takes advantage of the local resonance frequency shift caused by the iron particles, by using a pair of spectral-spatial RF pulses to excite and refocus only the off-resonant water protons in the vicinity of the particles while suppressing the on-resonant signal.

Susceptibility gradient mapping (SGM): The SGM technique involves post-processing of conventional 3D GRE T2* weighted complex images to calculate susceptibility gradients induced by the magnetite particles. A map of the susceptibility gradient vector provides a positive contrast image of the particle distribution.

Figure 1 shows MR images of a phantom containing four 10 µl spots of AMB-1 cells in gelatin, with Fe concentration of approximately 10, 25, 50 and 75 µg/ml. The positive contrast images (b,c) obtained with both techniques visualize the magnetite spots well, with good background suppression. Figure 1d shows that a linear correlation exists between the iron concentration and the sum of the signal intensity of all "positive voxels" within a region-of-interest at the spot location. A voxel is "positive" if its intensity is >5 times the standard deviation of the background.

Positive contrast MRI can potentially allow quantitation of the magnetotactic bacteria and can be a useful tool for studying cancer diagnosis and treatment evaluation in pre-clinical models.

References/Funding Source R21 CA140903-01 "Development of Contrast Agents from Bacterial Magnetite for Targeting and Visualizing Cancerous Tumors with MRI", AC Matin

Hybrid PRF-Thermometry in the Myocardium

V Rieke[1], W Grissom[2], AB Holbrook[1,3], MV McConnell[4], K Butts-Pauly[1]
Departments of [1]Radiology, RSL, [2]Bioengineering, [3]Cardiovascular Medicine, Stanford University, CA, USA; [3]GE Health Care, Munich, Germany

Objective: In recent years there has been increased interest to perform cardiac interventions such as EP ablation under MR-guidance. Directly monitoring the temperature rise during these procedures could potentially be helpful to verify successful ablation and predict treatment outcome. Here, we investigate the feasibility of monitoring temperature changes in the left ventricular myocardium in real-time. Temperature images based on the proton resonance frequency (PRF) shift are reconstructed using a hybrid method that combines multi-baseline subtraction and referenceless thermometry.

Materials and Methods: Short-axis free-breathing cardiac images were acquired in three volunteers (no heat applied) in real-time using spiral gradient echo acquisitions with 4-5 interleaves on a 3T scanner using echo times of 3 ms, 5 ms, and 7 ms.

Hybrid temperature image reconstruction was performed off-line in Matlab. The hybrid imaging model assumes that three sources contribute to image phase during thermal treatment: Background anatomical phase, spatially smooth phase deviations, and focal, heat-induced phase shifts.

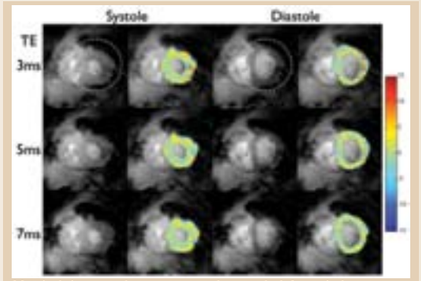

Magnitude images and temperature overlay onto the left ventricular myocardium showing the temperature uncertainty for three different echo times during systole and diastole. The dashed circle shows the circular regions for the hybrid temperature estimation.

For the referenceless portion of the processing, sixth-order background polynomials were used and the multi-baseline libraries were comprised of 150 images (sliding window reconstruction) acquired during free breathing, representing approximately three cardiac cycles. Temperature reconstruction was performed over circular regions of interest containing the entire left ventricle (Fig. 1). Temperature uncertainty was measured in the septum and the free ventricular wall in images during systole and diastole.

Results: The lowest temperature uncertainty was measured in the septum during systole, followed by septum during diastole and free wall during systole. The temperature uncertainty was always highest in the free wall during diastole. Increasing the echo time from 3 ms to 7 ms decreases the temperature uncertainty.

Conclusion: Temperature measurements in the left ventricular myocardium in real-time with a hybrid referenceless and multi-baseline method can achieve low temperature uncertainties that make in vivo thermal ablation monitoring feasible.

References/Funding Source NIH K99 HL097030, R01 CA121163, R21 EB007715. V Rieke, W Grissom, AB Holbrook, JM Santos, MV McConnell, K Butts-Pauly. Hybrid PRF-thermometry in the myocardium. 8th Interventional MRI Symposium, Leipzig, Germany, 2010.

MR-guided High Intensity Focused Ultrasound in Cadaver Breasts for Localization of Non-Palpable Breast Tumors

RR Bitton[1], E Kaye[1,2], BL Daniel[1], K Butts-Pauly[1]
Departments of [1]Radiology, RSL and [2]Electrical Engineering, Stanford University, CA

In breast conservation surgery, the current method to locate non-palpable breast tumors is pre-operative image-guided wire placement localization. However, wire localization is unable to demarcate irregularly shaped tumors, and positive tumor margins, which require repeat surgeries, are discovered in many patients [1]. As an alternative to wire localization, we propose using MR-Image guided High Intensity Focused Ultrasound (MRgHIFU) to create thermal lesions which circumscribe a non-palpable breast tumor, providing an excision guide during breast conservation surgery. This study investigates visibility and palpability of HIFU lesions in cadaver breast tissue.

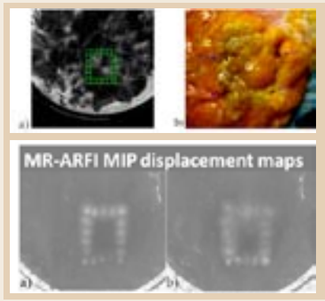

Figure 1. a) MRgHIFU planning image (T1w FSE fat saturated), green circles indicate sonications. b) Photograph of ex vivo human breast after ablation square perimeter. Arrows point to square demarcated by voids and tissue darkening.

Figure 2. MIP of MR-ARFI displacement maps of pre a) and post b) ablation spots. c) Percent displacement difference between pre and post ablations for sonications 1-18.

MRgHIFU was performed in a GE 3T scanner using ExAblate 2000. Acoustic Radiation Force Imaging (MR-ARFI) was applied to measure tissue displacement. MR-ARFI locates the ultrasound focus without heating, and measures changes tissue displacement, relating to tissue stiffness properties. Eighteen sonications (1MHz) were made in the cadaver breast, representing a non-palpable tumor perimeter. Ablation sonications were prescribed along both fibroglandular and fatty tissue. T1wFSE images showed a slight structural change during the heating phase of some sonications, where fat shrank towards the nearest heated fibroglandular tissue. Stiffening of the tissue, where sonications corresponded with fibroglandular tissue, could be felt upon palpation of the breast at room temperature. The ablations produced visible changes in the tissue, where voids in purely fat sonications and an overall darkening of the ablated square perimeter could be seen (Fig 1). Maximum Intensity Projections (MIP) of MR-ARFI maps of the tissue taken pre and post ablation show a reduction in the amount of displacement for 11 post ablation spots (Fig 2). These maps show a measured increase in palpability for those ablations where tissue displacement post heating is reduced given the same mechanical force.

References/Funding Source NIH/NCI T32 CA09695. [1] RJ Gray et al. "Randomized prospective evaluation of a novel technique for biopsy or lumpectomy of nonpalpable breast lesions." Ann Surg Oncol 2001;8.0. RR Bitton, E Kaye, BL Daniel, K Butts-Pauly, "MR guided HIFU in Cadaver Breasts for Pre-Operative Tumor Localization of Non-Palpable Breast Tumors as an Alternative to Needle Wire Localization," Proc. of the ISMRM, 2010.

MRI Tools for Focal Spot Visualization during FUS Breast Treatment

E Kaye[1,2], RR Bitton[2], K Butts-Pauly[2]
Departments of [1]Electrical Engineering and [2]Radiology, RSL, Stanford University, CA

Introduction: During the planning stage of MRI-guided focused ultrasound treatments in breast, the actual location of the focus is verified by visualization of a low temperature test spots using proton resonance frequency (PRF) thermometry. However, in fat PRF becomes unreliable. The alternative approaches are based on T1-weighted imaging with fast spin-echo (FSE) [1] and on displacement imaging with MR-ARFI. The goal of this study was to evaluate both methods in human ex vivo breast tissue.

Methods: For six focal locations, imaging was performed with ultrasound, using MR-ARFI and FSE. For FSE, repetition time (TR) was varied. Imaging was performed on a 3T MRI scanner equipped with a HIFU system, and timed such that the sonications and the scans ended at the same time. SNR of the signal at the focus was analyzed using MR-ARFI displacement maps and FSE magnitude difference images.

Results: The focal spot was apparent in the unprocessed MR-ARFI phase images, as shown inn Figure 1. For FSE, the focal spot was visible only on the difference images, but not on the unprocessed magnitude images. In the displacement maps the mean SNR was 43, and for the optimal TR of 500 ms in the FSE difference image the SNR was 11.5.

Conclusion: The results of this study show that T1-weighted imaging and MR-ARFI allow visualization of the ultrasound focal spot. MR-ARFI provided greater SNR at the focal spot and deposited 10 times less ultrasound energy than needed during FSE acquisition. Current MR-ARFI sequences require a longer scan time than FSE, but this could be mitigated in the future.

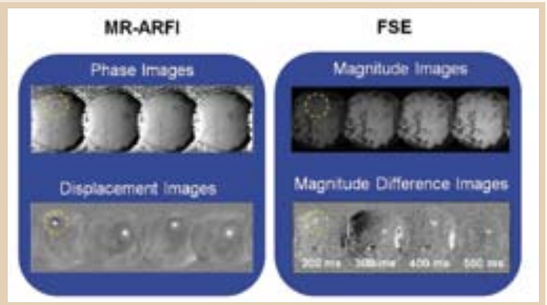

Figure 1. Example images for 4 out of 6 locations. Top-left: phase images obtained with encoding gradients in the opposite direction of the ultrasound beam; bottom-left: MR-ARFI displacement maps; top-right: FSE magnitude images obtained during sonications. Bottom – right: FSE difference images.

References/Funding Source [1] K Hynynen, et al., MRM, 2000,43:901-904. [2] N McDannold, et al., Med Phys, 35(8):3748-58, 2008. [3] J Chen, et al., MRM 2010;63(4):1050-1058. [4] R Sinkus, et al., Proc. of IEEE, 2008,96, 490-99.

Fabrication of CMUT Cells with Gold Center Mass for Higher Output Pressure

HS. Yoon[1], MC. Ho[1], N. Apte[2], P. Cristman[1], S. Vaithilingam[1], M. Kupnik[1], K. Butts-Pauly[3], B. T. Khuri-Yakub[1]
Departments of [1]Electrical Engineering, [2]Mechanical Engineering, [3]Radiology, Stanford University, CA

Capacitive micromachined ultrasonic transducer (CMUT) technology is a promising candidate for high intensity focused ultrasound (HIFU) therapy as it allows the fabrication of arbitrary array geometries and is inherently magnetic resonance (MR) compatible. In this study, we investigate a way to improve the output pressure of a single CMUT cell by a modification to the basic CMUT cell structure: adding a gold mass over the center of the top CMUT plate. Using the direct wafer bonding fabrication process we realized linear 1D CMUT arrays. On top of the 0.86 µm thick silicon plate, a 200-nm thick aluminum layer and a 10-nm thick titanium adhesion layer were deposited. A lift-off technique was used to deposit a gold mass on top of the adhesion layer, at the center of each cell. The 1-µm thick gold layer was deposited in multiple steps with intervening cool-down periods to ensure low thermal-induced stress between the gold and the metalized CMUT plates. Electrical impedance measurements of the devices reveal improved performance due to the gold mass, and the average resonance frequency in air for the elements in the 1D array decreased from 7 MHz to 3.6 MHz with a standard deviation of 0.125 MHz and 0.157 MHz, respectively. A direct comparison of cells with and without the gold mass in terms of measured output pressure at the surface of a single cell demonstrated a 23% improvement. When biased with a DC voltage equal to 75% of the pull-in voltage, the device with the gold mass delivered 1.875 MPa peak-to-peak surface pressure at a frequency of 2.6 MHz. The results indicate that adding a center-mass to regular CMUT cells improves device performance in terms of acoustic output pressure. In the future, we plan to investigate the acoustic crosstalk between cells and ways to mitigate it.

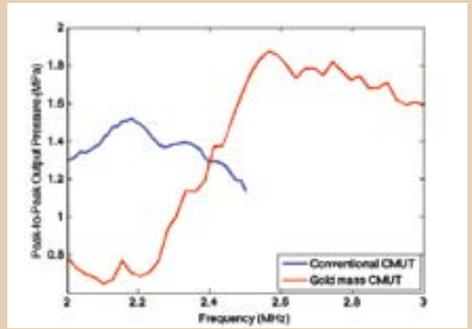

Surface pressure measurement of each device

References/Funding Source ISTU2010 proceedings.

Real Time MR-Guided Prostate Ablation with Transurethral Multisectored Ultrasound Applicators and Multi-slice Treatment Planning

AB Holbrook[1,2], P Prakash[3], P Jones[3], C Planey[1], JM Santos[4,5], CJ Diederich[3], K Butts-Pauly[1], FG Sommer[1]
Departments of [1]Radiology, RSL, [2]Bioengineering, [4]Electrical Engineering, Stanford University, CA; [3]Department of Radiation Oncology, University of California in San Francisco, San Francisco, CA; [5]HeartVista, Inc. Los Altos, CA

Introduction: The purpose of this work was to improve targeted prostate ablation with transurethral multisectored ultrasound applicators. To do this, an integrated imaging platform was developed to minimize setup and treatment time and also provide real-time temperature feedback. We incorporated integrated device localization, prostate-specific planning, and multi-slice MR thermometry in a single platform. We also developed temperature feedback control points which are transferred externally for automated control of ultrasound power.

Methods: Three pulse sequences were incorporated into our real-time imaging platform based on RTHawk: one for device visualization, a MR-tracking sequence for tracking coil and catheter localization, and a thermometry sequence. The software was divided into two parts: localization and planning/treatment monitoring.

For verification, a catheter with two tracking coils was inserted into a phantom placed in a GE Signa Excite 3.0T scanner. After acquisition of the MR-tracking sequence, we tested whether the control software was able to automatically acquire a localization sequence with the catheter centered in the image. In a second test, two interstitial applicators were placed inside a gel phantom. Regions of interest (ROIs) were defined in transverse slices, and the mean ROI temperatures were transmitted to external power control software. This external program monitored treatment of the target volume, shutting it off once adequate heating was achieved.

Results: In the MR-tracking validation, the tracking coil locations were automatically detected, and a slice was displayed and centered through both tracking coils. In the heating experiment, the software successfully passed temperature data to the power control software as heat increased inside the phantom. Upon reaching the desired temperature, the applicator automatically turned off. The imaging temporal resolution was 7.7 seconds/frame for five slices, sufficient for 5-15 minute treatments.

Conclusions: We have developed and performed initial testing of a real-time, MRI software package complete with catheter localization and multi-slice treatment prescription and monitoring. Although our experiments highlight separate phases of the software, all are integrated into one platform.

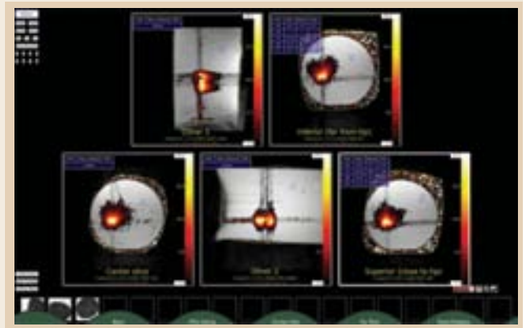

Multi-slice thermal ablation monitoring in a phantom. Regions of Interest (ROIs) send temperature information to the applicator control software, which modulates the delivered energy.

References/Funding Source RO1 CA121163, RO1 CA111981, P41 RR009784. AB Holbrook, P Prakash, P Jones, C Planey, JM Santos, CJ Diederich, K Butts-Pauly, FG Sommer. Multislice Treatment Planning and Control for Real Time MR-Guided Prostate Ablation with Transurethral Multisectored Ultrasound Applicators. Proceedings of 18th Joint Annual Meeting ISMRM-ESMRMB 2010. Stockholm, Sweden. May 1-7, 2010. AB Holbrook, P Prakash, P Jones, C Planey, JM Santos, CJ Diederich, K Butts-Pauly, FG Sommer. Real time MR-guided prostate ablation with transurethral multisectored ultrasound applicators and multislice treatment planning and control.10th International Symposium on Therapeutic Ultrasound.Tokyo, Japan.June 9-12,2010

Integrated MR and HIFU Control System: Towards Real Time Treatment of the Liver

AB Holbrook[1,2], C Dumoulin[3], JM Santos[4,5], Y Medan[6], K Butts-Pauly[1]
Departments of [1]Radiology, RSL, [2]Bioengineering, [4]Electrical Engineering, Stanford University, CA, USA; [3]Cincinnati Children's Hospital Medical Center, Cincinnati, OH, USA; [5]HeartVista, Inc., Los Altos, CA, USA; [6]InSightec, Ltd., Tirat Carmel, Israel

High Intensity Focused Ultrasound (HIFU) of the abdomen is a complex endeavor requiring integrated real time control of MRI imaging and the HIFU transducer. Last year we demonstrated our ability to define arbitrary treatment profiles in a real time environment, heating both a phantom and rabbit thigh in-vivo. This year we developed and tested additional capabilities critical for in vivo liver ablation.

Vessel tracking is used for guiding treatment planning in the presence of respiration. Additionally, respiration data via a respiratory bellows are registered to incoming images, allowing for transducer steering based on a combination of image and bellows guidance. The transducer orientation is located automatically via MR-tracking algorithms, and done so as a function of respiratory position. Multiple imaging pulse sequences are now available, including a high field of view (FOV) localization sequence, a reduced FOV spin echo planar imaging (EPI) MR-ARFI sequence for calibrating the focal spot, and a reduced FOV EPI thermometry sequence for monitoring the ablation. Finally, the thermometry processing was modified to reduced artifacts through the use of our newly developed hybrid referenceless-multi-baseline method.

The system improvements were tested with in vivo experimental data and with gel phantom experiments using an Insightec ExAblate 2000 extracorporeal transducer and a GE Signa Excite 3.0T scanner. Overall, artifacts were reduced and the calibration and monitoring imaging methods were greatly improved.

These new system additions will allow for a more tailored liver ablation platform, combining the demonstrated real-time ultrasound control with additional features to improve planning efficiency and ultimately treatment success.

Real-time application of HIFU and MR-ARFI for calibrating ablations before treatment in porcine liver in vivo. The treatment should be at the lower (green) dot; after calibration it is.

References/Funding Source RO1 CA121163, RO1 CA111981, P41 RR009784. AB Holbrook, CL Dumoulin, JM Santos, Y Medan, K Butts-Pauly. Integrated MRI and HIFU Control System: Towards Real Time Treatment of the Liver. Proceedings of 18th Joint Annual Meeting ISMRM-ESMRMB 2010. Stockholm, Sweden. May 1-7, 2010. AB Holbrook, CL Dumoulin, JM Santos, Y Medan, K Butts-Pauly. Integrated MRI and HIFU Control System: Towards Real Time Treatment of the Liver. 10th International Symposium on Therapeutic Ultrasound. Tokyo, Japan. June 9-12, 2010.

Neural and Behavioral Responses to Threatening Emotion Faces in Children as a Function of the Short Allele of the Serotonin Transporter Gene.

ME Thomason[1], ML Henry[1], JP Hamilton[1], J Joormann[2], DS Pine[3], M Ernst[3], D Goldman[3], K Mogg[4], BP Bradley[4], JC Britton[3], KM Lindstrom[3], CS Monk[5], LS Sankin[3], HMC Louro[1], IH Gotlib[1]
Departments of [1]Psychology, Stanford University, Stanford, CA, USA; [2]Department of Psychology, University of Miami, Miami, FL, USA; [3]Mood and Anxiety Program, National Institute of Mental Health, National Institutes of Health, USA; [4]Department of Psychology, University of Southampton, UK; [5]Department of Psychology, University of Michigan, Ann Arbor, MI, USA

Recent evidence suggests that a genetic polymorphism in the promoter region (5-HTTLPR) of the serotonin transporter gene (SLC6A4) mediates stress reactivity in adults. Little is known, however, about this gene-brain association in childhood and adolescence, generally conceptualized as a time of heightened stress reactivity. The present study examines the association between 5-HTTLPR allelic variation and responses to fearful and angry faces presented both sub- and supraliminally in participants, ages 9–17. Behaviorally, carriers of the 5-HTTLPR short (s)-allele exhibited significantly greater attentional bias to subliminally presented fear faces than did their long (l)-allele homozygous counterparts. Moreover, s-allele carriers showed greater neural activations to fearful and angry faces than did l-allele homozygotes in various regions of association cortex previously linked to attention control in adults. These results indicate that in children and adolescents, s-allele carriers can be distinguished from l-allele homozygotes on the basis of hypervigilant behavioral and neural processing of negative material.

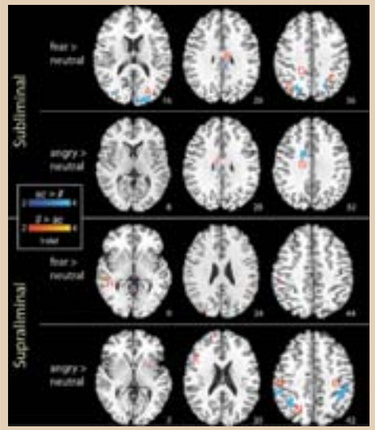

References/Funding Source National Institute of Mental Health [MH081583 to MET, and MH074849 to IHG]. NARSAD Young Investigator Award to MET NIMH-Intramural Research Program ME Thomason, ML Henry, JP Hamilton, J Joormann, DS Pine, M Ernst, D Goldman, K Mogg, BP Bradley, JC Britton, KM Lindstrom, CS Monk, LS Sankin, HMC Louro, IH Gotlib, (In Press) Neural and behavioral responses to threatening emotion faces in children as a function of the short allele of the serotonin transporter gene. Biological Psychology.

Variable Density Spiral-In/Out fMRI

C Chang[1,2], GH Glover[1,2]
Departments of [1]Electrical Engineering and [2]Radiology, Stanford University, CA

A variable-density spiral k-space trajectory is introduced for brain functional magnetic resonance imaging (fMRI). The proposed spiral trajectory consists of an Archimedean spiral from the k-space origin to an arbitrary fraction r of the maximum k-space radius, extending beyond this point with a variable-density spiral in which the sampling density decreases as the k-space radius increases. It therefore permits a reduction in readout time at the expense of undersampling only the high spatial frequencies, in which the energy in T2*-weighted brain images is typically low. The trajectory was implemented in a 2D spiral-in/out sequence, and single-shot high-resolution (1.71 x 1.71 mm2 in-plane) fMRI data were acquired from human volunteers. Compared to a two-shot uniform-density spiral sequence with the same spatial coverage and total scan time, the variable-density sequence yielded greater activation magnitudes with improved temporal efficiency and minimal artifacts.

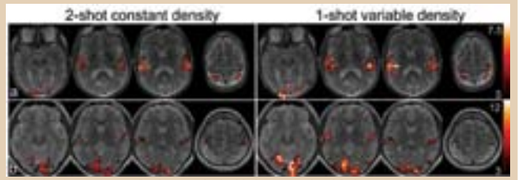

Activation (t-score) maps for data acquired with the conventional 2-shot constant-density sequence (left) and the single-shot variable-density spiral sequence (right), shown for 2 individual subjects (a, b). The activation maps for each subject are thresholded at the identical t-values.

References/Funding Source NIH F31-AG032168 to CC and P41-RR009784 to GHG. C Chang, GH Glover. Variable Density Spiral-In/Out fMRI. Mag. Res. Med. (submitted)

Selective Reduction of Cardiac Artifact in Breast MRI

R Rakow-Penner, BL Daniel, L Pisani, B Hargreaves, GH Glover
Department of Radiology, RSL, Stanford University, CA

Purpose: Cardiac motion causes significant artifact in breast MRI. Conventional slab saturation pulses cannot be applied to the heart without obscuring portions of the axillary breast tissue. We have implemented a 2D cylindrical saturation pulse that selectively saturates the heart and diaphragm.

Methods: We collected data on six healthy volunteers at 1.5T (GE Healthcare, Waukesha, WI). A 2D excitation was applied with spiral gradients in both x and z for an elliptical cylindrical superior-inferior prescription encompassing the heart. Gradient crushers followed the cylindrical excitation, thus dephasing and reducing the signal from the selected area. The heart saturation pulse was followed by a dual band spectral spatial RF pulse for bilateral breast excitation, and a 3D variable-density stack of spirals for acquisition. The TR for the saturation pulse is 12 ms, in addition to the 32 ms bilateral spiral pulse.

For analysis, three ROIs were drawn in each image: one in the heart, one in the glandular breast tissue, and one in the image background. To calculate the signal emanating from the outer area, the standard deviation of the outer ROI was normalized by dividing by the mean signal from the breast ROI.

Results: In spiral imaging, the ghosting artifact from the heart motion manifests as a swirling artifact (compared to ghosting in the phase encode direction present with Cartesian imaging). The artifact signal without heart saturation was on average1.3 times the artifact signal with heart saturation ($p<0.01$). On average, 58% of the heart signal was eliminated with heart saturation.

Conclusion: Elliptical cylindrical saturation of the heart significantly eliminates artifact from the heart in breast MR imaging without sacrificing important diagnostic information. This saturation pulse can be applied to many breast MR sequences and is particularly promising in spiral imaging.

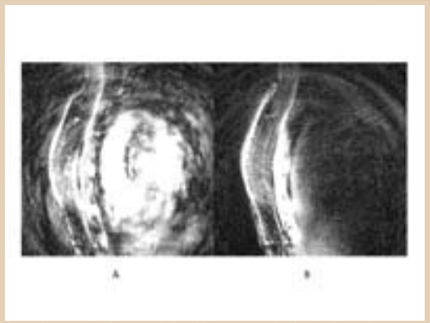

Breast images (A) without and (B) with heart saturation in a healthy volunteer. Notice the decreased artifact in (B).

References/Funding Source NIH P41-RR009874, California Breast Cancer Research Program Predoctoral Fellowship

Time-frequency Dynamics of Resting Brain Connectivity Measured with fMRI

C Chang[1,2], GH Glover[1,2]
Departments of [1]Electrical Engineering and [2]Radiology, Stanford University, CA

Most studies of resting-state ("intrinsic") functional connectivity using fMRI employ methods that assume temporal stationarity, such as correlation and data-driven decompositions computed across the duration of the scan. However, evidence from both task-based fMRI studies and animal electrophysiology suggests that intrinsic functional connectivity may exhibit dynamic changes within time scales of seconds to minutes. In the present study, we investigated the dynamic behavior of resting-state connectivity across the course of a single scan, performing a time–frequency coherence analysis based on the wavelet transform. We focused on the connectivity of the posterior cingulate cortex (PCC), a primary node of the default-mode network, examining its relationship with both the "anti-correlated" ("task-positive") network as well as other nodes of the default-mode network. It was observed that coherence and phase between the PCC and the anticorrelated network was variable in time and frequency, and statistical testing based on Monte Carlo simulations revealed the presence of significant scale-dependent temporal variability. In addition, a sliding-window correlation procedure identified other regions across the brain that exhibited variable connectivity with the PCC across the scan, which included areas previously implicated in attention and salience processing. Although it is unclear whether the observed coherence and phase variability can be attributed to residual noise or modulation of cognitive state, the present results illustrate that resting-state functional connectivity is not static, and it may therefore prove valuable to consider measures of variability, in addition to average quantities, when characterizing resting-state networks.

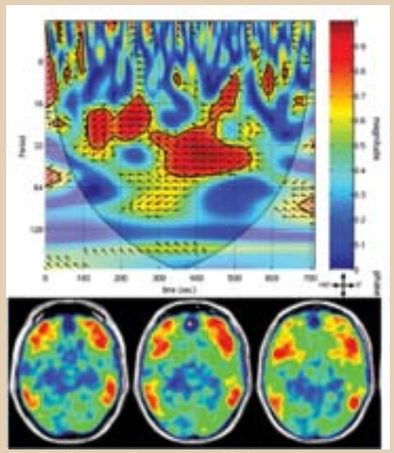

(Top) Time-frequency coherence between 2 brain networks across a resting-state scan, shown for 1 subject. Intensity reflects the magnitude of coherence, and the direction of arrows indicates phase. (Bottom) Map of default-mode connectivity variability, averaged over 12 subjects.

References/Funding Source NIH F31-AG032168 to CC and P41-RR009784 to GHG. C Chang, GH Glover, 2010. Time-frequency dynamics of resting-state brain connectivity measured with fMRI. Neuroimage 50, 81-98.

Hadamard-encoded BOLD fMRI for Reduced Signal Dropout

GH Glover, C Chang
Departments of Radiology and Electrical Engineering, Stanford University, CA

Introduction: BOLD fMRI suffers from signal dropout in frontal-orbital and lateral parietal/temporal regions from susceptibility differences between air and tissue induces intravoxel dephasing. By decreasing the slice thickness, dephasing is reduced and signal is regained, but at the expense of signal to noise ratio (SNR) in magnetically uniform regions of the brain (1). Here we introduce a novel solution: the use of Hadamard-encoding to simultaneously excite pairs of subslices that are subsequently combined incoherently using UNFOLD (2) to gain signal in dropout regions at no loss of SNR efficiency in uniform regions.

Methods: Alternately applying sine- and cosine-modulated Hadamard pulses (3) in a dynamic acquisition, two sub-slices of half the desired slice thickness are excited in-phase and out-of-phase (Fig. 1). Assuming there is a phase shift of φ between subslices because of the susceptibility-induced gradients, the resulting complex-valued time series contains magnitude components

$y(t) = \left[\rho_1^2(t) + \rho_2^2(t) \mp 2\rho_1(t)\rho_2(t)\sin(\phi(t))\right]^{1/2}$, where ρ_i are the magnitudes of the subslice signals, and the sign alternates with time frame t because of the alternating excitation. Squaring y(t) and taking its Fourier transform, one finds a component Y_1 with spectrum centered at DC corresponding to the term $\rho_1^2(t) + \rho_2^2(t)$ and a second component Y_2 centered at the Nyquist frequency corresponding to $2\rho_1(t)\rho_2(t)\sin(\phi(t))$ (Fig. 2). Applying an UNFOLD filter $H(\omega)$ to remove the Nyquist component, inverse transforming and taking the square root yields a reconstructed timeseries $\rho(t) = \left\{\Im^{-1}\left[\Im\left(y^2(t)\right)H(\omega)\right]\right\}^{1/2} = \left[\rho_1^2(t) + \rho_2^2(t)\right]^{1/2}$, i.e. the square root of the sum of squares of the two subslices. The influence of the intravoxel dephasing component φ is thereby removed.

The Hadamard method was implemented in a spiral-in/out pulse sequence (4). 60 2 mm thick subslices were acquired for 128 time frames. Timeseries corresponding to 4 mm slices were obtained from the magnitude reconstructed images as above using a two-point boxcar filter ($H(\omega) = \cos(\omega/\omega_{nyq})$). Functional data were obtained at 3T using a breath hold task to elicit activation in most of the brain (5). These scans were compared to a similar conventional method.

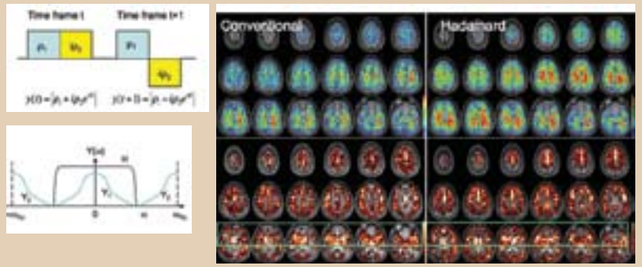

Fig. 1. Two time frames, showing Hadamard excitation of subslices ρi with alternating phase of ρ2.
Fig. 2. Spectrum of squared time series. Desired component $Y_1(\omega)$ centered at DC is selected by UNFOLD filter H.
Fig. 3. SFNR maps (top, 90-140) and activation maps (bottom, p<0.05) for one subject. Note increase in SFNR and activation with new method, especially in frontal regions, and slight gains in uniform regions.

Results: Figure 3 shows SFNR and activation maps for one volunteer. Note the recovery of signal in susceptibility regions and increase in SFNR from reduction of phase noise in the incoherent addition of subslices. Using the ROIs shown to highlight the compromised regions (green boxes, Fig. 3), an increase of 10.0% in activation extent was obtained with the Hadamard method.

Conclusion: The new method shows promise in diminishing signal dropout without loss of SNR efficiency, but with small loss in temporal resolution.

References/Funding Source NIH P41 RR009784. 1. S Lai, et al. Magn. Reson. Med 39:68 (1998). 2. B Madore, et al. Magn. Reson. Med 42:813 (1999). 3. SP Souza, et al. J. Comp. Assist. Tomog. 12:1026 (1988). 4. GH Glover, et al. Magn. Reson. Med 46:515 (1998). 5. ME Thomason, et al. NeuroImage 25:824 (2005). GH Glover, CE Chang, Hadamard-Encoded fMRI for Reduced Susceptibility Dropout. ISMRM Book of Abstracts, Barcelona 2010.

Reward Processing in Adolescents with First Episode Mania

M Singh[1], I Gotlib[2], R Kelley[1], X Cui[1], M Lum[1], E Adams[1], M Howe[1], K Chang[1], A Reiss[1]
Departments of [1]Psychiatry and Behavioral Sciences and [2]Psychology, Stanford University, CA

Objective: To evaluate performance and neural activation during reward processing in adolescents with first episode mania (BD) and healthy controls (HC), hypothesizing that those with BD will exhibit greater activation than will HC in the ventral striatum (nucleus accumbens) and amygdala in anticipating gains. These activations were predicted to be more robust with an affective prime preceding the reward task.

Methods: Adolescents (ages 13-18 years) with bipolar I disorder (N=21) diagnosed within the previous 9 months were recruited along with age and gender comparable healthy children (HC, N=23) without any psychiatric diagnoses. Subjects were given an in-scanner standardized monetary incentive delay (MID, Knutson et al., 2001) task with an antecedent mood induction. Functional magnetic resonance images were acquired with a 3T GE Signa scanner using a standard whole-head coil (General Electric, Milwaukee) and high-resolution, T1-weighted, spoiled GRASS images. A whole brain group analysis was performed by computing t-tests on contrast images for anticipated rewards and losses for each trial. The effects of priming on the groups were evaluated using a groupxprime ANOVA.

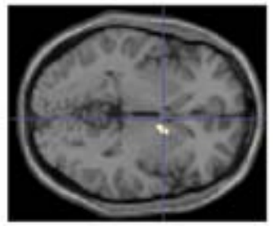

Increased activation in the nucleus accumbens in Healthy Controls relative to Adolescents with Bipolar Disorder while anticipating monetary gain.

Results: Within the HC group, increased activation was seen in the ventral striatum and ACC in gain anticipation. Within the BD group, increased activation was seen in the occipital lobe and supplemental motor area during gain anticipation. Between group comparisons showed significantly increased right nucleus accumbens activation in HC relative to BD participants while anticipating gains ($p<0.001$, uncorrected, extent = 40). Priming produced orbitofrontal activations in HC but not in BD ($p<0.01$, extent=20).

Discussion: Altered profiles of network activation were associated with reward processing in adolescent mania. BD adolescents show activations in predominantly visual cortical and motor preparatory regions in response to reward stimuli, whereas healthy adolescents show increased activation in prefrontal and ventrostriatal regions. Further studies characterizing reward processing in mania are warranted.

References/Funding Source Klingenstein Third Generation Foundation. Presented at the 55th Annual Meeting of the American College of Neuropsychopharmacology, Fort Lauderdale, FL, December 6-10, 2009.

Functional Connectivity in Patients with Chronic Neuropathic Pain

M Barad[1,2], E Sherman[1], J Brown[1], N Chatterjee[1], S Mackey[1]
Departments of [1]Anesthesia and [2]Neurology, Stanford University, CA

Cognitive behavioral therapy has long been used as a strategy for modulating chronic pain. Functional connectivity is an imaging technique to examine the strength of timecourse covariance of two neural entities. To better understand connectivity in the supraspinal modulation of pain, we looked at functional connectivity of the "pain matrix" as chronic pain patients modulated pain intensity with cognitive behavioral therapy.

Five patients with chronic NP in a limb were instructed and trained on the cognitive behavioral strategies of attention, distraction, and positive and negative reappraisal. Each subject completed 4 scans using each strategy to modulate their pain, and a resting state scan. After performing resting state fMRI using a 3T MRI, the connectivity for each subject was calculated as the pairwise correlation between average ROI time-courses. Subsequently, the average connectivity was determined by averaging across subjects. Finally, connectivity in different scans was compared using the Fisher's Z transformation.

The following results were significant at $p<0.05$. Compared to the resting state, attention decreased connectivity between the primary somatosensory cortex (S1)-insula. Distraction increased connectivity between the thalamus-S1, and between the prefrontal cortex (PFC)-insula, S1, thalamus, periaqueductal gray (PAG). Distraction decreased connectivity between the secondary somatosensory cortex (S2)-insula, S1, thalamus. Positive reappraisal increased connectivity between PFC-anterior cingulate cortex (ACC). Negative reappraisal increased connectivity between PFC-ACC, insula, S1, S2. Attention, as compared to distraction, decreased connectivity between the thalamus-S2, and increased connectivity between the thalamus-S1, and between PAG-PFC, thalamus. Negative reappraisal, as compared to positive reappraisal, decreased connectivity between S2-PFC.

This study demonstrates significant differences in the functional connectivity of chronic NP patients using different cognitive strategies. Our goal is to use this information to target areas and strategies to use in real-time fMRI, a non-invasive modulatory tool.

References/Funding Source AAN CRTF; NIH R21DA026092. Poster accepted for presentation at American Academy of Neurology 2010 annual conference, Toronto Canada, April 2010

Application of Support Vector Machines to the Detection of Chronic Pain

H Ung, J Brown, S Mackey
Department of [1]Anesthesia, Stanford University, CA

The subjective nature of pain makes an objective measurement difficult to produce. If such a measurement is possible, then this knowledge would assist in the management of patients whose self report of pain is either unavailable or called into question. Past studies have demonstrated that chronic pain is associated with gray matter (GM) atrophy, detectable by magnetic resonance imaging. We show that this decline of GM density can be used to distinguish between healthy and chronic low back pain (LBP) subjects with greater than chance accuracy. Structural MR scans from 100 subjects were segmented and spatially normalized to the standard MNI template using SPM8. Each image was resampled to 5x5x5 mm, resulting in approximately 1700 voxels. The average GM density within each voxel was used to generate the feature vectors for a linear support vector machine (SVM) classifier. Performance of the classifier was assessed using a k-fold cross validation scheme and significance was assessed with a Monte Carlo permutation test. The SVM classifier identified the presence or absence of LBP correctly 79% of the time ($p<0.01$). Sensitivity and specificity were 72% and 86% respectively. Regions of the brain important for driving the classifier include the left thalamus and parts of the ventromedial prefrontal cortex. These findings provide a promising outlook for using more advanced machine learning techniques to detect pain based on structural imaging data.

References/Funding Source Eli Lilly, the Redlich Pain Research Endowment, Rosenkrans Pain Research Endowment, NIH NS053961, NIH K99 DA023609. Poster presented at American Pain Society Conference, Baltimore MD, May 2010

Duloxetine and Placebo Alter Different Gray Matter Regions in Chronic Low Back Pain Patients

N Noor, N Chatterjee, A Crowell, S Mackey
Department of Anesthesia, Stanford University, CA

Chronic lower back pain (CLBP) affects millions of people and cost billions of dollars per year in the United States alone. Recent evidence indicates that chronic back pain may cause structural changes in brain gray matter (GM), suggesting that GM changes may be an important metric in evaluating the efficacy of pain treatments. In this double-blind crossover study, we used tensor based morphometry (TBM) to test our hypothesis that treatment with duloxetine (a specific serotonin-norepinephrine reuptake inhibitor) would cause GM changes that are distinct from those caused by treatment with placebo.

14 male subjects with CLBP were recruited. They rated pain as at least 4/10 on average for the two weeks prior to the start of the study and were not on pain medications. Study design was a double blind, placebo control, 12-week crossover study utilizing duloxetine as the active drug. Structural scans were conducted at baseline and at the end of each drug period.

Tensor based morphometry was used to evaluate structural changes between baseline and follow-up scans in a method similar to that outlined by Kipps et al (Kipps, J Neurol Neurosurg Psychiatry, 2005). Significant clusters were defined at $p<0.05$ corrected for multiple comparisons.

Both duloxetine and placebo caused changes in localized brain GM. These changes were distinct in that duloxetine led to increases in GM in bilateral caudate and decreases in GM in orbitofrontal and ventromedial prefrontal cortex, while placebo led to increases in GM in left anterior insula and bilateral caudate. Correlations with behavioral measurements are ongoing. Our study suggests separate brain mechanisms for duloxetine and placebo effects in chronic low back pain patients.

References/Funding Source Eli Lilly. Poster presented at American Pain Society Conference, Baltimore MD, May 2010

Human Brain Activity Identifies the Presence or Absence of Pain

J Brown, N Chatterjee, S Mackey
Department of Anesthesia, Stanford University, CA

Introduction: Currently, the most reliable method of assessing pain is self-report. If however, self-report is unavailable or called into question, pain may be ignored or discredited. Therefore, a biomarker for pain would help to better inform clinical decisions. Suggesting that patterns of brain activity might provide a biomarker for pain, regions of the human brain are more activated by painful stimuli than by non-painful stimuli. This study aims to use fMRI to determine the degree to which patterns of neural activity can predict the presence or absence of pain.

Methods: The protocol was approved by the Stanford Institutional Review Board, and subjects provided written, informed consent and completed the experiment. Using fMRI, we recorded brain activity during the presentation of both painful and non-painful thermal stimuli. Using maps of brain activity from 8 study participants, we trained a linear support vector machine (SVM) to classify heat stimuli as painful or non-painful. The accuracy of this SVM was assessed by applying it to 8 novel study participants.

Results: When using patterns of brain activity to predict whether or not a heat stimulus was painful, the SVM performed with 87% overall accuracy and with negative predictive values that exceeded 95%.

Conclusions: FMRI measurement of brain activity provides a clinically relevant biomarker for the presence or absence of pain. We show that the brain activity patterns associated with several individuals' subjective experiences of pain can be used to objectively identify the experience of pain in a different set of individuals.

References/Funding Source NRSA: 1F31GM08361-01 and RO1 NS053961-01. Talk and poster presented at American Academy of Pain Medicine 26th Annual Meeting in San Antonio, Texas. February, 2010.

Structural Brain Differences in Fragile X Syndrome and Idiopathic Developmental Delay

S Patnaik, K Chen, E Walter, Y Park, A Lightbody, A Reiss
Center for Interdisciplinary Brain Sciences Research, Department of Psychiatry, Stanford University, CA

Previous MRI studies of children and adolescents with fragile X syndrome have shown aberrant morphology in sub-cortical brain structures including enlargements of the caudate, thalamus and fourth ventricle. Automated anatomical parcellation and segmentation tools such as FreeSurfer have recently been successful in delineating brain structures (including deep-brain structures) in typically developing individuals. We have tested the feasibility of using FreeSurfer to segment deep-brain structures in young adults with fragile X syndrome and idiopathic developmental delay.

We scanned 30 young adults with fragile X syndrome ranging in age from 15 to 25 years (mean 21.84 ±2.7 years) and 13 with idiopathic developmental delay ranging in age 16 to 26 (mean 20.42 ± 3.2 years). Participants were group matched for age and IQ.

We obtained T1-weighted structural MRIs on a 3T MRI scanner (GE) at Stanford University. Images were analyzed using FreeSurfer's automated pipeline. Sub-cortical regions were obtained via FreeSurfer's volumetric segmentation methods (http://surfer.nmr.mgh.harvard.edu/). Resulting volumes for brain structures of interest were subject to a multivariate ANCOVA while covarying for age, gender, IQ and total tissue volume (total grey matter plus total white matter).

We found significant enlargements of the caudate, pallidum and thalamus bilaterally (all $p<0.005$) in fragile X syndrome as compared to the developmentally delayed control participants. In addition, we found marginally significant enlargements of the right putamen, bilateral lateral ventricles and the mid-posterior segment of the corpus callosum.

Our findings replicate previous differences in sub-cortical structures in a novel and under-studied sample of young adults with fragile X syndrome. In addition, we found the pallidum to be significantly enlarged in fragile X syndrome. This work provides evidence that FreeSurfer can be effectively used to investigate neuroanatomical structures in non-typically developing populations.

References/Funding Source NIH5R01-MH50047 (ALR). S Patnaik, K Chen, E Walter, Y Park, A Lightbody, A Reiss, (2010, July). Structural brain differences in fragile X syndrome and idiopathic developmental delay. Poster to be presented at the 12th annual International Fragile X Conference, Detroit, Michigan.

Neurochemical Deficits in Cerebellar Vermis in Offspring of Parents with Bipolar Disorder

M Singh[1], D Spielman[2], A Libby[1], E Adams[1], T Acquaye[1], M Howe[1], R Kelley[1], A Reiss[1], K Chang[1]
Departments of [1]Psychiatry and Behavioral Sciences and [2]Radiology, Stanford University, CA

Objectives: We aimed to compare concentrations of N-acetyl aspartate, myoinositol, and other neurometabolites in the cerebellar vermis of bipolar offspring and healthy controls to examine whether changes in these neuronal metabolite concentrations occur in bipolar offspring prior to the onset of mania. Methods: 9–17 year old children and adolescents with a familial risk for bipolar I or II disorder (22 bipolar offspring with subsyndromal mood symptoms, "SS"), and 25 healthy controls ("HC") were examined using proton magnetic resonance spectroscopy (1H-MRS) at 3T to study metabolite concentrations in an 8 cc voxel in the cerebellar vermis. Data was processed using LCModel (Provencher, 2001).

Results: Decreased myoinositol and choline concentrations in the vermis were seen in the SS group compared to HC ($p<0.01$).

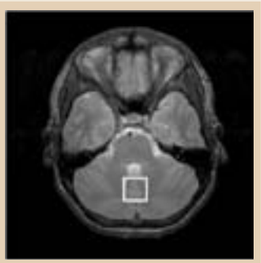

Anatomical localization of cerebellar vermis sampled in this study

Discussion: Decreased cellular metabolism and interference with second messenger pathways may be present in the cerebellar vermis in individuals at risk for BD as evident by decreased myoinositol and choline concentrations in this region. These results may be limited by a cross-sectional design, co-occurring diagnoses, and medication exposure. Longitudinal studies are necessary to determine if early neurochemical changes can predict the development of mania. Improved methods for identifying children with certain neurochemical vulnerabilities may inform preventive and early intervention strategies prior to the onset of mania.

References/Funding Source National Institute of Health (R01 MH077047-01, RR09784, and K23 MH085919), the National Alliance for Research on Schizophrenia and Depression (NARSAD), and Lucile Packard Children's Hospital Child Health Research Program. MK Singh, D Spielman, A Libby, E Adams, T Acquaye, M Howe, R Kelley, A Reiss, K Chang: Neurochemical Deficits in the Cerebellar Vermis in Child Offspring of Parents with Bipolar Disorder. (In review). Presented at the Annual Meeting of the American Academy of Child and Adolescent Psychiatry, Honolulu, HI, December 7-11, 2008.

Regional Grey Matter Accounts for Individual Differences at Risk for Developing Dyslexia in 5-6 Year Olds

JM Black[1], H Tanaka[1,2], L Stanley[1,2], M Nagamine[3], N Zakerani[1,2], A Thurston[1,2], S Kesler[1], C Hulme[4], H Lyytinen[5], GH Glover[6], AL Reiss[1], F Hoeft[1]
Departments of [1]Center for Interdisciplinary Brain Sciences Research (CIBSR), Department of Psychiatry and Behavioral Sciences, [6]Radiology, Stanford University, Stanford, CA; [2]Pacific Graduate School of Psychology, Redwood City CA; [3]Psychiatry, National Defense Medical College, Saitama Japan; [4]Psychology, University of York, York England; [5]Psychology and Child Research Center, University of Jyväskylä,Jyväskylä Finland

Family history and poor reading-related skills such as phonological awareness, rapid naming and letter knowledge in pre-readers (referred here as familial and behavioral risk, respectively) are critical predictors of developmental dyslexia. No studies have shown structural brain patterns that account for individual differences in risk for developmental dyslexia, especially in young children at the beginning of or before formal reading instructions are provided. Further, individual contributions of the two risk factors, familial and behavioral risks, have not been previously examined using neuroimaging. We examined 51 children (5 to 6 years of age) with varying degrees of familial and behavioral risks for developmental dyslexia and sought to demonstrate associations with brain morphometry. Results showed that greater maternal history of reading disability was associated with smaller bilateral prefrontal and parieto-temporal grey but not white matter volumes (with or without behavioral risk as a nuisance variable). No such relationship was observed for paternal reading history and behavioral risk. These results help to guide future neuroimaging research focusing on environmental and genetic influences and provide new information that may help predict which child will develop dyslexia in the future.

References/Funding Source NICHD HD054720, Lucile Packard Foundation for Children's Health, Dyslexia Foundation, Bette and Al Moorman Young Investigator Award, P41RR009784. Submitted to Proc Natl Acad Sci USA.

Subgenual Anterior Cingulate Cortex Reductions in Adolescents with First Episode Mania

M Singh[1], K Chang[1], M Chen[2], R Kelley[1], A Garrett[1], M Mitsunaga[1], L Bararpour[1], M Howe[1], A Reiss[1], I Gotlib[2]
Departments of [1]Psychiatry and Behavioral Sciences and [2]Psychology, Stanford University, CA

Objective: A range of prefrontal and subcortical volumetric abnormalities has been found in adults and adolescents with bipolar disorder. It is unclear, however, if these deficits are present early in the onset of mania or are a consequence of multiple mood episodes or prolonged exposure to medication. The goal of this study was to examine whether youth who recently experienced their first episode of mania are characterized by brain volumetric abnormalities.

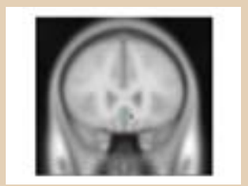

Adolescents with first-episode mania have smaller subgenual cingulate grey matter volume than do healthy adolescents on whole brain analysis (result shown in red at a statistical threshold of $p<0.05$, FWE-corrected and superimposed on manually traced left and right subgenual cingulate cortices).

Methods: Anatomical images from magnetic resonance imaging of 26 13-18-year-old adolescents with first-episode mania and 24 age-comparable healthy controls with no personal or family history of psychopathology were analyzed using whole-brain voxel-based morphometry (VBM) in SPM8.

Results: Compared with healthy controls, adolescents with mania had significantly less grey matter volume in the left subgenual cingulate cortex ($p<0.05$, FWE corrected).

Discussion: Adolescents with a recent onset of mania have smaller subgenual cingulate cortex volume than do their healthy counterparts, suggesting that this anomaly occurs early in the onset of, or may predate the disorder. Longitudinal studies are needed to examine the impact of this volumetric reduction on the course and outcome of this disorder.

References/Funding Source Klingenstein Third Generation Foundation. MK Singh, KD Chang, MC Chen, RG Kelley, A Garrett, M Mitsunaga, L Bararpour, M Howe, AL Reiss, IH Gotlib: Volumetric Reductions in the Subgenual Anterior Cingulate Cortex in Adolescents with First Episode Mania (In Review). Presented at the 65th Annual Meeting of the Society for Biological Psychiatry, New Orleans, LA, May 20-22, 2010.

Reward Processing in Adolescents with First Episode Mania

M Singh[1], I Gotlib[2], R Kelley[1], X Cui[1], M Lum[1], E Adams[1], M Howe[1], K Chang[1], A Reiss[1]
Departments of [1]Psychiatry and Behavioral Sciences and [2]Psychology, Stanford University, CA

Objective: To evaluate performance and neural activation during reward processing in adolescents with first episode mania (BD) and healthy controls (HC), hypothesizing that those with BD will exhibit greater activation than will HC in the ventral striatum (nucleus accumbens) and amygdala in anticipating gains. These activations were predicted to be more robust with an affective prime preceding the reward task.

Methods: Adolescents (ages 13-18 years) with bipolar I disorder (N=21) diagnosed within the previous 9 months were recruited along with age and gender comparable healthy children (HC, N=23) without any psychiatric diagnoses. Subjects were given an in-scanner standardized monetary incentive delay (MID, Knutson et al., 2001) task with an antecedent mood induction. Functional magnetic resonance images were acquired with a 3T GE Signa scanner using a standard whole-head coil (General Electric, Milwaukee) and high-resolution, T1-weighted, spoiled GRASS images. A whole brain group analysis was performed by computing t-tests on contrast images for anticipated rewards and losses for each trial. The effects of priming on the groups were evaluated using a groupxprime ANOVA.

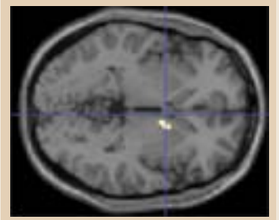

Increased activation in the nucleus accumbens in Healthy Controls relative to Adolescents with Bipolar Disorder while anticipating monetary gain.

Results: Within the HC group, increased activation was seen in the ventral striatum and ACC in gain anticipation. Within the BD group, increased activation was seen in the occipital lobe and supplemental motor area during gain anticipation. Between group comparisons showed significantly increased right nucleus accumbens activation in HC relative to BD participants while anticipating gains ($p<0.001$, uncorrected, extent = 40). Priming produced orbitofrontal activations in HC but not in BD ($p<0.01$, extent=20).

Discussion: Altered profiles of network activation were associated with reward processing in adolescent mania. BD adolescents show activations in predominantly visual cortical and motor preparatory regions in response to reward stimuli, whereas healthy adolescents show increased activation in prefrontal and ventrostriatal regions. Further studies characterizing reward processing in mania are warranted.

References/Funding Source Klingenstein Third Generation Foundation. Presented at the 55th Annual Meeting of the American College of Neuropsychopharmacology, Fort Lauderdale, FL, December 6-10, 2009.

Evaluating an Intensive Behavioral Intervention for Children and Adolescents with Fragile X Syndrome

SS Hall, JL Hammond, MA Hirt, AL Reiss
Department of Psychiatry and Behavioral Sciences, Stanford University, CA

This study will attempt to overcome putative specific learning dysfunction in children and adolescents diagnosed with Fragile X syndrome (FXS) using a stimulus equivalence (SE) teaching paradigm. Mathematical performance and brain activation prior to and following SE training will be examined. The efficacy of the intervention will be studied in comparison to a control group of gender, verbal IQ, and age-matched individuals diagnosed with non-specific developmental delay (DD) in order to understand the specificity of mathematical dysfunction exhibited by individuals with FXS. Performance in the targeted skill areas (fraction, pie chart, and decimal conversion) will be compared prior to and following SE training, using functional magnetic resonance imaging (fMRI) and behavioral metrics. It is hypothesized that following SE training, individuals with FXS will show gains in their discrimination of both trained and untrained mathematical relations, and will show increased activation in posterior parietal (PPC) and dorsolateral prefrontal cortex (DLPFC). In addition, we hypothesize that these regions will show increased functional connectivity compared to pre-test measures.

References/Funding Source National Institute of Mental Health (K08)

Changes in Brain Activation Following Family-focused Treatment in Youth at Risk for Bipolar Disorder

A Garrett[1], K Chang[1], D Miklowitz[3], M Howe[1], R Kelley[1], M Singh[1], G Glover[2], A Reiss[1],
[1]Departments of Psychiatry and Behavioral Sciences, and [2]Radiology, Stanford University, CA; [3]Department of Psychiatry, UCLA, CA

Objective: To investigate changes in brain activation associated with family focused treatment (FFT) in adolescents at high risk for developing bipolar disorder.

Background: Previous studies have found that FFT is effective in stabilizing symptoms of mania and depression in adolescent patients. This treatment may also be associated with changes in the function of brain regions associated with emotional responses.

Methods: Ten subjects with a family history of bipolar disorder and current subsyndromal symptoms completed scans at baseline and after 12 weeks of treatment (either treatment as usual or FFT). Functional magnetic resonance imaging scans were acquired using a spiral pulse sequence at 3T, while subjects viewed fearful and neutral faces. Whole brain data were processed in SPM5. Clusters of activation that changed significantly from baseline to follow-up were identified using a repeated measures ANOVA, and a dual threshold of p=.01, extent = 80. Mean activation in clusters that fell in a priori hypothesized regions was extracted. Due to the small sample size, all subjects were included in a single group, regardless of treatment condition.

Results: The whole brain repeated measures analysis showed that, from baseline to follow-up, the following changes occurred: (1) amygdala activation decreased, (2) dorsolateral and orbital prefrontal cortex activation increased. Further analyses showed that (a) higher activation in the right amygdala at baseline was found in subjects who showed the greatest clinical improvement in depressive symptoms at follow-up, (b) lower right DLPFC activation at baseline was associated with greater improvement in depressive and manic symptoms at followup (see Figure), and (c) greater increases in right orbitofrontal cortex activation from baseline to followup were associated with greater improvement in depressive and manic symptoms.

Conclusions: Clinical improvement is associated with functional changes in specific brain regions that have been implicated in emotion perception and regulation. These data also suggest that fMRI may help us to predict who will respond best to these treatments.

Aberrant Brain Activation During a Response Inhibition Task in Adolescent Eating Disorder Subtypes

J Lock, A Garrett, J Beenhakker, A Reiss
Department of Psychiatry and Behavioral Sciences, Stanford University, CA

Objective: Behavioral and personality characteristics associated with excessive inhibition and disinhibition are observed in patients with eating disorders. This study examined the neural correlates of inhibitory control in adolescents with these disorders. We hypothesized that patients with symptoms of binge eating and purging would show aberrant activation in regions associated with response inhibition, and that this pattern would differ from patients with restricting eating behaviors.

Methods: Thirteen adolescents with binge eating and purging, i.e., bulimia nervosa or anorexia nervosa, binge-purge subtype ,14 with anorexia nervosa, restricting subtype, and 13 healthy controls performed a rapid jittered event related Go-NoGo task. FMRI images were collected using a 3T GE scanner and a spiral pulse sequence. A whole-brain 3-group ANOVA in SPM5 was used to identify significant activation associated with the Main Effect of Group, for the comparison of correct NoGo versus Go trials. The mean activation in these clusters was extracted for further comparisons in SPSS.

Results: The binge-purge group showed significantly greater activation than the healthy control group in the bilateral precentral gyri, anterior cingulate cortex, and middle and superior temporal gyri, and greater activation compared to both controls and anorexia nervosa restricting type group in the hypothalamus and right dorsolateral prefrontal cortex. Within-group analysis found that only the anorexia nervosa, restricting group showed a positive correlation between percent correct on NoGo trials and activation in posterior visual and inferior parietal cortex regions.

Conclusions: The current study provides preliminary evidence that during adolescence, eating disorder subtypes may be distinguishable in terms of neural correlates of inhibitory control. This distinction is consistent with differences in behavioral impulsivity in these patient groups.

References/Funding Source Lucile Packard Children's Hospital at Stanford. In press at American Journal of Psychiatry

Neural Processing of Dynamic Social Stimuli

E Walter, A Lightbody, A Reiss
Center for Interdisciplinary Brain Sciences Research, Department of Psychiatry, Stanford University, CA

We performed fMRI with healthy volunteers to elucidate the brain circuits involved in processing short, naturalistic, "socially demanding" gestures. We created a stimulus set comprising two-second video clips of a live actor who performed either a social gesture (e.g. waving, handshake) or a non-social gesture that was matched for amount and direction of movement (e.g. reaching for mug, wiping counter). In half of the clips, the actor was facing the participant (i.e. facing the camera), and in the other half of the clips the actor was turned at an angle (i.e. as if they were addressing an unseen individual just off camera). To tease apart the influence of facial movements and eye gaze on gesture processing, we also created blurred versions of all stimuli.

Our novel design allowed us to tease apart many aspects of social cognition. We conducted a whole-brain functional MRI (3T) study using these movie stimuli. Participants were instructed to watch the short movie clips for a red dot to appear near the eyes/nose region on half of the clips, and were not given instructions regarding the social/non-social aspect of the stimuli.

All contrasts were performed using a whole-brain voxel-level threshold of $p<0.001$, cluster corrected at $p<0.05$. A contrast of all Social vs all Nonsocial gestures found significantly greater activation in the left occipital cortex (BA 19) and right middle occipital gyrus (BA 18) during Social gestures. Marginally significant activations were also found in the left fusiform gyrus (FFG, BA 19), right insula (BA 13) and right inferior frontal gyrus (IFG, BA 45). Nonsocial gestures more strongly activated left parietal regions, including the inferior parietal lobe (IPL, BA 40) and post-central gyrus (BA 5). Our analyses provide further support for the role of frontal and temporal cortex in the processing dynamic social stimuli.

References/Funding Source NIH5R01-MH50047 (ALR).

Longitudinal fMRI Study Exploring Differences in Response Inhibition in Fragile X Syndrome

K Chen, S Bray, S Patnaik, E Walter, P Mazaika, A Lightbody, A Reiss
Center for Interdisciplinary Brain Sciences Research, Department of Psychiatry, Stanford University, CA

Individuals with fragile X syndrome (FXS) have known difficulties with executive function tasks, including the inhibition of inappropriate responses. Single timepoint brain imaging studies have suggested that this difficulty is related to activation differences, relative to control participants, in regions such as the right ventrolateral prefrontal cortex (VLPFC) and anterior cingulate cortex (ACC). We used fMRI in a longitudinal design to explore changes in regional activation related to response inhibition in individuals with FXS, compared to healthy controls.

We scanned 10 individuals with FXS (5 females) and 14 typically developing participants (7 females) at two timepoints. The mean ages were 14±3.20 years at the first timepoint and 17.97±3.84 years at the second timepoint; on average the scans were separated by 3.97±1.81 years.

Participants performed a classic Go/NoGo task that requires inhibition of a prepotent response. For each subject we generated a general linear model that included block regressors for "go" and "go/nogo" blocks, with time 1 and time 2 scans modeled as separate sessions. We extracted contrast estimates for the "go/nogo" minus "go" blocks, as a measure of activation related to response inhibition, from our regions of interest (ROIs) (bilateral VLPFC, insula, and ACC). We used paired t-tests to identify time differences within groups, and repeated measures ANOVAs to test for time x group interactions, using age and gender as covariates.

FXS participants showed significant decreases in activation from time 1 to time 2 in the bilateral VLPFC, insula, and ACC, whereas the TD participants showed a significant decrease over time in the bilateral insula ($p<0.01$). When comparing longitudinal changes between groups, we found that the right pars opercularis of the inferior frontal gyrus ($p<0.001$) and bilateral ACC ($p<0.05$) showed a significant group x time interaction; activation in these regions decreased more over time in the FXS group compared to the TD group.

References/Funding Source NIH5R01-MH50047 (ALR). K Chen, S Bray, S Patnaik, E Walter, P Mazaika, A Lightbody, A Reiss. Longitudinal fMRI study exploring differences in response inhibition in fragile X syndrome. Poster presented at the 12th Annual International Fragile X Conference, Detroit, Michigan, July 2010.

Functional MRI Investigation of Executive Function Processes in Fragile X Syndrome

E Walter, K Chen, S Patnaik, A Lightbody, A Reiss
Center for Interdisciplinary Brain Sciences Research, Department of Psychiatry, Stanford University, CA

Individuals with fragile X syndrome (FXS) differ from control participants in the size and function of many brain areas, including the caudate, thought to be important for motor control, implicit learning and executive function processes.

We recruited young adult females diagnosed with FXS, Turner syndrome and idiopathic developmental delay to participate. Participants were scanned with functional magnetic resonance imaging (fMRI) while they performed two cognitive tasks thought to be mediated by the caudate: the Serial Reaction Time Task (SRTT) and the Stop-Signal Reaction Time Task (Stop Signal Task). The SRTT is a measure of implicit learning requiring simple button presses in random or sequential order. The Stop Signal Task measures the ability to withhold (inhibit) a prepotent response.

For the SRTT, young adult females with FXS activated the right caudate, inferior frontal gyrus and anterior cingulate cortex, as well as the left cerebellum and parahippocampal gyrus more strongly during the Sequential versus the Random blocks of trials than did controls. In contrast, those in the control group activated the left medial frontal gyrus more strongly than did the fragile X group for the same Sequential >> Random contrast. During the Stop Signal Task, those with FXS activated many more brain areas during the Stop trials, in comparison to the Go trials, than did the control participants. These brain regions included large regions in the right inferior frontal gyrus, medial frontal gyrus and anterior cingulate, as well as in the left insula. In contrast, the Stop>>Go contrast activated only left-lateralized motor areas more significantly in the control group relative to the group with FXS. (All reported results were performed using a threshold of $p<0.001$, with a cluster threshold of 20 voxels.)

References/Funding Source NIH5R01-MH50047 (ALR). E Walter, K Chen, S Patnaik, A Lightbody, A Reiss. Functional MRI investigation of executive function processes in fragile X syndrome. Talk to be given at the 12th annual International Fragile X Conference, Detroit, Michigan, July 2010.

Bolus Perfusion-Weighted Imaging Measurement Of Quantitative Cerebral Blood Flow Can Be Improved Using An Arterial Spin Label Derived Scaling Factor: A Comparative Xenon CT Study

G Zaharchuk[1], M Straka[1], A Shankaranarayan[2], DC Alsop[3], ME Marks[1], ME Moseley[1], R Bammer[1]
Departments of [1]Radiology, [2]Neurology, Stanford University, CA; [3]Appled Sciences Laboratory - West, GE Healthcare, Menlo Park, CA; [4]Radiology, Beth Israel Deaconess Hospital, Boston, MA

Bolus dynamic susceptibility contrast (DSC) perfusion-weighted imaging (PWI) and arterial spin labeling (ASL) are two methods of measuring cerebral blood flow (CBF) using MRI. Each has different strengths and weaknesses. ASL CBF levels are reliable in high flow regions, but suffer from errors and low SNR in regions with long arterial arrival times. PWI, particularly when using delay-invariant deconvolution, is in theory unaffected by long arrival times. However, absolute quantitation is challenging, due to uncertainties in AIF & VOF partial volume and the nonlinear relationship between transverse relaxivity and contrast concentration. This study describes a method that uses ASL CBF measurements in regions with short transit delays (as measured by Tmax) to scale PWI CBF measurements. Stable xenon CT was used as a gold standard for CBF. Practically, a single global scaling factor will never improve correlation within an individual patient. Also, the upper limit of the improvement in between-patients correlation is set by the accuracy of ASL. However, specifically in regions with long Tmax, we found improved CBF correlation for corrected bolus PWI compared to either uncorrected PWI or ASL CBF. While we used a 6 min high resolution ASL sequence as this is part of our standard imaging, in principle, much lower resolution ASL CBF maps with shorter acquisition times could be obtained, since the scaling factor is determined from a relatively large volume of tissue.

We conclude that the combined ASL-PWI method is superior to either method alone for measuring quantitative CBF with MRI.

References/Funding Source National Institute of Mental Health (K08)

Diagnostic Accuracy Of High-Resolution Multi-Shot Diffusion-Weighted MRI For The Detection Of Breast Cancer

WB Veldhuis, C Liu, Y Do, ME Moseley, BL Daniel
Departments of Radiology, Stanford University, CA

Diffusion-weighted imaging (DWI) may provide information - physically unrelated to microvascular changes detected by contrast-enhanced MRI - that can improve the specificity of MRI for breast cancer diagnosis. Attempts thus far to benefit from the information content that DWI may offer have been limited by the use of single-shot techniques, with inherent sensitivity to geometric distortions and limitations in detected lesion size. The aim of this HIPAA-compliant, IRB-approved study was to compare the sensitivity and specificity of high-resolution DWI of the breast to 'conventional' dynamic-contrast enhanced MRI, and to pathology. We performed a retrospective analysis of diffusion-weighted data sets acquired in 103 consecutive women (mean age 50.3 years, range: 15-81) undergoing 1.5T MRI for the evaluation of breast cancer. Pathological confirmation was obtained for all but one of the lesions marked as 'suspicious' on ftADC. As expected, the sensitivity of DCE-MRI was very high, with a lower specificity. The specificity of blind DWI and especially of the blind ftADC-analysis, was much higher. The present data suggest that a contrast-free MRI-protocol, that includes DW imaging, may have a clinically acceptable diagnostic performance. This is relevant in light of recent issues with gadolinium-induced nephrogenic systemic fibrosis, and may also be relevant to discussions on breast cancer screening with MRI. Lastly, we are aware that the conventional breast imaging protocol will include contrast-enhanced-sequences for some time to come. However, even with such a protocol, patients may still benefit from a diagnosis-modifying effect – in terms of up- or down-staging – of adding ftADC-maps to the analysis. For the current data set, retrospective addition of ftADC-mapping resulted in the correct downstaging of 22 of 65 pathology-verified lesions (data not shown). Large, multi-center validation will have to precede actual clinical implementation of this technique.

References/Funding Source Lucas Foundation, NCRR P41RR09784, KWF - Dutch Cancer Society, and NIH-5K99EB007182-02. WB Veldhuis, C Liu, Y Do, ME Moseley, BL Daniel. Diagnostic Accuracy Of High-Resolution Multi-Shot Diffusion-Weighted MRI For The Detection Of Breast Cancer. Proceedings of the ISMRM, 2009, Honolulu Hawaii.

Estimation of CBF Values Using Multi-Echo DSC-MRI: a Comparison with a Xenon CT

M Straka[1], G Zaharchuk[1], RD Newbould[2], GW Albers[3], ME Moseley[1], R Bammer[1]
Departments of [1]Radiology, [2]Electrical Engineering and [3]Stanford Stroke Center, Stanford University, CA

Spatial distortions in EPI sequences and clipping of vascular signals during bolus passage peak a scanning sequence for perfusion with multiple echoes and temporal enhancement (PERMEATE) was developed, in which the confounding artifacts should be reduced. Data acquired with first (short) echo should be used to properly recover the vascular signals, whereas the later echoes are used to determine signals in the tissue manifesting better signal-to-noise ratio therein. Such state-of-the-art perfusion acquisition is complemented by a PWI post-processing pipeline, including correction for partialvolume effect (PVE) in vascular signals and susceptibility effect of the paramagnetic tracer in large vessels. The purpose of this study was to evaluate the benefits of such advanced acquisition scheme with the PVE and bulk-blood corrections and to quantify the improvement of values in the computed quantitative perfusion maps. In this work, we have demonstrated the acquisition of diffusion-weighted whole brain volumes using a SSFP-3DRS sequence. Compared with other diffusion techniques, our approach can achieve much higher SNR with desired diffusion weighting and limited imaging time. The 3DRS sampling strategy also benefits from reduced sensitivity of subject motion. However, since only the 0th order phase error term can be extracted and corrected, images may still be contaminated by residual motion artifacts, especially for high b-values. A proper 3D navigator should help further improve the image quality, which is still under investigation. Furthermore, with its high SNR efficiency, SSFP-3DRS can be feasibly applied to acquire DTI volumes under even higher resolution, which is usually desirable for tractography.

References/Funding Source Lucas Foundation, and NCRR P41RR09784 . M Straka, G Zaharchuk, RD Newbould, GW Albers, ME Moseley, R Bammer. Estimation of CBF Values Using Multi-Echo DSC-MRI: a Comparison with a Xenon CT. Proceedings of the ISMRM, 2009, Honolulu Hawaii.

A Quantitative Comparison of NIRS and fMRI Across Multiple Cognitive Tasks

Xu Cui[1,2], Signe Bray[1,2], A Reiss[1,2]
[1]Department of Psychiatry and Behavioral Sciences and [2]Center for Interdisciplinary Brain Sciences Research, Stanford University, CA

INTRODUCTION: Near-infrared spectroscopy (NIRS) is an increasingly popular technology for studying brain function. NIRS offers several advantages relative to functional magnetic resonance imaging (fMRI), including the ability to measure concentration changes of both oxygenated and deoxygenated hemoglobin, finer temporal resolution, and ease of administration, as well as disadvantages, most prominently inferior spatial resolution, inability to directly measure signals from deep-brain structures, and decreased signal-to-noise ratio (SNR). In this study, we compared NIRS and fMRI signals to assess spatial and temporal similarities.

METHODS: Thirteen healthy adults (mean age 27.9, age range 21-42, 6 males) underwent simultaneous NIRS and fMRI scanning while they completed four experimental paradigms: left finger tapping (tap), go/no-go (nog), judgment of line orientation (jlo), and an N-back working memory task using visuospatial stimuli (vis). We performed detailed comparisons of the signals in both temporal and spatial domains.

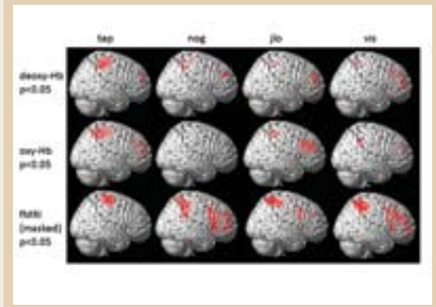

Activation maps measured with fMRI and NIRS. Channel positions projected onto the brain surface were normalized to a standard brain. fMRI activations were masked to show only regions covered by the NIRS probes.

RESULTS: We found that NIRS signals have significantly weaker SNR, but are nonetheless often highly correlated with fMRI measurements. Both SNR and the distance from scalp to brain contributed to variability in the NIRS/fMRI correlations. In the spatial domain, we found that a photon path forming an ellipse between the NIRS emitter and detector with a depth of ~14mm correlated most strongly with the BOLD response.

CONCLUSION: These findings suggest that, while NIRS can be an appropriate substitute for fMRI when studying brain activity related to certain cognitive tasks, care should be taken when designing NIRS studies to ensure that: 1) the spatial resolution is adequate for answering the question of interest and 2) the design accounts for weaker SNR, especially in brain regions further from the scalp.

References/Funding Source Shared Instrument grant (S10RR024657, ALR PI), the Stanford Institute for Neuro-Innovation and Translational Neurosciences (SINTN) fellowship (XC and ALR), NARSAD Young Investigator's Award, and Stanford University Lucas Center Radiology Seed Grant.

Reduced Field of View Imaging for Twice-Refocused Diffusion EPI using a Perpendicular Refocusing Slab

RL O'Halloran, S Holdsworth, S Skare, R Bammer
Department of Radiology, Stanford University, CA

Introduction: Imaging with a reduced field of view (rFOV) reduces distortion in EPI by acquiring fewer phase-encode lines. However, aliasing occurs when regions with signal are outside the phase field of view. ZOOM-EPI [1,2] is a method used to address this problem in which the refocusing slices are tilted relative to the first excitation (the 90 degree pulse). Here we use ZOOM-EPI with the refocusing pulses titled by 90 degrees to assure a sharp profile of the selected band. The approach is compared to a full FOV method in diffusion-tensor imaging DTI of the thoracic spine in one healthy volunteer.

Methods: MRI: Single-shot twice-refocused DTI of the thoracic spine was performed on a healthy volunteer using a 1.5T MRI scanner with a 4-channel spine coil. Three un-weighted (b=0 s/mm2) images and 60 diffusion-weighted directions (b = 500 s/mm2) were collected on 7 slices with a 4 mm slice thickness. Both the rFOV method and a conventional full FOV method were performed in a scan time of 3:12 min.

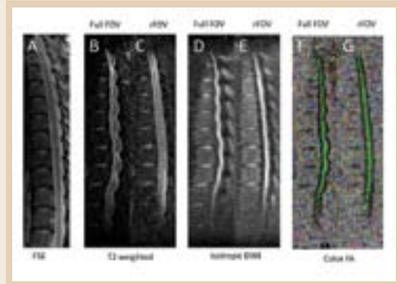

Figure 1: Thoracic spine images compared. The FSE (a) is shown for anatomical reference. The full FOV T2-weighted image (b) has much more distortion than the rFOV image (c). The DWI (d,e) and color FA (f,g) images show a similar effect .

Results and Discussion: The SNR of the rFOV implementation was approximately 67% of the SNR in the full FOV implementation, however the relative SNR was 12% higher in the rFOV image due to a lower achievable echo time. Images acquired with the rFOV method (Fig 1c,e,g) had far less distortion than the full FOV images (Fig 1b,e,f). The distortion in the full FOV images (Fig 1b,d,f) caused the spinal cord to have a serpentine appearance.

Conclusion: A rFOV method for DTI was presented that had significant reduction in distortion compared to full FOV EPI at the cost of modest reduction in SNR.

References/Funding Source 1 R01 EB008706, 1 R01 EB008706 S1, 5 R01 EB002711, 1 R01 EB006526, 1 R21 EB006860, Center of Advanced MR Technology at Stanford (P41RR09784), Lucas Foundation, Oak Foundation. GE Healthcare. Reduced Field of View Imaging for Twice-Refocused Diffusion EPI using a Perpendicular Refocusing Slab. RL O'Halloran, S Holdsworth, S Skare, R Bammer. In Proceedings of the 18th Annual Meeting of the ISMRM. 2452

Comparison Between Readout-Segmented (RS)-EPI and an Improved Distortion Correction Method for Short-Axis Propeller (SAP)-EPI

S Skare, SJ Holdsworth, K Yeom, PD Barnes, R Bammer
Department of Radiology, Stanford University, CA

'Short-Axis readout Propeller EPI' (SAP-EPI) and 'Readout-Segmented EPI' (RS-EPI) have been proposed for use in high resolution diffusion-weighted (DW) imaging. SAP-EPI and RS-EPI share common characteristics, in that k-space is traversed by several EPI 'segments' (referred to as blades (SAP-EPI) or blinds (RS-EPI)) in order to reduce the distortion and blurring that typically hampers EPI images. Our previous work comparing RS-EPI and SAP-EPI concluded that SAP-EPI suffers from considerably more blurring compared with RS-EPI despite attempts to correct for distortion. With an improved distortion correction method, we demonstrate that SAP-EPI results in a similar image resolution to RS-EPI for a given SNR normalized for scan time/slice.

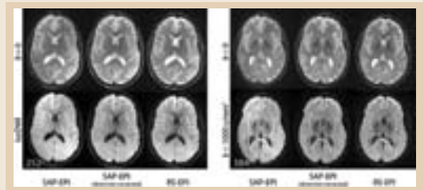

Comparison between SAP-EPI, distortion-corrected SAP-EPI, and RS-EPI on a healthy volunteer at matrix sizes of 252x252 (left) and 384x384 (right). SAP-EPI and RS-EPI datasets were acquired in equivalent scan times of 1:24min/volume.

All images were acquired on a 3T whole-body MRI unit using an 8-channel head coil. Scan-time matched SAP-EPI and RS-EPI DWI experiments were first performed on healthy volunteers using two matrix sizes: 256×252 (blade/blind width = 64) and 384×384 (blade/blind width = 96). Together with noise maps generated from repeated b = 0 scans, the scan time efficiency was calculated from the RS-EPI and distortion-corrected SAP-EPI images.

In our previous distortion correction implementation for SAP-EPI, the distorted blade data underwent two unnecessary sampling steps which now have been removed. Each of these resampling steps caused a slight loss in resolution, which also added a blur in the final image. For the new implementation presented in this work, we estimate (using the blade data itself) the ΔB_0 field in the laboratory space while using the original blade data in their own native coordinate systems, each having their unique 4×4 voxel-to-world matrix (defining its position and rotation) applied to the resampling coordinates.

The figure shows SAP-EPI, distortion-corrected SAP-EPI, and RS-EPI b = 0 and DW images acquired with matrix sizes of 2522 and 3842. The SAP-EPI images show considerably less blurring when corrected for distortion, with a resolution approaching that of the RS-EPI scan. The normalized SNR ratio (SNRSAP-EPI/SNRRS-EPI) was 1.3 and 1.6 for the 2522 and 3842 matrix sizes, respectively – indicating that one must scan RS-EPI approximately twice as long in order to achieve the same SNR as SAP-EPI. Looking at normalized noise maps for the 3842 acquisitions (data not shown) we found that at a comparative SNR the resolution is now very slightly reduced for RS-EPI.

This study demonstrates that SAP-EPI combined with an improved distortion-correction method and RS-EPI produce images of similar quality. At first glance, distortion-corrected SAP-EPI images appear more blurred than RS-EPI images. Without scan time restrictions, the unidirectional distortions in RS-EPI result in a sharper image, particularly with increasing resolution. However, one must scan RS-EPI approximately twice as long to achieve the same SNR. For an SNR-matched scenario the image quality of the two acquisitions very closely resemble each other – with a slight reduction in resolution for RS-EPI. In addition to the larger slice coverage/TR, SAP-EPI has one important advantage over RS-EPI in that for each blade, the stack of 2D slices forms a 'brick' in the image domain, making image domain 3D motion correction possible.

References/Funding Source NIH (1R01 EB008706, 1R01 EB008706S1, 5R01 EB002711, 1R01 EB006526, 1R21 EB006860), the Center of Advanced MR Technology at Stanford (P41RR09784), Lucas Foundation, Oak Foundation, and the Swedish Research Council (K2007-53P-20322-01-4). S Skare, SJ Holdsworth, K Yeom, PD Barnes, R Bammer, "Comparison Between Readout-Segmented (RS)-EPI and an Improved Distortion Correction Method for Short-Axis Propeller (SAP)-EPI" In: 18th Annual Meeting of the ISMRM. Stockholm, Sweden, 2010

R2/R2* Estimation Errors in Combined Gradient- and Spin-echo EPI Sequences due to Slice-profile Differences Between RF Pulses

H Schmiedeskamp, M Straka, R Bammer
Lucas Center, Department of Radiology, Stanford University, CA

There is increased interest in a combined acquisition of gradient-echo (GE) and spin-echo (SE) signals for applications in DSC-PWI and fMRI. One of the main reasons is the different sensitivity of GEs and SEs to different compartments of the underlying microvasculature. A multi-echo GE/SE-EPI pulse sequence allows one to simultaneously measure multiple EPI trains with R_2* and R_2 contrast. This facilitates T_1-independent calculations of $R_2^* = R_2 + R_2'$ and R_2 by least-squares fitting of the characteristic system of signal equations:

$S(t)^I = S_0^I \cdot exp(-t\cdot(R2+R2')) \text{ for } 0 < t < TE/2$ and $S(t)^{II} = S_0^{II} \cdot exp(-TE\cdot R2') \cdot exp(-t\cdot(R2-R2')) \text{ for } TE/2 < t \leq TE$.

In practice, the assumption that S_0 before and after the refocusing pulse is identical does not generally hold. This can be attributed to differences between the excitation and refocusing pulse profiles and requires careful attention. One potential remedy is to introduce an additional correction term δ that relates S_0^I prior to the refocusing pulse to the equilibrium signal after the 180° pulse by $S_0^I = \delta \cdot S_0^{II}$, so that the equations account for the differences in the excitation profiles.

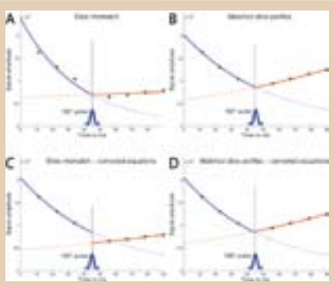

Comparison between SAP-EPI, distortion-corrected SAP-EPI, and RS-EPI on a healthy volunteer at matrix sizes of 252x252 (left) and 384x384 (right). SAP-EPI and RS-EPI datasets were acquired in equivalent scan times of 1:24min/volume.

Fig.1 shows the measured signal over an ROI in a phantom experiments (black dots) superimposed on the signal characteristics using fitted values for R_2, R_2', S_0^I and S_0^{II}. In case of mismatched slice profiles (Fig.1A/C), the non-corrected signal equations induced large overestimations of R2/R2* (RMS fit error = 659.1, cf. Fig.1A). By adding δ to the fitting function, the measured signal closely followed the fitted model (RMS error = 49.8, cf. Fig.1C). With minimal slice-profile mismatches, in this case achieved through single-slice acquisition (Fig.3B/D), results with both models were similar with a smaller RMS error in case of δ-correction (RMS = 75.5 instead of 112.8). If the slice profiles were truly identical, the 2 models would actually yield the same results.

The introduction of a factor δ to correct for discordances in slice profiles between excitation and refocusing pulses mitigated errors in the estimation of R2 and R2* in a pulse sequence that simultaneously measures GEs and SEs.

References/Funding Source Supported by NIH (1R01EB008706, 5R01EB002711, 1R01EB006526, 1R21EB006860), Center of Advanced MR Technology at Stanford (P41RR09784), Lucas & Oak Foundations. H Schmiedeskamp, M Straka, R Bammer. R2/R2* estimation errors in combined gradient- and spin-echo EPI sequences due to slice-profile differences between RF pulses. Proceedings of the Joint Annual Meeting of ISMRM/ESMRMB, Stockholm, Sweden. p 2962.

Reduced-FOV Diffusion Imaging with ZOnal Oblique Multislice (ZOOM) Combined with Readout-Segmented (RS)-EPI

SJ Holdsworth, S Skare, RL O'Hallaran, R Bammer
Department of Radiology, Stanford University, CA

Diffusion-weighted imaging (DWI) using echo-planar imaging (EPI) has been limited by geometric distortion and blurring, particularly in regions with large off-resonance effects such as in the spinal-cord and in regions of the brain residing near tissue/air interfaces. Geometric distortion in EPI is proportional to the FOV in the phase encoding direction (FOVpe), as well as the echo-spacing between adjacent echoes in the EPI train (Tro). To reduce FOVpe and avoid aliasing, here we use the zonal oblique multislice EPI (ZOOM-EPI) technique, which uses a tilted refocusing pulse. To reduce distortion further, Tro can be reduced by covering k-space with a series of consecutive segments or 'blinds', known as RS-EPI. Here we implemented the ZOOM pulse together with the RS-EPI trajectory (ZOOM-RS-EPI) to get the benefits of both methods for reducing distortion.

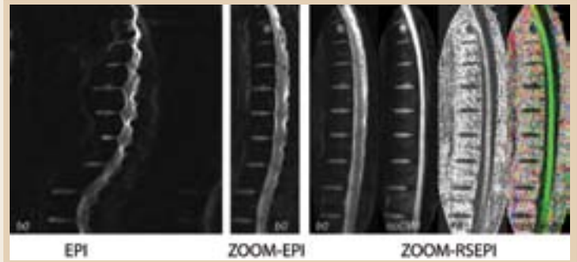

Comparison between the b = 0 s/mm2 images of a thoracic spine using full-FOV EPI, ZOOM-EPI and ZOOM-RS-EPI. For ZOOM-RS-EPI, the isotropic DWI (isoDWI, b = 500 s/mm2), fractional anisotropy (FA), and 1st eigenvector (colormap) are also shown. Note that there is less 'disc bulging' into the spinal canal and less blurring on the ZOOM-RS-EPI scans than on the ZOOM-EPI scans.

All diffusion images were acquired on a 3T whole-body GE system. ZOOM-EPI and ZOOM-RS-EPI thoracic spine DTI images were acquired on a volunteer using a 4-channel spine coil with the following parameters: rectangular FOV = 30 x 10cm, slthck = 4 mm, zoom-angle θ = 5º, TR = 3s, a matrix size = 200 x 60 (square pixels), partial Fourier (18 overscans), 24 isotropically distributed DW directions with b = 500 s/mm2, and a scan time of 9:48mins. ZOOM-RS-EPI used TEmin = 55 ms, 7 blinds of width = 32 and ZOOM-EPI used TEmin = 75 ms, and 7 NEX. For comparison, full FOV images were acquired.

The EPI and RS-EPI b = 0 s/mm2 images acquired with and without the use of rectangular FOV and ZOOM pulse is shown in the figure. As shown, geometric distortion can be reduced significantly with ZOOM-RS-EPI and also reduces the 'jagged' appearance of the spinal cord as shown in the b = 0 s/mm2 images.

This work shows that RS-EPI in combination with the ZOOM pulse in order to spatially select a region of interest may be useful for diffusion imaging of regions with large off-resonance effects. While the rectangular FOV used in this work (30cm x 10cm) reduced distortion by 30% (compared to a full FOV acquisition), RS-EPI further reduced the distortion by 33%. A disadvantage of RS-EPI is the reduced SNR efficiency compared with EPI. However the resulting RS-EPI DTI data shows high SNR 3T images acquired in a reasonable scan time for DTI, and the jagged appearance that often hampers the quality of EPI DW images is reduced significantly.

References/Funding Source NIH (1R01 EB008706, 1R01 EB008706S1, 5R01 EB002711, 1R01 EB006526, 1R21 EB006860), the Center of Advanced MR Technology at Stanford (P41RR09784), Lucas Foundation, Oak Foundation, and the Swedish Research Council (K2007-53P-20322-01-4). SJ Holdsworth, S Skare, RL O'Hallaran, R Bammer, "Reduced-FOV Diffusion Imaging with ZOnal Oblique Multislice (ZOOM) Combined with Readout-Segmented (RS)-EPI" In: 18th Annual Meeting of the ISMRM. Stockholm, Sweden, #1611, 2010

Diffusion-Weighted Imaging of the Abdomen with Readout-Segmented (RS)-EPI

SJ Holdsworth, S Skare, S Vasanawala, R Bammer
Department of Radiology, Stanford University, CA

Diffusion-weighted imaging (DWI) in the abdomen has proven useful for various pathologies, including liver lesion characterization and simple vessel suppression, diagnosis of diffuse renal disease, and detection of metastatic spread to lymph nodes. However, image distortions arising from the use of EPI has shown to be problematic. In this work we explore the use of Readout-Segmented (RS)-EPI, a technique with reduced distortion compared to EPI, for imaging the abdomen.

Breath-hold single-shot (ss)-EPI and ss-RS-EPI DW images were acquired on an adult volunteer using a 3T whole-body system using an 8-channel cardiac-array coil. Both sequences used a matrix size of 192 x 192, FOV = 34cm and an equivalent scan time. The figure shows a comparison between the b = 0 s/mm2 and isotropic b = 500 s/mm2 EPI and RS-EPI images. At an equivalent matrix size and scan time, RS-EPI appears sharper and less distorted. By using RS-EPI over EPI, the distortion was reduced by 50% at the expense of a lower SNR.

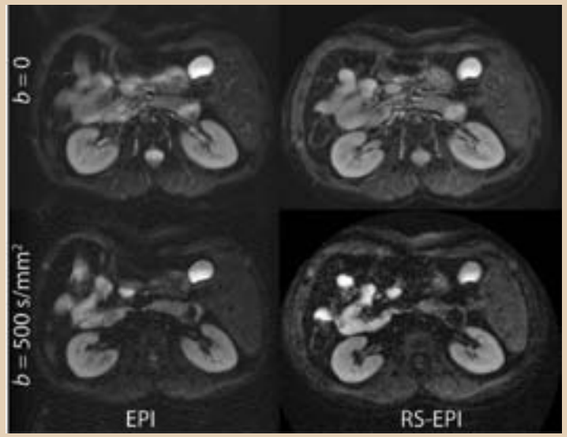

Comparison between ss-EPI and ss-RS-EPI DWI 30sec breath-hold images on a volunteer acquired at 3T.

This work shows that RS-EPI can be useful for DWI of the abdomen by reducing geometric distortion and blurring. Disadvantages of RS-EPI are the increased scan time compared with EPI as well as the increased risk of phase-artifacts that can occur between blinds. Further experiments will explore these effects under free-breathing and respiratory triggering.

References/Funding Source NIH (1R01 EB008706, 1R01 EB008706S1, 5R01 EB002711, 1R01 EB006526, 1R21 EB006860), the Center of Advanced MR Technology at Stanford (P41RR09784), Lucas Foundation, Oak Foundation, and the Swedish Research Council (K2007-53P-20322-01-4). SJ Holdsworth, S Skare, S Vasanawala, R Bammer, "Diffusion-Weighted Imaging of the Abdomen with Readout-Segmented (RS)-EPI" In: 18th Annual Meeting of the ISMRM. Stockholm, Sweden, #2647, 2010

Blood-Brain Barrier Permeability Measured by DCE MRI Predicts Perihematomal Edema Diffusivity

DB Aksoy[1], R Bammer[2], M Mlynash[1], SN Gupta[3], RW Snider[1], I Eyngorn[1], C Venkatasubramanian[1], N Fischbein[2], CA Wijman[1]
Departments of [1]Neurology and Neurological Sciences, [2]Radiology, Stanford University, CA; [3]GE Global Research Center, Niskayuna, NY

Introduction: Spontaneous intracerebral hemorrhage (ICH) is one of the deadliest forms of stroke. Secondary brain injury and edema formation contribute to high morbidity and mortality among ICH patients. B-brain barrier (BBB) disruption is potentially an important factor in the formation and progression of perihematomal edema. This study aims to quantify BBB injury by DCE MRI and to examine its relationship with perihematomal diffusivity, as a measure of vasogenic edema severity, utilizing diffusion weighted imaging (DWI).

Methods: 15 patients (60% female, 67.8±13.6 years) prospectively enrolled patients were examined using DCE MRI and DWI at approximately one week after symptom onset. All imaging was performed on a 1.5T GE Signa Excite scanner. Proton density weighted (PDW) and DCE MRI scans were used to map the native T1 times using a double-angle method. Flip angles were 5º for the PDW and 30º for the DCE MRI scans. PDW scanning was immediately followed by the DCE scans. To obtain both scans, axial spoiled gradient echo sequence were used with scan parameters as follows: TR/TE 7.8/3.4ms, slice thickness 5mm, 12 slices, FOV 220mm, matrix size 256x256, temporal resolution 14 sec/volume). Diffusion-weighted single-shot spin-echo EPI scans were performed with the following parameters: GRAPPA acceleration factor=3, b value=1000 sec/mm2, TR/TE=3000ms/60ms, slice thickness=5mm, flip angle=90º, FOV=240mm, matrix size=192x192. For DCE a 0.1 mM/kg Gd-DPTA bolus was administered. Total acquisition time for DCE MRI images was 420 seconds. An in-house written software developed in MATLAB (Mathworks, Natick, MA) was used for co-registering PDW and DCE MRI images. CINETool, an investigational pharmacokinetic analysis software (GE Healthcare, Waukesha, WI) was used for processing the DCE MRI data. Contrast agent dynamics in the brain tissue and a two-compartmental general kinetic model were used to estimate the forward leakage rate (Ktrans) at the region of interests. ROIs were placed immediately surrounding to the hematoma and control ROIs were chosen at the homologous location on the contralateral brain hemisphere. Wilcoxon signed rank test was used to analyze the forward leakage rates. Apparent diffusion coefficient (ADC) maps were co-registered with fluid attenuated inversion recovery (FLAIR) images using MIPAV software. The rim surrounding the hematoma was outlined on FLAIR images and mean ADC values for these ROIs were calculated. Correlation between ADC values and BBB permeability values was estimated using Spearman Rank test.

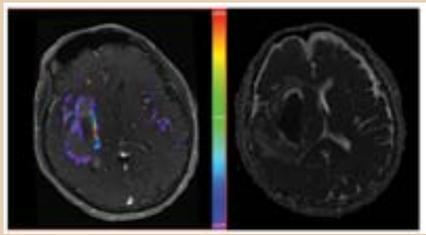

Color coded permeability (left) and ADC (right) maps of a patient. Increased permeability surrounding the hematoma and increased diffusivity are clearly visible.

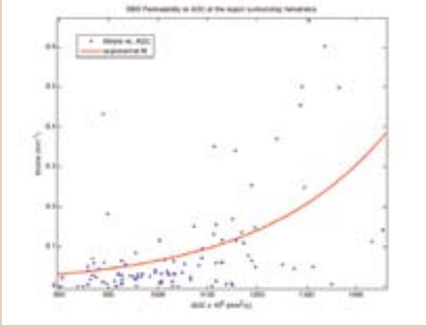

Correlation between BBB permeability and diffusivity in the region surrounding the hematoma is shown. Increased BBB injury is associated with high ADC values.

Results: Increased BBB permeability was observed at the region immediately surrounding the hematoma at one week after symptom onset. Forward leakage rate at the rim was 0.037min-1 (0.017-0.090) compared to 0min-1 (0-0) at the control ROI (Figure 1). ADC values in the region surrounding the rim were found to be 1021 (926-1142) x 10-6 mm2/sec. ADC values measured at one week after symptom onset highly correlated with BBB permeability at the ROI (R=0.50, p<0.0001)(Figure 2). Mean ADC values for each patient were also correlated with mean BBB leakage rate measured for each patient (R=0.74, p=0.041).

Discussion and Conclusion: In this study, we showed that BBB permeability assessed by DCE MRI correlates with ADC values in the region surrounding the hematoma at one week after symptom onset. Our findings suggest a strong relationship between BBB injury and severity of the vasogenic edema. A potential explanation would be a common injury process causing both BBB disruption and vasogenic edema. DCE MRI and DWI might be used as surrogate markers of BBB injury and edema formation and evolution in spontaneous intracerebral hemorrhage.

References/Funding Source NIH ROI NS034866-08 (Wijman), 2R01EB002711 (Bammer), 1R21EB006860 (Bammer) and the Neurocritical Care Society Career Development Fellowship in Cerebrovascular Disease and Neurotrauma (Venkatasubramanian).

Improving DSC-MRI by Orientation-corrected Phase-based AIF and VOF

M Straka[1], RD Newbould[2], GW Albers[3], R Bammer[1]
Department of [1]Radiology, [3]Stroke Center, Stanford University, CA; [2]GlaxoSmithKline, London, UK

Quantitative DSC-MRI perfusion imaging requires signal values that can be accurately converted to tracer concentration values but measuring vascular concentration (e.g. arterial input function AIF) remains challenging. Susceptibility agents induce a change in the resonance frequency that is linear with the tracer concentration and does not depend on T_1. This change in frequency can be assessed by change in MR signal phase and could potentially deliver better estimates of tracer concentration. The observable phase effect depends however on the orientation of the vessels relative B_0 (Eq. 1) and information about vessel orientation is thus warranted. To avoid extra cumbersome measurements we propose to estimate the vessel orientation from the magnitude data of the dynamic EPI scan itself.

Intravascular concentration of paramagnetic tracer can be estimated using equation below, where θ is the tilt angle of the vessel relative to B_0, t_{TE} is the echo time, $\Delta\varphi$ is the tracer-induced change of phase relative to the background phase, ρ is molar susceptibility of gadolinium (ρ = 0.026 ppm/mM in cgs units), and k is a currently unknown scaling factor (empirically determined k = 0.02). To estimateθ, so called tubular-filtering was employed.

$$c_v = k \frac{\Delta\varphi}{\rho \gamma_0 |E| \left| \cos^2\theta - \frac{1}{3} \right| t_{TE}}$$

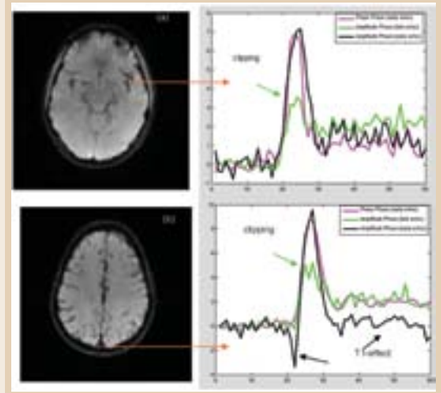

Vessel oriented perpendicular to B_0 (e.g. AIF in MCA) and (b) parallel to B0 (e.g. VOF in SSS). The plots show estimated concentration during bolus passage using phase-signal from early echo (purple), and magnitude signals from late echo (green) and early echo (black).

Figure shows vascular gadolinium concentration values that were obtained either from phase (first echo) or magnitude data (first and third echo). Moreover, the T_1-dependency of short-TE magnitude data at early bolus arrival can be clearly seen.

A new method for improving the estimation of vascular Gd concentration has been proposed. Major advantages of the phase-based approach are its immunity to log-Ricean transformed noise (present in perfusion signals when computed in magnitude data) and immunity to T1-artifacts as well as linearity of signal with respect to Gd concentration.

References/Funding Source NIH (1R01EB008706, 1R01EB008706S1, 5R01EB002711, 1R01EB006526, 1R21EB006860, 2R01NS039325-04A2), Center of Advanced MR Technology at Stanford (P41RR09784), Lucas Foundation, Oak Foundation and an anonymous philanthropist. Presented at the Conference of International Society for Magnetic Resonance in Medicine, Stockholm, Sweden (May 1-7, 2010).

Is Reduced CBV a Reliable Surrogate Marker for Infarct Core and Can It Be Used to Identify Lesion Mismatch?

M Straka[1], MG Lansberg[2], S Christensen[3], M Mlynash[2], DA De Silva[5], J-M Olivot[2], BC Campbell[4], GA Donnan[6], SM Davis[4], GW Albers[2], R Bammer[1], on behalf of the DEFUSE-EPITHET Investigators
Departments of [1]Radiology, [2]Stroke Center, Stanford University, CA; [3]Radiology, [4]Neurology, Royal Melbourne Hospital, University of Melbourne, Australia; [5]Natl Neuroscience Inst, Singapore General Hosp campus, Singapore; [6]Florey Neuroscience Institutes, Melbourne, Australia

Perfusion CT imaging in acute stroke lacks a clear marker for early identification of the ischemic core. Previous studies have suggested that CBV_{CT} correlates well with DWI, however these studies were limited by spatial coverage and time differences between CT and MRI. To assess whether CBV is an accurate surrogate for the ischemic core, we analyzed: 1) the relationship between CBV_{MR} and DWI lesion volumes, and 2) the agreement between Tmax/CBV_{MR} with Tmax/DWI for classification of mismatch.

133 cases with sufficient quality baseline DWI and PWI data from the DEFUSE-EPITHET pooled database were analyzed. The stroke core was identified by automated software using an absolute ADC threshold. The CBV lesions were manually outlined on relative CBV_{MR} maps guided by regions that were hyperintense on DWI. Critically hypoperfused tissue was defined as the PWI lesion with a Tmax > 6s. Ischemic core was defined by the DWI or CBV_{MR} volume. Mismatch was defined as PWI (Tmax >6s)/core ≥1.2 and an absolute mismatch volume ≥10ml.

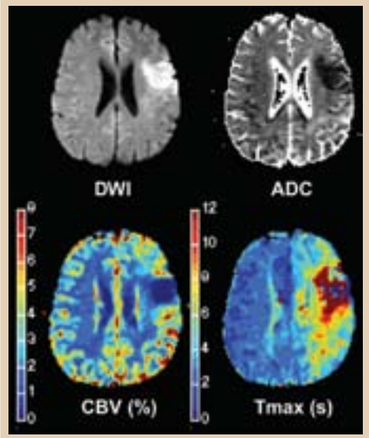

Acute-stroke case with core matched on DWI, ADC and CBV maps.

Correlation between CBV_{MR} and DWI lesion volumes among all cases was excellent (r^2=0.89; regression line CBV = 1.04*DWI – 2.26). However, in the subgroup of small lesions (DWI <= 10ml) the correlation was poor (r2=0.20). All correlations were statistically significant (p < 0.001). Using the PWI/DWI mismatch pattern as reference, the sensitivity of the Tmax/CBV_{MR} approach was 0.98 and specificity was 0.76. The Tmax/CBV_{MR} mismatch resulted in 90 true positive, 31 true negative, 10 false positive and 2 false negative results. In the majority of the discordant cases, the CBV_{MR} lesion was smaller than the DWI lesion.

The findings imply that DWI is superior to CBV_{MR} for detecting the early ischemic core even under optimized perfusion imaging circumstances.

References/Funding Source NIH (1R01EB008706, 1R01EB008706S1, 5R01EB002711, 1R01EB006526, 1R21EB006860, 2R01NS039325-04A2), Center of Advanced MR Technology at Stanford (P41RR09784), Lucas Foundation, Oak Foundation and an anonymous philanthropist. Presented at the International Stroke Conference in San Antonio, Texas, USA (Feb 23-26, 2010).

Remembering to Attend: Separating Attention and Memory Signals in Posterior Parietal Cortex

MR Uncapher[1], S DuBrow[1], JB Hutchinson[1], AD Wagner[1,2]
[1]Dept of Psychology and [2]Neurosciences Program, Stanford University, CA

While attention and declarative memory dynamically interact, the nature of these interactions remains underspecified. Recent proposals suggest that the consistent observation of functional activation in posterior parietal cortex (PPC) during episodic retrieval may reflect the engagement of attention mechanisms. However, a central tenet of these proposals is currently under debate; namely, whether separate attention and memory mechanisms exist in PPC, or whether PPC attention mechanisms are engaged in service of retrieval (by setting the stage for and then acting on the contents of memory during retrieval). To test these competing hypotheses, the present fMRI study incorporated an attentional orienting manipulation into a memory retrieval paradigm. Volunteers were scanned while being cued to orient attention to locations within trial-unique scenes in which trial-unique objects had been studied. To separate memory and attention effects in PPC, memory-based expectations (about object-scene and/or object-location associations) were either met or violated. We predicted functional heterogeneity in PPC, such that (1) dorsal PPC would exhibit top-down attentional orienting effects (when cues to shift spatial attention appeared), (2) temporoparietal junction would exhibit reflexive attentional reorienting effects (when expectations were violated), and (3) angular gyrus would exhibit memory recollection effects (when associative information was successfully retrieved). BOLD data revealed all three patterns, indicating that dorsal and ventral PPC attention mechanisms do not fully account for parietal activation during episodic retrieval. Rather, additional PPC mechanisms appear to be specifically engaged when retrieving associative information from memory. These findings add to an emerging literature indicating high functional heterogeneity within PPC.

References/Funding Source NIMH [5R01–MH080309 and F32–MH084475]

Resting-state fMRI is a Reliable Procedure for Mapping the Development of Neural Networks

ME Thomason [1,2], EL Dennis [1,2], AA Joshi [2,3], SH Joshi [2,3], ID Dinov [2,3], C Chang[4], ML Henry[1], RF Johnson[1], PM Thompson [2,3], AW Toga [2,3], GH Glover[4], IH Gotlib[1]
Departments of [1]Psychology, [4]Radiology, Stanford University, CA; [2]Laboratory of Neuro Imaging (LONI), Neurology, David Geffen School of Medicine, [3]Center for Computational Biology at UCLA, CA

Resting-state fMRI (rs-fMRI) is emerging as a powerful procedure for studying whole brain neural connectivity. In this study, we provide the first empirical evidence of the longitudinal reliability of rs-fMRI in children. We compared rest-retest measurements across spatial, temporal, and frequency domains for each of six intrinsic connectivity networks (ICNs) (cognitive and sensorimotor networks) both within and between scan sessions. Using Kendall's W, concordance in spatial maps ranged from .55 to .86 across networks and comparisons. R scores for temporal coherence between networks ranged from .36 between sessions to .66 within session. Finally, there were no differences across measurements in low-frequency power of the ICNs. These reliable measurements across multiple domains (spatial, temporal, and frequency) for resting state data in children indicate that these measures are reliable and useful for assessing the development of large-scale brain networks. The implications of these findings for task-free ICN studies in development are discussed.

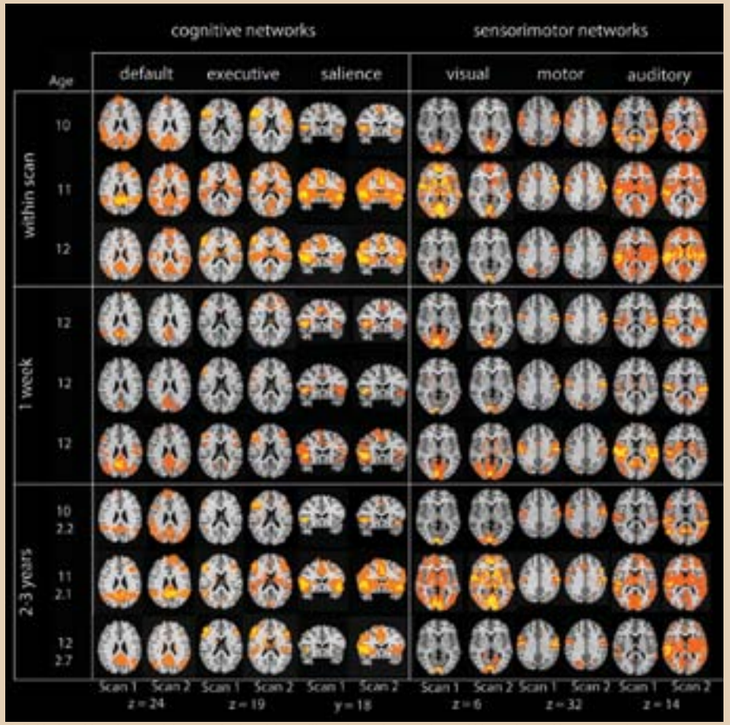

Individual seed-based connectivity maps for 6 participants illustrating each comparison (within-session, and between-session). Greater uniformity of connectivity maps is evident within participants (rows) as opposed to across participants (columns).

References/Funding Source National Institute of Health [MH081583 to MET, F31-AG032168 to CC, P41-RR009874 to GHG, MH074849 to IHG, U54-RR021813 and P41-RR013642 to AWT], National Science Foundation [0716055 and 0442992 to IDD], and by a NARSAD Young Investigator Award to MET. ME Thomason, EL Dennis, AA Joshi, SH Joshi, ID Dinov, C Chang, ML Henry, RF Johnson, PM Thompson , AW Toga, GH Glover, IH Gotlib. Resting-state fMRI is a reliable procedure for mapping the development of neural networks. Submitted

Steady-State Free Precession (SSFP) Diffusion Imaging Using 3D Rotating Spirals (3DRS)

J Zhang[1,2], C Liu[1], ME Moseley[1]
Departments of [1]Radiology and [2]Electrical Engineering, Stanford University, CA

Although signal in SSFP-DWI is composed of both spin echo and multiple stimulated echoes, experiments have shown that motion induced artifacts in SSFP-DWI can still be reduced by correcting navigated phase errors or averaging multiple DWI scans. In this work, we will present a SSFP 3D rotating spiral (3DRS) method for fast DWI and diffusion tensor imaging (DTI) acquisition, which is based on our previously reported 3D-SNAILS technique [1]. By combining SSFP-DWI and 3DRS readouts in this approach, high quality diffusion weighted volumes can be rapidly acquired with very high SNR efficiency and low sensitivity to motion artifacts. One key result of the proposed auto-calibrated kSPA algorithm is that the reconstruction kernel can be computed using calibration data acquired at any location. To accomplish that we only need to translate the surrounding sampling points to center at a set of grid points in the middle of the calibration region. We then repeat the reconstruction for each coil to form the final image similar to the GRAPPA algorithm.

In this work, we have demonstrated the acquisition of diffusion-weighted whole brain volumes using a SSFP-3DRS sequence. Compared with other diffusion techniques, our approach can achieve much higher SNR with desired diffusion weighting and limited imaging time. The 3DRS sampling strategy also benefits from reduced sensitivity of subject motion. However, since only the 0th order phase error term can be extracted and corrected, images may still be contaminated by residual motion artifacts, especially for high b-values. A proper 3D navigator should help further improve the image quality, which is still under investigation. Furthermore, with its high SNR efficiency, SSFP-3DRS can be feasibly applied to acquire DTI volumes under even higher resolution, which is usually desirable for tractography.

References/Funding Source NIH-1K99NS057943, Lucas Foundation, and NCRR P41RR09784. J Zhang, C Liu, ME Moseley. Steady-State Free Precession (SSFP) Diffusion Imaging Using 3D Rotating Spirals (3DRS). Proceedings of the ISMRM, 2009, Honolulu Hawaii.

High-Resolution, Fat-Suppressed, Diffusion-Weighted MRI Of The Breast Using A Self-Navigated Multi-Shot Technique

WB Veldhuis, C Liu, R Bammer, BL Daniel, ME Moseley
Departments of Radiology, Stanford University, CA

For breast MRI, with increasing resolution the readout time for conventional single-shot MR lengthens to the point that blurring and geometric distortions impair image acquisition. The strong gradients needed for diffusion-weighting (DW) worsen this problem. Parallel imaging can partially reduce these distortions, which was recently shown for breast MRI, using ASSET. Another approach is to use a multishot technique, such as SNAILS: a fat-saturated twice-refocused spin echo sequence with an analytically designed interleaved variable-density spiral readout trajectory, which has been applied successfully to high-resolution DWI in the brain. We assess its technical feasibility in the body, for breast MRI, and compare it to ASSET-DW-EPI in healthy volunteers to show ASSET-EPI and SNAILS diffusion-weighted images.

Even with ASSET, DW-EPI was not possible at a 256x256 matrix size. SNAILS allowed distortion free acquisition of 256x256 resolution images. In addition, the high resolution and relative insensitivity to motion of SNAILS, allowed for high quality multiplanar reformats with the 'PET-like' contrast-reversal now popular in DWI screening studies.

For SNAILS there was no significiant difference in ADC values measured at 256x256 or at 128x128 matrix size. For DW-EPI ADC values could not be reliably determined at 256x256 matrix size; The values obtained with DW-EPI at 128x128 resolution fall within the range of values reported in the literature, which vary mainly with varying b-value. The results suggest that with identical prescribed b-values, difference in sequence design can cause within-subject variation of ADC values. We conclude that free-breathing, high-resolution DWI of the breast using SNAILS, is feasible at clinically available gradient-strengths, within reasonable acquisition times.

References/Funding Source Lucas Foundation, NCRR P41RR09784, KWF - Dutch Cancer Society, and NIH-5K99EB007182-02. B Veldhuis, C Liu, R Bammer, BL Daniel, ME Moseley. High-Resolution, Fat-Suppressed, Diffusion-Weighted MRI Of The Breast Using A Self-Navigated Multi-Shot Technique. Proceedings of the ISMRM, 2009, Honolulu Hawaii.

Benign-Malignant Lesion Differentiation Using Functional ADC-Thresholding – Allowing Expert Radiologist Interpretation – Versus Conventional Thresholding Based On ADC Cut-Off Values

WB Veldhuis, C Liu, Y Do, TJ Brosnan, ME Moseley, BL Daniel
Department of Radiology, Stanford University, CA

Diffusion-weighted imaging (DWI) may aid in the discrimination of benign from malignant (breast) lesions. Approaches to benefit from the information contained in the DWI dataset have mostly been based on trying to define a cut-off value for the lesion ADC. This may be limiting because of the relatively low SNR, the relatively high variability of lesion ADC - even within one hospital or patient population - and the limited potential of the results to be extrapolated to different field strengths, pulse-sequences or b-values. We used an approach in which the high CNR of DWI and the quantitative information of the ADC are presented to the radiologist in a "functionally-thresholded ADC (ftADC) map" that increases the conspicuity of lesions of interest, much like phase-images are used to increase vascular conspicuity in susceptibility-weighted imaging. Radiologists can "window-level" ftADC-maps at their discretion and diagnose a lesion as "ftADC-bright" without having to choose an ADC-threshold value; Similar to, for example, a cystic lesion being interpreted as "T2-bright" without using T2-cut-off values. We performed a retrospective, HIPAA-compliant, IRB-approved analysis of DW data sets of 103 consecutive women who underwent 1.5T MRI for the evaluation of breast cancer. Conventional ADC-thresholding was compared to ftADC-mapping and to dynamic contrast-enhanced (DCE) MRI, for all pathology-verified lesions.

The results confirm that lower ADCs are correlated with a higher chance of a malignant diagnosis, but that the discriminatory power of setting an ADC cut-off value – evaluated using ROC curves – is low. In addition, attempts to reduce variability by within-patient normalization of lesion ADC to muscle ADC are shown to be unsuccessful. ftADC-mapping may improve lesion discrimination in (breast) MRI. In theory, after large-scale validation of the results, a significant number of patients could be downstaged from BIRADS-3 and possibly even from BIRADS-4, to a benign diagnosis, and thus be spared a biopsy.

References/Funding Source Lucas Foundation, NCRR P41RR09784, KWF - Dutch Cancer Society, and NIH-5K99EB007182-02. WB Veldhuis, C Liu, Y Do, TJ Brosnan, ME Moseley, BL Daniel. Benign-Malignant Lesion Differentiation Using Functional ADC-Thresholding – Allowing Expert Radiologist Interpretation – Versus Conventional Thresholding Based On ADC Cut-Off Values. Proceedings of the ISMRM, 2009, Honolulu, Hawaii.

Diffusion Tensor Imaging Finds Different Patterns of Associations Between White Matter Microstructure, Age and Language Skills in Preterm and Full-term Children

ES Lee[1], JD Yeatman[2], R Bammer[3], HM Feldman[1]
Departments of [1]Pediatrics, [2]Psychology and [3]Radiology, Stanford University, CA

Background: Children born preterm have lower IQ and weaknesses in language and reading compared to full-term peers. White matter injury to periventricular regions is thought to be the major cause of these cognitive problems. In typically developing children, white matter matures from childhood to adolescence.

Objective: To contrast white matter microstructure in children born preterm and full term controls in relation to age, IQ, language and reading scores.

Methods: Preterms (n=19, mean age 11.9 yr) and controls (n=15, mean age = 13.4 yr) were assessed on the following: IQ (Wechsler Abbreviated Scales of Intelligence), linguistic processing speed (Test for Reception of Grammar – Revised), verbal memory (Clinical Evaluation of Language Fundamentals – 4th Edition), and reading decoding and passage comprehension (Woodcock-Johnson Tests of Achievement – 3rd Edition). Four DTI acquisitions of 60, 2mm-thick slices were collected in 30 different diffusion directions (b = 900). DTI data were pre-processed with FSL Diffusion Toolbox. Tract-Based Spatial Statistics based on fractional anisotropy (FA) defined the centers of major white matter tracts throughout the brain. We evaluated group differences in the FA of these tracts and also ran correlations with age, scores, and FA. After correcting for multiple comparisons, we set $p < .05$.

Results: Age was correlated with FA in controls $p < .05$, but not in preterms. The regions of significant differences included the corpus callosum (CC), superior longitudinal fasciculus (SLF), and inferior frontal occipital fasciculus (IFO). Preterms and controls did not differ in FA. A comparison of preterms with IQ < 100 (n=8), preterms with IQ > 100 (n=11) and controls showed significant differences after covarying for age, $F = 4.97$, $p < .01$. Correlations of FA with verbal memory, vocabulary, and decoding in preterms approached significance $p < .06$ but not in controls. The regions of significant differences in verbal memory and vocabulary included the IFO. Regions of differences in decoding also included the SLF and CC.

Discussion: High functioning preterm children appear to have normal white matter microstructure. Perinatal white matter injury in low functioning preterm children affects brain structure and function into adolescence. White matter microstructure did not explain individual differences in function in controls.

References/Funding Source Accepted for presentation at Society for Neuroscience Annual meeting, Nov 15, 2010, San Diego CA

An fMRI Investigation of Individual Differences in Auditory Sentence Comprehension in Adolescent Children Born Prematurely

LHF Barde[1], JD. Yeatman[2], ES. Lee[1], GH Glover[2], HM Feldman[1]
Departments of [1]Pediatrics and [2]Psychology, Stanford University, CA

Despite evidence that premature birth has long-range adverse outcomes on functional language ability, the dynamic properties of the neural network for sentence comprehension have not been previously well characterized in this population. This study used event-related fMRI to explore the effects of prematurity on auditory sentence comprehension. Twelve adolescents between the ages of 9-14 years (8 male, mean gestational age = 28.6 weeks) performed a cross-modal sentence-picture verification task where sentence length and difficulty were manipulated in a 2 x 2 factorial design. Participants had general cognitive (WASI), vocabulary (PPVT-III), and language skill (CELF) scores in the normal range (mean scores: 114.3, 122.2, and 103.8, respectively). Preliminary analyses of the imaging data found task related activation in superior temporal cortex bilaterally. Moreover, changes in activation in both regions covaried with individual participant's vocabulary and language skill. Similarly, increased sentence length and difficulty were associated with activations in bilateral temporal cortex. Thus, individual differences in vocabulary and language skill were associated with changes in activation of the neural network for auditory sentence comprehension in response to changing task demands. Interestingly, the neural activations in this group of preterm born adolescents was less extensive than found in a group of full-term born adolescents (Yeatman, Ben-Shachar, Glover, & Feldman, 2010). Subtle white matter injury in children born prematurely may change patterns of activation in response to task difficulty.

References/Funding Source Accepted for presentation at Society for Neuroscience Annual meeting, Monday Nov 15, 2010 1:00 PM - 5:00 PM San Diego CA

Expected Value Information Improves Financial Risk Taking Across the Adult Life Span

GR Samanez-Larkin, AD Wagner, B Knutson
Departments of Psychology, Stanford University, CA

When making decisions, individuals must often compensate for cognitive limitations, particularly in the face of advanced age. Recent findings suggest that age-related variability in striatal activity may increase financial risk-taking mistakes in older adults. In two studies, we sought to further characterize neural contributions to optimal financial risk taking and to determine whether decision aids could improve financial risk taking. In Study 1, neuroimaging analyses revealed that individuals whose mesolimbic activation correlated with the expected value estimates of a rational actor made more optimal financial decisions. In Study 2, presentation of expected value information improved decision making in both younger and older adults, but the addition of a distracting secondary task had little impact on decision quality. Remarkably, provision of expected value information improved the performance of older adults to match that of younger adults at baseline. These findings are consistent with the notion that mesolimbic circuits play a critical role in optimal choice, and imply that providing simplified information about expected value may improve financial risk taking across the adult life span.

References/Funding Source Financial Industry Regulatory Authority Investor Education Foundation and US National Institute on Aging grants AG030778, AG024957 and AG017253. G.R.S.L. was supported by National Institute on Aging fellowship AG032804 and A.D.W. was supported by National Institute of Mental Health grant MH080309. GR Samanez-Larkin, AD Wagner, B Knutson. (in press) Expected value information improves financial risk taking across the adult life span. Social Cognitive and Affective Neuroscience.

Core White Matter Characteristics Related to Behavioral Problems in 9-16 Year Old Preterm and Full-term Children

[1]ES Lee, [1]IM Loe, [2]R Bammer, [1]HM Feldman
Departments of [1]Pediatrics and [2]Radiology, Stanford University, CA

Purpose:Preterm children have more behavior problems, including inattention and anxiety symptoms, than full-term peers. To date, the only study on behavior, white matter (WM) microstructure, and prematurity found areas of abnormal WM, e.g. internal and external capsules and long fascicles, in 15-year-old preterms were related to inattention, social deficits, and overall mental health, but not specifically to anxiety or hyperactivity (Skranes et al., 2007). Methods:Preterms (n=19, mean age 11.9 yr) and full-term controls (n=15, mean age 13.4 yr) were assessed on the CBCL, a standardized behavior rating scale. Outcomes were t scores for anxiety (Anx), social (Soc), attention (Att), and Externalizing (EXT, rule-breaking and aggressive behavior) problems. DTI data were pre-processed with FSL Diffusion Toolbox. Tract-Based Spatial Statistics, based on fractional anisotropy (FA), defined the centers of major WM tracts throughout the brain. We evaluated correlations between FA of tract centers and behavior symptom scores. We set $p<.05$ after correction for multiple comparisons. Results:Preterm and control groups did not differ in FA in the centers of major WM tracts; however, behavior scores correlated with FA. More Anx ($p<.01$), Att ($p<.01$), EXT ($p<.05$), and Soc ($p<.07$) problems were associated with lower core FA in multiple tracts. Tracts correlated with Anx included corpus callosum (CC), left (L) superior longitudinal fasciculus (SLF), inferior fronto-occipital fasciculus (IFO), inferior longitudinal fasciculus (ILF), posterior limb of internal capsule (PLIC), right (R) external capsule (EC), cingulum (CNG), corona radiata (CR), and cerebral peduncle (CP). Tracts correlated with Att overlapped in CC, L SLF, IFO, ILF, L PLIC, CNG, CR, and CP; but also included R SLF, L anterior limb of IC (ALIC), and L EC. Tracts correlated with EXT overlapped in CC, L SLF, IFO, ILF, and CR; but included L ALIC and L EC, similar to Att. Tracts correlating with Soc included CC, L SLF, L IFO, L ILF, and CR. Conclusion: Compared to a previous study, we found additional links between anxiety and externalizing problems and core WM microstructure. We replicated findings for attention and social problems even when preterms as a group had no obvious WM damage compared to full-terms. Our study found significant associations using a more conservative WM analysis method while including a wider age range of children.

References/Funding Source Accepted for Presentation at the Society for Developmental and Behavioral Pediatrics, September 12, 2010, Boston MA

White Matter Characteristics Correlate with Executive Function Skills in Preterm and Full-term Children

IM Loe[1], ES Lee[1], R Bammer[2], HM Feldman[1]
Departments of [1]Pediatrics and [2]Radiology, Stanford University, CA

Purpose:Executive function (EF) skills are an interrelated set of abilities that include working memory, organization and planning. Preterm children have difficulties with EF skills compared to full-term peers. Diffuse white matter injury in preterm children is common. Little is known about the relationship between white matter injury and EF problems in preterm children. Methods:Preterms (n=19, mean age 11.9 yr) and controls (n=15, mean age 13.4 yr) were assessed on the CANTAB, a computerized EF battery. Outcome measures for each task: Spatial Working Memory (SWM, working memory for spatial location) strategy score; Stockings of Cambridge (SOC, a complex measure of spatial planning, organization and response inhibition) problems solved in minimum moves (PS); Spatial Span (SSP, a measure of spatial memory capacity) span length (SL). Four diffusion tensor imaging (DTI) acquisitions of 60, 2mm-thick slices were collected in 30 different diffusion directions (b = 900). DTI data were pre-processed with FSL Diffusion Toolbox. Tract-Based Spatial Statistics based on fractional anisotropy (FA) defined the centers of major white matter tracts throughout the brain. We evaluated correlations between FA of these tracts and EF skills, covarying by age. We set $p<.05$ after correcting for multiple comparisons. Results: Preterm and control groups did not differ in FA; however, EF skills were correlated with FA. SWM strategy was negatively correlated with FA; better strategy was associated with higher FA, $p<.01$. Regions of significant correlation include corpus callosum (CC), bilateral (B) superior longitudinal fasciculus (SLF), and B inferior fronto-occipital fasciculus (IFOF). SOC PS was positively correlated with FA; better overall performance on a complex EF task was associated with higher FA, $p<.05$. Significant regions include CC, B SLF, and B IFOF. SSP SL showed a trend for positive correlation with FA, $p<.09$. Conclusion: Preterm and full term children show significant associations between EF skills and white matter microstructure in multiple brain regions. These regions include long tracts which run from posterior temporal and occipital regions to frontal regions implicated in EF. Though preterm children as a group did not have obvious white matter damage compared to full-term controls, a measure of white matter microstructure was sensitive to individual differences in EF in children and adolescents.

References/Funding Source Accepted for Presentation at the Society for Developmental and Behavioral Pediatrics, September 12, 2010 Boston MA

Variability in Nucleus Accumbens Activity Mediates Age-related Suboptimal Financial Risk Taking

GR Samanez-Larkin[1], CM Kuhnen[2], DJ Yoo[1], B Knutson[1]
Departments of [1]Psychology, Stanford University, CA; [2]Kellogg School of Management, Northwestern University

As human life expectancy continues to rise, financial decisions of aging investors may have an increasing impact on the global economy. In this study, we examined age differences in financial decisions across the adult life span by combining functional neuroimaging with a dynamic financial investment task. During the task, older adults made more suboptimal choices than younger adults when choosing risky assets. This age-related effect was mediated by a neural measure of temporal variability in nucleus accumbens activity. These findings reveal a novel neural mechanism by which aging may disrupt rational financial choice.

References/Funding Source National Institute on Aging Grant AG030778, the Financial Industry Regulatory Authority Investor Education Foundation, and Center on Advancing Decision Making in Aging Grant AG024957. G.R.S.-L. is supported by National Institute on Aging Award AG032804. GR Samanez-Larkin, CM Kuhnen, DJ Yoo, B Knutson. (2010) Variability in nucleus accumbens activity mediates age-related suboptimal financial risk taking. Journal of Neuroscience, 30(4), 1426–1434.

Content-sensitive Novelty Encoding in the Medial Temporal Lobe: Insights from High-resolution fMRI and Distributed Pattern Analysis

J Liang[1], A Wagner[2], A Preston[1]
[1]University of Texas at Austin, Austin, TX; [2]Stanford University, Stanford, CA

The ability to distinguish between novel and familiar stimuli plays a critical role in orienting toward behaviorally salient and rewarding events. Current theories of medial temporal lobe (MTL) function propose that distinct MTL regions may differ in their sensitivity to novelty based on information content. For example, the anatomical projections between sensory processing regions and perirhinal and parahippocampal cortices suggest that these regions are sensitive to visual object and visuospatial content respectively. However, the representation of different stimulus content need not be modular and may instead be distributed in a graded manner both within and across subregions. To answer this question, we employed high-resolution functional MRI and an incidental novelty detection task using five stimulus classes (faces, scenes, visual words, spoken words, sounds). Univariate statistics revealed a graded distribution of face and scene novelty responses along the anterior-posterior axis of MTL cortex. Novelty responses in hippocampus were isolated to the anterior subfields and were similar across content. Additional multivoxel pattern analyses revealed that despite overall sensitivity to specific content, MTL cortical regions maintained an ability to classify information of non-preferred content. In contrast, hippocampal subfields DG/CA3 and CA1 failed to accurately discriminate between different content types, though subiculum demonstrated significant classification accuracy for faces and scenes. Together, these findings support a graded distribution of content-sensitive novelty responding along the anterior-posterior axis of MTL cortex and provide evidence for content-general novelty encoding in the hippocampus.

References/Funding Source Presented at Cognitive Neuroscience Society 2010

Learning Exceptions to the Rule: High-Resolution fMRI of Hippocampal Subfield Contributions to Category Learning

T Davis, BC Love, AR Preston
University of Texas at Austin, Austin, TX

The medial temporal lobe (MTL) and its connections with midbrain, prefrontal cortex (PFC), and striatum have been implicated in different forms of novelty processing. In the present study, we examine a unique novelty detection task where subjects learn categories containing items that violate a salient regularity. These "exceptions to the rule" are novel in the context of their categories because they share critical features with an opposing category, and must be learned and stored separately to enable correct categorization. Previous theoretical (Love & Gureckis, 2007) and whole-brain fMRI (Davis, Love, & Preston, submitted) research suggests that the hippocampus is engaged during exception learning and is modulated by midbrain, PFC, and striatum. The current study employs high-resolution fMRI techniques to investigate the role of hippocampal subfields in exception learning. High-resolution methods extend our previous whole-brain results by allowing us to dissociate the function of individual hippocampal subfields and MTL cortical regions. Within the MTL, our results reveal that CA1 and a combined region of CA2,3 and dentate gyrus are recruited during categorization of exception items as well as in response to categorization errors. Such findings are consistent with theories suggesting that the hippocampal circuit acts as a comparator to evaluate incoming information by comparing it with previously stored representations and forming new representations in response to prediction error. Specifically, we suggest that the CA fields and dentate gyrus are recruited both to encode new representations when exceptions are first encountered and to retrieve these representations when needed for accurate exception performance.

Detection of Sequence Violations in the Medial Temporal Lobe: Subregional Contributions to Memory-based Prediction Through High-resolution fMRI

JC Liang, D Zeithamova, AR Preston
University of Texas at Austin, Austin, TX

Current research proposes that medial temporal lobe (MTL) subregions perform distinct computations to enable comparison between past and present experience. Hippocampus is thought to play a unique role in the detection of sequence novelty, wherein associated items appear in a new order. However, it is unclear how hippocampal subregions and surrounding MTL cortex differentially contribute to novelty detection, and whether content-sensitive networks are differentially engaged when novelty is restricted to a certain class of content. Here, we used high-resolution fMRI to measure MTL responses to temporal sequence violations while subjects performed an incidental 1-back detection task. Trials consisted of two consecutive sequence presentations. In the first, participants observed a sequence of four object-scene pairs. In the second presentation, the same set of object-scene pairs were presented again in one of six conditions. In the repeated condition, the initial sequence was repeated in the same order. In the half condition (H), the order of the third and fourth object-scene pairs was switched. In the object-half (OH) condition, the order of objects in the third and fourth pair was switched. In the scene-half (SH) condition, the order of scenes was switched. In the novel (N) condition, the order of all four objects and scenes was scrambled. Finally, a familiar condition consisted of pre-exposed sequences seen repeatedly throughout the experiment. By comparing activation during the half conditions with novel sequences, we isolated responses that reflect novelty responses cued by a violation of expectation based on temporal order (a mismatch) from novelty responses that reflect novel associations per se. Furthermore, comparison of OH, SH, and novel sequences sought to reveal MTL regions that signal content-based mismatch responding. Preliminary analyses identified distinct populations of voxels that were sensitive to violations of object order (OH > N) and violations of scene order (SH > N) as well as voxels that were sensitive to violations based solely on overall temporal order (H > N). These associative mismatch responses were primarily restricted to hippocampal subfields. By contrast, MTL cortical regions showed sensitivity to novelty that was predominantly related to the amount of previous exposure when comparing novel to highly familiar sequences. These results expand on previous findings to suggest that hippocampal responses to associative novelty can be distinguished by the class of content being violated, and that MTL cortical regions show sensitivity to the familiarity status of stimulus configurations based on the amount of exposure.

References/Funding Source To be presented at Society for Neuroscience 2010

Motivation During Associative Encoding Influences Subsequent Recall Responses in Medial Temporal Subregions

SM Wolosin, D Zeithamova, AR Preston
University of Texas at Austin, TX

Emerging evidence suggests that hippocampal memory processing is modulated by reward, resulting in enhanced encoding of episodic information—long-term memory for events. Current theories further propose that memory processing in hippocampal subregions may be differentially influenced by reward. While previous research has examined reward influences on episodic encoding, no study to date has examined how motivation during encoding influences hippocampal responses at retrieval. Using high-resolution functional magnetic resonance imaging (fMRI), the present study investigated the function of medial temporal lobe (MTL) subregions, including hippocampal subfields, midbrain, and nucleus accumbens during cued recall of associations learned under varying conditions of reward. During encoding, high-value or low-value monetary cues preceded object pairs indicating potential reward for successful retrieval of the associations. At retrieval, participants were presented with a cue object (a single object from a studied pair) and were asked to recall and imagine the associated object during a delay period. At the end of the trial, participants viewed a probe object and judged whether the probe was the correct object (a "match") or another object viewed at encoding, but as part of a different pair (a "mismatch"). Behaviorally, cued recall performance was superior for high-value compared to low-value pairs. fMRI analysis revealed regions in hippocampus, including dentate gyrus/CA2,3, CA1, and subiculum, as well as parahippocampal cortex and nucleus accumbens that demonstrated greater cue and delay period activation for high-value compared to low-value associations. Importantly, such reward-based modulation of cue and delay period activation was observed in the absence of explicit reward cues. Of these regions, left CA1 uniquely showed an interaction between reward status and retrieval based success effects where activation differed for correct and incorrect trials only for high-value associations. At probe, several MTL regions demonstrated match responses with greater activation for correct match probes relative to correct mismatch probes. In these probe-sensitive regions, match effects in left CA1 and left dentate gyrus/CA2,3 were limited to high-value trials. Together these findings suggest that motivation during encoding affects subsequent associative retrieval processing in MTL subregions, and highlight that within the hippocampus CA1 may play an important role incorporating motivational salience into episodic retrieval processes.

Reduced Hippocampal Activity During Encoding in Cognitively Normal Adults Carrying the APOE ε4 Allele

MM Adamson[1,2], J Hutchinson[3], A Shelton[4], A Wagner[3], JL Taylor[1,2]
Departments of [1]Veterans Affairs and Sierra-Pacific MIRECC, Palo Alto, CA; [2]Psychiatry and Behavioral Sciences, [3]Psychology, Stanford University, Stanford, CA; [4]Psychological and Brain Sciences, John Hopkins University, Baltimore, MD

Apolipoprotein (APOE) ε4-related differences in memory performance have been detected before age 65. The hippocampus and the surrounding medial temporal lobe (MTL) structures are the first site affected by Alzheimer's Disease (AD) and the MTL is the seat of episodic and visuospatial memory. However, reports on APOE ε4-related differences in these brain structures are not consistent in either cross-sectional or longitudinal structural and functional magnetic resonance imaging (fMRI) studies. In addition, there is increasing evidence that the brain activity at baseline (defined as the activity during fixation or rest) may be different in APOE ε4 carriers compared to non-carriers. In this fMRI study, cognitively normal APOE ε4 carriers and non-carriers engaged in a perspective-dependent learning task (Shelton and Gabrieli, 2002) previously shown to activate MTL structures in older participants (Borghesani et al., 2008). A low-level, visually engaging dot-control task was used for comparison to provide non-MTL-based activity, in addition to fixation. Consistent with the primary hypothesis, APOE ε4 carriers showed less activation than non-carriers in the hippocampus proper during encoding. Specifically, when the encoding of the two perspectives was contrasted against the dot-control task the encoding-related activation was significantly lower in carriers than non-carriers. No ε4-related differences in the hippocampus were found when encoding during the two perspective tasks was compared with fixation. Lower activation, however, was not global as the encoding-related activation was not different between APOE ε4 carriers and non-carriers in bilateral middle occipital region. The present study illustrates APOE ε4-related differences during encoding in the hippocampus proper and underscores the role of low level control contrast for complex encoding tasks. The results of this study have implications for fMRI studies that investigate the task-positive network (TPN) and default-mode network (DMN) in APOE ε4 carriers to help evaluate AD risk in the otherwise cognitively normal population.

Neural Basis Of Hypnotizability Revealed By Resting State Functional Connectivity

F Hoeft , J Gabrieli, S Whitfield-Gabrieli, B Haas, R Bammer, V Menon, D Spiegel
Department of Psychiatry and Behavioral Sciences, Stanford University, CA

Hypnotic induction and suggestion modulate activity in brain regions associated with cognitive processes being manipulated in people who are hypnotizable, but the neural mechanism of hypnotizability itself remains unknown. Here we examined intrinsic functional connectivity of cognitive networks in high and low hypnotizable individuals. High- compared to low-hypnotizable individuals showed greater co-activation between the salience and executive-control networks, two key brain networks that can be readily indentified in resting state fMRI. Critically, only highly-hypnotizable individuals recruited executive control regions, most notably the left dorsolateral prefrontal cortex (DLPFC), into the salience network, a network that includes most prominently the anterior cingulate cortex (ACC), anterior insula, amygdala and the ventral striatum. High- compared to low- hypnotizable individuals also showed greater intrinsic functional connectivity between left DLPFC and ACC. These results were found in the absence of structural (grey and white matter measures by T1 MRI voxel-based morphometry [VBM] and diffusion tensor imaging [DTI]) differences. The hypnotic experience may involve enhanced focus of attention or working memory that reduces conflict detection, enhancing engagement in cognitive and perceptual tasks. Altered functional connectivity in DLPFC and ACC may underlie hypnotizability.

References/Funding Source Nissan Research Center (D.S.), the Randolph H. Chase, M. D. Fund II (D.S.), the Jay and Rose Phillips Family Foundation (D.S.) and P41 RR09784 (P.I. Dr. Gary Glover). We sincerely thank Dr. Lisa Butler, Liz Seibert, and Emily Dennis for their invaluable work on the project.

Flow Separation Control in a Conical Diffuser with an Annular Inlet

K Lo, C Elkins, J Eaton
Department of Mechanical Engineering, Stanford University, Stanford, CA

In a combined cycle power plant, the high velocity exhaust from the power turbine has to be slowed down before reaching the steam generator. A conical diffuser is commonly used behind the turbine to slow down the flow and recover pressure. The inlet to the diffuser is an annulus due to the annular flow passage of the turbine. A large central separation bubble forms if the central hub ends abruptly because the flow is incapable of negotiating around a sharp corner. This separation causes non-uniform flow into the steam generator, and imposes fatigue loading on downstream components. Both have negative effects on the performance and the longevity of the steam generator. A long streamlined tail cone at the end of the hub can eliminate the separation, but it is often unfeasible for structural reasons. Experiments were performed in scaled flow models to investigate various means to manage both the central separation bubble and any separation on the outer diffuser walls. The Reynolds number is 66000 based on the annulus bulk velocity and hydraulic diameter. Full-field, three-component velocity data were measured in a series of diffuser models using phase contrast magnetic resonance velocimetry. The central separation bubble behind the hub extends the full length of the diffuser in the absence of any control. A Coanda jet at the end of the hub can strongly reduce or completely eliminate the central separation bubble, depending on the jet blowing ratio. However this can cause separation from the conical diffuser walls in some cases. A backward facing step in the outer diffuser wall acts to fix the location of separation making it more amenable to control. Several control mechanisms for this outer separation bubble are under investigation.

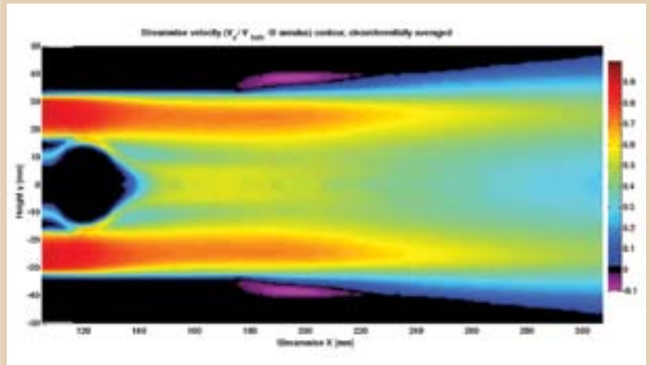

Velocity contour of the flow in a step diffuser. Flow direction is from left to right. Purple indicates reverse flow with negative velocity. A Coanda jet at a blowing ratio of 1 is attached to the end of the hub. There is no central separation bubble behind the hub, as indicated by positive velocity in that region. A backward facing step in the outer diffuser wall starts at x = 171mm. The step fixes the location of separation, which starts at the back of the step and reattaches at around x = 220mm.

Measurements of 3D Velocity and Scalar Field for a Film-cooled Airfoil Trailing Edge

M Benson, C Elkins, J Eaton
Department of Mechanical Engineering, Stanford University, Stanford, CA

Turbine blade tips commonly are cooled by venting air through slots upstream of the trailing edge. The effectiveness of this approach is governed by the rate of mixing of the coolant with the mainstream flow. Experiments were conducted for a simple airfoil with a modern trailing edge cooling geometry. The full 3D coolant concentration distribution was measured using MRI. The scans measured the concentration distribution with a spatial resolution of 0.5 mm3 and an uncertainty near 5%. Magnetic Resonance Velocimetry (MRV) was used to provide 3D, mean velocity measurements in the identical flow. The coupled concentration and velocity measurements were used to develop a qualitative picture of the flow structures contributing to the rapid mixing. Surface concentration measurements provide film cooling effectiveness data, which were compared for validation purposes with traditional thermal measurements, with substantially lower uncertainty in the MR-based measurements.

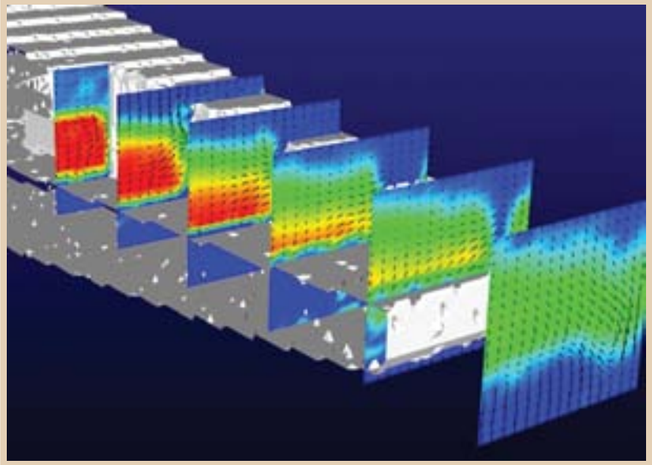

Combined Velocity and Concentration Measurements

References/Funding Source Army Research Office, General Electric. M Benson, C Elkins, P Mobley, M Alley, J Eaton. (2010). Three-dimensional concentration field measurements in a mixing layer using magnetic resonance imaging. Exp Fluids, 49(1), 43-55. M Benson, C Elkins, P Mobley, M Alley, J Eaton. (2008). Quantitative Mixing Measurements Using MRI of the D2O, H2O System. Presented at American Physical Society Division of Fluid Dynamics Meeting, San Antonio, TX, Nov 23-25. M Benson, C Elkins, J Eaton. (2010). Measurements of 3D velocity and scalar field for a film-cooled airfoil trailing edge. To be presented at American Physical Society Division of Fluid Dynamics Meeting, Long Beach, CA, Nov 21-23.

fMRI of Emotional Reactivity, Cognitive Regulation, and CBT for Social Phobia

J Gross, P Goldin
Department of Psychology, Stanford University, CA

The overall goal of this study is to elucidate the neural bases of emotional reactivity and cognitive regulation in social phobia (SP) and to identify the neural mechanisms underlying therapeutic change associated with cognitive-behavioral therapy (CBT) for SP. In this randomized clinical trial study, patients with social anxiety disorder are randomly assigned to CBT or waitlist, and are administered a battery of assessments in order to examine therapeutic change and change in brain systems related to emotion reactivity and regulation.

To date, 115 adults have entered the study, including 40 non-psychiatric healthy controls, and 75 adults diagnosed with generalized social anxiety disorder (who have been randomized to either immediate CBT or waitlist followed by CBT). 2 Group (CBT, Waitlist) x 2 Time (Pre Time 1, Post Time 2) repeated-measures ANOVAs have demonstrated a significant interaction of group by time showing that, compared to waitlist participants, CBT completers have lower social anxiety symptom severity (Liebowitz Social Anxiety Scale; $F=5.24$, $p<.05$, $eta^2=.42$) and fear of negative evaluation (BFNE; $F=5.90$, $p<.05$, $eta^2=.38$).

fMRI sessions include experiments that directly assess emotional reactivity and regulation across three different types of emotional probe stimuli. Based on data from the first 58 patients with social anxiety disorder who have completed assessments, from Time 1 (Baseline) to Time 2 (either CBT or waitlist), we are observing (a) a reduction in negative emotion reactivity to negative social self-beliefs for the CBT but not for the WL group, and (b) increased effectiveness of cognitive reappraisal of negative social self-beliefs for the CBT, but not the WL group. Brain analysis is showing increased recruitment of cognitive regulation related PFC areas and decreased activity in emotion related limbic region.

References/Funding Source R01 MH076074-01A1 Awarded to James Gross. P Goldin, T Manber-Ball, K Werner, R Heimberg, J Gross. (2009). Neural mechanisms of emotion regulation of negative self-referential beliefs in social anxiety disorder. Biological Psychiatry, 66, 1091-9. PR Goldin, S Hakimi, T Manber, T Canli, J Gross. (2009). Neural bases of social anxiety disorder: emotional reactivity and cognitive regulation during social and physical threat. Archives of General Psychiatry, 66, 170-180.

Deficits in Anterior Cingulate-Amygdalar Circuitry During Implicit Emotion Regulation in Anxiety

A Etkin[1], KE Prater[1], F Hoeft[1,2], V Menon[1,3], AF Schatzberg[1]
Departments of [1]Psychiatry and Behavioral Sciences, [2]Center for Interdisciplinary Brain Science Research, [3]Neuroscience, Stanford University, CA

Objective: Clinical data suggest that abnormalities in the regulation of emotional processing contribute to the pathophysiology of generalized anxiety disorder, yet these abnormalities remain poorly understood at the neurobiological level. We recently reported in healthy volunteers that the pregenual anterior cingulate regulates emotional conflict on a trial-by-trial basis by dampening activity in the amygdala. We also showed that this process is specific to the regulation of emotional, compared to non-emotional, conflict. Here we examined whether this form of non-instructed emotion regulation is perturbed in generalized anxiety disorder.

Methods: 17 patients and 24 healthy comparison subjects, were studied using functional magnetic resonance imaging while they performed an emotional conflict task, which involved categorizing facial affect while ignoring overlayed affect label words. We compared trial-by-trial changes in conflict regulation using behavioral and neural measures.

Results: Healthy subjects effectively regulated emotional conflict from trial-to-trial, even though they were unaware of having done so. By contrast, generalized anxiety disorder patients were completely unable to regulate emotional conflict and failed to engage the pregenual anterior cingulate in ways that would dampen amygdalar activity. Moreover, multivariate pattern classification using brain activity during conflict regulation discriminated between patients and controls with high accuracy.

Conclusions: Our data demonstrate that patients with generalized anxiety disorder show significant deficits in the non-instructed and spontaneous regulation of emotional processing. Conceptualization of anxiety as importantly involving abnormalities in emotion regulation, particularly a type occurring outside of awareness, may open up avenues for novel treatments, such as by targeting the medial prefrontal cortex.

Neural Mechanisms Underlying MBSR in Healthy and Socially Phobic Individuals

J Gross, P Goldin
Department of Psychology, Stanford University, CA

The overall goal is to identify the neural mechanisms associated with Mindfulness-Based Stress Reduction (MBSR). Clinical research has shown that MBSR reduces psychological distress and increases well-being, but the mechanisms underlying these changes in not well described. Basic research has examined the neural bases of emotion and emotion regulation, but this research has not examined changes following MBSR. We employ a translational framework that characterizes the impact of MBSR on emotion regulation in terms of interactions between ventral emotion-generative brain regions and dorsal emotion-regulatory brain regions. We propose to compare the effects of MBSR and an active control condition (ACC) in participants with generalized social phobia (SP). SP will be randomly assigned to MBSR or ACC and assessed using self-report inventories and functional magnetic resonance imaging (fMRI) before and after MBSR and the ACC. Aim 1 investigates the effects of MBSR on anxiety and well-being. For the MBSR participants, we expect significant (a) decreases in anxiety, and (b) increases in well-being at immediately post-intervention and at the 3-month follow-up compared to pre-intervention. For the ACC participants, we expect no change in anxiety or well-being from pre- to post-intervention. Aim 2 investigates the effects of MBSR on attentional and cognitive emotion regulation. We expect MBSR participants to show improvements in attentional regulation, but no change in cognitive regulation from pre- to post-intervention, as indicated by (a) greater reductions in negative emotion ratings, (b) greater reductions in ventral emotion-generative brain regions, as well as (c) greater increases in attention-related dorsal emotion-regulatory brain regions. We do not expect ACC participants to show changes in either form of regulation from pre- to post-ACC. Aim 3 investigates whether MBSR-related changes in attentional emotion regulation mediate MBSR treatment response (decreases in anxiety and increases in well-being) at post-treatment and at the 3-month follow-up.

References/Funding Source R21 AT003644 Awarded to James Gross. PR Goldin, J Gross. (2010). Effect of mindfulness training on the neural bases of emotion regulation in social anxiety disorder. Emotion, 10, 83-91. PR Goldin, W Ramel, J Gross. (2009). Mindfulness meditation training and self-referential processing in social anxiety disorder: behavioral and neural effects. Journal of Cognitive Psychotherapy, 23, 242-257

The Feasibility of Detecting Neuroanatomical Effects of Type 1 Diabetes Mellitus in Young Children

T Aye[1], S Kesler[2], S Hoang[1], D Wilson[1], A Reiss[2], B Buckingham[1]
Departments of [1]Pediatric Endocrinology and Diabetes, [2]Center for Interdisciplinary Brain Sciences Research, Stanford University, CA

Type 1 diabetes mellitus (T1DM) impacts the developing brain and both hypoglycemia and hyperglycemia have been associated with neurocognitive and neuroanataomical changes. Young children with T1DM have wide excursions in blood glucose during a period when the brain is undergoing dynamic changes including myelination and repair of synapses. Therefore, we hypothesized that frequent exposure to hypoglycemia and hyperglycemia during early childhood may potentially lead to changes in brain anatomy. Young children, ages 3 to less than 10 years, with TIDM and age, gender and socioeconomic matched healthy controls completed age non-sedated MRI scans of the brain. Ninety-three percent of the children successfully MRI scanning respectively. In our cohort of 28 children with T1DM and 17 healthy controls, we found similar grey matter (GM: 862 ± 101 mm^3 vs 838 ± 95 mm^3), white matter (WM: 377 ± 63 mm^3 vs 370 ± 57 mm^3) and hippocampal (6. 3 ± 0.8 mm^3 vs 6.1 ± 0.8 mm^3) volumes in subjects between the two groups. However, after controlling for age and gender, we detected a significant diagnosis by age interaction (p=0.005) such that WM volume was unchanged in older children with T1DM, in contrast to healthy controls who showed the (expected) normal increase in WM volume with age. A similar trend was detected for hippocampal volume (diagnosis x age: p=0.07). We also noted that those T1DM children who had experienced seizures showed significantly reduced GM (p=0.049) and WM (p=0.049) volumes relative to children with T1DM who had not experienced seizures. We show that it is feasible to perform MRI in young children with T1DM and that early signs of neuroanatomical variation may be present in this population. Larger cross-sectional and longitudinal studies of neuroanatomy are needed to define the impact of T1DM on the developing brain.

References/Funding Source Weisgerber Foundation. American Diabetes Association June 2010

Dominance of Task-positive Over Default-mode Network Activity Mediates Adaptive and Maladaptive Rumination in Major Depressive Disorder

JP Hamilton, DJ Furman, C Chang, ME Thomason, E Dennis, IH Gotlib
Department of Psychology, Stanford University, CA

Major Depressive Disorder (MDD) has been associated reliably with ruminative responding that involves both adaptive and maladaptive components. Relative levels of activity in the task-positive network versus the default-mode network (TPN and DMN) of the intrinsic functional macro-architecture of the brain may represent an important neural substrate of adaptive and maladaptive ruminating in MDD. We estimated TPN dominance over DMN from blood-oxygen-level dependent data collected during eyes-closed rest in depressed and never-depressed persons. We calculated correlations between TPN dominance over DMN and the depressive, brooding, and reflective subscales of the Ruminative Responses Scale, correcting for associations between these measures and severity of depression.

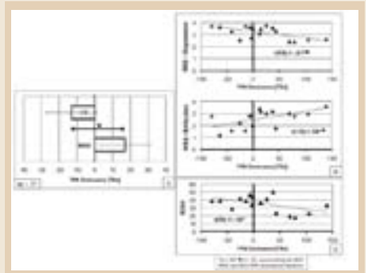

Further, for both groups of participants we estimated RFIC response during initiations of ascent in TPN and in DMN activity. We observed in MDD increased TPN dominance over DMN that was negatively correlated with maladaptive depressive rumination and positively correlated with adaptive, reflective rumination (see figure below). We also found in depressed participants increased RFIC activation at the onset of ascents in TPN activity that was positively correlated with TPN dominance over DMN. The current results show in MDD an adaptive relation between the TPN and DMN that appears to be instigated by RFIC-mediated awareness of negative emotional states.

Investigating Neural Primacy in Major Depressive Disorder: Multivariate Granger Causality Analysis of Resting-state fMRI Time-series Data

JP Hamilton, G Chen, ME Thomason, ME Schwartz, IH Gotlib
Department of Psychology, Stanford University, CA

Major Depressive Disorder (MDD) has been conceptualized as a neural network-level disease. Few studies of the neural bases of depression, however, have used analytic techniques that are capable of testing network-level hypotheses of neural dysfunction in this disorder. Moreover, of those that have, fewer still have attempted to determine directionality of influence within functionally abnormal networks of structures. We used multivariate Granger causality analysis — a technique that estimates the extent to which preceding neural activity in one or more seed regions predicts subsequent activity in target brain regions — to analyze blood-oxygen-level dependent (BOLD) data collected during eyes-closed rest in depressed and never-depressed persons. We found that activation in the hippocampus predicted subsequent increases in ventral anterior cingulate cortex (vACC) activity in depression, and that activity in medial prefrontal cortex and vACC were mutually reinforcing in MDD. Hippocampal and vACC activation in depressed participants predicted subsequent decreases in dorsal cortical activity (see figure below). This study shows that, on a moment-by-moment basis, there is increased excitatory activity among limbic and paralimbic structures, as well as increased inhibition in activity of dorsal cortical structures, by limbic structures in depression; these aberrant patterns of effective connectivity implicate disturbances in the mesostriatal dopamine system in depression. These findings advance neural theory of depression by detailing specific patterns of limbic excitation in MDD, by making explicit the primary role of limbic inhibition of dorsal cortex in the cortico-limbic relation posited to underlie depression, and by presenting an integrated neurofunctional account of altered dopamine function in this disorder.

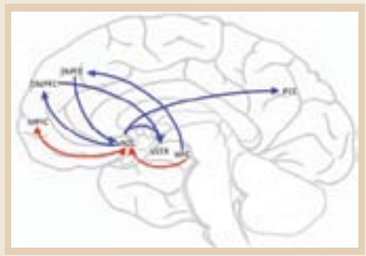

The Neural Temporal Dynamics of the Intensity of Emotional Experience

CE Waugh[1], JP Hamilton[1], IH Gotlib[1]
Department of Psychology, Stanford University, CA

Despite the fact that emotions involve multiple time-varying components, little is known about the underlying neural basis of these temporal dynamics. In this paper, we assess these temporal dynamics by using time-varying hemodynamic response functions (HRF) to model BOLD responses to emotional stimuli. We show that these time-varying HRFs lead to a better fit to the BOLD data and yield larger areas of significant activation than do conventional gamma-based canonical HRFs. We also report for the first time that intensity of emotional experience is associated with both magnitude and duration of brain activation. Specifically, greater negative emotional intensity was associated with greater magnitude of activation in the occipital cortex and with longer duration of activation in regions along the cortical midline associated with self-referent processing: the anterior medial prefrontal cortex and the posterior cingulate cortex. These data significantly advance our understanding of how the brain processes emotion and suggest that the intensity of a negative emotional experience is due in part to elaborative self-referent processing that is captured by the duration of neural activity in cortical midline structures. These data also underscore the importance of using modeling techniques that will help elucidate the chronometry of both normal and psychopathological emotional processes.

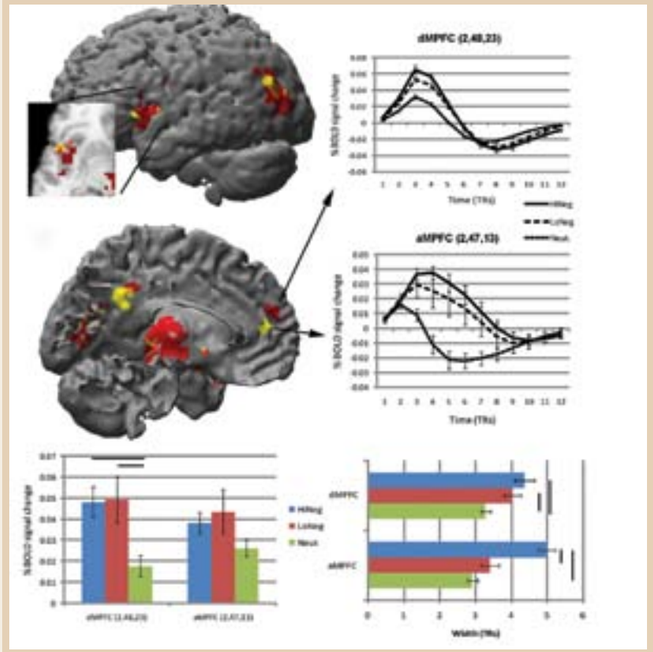

Brain regions showing significantly greater height of activation (red), width of activation (yellow), and both (orange) to the HiNeg (vs. neutral) pictures. The line graphs are the estimated HRFs from the aMPFC and dMPFC, which show non-overlapping differences in activation width and height, respectively (shown in the bar graphs). All error bars are standard error of the mean. Solid lines above bars represent significant differences at $p < .01$.

References/Funding Source Grant MH079651 from the National Institute of Mental Health to J. Paul Hamilton, and by a Distinguished Scientist Award from NARSAD and Grant MH074849 from the National Institute of Mental Health to Ian H. Gotlib. CW Waugh, JP Hamilton, IH Gotlib. (2010). The neural temporal dynamics of the intensity of emotional experience. Neuroimage, 49, 1699-1707.

Psychophysical and Neural Investigations of Congenital Prosopagnosia

N Witthoft, S Poltoratski, G Golarai, A Liberman, K Grill-Spector
Department of Psychology and Neurosciences Program, Stanford University, CA

Congenital prosopagnosia is a lifelong specific deficit in identifying faces that is not the result of stroke or other brain injury or gross physiological abnormality. fMRI in prosopagnosics has been inconclusive in revealing the neural basis with the largest such study (n=6) failing to find any differences between prosopagnosics and controls in ventral occipito-temporal visual cortex. Nonetheless, it is plausible that there are some differences between prosopagnosics and controls in the functional profile of face-selective regions in ventral visual regions. In ongoing work we have identified 14 prosopagnosics who show poorer performance than controls on tests of face recognition Additionally, our prosopagnosic group performed worse on the NEPSY-II Test of Emotional Development, suggesting a subtle impairment in their perception of facial affect. Consistent with a deficit specific to face memory/perception, our subjects do not differ from controls in recognition of famous places, or recognition memory for scenes and objects. We have collected and analyzed fMRI data from 10/14 subjects. In the scanning experiment, subjects viewed blocks of faces, places, and objects, alternating with fixation. Previously published data (Golarai et al 2010) from 9 adults who participated in identical experiments was used for comparison. Anatomical regions of interest containing ventral visual cortex were drawn in each subject, extending anteriorly from V4, 2/3 of the distance to the temporal pole. The ROI was bounded medially by the collateral sulcus and laterally by the occipital temporal sulcus. Within this ROI we found no differences between our prosopagnosics and controls in the spatial extent of object-selective (objects>scrambled) or place-selective activations (places>objects). However, prosopagnosics had fewer face-selective voxels in the right hemisphere (faces>objects), suggesting prosopagnosics may differ from controls in the extent of face selectivity in ventral visual cortex.

References/Funding Source NSF: BCS 0920865 and NIH: NRSA 1F32EY018533-01

High-resolution fMRI Reveals Separate Limb-selective Activations Surrounding Area hMT+

KS Weiner[1], K Grill-Spector[1,2]
Department of [1]Psychology and [2]Neuroscience Institute, Stanford University, CA

Standard functional magnetic resonance imaging (fMRI) studies have identified overlapping regions in human lateral occipitotemporal cortex (LOTC) that are motion-selective (area hMT+) and body part-selective (the extrastriate body area, EBA). Using high-resolution fMRI (HR-fMRI), we examined the fine-scale spatial organization of these regions relative to each other, as well as to known visual field maps in LOTC, specifically, LO-1/2 and TO-1/2. We scanned seven healthy individuals in four experiments across three scanning sessions. In Session 1 (resolution of 1.5 x 1.5 x 3 mm), we conducted experiments to localize the EBA and hMT+. In Session 2 (resolution of 3 mm isotropic voxels), we implemented standard retinotopic mapping using a rotating wedge to map polar angle and expanding rings to map eccentricity. In Session 3 (resolution of 1.5 x 1.5 x 1.5 mm), we probed the representation of stimulus type and position by presenting 2.5° images of faces, limbs, and houses in five visual field positions. First, our results indicate two separate limb-selective activations that minimally overlap hMT+, rather than a single EBA that highly overlaps with hMT+. These activations have consistent anatomical boundaries across subjects. Specifically, there is a limb-selective activation located anterior to hMT+ on the medial temporal gyrus (MTG) and a separate posterior limb-selective activation located on the lateral occipital sulcus (LOS). Second, the MTG activation typically overlaps with TO-2 and consistently extends outside established retinotopic maps, while the LOS activation falls on retinotopic regions LO-2 and TO-1. Third, there are differential position sensitivities across ROIs, where the MTG activation illustrates a foveal bias, and the LOS activation illustrates a contralateral bias. Overall, our HR-fMRI measurements illustrate a series of limb-selective activations that 1) minimally overlap hMT+, 2) have separate anatomical boundaries, 3) overlap distinct visual field maps, and 4) have differential sensitivity to stimulus position. These results demonstrate a consistent organization of distinct limb-selective activations with differing functional properties surrounding hMT+, which challenges the traditional view of highly overlapping body part- and motion-selective areas in LOTC.

Face-selective Activation in the Posterior Super Temporal Sulcus is Similar Across Children, Adolescents, and Adults

A Liberman, G Golarai, J Yoon, K Grill-Spector
Department of Psychology, Stanford University, CA

Regions in the posterior superior temporal sulcus (pSTS) in humans respond more strongly to face versus non-face stimuli and are thought to be involved in processing dynamic aspects of faces. Functional magnetic resonance imaging (fMRI) studies of this region report conflicting results on the development of face-selective activations from childhood to adulthood. Some studies reported no face-selective activation in 5-8 year olds and other studies reported comparable activation in 7-11 year olds and adults. To better understand the development of this region, we used fMRI in a 3T scanner to identify face-selective activations in 6 children (ages 8-11 years), 14 adolescents (ages 12-16) and 10 adults (ages 18-40). Subjects viewed blocks of pictures of men, boys, cars, abstract objects, indoor and outdoor scenes while fixating and performing a 1-back task. We measured the spatial extent of face-selective activation in an anatomically-defined pSTS region of interest (ROI). This ROI included the ascending and horizontal posterior segments of the STS as well as the portions of the angular gyrus and middle temporal gyrus that bordered the pSTS. In each subject, we measured the spatial extent of face-selective activation within this anatomically-defined pSTS. Using a standard contrast (faces > objects, $p<10^{-3}$), we found face-selective activations in all age groups (left: 6/6 children, 12/14 teens, and 9/10 adults; right: 5/6 children, 11/14 adolescents and 10/10 adults). There was no significant difference in the volume of activation between the three age-groups, but female subjects showed significantly larger activations than males (right pSTS, p=0.044; left pSTS, p=0.009). (Since our stimuli consisted only of male faces, future examinations of putative gender effects should be conducted using images of male and female faces). Similar results were found when activations were measured at different thresholds ($10^{-6} < p < 10^{-2}$) in each hemisphere, except for a trend of smaller volume of activation in adolescents than adults. Outside of the scanner, subjects participated in an IQ test, a facial affect recognition test (NEPSY-II), a face, object and place recognition memory test and the Benton Facial Recognition task. We found no significant correlations between face-selective pSTS activation volumes and performance in any of the tasks. In conclusion, our results suggest that the volume of face selective activations in this region is adult like by 8 years of age.

References/Funding Source NSF: BCS-0617688; NIH: 1R21EY017741; NSF: BCS 0920865. This work will be presented as a poster at SFN 2010.

Parietal Contributions to Episodic Retrieval: Effects of Memory and Decision Criteria

JB Hutchinson[1], MR Uncapher[1], AD Wagner[1,2]
Departments of [1]Psychology and [2]Neuroscience Program, Stanford University, CA

While neuroimaging studies of episodic retrieval have consistently revealed activation in posterior parietal cortex (PPC), there remains much debate about the functional roles of dorsal and ventral PPC regions in memory. A parallel literature implicates PPC in processes engaged during perceptual decision-making, suggesting similar processes may also contribute to episodic retrieval. The current fMRI study manipulated decision criteria in order to disentangle PPC responses associated with mnemonic evidence from responses associated with decision processes. Participants incidentally encoded visually presented words, and were subsequently scanned while performing two recognition memory tests. In the first test, a between-subject instructional manipulation varied whether participants made a 1-5 point confidence rating about item novelty or item familiarity. In the second test, participants performed a standard old/new recognition task (making old/new/unsure responses). PPC regions showing greater activation during hits vs. correct rejections (i.e., "old/new effects") on this latter test were interrogated for sensitivity to instructional framing in the confidence-rating test. Initial results suggest that old/new sensitive regions in the inferior parietal lobule, near the intraparietal sulcus, are insensitive to decision criteria. Additional a priori region of interest analyses suggest that a region within the superior parietal lobule tracks the decision uncertainty, whereas a region of angular gyrus demonstrates an inverse pattern. These findings underscore that multiple interacting processes within PPC contribute to episodic retrieval.

References/Funding Source NIMH (5R01–MH080309). JB Hutchinson, MR Uncapher, AD Wagner (2010) Parietal Contributions to Episodic Retrieval: Effects of Memory and Decision Criteria. For: Cognitive Neuroscience Society, Montreal, Canada.

Characterizing Face Representations in the Ventral Stream: Effects of Physical Variability and Distance from the Average Face

R Davidenko[1], K Grill-Spector[1,2]
Departments of [1]Psychology, [2]Neuroscience Institute, Stanford University, CA

fMRI research has identified regions in the human fusiform gyrus (FFA) and inferior occipital gyrus (IOG) that respond selectively to faces, but the mechanisms by which neurons in these regions represent different faces is highly debated. A prominent view posits that face-selective neurons employ a norm-based representation, responding more strongly to distinctive faces that deviate from the average face in particular directions in face space. However, in humans, evidence for this view is based on block-design fMRI experiments in which the within-block physical variability of face stimuli is not controlled across different blocks. If blocks of distinctive faces also contain more physically variable faces than blocks of typical faces, a larger BOLD response to distinctive blocks may indicate less adaptation during these high-variability blocks rather than preferential tuning to distinctive faces. In 3 studies (8-10 subjects each), we measured responses of FFA, IOG, and an object-selective region (LO) using fMRI at 3T. We manipulated distance from the average face (distinctiveness) independently from the physical variability of face stimuli using a perceptually validated silhouette face space. When physical variability and distinctiveness co-varied (Study 1), we replicated previous studies and found stronger responses during distinctive (and high-variability) blocks in FFA and IOG. However, we found the same pattern in LO, suggesting general adaptation to low-variability blocks rather than evidence for a face coding mechanism. In contrast, when physical variability was held constant across blocks (Study 2), responses in FFA and IOG (but not LO) were stronger during typical face blocks, providing new evidence of a typicality preference in FFA and IOG. A key prediction of the norm-based model is that blocks of faces sampled from multiple directions in face space relative to the average face should activate a larger neural population and thus yield a stronger BOLD response than blocks of faces sampled from a single direction. Contrary to this prediction, we found that FFA and IOG responses did not differ across these two types of blocks when physical variability was matched (Study 3). Our results highlight the importance of controlling the physical variability of stimuli when investigating the functional properties of ventral visual cortex. Further, responses in FFA and IOG across all 3 studies can be explained by an exemplar-tuned neural population that allocates more neurons with sharper tuning to frequently experienced, typical faces near the average face. We propose similar coding principles may underlie the representation of other visual categories.

High-resolution Investigation of Pattern Separation in the Medial Temporal Lobe

VA Carr[1], SE Favila[2], AD Wagner[1,3]
Departments of [1]Psychology, [2]Human Biology, and [3]Neurosciences, Stanford University, Stanford, CA

Tension is thought to exist within the medial temporal lobe (MTL) when events share overlapping features, such that some subfields readily encode a given event as distinct from previously-experienced events (e.g., pattern separation), whereas others generalize across similar events. In an effort to better characterize putative functional heterogeneity among MTL subfields, two studies were conducted examining the manner in which subfields respond to parametric manipulations of either item or relational similarity. In both cases, participants were scanned using high-resolution fMRI and a rapid adaptation paradigm in which trials began with presentation of a novel stimulus, followed by a stimulus varying in similarity to the novel stimulus. We hypothesized that (a) when two stimuli were identical, adaptation would be seen across all MTL subfields, and (b) critically, different levels of adaptation would appear across subfields as a function of stimulus similarity. Analyses were performed in two ways: (1) participant's images were kept in native space, and activity was extracted from anatomical regions of interest (ROI), (2) participant's images were registered into a group template using an ROI-alignment technique (ROI-AL) to allow for group-level voxel-based analyses. Results reveal regional adaptation differences between the hippocampus and MTL cortices in both studies, as well as subregional differences within the hippocampus such that CA/dentate gyrus plays the clearest role in pattern separation.

References/Funding Source NIMH(5RO1-MH076932), NARSAD

White Matter of the Early Visual Pathways

N Levin[1,2], E Rykhlevskaia[2], LM Perry[2], RF Dougherty[2], A Mezer[2], A Sherbondy[2], BA Wandell[2]
Departments of [1]Hadassah University Hospital, Jerusalem, Israel; [2]Psychology, Stanford University, CA, USA

Vision is initiated by absorptions in the photoreceptors within the retina. Beginning with the output neurons of the retina, the ganglion cells, a series of long range white matter tracts communicate visual signals to the visual cortex. These white matter structures in the early visual pathways can be reliably identified using diffusion-tensor imaging (DTI) and fiber tractography. The clinical use of DTI in Ophthalmology is limited by the lack of a normal standard of reference. We collected anatomical and diffusion-weighted images on a 1.5T G.E. MR scanner on 60 hemispheres from a normal subject pool and used a new probabilistic tractography algorithm to identify the anterior visual pathways. We identified the optic tracts, optic radiations and occipital callosal pathways in all subjects (N=30); the reconstructed pathways were in good agreement with known anatomy. We summarize the morphometric properties of these pathways, including length and volume of the different pathways and compare our measurements to what is reported in the autopsy literature. The cross-section area of the occipital callosal bundle in the mid-sagittal plane is correlated with the cross-section area of the full corpus callosum ($r = 0.47$, $p< 0.001$). We report diffusivity measurements including fractional anisotropy, longitudinal and radial diffusivities. We have discovered significant right vs. left differences in the optic radiations and the occipital cross callosal fiber bundles. This in vivo database of sighted adult visual pathways can be used as a standard for comparison to disease states, unusual cases involving developmental plasticity and recovery from damage.

Locations of the principal early visual white matter bundles. The large sphere in the middle sagittal location shows the optic chiasm. After the optic nerve fibers meet and cross at the chiasm, they form the optic tract. Each contains information about one hemifield. The optic tract fibers (saturated red and blue) project to the left and right lateral geniculate nucleus, which are shown as smaller spheres. Fibers from the LGN connect to the calcarine sulcus (primary visual cortex) and form the optic radiation (pale red and blue). Some of the fibers travel directly posterior, while others make an anterior turn before heading posterior, which forms Meyer's loop. The occipital-lobe to callosal projection (green) carries signals that communicate between the two hemispheres.

References/Funding Source NEI EY03164

White Matter Callosal Projections from Superior Temporal Region Predict Phonological Skills in Children

AM Kevan[1], LM Perry[1], EI Rykhlevskaia[1], M Ben-Shachar [1,2], AJ Sherbondy[1], RF Dougherty[1], BA Wandell[1]
Departments of [1]Psychology, Stanford University, CA, USA; [2]Linguistics and Gonda Brain Research Center, Bar Ilan University, Israel

Multiple groups report a correlation between phonological processing and diffusion measures in a posterior region of the callosum (Dougherty 2007; Odegard 2009; Frye 2009). Callosal fibers from this region pass through a complex region of intersecting fibers that obscures their cortical projection zone. We used a combination of probabilistic tractography and fMRI measures to examine three competing hypotheses about the likely cortical destination of these callosal fibers. Specifically, we asked whether the callosal fibers project to (a) hMT+, (b) visual word form area (VWFA) or, (c) posterior superior temporal cortex (pSTC). We obtained diffusion (DTI), functional (fMRI), and phonological measures in typically developing children. Speed judgment localizers (Ben-Shachar 2007) were used to define left hMT+; word localizers were used to define VWFA; in 8 children rhyme judgment localizers identified left pSTC, and using the Desikan-Killiany Atlas (Fischl 2004), we identified the likely position of the pSTC in the remaining children.

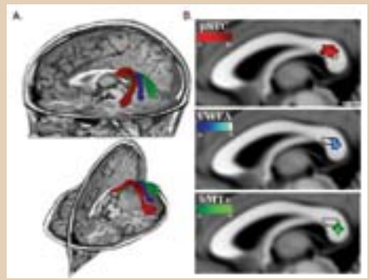

(A) Three-dimensional renderings of the trajectories of: pSTC (red), VWFA (blue), and hMT+ (green) callosal fibers. (B) Degree of overlap between temporal-callosal fibers previously shown to correlate with phonological processing skill (black outline) and the projection regions of the pSTC, VWFA, and hMT+ callosal fibers. Heat maps show the percentage of children who had fibers in a given voxel: pSTC (n=55), VWFA (n=32), and hMT+ (n=29). (Scale bar: 1cm).

We used a probabilistic algorithm (Sherbondy 2008) to identify the most likely pathways between the callosum and either (a) hMT+, (b) VWFA, or (c) pSTC. We also measured diffusivity along each of the callosal pathways and compared diffusivity with behavioral measures of phonological awareness. Fibers of the left pSTC project to the same callosal region previously shown to correlate with phonological performance. Our data also show a correlation between phonological awareness, and fractional anisotropy and radial diffusivity on the pSTC fiber track. In contrast, the hMT+ and VWFA callosal fibers project to a different region in the posterior callosum, and their diffusion properties do not correlate with phonological awareness. Combining fiber tracking and functional MRI, we conclude that callosal fibers correlated with reading measures project to pSTC. Further, the correlations between diffusion measures and behavior suggest that these fibers carry signals essential for the phonological processing.

References/Funding Source NIH Grant EY15000. AM Kevan[1], LM Perry[1], EI Rykhlevskaia[1], M Ben-Shachar[1,2], AJ Sherbondy[1], RF Dougherty[1], BA Wandell[1]. (2010). White matter callosal projections from superior temporal phonological regions predict reading skills in children. Society for Neuroscience annual meeting, San Diego. CA.

Anatomical Properties of the Arcuate Fasciculus Predicts Phonological and Reading Skills in Children

JD Yeatman[1], RF Dougherty[1], E Rykhlevskaia[1], GK Deutsch[1], BA Wandell[1], M Ben-Shachar[2]
Departments of [1]Psychology, Stanford University, CA, USA; [2]The Gonda Multidisciplinary Brain Research Center and English Department, Bar Ilan University, Israel

The left arcuate fasciculus (AF) is thought to comprise fibers that carry essential information for processing language. Yet, prior studies based on whole-brain group comparisons suggested that the essential reading-related white matter pathway is in the corona radiata, adjacent to the arcuate fasciculus, but not in the arcuate itself. We identified the left arcuate fasciculus using fiber tractography in each of fifty typically developing children. We identified the tract by a standard protocol that required establishing key waypoints and properties of the arcuate. By identifying this track in individual children, we could directly confront the hypothesis that diffusion properties within the left arcuate are correlated with behavioral measures of reading and reading-related skills. Averaged across the entire arcuate, fractional anisotropy in the left AF is negatively correlated with phonological awareness. The FA differences arise because better readers have larger radial diffusivity (RD) and equal axial diffusivity (AD) compared to poor readers. Diffusion properties of the right AF were not associated with any of the targeted behavioral measures. Fractional anisotropy varies considerably along the arcuate. While the mean FA of the AF varies from 0.36 to 0.45 between subjects, within a subject along the length of the AF the value can vary from 0.23 to 0.66. Through analysis of the fibers passing near the AF, we observed that the lowest FA region arises because of crossing fibers destined for the parietal lobe. The correlation between FA and phonological awareness is highest in the left AF region with the highest FA. Finally, decreased AF laterality was associated with better phonological memory; and this association was stronger for females (r = -0.52) than males (r = -0.33). Decreased AF laterality was associated with better basic reading scores in females, but not in males. We find that the diffusion properties within the arcuate are predictive of performance on a phonological awareness task.

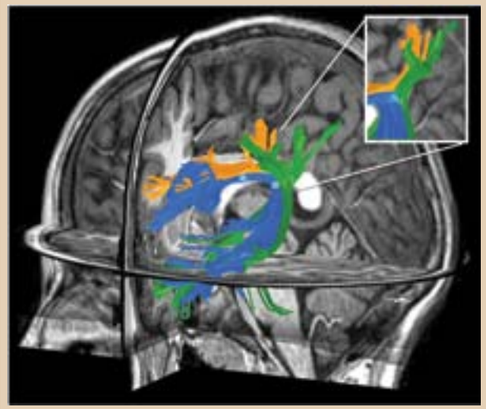

Arcuate fasciculus (AF) connects regions in the temporal lobe to the frontal lobe. The blue curves show estimates of the AF in a single child. The green and orange curves show estimates of nearby tracts. The inset shows the detail where the three fiber tracts come together at the main arc of the arcuate. The two small spheres show the points of the highest (anterior) and lowest (posterior) regions of fractional anisotropy in along the AF. The region of low anisotropy occurs at the point where the multiple tracts converge.

References/Funding Source NIH EY 015000

Molecular imaging is the art of looking inside of a living organism or cell to evaluate biological processes, observe normal cell behavior, identify aberrant behaviors, and develop interventions to halt or rectify such abnormalities. Through molecular and functional imaging we have made huge strides in bridging many other disciplines such as, biology, chemistry, physics, and computer science and ultimately changing and improving how we use imaging in medicine.

Minocycline Prevents Development of Neuropathic Pain by Mitigating Macrophage Recruitment to Site of Nerve Injury as Shown with USPIO-MRI

P Ghanouni, D Behera, S Biswal
Department of Radiology, MIPS, Stanford University, CA

Objective: Minocycline has proven anti-nociceptive effects, delaying the development of allodynia/hyperalgesia after peripheral nerve injury. However, the mechanism by which this occurs remains unclear. Inflammatory cells, in particular macrophages, are critical components of the response to nerve injury. Using USPIO-MRI to monitor macrophage trafficking, the purpose of this project is determine whether minocycline modulates macrophage trafficking to site of nerve injury which, in turn, results in altered pain thresholds.

Methods: Animal experiments were approved by Stanford IACUC. A model of neuropathic pain was created using the Spared Nerve Injury (SNI) model which involves ligation of 2 out of the 3 branches of the left sciatic nerve in the left thigh of adult Sprague-Dawley rats. Animals with SNI and uninjured animals (control) were then injected with/without USPIOs (300µmol/kg IV) and with/without minocycline (50mg/kg IP) (n=3 in each group). Bilateral sciatic nerves were scanned with a volume coil in a 7T magnet at 1, 4, and 7 days after USPIO administration. Fluid-sensitive FIESTA images (TR/TE/FA 11/22/20, in-plane resolution 110µm2, slice thickness of 1mm) were obtained. Using Osirix image analysis software, ROIs were placed on bilateral sciatic nerves to quantify signal intensity which were normalized to background signal in the muscle. Pain behavior modulation by minocyclinewas measured using the Von Frey filament test. The data was analyzed with using GraphPad Prism software.. Significance is $p<0.05$. Sciatic nerves were ultimately harvested at day 7, fixed in 10% buffered formalin and stained for the presence of iron oxide-laden macrophages.

Results: Behavioral measurements confirmed the presence of allodynia in the neuropathic pain model (50% paw withdrawal threshold of 3.86+/-0.34) while the uninjured (4.85+/-0.16) and minocycline-treated injured group (4.90+/-0.08) had significantly higher paw withdrawal thresholds ($p<0.011$). Decreased MR signal is observed in the SNI group that received USPIOs (3.3+/-0.5%) compared to the minocycline-treated SNI group that received USPIOs (15.2+/-4.5%) and minocycline-treated group (no USPIOs; 41.2+/-2.3%) ($p<0.04$). Histology of harvested sciatic nerve specimens confirmed the presence USPIOs at the nerve injury site in the SNI group without minocycline treatment.

Conclusion: Animals with neuropathic pain in the left hindpaw show increased trafficking of USPIO-laden macrophages to the site of sciatic nerve injury. Minocycline appears to retard the migration of macrophages to the nerve injury site, which may partly explain its anti-nociceptive effects. USPIO-MRI is an effective tool to study the role of macrophages in the development of neuropathic pain.

[18F]Saxitoxin PET-MRI: A New PET-based Method for Imaging Pain in Living Subjects

FT Chin[1], A Hoehne[1], W Parsons[2], D Behera[1], J Dubois[2], S Biswal[1]
Departments of [1]Radiology, MIPS and [2]Chemistry, Stanford University, CA

Purpose: The sensation of pain is dependent upon voltage-gated sodium channels (Na_V), which are essential to generation of action potentials and nerve impulse conduction. Na_V isoforms are known to be increased in peripheral sensory neurons in chronic and neuropathic pain. The radiofluorination of saxitoxin (STX), a non-protein neurotoxin that binds Na_V channels with high affinity, and evaluation of [18F]STX in living rats using positron emission tomography-magnetic resonance imaging (microPET-MRI) can potentially be used to identify neuropathic changes in living subjects.

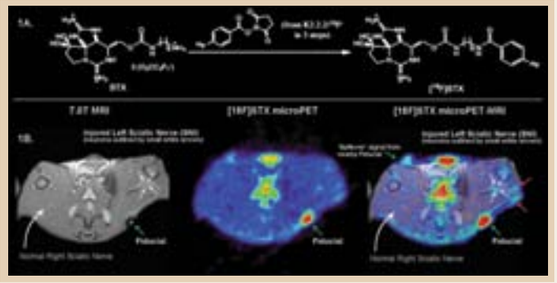

Methods: N-succinimidyl 4-[18F]fluorobenzoate ([18F]SFB) was made via nucleophilic substitution using a commercially-available automated radiochemistry module. The conjugation of [18F]SFB with STX (synthesized in-house) afforded [18F]STX (Figure 1A) with a minimum specific radioactivity of 1.3 Ci/μmol (48 GBq/μmol) and radiochemical purity ≥93% in a total synthesis time of about 3.5 h from end of bombardment (n=3). *In vivo* biodistribution of [18F]STX was assessed via 60 minute dynamic imaging of neuropathic pain-model rats (Spared Nerve Injury (SNI) of the left sciatic nerve) using small animal PET-MRI (microPET-MRI). Biodistribution studies via radioactivity measurements in organs using a gamma counter was also performed (n=3).

Results: MicroPET-MRI images and individual organ measurements showed accumulation of [18F]STX in the kidneys (10.7±8.9% ID/gm). No significant uptake was seen in bone (0.03±0.02% ID/gm). [18F]STX was observed in the injured left sciatic nerve nerve region at 15 min p.i. (small white arrows; Figure 1B). Adjacent areas around the injured nerve also showed increased uptake (small red arrows). The control intact right sciatic nerve by comparison showed no significant uptake (large white arrow).

Conclusions: [18F]STX shows tremendous potential as a specific radioligand for visualizing Na_V channels *in vivo*. Since [18F]STX is the only reported radioligand targeting Na_V channels to date, it is a valuable lead compound for future tracer development to image pain and facilitate future image-guided therapies for humans.

Oral Manganese as an MRI Contrast Agent for the Detection of Nociceptive Activity

KE Jacobs[1], D Behera[1], GE Gold[1], M Moseley[1], J Rosenberg[1], D Yeomans[2], S Biswal[1]
Departments of [1]Radiology and [2]Anesthesia, Stanford University, CA

Manganese-enhanced magnetic resonance imaging (MEMRI) is a potentially powerful diagnostic method for identifying neural regions of pain processing for image-guided interventions. Manganese can enter nerves via voltage-gated calcium channels, which are selectively upregulated in pain. We gave manganese by oral gavage to two rat groups: one with spared injury of their sciatic nerves and a sham-operated group. We found that rats with spared nerve injury have increased manganese ion uptake and retention in their nerves compared to the nerves of sham-operated rats as shown by increased MR signal and nerve concentrations. Therefore, manganese can specifically enhance nerves associated with pain.

[18F]Fluoride Ion PET-CT Predicts Painful Metastatic Bone Lesions in the Thoracolumbar Spine

V Rao[1], A Iagaru[1], E Graves[2], S Biswal[1]
Department of [1]Radiology and [2]Radiation Oncology, Stanford University, CA

Purpose: [18F]Fluoride ion PET-CT has emerged as a powerful and sensitive approach to studying areas of bone remodeling and turnover. The purpose of this study is to determine if there is a relationship between the extent of [18F]fluoride ion uptake in the thoracolumbar spine and presence of thoracolumbar back pain in patients suffering from osseous metastatic disease.

Method: IRB approval was attained. A retrospective review of 15 whole body [18F] fluoride ion PET-CT, which included 4 women and 12 men from ages 19-81. The same subjects had also received a [18F]FDG PET/CT study with an average interval of 6.3 days (range 1-28 days) between studies. Subjects fell into 1 of 3 categories: 1) Subjects with metastatic lesions to the thoracolumbar spine and described 'back pain' on the entrance questionnaire (n=3), 2) Subjects with metastatic disease to the spine and described 'no pain' (n=6), and 3) Subjects (control) who described 'no pain' on their entrance questionnaire and had no metastatic lesions to the spine (n=6). Using the transaxial CT to define the margins of the bone, representative rounded region of interests (ROIs) were placed at each vertebral level of the study from T1 to S1 in both [18F]fluoride ion and [18F]FDG PET-CT studies. Mean SUV was recorded at each level and each patient was assigned a maximum mean SUV for their entire thoracolumbar spine. Data was analyzed using RT_Image analysis software and t-test with unequal variances. Significance is $p<0.05$.

Results: Patients with spinal osseous metastases to the thoracolumbar spine and 'back pain' had significantly higher mean [18F]fluoride ion SUV (27.7+/-11.8) than those with spinal metastases but 'no pain' (11.4+/-3.5) and those without metastatic disease (7.9+/-0.7) ($p<0.013$). By comparison, no significance difference was observed in [18F]FDG uptake between the 3 groups. FDG SUV of mets with back pain, mets with no back pain and no mets were 6.9+/-0.1, 2.9+/-1.4 and 3.9+/-2.7, respectively ($p<0.11$).

Conclusion: Significantly increased [18F]fluoride uptake is observed in painful metastatic lesions compared to non-painful lesions of the thoracolumbar spine canal in subjects describing low back pain.

[18F]Fluoride ion PET-CT may be helpful in predicting which metastatic lesions will be painful in the thoracolumbar spine, allowing for treatment planning.

Noninvasive Molecular Imaging of Radioactive Probes Using Optical Imaging Techniques

H Liu[1,4], G Ren[1], Z Miao[1], X Zhang[1,4], X Tang[3], P Han[4], SS Gambhir[1,2], Z Cheng[1]
Departments of [1]Radiology, MIPS, Bio-X Program, [2]Bioengineering, Stanford University, CA, USA; [3]Physics, University of Notre Dame, IN, USA; [4]Institute of Radiation Medicine, Chinese Academy of Medical Sciences, Tsinghua University, Tianjin

Objectives: Radioactive molecular probes are generally imaged with nuclear imaging modalities such as single photon emission computed tomography (SPECT) and positron emission tomography (PET). Optical imaging techniques have been discovered to be able to image PET probes such as 2-deoxy-2-[18F]fluoro-D-glucose ([18F]FDG) in small animals recently. Here we further demonstrated that conventional optical imaging techniques could be very useful for non-invasively monitoring *in vivo* behaviors of a variety of radioactive probes labeled with ^{18}F, ^{131}I, ^{90}Y, etc.

Methods: By taking the advantages of low energy window of light (1.2-3.1 eV, 400-1000 nm) resulting from radiation, radionuclides that emit charged particles such as β+ and β- can be successfully imaged with optical imaging instruments.

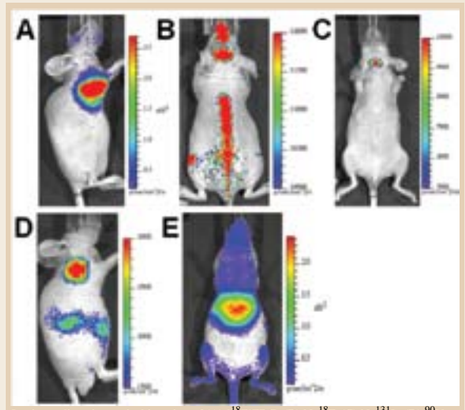

In vivo radioactive optical imaging of (A) [18F]FDG, (B) $Na^{18}F$, (C) $Na^{131}I$, (D) ^{90}Y-RGD-BBN and (E) $^{90}YCl_3$.

Results: High quality of *in vivo* optical images were obtained for several radioactive probes including [18F]FDG, $Na^{18}F$, $Na^{131}I$, $^{90}YCl_3$ and a ^{90}Y labeled peptide that specifically targets prostate cancer.

Conclusion: These studies demonstrate that optical imaging of radioactive probes is a generalizable technique. It provides a new molecular imaging strategy and will likely have significant impacts in both small animal and clinical imaging.

References/Funding Department of Radiology, Stanford University (to Z.C.), a China Scholarship Council fellowship (to H.L.), the National Cancer Institute (NCI) In Vivo Cellular Molecular Imaging Center (ICMIC) grant P50 CA114747 (to S.S.G.), and R01 CA119053 (to Z.C.). HG Liu, G Ren, Z Miao, XF Zhang, X Tang, PZ Han, SS Gambhir, Z Cheng. Molecular Optical Imaging with Radioactive Probes. PLoS ONE, 5(3): e9470.

In Vivo Multiplexed Optical Imaging with Radiation Luminescence Excited Quantum Dots

H Liu[1,4], X Zhang[1,4], B Xing[3], P Han[4], SS Gambhir[1,2], Zhen Cheng[1]
Departments of [1]Radiology, MIPS, Bio-X Program, [2]Bioengineering, Stanford University, CA; [3]Division of Chemistry and Biological chemistry, Nanyang Technological University, Singapore; [4]Institute of Radiation Medicine,Tsinghua University, Tianjin

Objectives: Quantum dots (QDs) have drawn much attention for their potential biomedical applications and have been widely explored as effective fluorescent sensors for *in vitro* and *in vivo* studies. Self-illuminating QD conjugates could circumvent some disadvantages of QDs, such as background autofluorescence and poor tissue penetration of the excitation photons. Hereby, we report a new method to illuminate QDs by radiation luminescence as an internal light source.

Methods: The low energy window of light resulting from radioactive materials such as ^{131}I was used to excite QDs both *in vitro* and *in vivo*. The resulted fluorescence was detected by IVIS spectrum optical imaging systems. Different wavelengths emitted by QDs were analyzed by Living Image software.

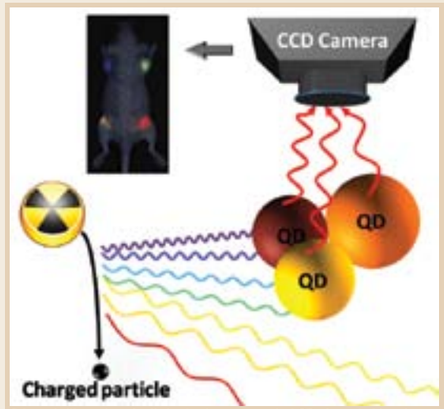

Schematic illustration of radiation luminescence excited QDs for optical imaging..

Results: The radionuclide ^{131}I excited QDs can produce fluorescence for both *in vitro* and *in vivo* imaging. Multiplexed QDs imaging was also achieved using this method.

Conclusion: This study provides an alternate strategy for design of self-illuminated optical imaging agents. Radiation luminescence excited QDs can also be readily adapted with single photon emission computed tomography (SPECT) or positron emission tomography (PET) for dual-modality imaging.

References/Funding National Cancer Institute (NCI) R21 CA121842 (to Z.C.), NCI Center of Cancer Nanotechnology Excellence Grant U54 CA119367 (to S.S.G.), an A_Star BMRC (07/1/22/19/534) grant from Singapore (to B.X.), and the China Scholarship Council fellowship (to H.L.). HG Liu, XF Zhang, B Xing, PZ Han, SS Gambhir, Z Cheng*. Radiation Luminescence Excited Quantum Dots for In Vivo Multiplexed Optical Imaging, Small, 6(10): 1087-1091.

Small Animal PET Imaging of HER2 Positive Tumors with a Novel ^{18}F-labeled Two-Helix Peptide

Z Miao[1,2], G Ren[1,2], L Jiang[1,2], H Liu[1,2], JM Webster[3], R Zhang[3], M Namavari[1,2], SS Gambhir[1,2], F Syud[3], Z Cheng[1,2]
Departments of [1]Radiology, MIPS, [2]Bio-X Program, Stanford University, CA; [3]Global Research, General Electric Company, Niskayuna, NY

Objectives: Two-helix peptides (~ 5 KDa) against human epidermal growth factor receptor type 2 (HER2) have been discovered in our previous research. In this study we aimed to develop an ^{18}F labeled 2-helix small peptide for positron emission tomography (PET) imaging of HER2 positive tumors.

Method and Results: An aminooxy functionalized 2-helix peptide (MUT-DS) with high HER2 binding affinity was synthesized through the conventional solid phase peptide synthesis. The purified linear peptide was cyclized by I_2 oxidation to form a disulfide bridge. The cyclic peptide was then labeled with a radiofluorination synthon, 4-^{18}F-fluorobenzyl aldehyde (^{18}F-FBA), through the aminooxy functional group at the peptide N-terminus (30% yield, non-decay corrected). The resulting PET probe, ^{18}F-FBO-MUT-DS, displayed a high specific activity (20-32 MBq/nmol, at the end of synthesis). Cell uptake assays showed high and specific cell uptake (~40 % applied activity at 1 h, 37 ˚C) by incubation the probe with HER2 high-expressing SKOV3 ovarian cancer cells. The affinities (K_D) of MUT-DS and ^{19}F-FBO-MUT-DS as tested by Biacore analysis were 2 and 1 nM, respectively. In vivo small-animal PET imaging demonstrated fast tumor targeting, high tumor accumulation and good tumor-to-normal tissue contrast of ^{18}F-FBO-MUT-DS. Biodistribution studies further demonstrated that the probe had excellent tumor uptake (6.92 %ID/g at 1 h postinjection) and was cleared through both liver and kidneys. Co-injection of the probe with 500 μg of HER2 Affibody protein reduced the tumor uptake (6.92 *vs.* 1.84 %ID/g).

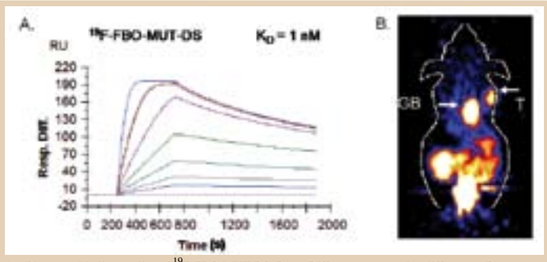

(A) Biosensor binding studies of ^{19}F-FBO-MUT-DS. Resp. Diff. means respective difference. (B) A representative ^{18}F-FBO-MUT-DS microPET image of a nude mouse bearing SKOV3 tumor on right shoulder at 2 h post-injection. T: tumor, GB: gallbladder.

Conclusion: ^{18}F-FBO-MUT-DS displays excellent HER2 targeting ability and tumor PET imaging quality. Two helix small proteins are suitable for development of ^{18}F based PET probes.

References/Funding California Breast Cancer Research Program 14IB-0091 (Z.C.) and an SNM Pilot Research Grant (to Z.C.). Z Miao, G Ren, L Jiang, H Liu, JM Webster, R Zhang, M Namavari, SS Gambhir, F Syud, Z Cheng. “Small-animal PET imaging of HER2 positive tumors with a novel 18F-labeled two-helix peptide.” WMIC 2010 meeting (poster).

Evaluations of In Vivo Distributions of Peptoids Using microPET

G Ren[1], J Seo[2], Z Miao[1], H Liu[1], Y Wang[1], M Park[2], A Barron[2], Z Cheng[1]
Departments of [1]Radiology, MIPS, Bio-X Program and [2]Bioengineering, Stanford University, CA

Objectives: Peptoid represents a novel class of emerging molecules for pharmaceutical development. However very limited studies have been reported to understand the in vivo absorption, distribution and metabolism of peptoids. In this study, the in vivo biodistribution of three peptoids with antimicrobial activity were investigated using micro-positron emission tomography.

Methods: DOTA conjugated peptoids (named as 1, 2 and 3) and control peptides (4 and 5) were synthesized by a solid-phase peptide synthesizer. The RP-HPLC purified and MALDI-TOF-MS confirmed compounds were then labeled with a positron emitter 64Cu (t1/2 = 12.7 hours). About 30 µCi of 64Cu labeled compounds were intravenously injected into BALB/c mice through tail vein. At different time points postinjection, microPET and biodistribution studies were performed.

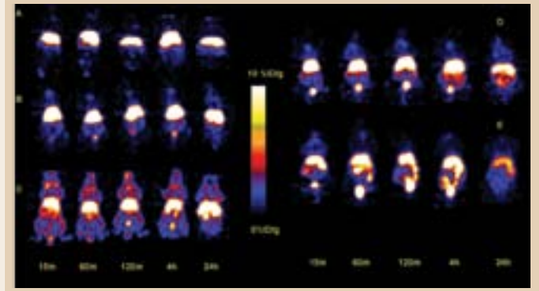

Representative decay-corrected coronal small-animal PET images of Balb/c mice at different time points after intravenous injection of peptoid 1 (A), 2 (B), 3 (C), and peptide 4 (D) and 5 (E) (n=4 for each group).

Results: All radiolabeled compounds showed excellent radiochemical purity (> 95%) and serum stability. Peptoids displayed high liver uptakes and long retention compared with the control peptides, suggesting their high hydrophobicity. Compared with 1 and 2, peptoid 3 exhibited lower liver while higher kidney uptake at both 2 and 24 h post-injection. MicroPET imaging also revealed that three peptoids and two peptides displayed different distribution patterns, especially in liver and bladder. Compared to peptoids, the bladder activities of both peptides were much higher than those of peptoids 1 and 2 (Figure).

Conclusions: In summary, these results suggest that the in vivo pharmacokinetics could be finely tuned by modifications of peptoid structure. The microPET could monitor the in vivo biodistribution of peptoids and provide useful information for the rational design and optimization of peptoid with various biological functions.

References/Funding DOD_PCRP. “Evaluation of in vivo distribution of peptoids using microPET”, Mar 21-25, 2010. American Chemical Society Meeting, San Francisco, CA, USA. G Ren, J Seo, HG Liu, Z Miao, A Barron, Z Cheng. PET Imaging of Peptoid Biodistribution. Journal of Medicinal Chemistry, to be submitted, 2010 July.

Targeting of HER2-Expressing Tumors Using Affibody-HSA Bioconjugates

S Hoppmann, Z Miao, H Liu, S Liu, G Ren, Z Cheng
Department of Radiology, MIPS, Stanford University, CA

Objectives: Affibody molecules represent a novel class of new protein scaffolds for cancer imaging and drug development. One major drawback, however, is their extremely high renal uptake, which is a concern for the imaging of tumors adjacent to the kidneys in positron emission tomography (PET) studies as well as for the use of Affibody molecules as radiotherapeutic agents. The purpose of this study is to explore whether human serum albumin (HSA) could be used to change the *in vivo* behaviors of Affibody proteins.

Methods: HSA was modified by 1,4,7,10-tetraazacyclododecane-1,4,7,10-tetraacetic acid (DOTA-NHS) ester and the bifunctional crosslinker sulfosuccinimidyl 4-[N-maleimidomethyl]cyclohexane-1-carboxylate (Sulfo-SMCC), respectively. The *HER2* Affibody analog Ac-Cys-$Z_{HER2:342}$ was then covalently conjugated to HSA, and the resulting bioconjugate DOTA-HSA-$_{ZHER2:342}$ was further radiolabeled with ^{64}Cu and ^{111}In and evaluated *in vitro* and *in vivo*.

Results: It was found that up to five Affibody molecules were covalently conjugated to one HSA molecule. MicroPET and single photon emission computed tomography (SPECT) imaging in SKOV3 tumor-bearing mice displayed high tumor and liver uptakes and moderate kidney accumulations. These results were coherent to the biodistribution data: ^{111}In-DOTA-HSA-$Z_{HER2:342}$ demonstrated high tumor uptakes (16.26 %ID/g) and liver uptakes (14.11 %ID/g) and relatively low kidney uptakes (6.06 %ID/g) at 24 h post injection (p.i.). Coinjection of Ac-Cys-$Z_{HER2:342}$ could significantly reduce the SKOV3 tumor uptake to 51% of the corresponding nontreated tumor uptake at 4 h post-injection ($P < 0.01$).

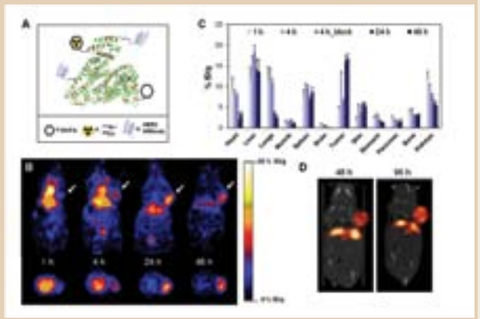

Radiolabeled Affibody-HSA Bioconjugates for *HER2* Targeting. (A)Illustration of radiolabeled DOTA-HSA-$Z_{HER2:342}$ bioconjugates. (B) Representative small-animal PET images of SKOV-3 tumor bearing mice at different time points after intravenous injection of ^{64}Cu-DOTA-HSA-$Z_{HER2:342}$ (n=5). (C) Biodistribution in SKOV-3 tumor bearing mice at different time points after intravenous injection of ^{111}In-DOTA-HSA-ZHER2:342. (n=3). (D) Representative small-animal SPECT-CT images of SKOV-3 tumor bearing mice at different time points after intravenous injection of ^{111}In-DOTA-HSA-$Z_{HER2:342}$ (n=3).

Conclusion: Radiolabeled DOTA-HSA-$Z_{HER2:342}$ Affibody conjugates are promising for imaging of *HER2* positive cancer. Furthermore, they are suitable for labeling with radiolanthanides such as ^{90}Y or ^{177}Lu for radiotherapeutic applications. More importantly, the concept of using HSA to alternate the pharmacokinetic of biomolecules such as Affibody scaffolds may be generalizable for design of many other targeting molecules.

References/Funding ICMIC, SU Radiology. “Chemically Conjugated Affibody-HSA for PET Imaging of HER2-Expressing Tumors”, Sep 8-11, 2010. World molecular Imaging Conference, Kyoto, Japan. “Chemically Conjugated Affibody-HSA as a Potential Radiotherapeutic Agent for Treatment of HER2-Positive Cancer” , Sep 8-11, 2010. World molecular Imaging Conference, Kyoto, Japan. S Hoppmann, Z Miao, S Liu, H Liu, G Ren, A Bao, Z Cheng. Radiolabeled Affibody-Albumin Bioconjugates for HER2 Positive Cancer Targeting. Journal of Nuclear Medicine (IF: 6,424), to be submitted, 2010 July.

^{111}In Labeled Knottins for Tumor Angiogenesis Targeting

G Ren[1], Z Miao[1], H Liu[1], R Kimura[2], Y Wang[1], J Cochran[2], Z Cheng[1]
Departments of [1]Radiology, MIPS, Bio-X Program and [2]Bioengineering, Stanford University, CA

Objectives: Integrin receptors play a pivot role in tumor angiogenesis. Engineered ecballium elaterium trypsin inhibitor II (EETI-II) knottin miniproteins 2.5D and 2.5F have shown high binding affinities (10-30 nmol/L) to integrin receptors. These peptides labeled with ^{64}Cu have been examined for micro-positron emission tomography (μPET) imaging of tumor integrin receptors, and they have displayed excellent tumor targeting ability and imaging quality. In this study, 2.5D and 2.5F were further labeled with ^{111}In, a single photon emission computed tomography (SPECT) radionuclide with relatively long half life, in order to evaluate the potential applications of EETI-II knottins for tumor SPECT imaging and radiotherapy.

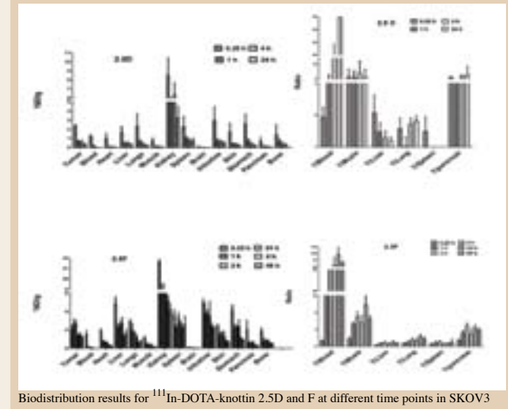

Biodistribution results for ^{111}In-DOTA-knottin 2.5D and F at different time points in SKOV3 tumor bearing mice (n=4). Data are expressed as the percentage administered activity (injected dose) per gram of tissue (%ID/g) or ratios between tumor and organs.

Methods: 2.5D and 2.5F were synthesized, purified and site-specifically conjugated with 1, 4, 7, 10-tetraazacyclododecane-N, N′, N″,N‴-tetraacetic acid (DOTA). The resulting bioconjugates were then labeled with $^{111}InCl_3$ and tested for their stability in mouse serum. The ^{111}In-radiocomplexes were further tested for cellular uptake, *in vivo* biodistribution and microSPECT/computed tomography (μSPECT/CT) imaging in murine xenograft bearing human SKOV3 ovarian cancer.

Results: DOTA conjugated knottins preserve high binding affinity. The ^{111}In-DOTA-knottins were stable in mouse serum under 37˚C for 24 hr. Compared with ^{111}In-DOTA-2.5D, 111In-DOTA-2.5F displayed higher uptakes in both SKOV3 cells and tumors. ^{111}In-DOTA-2.5F also exhibited longer tumor retention *in vivo* (Figure). Finally, both knottins showed higher tumor uptakes than that of ^{111}In labeled monomeric c(RGDfK).

Conclusions: Both knottins are promising probes for SPECT imaging of $\alpha_v\beta_3$ positive tumors. Knottin 2.5F may be more appealing to angiogenesis targeted radiotherapy due to its better pharmacokinetic profile *in vivo*.

References/Funding NIH. “Novel knottin miniproteins for tumor angiogenesis targeting”, June 3-7, 2010. Society of Nuclear Medicine, Salt Lake City, UT, USA. G Ren, Z Miao, H Liu, RH Kimura, Y Wang, J Cochran, Z Cheng. Knottin Miniproteins for Tumor Angiogenesis Targeting. to be submitted, 2010 July.

A Cy5.5 Labeled Affibody Molecule for Near-infrared Fluorescent Optical Imaging of Epidermal Growth Factor Receptor Positive Tumors

Z Miao, G Ren, H Liu, L Jiang, Z Cheng
Department of Radiology, MIPS, Bio-X Program, Stanford University, CA

Objectives: Affibody protein is an engineered protein scaffold with a three-helical bundle structure. Affibody molecules of small size (7 kD) have great potential for targeting cancer biomarkers in vivo. In this study, we aimed to develop an Affibody based molecular probe for *in vivo* optical imaging of epidermal growth factor receptor (EGFR) positive tumors,

Method and Results: An anti-EGFR Affibody molecule, Ac-Cys-$Z_{EGFR:1907}$ (7 kD), was site-specifically conjugated with a near infrared (NIR) fluorescence dye, Cy5.5-mono-maleimide. Using fluorescent microscopy, the binding specificity of the probe Cy5.5-$Z_{EGFR:1907}$ was measured using high EGFR expressing A431 cells and low EGFR expressing MCF7 cells. The EGFR binding affinity of Cy5.5-$Z_{EGFR:1907}$ (K_D) was 43.6 ± 8.4 nM as determined by flow cytometry. For in vivo imaging study, the probe showed fast tumor targeting and good tumor contrast as early as 0.5 h post-injection in A431 tumors, while MCF7 tumors could be barely visualized. Ex vivo imaging study also demonstrated that Cy5.5-$Z_{EGFR:1907}$ had high tumor, liver and kidney uptakes at 24 h p.i..

Conclusion: Cy5.5-$Z_{EGFR:1907}$ shows good affinity and high specificity to EGFR. It is a promising NIR probe for EGFR targeted cancer optical imaging.

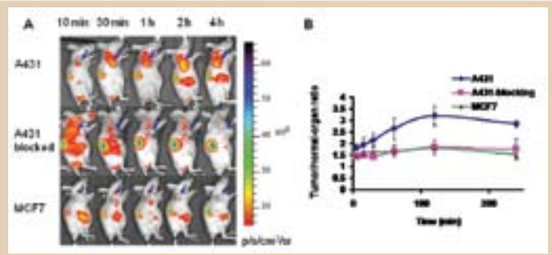

(A) In vivo fluorescence IVIS-200 imaging of subcutaneous A431 and MCF7 tumor-bearing nude mice at 10 min, 30 min, 1, 2, and 4 h. Cy5.5-$Z_{EGFR:1907}$ (0.5 nmol) with (bottom) or without (top) co-injection of unlabeled Affibody $Z_{EGFR:1907}$ (300 μg) were injected. Arrows indicate the location of tumors. (B) ROI analysis of tumor-to-normal tissue ratios of Cy5.5-$Z_{EGFR:1907}$ in mice bearing A431 tumor at 10 min to 4 h p.i. (n = 3).

References/Funding California Breast Cancer Research Program 14IB-0091 (Z.C.) and an SNM Pilot Research Grant (to Z.C.). Z Miao, G Ren, H Liu, L Jiang, Z Cheng. "A Cy5.5 Labeled Affibody Molecule for Near-infrared Fluorescent Optical Imaging of Epidermal Growth Factor Receptor Expression." Journal of Biomedical Optics. 2010. Accepted.

Small-Animal PET Imaging of Human Epidermal Growth Factor Receptor Positive Tumor with a ^{64}Cu Labeled Affibody Protein

Z Miao, G Ren, H Liu, L Jiang, Z Cheng
Department of Radiology, MIPS, Bio-X Program, Stanford University, CA

Objectives: Epidermal growth factor receptor (EGFR) has become an attractive target for cancer molecular imaging and therapy. Affibody proteins against EGFR have been reported recently. We thus are interested in evaluating their potential for positron emission tomography (PET) imaging of EGFR positive cancers.

Methods: An Affibody molecule (Ac- Cys-$Z_{EGFR:1907}$) binding to EGFR was prepared through conventional solid phase peptide synthesis. The purified protein was site-specifically coupled with the 1,4,7,10-tetraazacyclododecane-1,4,7-tris-aceticacid-10-maleimidethylacetamide (maleimido-mono-amide-DOTA) to produce the bioconjugate, DOTA-$Z_{EGFR:1907}$, and it was then radiolabeled with 64Cu and evaluated in vitro and in vivo in EGFR positive A431 epidermoid carcinoma cancer cells.

Results: ^{64}Cu labeled Affibody molecule, ^{64}Cu-DOTA-$Z_{EGFR:1907}$, displayed a moderate specific activity (5-8 MBq/nmol). Cell uptake assays by pre-incubating with or without Ac-Cys-$Z_{EGFR:1907}$ showed high EGFR specific uptake (20% applied activity at 0.5 h) in A431 cells. The binding affinity (KD) of ^{64}Cu-DOTA-$Z_{EGFR:1907}$ as tested by cell binding assay was 20 nM. The serum stability study demonstrated excellent stability of the probe with >95% intact probe after 4 h of incubation in mouse serum. In vivo small-animal PET imaging revealed fast tumor targeting, high tumor accumulation (~10% ID/g at 1 h p.i.), and good tumor-to-normal tissue contrast of the probe spiked with a wide dose range of Ac-Cys-$Z_{EGFR:1907}$. Biodistribution studies further demonstrated that the probe had high tumor, blood, liver, and kidney uptakes, while blood radioactivity dropped dramatically at increased spiking doses of cold Affibody molecule. Co-injection of the probe with 500 μg of Ac-Cys-$Z_{EGFR:1907}$ for blocking could significantly reduce the tumor uptake.

Conclusions: ^{64}Cu-DOTA-$Z_{EGFR:1907}$ has great potential for PET imaging of EGFR positive tumors. The probe spiked with cold Ac-Cys-$Z_{EGFR:1907}$ can improve tumor imaging contrast, which may have important clinical applications.

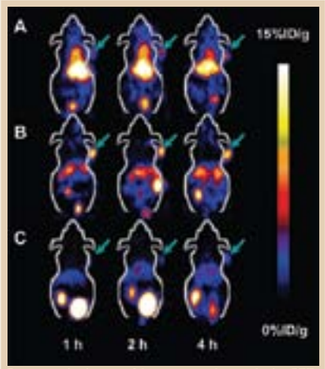

Representative images of decay corrected coronal microPET images of nude mice bearing the A431 tumor on the right shoulder at 1, 2, and 4 h after tail vein injection of ^{64}Cu-DOTA-$Z_{EGFR:1907}$ (1.11-1.85 MBq) spiked with 0 μg (A), 50 μg (B), and 500 μg (C) of Ac-Cys-$Z_{EGFR:1907}$. Arrows indicate the location of tumors.

References/Funding California Breast Cancer Research Program 14IB-0091 and an SNM Pilot Research Grant. Z Miao, G Ren, H Liu, L Jiang, Z Cheng. "Small-animal PET imaging of human epidermal growth factor receptor positive tumor with a ^{64}Cu labeled affibody protein." Bioconjug Chem 2010;21(5):947-54.

Effect of Inter- and Intra- User Variability in Quantification of Molecular Imaging Data

F Habte[1,2], S Budhiraja[1,2], T Doyle[2,3], CS Levin[1,2], D Paik[1,2]
Departments of [1]Radiology, [2]Radiology, MIPS, [3]Pediatrics, Stanford University, CA

In molecular imaging, absolute image quantitation is generally considered to be critical since it reduces subjectivity and provides important additional information that adds confidence in the data analysis process. Quantitation, however, heavily depends on the region of interest (ROI) analysis method, which normally is performed by manually defining an ROI and querying its statistics. Depending on how the ROI is drawn, the geometry and size of the ROI and the specific software tool used introduce variability and limit the accuracy. To characterize variability, nine experienced users with no restriction on data analysis tools were selected to read five different data sets three times for each data set. The images were acquired using microPET. In addition, we conducted a survey to study the users' confidence and subjectivity involved in the analysis. Our result indicates that high inter-user variability (s.d. > 30% of the inter-user mean) occurred while the intra-user variability is relatively low (s.d. < 10% of the inter-user mean). We also observed a pattern where each user consistently either under- or over-estimates the mean quantitative value, demonstrating the high degree of subjectivity. There was no direct correlation observed between the inter-user variability and confidence of the users on drawing the specific ROIs. Thus, software tools capable of defining ROIs semi-automatically may be required to improve quantitation accuracy and reduce variability in analysis of molecular imaging data.

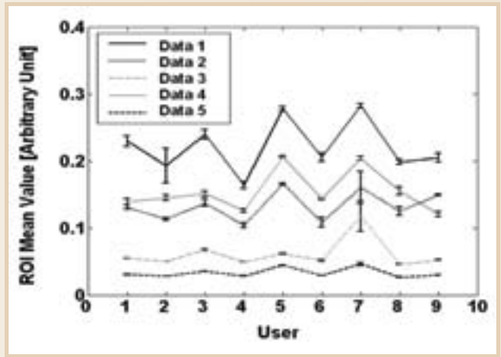

Inter- and Intra- user variability study o five-image data sets acquired using microPET.

References/Funding Poster Session 3b: Imaging Methodology and Instrumentation. September 26, 2009 / 16:00-17:30 / Room: 513. www.wmicmeeting.org/abstracts/data/papers/1143.html

Quantitation Error Assessment for Small Animal PET

F Habte[1,3], CH Nielsen[1,3], G Ren[1,3], S Yaghoubi[1,3], N Withofs[1,3], T Doyle[2,3], J Pisani[1,3], CS Levin[1,3], SS Gambhir[1,3], D Paik[1,3]
Departments of [1]Radiology, [2]Pediatrics, [3]Radiology, MIPS, Stanford University, CA.

Image quantitation in PET depends on many factors including pre-scan animal preparation, accuracy of calibrations, understanding error correction mechanisms and reliability of the entire data analysis procedure. Hence, the goal of this study is to identify the major sources of errors and optimize data analysis procedures to improve accuracy. We monitored the accuracy of calibration parameters on a monthly basis and compared the biodistribution of various organs/tumors using both microPET and a gamma-counter. We also conducted a phantom study with F-18 filled spheres to demonstrate the consistent underestimation of organ activity observed by microPET in various studies for organs expressing high tracer uptake. The biodistribution comparison showed close agreement (< 10% difference) for organs/tumors with lower uptake (> 10 uCi/mL) while significantly larger difference (> 30%) for organs with higher uptake. This observation was in close agreement with previous studies. We further verified the significant underestimation of PET concentration for regions with high tracer uptake using phantom studies. In our study, we have applied the vendor recommended attenuation and scatter corrections despite their minimum effect on mouse imaging. On the other hand, the vendor recommended global deadtime correction has limitations showing consistent count loss in high activity (>10 uCi/mL) regions of interest. This suggests that further evaluation of the microPET deadtime correction methods may be needed or additional post-reconstruction deadtime correction should be applied for more accurate quantitation.

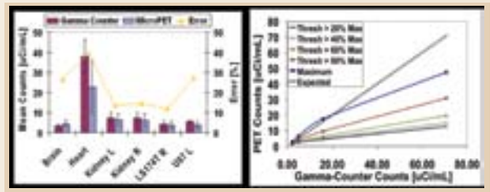

A. Biodistribution comparison of PET to gamma-counter results, and B. Phantom study demonstrating the significant under estimation of PET for regions with relatively high tracer concentration.

References/Funding Bayer Schering. Poster Session 3b: Imaging Methodology and Instrumentation. September 26, 2009 / 16:00-17:30 / Room: 513.

Continuous, Quantitative, Molecular Monitoring of a Near Infrared Fluorophore Using a Novel, Microfabricated, Implantable Biosensor

N Parashurama[1], TD O'Sullivan[2], A de la Zerda[1], O Levi[3], JS Harris[2], SS Gambhir[1]
Departments of [1]Radiology, [2]Electrical Engineering, Stanford University, CA, USA; [3]Institute of Biomaterials and Biomedical Engineering, Electrical and Computer Engineering, University of Toronto, ON, Canada.

Current approaches to detect fluorescence in anesthetized subjects utilize CCD cameras and generally take snapshots of a particular molecular process. Alternatively, continuous molecular monitoring in a freely moving subject would be useful in preclinical disease models for monitoring drug delivery, stem cell growth, and metastases. With these objectives in mind, we fabricated a novel cylindrical device (8mm diameter) containing a 1.5mW, 670nm vertical-cavity surface-emitting laser (VCSEL), un-cooled Gallium Arsenide photodiode, an integrated collimation lens, and a commercially available fluorescence emission filter. The field of view was (3x3x3 mm), and for Cy5.5 dye, the in vitro sensitivity was 100nM (R2= 0.891), with signal saturation at 30μM. The in vivo sensitivity curve was linear (R2= 0.856) and correlated well with CCD camera data (R2=0.99), and the in vivo sensitivity was 1μM. We then utilized this device in a glioblastoma (U87 cell line) tumor xenograft model in nude mice in which Cy5.5-RGD specifically binds to integrin receptors on tumor cells. After tail-vein injection of Cy5.5-RGD (50μM in 50μl), the signal was background corrected, and signal to noise ratio was 23.69 ± 2.73 in tumors and 7.59 ± 1.39 in non tumor tissue. This data was statistically significant (P<0.018, N=2 mice). This agreed with the specificity of RGD-Cy5.5 uptake in tumors versus control tissue. Furthermore, we were able to continuously monitor probe uptake, and compare kinetics between mice. We found that the 90% of the max signal occurs at 13.27 ± 4.11 minutes (N=3 mice). Lastly, we demonstrated intraperitoneal (IP) injection of the Cy5.5-RGD (50μM in 50μl) resulted in a delayed 90% of the max signal (approximately 55 minutes) when compared to tail vein injection (approximately 13 minutes). This is the first demonstration of using a VCSEL for the detection of a molecular probe and is a proof-of-principle that should allow expansion of this technology for implanting sensors in freely moving subjects.

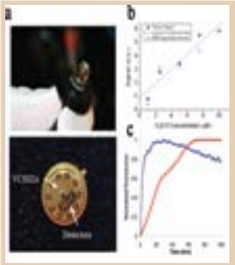

Integrated biosensor for continuous sensing a) Top Panel- The VCSEL (vertical cavity surface emitting laser) and detector integrated sensor device Bottom Panel- The microfabricated in integrated sensor design with laser and detector on same chip c) The sensor detecting Cy5.5 dye in a live mouse d) Kinetic sensing data demonstrating increased signal after IV injection of RGD-Cy5.5 for two different sensors within one tumor, and control site away from tumor.

Molecular Imaging of Oncogene Targeted Cancer Therapy

H Fan-Minogue[1,2], R Paulmurugan[1,2], CT Chan[1,2], Z Cao[3], DW Felsher[3], SS Gambhir[1,2]
Departments of [1]Radiology, [2]Radiology, MIPS, [3]Medical Oncology, Stanford University, CA

Oncogene signaling pathways have been identified as essential for cancer progression and regression and are hence considered attractive candidates for targeted cancer therapy. We developed for the first time a bioluminescent sensor system that can detect in living animals the activation of the cytoplasmic MYC (c-Myc) oncogene. This sensor system utilizes protein-assisted complementation of split firefly luciferases (Nfluc 398/Cfluc 394) that are fused to a specific phosphorylation motif in the Myc Box I and a selected phospho-recognition domain in GSK3β respectively, to report phosphorylation dependent c-Myc activation and interaction with GSK3β. Extensive optimization and validation of the sensor system has been done ex vivo to achieve optimal sensitivity and selectivity. The optimal sensors showed more than a two-fold signal reduction when the phosphorylation site of the sensor was abolished, and complete signal recovery with slight increase ($p<0.05$) when there was a constitutively phosphorylated site. In SK-BR-3 breast cancer cells, the sensor signal was more than four-fold higher than that in CHO normal cells ($p<0.05$), which correlated ($R2=0.98$) with the endogenous phosphorylation status of c-Myc in those cells. Upon inhibition of c-Myc signaling by Atovarstatin (AT) (0μM to 50μM), which efficiently prevents MYC phosphorylation induced lymphomagenesis, the SK-BR-3 stable cells expressing the sensor system showed a dose dependent signal reduction that correlated with the endogenous c-Myc phosphorylation ($R^2=0.99$), but not those expressing the full length firefly luciferase. In vivo, mouse xenografts (N=4) of SK-BR-3 sensor stable cells treated intra-tumorally with AT (250mM) already showed 20% and 50% signal reduction at the 8th and 13th day respectively of the treatment compared to those treated intra-tumorally with PBS, which is significantly prior to the detectable difference in tumor size (20 days after treatment). This sensor system may provide an important way to not only monitor therapeutic activity of oncogene targeted drugs in vivo, and thus facilitate cancer drug development, but also detect and assess cancer response to therapy at earlier time points.

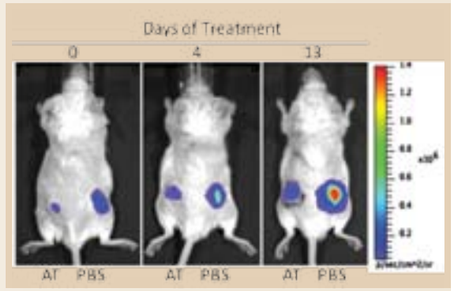

References/Funding Poster Session 1c: Therapy including Drug Therapy, September 24, 2009 / 16:00-17:30 / Room: 514. Bayer Schering.

A Novel Strategy for Repetitive, Non-invasive Monitoring of the Efficacies of Histone Deacetylase 6 (HDAC6) Inhibitors in Living Subjects

CT Chan[1], JE Bradner[2], RE Reeves[1], SL Schreiber[3], R Paulmurugan[1], SS Gambhir[1]
Department of [1]Radiology, Stanford University, CA; [2]Hematologic Oncology, Dana-Farber Cancer Institute, Boston, MA; [3]Chemistry and Chemical Biology, Harvard University, MA.

Heat Shock Protein 90(Hsp90)/p23 interactions are crucial for proper folding of proteins in cancer and neurodegenerative diseases. Hsp90 and HDAC6 inhibitors block Hsp90(α/β)/p23 interactions by preventing ATP binding and leading to hyperacetylation of Hsp90,respectively. A split Renilla Luciferase complementation system [Cancer Res 68:216-26] was used for indirect monitoring of Hsp90(α/β)/p23 interactions by bioluminescence imaging (BLI) in cell culture and living mice in response to different HDAC inhibitors. Class II (APHA & Trichostatin) and HDAC6 inhibitors (Tubacin[Tuba] & WT161) led to disruption of Hsp90(α/β)/p23 interactions and increased expression of $p21^{waf1}$ and acetylated α-tubulin (act-αtub). Their efficacies were enhanced by the addition of the Hsp90 inhibitors PUH71/17DMAG. HDAC1 inhibitor MS275 and the control compound Niltubacin had no effect on Hsp90/p23 interactions (Fig.1A) nor the expression of $p21^{waf1}$ and act-αtub. The efficacy of Tuba in disruption of Hsp90/p23 interactions in living mice were evaluated by BLI (Fig.1B). Relative to 0 hr, BLI signals in mice treated with Tuba (25 mg/kg,23 hrs) were 33±14% and 70±11% of Hsp90α/p23 and Hsp90β/p23 interactions, respectively ($p< 0.05$ compared to respective carrier control treated mice)[Fig. 1B]. Combination of Tuba with PU-H71 led to further reduction in Hsp90(α/β)/p23 interactions. The efficacy of Tuba was confirmed by increased expression of act-αtub in excised tumors. Non-invasive monitoring of the efficacy of HDAC inhibitors, alone in combination with Hsp90 inhibitors will significantly accelerate the development of HDAC6 inhibitors and combinatorial therapies.

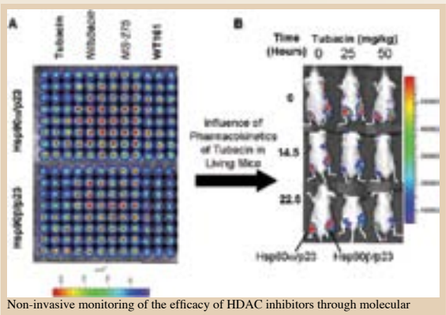

Non-invasive monitoring of the efficacy of HDAC inhibitors through molecular imaging of the disruption of Hsp90(α/β)/p23 interactions in cell culture and in living mice. A. 293T cells stably expressing Hsp90(α/β)/p23 split RL reporters were treated with HDAC6 inhibitors Tubacin and WT161 or HDAC1 inhibitor MS275 or the control Niltubacin for 24 hours prior to BLI. B. The efficacy of Tubacin in disruption of Hsp90(α/β)/p23 interactions in living mice were monitored by repetitive BLI upon injection of the RL substrate coelentarazine.

References/Funding Poster Session 3c: Therapy including Drug Therapy, September 26, 2009 / 16:00-17:30 / Room: 514. Bayer Schering.

Clinical-grade [^{18}F]FPPRGD2: An Automated Multi-step Radiosynthesis for Human PET Studies

FT Chin, B Shen, S Liu, RA Berganos, E Chang, E Mittra, X Chen, SS Gambhir
Department of Radiology, Stanford University, CA

Introduction. In positron emission tomography (PET) imaging, radiolabeled RGD-peptides are one of the most promising radiotracers for noninvasive imaging of $\alpha_v\beta_3$ expression for potential applications in tumor staging, monitoring response to therapy, and characterizing metastatic potential. Here we report a reliable, routine and automated radiosynthesis of a new clinical-grade ^{18}F-RGD-peptide tracer ([^{18}F]FPPRGD$_2$) which is formed by conjugating 4-nitrophenyl-2-[^{18}F]fluoropropionate ([^{18}F]NPE) as a prosthetic group with the PEG$_3$-E[c(RGDyK)]$_2$ peptide and was evaluated both in mouse and human. Experimental. Optimized radiochemistry was performed in a GE TRACERLab FX$_{FN}$ synthesis module with a customized module (CM). [^{18}F]NPE was prepared [1] and purified by prep-HPLC. [^{18}F]NPE fraction was transferred into the CM and processed with a C-18 SPE cartridge. Trapped [^{18}F]NPE was eluted with Et_2O and passed through a Na_2SO_4 drying cartridge. Et_2O was removed by He stream and then a peptide solution (2 mg/200 μL DMSO/40 μL DIPEA) was added to the vial containing dried [^{18}F]NPE. Peptide mixture was heated at 60 ˚C for 20 min, acidified, and then purified by prep-HPLC. Formulated [^{18}F]FPPRGD$_2$ was sterile-filtered and then analyzed for quality control. Imaging with clinical-grade [^{18}F]FPPRGD$_2$ in mouse and human were completed by microPET and human PET scanners. Results and Discussion. All radiochemical yields (RCY ± SD) are decay-corrected to end-of-bombardment. After 170 min radiosynthesis, [18F]FPPRGD2 afforded consistent RCYs (14.4 ± 2.8%; n = 5) with specific radioactivity of 900 ± 257 mCi/μmol (33.3 ± 9.5 GBq/μmol). High radiochemical and chemical purities exceeded 99% via HPLC analysis. As a better alternative to traditional rotavaporation alone (9.9 ± 2.8%, n = 3), more [^{18}F]NPE is available for peptide coupling when the SPE process uses Et_2O and a Na_2SO_4 cartridge (91.8 ± 2.6%, n = 9) followed by gentle evaporation of Et_2O with a He stream in the CM. The Na_2SO_4 cartridge gave higher coupling yields (79.3 ± 8.5%, n = 9 vs. without cartridge 30 ± 35%, n = 3) since residual moisture was removed after SPE processing of [^{18}F]NPE. PET imaging in mouse (Normal/Tumor-xenografted*: bladder>>kidneys>gut/liver>>tumor*/brain/feces) and initial biodistribution studies in human have been done. Conclusion. A multi-step radiosynthesis of clinical-grade [^{18}F]FPPRGD$_2$ was implemented in a commercial automated synthesis module with a CM to provide the tracer routinely for animal/clinical PET studies.

References/Funding [1] Guhlke, S. et. al. (1994) Appl. Radiat. Isot. 45, 715-727.

Enhanced Ultrasound-Mediated Gene Delivery with Cationic Microbubbles in a Mouse Model of Tumor Angiogenesis

DS Wang[1], MA Pysz[1], R Paulmurugan[1], C Panje[1], SS Gambhir[1], M Schneider[2], JK Willmann[1]
Department of [1]Radiology, MIPS, Stanford University, CA, USA; [2]Bracco Research SA, Switzerland

Sonoporation with ultrasound (US) and microbubbles (MBs) is a promising strategy for efficient gene therapy. While maintaining US contrast properties, MBs may be modified into vehicles for therapeutic delivery. This study sought to determine whether novel cationic MBs, which directly bind DNA through charge interactions, would enhance US-mediated gene delivery (UMGD) in a mouse model of tumor angiogenesis.

By varying shell composition, cationic (zeta potential +28mV) and control neutral MBs were produced. Plasmids encoding for red shifted click beetle luciferase (CBluc) driven by a CMV promoter were charge coupled with cationic MBs and used for in vitro UMGD in SVR cells, an angiosarcoma-like cell line. Luciferase activity was evaluated in 24hrs. To establish mouse models of tumor angiogenesis, SVR cells were implanted subcutaneously in nude mice hindlimbs. Regional in vivo UMGD was performed by insonation (2W/cm2, 50% duty cycle, 5min) of tumor xenografts after tail vein administration of plasmid-bearing cationic MBs. CBluc expression was assessed 12, 24, 36, and 48hrs following UMGD.<p>SVR cells transfected by UMGD with cationic MBs expressed luciferase in vitro. As shown in the table and figure, in vivo CBluc activity of tumor-bearing hindlimbs was significantly increased at 12, 24, 36, and 48hrs ($P<0.05$, all time points) in mice who received US and cationic MBs ($N=7$) relative to those who received US and neutral MBs ($N=4$), US but no MBs ($N=4$), and cationic MBs but no US ($N=4$). In vivo expression was validated ex vivo.

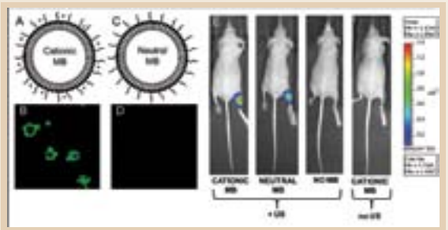

Figure 1: Representative images of CBluc expression in hindlimb tumor xenografts 36hrs after UMGD using A) cationic, B) neutral, and C) no MBs. For negative control D), mice received cationic MBs but no US. Figure 2: †P<0.05 vs B to D

Cationic MBs enhance UMGD in a mouse model of tumor angiogenesis. These MBs may be further modified for molecular targeting, providing a promising theranostic approach for targeted gene delivery and imaging of tumor neovasculature.

References/Funding Poster Session 2d: Development/Novel Use of Imaging Probes, September 25, 2009 / 16:00-17:30 / Room: 516.

Affibody Based Molecular Probes for EGFR PET and Optical Imaging

Z Miao[1,2], G Ren[1,2], L Jiang[1,2], H Liu[3,2], Y Wang[1,2], Z Cheng[1,2], SS Gambhir[2,1]
Departments of [1]Radiology, [2]Radiology, MIPS, Stanford University, CA, USA; [3]Institute of Radiation Medicine, Peking Union Medical College, China

The purpose of this study is to site-specifically label an Affibody protein (Ac-Cys-ZEGFR:1907) binding to epidermal growth factor receptor (EGFR) with Cy5.5 and 64Cu-DOTA , investigate its in vitro cell uptake and binding specificity, study Cy5.5-ZEGFR:1907 and 64Cu-DOTA-ZEGFR:1907 in vivo tumor imaging ability, and evaluate the potential of EGFR PET imaging with 64Cu-DOTA-ZEGFR:1907 for clinical translation. Methods: Molecular probe Cy5.5-ZEGFR:1907 and 64Cu-DOTA-ZEGFR:1907 were made through solid peptide phase synthesis of Ac-Cys-ZEGFR:1907 followed by site-specific conjugation with Cy5.5-mono-maleimide and DOTA-mono-maleimide respectively. DOTA-ZEGFR:1907 was then labeled with 64Cu in sodium acetate buffer (pH=5.0) at 40 oC. Cell uptake assay was performed using EGFR expression A431 cell line (cervical cancer cell line) with/without pre-incubation of unlabeled Ac-Cys-ZEGFR:1907 for blocking. Cy5.5-ZEGFR:1907 (500pmol) or 64Cu-DOTA-ZEGFR1907 (40-70 μCi) was injected into A431 tumor bearing nude mice through tail-vein for optical imaging and microPET imaging respectively. Bio-distribution studies were performed at 1, 4 and 24 hours post-injection (p.i.). Results: In vitro microscopy study showed that majority of Cy5.5-ZEGFR:1907 specifically bound to A431 cell surface in 1 h. Optical imaging of Cy5.5-ZEGFR:1907 successfully demonstrated EGFR receptor mediated targeting to A431 tumor. For radiolabeled probe, it displayed high (27% at 1 h) and specific in vitro cell uptake. In vivo microPET imaging showed high tumor accumulation (> 10 %ID/g at 4 h p.i.) and good contrast of 64Cu-DOTA-ZEGFR:1907. Bio-distribution studies demonstrated that 64Cu-DOTA-ZEGFR:1907 had high tumor uptakes, and also high blood, liver and kidney uptakes, while kidney and blood uptake dropped significantly 24 h p.i.. Conclusions: Cy5.5 and 64Cu labeled ZEGFR:1907 can provide high sensitivity, receptor specific optical and PET imaging of EGFR positive tumors. 64Cu-DOTA-ZEGFR:1907 is mainly clearly through kidney-urinary system. Three-helix Affibodies are excellent protein scaffolds for the development of PET probes for clinical translation.

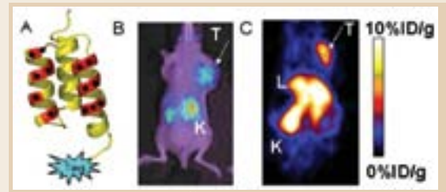

Three-helix Affibody based probe ^{64}Cu-DOTA-$Z_{EGFR:1907}$ and Cy5.5-ZEGFR:1907 for EGFR PET and optical imaging. (A) Cartoon of Affibody based probes, the black dots and red regions indicate the amino acid residues responsible for receptor binding. Optical (B) and microPET imaging (C) of a mouse bearing A431 tumor xenograft at 2 h p.i.. Arrows were pointed at tumors. T, tumor; L, liver; K, kidney.

References/Funding Bayer Schering, Poster Session 2d: Development/Novel Use of Imaging Probes, September 25, 2009 / 16:00-17:30 / Room: 516.

An 18F-Labeled Knottin Peptide for Tumor αvβ3 Integrin PET Imaging

Z Miao[2,1], G Ren[2,1], L Jiang[2,1], R Kimura[4,3], JR Cochran[4,3], Z Cheng[2,1], SS Gambhir[2,1]
Departments of [1]Radiology, [2]Radiology, MIPS, [3]Bio-X program, [4]Bioengineering, Stanford University, CA

Knottins are small constrained polypeptides that share a common disulfide-bonded framework and a triple-stranded beta-sheet fold. Our objectives were to: 1) site-specifically label an integrin αvβ3 binding knottin peptide, 2.5D, with 18/19F, 2) characterize 18F labeled 2.5D (18F-FB-2.5D) in living subjects with microPET imaging methods, and 3) evaluate the translational potential of 18F-FB-2.5D. Methods: 2.5D was prepared by solid phase synthesis and oxidized using glutathione. 2.5D was reacted with N-succinimidyl-4-18/19F-fluorobenzoate (18/19F-SFB) in DMSO at 60 oC. Competition binding assays were performed with human glioblastoma U87MG cells using 125I-labeled echistatin. Approximately 100 uCi 18F-FB-2.5D, with and without a molar excess of c(RGDyK), was injected via the tail vein of U87MG tumor bearing mice for microPET imaging performed at 0.5 h, 1 h post-injection (p.i.) In addition, biodistribution studies were conducted at 0.5 h p.i. Finally, dynamic microPET scanning for a 35 min p.i. duration was also performed. Results and Conclusions: 19F-FB-2.5D competed with 125I-echistatin for binding to cell surface integrins with an IC50 of 162 ± 21 nM. Radiofluorinated 2.5D displayed a high specific activity (75-100 GBq/μmol) throughout the course of our studies. In vivo microPET imaging showed that the radiotracer rapidly accumulated at the tumor (2.7%ID/g, n=3), and also rapidly cleared through the kidneys. These pharmacokinetics leads to promising tumor-to-normal tissue contrast (Figure1). Biodistribution studies demonstrated that 18F-FB-2.5D had moderate tumor uptakes at 0.5 h p.i. and that co-injection of c(RGDyK) significantly reduced tumor uptake (1.90 ± 1.15 %ID/g vs 0.57 ± 0.14 %ID/g, 70% inhibition, $P<0.05$). Dynamic scanning showed high kidney uptake at early time points (51.8 %ID/g at 4 min p.i.), followed by rapid clearance within a half an hour (6.2 %ID/g at 35 min p.i.), Finally, the probe displayed relatively low uptake in the liver (1.5 %ID/g at 35min p.i.). Collectively, knottins are excellent peptide scaffolds for development of PET probes for clinical translations.

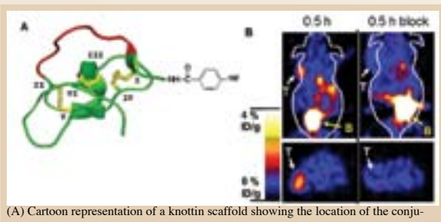

(A) Cartoon representation of a knottin scaffold showing the location of the conjugated radiolabel. The loop that was mutated for integrin binding is indicated in red. (B) The coronal and transaxial microPET images of U87MG tumor-bearing mice at 0.5 h after injection of 18F-FB-2.5D with or without c(RGDyK) co-injection. Tumor(T) and Bladder(B) are indicated by arrows.

References/Funding Bayer Schering, Poster Session 2d: Development/Novel Use of Imaging Probes, September 25, 2009 / 16:00-17:30 / Room: 516

A Novel Synthesis of 2'-Deoxy-2'-[^{18}F]fluoro-9-β-D-arabino-fluranosylguanine ([^{18}F]F-AraG), for Imaging T Cell Activation with PET

M Namavari[1], Y-F Chang[1], B Kusler[1,2], S Yaghoubi[1], BS Mitchell[1,2], SS Gambhir[1]
Departments of [1]Radiology and [2]Medicine/Oncology, Stanford University, CA

2'-Deoxy-9-β-D-arabino-furanosylguanine (AraG) is a guanosine analog that has proven efficacy in the treatment of T cell lymphoblastic disease. It is metaboloized in a unique fassion by deoxyguanosine kinase and incorporated into mitochondrial. Also, 2'-deoxy-2'-fluoro-9-β-D-arabino-furanosylguanine (F-AraG) is known to exhibit selective T-cell toxicity. We were therefore intersted in the synthesis of 2'-deoxy-2'-[^{18}F]fluoro-9-β-D-arabino-furanosylguanine ([^{18}F]F-AraG) as a novel PET imaging agent. We report for the first time the synthesis of ([^{18}F]F-AraG) as an imaging agent. The partially protected 2-N-acetyl-6-O-((4-nitrophenyl)ethyl)guanosine derivative 1 was converted to 3',5'-di-O-trityl (2) and 2',5'-di-O-trityl (3) derivatives. Trityl derivatives 2 and 3 were separated on a silica gel column. Treatment of trityl derivative 2 with CF_3SO_2Cl/DMAP afforded 2-N-acetyl-6-O-((4-nitrophenyl) ethyl)-9-(3',5'-di-O-trityl-2'-O-trifyl-β-D-ribofuranosyl)guanine (4, 65%) as a precursor for([18F]F-AraG. [^{18}F]F-AraG was prepared from precursor 4 in 8-12 % radiochemical (decay corrected). The specific activity ranged 0.6-1.3 Ci/μmol. The synthesis utilizes the reaction between the leaving group triflate in 4 and anhydrous [^{18}F]KF/Kryptofix 2.2.2 at 85 oC for 40 minutes to produce 2-N-acetyl-6-O-((4-nitrophenyl)ethyl)-9-(3',5'-di-O-trityl-[^{18}F]-2'-fluoro-β-D-arabinofuranosyl)guanine (5). Finally, acid hydrolysis of 5 produces the final [^{18}F]F-AraG. Preliminary cell uptake experiments indicate that the CCRF-CEM cell line and activated primary thymocytes take up the [^{18}F]F-AraG. Competition assays show that the cold derivative F-AraG competes with the uptake of 8-[3H]-AraG, indicating similar uptake pathways. In conclusion, for the first time to our knowledge, [^{18}F]F-AraG has been successfully synthesized by direct fluorination of an appropriate precursor of a guanosine nucleoside. This approach also maybe useful for the synthesis of other important PET probes such as [^{18}F]FEAU, [^{18}F]FMAU and [^{18}F]FBAU which currently are synthesized by multiple steps and involved lengthy purification processes.

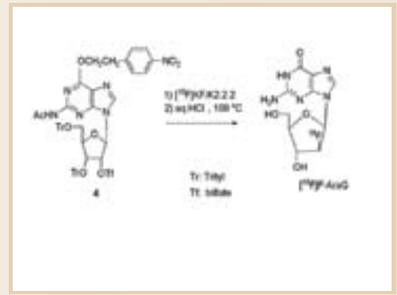

References/Funding Bayer Schering, Poster Session 1d: Development/Novel Use of Imaging Probes, September 24, 2009 / 16:00-17:30 / Room: 516.

111In-Labeled Agouti Related Proteins for SPECT/CT Imaging of Tumor αvβ3 Integrin

L Jiang[1,2], Z Miao[1], R Kimura[1], G Ren[1], H Liu[1], AP Silverman[1], P Li[2], SS Gambhir[1], JR Cochran[1], Z Cheng[1]
Departments of [1]Radiology, MIPS, Stanford, CA, USA; [2]Department of Nuclear Medicine, Ruijin Hospital, Shanghai, China

Agouti-related protein (AgRP) is a 4-kDa cystine-knot peptide of human origin with four disulfide bonds and four solvent exposed loops that are amenable to directed evolution. By replacement of a six amino acid loop in AgRP with a nine amino acid loop containing an RGD motif, engineered AgRP mutants that bind to αvβ3 integrin with high affinity and high specificity have been discovered. In this study, the AgRP mutant 7C was labeled with 111In and used for SPECT/CT imaging of αvβ3 integrin expression in living subjects. Methods: AgRP 7C was synthesized using solid-phase peptide synthesis and an oxidative folding reaction. 1, 4, 7, 10-tetra-azacyclododecane-N, N', N'', N''' -tetraacetic acid (DOTA) was site specifically coupled to the N-terminus of the peptides. Receptor competition binding assay was then performed to measure the αvβ3 integrin binding affinity of the resulting bioconjugate. Radiolabeling of DOTA-7C was achieved by incubating the peptide with 111InCl3 in NaOAc buffer (pH 5.5) at 80 oC for 45 min. Biodistribution and microSPECT/CT imaging studies were then performed to evaluate the in vivo performance of the probes using mice bearing U87MG xenografts. Results: DOTA-conjugated AgRP 7C displayed high αvβ3 integrin binding affinity (nM range), and was easily labeled with 111In in high yield and purity (>99%). Moreover, this SPECT probe exhibited excellent stability in PBS buffer (pH 7.4) and mouse serum. 111In-DOTA-7C showed good U87MG tumor uptake (5.74±1.60 and 1.17±0.21 %ID/g at 0.5 and 24 h, respectively). High tumor-to-normal organ ratios were also obtained for this probe (25.8 and 39.8 at 2 h for tumor-to-blood and tumor-to-muscle, respectively). The tumor uptake of 111In-DOTA-7C could also be specifically inhibited by co-injection with large excess of the αvβ3 integrin-binding peptide c(RGDyK). Finally, excellent and specific tumor imaging of 111In-DOTA-7C was also demonstrated by small-animal SPECT/CT imaging at 1 h after injection. Conclusion: AgRP peptide 7C labeled with 111In exhibited high tumor uptake, demonstrating great potential for SPECT/CT imaging of αvβ3 integrin expression in living subjects.

References/Funding Bayer Schering, Poster Session 1d: Development/Novel Use of Imaging ProbesSeptember 24, 2009 / 16:00-17:30 / Room: 516

Intravital Molecular Imaging of the Birth of a Tumor From Cancer Stem Cells Using Intravital Microscopy

N Parashurama[1], N Lobo[2], MF Clarke[2], SS Gambhir[1]
Departments of [1]Radiology, MIPS and [2]Institute for Stem Cells and Regenerative Medicine, Stanford University, CA

Despite phenotypic enrichment of breast cancer stem cells (CSC), the early detection of breast cancer by targeting CSC remains elusive. We hypothesized that incorporating imaging into CSC assays could provide novel insights into the early mechanisms of tumor initiation from CSC. Furthermore, we reasoned that imaging CSC can be done in the adult, postnatally developing mammary gland, and regenerating mammary gland after transplantation. To image the 4th adult mammary gland, a surgical flap was created and stabilized in an anesthetized, transgenic, virgin, BL6 eGFP (and DsRed) female mouse in which mammary ducts express high levels of fluorescent protein. Mammary ducts and lobules could be visualized with 4, 10, and 20x objectives in both adult (N=10) and developing (age= 3- 4.5 weeks, N= 4) eGFP+ mice. This technique, which utilizes a multichannel intravital microscope, has a spatial resolution of approximately 1 µm, and depth penetration of approximately 150µm. Furthermore, vascular structures, ranging

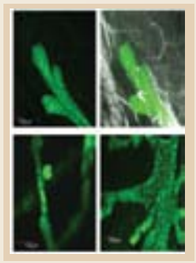

from 1-500µm, were imaged using a fluorescent (750nm) intravascular dye (N=5 mice). To image regenerating mammary ducts, 50,000 cells of an eGFP+, Lin- population, which contains rare mammary stem cells, were transplanted into the cleared fat pads of wild type hosts. Regenerating glands were repetitively imaged at 8 and 12 weeks after transplantation (N=5). Importantly, cellular structures in living subjects could be resolved for the first time in all systems. Furthermore, we imaged 5000 Lineage-, CD44+, human breast CSC that had been lentivirally transduced with reporter gene expressing tomato fluorescent protein, and transplanted into the mammary fat pad of NOD-SCID mice for 10 days. Having established these systems, we will image single CSC, in both mouse and humans, and corresponding changes in microvasculature in tandem. These approaches should markedly change our understanding of breast tumor development in living subjects, and advance the early detection of, or early therapeutic targeting of CSC.

Immobilized Activatable Bioluminescent Probes for In Vivo Imaging of Protease Activity in Tumors

J Rao, Z Xia
Department of Radiology, Stanford University, CA

We report here a novel strategy for in vivo imaging of enzyme activity at tumor, which provides a powerful tool for in vivo study the roles of enzymes in tumor biology and dynamic imaging of tumor response to drug treatment. In previous examples, fluorescent activatable probes are designed to image enzymes particularly proteases. One of the concerns with these examples is whether the enhanced fluorescence signal observed in tumors all came from the enzyme activation at the tumors or some came from enzymes at other locations but accumulated at the tumors due to the enhanced permeation effect (EPR). In addition, in spite of the amplification feature of the design, the observed contrast in vivo is generally small in these examples. In this presentation, we describe an immobilized activatable bioluminescent probe that we believe is able to truly image the extracellular protease activity in vivo. First, we took advantage of bioluminescence resonance energy transfer and generated a chemically quenched bioluminescent protein the conjugation with small chemical dyes. Protease cleavage led to the release of the quencher from the protein and thus the activation of the emission from the bioluminescent protein. This bioluminescence based detection offers a much greater sensitivity than the fluorescence based imaging. Furthermore, to ensure that the activated protein does not travel within the body and get accumulated into the tumors, we further fused the probe with the collagen binding protein. The binding of the probe to the abundant collagens restrained the probe mobility so the enzyme activated signals precisely reflect the local enzyme activity at tumor (Figure 1). With the designed probe, we were able to image the MMP activity exclusively in tumors with high sensitivity. Our approach opens a new avenue for study enzyme functions in vivo, which may have a significant impact on cancer research and tumor treatment.

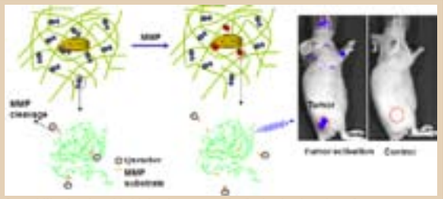

Immobilized activatable bioluminescent probe for in vivo imaging of enzyme activity. Bioluminescent proteins are chemically quenched with small dyes but can be activated by protease cleavage to restore the emission. Furthermore, the probe is fused to a collagen binding protein so it is immobilized at the extracellular matrix. MMP activity can thus be locally mapped and imaged.

References/Funding Poster Session 1d: Development/Novel Use of Imaging Probes, September 24, 2009 / 16:00-17:30 / Room: 516

Engineering Attenuated Salmonella Typhimurium to Selectively Target and Deliver Protein in Infarcted Myocardium

UN Le[1], J-S Kwon[2], VH Nguyen[1], HS Kim[3], SN Jiang[1], Y Hong[4], MG Shin[5], JH Rhee[4], H-S Bom[1], SS Gambhir[6], Y Ahn[2], HE Choy[4], J-J Min[1,7]
Departments of [1]Nuclear Medicine, [2]Cardiovascular Medicine, [3]Forensic Medicine, [4]Microbiology, [5]Laboratory Medicine, Chonnam National University Medical School, South Korea; [6]MIPS, Department of Radiology & Bioengineering, Bio-X Program, Stanford University, CA, USA; [7]Bioimaging Research Center, Gwangju Institute of Science and Technology, South Korea

Gene-based therapeutic approaches offer a potential strategy to redress myocardial dysfunction for the patients with refractory angina despite conventional medical or surgical treatment. Optimizing the specific affinity of the cardiac vectors would improve the efficiency of gene/protein delivery, and reduces unwanted transfection of non-cardiac tissues. However, none of the cardiac vectors so far have specificity for the infarcted myocardium. In this study, we explored bacterial tropism for infarcted myocardium. We constructed a Salmonella typhimurium defective in ppGpp synthesis to express and secrete the reporter gene (RLuc8) by the regulation of an inducible P_{BAD} promoter. A bacterial expression plasmid encoding a variant of Renilla luciferase (RLuc8) was constructed, in which the pelB leader sequence and a histidine tag (6x His) were fused to the amino- and carboxy-terminus, respectively, of RLuc8. An occlusion at the left coronary artery generated the myocardial infarction (MI) in the left ventricle of Sprague-Dawley rats. $2x10^8$ cfu of the Salmonellae were intravenously injected and bacterial tropism for MI was observed by cooled CCD camera. To assess the systemic or local toxicity after bacterial injection, we measured C-reactive protein and procalcitonin in the rats' serum and measured infarct size by TTC staining before and after bacterial injection. The Salmonella were found to accumulate in infarcted myocardium. RLuc8 gene delivered by the engineered Salmonellae was expressed and its translated product was secreted specifically in the infarcted myocardium under the stringent control of the P_{BAD} promoter after L-arabinose administration. No sign of serious local or systemic inflammatory reactions was noted following intravenous administration of attenuated Salmonella. Thus, MI-targeting bacteria can potentially deliver therapeutic molecules to salvageable myocardium. Taken together, the development of MI-targeting bacteria opens many new avenues for molecular imaging and therapy, including tissue-specific targeting with signal amplification based on bacterial proliferation, in vivo tissue-specific drug delivery, and the design of imageable therapeutic probes.

NIR Fluorescence Imaging of Melanocortin 1 Receptor Expression with A Cy5.5-α-MSH Analog

H Liu[1,2], G Ren[1], Z Miao[1], P Han[2], SS Gambhir[1], Z Cheng[1]
Department of [1]Radiology, MIPS, Bio-X Program, Stanford University, CA, USA; [2]Institute of Radiation Medicine, Chinese Academy of Medical Sciences, Peking Union Medical College, Tianjin, China.

The α-melanocyte-stimulating hormone (α-MSH) receptor (melanocortin type 1 receptor, or MC1R) is known to be overexpressed in most of murine and human melanoma, making it a promising molecular target for melanoma imaging and therapy. The purpose of this study was to evaluate a near-infrared fluorophore, Cy5.5 conjugated α-MSH analog (CyMSH, Fig.a), as a contrast agent to visualize tumor MC1R expression in vivo. Methods: α-MSH analog containing α-MSH core sequences, His-D-Phe-Arg-Trp, was designed and synthesized using Fmoc/HBTU chemistry on a solid-phase peptide synthesizer and conjugated with Cy5.5 through the N-terminal cysteine. The binding affinity was determined using a competitive receptor binding assay. Melanoma B16F10, TXM13 and A375M, which has high, medium and low MC1R expression, respectively, were chosen to evaluate the MC1R imaging profiles of CyMSH in vitro and in vivo. Results: CyMSH was successfully synthesized and displayed high MC1R binding affinity (0.6nmol/L). In vitro cell fluorescence imaging study revealed that the probe showed high, medium and low cell staining in B16F10, TXM13 and A375M cell lines, respectively, which was in consistence with their receptor expression levels. Co-incubation the probe with a large excess of the α-MSH peptide NDP specifically inhibited the probe uptakes in B16F10 and TXM13 cells. In vivo optical imaging detected little fluorescence in B16F10 tumor (Fig.b), which was mainly caused by the high melanin content in B16F10 tumor that absorbed nearly all excitation and emission NIR lights. To the contrary, melanoma TXM13 with much less melanin content and medium level of MC1R expression could be clearly visualized with CyMSH (Fig.c). Finally, amelanotic A375M with the lowest MC1R expression showed poor tumor/normal contrast (Fig.d). Conclusion: This study suggests that the combination of the specificity of α-MSH peptide with NIR fluorescence detection may be applied to molecular imaging of MC1R expression in melanoma with low melanin content.

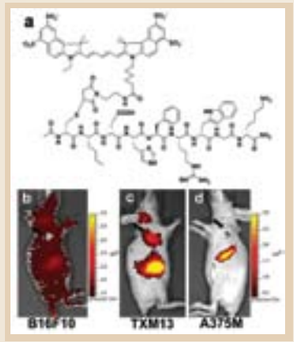

References/Funding Bayer Schering, Poster Session 1d: Development/Novel Use of Imaging Probes, September 24, 2009 / 16:00-17:30 / Room: 516

Preclinical Evaluation of Raman Nanoparticles for Their Potential Use in Clinical Endoscopic Imaging

C Zavaleta, KB Hartman, Z Miao, Z Cheng, SS Gambhir
Department of Radiology, MIPS, Stanford University, CA

Raman spectroscopy continues to prove itself as a powerful non-invasive molecular imaging tool to evaluate nanoparticle delivery in preclinical models. Its pM sensitivity and multiplexing capabilities are unsurpassed. However, its limited depth of light penetration hinders direct clinical translation. Therefore, a more suitable way to harness its attributes in a clinical setting would be to couple Raman spectroscopy with endoscopy. It was recently reported that flat lesions in the colon were five times more likely to contain cancerous tissue than polyps detected by conventional colonoscopy. The use of an accessory Raman endoscope in conjunction with locally administered tumor targeting Raman nanoparticles during a routine colonoscopy could offer a new way to sensitively detect these dysplastic flat lesions. In this study we evaluated the natural biodistribution of gold surface enhanced Raman scattering (SERS) nanoparticles by radiolabeling them with ^{64}Cu and imaging their localization over time using microPET. Mice were injected either intravenously (IV) or intrarectally (IR) with approximately 100 μCi of ^{64}Cu-SERS nanoparticles and imaged with microPET at various time points: immediately, 30 m, 2, 5, and 24 h post injection. Three mice from each group (IV and IR) were sacrificed at 2, 5 and 24 h and their organs were collected, weighed and counted in a gamma counter to determine % injected dose per gram (%ID/g). Quantitative biodistribution data obtained from each organ correlated well with the corresponding microPET images, revealing that mice injected IV had significantly higher uptake ($p<0.05$) in the liver (5h=18.9% ID/g) (24h=4.8% ID/g), as opposed to mice injected IR (5h=1.27% ID/g) (24h=0.3% ID/g). Mice injected IR showed localized uptake in the large intestine (5h=9% ID/g) (24h=4.3% ID/g) with minimal uptake in other organs. Raman imaging of the excised tissues confirmed the presence of SERS nanoparticles within tissues of interest. These results suggest that topical application of SERS nanoparticles in the colon appears to minimize their systemic distribution, thus avoiding potential toxicity and supporting the clinical translation of Raman spectroscopy as an endoscopic imaging tool.

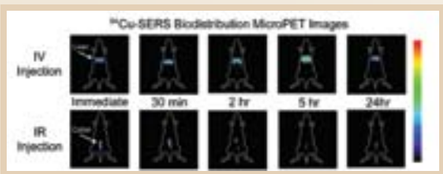

MicroPET imaging in mice after either intravenous (IV) or intrarectal (IR) administration of Cu-64 labeled SERS nanoparticles at various time points post injection. The SERS nanoparticles appear to localize in the liver immediately after IV injection and remain in the liver over 24 hours whereas the SERS nanoparticles injected IR remain localized in the colon over 24 hours. Colored scale bar to right represents Cu-SERS uptake where red represents most uptake and black represents no uptake.

References/Funding Bayer Schering, Poster Session 3d: Development/Novel Use of Imaging Probes, September 26, 2009 / 16:00-17:30 / Room: 516

Gd-encapsulated Porous Polymersomes as Highly Efficient MRI Contrast Agents

Z Cheng, DL Thorek, A Tsourkas
Department of Bioengineering, University of Pennsylvania, PA

The use of Gd-encapsulated nanovesicles as MR contrast agents has largely been ignored due to the detrimental effects of the slow water exchange rate through the vesicle bilayer on the relaxivity of encapsulated Gd. Here, we describe the facile synthesis of porous polymer nanovesicles that exhibit improved permeability to water flux, high structural stability, and a large capacity to store chelated Gd within the aqueous core. The porous polymersomes, 130 nm in diameter, were produced through the aqueous assembly of the polymers, PEO(1300)-b-PBD(2500) (PBdEO) and PEO(2000)-b-PCL(2700). Subsequent hydrolysis of the caprolactone (PCL) block resulted in a highly permeable outer membrane. To prevent the leakage of small Gd-chelate through the pores, Gd was conjugated to PAMAM dendrimer via DTPA dianhydride prior to encapsulation. As a result of the slower rotational correlation time of Gd-labeled dendrimers, the porous outer membrane of the nanovesicle, and the high Gd payload, the nanovesicles were found to exhibit a relaxivity (R1) of 292,109 mM-1 s-1 per particle. The polymersomes were also found to exhibit low cellular toxicity and a long circulation half-life. Here, the design, assembly, characterization and application of the paramagnetic polymersomes will be presented.

References/Funding Poster Session 2d: Development/Novel Use of Imaging Probes, September 25, 2009 / 16:00-17:30 / Room: 516

Secretory Gaussia Luciferase (sGLUC)-monomeric Red Fluorescence protein (mRFP)-truncated Herpes Simplex Virus Thymidine Kinase (tTK) Triple Fusion Improves Intracellular Luciferase Activity and Enhances its Imaging Applications in Small Animals

R Paulmurugan[1,2], A Sathirachinda[2], BC Ahn[2,3], H Fan-Minogue[1,2], CT Chan[1,2], TF Massoud[4,2], SS Gambhir[1,2]
Departments of [1]Radiology and Bioengineering, Bio-X Program, [2]Radiology, MIPS, Stanford University, CA, USA; [3]School of Medicine, Kyungpook National University, Daegu, South Korea; [4]Radiology, University of Cambridge, Cambridge, United Kingdom

Gaussia luciferase, a bioluminescent photoprotein that uses coelenterazine as its substrate, has potential as a reporter gene for different biological applications. In this study we report that the 16-amino acids (1-16) at the N-terminus of this protein are not only important for the secretory nature of this protein, but are also critical for its rapid maturation and proper functionality. We constructed a series of vectors expressing GLUC fusions and N-terminal truncation/substitution (see Figure) to prove the importance of the secretory peptide, and also to improve its intracellular retention for small animal imaging. The 293T, SKBr3 and CHO cells transfected with these constructs were assayed for GLUC-activity immediately after lysis and, at 2, 5, 12, 24, 48, 72 and 120 hrs post-lysis. The results showed significant improvement in the intracellular activity only from the sGLUC fused to mRFP-tTK (10-fold). The cells transfected with tGLUC, tGLUC-GFP and TK-Leader-tGLUC showed minimal intracellular activity when assayed immediately after lysis (<1.0% of sGLUC), the signal increased over time and stabilized at 72 hr. The activity by tGLUC measured at 72 hr was 120±10-fold higher than the initial activity and was □80% of the sGLUC activity. Tumor xenografts of 293T cells stably expressing tGLUC-GFP, sGLUC-GFP and sGLUC-mRFP-tTK in mice (N=11) were imaged for GLUC, GFP and mRFP signals over time. The imaging results showed no GLUC-signals from the cells transfected with tGLUC-GFP, but showed significant level of fused GFP signal ($p<0.001$). The sGLUC with C-terminal fusions showed a constant intracellular GLUC-signal over time, indicating the importance of the secretory peptide for GLUC-maturation. The enhanced fluorescent signal from GFP and RFP fused to the GLUC, than the corresponding fusions with other bioluminescent reporters, indicates its minimal steric hindrance. In conclusion, we have successfully developed a novel triple fusion that enhances imaging intracellular GLUC protein in small animals.

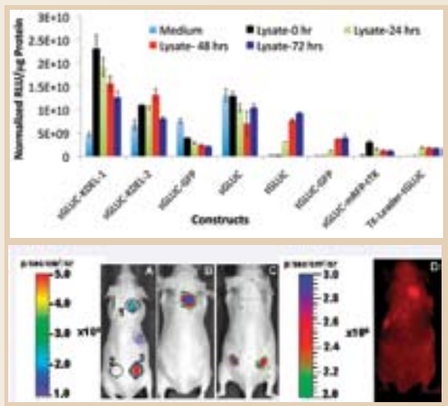

References/Funding Bayer Schering, Poster Session 2f: In Vivo Studies, September 25, 2009 / 16:00-17:30 / Room: 519

The Microscale Journey of Targeted Carbon Nanotubes Imaged Using Intravital Microscopy: from Circulation to Tumor Cells in Living Subjects

BR Smith[1], C Zavaleta[1], Z Liu[2], J Prescher[1], J Ramunas[3], R Tong[4], X Chen[1], H Dai[2], SS Gambhir[1]
Departments of [1]Radiology, MIPS, [2]Chemistry, [3]Neuroscience, [4]School of Medicine, Stanford University, CA.

Though nanoparticles have become invaluable in the molecular imaging toolkit, little is known about the mechanisms by which they target disease sites. To overcome this critical hurdle, we visualized targeted single-walled carbon nanotubes (SWNTs) entering tumor vasculature, specifically binding luminal targets, extravasating from vessels, and binding to tumor cells. To understand the fundamental mechanisms underlying SWNT tumor uptake, we confirmed and correlated our intravital microscopy (IVM) results with macroscopic Raman imaging, which quantitatively detects the SWNTs' intrinsic Raman signal. Targeted SWNTs were prepared by conjugating RGD peptides (targeting αvβ3-integrins expressed on tumor neovasculature and some tumor cells) and Cy5.5 dye. Dorsal chambers were surgically implanted into mice and EGFP-U87MG tumor cells (expressing αvβ3-integrins) or EGFP-SKOV3 were inoculated. 25 mice (U87MG, SKOV-3, no tumor) were imaged with RGD-SWNTs (~60 pmol) and controls. Using IVM and Raman, mice were imaged during injection and frequently during the following month. Unlike controls, RGD-SWNTs were observed to bind tumor blood vessels. Within hours, SWNTs extravasated in U87MG tumor beds, but not in SKOV-3. While both RGD and control SWNTs were observed associated with some tumor cells in U87MG tumors, RGD-SWNTs not only bound more ($P<0.0001$), but they differentially bound tumor cells over time compared with controls ($P<0.007$) and they persisted in tumor for over a month. Control SWNTs cleared within ~1 week. Also, we unexpectedly observed uptake of SWNTs by circulating white blood cells, which subsequently trafficked to tumor; FACS confirmed these results. In summary, IVM allowed detailed exploration of SWNT uptake in tumor, particularly unanticipated features. This work offers unprecedented understanding of the mechanisms/temporal framework of nanoparticle tumor uptake, which will translate into superior properties for clinical use.

(Left) Image taken soon after RGD-SWNTs cleared from vessels (~6 hrs post-injection). Arrows indicate where RGD-SWNTs specifically bound vessels. (Right) Single frame capture chosen from a movie in which SWNT-laden WBCs are moving through tumor blood vessels at ~4 hours post-injection. Arrows designate circulating WBCs.

Direct Microscale Visualization of Targeted Quantum Dot Binding in Multiple Tumor Models of Living Mice using Intravital Microscopy

BR Smith[1], Z Cheng[1], A De[1], AL Koh[2], R Sinclair[2], SS Gambhir[1]
Departments of [1]Radiology, MIPS and [2]Materials Science and Engineering, Stanford University, CA

Targeted nanoparticles have begun to make major contributions in cancer diagnosis and monitoring of therapeutic response. However, comprehension of the mechanisms by which nanoparticles target tumors is critically lacking. Mechanistic insight is essential because it will lead to: 1. Selection of the appropriate diagnostic entity for each disease/disease site 2. Optimization of nanoparticle parameters for superior targeting efficiency, and 3. Regulatory approval for nanoparticle formulations. We employed intravital microscopy to directly image the process of quantum dots (qdots) targeting tumor. In three different tumor models and two animal models, we surprisingly found that targeted qdots bound to tumor blood vessels only as aggregates, rather than as individual units. Further, we showed that in two of the three tumor models tested, qdots did not extravasate. We conjugated cyclic-RGD (targeting αvβ3-integrins localized on tumor blood vessels and some tumor cells) to near-infrared emitting (800 nm) qdots of ~20 nm hydrodynamic diameter. EGFP-SKOV-3, EGFP-LS174T, and EGFP-U87MG cells were implanted into the ears of mice or in surgically implanted dorsal window chambers (DSC) to form tumors. We injected AngioSense dye and ~50 pmol qdots into tail veins of mice to visualize the arrival and binding of qdots to tumor vessels. We observed RGD-conjugated qdot aggregates binding tumor blood vessels significantly ($P<0.001$) more than controls (RAD, RGD-block, bare (no peptide) qdots, and RGD-qdots in normal mice) in all tumor models. Interestingly, binding occurred more in the SKOV-3 DSC condition than in any other. We also showed that while we are capable of visualizing disperse qdot binding with our instrument, it did not occur in any of our models. Furthermore, while qdots did not extravasate in SKOV-3 nor LS174T models, we imaged their extravasation in our U87MG tumor model. We have thus demonstrated the utility of intravital microscopy to extract critical information that will aid in future nanoparticle design and approval in cancer diagnostics.

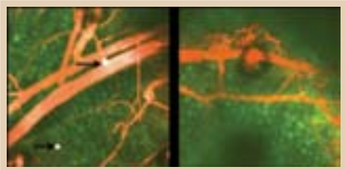

RGD-qdots were observed binding to tumor blood vessels significantly more ($P<0.001$) than RAD-qdots. In typical images, RGD-qdot aggregates (left) bound to neovasculature, while RAD-qdots (right) did not as shown here in the SKOV-3 ear model.

Noninvasive Imaging of Cancer Gene Therapy in Orthotopic Mouse Models Using A Novel Systemically Delivered Bi-Directional Transcriptional Targeting Vector

BC Ahn[1,4], YI Kim[2], S Ray[1], R Katzenberg[2], LV Hofmann[2], SS Gambhir[1,3]
Departments of [1]Radiology, MIPS, [2]Interventional Radiology, [3]Bioengineering, Stanford University, CA, USA; [4]Nuclear Medicine, Kyungpook National University, South Korea

Weak cancer specific promoters, such as Survivin promoter(pSurv), need an amplification strategy to be used for cancer gene therapy. Gene therapy ideally requires non invasive tools to image the delivery of therapeutic genes. We report the development of a novel adenoviral vector carrying a bidirectional transcriptional amplification GAL4-VP2 system which can amplify pSurv activity leading to correlated expression of a reporter gene (firefly luciferase; FL) and a therapeutic gene (TRAIL) [Ad-pSurv-TRAIL-G8-FL]. Methods; MCA-RH7777 (Morris hepatoma) and BRL 3A (Buffalo rat liver) cells were transfected with 100 MOI Ad-pSurv-TRAIL-G8-FL and bioluminescence imaging (BLI) was performed at 72 hrs. Comparison of FL and TRAIL activities was also performed with HCT116 cells. For animal studies, MCA-RH7777 cells(1x106) were surgically implanted in the liver of Buffalo rats. Tumor formation was confirmed with FDG-PET at 14 days after implantation. 109 PFU of Ad-pSurv-TRAIL-G8-FL was administered via tail-vein. BLI was performed to evaluate FL expression in tumor and non-tumor regions at 2d after the virus delivery. Results; MCA-RH7777 cells show 3 fold higher FL activity than BRL 3A cells (4.2X107±4.2X106 vs. 1.4 X107±1.9X106p/s/cm2/sr, $p=0.002$). Expression levels of FL and TRAIL were well correlated ($R2=0.93$). PET imaging 2 wks after tumor implantation showed FDG uptake in tumor implanted area (0.62±0.13%ID/gm). Tumor region showed 29 fold higher light output than normal liver(9.2 X103 vs. 3.1X102p/s/cm2/sr, $p=0.02$) in BLI. Conclusions; An adenoviral vector carrying Survivin promoter driven both the TRAIL therapeutic gene and the FL reporter gene is more active in hepatoma cell lines compared to normal liver cell lines. Most importantly, we report for the first time the iv injection of such a vector to achieve highly specific liver tumor targeting in living rats. The bidirectional transcriptional amplification system using GAL4-VP2 preserves promoter specificity and has the capability of showing therapeutic gene expression non-invasively in a rat orthotopic hepatic tumor model.

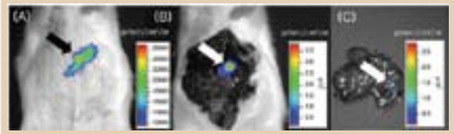

(A) Intact Rat, (B) open abdomen, (C) ex vivo bioluminescence imaging after tail-vein injection of gene delivery vehicle followed by D-Luciferin intraperitoneal delivery 48 hours later. Luciferase activity is only observed from the area of implanted tumor showing highly specific targeting (Arrow).

References/Funding Bayer Schering.

Ultra High Sensitivity Targeted Photoacoustic Imaging Agents for Cancer Early Detection in Living Mice

A de la Zerda[1,2], Z Liu[3], SI Bodapati[2], R Teed[2], C Zavaleta[2], S Vaithilingam[1], X Chen[2], B Khuri-Yakub[1], H Dai[3], SS Gambhir[2,4]
Departments of [1]Electrical Engineering, [2]Radiology, [3]Chemistry, [4]Bioengineering, Stanford University, CA

Photoacoustic molecular imaging of living subjects offers high spatial resolution at increased tissue depths compared to optical imaging strategies. We have recently demonstrated single walled carbon nanotubes (SWNTs) conjugated to Indocyanine Green (SWNT-ICG) as targeted photoacoustic imaging agents in-vitro. In the current work, we created a significantly improved SWNT-ICG particle with over 1000-times better sensitivity than plain SWNT and demonstrated their ability to target tumors when injected intravenously to a living mouse. The targeted SWNT-ICG particles were synthesized by coupling of ICG molecules to the surface of SWNT-RGD particles through pi-pi stacking interactions. Control SWNT-ICG particles were created using the untargeted SWNT-RAD instead. We verified the particles are stable in serum and target αvβ3 integrin through cell uptake studies with U87 cells. We found the photoacoustic signal produced by the particles to be highly linear to their concentration both in phantom studies ($R2 = 0.99$) as well as in living mice injected with the particles subcutaneously ($R2 = 0.971$). We further measured the detection sensitivity of SWNT-ICG in living mice ($n = 3$ mice) and found it to be 30 pM. This represents more than 3 orders of magnitude improvement compared to plain SWNTs sensitivity in living mice ($p < 0.05$). Furthermore, xenograft-bearing mice were tail-vein injected with RGD-targeted SWNT-ICG. At 2 hours post-injection, mice injected with the RGD-targeted particles showed 2.1-times higher photoacoustic signal in the tumor compared to mice injected with control particles ($p < 0.05$, $n = 4$ mice). Finally, we demonstrated the superiority of the SWNT-ICG-RGD particles by incubating them with U87 cells and detecting in living mice 1000-times such cells than if the cells were incubated with plain SWNT-RGD. This is the first photoacoustic imaging agent tested and targeted in living animals that we know of that can reach such a high sensitivity of 30 pM.

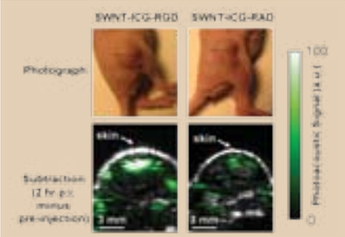

Mice injected with RGD-targeted SWNT-ICG showed significantly higher photoacoustic signal at 2 hours post-injection compared to mice injected with control particles.

References/Funding Bayer Schering.

A Novel Smart Agent for Photoacoustic Molecular Imaging

KB Hartman, A Dragulescu-Andrasi, J Levi, A de la Zerda, SS Gambhir
Department of Radiology, MIPS, Stanford University, CA

Photoacoustic imaging is an exciting new modality that offers higher spatial resolution and deeper penetration than traditional optical imaging. We have designed an activatable (smart) photoacoustic molecular imaging agent which can be activated by matrix metalloprotease-2 (MMP-2), a secreted enzyme commonly present in many cancers. The smart probe developed couples a fluorescent dye (cy5.5) to a photoacoustic dye via an enzyme-recognized peptide sequence (RVGLP). In close spatial proximity, the fluorescent dye silences the photoacoustic dye because of its significantly greater coefficient of absorption (approximately 3-6-fold greater). A scrambled control peptide sequence (PGLRV) probe was also synthesized. Upon cleavage of the enzyme-specific peptide sequence, diffusion of the photoacoustic dye away from the fluorescent dye allows it to produce a greater photoacoustic signal. The activated and control probes were each incubated with either the activated enzyme (recombinant human MMP-2, 37 °C) or the non-activated enzyme (0 °C) for 1 hour prior to suspension in an agar phantom. The samples were at a concentration of approximately 100 μM and imaged in triplicate. The measured photoacoustic signals for the agar alone, unactivated probe, and activated smart probe were 232 relative units (RU) +/- 35 RU, 2751 RU +/- 306 RU, and 3529 RU +/- 255 RU, respectively. All combinations of data comparisons are statistically significant ($p<0.05$). The scrambled control probe did not lead to any detectable cleavage.Mouse studies with the activatable probe show a statistically significant ($p<0.05$) signal enhancement of 256,260 RU +/- 105,802 RU as compared to normal regions of the mouse where the signal is 802 RU +/- 101 RU. These experiments validate the first photoacoustic smart probe and the strategies developed can be used to synthesize other smart probes after further validation in various mouse models.

Design and Testing of a Novel Ultrasound Contrast Agent for Molecular Ultrasound Imaging of Tumor Angiogenesis

JK Willmann[1], R Kimura[1,2], N Deshpande[1], AM Lutz[1], JR Cochran[2], SS Gambhir[1,2]
Departments of [1]Radiology and [2]Bioengineering, Stanford University, CA.

Molecular ultrasound imaging is increasingly being recognized as a promising and powerful molecular imaging tool. In this proof-of-principle study we hypothesized that a new class of molecular ultrasound contrast agents could be developed using small (~3 kDa), conformationally constrained integrin-binding peptides that are coupled onto the surface of contrast microbubbles. Directed evolution was used to engineer a small, disulfide-constrained cystine knot peptide (knottin) to bind to αvβ3-integrins with nanomolar affinity (knottinIntegrin). A molecular ultrasound imaging contrast agent was designed by attaching the knottinIntegrin onto the shell of perfluorocarbon-filled microbubbles (MB-Knottinintegrin). A knottin peptide with a scrambled sequence was used to create control microbubbles (MB-KnottinScrambled). Binding of MB-Knottinintegrin and MB-KnottinScrambled to αvβ3-integrin-positive cells and control cells was assessed and compared to microbubbles labeled with anti-αvβ3-integrin monoclonal antibodies (MBαvβ3) and microbubbles labeled with c(RGDfK) (MB-cRGD). In vivo imaging signal of contrast-enhanced ultrasound using the different types of microbubbles was quantified in 49 mice bearing human ovarian adenocarcinoma xenograft tumors. Tumor tissue was stained for αvβ3 integrin and CD31, a vascular endothelial cell marker. MB-KnottinIntegrin attached significantly more ($P<.0001$) to αvβ3-integrin-positive cells (0.47±0.21 microbubbles per cell) than to control cells (0.02±0.02). Control MB-KnottinScrambled adhered less to αvβ3-integrin-positive cells (0.17±0.12) than MB-KnottinIntegrin. After blocking of integrins, attachment of MB-KnottinIntegrin to αvβ3-integrin-positive cells significantly decreased ($P<.04$). In vivo ultrasound imaging signal was higher following administration of MB-KnottinIntegrin compared to MBαvβ3, MBcRGD, and control MB-KnottinScrambled ($P<.018$). Following in vivo blocking of integrin receptors, the imaging signal after administration of MB-KnottinIntegrin significantly ($P<.018$) dropped by 64%. Ex vivo immunofluorescence confirmed integrin expression on tumor endothelial cells of human ovarian adenocarcinoma xenograft tumors. In summary, our study shows that knottin peptides are a promising platform for designing novel contrast agents for molecular ultrasound imaging of tumor angiogenesis. The design of small, evolvable peptide ligands that can be coupled with the surface of microbubbles may facilitate the translation of molecular ultrasound from preclinical animal models to clinical applications in patients in the near future.

Multivalent ^{64}Cu-α-MSH Analogs for MicroPET Imaging of Melanocortin 1 Receptor Expression

H Liu[1,3], Z Miao[1], G Ren[1], L Jiang[1], R Kimura[2], JR Cochran[2], P Han[3], Z Cheng[1]
Departments of [1]Radiology, MIPS, Bio-X Program, [2]BioEngineering, Stanford University , CA, USA; [3]Institute of Radiation Medicine, Chinese Academy of Medical Sciences, Peking Union Medical College, Tianjin, China.

Multivalent peptides have been explored as a useful strategy to construct molecular imaging probes and drug delivery carriers. It is generally accepted that multivalency has advantages over monovalency for improving binding affinities and even activity. Herein by using multivalent α-melanocyte stimulating hormone (α-MSH) analogs, B16F10 melanoma-bearing mice and microPET imaging technology, we systematically investigated the influence of multivalent effect on α-MSH analogs' binding affinity and in vivo melanoma targeting profiles. Methods: Three α-MSH analogs named as MSH1, MSH2 and MSH4 were designed and synthesized, which contained one, two or four valency of an α-MSH core sequence, His-d, Phe-Arg-Trp, respectively (Fig. a). α-MSH analogs tetramer was constructed using the multiple antigenic peptide (MAP) scaffold. 1,4,7,10-tetraazacyclododecane-1,4,7,10-tetraacetic acid (DOTA) was conjugated to the lysine residue of peptides for radiolabeling with a PET radioisotope, 64Cu. In vitro binding affinity assays were performed with B16F10 melanoma cell line. After radiolabeling with 64Cu, the in vivo performances of the peptides were evaluated in subcutaneous B16F10 melanoma xenografted mice by microPET imaging followed by biodistribution studies. Results: In the receptor competition binding assays, DOTA-MSH4 showed highest binding affinity (IC50= 1.00 nM) which is consistent with its highest ligand density. However, in vivo study demonstrated poor performance of MSH4 as an imaging agent due to its lowest tumor uptake and highest kidney accumulation. In comparison, DOTA-MSH2 displayed medium affinity (IC50=2.06 nM), yet highest tumor uptake and lowest kidney accumulation (Fig. b). Further blocking study of DOTA-MSH2 confirmed its tumor targeting specificity in vivo. Conclusion: Multivalency effects have complex impact to peptides' in vivo behaviors. Eventhough MSH tetramer shows the higher binding affinities in vitro, the better in vivo tumor targeting ability is achieved by MSH dimer. Cu-64 labeled dimeric DOTA-MSH2 has been identified as an ideal melanoma PET imaging probe.

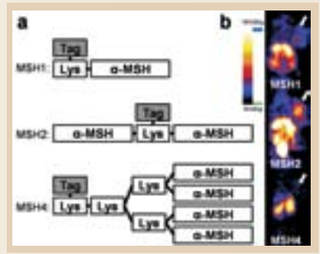

Imaging Tumor Neovascularization in Transgenic Mouse Models Using Novel PET ^{64}Cu-DOTA-Knottin Peptide

CH Nielsen[1,2], N Withofs[1], R Kimura[1], PT Tran[3,4], Z Miao[1], JR Cochran[5], Z Cheng[1], DW Felsher[3], JK Willmann[1], SS Gambhir[1,5]
Departments of [1]Radiology, MIPS, [3]Division of Oncology, Medicine & Pathology, [4]Radiation Oncology, [5]Bioengineering, Stanford University, CA, USA; [2]Cluster for Molecular Imaging, Clinical Physiology, University of Copenhagen, Denmark

Despite advances in cancer management the mortality of lung cancer is still strikingly high. A major problem is that lung cancer patients typically are diagnosed when they have advanced stage disease thus eliminating the option of curative surgery. Once a tumor reaches 1-3 mm in diameter it is dependent on angiogenesis to support further growth. In this study we demonstrate the potential of using a novel 64Cu-DOTA-Peptide (Knottin 2.5F) to image angiogenesis (through $\alpha_v\beta_3$, $\alpha_v\beta_5$, and $\alpha_5\beta_1$ targeting) associated with malignancy in a transgenic mouse model mimicking the development of lung cancer. Conditional transgenic mice with the oncogenes cMyc and K-ras induced by doxycyline were screened for lung lesions using respiratory gated microCT. Mice (N=7) with positive CT findings underwent microPET/microCT imaging with Knottin 2.5F (~100 μCi). In addition mice were imaged with FDG-microPET/microCT. The PET-tracers uptake in the lesions was estimated by volumetric ROIs drawn based on the microCT images and tumor to normal lung ratios calculated. Ex vivo gamma counting was also performed on tumor- and normal lung sections and tumor tissue was stained for integrins (α_v-subunit) and CD31. Lung lesions, as small as 3^3 mm^3 in volume, were successfully imaged with Knottin 2.5F and FDG. Overall, the %ID/g in the tumors was lower for Knottin 2.5F compared to FDG, but the tumor to normal lung ratio (6.01±1.92 vs. 4.36±2.15) was significantly higher ($P\leq0.04$) for Knottin 2.5F. Ex vivo gamma counting supported the PET findings showing higher uptake in tumor sections than in normal lung. Immunofluorescence confirmed expression of integrins (α_v-subunit) on tumor vasculature. In conclusion, we demonstrate the feasibility of using Knottin 2.5F as an imaging agent to image angiogenesis occurring during tumorigenesis in a transgenic mouse model. Knottin 2.5F yields a higher tumor to background ratio as compared to FDG and shows minimal uptake in the thorax making it a promising imaging agent to characterize lung lesions. The improved visualization may facilitate better characterization of malignant lesions in patients undergoing PET/CT.

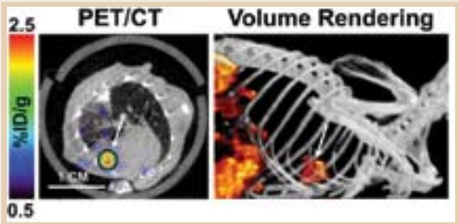

Left: MicroPET/microCT cross section of a transgenic mouse imaged with Knottin 2.5F. A nodule ~33mm3 immediate adjacent to the heart is clearly visible (arrow). Right: Volume rendering of the same mouse. The Knottin 2.5F uptake is shown in color. Uptake is seen in the liver (left). The low background in the lungs makes it easy to delineate the nodule (arrow).

References/Funding Bayer Schering, Scientific Session 9: Cancer Session I: Hypoxia and Angiogenesis, September 24, 2009 / 14:15-14:30 / Room: 710A

Monitoring Adoptive Cellular Immunotherapy in Glioma Patients Using PET Reporter Gene Imaging

S Yaghoubi[1], M Jensen[2], N Satyamurthy[3], F Habte[1], D Paik[1], J Czernin[3], SS Gambhir[1]
Department of [2]Cancer Immunotherapeutics and Tumor Immunology, Beckman Research Institute, Duarte, CA; [3]Molecular and Medical Pharmacology, UCLA, CA; [1]Radiology, MIPS, [2]Bioengineering, Stanford University, CA

Noninvasive imaging of cell trafficking should allow early assessment of efficacy and potential adverse effects of adoptive cellular immunotherapy in cancer patients. Under a FDA authorized IND (61,880), we have imaged the biodistribution of the positron emission tomography (PET) reporter probe, 9-[4-[18F]fluoro-3-(hydroxymethyl)butyl]guanine ([^{18}F]FHBG) in glioma patients (two hours after injecting < 7 mCi intravenously). These patients had recurrent glioblastoma multiforme. They were infused autologous cytolytic T lymphocyte (CTL) clones (12 sessions, 10^7 to 10^8 cells each session) into the site of surgically removed recurrent tumor. The CTLs expressed Herpes Simplex virus type 1 thymidine kinase (HSV1-tk) PET reporter gene (confirmed by Ganciclovir sensitivity and tritiated Penciclovir uptake assays) and IL-13 zetakine. We previously reported the case of a glioma patient imaged with [^{18}F]FHBG only after cell infusions (Yaghoubi et. al. Nature Clinical Practice Oncology 6(1): 53-58). In this patient we observed tumor signals that were about 2.6 fold higher, when compared to tumor signals in control glioma patients who had not been infused CTLs. Biopsy had confirmed presence of CTLs at tumor resection site as well as in a newly formed tumor in the corpus callosum. Here, we report imaging another patient who was imaged both before and after CTL infusions with [^{18}F]FHBG. The Figure illustrates brain [^{18}F]FHBG PET images pre and post CTL infusions. Comparing Tumor/brain intensity ratios, the ratio is 1.6 fold higher after cell infusions. Comparing tumor/meninges ratios, the ratio is 4.2 fold higher after cell infusions. Another observed difference is that in pre-cell infusions the signal is observed on the walls of the tumor resection site; whereas after infusions, the signal emanates from the whole resection site. Additional studies are planned for imaging patients pre and post CTL infusions that should allow statistical analysis. Meanwhile, these recent data, using the pre-scan of the same patient as a control image provide further demonstration of PET reporter gene based imaging of therapeutic cells in cancer patients.

Photoacoustic Imaging of the Eye for Improved Disease Detection

A de la Zerda[1,2], YM Paulus[3], DM Moshfeghi[3], SS Gambhir[2,4]
Departments of [1]Electrical Engineering, [2]Radiology, [3]Ophthalmology, [4]Bioengineering, Stanford University, CA

Ophthalmologists lack good functional and molecular imaging tools for the evaluation of angiogenesis in patients. Solving this need would allow earlier detection and improved intervention to multiple ophthalmic diseases including macular degeneration and ocular malignancies. We report on the first demonstration of photoacoustic retinal imaging in living animals. The photoacoustic device can not only be used with photoacoustic contrast agents for molecular imaging but can be used without contrast agents, in which case the eye blood vessels are visualized. The device has high spatial resolution (250 µm) and high depth of penetration allowing it to visualize the retina, choroid, sclera and optic nerve. This is particularly important as most eye diseases originate deep in the eye where they cannot be visualized with existing imaging tools. The device illuminates the eye with a wide laser beam at a safe power (800 nm wavelength at 0.5 mJ/cm2). The light is absorbed by hemoglobin producing ultrasound waves that emerge from the eye and detected by an ultrasound transducer. The transducer scans the eye from multiple locations creating a three-dimensional map of blood distribution in the eye. We scanned living rats and rabbits eyes (n = 3 of each animal) and enucleated pigs eyes (n = 3). Along with the photoacoustic scan, we acquired an ultrasound scan to visualize the eye's anatomy. The field of view included most of the eyeball (~2 cm in diameter) and time of acquisition was 20 minutes using a 25 MHz transducer (Fig. 1). This is the first demonstration of photoacoustic ocular imaging in living animals. Such system has uses not only in clinical diagnosis but also in the drug development process where ophthalmic diseased animal models can be scanned for the first time with high depth of penetration.

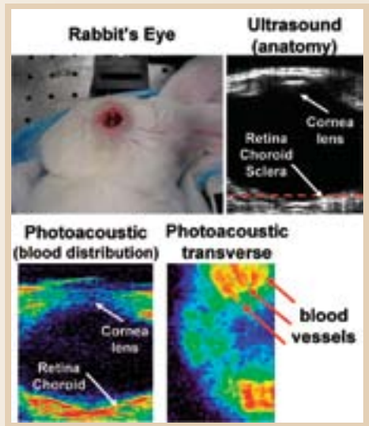

Photoacoustic and ultrasound images of a live rabbit's eye. Using safe laser exposure, photoacoustic signals were measured to image both the retina and choroid visualizing individual blood vessels.

Molecular Imaging of Cell Transplantation in Porcine Myocardium Using Clinical MRI and PET-CT

N Parashurama[1], BC Ahn[1,4], D Yerushalmi[1], C Zavaleta[1], J Chung[2], JC Swanson[3], F Ikeno[2], T Teramoto[2], J Lyons[2], S Bhaumik[5], S Yaghoubi[1], P Yang[2], PG Yock[2], RC Robbins[3], SS Gambhir[1]
Departments of [1]Radiology, MIPS, [2]Cardiovascular Medicine, [3]Cardiothoracic Surgery, Stanford University, CA, USA; [4]Nuclear Medicine, Kyungpook National University, Daegu, South Korea; [5]GE Global Research Center, General Electric, Niskayuna, NY, USA

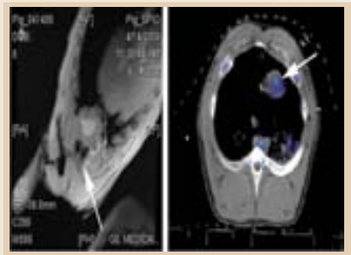

Imaging cells after cardiac cellular therapy could be a promising approach to optimizing this new treatment strategy. Marrying the strengths of cardiovascular MRI (high spatial resolution) and PET (high sensitivity) enhances the ability to assess the cell location, viability, survival, and myocardial response to treatment. To build on our previous swine studies with adenovirally transduced cells, Rat Mesenchymal Stem Cells (rMSC) were stably transduced with a second generation, self-inactivating lentivirus carrying a ubiquitin-driven triple fusion (TF) reporter gene (RG), comprised of green fluorescent protein (GFP), firefly luciferase (Fluc) and a mutant truncated herpes simplex virus type 1 thymidine kinase (HSV1-tsr39tk). These TFRG expressing rMSC were loaded overnight with 12 µg/ml Iron bearing SPIO particles (35nm) using a protamine transfection technique. To determine sensitivity, 3 injections of SPIO particles, at varying concentrations, were made into swine hearts, and a T2 weighted sequence, a short axis, Fiesta sequence, was applied to the 3T MRI. Injection of 5mg/ml of SPIO resulted in an SNR (signal to noise ratio) of 0.81, injection of 12µg/ml resulted in an SNR of 4.65, and injection of 4 µg/ml resulted in an SNR of 5.73, where decreasing dose of SPIO leads to an increased signal intensity (N=2 swine). The MRI allowed simple detection of injection site after injection of 150-220 x106 cells. Next, clinical PET-CT was performed dynamically op to five hours after injection of F18-FHBG (14 mCi), and nine hours after injection of the rMSC. Uptake of probe was measured as a SNR ratios 1.34 and 1.16 each injection (N=2 swine). Cell injection sites were localized to areas of heart by MRI T2 weighted images. Future work will aim to use swine TFRG-MSC in survival models of swine infarction. Studies of PET reporter genes in large animals should help translate stem cells to the clinic and establish the role for molecular imaging in monitoring stem cell therapies.

Acceleration of PET Monte Carlo Simulations using the Graphics Hardware Ray Tracing Engine

Z Wang[1], PD Olcott[1,2], CS Levin[1,3,4,5]
Departments of [1]Radiology, [2]Bio-engineering, [3]Radiology, MIPS, [4]Electrical Engineering, [5]School of Medicine, Stanford University, CA

Recent improvements in the computing power and programmability of graphics processing units (GPUs) have enabled the possibility of using GPUs for the acceleration of scientific applications, including time-consuming simulations in physics. This paper describes the acceleration of a Monte Carlo high energy photon ray tracer called GRAY using NVIDIA OptiX ray tracing engine on GPUs. Monte Carlo simulations guide the design of advanced PET systems, data correction schemes, and image reconstruction algorithms. GPU acceleration of these simulations makes these studies more practical while avoiding the need of a large, expensive computer cluster. We describe the GPU-based computation and how it is mapped onto the many parallel computational units now available on the NVIDIA GTX 200 series GPUs. For a whole body PET benchmark, a speedup of 5.2X was achieved on a single GTX285 GPU over the GRAY code executed on an AMD Athlon 3200+ processor using 1 CPU core, with equivalent accuracy. Compared to PET system simulations run on the standard Monte Carlo package known as "GATE", the speedup is 53.6-fold.

GPU ray tracing engine receives radionuclide distribution, phantom, detector system geometry and material database, calculates intersection properties and sends back this information to the main routine.

References/Funding Stanford Bio-X Graduate Fellowship (Olcott), and grants R01 CA110956, ARRA R01CA119056-04S1, and R01 CA120474. 1) CS Levin, M Dahlbom, E Hoffman, "A Monte-Carlo correction for the effect of Compton-scattering in 3D PET brain imaging," IEEE TRANSACTIONS ON NUCLEAR SCIENCE, vol. 42, no. 4, pp. 1181-1185, Aug. 1995. 2) CH Holdsworth, C. S. Levin, M. Janecek, M. Dahlbom, and E. J. Hoffman, "Investigation of accelerated Monte Carlo techniques of PET simulation and 3D PET scatter correction," IEEE Trans. Nucl. Sci., vol. 48, pp. 74 – 81, 2001. 3)P. D. Olcott, S. R. Buss, C. S. Levin, G. Pratx, C. K. Sramek, "GRAY: High Energy Photon Ray Tracer for PET Applications," in IEEE Nuclear Science Symposium Conference Record, vol. 4, pp. 2011 – 2015, 2006.

Effects of External Shielding on the Performance of a 1 mm³ Resolution Breast PET Camera

A Vandenbroucke[1], D Innes[1], CS Levin[1,2,3]
Departments of [1]Radiology, MIPS, [2]Bioengineering, [3]Electrical Engineering, Stanford University, CA

We are constructing a 1 mm³ resolution, high sensitivity breast-specific PET camera, whose imaging heads will consist of many layers of 8x8 arrays of 1x1x1 mm³ LYSO crystals coupled to PSAPDs.

This paper investigates the effects of shielding on out-of-field background event rate from highly vascular organs like heart, liver, spleen and brain. In order to optimize the performance of the breast specific PET camera, we must address this background by proper external shielding, which reduces the single photon event rate. This avoids data acquisition saturation and reduces the amount of scatter and random coincidences, which enhances the image SNR. Shielding should ideally reduce out-of-field activity while maintaining a high sensitivity for photons emitted from the breast.

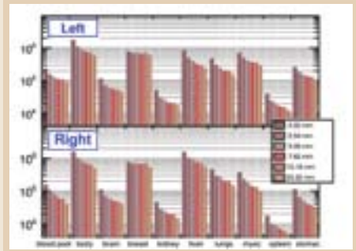

Reduction in counts from various organs for different shielding thickness. Note that the counts from the breast remain quasi constant, indicating that the shielding only slightly reduces the valid counts from the breast.

Shielding design is studied using the Monte-Carlo simulation package GRAY, which supports complex mesh based primitives for phantoms and detector shapes. An anatomically accurate model of the female torso based on the realistic NURBS CArdiac Torso (NCAT) phantom is used, which was manipulated to include a slight breast compression to a width of 7.5 cm.

The detector configuration in the simulation is based on its CAD drawings. As shielding material we use an alloy of 97% tungsten, 2.1% Ni and 0.9% Fe, which has a density of 18.5 g/cm³ and a high atomic number Z. Different shielding thicknesses and locations are investigated and their influence on the system count rate is analysed.

We show that the maximum count rate is reduced by 45% (57 %) when placing 2.54 mm (5.08 mm) of tungsten shielding around the panels. The highest observed event rate per ASIC is 19 kHz (15kHz), which is well below the 83 kHz maximum estimated count rate of our data acquisition system. The out of field background is reduced by 35 and 40 % (42 and 47%) for left and right breast respectively.

References/Funding NIH grants R01CA119056, ARRA R01CA119056-S1 and DOD BC094158. Accepted for presentation at IEEE MIC, Nov 2010, Knoxville, TN.

Compact Readout Electronics Module for a High Resolution Breast-Dedicated PET System

PD Reynolds[1,2], A Vandenbroucke[2], F Lau[1,2], CS Levin[2]
Departments of [1]Electrical Engineering, [2]Radiology, MIPS, [3]Bioengineering, Stanford University, CA

We have developed and tested a compact readout electronics module for use in our 1 mm3 resolution breast-dedicated PET system. The system consists of two 9 cm x 16 cm x 38 cm panels, with each panel requiring 9,216 channels of charge sensing circuitry. To fit this volume, along with front end and auxiliary electronics, the size of the readout electronics needs to be small. The compact readout electronics module can read 64 channels in an 8 cm x 8cm x 0.4 cm volume.

The module is based on the NOVA RENA-3 readout ASIC, which consists of 36 configurable channels of preamplifier, Gaussian shaper, trigger and timestamp circuitry. The module incorporates two RENA-3 chips, and due to detectors limitations, 32 channels from each chip. A Xilinx XC3S200A is used for control logic and communication in the module. Each RENA has its own 12-bit analog to digital converter and dedicated transfer link for high speed readout.

Top, the compact readout electronics module. Bottom, collected data demonstrates readout capability through the individual crystal separation in the flood histograms.

A pulser signal of several amplitudes is used to generate charge for testing each channel. The standard deviation of the amplitude for each measurement is typically less than 1.5 ADC counts. This translates into an amplitude resolution of the readout electronics of less than 0.15% in the center of the dynamic range. The timing resolution of pulser data measures around 1.33 ns FWHM.

Four position sensitive avalanche photodiodes (PSAPD) with 8x8 arrays of 1x1x1 mm3 LSO crystals were connected to the readouts and coincidence data was collected. All crystals are visible in position flood histograms. The per crystal energy resolution shows the 511keV photo peak with 10.9% energy resolution. PSAPD coincidence time resolution measures 6.71 ns FWHM.

References/Funding NIH R01CA119056, R01CA119056-S1(ARRA), R33 EB003283, and R01CA120474. Accepted for presentation at the 2010 IEEE Medical Imaging Conference, October 30, 2010, Knoxville, Tenessee, U.S.A.

Key Physical Factors for DoI-compensated ToF PET: Understanding Scintillation-photodetector Features

VC Spanoudaki[1], CS Levin[1,2]
Departments of [1]Radiology, MIPS, [2]Electrical Engineering, Stanford University, CA

We are investigating 511 keV photon detectors for PET with combined time of flight (ToF) and depth of interaction (DoI) features. Such an advance would enable image signal-to-noise ratio (SNR) as well as spatial resolution uniformity improvements. This study investigates the inter-dependence of these features and experiments with ToF-DoI detector design parameters. We also present a study of the detection process chain, from interaction of the annihilation photons within the crystal volume through signal formation in the photodetector, using both simulations and experiments with LYSO crystals coupled to silicon photmultipliers (SiPM). The modeled and measured performances demonstrate the dependence of time resolution on crystal thickness, surface treatment and DoI. Time resolution degrades with increasing crystal length (up to 150%/50% degradation in simulation/measurement going from 5 to 20 mm crystal lengths). The effect of crystal surface on time resolution has a complex dependence on crystal length (measured 10% improvement for a 5 mm rough crystal vs. 20% improvement for a 20 mm polished crystal) due to time response variations on DoI for rough versus polished crystals (up to 50%/20% time resolution degradation in simulation/experiment over an 11 mm DoI range within a 20 mm length crystal). Simulations show a dependence of time resolution on individual photoelectron trigger level (15% maximum observed difference for rough crystals) indicating statistical inaccuracies associated with the arrival of the first few photoelectrons. For investigating the effect of the above factors on detector pulse shape we present an electrical model that simulates the individual photoelectron signal pile-up of a SiPM consisting of several thousand microcells. The model uses parameters derived from the above optical photon tracking model, and predicts a dependence of signal pulse shape on DoI for 3x3x20 mm3 crystal elements (70% stronger for polished crystals over a 16 mm range of DoI).

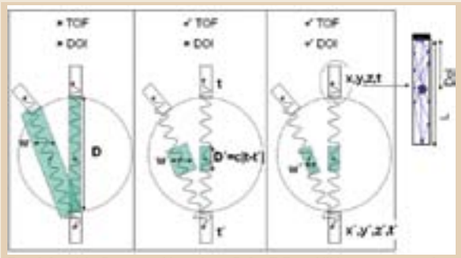

From left to right: Detectors without photon DoI or ToF capabilities cannot accurately localize where the annihilation event occurred along a tube of response (ToR) between two detectors (left). Based on the difference of the annihilation photon flight time this information becomes more precise (middle). Based on DoI the width of the ToR becomes narrower, for oblique lines offset from the center (right).

References/Funding AXA Research Fund. Accepted for presentation at the 2010 IEEE Medical Imaging Conference, 31 Oct.-6 Nov, Knoxville, TN

Cross-strip Capacitive Multiplexing and Electro-optical Coupling for Silicon Photomultiplier Arrays for PET Detectors

P Olcott[1,2], H Peng[1], CS Levin[1,2]
Departments of [1]Radiology, MIPS and [2]Bioengineering, Stanford University, CA

A key component for the development of simultaneous, PET/MR is a PET block detector that has a low number of readout channels, non-magnetic components, and little or no mutual influence between PET and MR systems. We have developed a differential multiplexing circuit for silicon photomultipliers (SiPM) that uses capacitors instead of resistors. We demonstrated that that two different arrays, 4 x 4 array of 3.2 mm x 3.2 mm x 20 mm and a 6 x 6 of 2.13 mm x 2.13 mm x 20 mm SiPM devices can be multiplexed into four signals with excellent spatial (peak-valley ratio >3), energy (22.3 +/- 0.3% energy resolution at 511 keV, and timing resolution (2.5 ns FWHM) using a variety of scintillation crystal designs. Output signals from the multiplexing circuit can directly drive telecommunication-grade lasers without using active amplifiers to transmit the energy and fast timing information of the scintillation block detector out of the MR, using multi- mode optical fibers, rather than coaxial cables, using a custom designed laser alignment block. This multiplexed, laser coupled block detector has a significant reduction in the number of readout channels while having a very low electrical footprint. These two technologies will be a key enabler of SiPM technology for high resolution small animal and clinical PET/MR.

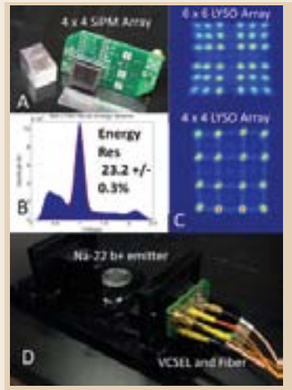

(A) A PET/MR block detector consists of a 6x6 array of 2.2 mm x 2.2 mm x 20 mm or a 4x4 array of 3.2 mm x 3.2 mm x 20 mm LYSO scintillation crystals coupled to a 4x4 array of 3.2 mm x 3.2 mm Silicon Photomultipliers (SiPM) detectors was electro-optically coupled to Vertical Cavity Surface Emitting Lasers (VCSELs) using a novel electrical multiplexing circuit. A MR compatible test setup (D) was able to resolve all 6x6 (Peak-valley 8:1) and 4x4 (Peak-Valley 22:1) crystals (C) on the array with an (B) energy resolution of 25.9 +/- 0.3% FWHM at 511 keV.

References/Funding GE PET/MR Research Grant, Society of Nuclear Medicine 2008 Pre-doctoral Fellowship, Bio-X Graduate Fellowship. [1] Olcott, H Peng, CS Levin, “Novel electro-optical coupling technique for magnetic resonance-compatible positron emission tomography detectors.” Mol Imaging (2009) vol. 8 (2) pp. 74-86. [2]P. Olcott, H Peng, CS Levin, “Cross-strip capacitive multiplexing and electro-optical coupling for silicon photomultiplier arrays for PET detectors”, IEEE NSS-MIC Conference, Orlando, FL, September, 2009

New Front-end IC with Fast Timing for Semiconductor Photodetectors

F Lau[1], M Horowitz[1], CS Levin[1,2]
Departments of [1]Electrical Engineering, [2]Radiology, Stanford University, CA

In order for the spatial and contrast resolution of PET to improve, we need PET systems with densely-packed sensors and high performance, highly integrated electronics. A PET system with small detector pixels (e.g., 1mm^3 in size) results in thousands of electronic readout channels, and this necessitates using integrated circuits (IC) for the front-end electronics. An IC is a miniaturized electronic circuit that has been fabricated on the surface of a thin piece of silicon semiconductor material. The front-end ICs currently available do not have the required dynamic range and time resolution.

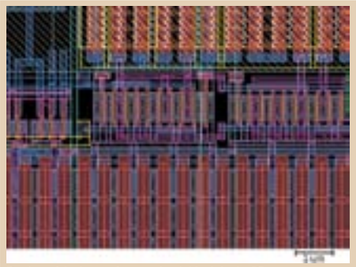

Portion of the layout for one circuit block in the IC.

We are designing a front-end mixed-signal IC with an innovative architecture that enables the analog circuits to be combined with the analog-to-digital converter (ADC) in a single IC, while consuming much less power and having a smaller electronic footprint than conventional techniques. The output of the IC will be fully digital, so it is robust against amplitude noise and pulse width jitter and also facilities multiplexing of the IC outputs. The IC will be programmable so that it can be used with both avalanche photodiode (APD) and silicon photomultiplier (SiPM) PET detectors. When completed, we are interested in sharing this IC with medical imaging researchers at Stanford and other institutions so that they can use it in their data acquisition systems.

The IC will have fast timing capability, i.e., it will be able to measure the time of the pulses from the PET detectors with about 100 ps time resolution. Therefore, it could be used in time-of-flight (ToF) PET. We are targeting an analog bandwidth of 2 GHz. The size of the IC is estimated to be 1mm3. Its small size facilitates the development of a highly compact and portable PET system form factor, which is especially important for our targeted application: breast-dedicated PET.

References/Funding California Breast Cancer Research Program Dissertation Grant and the Stanford BioX Graduate Student Fellowship

Fully 3-D Time-of-Flight PET Image Reconstruction from List-mode Data Using GPUs and CUDA

J Cui[1], G Pratx[2], S Prevrhal[5], CS Levin[1,3,4]
Departments of [1]Electrical Engineering, [2]Radiation Oncology, [3]Radiology, [4]Radiology, MIPS, Stanford University, CA; [5]Philips Healthcare, CA

List-mode processing is an efficient way of dealing with the sparse nature of PET datasets and is the processing method of choice for time-of-flight (ToF) PET because data are collected in list-mode. We present a novel method of computing line projection operations required for list-mode ordered-subsets expectation-maximization (OSEM) for fully 3-D PET image reconstruction on a graphics processing unit (GPU) using the Compute Unified Device Architecture (CUDA) framework. Our method overcomes challenges such as compute thread divergence and exploits GPU capabilities such as shared memory and atomic operations. Each thread block takes a set of tubes-of-response (TORs), and assigns one TOR to a thread. In the forward projection stage, the threads process the TORs independently, and accumulate the contribution of the voxels to the TORs by looping over the voxels that can potentially intersect with the TOR. In the backprojection stage, the threads accumulate the contribution of the TORs to the voxels, and atomic operations are used to ensure data race conditions between different threads. The benefits of the GPU-CUDA implementation compared with previously studied GPU-OpenGL/Cg-based methods include easier implementation and maintenance, better utilization of the resources of the GPU (shared memory and atomic operations), and faster extension to more accurate projection models. When applied to line projection operations for list-mode time-of-flight PET this new GPU-CUDA implementation is 120X faster than a reference CPU implementation. The image quality is preserved with root mean squared (RMS) deviation between the images generated using the CPU and the GPU being 0.08%, which has negligible effect in typical clinical applications.

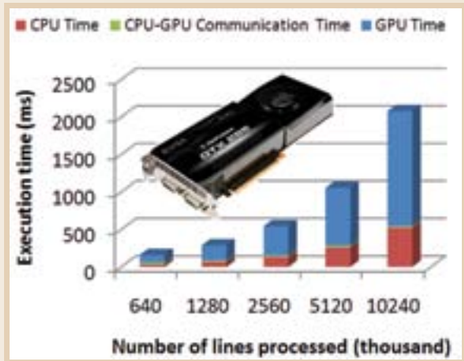

Execution time for processing varying numbers of lines for GPU versus CPU implementations of the list-mode 3D-OSEM iterative tomographic image reconstruction algorithm. The proportional relationship between the number of lines and the execution time indicates low overhead and good scaling of the implementation. The insert image shows the GPU that we used.

References/Funding Philips Healthcare and NIH grants R01 CA110956, ARRA R01CA119056-04S1, and R01 CA120474. Accepted for presentation at the 2010 IEEE Medical Imaging Conference, October 30, 2010, Knoxville, Tenessee, U.S.A.

Thermal Regulation for a 1mm^3 Resolution PET Camera based on Avalanche Photodiodes: Design, Simulation and Experimental Verification

J Zhai[1,2], A Vandenbroucke[1], CS Levin[1]
Departments of [1]Radiology, MIPS and [2]Computer Science, Stanford University, CA

We are prototyping a lutetium yttrium oxyorthosilicate (LYSO) - position sensitive avalanche photodiode (PSAPD) based positron emission tomography (PET) camera with 1mm3 spatial resolution. The detector module within the camera consists of a pair of 8X8 arrays of 1mm^3 LYSO crystals coupled to two PSAPDs.

The PSAPDs are mounted on a Kapton flex circuit covered with Liquid Crystal Polymer (LCP). An alumina frame is used to prevent sparks from high voltage (HV) lines and to provide rigidity. Many rows of these modules will be stacked to form a panel head. The full camera will consist of two such panels. Annihilation radiation enters the crystals edge-on.

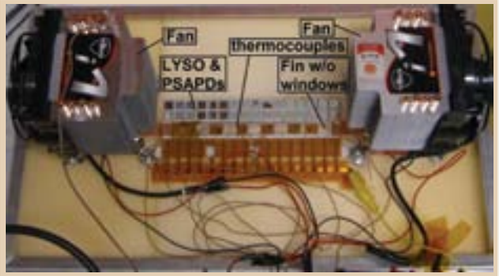

Experimental device for temperature measurement using fin without windows to cool PSAPDs

Given the design of the PET imaging system, many PSAPDs will be closely packed together. It is well known that the 1cmX1cm PSAPDs will heat up by 2 to 4 mW when biased and are sensitive to temperature. In particular, the gain of PSAPD varies with temperature, which may impair system performance.

We completed the design of the thermal regulation plan for these PSAPDs. Results were validated by both the experiments and finite volume simulations. We investigated the temperature profile of the layer of PSAPD detectors residing in the system and design the thermal regulation system for the front end of the PET camera.

We concluded that the design of a heat-dissipating fin structure with "windows" that border the scintillation crystal arrays of 16 adjacent detector modules per layer has the best heat dissipation effects compared to a design without the windows. For the fin with windows, the temperature difference from center to near the edge is 0.97˚C in simulation and 1.2˚C in experiment. The total cooling power is 0.08W per half of the fin.

References/Funding NIH-NCI grants R01 CA119056, R01 CA119056-S1(ARRA), a grant from the DoD BCRP, and CSC Graduate Fellowship. [1] A Vandenbroucke, J Lee, F Lau, P Reynolds, CS Levin, IEEE NSSMIC, pp. M13-135, 2009. [2] F Lau, A Vandenbroucke, P Reynolds, P Olcott, M Horowitz, CS Levin, IEEE NSS Conference Record, pp. 3871 - 3874, 2008. The work has been accepted for presentation at the 2010 IEEE Medical Imaging Conference, Nov/8/2010, Knoxville, TN.

Spatial Resolution Improvement by ML Estimation in a 3D Positioning CZT Detector for PET

Y Gu[1,2], G Chinn[2], A Bousselham[2], CS Levin[1,2]
Departments of [1]Electrical Engineering and [2]Radiology, MIPS, Stanford University, CA

We are developing a 1 mm resolution small animal PET system using cadmium zinc telluride (CZT) photon detectors capable of positioning the 3D coordinates of individual photon interactions. The detectors are 40×40×5 mm^3 monolithic CZT crystals patterned with a cross-strip electrode design. Spatial localization along the *x*-*y* plane i.e. parallel to the electrode planes, is achieved by finding the intersection of the anode and cathode strips that trigger signal readout. Localization along the *z* direction i.e. the interaction depth orthogonal to the electrode planes, can be achieved by observing the ratio of the cathode and anode pulse heights i.e. the C/A ratio. However due to factors such as finite energy resolution, measurement noise and photon Compton scatter within the detector, the C/A ratio to *z* relationship is statistical in nature and offers limited estimation accuracy.

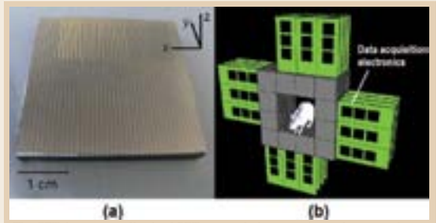

The CZT detector, small animal PET system design, experimental setup, and comparison of results. (a) Anode side of the 40×40×5 mm^3 cross-strip CZT detector, (b) 3-D high-resolution small animal PET system under development using CZT detectors with a 8×8×8cm^3 field of view.

We explore the use of the maximum likelihood (ML) approach for estimating the *z*-coordinate based on both the C/A ratio as well as the difference between a photon interaction's anode and cathode time stamps – or simply Δt. The time difference Δt arises due to the finite drift velocity of carriers in CZT and the different widths of the anode and cathode strips. Importantly, similar to C/A, Δt provides depth information as it varies systematically with *z*.

A novel 40×40×5 mm^3 prototype detector was edge illuminated at varying depths along its 5 mm thickness using a ^{137}Cs source through a lead collimator with a 0.635 mm wide slit. Using Parzen-window density estimation, the experimental data was used to calculate the empirical joint PDF P(*z*, C/A, Δt). The ML estimator based on the corresponding P(*z*|C/A, Δt) realized a 0.83 mm RMS (1.54 mm FWHM) resolution along the *z* direction, which is a 38.5% (23.8% in terms of FWHM) improvement compared to when C/A alone was used.

References/Funding NIH-NCI R01 CA120474 and Postdoctoral Fellowship from the Swedish Research Council. Accepted for presentation at the 2010 IEEE Medical Imaging Conference, Oct. 30 – Nov. 6, Knoxville, Tennessee.

Nanophotonic Optical Temporal Correlation for Positron Emission Tomography

A Grant[1], P Olcott[1], CS Levin[1,2]
Departments of [1]Bioengineering and [2]Radiology, Stanford University, CA

Positron emission tomography (PET) enables non-invasive cellular and molecular assays of any tissue (deep or shallow) within a living subject. PET requires temporal correlation of the two 511 keV "annihilation photons" simultaneously emitted for every PET tracer radioactive decay. Time-of-flight (TOF)-PET uses photon arrival time measurements that provide information on the two-photon emission location within the body to substantially increase image signal-to-noise ratio, enabling significant improvements in disease visualization and quantification, or large reduction in injected dose and/or scan time. Precise photon arrival time information requires very high temporal resolution, however. We have developed a technique to convert the 511 keV photon information into coherent infrared light pulses. We hypothesize that purely optical temporal correlation of these light pulses from coincident 511 keV photons based on nanophotonic crystals rather than conventional electronic coincidence processing will significantly improve photon arrival time resolution (<100 ps), advancing TOF-PET performance. Additionally, this approach greatly simplifies the data acquisition system since it eliminates the need for fast timing electronics. Spatial, timing, and energy information from incoming photons is optically encoded in the nanophotonic crystals with pulses of light that are delayed for precise amounts of time, each delay value corresponding to an individual detector channel. Detector channels are then optically multiplexed to allow a single readout for the entire system (a fast photodetector). We will design and fabricate 16-channel nanophotonic chips with characteristic light delays up to 4 ns in 10 ps increments to test our novel all-optical annihilation photon coincidence processing scheme, and compare the coincidence time resolution results with those obtained through conventional electronic methods.

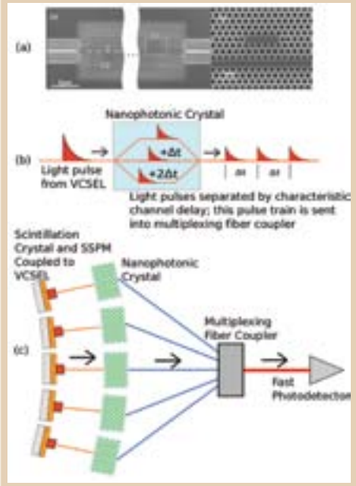

(a) Nanophotonic waveguide capable of introducing delays in light (Pan, J., et al. Applied Physics Letters, 2008. 92, 103114); (b) Single channel detail of pulse channel encoding scheme in a nanophotonic crystal. The crystal splits the incoming light into 3 pulses and introduces characteristic delay time Δt (unique to that channel) between them before recombining the pulses into one channel. This characteristic delay corresponds to only one detector channel in the system (VCSEL: vertical cavity surface emitting laser); (c) Portion of detector ring showing propagation of scintillation pulses along fibers through system in direction of arrows. Each nanophotonic crystal introduces a characteristic delay as shown in (b). The characteristic delay is unique and known for each detector channel of the system. Analyzing the time between consecutive pulses on the fast photodetector readout tells us which channels received 511 keV photon hits (SSPM: solid-state photomultiplier).

References/Funding NIH U54CA119367, Sub-Award

New Photon Detectors Based on Position Sensitive Solid State Photomultipliers for High Resolution PET

F Taghibakhsh[1], PD Olcott[1,2], CS Levin[1,2,3]
Departments of [1]Radiology, MIPS, [2]Bioengineering, [3]Electrical Engineering, Stanford University, CA

High resolution detectors are essential components of an effective positron emission tomography system dedicated to breast imaging. Enhancing detector resolution down to 1mm usually results in increased cost due to increased number of photodetectors/processing channels unless, as one approach, position sensitive detectors are used to keep number of processing channels at a manageable level.

We are developing a high-resolution PET detector block based on position sensitive solid state photomultipliers (PS-SSPM) to arrive at detector resolution of 1 mm or better. PS-SSPMs are new developments in photodetection technology that combine high gain and low voltage properties of silicon photomultipliers (SiPM) with the position encoding capability of position sensitive avalanche photodiodes (PSAPD). They basically consist of a silicon photomultiplier integrated with a built-in resistive network at device level. Based on our demonstrated experience in design and development of block detectors using both PS-APDs and SiPMs, we expect PS-SSPMs provide advantages of superior positioning and timing capability as well as magnetic field invariability for PET/MRI multimodality applications.

We have considered coupling of scintillator crystal arrays of 1.0 mm and 0.8 mm pitch to a 25 mm2 SP-SSPM with four outputs. Our preliminary results show that in case of 1.0 mm pitch crystals, the PS-SSPM can resolve all 16 crystals and the 511 keV photopeak energy resolution obtained from the overall energy spectra of the crystal array is 15% at FWHM (this result is reported without offset correction). After positioning and correction for regular segmentation, the average peak to valley ratio was calculated to be 18.25 with sigma of 4.8. For the 0.8 mm pitch crystal array, the PS-SSPM can resolve all 36 crystals.

This work continues with full characterization of PS-SSPMs and addition of depth of interaction resolving capability to the detector block to address requirements of PET detectors for high resolution imaging.

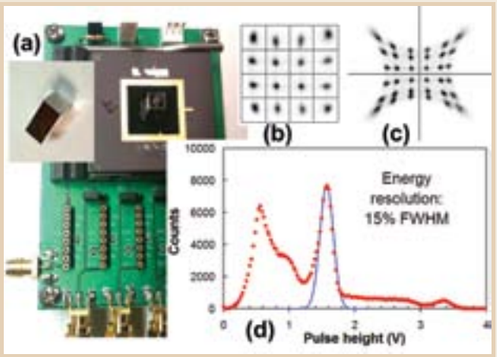

(a) Image of the PS-SSPM photodetector package and adapter board and a 6x6 array of crystals with 0.8 mm pitch. (b) The flood image for a 1 mm pitch 4x4 crystal array corrected for regular segmentation. (c) Anger logic flood image for the 6x6 crystal array with 0.8 mm pitch. (d) The overall energy spectrum for the 4x4 array of crystals with 1.0 mm pitch. The energy resolution of the photopeak is 15%.

References/Funding NSERC PDF (Natural Sciences and Engineering Council of Canada post-doctoral fellowship).

Mixture Model for Fast Estimation of Positron Annihilation Position

P Olcott[1], E Gonzalez[2], A Vandenbroucke[4], CS Levin[1,3,4]
Departments of [1]Electrical Engineering, [2]SMIS, [3]Radiology, [4]Radiology, MIPS, Stanford University, CA

We present an appropriate mixture model of exponential distributions to describe the variation of the positron endpoint in tissue. The physics of positron trajectories through tissue was simulated by a Monte-Carlo simulator based on elastic scattering from the nucleus, inelastic collisions with atomic electrons, hard elastic collisions producing delta electrons, and the positron emission energy spectra. Data from this comprehensive physics based Monte Carlo simulation was fed into the Expectation Maximization (EM) algorithm, and adapted to a binary mixture of exponential distributions. This binary mixture distribution provides a fast and accurate way to estimate positron-range for PET Monte Carlo simulation packages. For 18-F and 15-O point source simulations, the root mean square (rms) deviations within 2xFWHM between this mixture model and the full Monte Carlo simulation of positron endpoints probabilities was 4 and 7%, respectively.

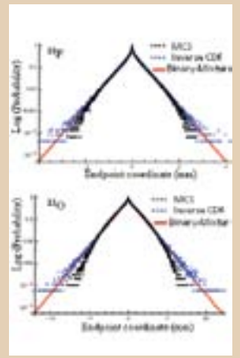

Physics simulated positron track endpoints (in water) using Monte Carlo Simulation (MCS), the binary mixture with parameters fitted to MCS, and the random sampling of the inverse CDF of the binary mixture

References/Funding Stanford Bio-X Graduate Fellowship (Olcott), Stanford Molecular Imaging Scholars (SMIS) program (NIH-NCI grant R25 CA118681)(Gonzalez), and grants R01 CA110956, ARRA R01CA119056-04S1, and R01 CA120474. Accepted for oral presentation at the 2010 IEEE Medical Imaging Conference. 30 October - 6 November, Knoxville, TN, USA

Optical Network-based PET DAQ System: One Fiber Optical Connection

E Kim[1,4], PD Olcott[1,5], CS Levin[1-6]
Departments of [1]Radiology, [2]Radiology, MIPS, [3]Bio-engineering, [4]Molecular Imaging Instrumentation Lab (MIIL), [5]Bio-X program, [6]Electrical Engineering, Stanford University, CA

Our work describes important and exciting advances in data acquisition system (DAQ) design for positron emission tomography (PET) that are possible with new high speed signal and optical network technology. Typically, a DAQ system is composed of many interconnected DAQ boards using high-speed links. Interconnections between PET DAQ boards involve transmission of event data, control signals, and a synchronization clock. Conventionally, the "tree" interconnection topology was used to handle high event data rates, however as the serial link and electronic computation speed have been improved, the "daisy-chained" interconnection scheme has become possible. The daisy-chain structure has improved the scalability as compared to the tree connection but has a lower single photon event throughput. High-speed serial optical networks can improve the throughput while further minimizing the interconnection between the DAQ boards. This newer approach can also be used to synchronize all the DAQ boards using the built in clock-recovery functionality inherent to optical data transmission links.

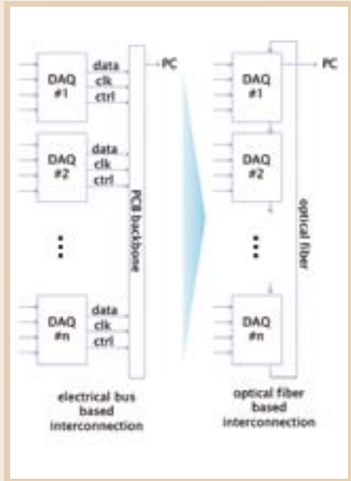

Comparison of DAQ interconnection based on electrical bus and optical fiber

We are developing DAQ boards for an MRI compatible PET brain scanner using the Fibre Channel 4.25Gbps optical standard to interconnect boards in a daisy-chained structure. For processing 576 differential detector signals, 18 DAQ boards are interconnected with only 18 optical patch cables and globally synchronize all the analog-to-digital converters (ADCs) and time-to-digital converters (TDCs) in the system. By replacing the signal lines used for parallel buses, serial buses, and clock signals with a single optical fiber channel, we minimized the number of interconnections between each DAQ board, which greatly simplifies the scaling process. Our design analysis predicts that the singles event throughput will be 80Mevents/sec using standard and easily available, optical interconnections and the required transmission buffer and coincidence memory sizes are 120 bits and 11k bits, respectively.

References/Funding GE Healthcare and a post-doctoral fellowship from TLI, Inc. Accepted for oral presentation at the 2010 IEEE Medical Imaging Conference, October 30, 2010, Knoxville, Tenessee, U.S.A.

Multiplexing PET Detectors with Noise Robust Compressed Sensing Decoder

G Chinn[1], P Olcott[1,2], CS Levin[1,2]
Departments of [1]Radiology, MIPS, [2]Bioengineering, Stanford University, CA

We present a novel method for multiplexing PET detectors using the theory of "compressed sensing" (CS). Photon events recorded by a PET camera are sparse in the natural pixel basis. Current multiplexing schemes used for PET cameras are noise robust but, multiple interaction events appear as a single interaction with an energy-weighted average position. CS theory can be used to specify multiplexing topologies that reduce the number of readout channels while resolving multiple interactions. The ability to distinguish multiple interaction events from single interaction events can improve the spatial resolution of PET. However, conventional CS decoders using L1 norm minimization are not robust in the presence of noise. Therefore, we have developed a new method for decoding multiplexed detector signals that optimizes the SNR of the decoded detector pixel signals using a modified L1 norm minimization (ML-CS). The new decoder can improve SNR by up to 60% over the conventional distance-weighted multiplexing schemes such as cross-strips and Anger logic. This multiplexing scheme combined with previously developed multiple interaction positioning algorithms can dramatically improve the spatial resolution of PET without any loss of energy or time resolution.

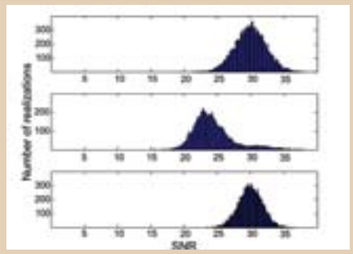

Shown are the distribution decoded detector signals for a multiplexed 8x8 pixel PET camera with a photopeak energy signal of "30" and a variance of "1" (power SNR of 900) is input into the detector for 10,000 trials of (top) conventional cross-strip multiplexing, (middle) CS, and (bottom) ML-CS. CS performs poorly in noise with a bias a larger variance while the proposed ML-CS algorithm is unbiased and reduces noise variance by 40% compared to the conventional multiplexing scheme.

References/Funding Stanford Bio-X Graduate Fellowship, NIH-NCI grants R01 CA110956 and R01 CA120474. Accepted for presentation at the IEEE NSS-MIC 2010, Knoxville, Tn.

Facile Synthesis, Silanization, and Biodistribution of Biocompatible Quantum Dots

N Ma[1], AF Marshall[2], SS Gambhir[1], J Rao[1]
Departments of [1]Radiology, MIPS and [2]Geballe Laboratory for Advanced Materials, Stanford University, CA

We reported a facile strategy for the synthesis of silica-coated quantum dots (QDs) for in vivo imaging. All the QD synthesis and silanization steps are conducted in water and methanol under mild conditions without involving any organometallic precursors or high-temperature, oxygen-free environments. The as-prepared silica-coated QDs possess high quantum yields and are extremely stable in mouse serum. In addition, the silanization method developed here produces nanoparticles with small sizes that are difficult to achieve via conventional silanization methods. The silica coating helps to prevent the exposure of the QD surface to the biological milieu and therefore increases the biocompatibility of QDs for in vivo applications. Interestingly, the silica-coated QDs exhibit a different biodistribution pattern from that of commercially available Invitrogen QD605 (carboxylate) with a similar size and emission wavelength. The Invitrogen QD605 exhibits predominant liver (57.2% injected dose (ID) g-1) and spleen (46.1% ID g-1) uptakes 30 min after intravenous injection, whereas the silica-coated QDs exhibit much lower liver (16.2% ID g-1) and spleen (3.67% ID g-1) uptakes but higher kidney uptake (8.82% ID g-1), blood retention (15.0% ID g-1), and partial renal clearance. Overall, this straightforward synthetic strategy paves the way for routine and customized synthesis of silica-coated QDs for biological use.

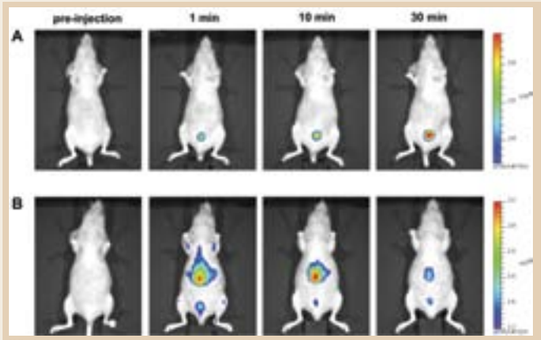

Whole-body imaging of silica-coated QDs and Invitrogen QDs. A) Representative whole-body fluorescence images of a nude mouse injected with silica-coated QDs during a 30 min time course. A strong signal from the bladder was observed, which indicated the possible renal clearance of silica-coated QDs (Five mice were examined and the results remained consistent.) B) Representative whole-body fluorescence images of a nude mouse injected with Invitrogen QD605 during a 30 min time course. The main signal comes from the liver. (Five mice were examined and the results remained consistent.)

References/Funding National Cancer Institute (Grant 1R01CA135294-01) , The Stanford University National Cancer Institute Centers of Cancer Nanotechnology Excellence (Grant 1U54CA119367-01). N. Ma, A. F. Marshall, S. S. Gambhir, J. Rao Small 2010, 6, 1520-1528

Non-invasive Molecular Imaging of Histone Tail Methylation in Living Animals

TV Sekar[1,2,3], A Dhanabalan[1,2,3], R Paulmurugan[1,2,3]
Departments of [1]Radiology, [2]Radiology, MIPS, [3]Canary Center at Stanford, Stanford University, CA

Histone modifications such us histone methylation and histone acetylation, are two important epigenetic processes which play key roles in maintaining a) Chromatin structure in heterochromatic region, and b) Gene expression in euchromatic region. Methylation of amino acids lysine and/or arginine residues at the NH2- terminal tail of histones (H3: Lys 4, 9, 27 and 36, and H4: Lys 20) by histone methyltransferases (HMTs) recruits chromodomains from heterochromatin-associated proteins (HP1) and forms a complex that functionally remodels chromatin structure, and regulation of gene expression. As epigenetic regulators are considered important players in maintaining cellular homeostasis, an *in vivo* imaging method of monitoring this cellular process may accelerate drug development for different diseases, including cancer. From this study, we have developed a bioluminescence resonance energy transfer (BRET) sensor that can optically image histone-methylation in cells and in living animals. A mutant renilla luciferase (Ex/Em:535/560nm), in combination with Turbo-RFP-FP635 (Ex/Em:588/635nm), was used to construct a vector expressing fusion protein with the histone methylation domain (H3-K9) and a chromodomain (HP1), connected by a specific linker peptide (RL8.6-Link-HP1-Link-K9-Link-Turbo-RFP-FP635). A similar sensor with Lys-27 peptide that normally interacts with the chromodomain of polycomb protein was used as control. The 293T-cells stably expressing K9-sensor was studied by inducing with different epigenetic modulators [valproic acid (VPA), TSA, and 5-Azacytidine] previously known to inhibit HDAC activity. The results showed an increase in the BRET signal (~2.5±0.5 fold) only by the sensor that has H3-K9-peptide with chromodoamin of HP1 protein and not by H3-K27 and polycomb proteins. Fluorescent microscopy imaging of cells showed a significant (P<0.5) methylation mediated increase in the level of Turbo-RFP signal. The tumor xenografts of cells expressing the sensor showed a similar level of VPA induced increase in living animals. The western blot analysis of H3 protein showed no change in endogenous level of its expression in response to the modulators further confirming the specificity of the system. The developed BRET system is sensitive and has the advantage of being used for the screening and pre-clinical evaluation of new drugs targeting this epigenetic regulator to test for different therapeutic applications.

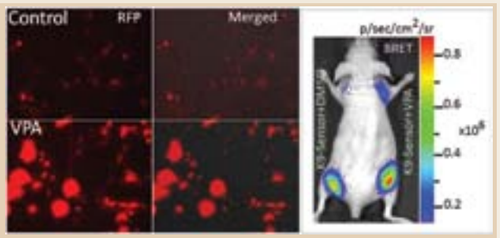

Sensor to image histone tail methylation in living animals

References/Funding Department of Radiology

18F-5-fluorouracil Dynamic PET/CT Reveals Decreased Tracer Uptake After Bevacizumab in Colorectal Metastasis

MH Zissen[1], P Kunz[1], G Fisher[2], A Quon[2]
Departments of [1]Medicine (Oncology), [2]Radiology, MIPS, Stanford University, CA

Purpose: The aim of this study was to evaluate the potential for 18F-5-fluorouracil (18F-5FU) PET/CT to reveal differences in 5FU uptake in metastatic colorectal cancer before and after treatment with bevacizumab.

Method and Materials: This was a pilot study of five consecutive patients (4 female, 1 male; mean age, 54.6 years; range, 27-85 years) with newly diagnosed and untreated metastatic colorectal adenocarcinoma. The presence of cancer was confirmed by histopathological analysis and patients served as their own internal control. Each patient underwent baseline 18F-5FU PET/CT scanning prior to treatment with bevacizumab, then received a 90-minute infusion of bevacizumab at a dose of 7.5 mg/kg (mean dose, 437.4 mg; range, 350-518 mg).

Approximately 24 hours post-bevacizumab, patients underwent a second 18F-5FU PET/CT. Using CT as an anatomical reference, manually drawn regions-of-interest (ROIs) were drawn around the aorta and all colorectal metastases and time-activity-curves (TAC) were generated at each tumor site. Differences between pre- and post-bevacizumab SUVmax and 5-minute Area Under the Curve ratios (AUCtumor/AUCaorta) were calculated for each lesion as the primary outcome measures.

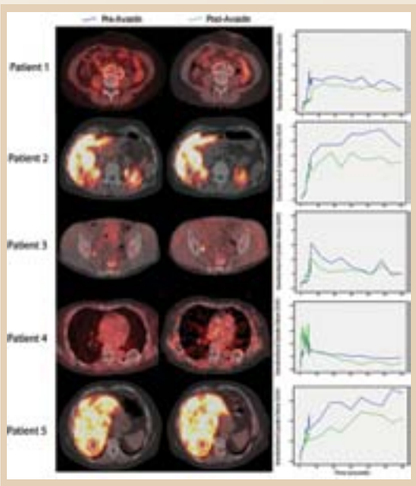

Results: The sizes of the metastatic lesions ranged from the smallest lesion measuring 3.04 cm x 1.50 cm to the largest measuring 4.19 cm x 2.76 cm. At baseline, the average SUVmax for 18F-5FU uptake at the metastatic sites 5-minutes after tracer infusion was 3.9 ± 1.4 (range, 0.98 to 8.06) and was not significantly different in patients 24-hours after the administration of bevacizumab, 3.1 ± 1.13 (range, 0.45 to 6.6, p = 0.125). In each of the 5 subjects, the 5-minute AUCtumor/AUCaorta ratio decreased 24 hours after treatment. At baseline, the mean AUCtumor/AUCaorta was 1.24 ± 0.30 (range, 0.424 to 2.14) and was significantly lower in patients 24-hours after the administration of bevacizumab, 1.06 ± 0.32 (range, 0.23 to 2.13, p = 0.04). This represents an average decline in the AUCtumor/AUCaorta of 20.2% (range, 0.4% to 45%).

Conclusion: In this pilot study of five patients with metastatic colorectal carcinoma, 18F-5FU PET/CT scanning revealed a significant decrease in tumor uptake 24 hours post-bevacizumab.

Clinical Relevance/Application: The ability of 18F-5FU PET/CT to visually demonstrate differential chemotherapy delivery may allow for improved therapy monitoring and treatment efficacy in patients with advanced colorectal cancer.

Quantification of Inflammation in Inflammatory Bowel Disease by Molecular Ultrasound Imaging

N Deshpande, Y Ren, K Foygel, M Schneider, PJ Pasricha, JK Willmann
Department of Radiology, MIPS, Stanford University, CA

Inflammatory bowel disease (IBD) is a chronic relapsing and remitting inflammatory condition of the gastrointestinal tract that needs regular and accurate monitoring. The goal of our study was to assess the potential of molecular ultrasound (US) imaging using microbubbles (MB) targeted to the inflammation marker P-selectin ($MB_{P\text{-selectin}}$) to quantify inflammation and to predict remission of inflammation following treatment in a chemically-induced colitis mouse model. Binding affinity and specificity of $MB_{P\text{-selectin}}$ was tested in a flow chamber under flow shear stress conditions (at 100 sec^{-1}). In vivo binding specificity of $MB_{P\text{-selectin}}$ to P-selectin was tested in 10 mice with colitis (induced by rectal administration of TNBS) and in 10 control mice without colitis using non-linear in vivo US imaging (25 MHz). Furthermore, in vivo molecular US imaging signal in treated (n=6; prednisolone therapy) versus non-treated (n=6; saline only) mice was compared over 3 subsequent treatment days. Attachment of $MB_{P\text{-selectin}}$ was significantly (p=0.01) higher to P-selectin positive (stimulated by TNF-alpha) than unstimulated endothelial cells and compared to $MB_{Control}$ (p=0.003). Furthermore, attachment of $MB_{P\text{-selectin}}$ significantly (R^2 >0.8, p=.01) correlated with expression levels of P-selectin on endothelial cells as quantified by flow cytometry. In vivo US signal of colitis was significantly higher (p=0.0003) with $MB_{P\text{-selectin}}$ compared with $MB_{Control}$ (Figure), and significantly (p=0.01) dropped by 53% following injection of blocking antibodies. In treated animals, in vivo US imaging signal significantly (p=.03) decreased during the course of treatment while in non-treated mice US signal in the colon wall remained elevated. In vivo US imaging signal significantly (R^2 >0.6; p=.04) correlated with P-selectin expression levels as assess by ex vivo assays (WB and IF). In conclusion, molecular US using $MB_{P\text{-selectin}}$ allows non-invasive in vivo quantification and monitoring of inflammation at the molecular level in a chemically-induced colitis mouse model. This study lays the foundation for an eventual future clinical translation of molecular US imaging for monitoring inflammation in IBD.

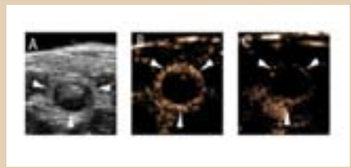

Figure. (A) Transverse B-mode image of the colon wall (white arrows) in a mouse with TNBS-induced colitis using a high-resolution US scanner. Molecular ultrasound imaging signal in colon wall (arrows) following injection of $MB_{P\text{-selectin}}$ (B) was significantly higher compared to control conditions following injection of $MB_{Control}$ (C), suggesting binding specificity of MBP-selectin to P-selectin in inflamed colon wall

Cationic and Neutral Microbubble and DNA Dose Effects on Ultrasound-mediated Gene Delivery In Vivo

C Panje[1], MA Pysz[1], DS Wang[1], Y Ren[1], M Schneider[2], JK Willmann[1]
Department of [1]Radiology, MIPS, Stanford University, CA, USA; [2]Bracco Research, Geneva, Switzerland.

Ultrasound (US)-mediated sonoporation using contrast microbubbles (MB) is a promising strategy for therapeutic gene delivery. The purpose was to assess the influence of different MB and DNA doses on in vivo gene delivery to skeletal muscles in mice using novel cationic and neutral MB. Cationic and neutral MB were characterized for their charge and amount of bound plasmid DNA encoding Firefly luciferase (pFluc). Protective effects of cationic MB in binding DNA were tested by incubating pFluc-MB mixtures with DNase and assessing the extent of degraded DNA. US-mediated gene delivery of 4 µg pFluc to endothelial cells with 5E7 cationic or neutral MB was performed and quantified using the luciferase assay kit. US-mediated in vivo gene delivery to hindlimb skeletal muscle was performed with varying cationic and neutral MB (1E7, 5E7, 1E8, or 5E8 with 50 µg pFluc) or pFluc doses (10, 17.5, 25, 37.5, or 50 µg with 1E8 MB). Bioluminescence imaging was performed every 24h post-transfection to compare each dose and to negative control conditions (no MB or US). pFluc binding of cationic MB was significantly (P<0.01) higher and more protective to DNase degradation than neutral MB. Fluc activity using cationic MB was significantly higher both in cell culture (P<0.01) and in vivo (P<0.006) experiments and was significantly lower in negative controls (P<0.002). The magnitude of in vivo gene delivery using cationic compared to neutral MB increased linearly (R2=0.9) with the amount of bound pFluc (P<0.05). Cationic MBs bound with 10 µg pFluc (30% bound fraction) resulted in 3.4-fold higher gene delivery compared to neutral MB. In contrast, cationic MB mixed with 50 µg pFluc (6% bound fraction) resulted in only 1.3-fold higher gene delivery compared to neutral MB. US-mediated gene delivery is more efficient with cationic compared with neutral MBs when the fraction of bound DNA is maximized.

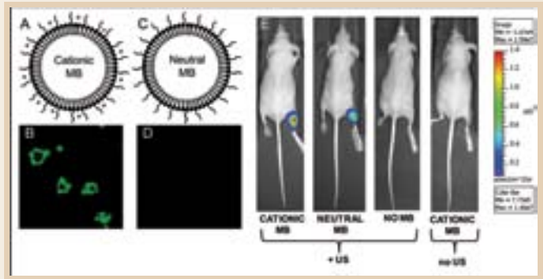

YOYO-1-labeled pFluc (green) binds to cationic (A) but not to neutral (C) microbubbles (MB) as evidenced by confocal microscopy (B, D). In vivo bioluminescence imaging of ultrasound-mediated delivery of 50 µg pFluc mixed with $1x10^8$ MB demonstrates significantly higher imaging signal in skeletal muscles when using cationic versus neutral MB and compared to control conditions (no MB, no US). Differences between cationic and neutral MB was highest when the fraction of bound DNA was maximized.

References/Funding RSNA Seed grant RSD0809, the Howard S. Stern Research Grant of the Society of Gastrointestinal Radiologists, NCI ICMIC CA114747 P50 developmental grant, NIH R21 CA139279, the SMIS NIH fellowship program R25 CA11868, and the Canary Foundation. 2010 World Molecular Imaging Congress, Kyoto, Japan. Oral presentation on Sept. 11, 2010.

Longitudinal Assessment of Expression Levels of Tumor Angiogenic Markers with Molecular Ultrasound Imaging

N Deshpande, Y Ren, K Foygel, J Rosenberg, JK Willmann
Department of Radiology, MIPS, Stanford University, CA

The purpose of this study was to evaluate molecular ultrasound (US) to non-invasively assess the temporal expression levels of three angiogenic markers, $\alpha_v\beta_3$ integrin, endoglin, and VEGFR2 on tumor vascular endothelial cells *in vivo*. Three types of targeted microbubbles ($MB_{Integrin}$, $MB_{Endoglin}$, MB_{VEGFR2}) were designed and the binding specificity of MB to their respective targets was tested on endothelial cells (positive and negative for angiogenic marker expression) under flow shear stress conditions (at 100 sec^{-1}) in a flow chamber. In vivo molecular US imaging using the three different MB was performed at three different tumor stages (small, medium, large size) of three different subcutaneous tumor xenografts (breast, ovarian, pancreatic cancer) in mice (n=48) and was correlated with angiogenic marker expression levels as assessed by western blotting. Attachment of all three targeted MB was significantly (p=0.003) higher to positive than to negative cells and the attachment was significantly (p=0.026) decreased by blocking antibodies. The number of attached targeted MB significantly (R^2>0.8, p=.0001) correlated with the expression levels of the angiogenic markers on cell lines as assessed by flow cytometry. For breast and ovarian cancer, endoglin expression was significantly higher than $\alpha_v\beta_3$ integrin (p=0.005) and VEGFR2 (p=0.0003) expression in small and medium tumors as assessed by in vivo US imaging. In contrast, in pancreatic cancer, $\alpha_v\beta_3$ integrin was highest in small tumors compared to endoglin and VEGFR2 (p=0.05) and endoglin expression peaked in medium and large tumors. In all tumors types, expression levels of all markers were lowest (p=0.005) in large tumors (Figure). In vivo US imaging signal significantly (R^2>0.6; p<.05) correlated with ex vivo western blotting results for all three markers. In conclusion, molecular US imaging allows non-invasive assessment of the expression levels of different tumor angiogenic markers that vary during tumor growth in various subcutaneous human tumor xenografts. The results provide insights into tumor angiogenesis biology and may help in defining imaging targets for both early cancer detection and treatment monitoring using molecular US imaging.

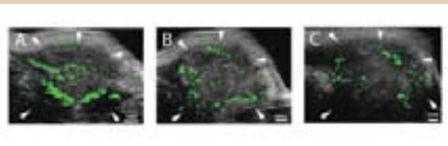

Transverse contrast-enhanced ultrasound images of a subcutaneous breast cancer tumor graft (arrows) in a nude mouse, imaged longitudinally at small (A), medium (B), and large (C) tumor sizes following intravenous administration of $MB_{Endoglin}$(Scale bar lower right corner equals 1mm). Endoglin expression (shown as green overlay on B-mode images) was highest at small tumor size and decreased at medium and large tumor sizes

A Novel Motion Correction Technique for Contrast-enhanced Ultrasound Imaging of Tumor Vascularity

MA Pysz[1], I Guracar[2], K Foygel[1], JK Willmann[1]
Department of [1]Radiology, MIPS, Stanford University, CA; [2]Siemens Medical Solutions, Mountain View, CA.

The purpose of our study was to develop and test a real-time adjustable motion correction algorithm for contrast-enhanced ultrasound (CEUS) imaging in human colon cancer xenografts in mice receiving vascular disruptive tumor treatment. A motion correction technique that measured horizontal and vertical B-mode pixel displacements using sum of absolute difference in a size- and location-adjustable tracking box, was incorporated into the software of a clinical US scanner (Sequoia Acuson 512, Siemens). Contrast-enhanced US imaging in the maximum intensity projection mode (14 MHz, MI=0.26) was performed on subcutaneous human colon cancer xenografts (implanted on backs of mice). Extent of tumor vascularity (expressed as % contrast area) was calculated in real-time with and without motion correction in tumors with different grades of vascularity (low, moderate, high; n=16), and in mice with (n=5) and without (n=5) treatment with a vascular disrupting agent (VDA). In moderately vascularized tumors, the effect of motion correction on the measured tumor vascularity was significantly (P<.001) higher (mean differences, 13.3% ± 2.3%) compared with tumors with low (mean differences, 3.2% ± 2.7%) or high (mean differences, 4.8% ± 2.5%) vascularity. The differences in tumor vascularity measurements with and without motion correction were also highest in animals taking a spontaneous deep breath when the tumors were moderately vascularized (mean differences, 25.4% ± 5.2%; Figure) compared to low (mean differences, 13.4% ± 7.2%) and highly (mean differences, 12.0% ± 10.0%) vascularized tumors. Following VDA treatment, tumor vascularity significantly (P=.003) decreased on motion-corrected images (51.7% ± 25.1% to 19.7% ± 11.4%), whereas vascularity minimally increased (P=.03) in non-treated mice (from 64.0% ± 15.4% to 70.7% ± 18.9%). In conclusion, the effects of real-time motion correction for CEUS imaging of tumor vascularity substantially depend on the grade of tumor vascularity and the extent of motion, and may improve CEUS imaging for treatment monitoring.

Subcutaneous human colon cancer xenograft imaged with contrast-enhanced ultrasound with (left) and without (right) novel real-time adjustable motion correction technique. Note substantial difference of measured tumor vascularity in mouse taking a spontaneous deep breath. A region of interest (yellow line) was placed to outline the tumor boundaries.

References/Funding RSNA Seed grant RSD0809, the Howard S. Stern Research Grant of the Society of Gastrointestinal Radiologists, NCI ICMIC CA114747 P50 developmental grant, NIH R21 CA139279, the SMIS NIH fellowship program R25 CA11868, and the Canary Foundation. 2010 World Molecular Imaging Congress, Kyoto, Japan. Poster presentation on Sept. 10, 2010.

A Novel MicroRNA Cocktail for Improving Survival of Transplanted Cardiac Progenitor Cells

S Hu, F Lan, M Huang, JC Wu
Department of Radiology, Stanford University, CA

Introduction: Ischemic heart disease is the leading cause of death in the United States. Cardiac progenitor cells (CPCs) have shown great promise for cardiac regenerative medicine. MicroRNAs (miRNAs) are small non-coding RNAs of 21-23 nucleotides in length which negatively regulate gene expression. We hypothesize that screening for a pro-survival/anti-apoptotic miRNAs cocktail can improve the survival of CPCs and enhance cell therapy after myocardial infarction (MI).

Methods: Sca-1$_+$ CPCs were isolated from transgenic mice (constitutively expressing luciferase and eGFP) through cultured ventricle explants followed by Sca-1$_+$ purification with anti-Sca-1 microbeads. CPCs were transduced with individual lentiviral vectors carrying precursor of miR-21, miR-24, miR-221, a cocktail of all 3 miRNAs, or GFP as control. For in vitro testing, CellTiter-Fluor™ Cell Viability Assay was used after challenge with serum free medium for 24 hrs. For in vivo testing, we injected the transfected cells intramuscularly. For targets bioinformatics prediction, we employed miRanda and TargetScan algorithms to evaluate the potential targets of these miRNAs.

Results: FACS indicated that isolated CPCs are more than 95% Sca-1$^+$ and CD45- cells. CPCs transduced with individual lentivirus showed higher cellular viability. More importantly, CPCs with miRNAs cocktail transduction showed highest cellular viability. Following intramuscular injection, CPCs expressing miRNAs showed significantly more robust bioluminescence signals compared to control CPCs at day 14 (18,734±1241 vs. 12,783±912 p/s/cm^2/sr; P<0.05). Bioinformatics assay indicated many apoptotic genes were targets of these 3 miRNAs which are putatively suppressed by these miRNAs, including Casp3, Casp8ap2, Bax, Pdcd4, and Fasl. Similarly, Foxo3, Bcl2l11 and Ak2 are apoptotic activators or effectors that were predicted to be potential suppression targets by all the three miRNAs.

Conclusion: miRNAs cocktail can improve CPC survival both in vitro and in vivo. miRNAs preconditioned CPCs may represent a potential strategy to improve cell survival after transplantation.

Upregulation of Major Histocompatibility Complex and Co-signaling Molecules on Human Embryonic Stem Cells in Allogeneic Humanized Mice

JI Pearl, R-J Swijnenburg, S Schrepfer, J Yu, F Cao, H Vogel, JC Wu
Department of Radiology, MIPS, Stanford University, CA

Introduction. Human embryonic stem cells (hESCs) hold promise to serve as an unlimited source of cells for therapeutic transplantation. However, the immunological properties of hESCs in a human allogeneic transplantation setting are unknown. We investigated the immunological phenotype of hESCs and the changes that occur upon interaction with allogeneic human lymphocytes *in vivo*.

Methods and results. hESC (H9 line) were cultured in feeder-free conditions. hESC-derivatives were obtained by embryoid body formation during 7 days, followed by spontaneous differentiation on gelatin-coated plates for an additional 7 to 21 days. Immunophenotyping was performed by FACS analysis of hESC and hESC-derivatives in resting state or after a 3-day treatment with Interferon (IFN)-γ (50ng/ml). hESC expressed class-I major histocompatibility (MHC), β-2 microglobulin, ICAM-1 and LFA-3 antigens and were negative for MHC-II, CD40, B7-1, B7-2 and B7-H1 antigens (Figure 1). IFN-γ treated hESC-derivatives expressed B7-H1 from differentiation day 14 and MHC-II at day 28. Immunodeficient NOD-scid Il2rγ^{null} mice were reconstituted with human peripheral blood mononuclear cells (hPBMCs, 2x10^7) by tail vein injection. hPBMC engraftment was confirmed by FACS analysis of human CD45$^+$ cells in mouse peripheral blood at 2 and 4 weeks following injection (n=12) (Figure 2). H9 hESC (5x10^4), transduced to express firefly luciferase and eGFP reporter genes, were injected into the spleen of hPBMC reconstituted (n=6) or non-reconstituted (n=4) mice. At 4 weeks, intrasplenic teratomas were harvested and digested into single cell suspension by incubation in collagenase D. FACS analysis of GFP$^+$ hESC-derived teratoma cells from hPBMC reconstituted animals revealed robust upregulation of MHC-I, MHC-II, β-2 microglobulin, ICAM-1 and B7-H1 (Figure 3 and Table 1), as compared to non-reconstituted mice. Expression of LFA-3 did not change and B7-1/2 antigens were not observed.

Conclusion. For the first time, the imunological phenotype of hESC was investigated in a clinically relevant human allogeneic transplantation model. Upon interaction with allogeneic lymphocytes *in vivo*, hESC-derivatives upregulate MHC and co-signaling molecules. These data suggest that the immunogenicity of hESC-derivatives increases progressively following allogeneic transplantation. Nevertheless, progressive upregulation of B7-H1 could provide immunomodulatory action.

Donor Cell Memory in Human Induced Pluripotent Stem Cells

Z Ghosh, KD Wilson, Y Wu, S Hu, T Quertermous, JC Wu
Department of Radiology, Stanford University, CA

Human induced pluripotent stem cells (hiPSCs) generated by de-differentiation of adult somatic cells offer potential solutions for the ethical issues surrounding human embryonic stem cells (hESCs) as well as their immunologic rejection after cellular transplantation. However, although hiPSCs have been described as "embryonic stem cell-like", these cells have a distinct gene expression pattern compared to hESCs, making incomplete reprogramming a possibility. It is unclear whether a difference in the tissue of origin contributes to these differences. To answer these vital questions, careful transcriptional profiling analysis is necessary to investigate the exact reprogramming state of hiPSCs, and the extent that the impression of the tissue of origin contributes to the reprogramming process in cells. We compared the gene profiles of hiPSCs derived from fetal fibroblasts, neonatal fibroblasts, adipose stem cells, and keratinocytes to hESCs and their corresponding donor cells to determine the overall degree of reprogramming within each hiPSC line. Global clustering of gene expression profiles showed the "distance" between each hiPSC line and their donor cells, as well as hESCs. Bioinformatic analysis of the genes that have a similar mode of regulation in hiPSCs and their corresponding donor cells thus established the degree of genetic memory of hiPSCs with respect to their cells of origin. Our study reveals that retention of gene expression memory of the donor cell type contributes to the difference between gene expression profiles of hiPSCs with hESCs, and adds to the incompleteness in reprogramming. Further, the status of reprogramming in hiPSCs reveals that fetal fibroblast-derived hiPSCs are closer to hESCs, followed by adipose, neonatal fibroblast, and keratinocyte derived hiPSCs.

Manganese-Enhanced Magnetic Resonance Imaging (MEMRI) Highlights Injured Peripheral Nerves in Neuropathic Pain (Chronic Constrictive Injury)

D Behera and S Biswal
Department of Radiology, MIPS, Stanford University, CA

Objective: Manganese-enhanced MRI (MEMRI) is a surrogate method to interrogate calcium fluxes in nervous system since Mn2+ physiologically follows calcium and is a T1 shortening agent. Our purpose is to validate MEMRI for detection of changes in lumbar nerves related to neuropathic nociception in a model of Chronic Constrictive Injury.

Methods: Animal experiments were approved by Stanford IACUC. A neuropathic pain model was created by Chronic Constrictive Injury (CCI) of the left sciatic nerve of Sprague-Dawley rats by placing four interrupted loose ligatures on the nerve. Rats were allowed to heal for four weeks. Rats with CCI (n=5) and uninjured animals (control; n=3) were evaluated for allodynia in the hind paws using von-Frey's filaments. All MRI experiments were performed on a small animal MR imaging unit (7T, Microsigna) and T1 weighted Fast Spin Echo images were obtained of the lumbosacral region. Baseline scans were obtained on all rats before MnCl2 administration. Then all rats were injected with $MnCl_2$ (30mM; 1 ml/100 gm; IP) and scanned again 24 hours after injection. ROIs (RT_Image image analysis software) were placed on sciatic nerves bilaterally, just inferior to L6 vertebra, at the level of sacral promontory to quantify the degree of manganese enhancement, which were normalized to background signal in the muscle (normalized signal). Statistical analysis of normalized MEMRI signal intensities was performed with ANOVA with variable sample sizes (n=5 in CCI group; n=3 in control group). Von-Frey test results were assessed by paired t-test for difference in mean 50% threshold values of the left and right paws of CCI rats. Data are reported at mean±standard deviation.

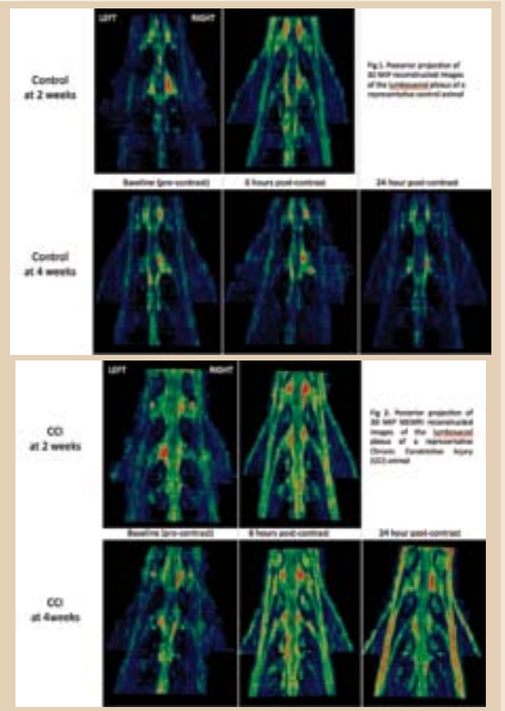

Results: Allodynia was illustrated in left hindpaws of CCI rats (50% paw withdrawal thresholds; mean log stiffness: left paw 4.35±0.46, right paw 5.00±0.19; p=0.0117). No difference was seen between the right and left paws of control rats (left paw 5.07±0.05, right paw 5.02±0.10; p=0.42).

Increased normalized MEMRI signal is seen in the CCI rats (Fig. 2; baseline 1.31±0.04; post-$MnCl_2$ 1.8±0.08) compared to control rats (Fig. 1; baseline 1.32±0.10; post-$MnCl_2$ 1.56±0.23); p=0.0082. No statistical difference was seen in normalized signal between left and right sides.

Conclusion: Rats with neuropathic pain show increased manganese uptake on MEMRI in vivo. MEMRI Functional Neurography can be used to assess pain-activated neural pathways.

^{18}F-FDG PET-MRI can be Used to Identify Injured Peripheral Nerves in a Model of Neuropathic Pain

D Behera and S Biswal
Department of Radiology, MIPS, Stanford University, CA

Purpose: Increased spontaneous neural activity and metabolic changes are known to occur in injured nerves and are largely attributed to the symptoms of neuropathic pain. Using ^{18}F-Fluorodeoxyglucose (^{18}FDG) positron emission tomography-magnetic resonance imaging (PET-MRI), we wanted to determine whether increased ^{18}F-FDG uptake is observed in injured peripheral nerves in a rodent model of neuropathic pain and whether the addition of MRI promoted improved localization ^{18}FDG uptake in peripheral nerves.

Materials and Methods: Animal experiments were approved by Stanford IACUC. Neuropathic pain model of spared-Nerve Injury (SNI) was created in adult male Sprague-Dawley rats (n=3) by ligating and transecting branches of the left sciatic nerve. The right hind limb was used as control. The rats were allowed 4 weeks to heal and develop pain. Presence of pain was confirmed by testing for allodynia using von-Frey's filaments. For imaging, each rat was given 500 μC of ^{18}FDG intravenously under anesthesia and kept under anesthesia for about 1 hour, until imaging. Animals were held rigidly in a transportable holder. Fiducials, containing both water and dilute amount of ^{18}F-FDG were placed against the animal. Ten minute static scans of the thighs were obtained using a small animal PET (microPET; R4 microPET, Siemens) and T1-weighted fast spin echo images were obtained using a 7T small-animal MRI (microMRI; Magnex). MicroPET-MR image fusion was performed using Amide image analysis software. MicroMR images were used to define the anatomic localization of the peripheral nerves and placement of the ROI. Radioactivity counts were then recorded from the fused microPET images. Volumetric ROIs were placed on 2 mm segments of sciatic nerves, proximal to the level of injury in both sciatic nerves of each animal. Additionally, background ROIs of 2 x 2 x 2 mm were placed in the adjacent muscle on each side. The maximum signal in each ROI was normalized to the mean signal within the respective background ROIs to obtain a signal-to-background ratio (SNR). Data were analyzed for statistical significance using paired t-tests in Excel.

Results: Presence of allodynia in the operated limb was confirmed. The 50% paw withdrawal threshold 2.6 ± 0.1 and 4.3 ± 0.2 on the SNI and control side, respectively (p<0.01). Significantly increased ^{18}FDG SNR is seen in the SNI nerve (2.2 ± 0.3) compared to control side (1.3 ± 0.4) (p<0.03).

Conclusion: Animals with neuropathic pain show increased ^{18}FDG uptake in the affected nerve. PET-MRI can be effectively used to localize 18FDG uptake in peripheral nerves.

Clinical Relevance: Constant and spontaneous activity of nociceptive neurons in neuropathic pain induces metabolic changes in such neurons. Using PET alone to identify injured peripheral nerves is difficult given the limited spatial resolution of PET. Identification and localization of chronic pain generators is difficult. The hybrid ^{18}F-FDG PET-MRI method can potentially be used to accurately localize injured peripheral nerves in neuropathic pain.

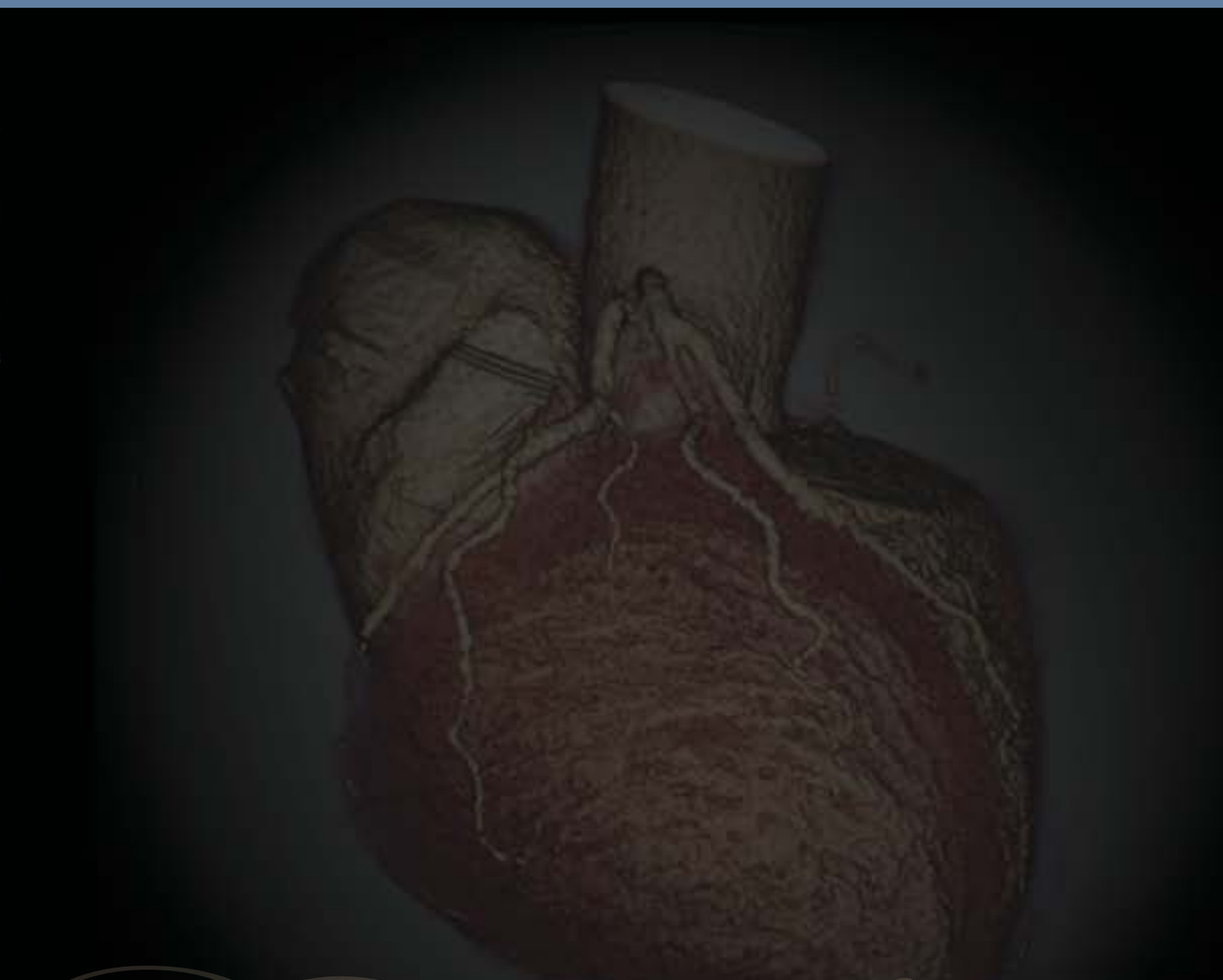

Publicc

Peer-Reviewed Presentations at Scientific Meetings

ISMRM 2010 (May 1-7, Stockholm, Sweden)

Aksoy M, Bammer R, Mlynash, Gupta, Snider, Eyngorn, Venkata-subramanian, Fischbein, Wijman	Blood-Brain Barrier Permeability Measured by DCE MRI Predicts Perihematomal Edema Diffusivity.
Aksoy M, Forman, Straka M, Cukur, Holdsworth, Skare, Santos, Hornergger, Bammer R	Hybrid Prospective & Retrospective Head Motion Correction System to Mitigate Cross-Calibration Errors.
Aksoy M, Forman, Straka M, Holdsworth, Skare, Hornegger, Bammer R	Fast Cross-Calibration Between MR Scanner and Optical System for Prospective Motion Correction.
Aksoy M, Forman, Straka M, Holdsworth, Skare, Santos, Hornegger, Bammer R	Improved Prospective Optical Motion Correction for DTI USing an Extended-Field-of-View and Self-Encoded Marker.
Aksoy M, Holdsworth, Skare, Bammer R	Effects of b-Matrix Correction on Fiber Tractography in High Resolution DTI with Short-Axis Propeller EPI.
Alley, Beatty, Hsiao, Vasanawala	Reducing the Scan Time of Time-Resolved, 3D Phase Contrast Imaging with 2D Autocalibrated Parallel Imaging.
Balchandani P, Pauly J, Spielman D	Self-Refocused Adiabatic Pulse for Spin Echo Imaging at 7T.
Balchandani P, Spielman D	Adiabatic Magnetization Preparation Pulse for T2-contrast at 7 Tesla.
Bammer R, Yeom, Holdsworth, Skare	High-Resolution Diffusion-Weighted Imaging of the Orbits Using Readout-Segmented EPI.
Bitton, Kaye, Daniel BL, Butts Pauly K.	MR guided HIFU in Cadaver Breasts for Pre-Operative Tumor Localization of Non-Palpable Breast Tumors as an Alternative to Needle Wire Localization.
Chang, Glover G	Variable density spiral fMRI.
Chen CA, Chen W, Goodman, Hargreaves B, Koch, Lu, Brau, Draper C, Delp, Gold G	SEMAC and MAVRIC for Artifact-Corrected MR Imaging around Metal in the Knee.
Dong, Worters, Wu, Cukur, Hargreaves B, Nishimura, Vasanawala	Rapid Non-Contrast-Enhanced Renal Angiography using Multiple Inversion Recovery.
Engstrom, Nordell A, Martensson, Nordell B, Bammer R, Skare	Isotropic resolution in Diffusion Weighted Imaging using 3D multi-slab, multi-echo Echo Planar Imaging.
Forman, Aksoy M, Straka M, Hornegger, Bammer R	Improved Pose Detection for Single Camera Real-Time MR Motion Correction Using a Self-Encoded Marker.
Forman, Aksoy M, Straka M, Nornegger, Bammer R	Self-Encoded Marker Design for Adaptive Optical Real-Time Motion Correction.
Glover G, Chang	Hadamard-Encoded fMRI for Reduced Susceptibility Dropout.
Gold G, Vasanawala, Lu, Chen CA, Chen W, Pauly J, Butts Pauly K., Goodman, Hargreaves B	MRI near Metallic Implants using SEMAC: Initial Clinical Experience.
Grandlund, Staroswiecki, Alley, Daniel, Hargreaves B	High Resolution T2 Breast Imaging using FADE.
Grissom, Holbrook A, Rieke, Lustig, Santos, Swaminathan, McConnell, Butts Pauly K.	Hybrid Multi-baseline and Referenceless PRF-shift Thermometry.
Gu, Zahr, Spielman D, Sullivan, Pfefferbaum, Mayer D	Quantification of Glutamate and Glutamine using CT-PRESS at 3T.

Peer-Reviewed Presentations at Scientific Meetings

ISMRM 2010 (May 1-7, Stockholm, Sweden)

Halloran, Aksoy M, Kober, Bammer R	Simple Self-Gating for Compensation of Respiratory Motion using a Spiral k-Space Trajectory.
Han, Hargreaves B	Combined Excitation and Partial Saturation to Reduce Inflow Enhancement.
Han, Hargreaves B, Daniel, Alsop, Robson, Han, Worters, Shankaranarayanan	Breast Perfusion Imaging Using Arterial Spin Labeling.
Hargreaves B, Gold G, Pauly J, Butts Pauly K.	Adaptive Slice Encoding for Metal Artifact Correction.
Hargreaves B, Lu, Butts Pauly K., Pauly J, Gold G	Fat-Suppressed and Distortion-Corrected MRI Near Metallic Implants.
Holbrook A, Dumoulin, Santos, Medan, Butts Pauly K.	Integrated MRI and HIFU Control System: Towards Real Time Treatment of the Liver.
Holbrook A, Prakash, Jones, Planey, Santos, Diederich, Butts Pauly K., Sommer G	Multislice Treatment Planning and Control for Real Time MR-Guided Prostate Ablation with Transurethral Multisectored Ultrasound Applicators.
Holdsworh, Skare, Vasanawala, Bammer R	Diffusion-Weighted Imaging of the Abdomen with Readout-Segmented (RS)-EPI.
Holdsworth, Skare, O'Hallaran, Bammer R	Reduced-FOV Diffusion Imaging with ZOnal Oblique Multislice (ZOOM) combined with Readout-Segmented (RS)-EPI.
Holdsworth, Yeom, Skare, Barnes PD, Bammer R	Clinical Application of Readout-Segmented (RS)-EPI for Diffusion-Weighted Imaging in Pediatric Brain.
Hu, Glover G	RF Excitation Encoding: A Fast Imaging Technique for Dynamic Studies.
Hurd R, Mayer D, Yen YF, Tropp, Pfefferbaum, Spielman D	Cerebral Dynamics and Metabolism of Hyperpolarized [1-13C] Pyruvate using Time Resolved Spiral-Spectroscopic Imaging.
Jordan, Worters, Vasanawala, Daniel, Alley, Kircher, Herfkens, Hargreaves B	Optimization and Comparison of Non-Contrast-Enhanced Inflow-Sensitive Inversion Recovery bSSFP for Renal and Mesenteric MRA at 1.5T and 3.0T.
Josan S, Holbrook A, Kaye, Law, Butts Pauly K.	Analysis of Focused Ultrasound Hotspot Appearance on EPI and Spiral MR Imaging.
Josan S, Yen YF, Hurd R, Pfefferbaum, Spielman D, Mayer D	Application of Double Spin-Echo Spiral Chemical Shift Imaging to Rapid Metabolic Imaging of Hyperpolarized [1-13C]-Pyruvate.
Josan S, Yen YF, Hurd R, Pfefferbaum, Spielman D, Mayer D	Double Spin-Echo Spiral Chemical Shift Imaging for Rapid Metabolic Imaging of Hyperpolarized [1-13C]-Pyruvate.
Kaye, Bitton, Butts Pauly K.	Focal Spot Visualization in MRgFUS of the Breast: MR-ARFI vs. T1-weighted FSE.
Kaye, Butts Pauly K.	SNR Trade-offs in MR-ARFI of Focused Ultrasound in the Brain.
Khalighi, Sacolick, Dixon, Watkins, Josan S, Rutt BK	Fast and Robust B1 Mapping at 7T by the Bloch-Siegert Method.
Khalighi, Sacolick, Rutt BK	Signal to Noise Ratio Analysis of Bloch-Siegert B1+ Mapping.
Kim, Sung, Han, Alley, Lu, Hargreaves B	Phase Correction in Bipolar Multi-Echo Sequence Water-Fat Separation for Off-Isocenter Imaging.
Kim, Sung, Hargreaves B	Robust Field Map Estimation Using Both Global and Local Minima.
King, Rieke, Butts Pauly K.	MR-Guided Focused Ultrasound Ablation of the Rat Liver.
Kitzler, Su, Zeineh, Deoni, Harper-Little, Leung, Kremenchutzky, Rutt BK	mcDESPOT-Derived Demyelination Volume in Multiple Sclerosis Patients Correlates with Clinical Disability and Senses Early Myelin Loss.

Peer-Reviewed Presentations at Scientific Meetings

ISMRM 2010 (May 1-7, Stockholm, Sweden)

Kopeinigg, Aksoy M, Forman, Bammer R	3D TOF Angiography using Real Time Optical Motion Correction with a Geometric Encoded Marker.
Li, Chen, Beatty, Brau, Hargreaves B, Busse, Gold G	SNR Quantification with Phased-Array Coils and Parallel Imaging for 3D-FSE.
Li, Chen, Rosenberg, Beatty, Brau, Kijowski R, Hargreaves B, Busse, Gold G	Improving Isotropic 3D FSE Methods for Imaging the Knee.
Lillaney, Bennett, Fahrig R	Motor Design for an MR-compatible Rotating Anode X-ray Tube.
Lu, Butts Pauly K., Gold G, Pauly J, Hargreaves B	Compressive Slice Encoding for Metal Artifact Correction.
Lu, Butts Pauly K., Gold G, Pauly J, Hargreaves B	Noise Reduction in Slice Encoding for Metal Artifact Correction Using Singular Value Decomposition.
Mayer D, Yen YF, Takahashi, Josan S, Tropp, Pfefferbaum, Hurd R, Spielman D	Dynamic and High-Resolution Metabolic Imaging of the Rat Brain In Vivo Using Hyperpolarized [1-C]-Pyruvate.
Mayer D, Yen YF, Takahashi, Tropp, Rutt BK, Hurd R, Spielman D, Pfefferbaum	Single-Shot Spiral Chemical Shift Imaging in the Rat In Vivo with Hyperpolarized [1-C]-Pyruvate.
Nnewihe A, Grafendorfer T, Daniel BL, Calderon P, Alley MT, Robb F, Hargreaves B	16-Channel Custom-Fitted Bilateral Breast Coil for Parallel Imaging in Two Directions.
O'Hallaran, Holdsworth, Skare, Bammer R	Reduced Field of View Imaging for Twice-Refocused Diffusion EPI using a Perpendicular Refocusing Slab.
Ouriadov, Thind, Farag, Friesen Waldner, Wang, Chen, Fox, Rutt BK, Scholl, McKenzie, Santyr	Extending the Data Acquisition Window for Hyperpolarized 13C Metabolite Mapping Using Variable Flip Angles.
Quist, Hargreaves B, Morrell, Gold G, Bangerter	Region-Growing Reconstruction for Large-Angle Multiple-Acquisition bSSFP.
Rakow-Penner R, Daniel, Glover G	A Pilot Study Comparing Blood Oxygen Level Dependent (BOLD) Contrast in the Human Healthy and Malignant Breast.
Schmiedeskamp, Straka M, Bammer R	R2/R2* Estimation Errors in Combined Gradient- and Spin-echo EPI Sequences Due to Slice-profile Differences Between RF Pulses.
Schmiedeskamp, Straka M, Jennuleson, Zaharchuk G, Bammer R	T1-independent Vessel Size Imaging with Multi-gradient- and Spin-echo EPI.
Senadheera, Mayer D, Darpolor, Yen YF, Xing, Spielman D	In Vivo Detection of Radiation-Induced Metabolic Response in Rat Kidneys by 13C Hyperpolarized MRSI.
Shapiro L, Jenkins, Stevens, Li, Chen, Brau, Hargreaves B, Gold G	Isotropic MRI of the Upper Extremity with 3D-FSE-Cube.
Skare, Bammer R	Jacobian Weighting of Distortion Corrected EPI Data.
Skare, Holdsworth, Bammer R	Diffusion Weighted Image Domain Propeller EPI (DW iProp EPI).
Skare, Holdsworth, Bammer R	Image Domain Propeller FSE (iProp-FSE).
Skare, Holdsworth, Yeom, Barnes PD, Bammer R	Comparison Between Readout-Segmented (RS)-EPI and an Improved Distortion Correction Method for Short-Axis Propeller (SAP)-EPI.
Staroswiecki, Bangerter, Gold G, Hargreaves B	Comparison of SPGR and Balanced SSFP for Sodium Knee Imaging.

Peer-Reviewed Presentations at Scientific Meetings

ISMRM 2010 (May 1-7, Stockholm, Sweden)

Staroswiecki, Granlund, Aley, Gold G, Hargreaves B	T2 Maps and Diffusion-Weighted Imaging of Knee Cartilage with a DESS Sequence at 3T.
Straka M, Albers, Bammer R	Equivalence of CBV Measurement Methods in DSC-MRI.
Straka M, Albers, Bammer R	Robust Arterial Input and Venous Output Function Detection for Automatic Processing in DSC-MRI.
Straka M, Lee, Lansberg, Mlynash, Albers, Bammer R	Is Reduced CBV a Reliable Surrogate Marker for Infarct Core and Can It Be Used to Identify Lesion Mismatch?
Straka M, Newbould, Sramek, Albers, Bammer R	Improving DSC-MRI by Orientation-corrected Phase-based AIF and VOF.
Sung, Hargreaves B	High-frequency Subband Compressed Sensing MRI.
Townsend, King, Zaharchuk G, Butts Pauly K.	MR-guided unfocused ultrasound disruption of the rat blood-brain barrier.
Vogelsong, Staroswiecki, Hargreaves B, Han, Fattor, Friedlander, Shah, Beaubien, Gold G	Comparison of T1ρ, T2 mapping, and sodium MRI of osteoarthritic cartilage in vivo.
Wade, McKenzie, Rutt BK	No Inversion Double Angle Look-Locker (niDALL) for Flip Angle Mapping.
Wade, McKenzie, Rutt BK	Transient RF Spoiling for 3D Look-Locker Acquisitions.
Waldner, Wang, Chen, Oriadov, Fox, Rutt BK, Scholl, Santry, McKenzie	Parallel MRI Acceleration of Dynamic and High Resolution Hyperpolarized 13C MRI.
Watkins, Staroswiecki, Bangerter, Hargreaves B, Gold G	High SNR Dual Tuned Sodium/Proton Knee Coil.
Worters, Hargreaves B	Transient Balanced SSFP Imaging with Increased Signal by Variable Flip Angles.
Xu, Mayer D, Gu, Yen YF, Josan S, Johansson, Tropp, Hurd R, Spielman D	Quantitation of In-Vivo Metabolic Kinetics of Pyruvate using Hyperpolarized 13C Magnetic Resonance Spectroscopic Imaging.
Yen YF, Le Roux, Mayer D, Takahashi, Tropp, Spielman D, Pfefferbaum, Hurd R	Exploring Multi-shot non-CPMG for Hyperpolarized 13C Metabolic MR Spectroscopic Imaging.
Zaharchuk G, Olivot, Bammer R, Shankaranarayanan, Mlynash, Albers, Moseley M	Arterial Spin Label Imaging of Transient Ischemic Attack.
Zahr, Gu, Mayer D, Spielman D, Sullivan, Pfefferbaum	Glutamate and Glutamine Changes Induced by Ethanol Treatment in the Rat Brain Detectable with CT-PRESS at 3T.
Zeineh, Kitzler, Atlas, Rutt BK	Increased Detectability of Alzheimer Plaques at 7T vs. 3T using High Resolution bSSFP.

Peer-Reviewed Presentations at Scientific Meetings

RSNA 2009 (Nov 29-Dec 4, Chicago, Illinois)

Barth R.	MR Imaging of the Fetal Chest.
Chan F.	MR Imaging.
Chan F.	Pediatric Cardiac-gated CT Imaging.
Chan F.	Pediatric Series: Chest/Cardiovascular Imaging.
Deshmukh S.	Compressed Sensing Fetal MRI.
Desser T.	Abdominal Fat Necrosis: Imaging Spectrum.
Do BH	A Natural Language Processor to Detect Uncertainty and Recommendations in Radiology Reports.
Do BH	J-Viewer: A Free Javascript Library for Creating Web (and iPhone) Teaching Files with Simple PACS Functionality.
Do BH	RadTF: An NLP-generated Teaching File.
Do BH	Vascular Ultrasound: Unusual Intravascular Abnormalities, Pitfalls and Don't Miss Lesions.
Do BH	XRAYHEAD MSK ONLINE: A Radiology Teaching File Based on RSNA's RadLex.
Gao H.	A New Algorithm for Scatter CorrectioninX-ray CT Using Primary Modulator.
Gayer G.	There Is What, Where Foreign Objects within the Abdominal Cavity Encountered on CT.
Ghanouni P.	Minocycline Prevents Development of Neuropathic Pain by Mitigating Macrophage Recruitment to Site of Nerve Injury as Shown with USPIO-MRI.
Girard-Hughes E.	Characterization of Radiofrequency Ablation Lesions with Iodine Contrast-enhanced Cardiac C-arm CT.
Gold G.	Advanced Imaging of Cartilage.
Gold G.	Three-dimensional FSE Cube for Detection of Hip Pathology with MR Arthrography.
Hallett R.	Postprocessing, Work Flow, and Interpretation.
Hsiao A.	An Integrated Computational Approach to Cardiovascular 4D Flow MRI.
Iagaru A.	Prospective Evaluation of 99mTc-MDP Scintigraphy, 18F NaF PET/CT, 18F FDG PET/CT, and Whole-Body MRI for Detection of Skeletal Metastases.
Kamaya A	BOOST: Gastrointestinal Case-based Review.
Lee C.	Incidental Extracardiac Findings on Screening Coronary Computed Tomography: Clinical and Economic Impact.
Mittra E.	Accuracy of Tumor Measurements by 18F-FDG PET.
Newman B.	Disorders of the Large Airways in the Pediatric Population.
Phangureh V.	Visualization of Long Term Endograft Migration Patterns after Endovascular Abdominal Aortic Aneurysm Repair (EVAR).
Rao V.	[18F] Fluoride Ion PET-CT Predicts Painful Metastatic Bone Lesions in the Thoracolumbar Spine.
Roos J.	Contrast Medium.
Rubin DL	iPad:A Tool for Creating Semantic Annotations in Radiology Images.
Rubin DL	Technical capabilities of RadLex in Proteacute; Geacute: From Lexicon to Ontology.
Rubin DL	Utility of Terminologies for Image Annotation and Information Retrieval.

Peer-Reviewed Presentations at Scientific Meetings

RSNA 2009 (Nov 29-Dec 4, Chicago, Illinois)

Rubin G.	Cardiac CT Mentored Case Review: Part II.
Rubin G.	Computer-aided Detection of Lung Nodules.
Rubin G.	Coronary Artery Disease I: Native Vessel Disease.
Schmitzberger F.	Assessing Display Quality for Trials on Lung Nodule CT-Scans Using Existing Non-specialized Monitors.
Segall G.	Case-based Review of Nuclear Medicine: PET/CT Workshop on Cancers of the Thorax.
Shin, Lewis	Research and Education Foundation Support Award: Unusual Intravascular Abnormalities: Pitfalls and Don't Miss Lesions.
Starman J.	A New Method for Lag Reduction in Flat-Panel X-ray Detectors.
Sze, Daniel Y.	Endovascular Treatment of Occlusive Diseases.
Ueda T.	Configuration by Incomplete Endograft Apposition to the Aortic Arch: Significant Risk of Endoleak Formation after Thoracic Endovascular Aortic Repair.
Wang D.	Cationic Microbubble Contrast Agents Enhance Ultrasound-Mediated Gene Delivery in a Mouse Model of Tumor Angiogenesis.
Willmann J.	Engineered Knottin Peptides: A New Platformfor the Design of Novel Molecular Ultrasound Contrast Agents for Imaging Tumor Angiogenesis.

SNM 2010 (June 5-9, Salt Lake City, Utah)

Draper C, Fredericson M, Besier T, Beaupre G, Delp S, Gold G, Quon A.	Correlation Between MRI and NaF PET/CT in Patients with Patellofemoral Knee Pain.
Eikman E, Segall G, Greenspan B, Jacene H, Heston T, Strauss H, Berman C, Walker R, Gatenby R.	Standard Image Descriptors for the Provisional Molecular Imaging Reporting System (pMIRS) for Thoracic Tumors.
Ren G, Miao Z, Liu H, Kimura R, Cheng Z	Novel Knottin Miniproteins for Tumor Angiogenesis Targeting.
Liu H, Ren G, Miao Z, Zhang X, Tang X, Han P, Gambhir SS, Cheng Z	Noninvasive Molecular Imaging of Radioactive Tracers Using Optical Imaging Techniques.
Liu H, Zhang X, Xing B, Han P, Gambhir SS, Cheng Z	In Vivo Multiplexed Optical Imaging with Radiation Luminescence Excited Quantum Dots.
Jiang L, Miao Z, Kimura R, Liu H, Bao A, Cutler C, Li P, Cheng Z.	Preliminary Evaluation of 177Lu Labeled Knottin Peptides as Novel Integrin Targeted Agents in a Human Glioma Xenografted Mice Model.
Kedziorek D, Gilson W, Fu Y, Barnett B, Huang G, Bulte J, Hofmann L, Kraitchman D.	A Novel X-ray-visible Microencapsuled Mesenchymal Stem Cell Therapy for Peripheral Arterial Disease.
Mittra E, Goris M, Iagaru A, Kardan A, Liu S, Shen B, Chin F, Chen X, Gambhir SS.	First in Man Studies of [18F]FPPRGD2: A Novel PET Radiopharmaceutical for Imaging αvβ3 Integrin Levels.
Peng H, Levin CS	Would a High Resolution Cardiac-dedicated PET System Improve Quantification of Myocardial Blood Flow?
Tang C, Dhawan V, Poston K, Feigin A, Eidelberg D	Accurate Differential Diagnosis of Parkinsonism by Pattern Analysis of Metabolic Imaging Data.

Peer-Reviewed Presentations at Scientific Meetings

WMIC 2009 (Sept 23-26, Montreal, Canada)

Byeong A.	Noninvasive Imaging of Cancer Gene Therapy in Orthotopic Mouse Models Using A Novel Systemically Delivered Bi-Directional Transcriptional Targeting Vector.
Chan C, Reeves R, Geller R, Yaghoubi S, Solow-Cordero D, Gambhir S	A Novel High-Throughput Strategy (HTS) Coupled with Molecular Imaging for Discovery of an Isoform-Selective Inhibitor of Heat Shock Protein 90 Alpha (Hsp90α) in Living Subjects.
Chan C, Bradner J, Reeves R, Schreiber S, Paulmurugan R, Gambhir S	A Novel Strategy for Repetitive, Non-invasive Monitoring of the Efficacies of Histone Deacetylase 6 (HDAC6) Inhibitors in Living Subjects.
Chin F, Shen B, Liu S, Berganos R, Chang E, Mittra E, chen X, Gambhir S	Clinical-grade [18F]FPPRGD2: An Automated Multi-step Radiosynthesis for Human PET Studies.
de la Zerda A, Paulus Y, Moshfeghi D, Gambhir S	Photoacoustic Imaging of the Eye for Improved Disease Detection.
de la Zerda A, Liu Z, Bodapati S, Teed R, Zavaleta C, Vaithilingam S, Chen X, Khuri-Yakub B, Dai, H, Gambhir S	Ultra High Sensitivity Targeted Photoacoustic Imaging Agents for Cancer Early Detection in Living Mice.
Doyle T.	Construction and Use of a Simple Multi-modality, Multi-animal Mouse Holder.
Fan-Minogue H, Paulmurugan R, Chan C, Cao Z, Felsher D, Gambhir S	Molecular Imaging of Oncogene Targeted Cancer Therapy.
Habte F, Budhiraja S, Doyle T, Levin CS, Paik D	Effect of Inter- and Intra- user Variability in Quantification of Molecular Imaging Data.
Habte F, Nielsen CH, Ren G, Yaghoubi S, Withofs N, Doyle T, Pisani L, Levin C	Quantitation Error Assessment for Small Animal PET.
Hardy J, Pisani L, Contag C	Multimodal Imaging of Transplacental Infection and Subsequent Birth Defects.
Kimura R, Miao Z, Cheng Z, Cochran J, Gambhir S	A Dual-labeled Cystine Knot Peptide for PET and Near-infrared Fluorescence Imaging of Integrin Expression in Living Subjects.
Kode K, Shachaf C, Elchuri S, Nolan G, Paik D	Parametric Modeling of Raman Spectra of Nanoparticles for Quantitative Unmixing.
Kode K, Zavaleta C, Gambhir SS, Paik D	Quantitative Unmixing of Spectra for Raman Molecular Imaging of Living Subjects.
Le U, Kwon, Nguyen, Kim, Jiang, Hong, Shin, Rhee, Bom, Gambhir SS, Ahn, Choy, Min	Engineering Attenuated Salmonella Typhimurium to Selectively Target and Deliver Protein in Infarcted Myocardium.
Lei J, Miao, Kimura R, Ren, Liu, Sliverman, Li, Gambhir SS, Cochran, Cheng	111In-Labeled Agouti Related Proteins for SPECT/CT Imaging of Tumor αvβ3 Integrin.
Lei J, Kimura, Miao, Silverman, Ren, Liu, Li, Gambhir, Cheng	Agouti-Related Protein: An Excellent Peptide Scaffold for In Vivo Tumor Molecular Imaging.
Hartman, Dragulescu-Andrasi, Levi, de la Zerda A, Gambhir SS	A Novel Smart Agent for Photoacoustic Molecular Imaging.
Liu, Miao, Ren, Jiang, Kimura R, Cochran, Han, Cheng	64Cu-Labeled Multivalent α-Melanocyte Stimulating Hormone Analogs for MicroPET Imaging of Melanocortin 1 Receptor Expression.

Peer-Reviewed Presentations at Scientific Meetings

WMIC 2009 (Sept 23-26, Montreal, Canada)

Liu H, Ren, Miao, Han, Gambhir SS, Cheng	Near-infrared Fluorescence Imaging of Melanocortin 1 Receptor Expression with A Cy5.5-Labeled α-Melanocyte-Stimulating Hormone Analog.
Miao Z, Levi, Cheng	Affibody Based Molecular Probes for EGFR PET and Optical Imaging.
Miao Z, Ren, Liu, Kimura R, Jiang, Cochran, Gambhir SS, Cheng	An 18F-Labeled Knottin Peptide for Tumor αvβ3 Integrin PET Imaging.
Namavari M, Chang, Kusler, Yaghoubi S, Mitchell, Gambhir SS	A Novel Synthesis of 2'-Deoxy-2'-[18F]fluoro-9-β-D-arabino-fluranosylguanine ([18F]F-AraG).
Nielsen C, Withofs, Kimura R, Tran, Miao, Cochran, Cheng, Felsher, Willman, Gambhir SS	Imaging of Tumor Neovascularization in Transgenic Mouse Models Using a Novel PET 64Cu-DOTA-Knottin Peptide.
Parashurama N, O'Sullivan, de la Zerda A, Levi, Harris, Gambhir SS	Continuous, Quantitative, Molecular Monitoring of a Near Infrared Fluorophore Using a Novel, Microfabricated, Implantable Biosensor.
Parashurama N, Lobo, Clarke, Gambhir SS	Intravital Molecular Imaging of the Birth of a Tumor From Cancer Stem Cells Using Intravital Microscopy.
Parashurama N,	Molecular Imaging of Cell Transplantation in Porcine Myocardium Using Clinical MRI and PET-CT.
Paulmurugan R.	Secretory Gaussia Luciferase (sGLUC)-monomeric Red Fluorescence protein (mRFP)-truncated Herpes Simplex Virus Thymidine Kinase (tTK) Triple Fusion Improves Intracellular Luciferase Activity and Enhances its Imaging Applications in Small Animals.
Peng H.	Preclinical and Clinical PET Detector Design Considerations Using Silicon Photomultipliers (SPM).
Pysz M.	Maximum Intensity Persistence Analysis is a Sensitive and Reliable Tool to Quantitate Tumor Angiogenesis with Ultrasound Imaging.
Pysz M.	Pre-clinical Evaluation of Novel Clinically-Translatable KDR-Targeted Microbubbles for Molecular Ultrasound Imaging of Angiogenesis in Cancer.
Ra H.	In Vivo Microscopy in Mouse Models of Monogenic Skin Disease.
Rao J.	Immobilized Activatable Bioluminescent Probes for In Vivo Imaging of Protease Activity in Tumors.
Rao J.	In Vivo Bioluminescence Imaging of Furin Activity in Breast Cancer Cells Using Luminogenic Substrates.
Rao J.	In Vivo Imaging of Tuberculosis with Near Infrared Fluorogenic Probes.
Ren G.	Discovery and In Vivo Evaluation of Two-Helix Small Proteins for HER2 Molecular Imaging.
Ribot E.	In Vivo Detection of Both Single Cells and Developing Metastases using SSFP at 1.5T.
Blankenberg F, Levashova, Sarkar, Pizzonia, Backer, Backer	Molecular Imaging Assessment of Tumor VEGF Receptors In Vivo in Response to Treatment with Pazopanib, a Small Molecule TKI under Clinical Development.
Smith B.	Direct Microscale Visualization of Targeted Quantum Dot Binding in Multiple Tumor Models of Living Mice using Intravital Microscopy.
Smith B.	The Microscale Journey of Targeted Carbon Nanotubes Imaged Using Intravital Microscopy: from Circulation to Tumor Cells in Living Subjects.
Sun X.	Imaging Guided Immunotherapy of Head-Neck Squamous Cell Carcinoma with Cetuximab in Animal Models.
Townson J.	Quantifying Differential Response of Solitary Cancer Cells and Growing Metastases to Treatment in Whole Mouse Liver using Magnetic Resonance Imaging.
Van de Ven S.	Molecular Imaging using Nanotubes and a Clinical Optical Breast Imaging System.

Peer-Reviewed Presentations at Scientific Meetings

WMIC 2009 (Sept 23-26, Montreal, Canada)

Wang D.	Enhanced Ultrasound-Mediated Gene Delivery with Cationic Microbubbles in a Mouse Model of Tumor Angiogenesis.
Willmann J.	Design and Testing of a Novel Ultrasound Contrast Agent for Molecular Ultrasound Imaging of Tumor Angiogenesis.
Yaghoubi S.	Monitoring Adoptive Cellular Immunotherapy in Glioma Patients Using PET Reporter Gene Imaging.
Yerushalmi D.	Factors Affecting Partial Volume Correction of PET-CT Images Based on the Method of Recovery Coefficients.
Zavaleta C.	Preclinical Evaluation of Raman Nanoparticles for Their Potential Use in Clinical Endoscopic Imaging.
Zhan K.	Small Molecule Probes for Live Cell Imaging of Membrane Proteins with an N-Terminal Cysteine.
Mackanos MA, Helms MW, Contag C.	Laser Guided Genomic Analysis of Tissue Response to Laser Induced Thermal Stress.
Bu L, Chen K, Xie J, Huang J, Sun KW, Wang YA, Chua M-S, So S, Shen B, Chen X.	Magnetic Resonance Imaging of orthotropic hepatocellular carcinoma in mice with Different Iron oxide nanoparticles.
Lee S, Xie J, Choi KY, Kim K, Kwon IC, Chen X.	Multi-Ferroic Activatable Probes for Protease Imaging.
Gao J, Chen K, Xie R, Peng X, Gambhir SS, Chen X.	Ultrasmall Near-infrared Non-Cadmium Quantum Dots for Tumor Imaging.
Wang K, Shen B, Huang T, Chen X.	Use of Fluorescent Labeled Epidermal Growth Factor to In Vivo Image Hepatocellular Carcinoma Xenografts.
Parashurama N, Ahn BC, Yerushalmi D, Zavaleta C, Chung J, Swanson JC, Ikeno F, Teramoto T, Lyons J, Bhaumik S, Yaghoubi S, Yang P, Yock PG, Robbins RC, Gambhir SS.	Molecular Imaging of Cell Transplantation in Porcine Myocardium Using Clnical MRI and PET-CT.
Haeberle H.	Tarted Peptides for Medulloblastoma Identified with Phage Display.
Lee S, Chen X, Kwon IC, Kim K.	Polymeric Nanosensor for Imaging Matrix Metalloproteinase Expression.

Other Scientific Meeting Presentations

Other Presentations 2010

Barnes P.	Controversies in Forensic Science and Medicine: Towards Resolution in the 21st Century. Child Abuse, NAI, and the Mimics: Controversies in the Era of Evidence-Based Medicine Seminar; September 24-25, 2009; Ontario, Canada.
Beaulieu C.	Imaging of Osseous Stress Injuries. Annual Winter Diagnostic Imaging Update; January 4-8, 2010; Beaver Creek, CO.
Beaulieu C.	Knee MRI. Annual Current Concepts of Magnetic Resonance Imaging; October 12-15, 2009; Monterey, CA.
Beaulieu C.	MDCT in Sports Injuries: What's the Point? Annual International Symposium on Multidetector-Row CT; May 19-22, 2009; San Francisco, CA.
Beaulieu C.	Musculoskeletal MDCT: Simple but Effective Protocols. Annual International Symposium on Multidetector-Row CT; May 19-22, 2009; San Francisco, CA.
Beaulieu C.	Optimizing MDCT of the Musculoskeletal System. Annual Winter Diagnostic Imaging Update; January 4-8, 2010; Beaver Creek, CO.
Beaulieu C.	Who Wants to be a Millionaire, the MSK Version. Annual Winter Diagnostic Imaging Update; January 4-8, 2010; Beaver Creek, CO.
Chan F.	Cardiac CT for Non-coronary Applications. Annual Spring Diagnostic Imaging Update; March 22-26, 2010; Maui, HI.
Chan F.	Cardiac MRI for Valvular Heart Disease. Annual Spring Diagnostic Imaging Update; March 22-26, 2010; Maui, HI.
Chan F.	Choosing Between Cardiac MRI and Cardiac CT: The Right Tool for the Right Problem. Annual Spring Diagnostic Imaging Update; March 22-26, 2010; Maui, HI.
Chan F.	Congenital Aberrant Coronary Arteries: What is Lethal, What is Not. Annual International Symposium on Multidetector-Row CT; May 19-22, 2009; San Francisco, CA.
Chan F.	CT Coronary Angiography - Techniques, Indications, and Radiation Risks. Annual Spring Diagnostic Imaging Update; March 22-26, 2010; Maui, HI.
Chan F.	Radiation in Pediatric Cardiac CTA: Myth and Reality. Annual International Symposium on Multidetector-Row CT; May 19-22, 2009; San Francisco, CA.
Chan F.	Reading with the Professor - Cardiac MDCT. Annual International Symposium on Multidetector-Row CT; May 19-22, 2009; San Francisco, CA.
Chen C, Chen W, Goodman S, Hargreaves B, Koch K, Lu W, Brau A, Gold G.	Correction of Metal-Induced MRI Artifacts in the Knee with MAVRIC and SEMAC Sequences. Annual Orthopedic Research Society Meeting; March 6-9, 2010; New Orleans, LA.
Cheng Z.	Molecular Probe Discovery with Protein Scaffold Based Approach. Korea Atomic Energy Research Institute; March 16-17, 2010; Jeongeup, Korea.
Church DG, Vasanawala SS, Rosenthal DN, Newman B, Chan FP.	MRI Diagnosis of Endocardial Fibroelastosis – A Comparison with Echocardiography. Annual Society for Pediatric Radiology Meeting; April 21-25, 2009; Carlsbad, CA.
Colen TW, Vasanawala SS, Newman B, Chan FP.	Coronary CT Angiography Dose Reduction in Children from 2006 to 2008. Annual Society for Pediatric Radiology Meeting; April 21-25, 2009; Carlsbad, CA.
Daniel B.	Back to the Future: Breast MRI Without Gadolinium? Annual Symposium on Breast MRI; October 23, 2009; Las Vegas, NV.
Daniel B.	Body MR - Emerging Techniques and Applications. Annual Current Concepts of Magnetic Resonance Imaging; October 12-15, 2009; Monterey, CA.
Daniel B.	Breast MRI for Local Staging. Annual Advances in Breast Imaging and Interventions; March 3, 2010; Las Vegas, NV.
Daniel B.	MR of the Abdomen: Common Techniques and What They Show. Annual Current Concepts of Magnetic Resonance Imaging; October 12-15, 2009; Monterey, CA.
Daniel B.	MRI of Silicone Breast Augmentation. Annual Symposium on Advances in Breast MRI; October 23 2009; Las Vegas, NV.

Other Scientific Meeting Presentations

Other Presentations 2010

Daniel B.	MRI of the Breast. Annual Current Concepts of Magnetic Resonance Imaging; October 12-15, 2009; Monterey, CA.
Daniel B.	MRI of the Prostate. Annual Current Concepts of Magnetic Resonance Imaging; October 12-15, 2009; Monterey, CA.
Daniel B.	Screening for Breast Cancer with Contrast-Enhanced MRI. Annual Advances in Breast Imaging and Interventions; March 3, 2010; Las Vegas, NV.
Desser T.	Abdominal Vascular Emergencies. Annual Spring Diagnostic Imaging Update; March 22-26, 2010; Maui, HI.
Desser T.	Imaging of Colorectal Cancer. Annual Spring Diagnostic Imaging Update; March 22-26, 2010; Maui, HI.
Desser T.	MDCT of the Small Bowel. Annual Spring Diagnostic Imaging Update; March 22-26, 2010; Maui, HI.
Desser T.	Understanding THIDS and THADs. Annual International Symposium on Multidetector-Row CT; May 19-22, 2009; San Francisco, CA.
Desser T.	Understanding THIDS and THADs. Annual Spring Diagnostic Imaging Update; March 22-26, 2010; Maui, HI.
Draper C, Besier T, Fredericson M, Santos J, Beaupre G, Delp S, Gold G.	Patellar Maltracking Patterns Differ with Gender. Annual Orthopedic Research Society Meeting; March 6-9, 2010; New Orleans, LA.
Fahrig R.	Image Guidance During Interventions: Beyond Fluoroscopy. Symposium of the Dept of Medical Biophysics at the University of Toronto; May 16, 2009; Toronto, Canada.
Fahrig R.	Scatter in MDCT: Hardware and Software Correction. Annual International Symposium on Multidetector-Row CT; May 19-22, 2009; San Francisco, CA.
Fischbein N.	Anterior and Central Skull Base. Neuroradiology in Aspen: Update 2009; August, 2009; Aspen, CO.
Fischbein N.	CT and MR of Stroke. Neuroradiology in Aspen: Update 2009; August, 2009; Aspen, CO.
Fischbein N.	Head and Neck Imaging. Annual Current Concepts of Magnetic Resonance Imaging; October 12-15, 2009; Monterey, CA.
Fischbein N.	Imaging the Myelopathic Patient. Neuroradiology in Aspen: Update 2009; August, 2009; Aspen, CO.
Fischbein N.	Intracranial Infection. Neuroradiology in Aspen: Update 2009; August, 2009; Aspen, CO.
Fischbein N.	Nasopharynx Cancer: Staging and Patterns of Spread. Annual meeting of the American Society of Nuroradiology; May 21, 2009; Vancouver, BC.
Fischbein N.	Spine MRI. Annual Current Concepts of Magnetic Resonance Imaging; October 12-15, 2009; Monterey, CA.
Fischbein N.	The Nasopharynx: Cancer and Pattersn of Tumor Spread. Annual meeting of the American Society of Head and Neck Radiology; October 9, 2009; New Orleans, LA.
Fischbein N.	White Matter Disease. Neuroradiology in Aspen: Update 2009; August, 2009; Aspen, CO.
Fleischmann D.	3D and 4D Imaging of the Aortic Root. Symposium on Multislice CT of the Chinese Society of Radiology & Stanford University; August 13-15, 2009; Dalian, China.
Fleischmann D.	Acute Aortic Dissection: New Insights from CT. 9th International MDCT Symposium; October 13, 2009; Tokyo, Japan.
Fleischmann D.	Acute Aortic Dissection: New Insights from CT. Symposium on Multislice CT of the Chinese Society of Radiology & Stanford University; August 13-15, 2009; Dalian, China.
Fleischmann D.	Complicated Type B Dissections. Annual International Symposium on Multidetector-Row CT; May 19-22, 2009; San Francisco, CA.
Fleischmann D.	How to Control Arterial Enhancement for Subsecond Scans. Annual International Symposium on Multidetector-Row CT; May 19-22, 2009; San Francisco, CA.

Other Scientific Meeting Presentations

Other Presentations 2010

Fleischmann D.	In Pursuit of the Heart - History of Cardiac CT. Symposium on Multislice CT of the Chinese Society of Radiology & Stanford University; August 13-15, 2009; Dalian, China.
Fleischmann D.	In Search of the Intimomedial Flap: Unusual Type A Dissections. Annual International Symposium on Multidetector-Row CT; May 19-22, 2009; San Francisco, CA.
Fleischmann D.	Injection Protocol Design for Fast Cardiovascular CT. Symposium on Multislice CT of the Chinese Society of Radiology & Stanford University; August 13-15, 2009; Dalian, China.
Fleischmann D.	Lower Extremity CT-Angiography. 6th Internationales MDCT Symposium; January 27-30, 2010; Garmisch-Partenkirchen, Germany.
Fleischmann D.	Understanding Arterial Contrast Medium Dynamics for Cardiovascular CT. Annual International Symposium on Multidetector-Row CT; May 19-22, 2009; San Francisco, CA.
Gambhir S.	A New Generation of Molecular Imaging Strategies. Second Asian Congress of Radiation Research; May, 2009; Seoul, South Korea.
Gambhir S.	Molecular Imaging in Drug Development. Johnson & Johnson Excellence in Science Symposium; November, 2009; New Brunswick, NJ.
Gambhir S.	Molecular Imaging: Challenges and Future Perspectives. BSP World Health Summit; October, 2009; Berlin, Germany.
Gambhir S.	Molecular Imaging: Future Perspectives. NCI Alliance for Nanotechnology; November, 2009; Manhattan Beach, CA.
Gold G.	Advanced MSK MRI. Annual Current Concepts of Magnetic Resonance Imaging; October 12-15, 2009; Monterey, CA.
Gold G.	Femoracetabular Impingement. Annual SCBT-MR Meeting; March 7-11, 2010; San Diego, CA.
Gold G.	MRI of the Elbow. MRI in Clinical Practice; March 17-19, 2010; Park City, UT.
Gold G.	MRI of the Hip. MRI in Clinical Practice; March 17-19, 2010; Park City, UT.
Gold G.	MRI of the Knee. MRI in Clinical Practice; March 17-19, 2010; Park City, UT.
Gold G.	MRI of the Shoulder. MRI in Clinical Practice; March 17-19, 2010; Park City, UT.
Gold G.	Stress Injuries in Athletes. Annual SCBT-MR Meeting; March 7-11, 2010; San Diego, CA.
Gu Y, Levin CS.	Effects of Multiple Interaction Photon Events on Measuring Position and Arrival Time in a CZTbased High-resolution Small Animal PET System. IEEE Medical Imaging Conference; October 25-31, 2009; Orlando FL.
Gu Y, Levin CS.	Photon Interaction Rate Studies for a Semiconductor-Based High-Resolution Small Animal PET System. IEEE Medical Imaging Conference; October 25-31, 2009; Orlando FL.
Hargreaves B.	3.0T: New Physics and Opportunities. Annual Symposium on Advances in Breast MRI; October 23 2009; Las Vegas, NV.
Hargreaves B.	Artifacts in MRI. Annual Current Concepts of Magnetic Resonance Imaging; October 12-15, 2009; Monterey, CA.
Hargreaves B.	Body MRI Concepts. Annual Current Concepts of Magnetic Resonance Imaging; October 12-15, 2009; Monterey, CA.
Hargreaves B.	Breast MRI Artifacts. Annual Symposium on Advances in Breast MRI; October 23 2009; Las Vegas, NV.
Hargreaves B.	Breast MRI: Review of Physics and Acronyms. Annual Symposium on Advances in Breast MRI; October 23 2009; Las Vegas, NV.
Hoffmann L.	Hands-on Device Instruction. IX Curso Internacional "Hands On" en Cirugia Invasiva Minima y Radiologia Intervencionista; October 30, 2009; Buenos Aires, Argentina.
Hoffmann L.	How I Do It: Chronic DVT. Annual LAVA: Latest Advances in Inverventional Techniques; July 27-30, 2009; Maui, HI.

Other Scientific Meeting Presentations

Other Presentations 2010

Hoffmann L.	Interventional Oncology + Molecular Imaging = The Future Of Cancer Therapy. Annual Symposium on Current Issues and New Techniques in Interventional Radiology and Endovascular Therapy; November 18-20, 2009; New York, NY.
Hoffmann L.	IRE: Is It The Holy Grail For The Treatment Of Pancreatic Cancer? Annual Symposium on Current Issues and New Techniques in Interventional Radiology and Endovascular Therapy; November 18-20, 2009; New York, NY.
Hoffmann L.	Irreversible Electroporation for Pancreatic Cancer. IX Curso Internacional "Hands On" en Cirugia Invasiva Minima y Radiologia Intervencionista; October 30, 2009; Buenos Aires, Argentina.
Hoffmann L.	New Horizons in Interventional Oncology. Annual LAVA: Latest Advances in Inverventional Techniques; July 27-30, 2009; Maui, HI.
Hoffmann L.	Percutaneous biliary neoanastomosis. A New Option for an Old Problem. IX Curso Internacional "Hands On" en Cirugia Invasiva Minima y Radiologia Intervencionista; October 30, 2009; Buenos Aires, Argentina.
Hoffmann L.	Portal Bvein and SMV Thrombosis: Should I Treat it, and if so, How? Annual LAVA: Latest Advances in Inverventional Techniques; July 27-30, 2009; Maui, HI.
Hoffmann L.	SFA/Popliteal/Tibial Disease. Current Status of Angiogenesis in Patients with Non Reconstructible PVD. Annual Symposium on Current Issues and New Techniques in Interventional Radiology and Endovascular Therapy; November 18-20, 2009; New York, NY.
Hoffmann L.	Stem cells and Gene Therapy: The Next Frontier for Image-guided Interventions. IX Curso Internacional "Hands On" en Cirugia Invasiva Minima y Radiologia Intervencionista; October 30, 2009; Buenos Aires, Argentina.
Hoffmann L.	Venous Thromboembolic Disease. Tips and Tricks for Stenting Chronic Venous Occlusions. Annual Symposium on Current Issues and New Techniques in Interventional Radiology and Endovascular Therapy; November 18-20, 2009; New York, NY.
Hoffmann L.	Why Develop a DVT Practice. Annual LAVA: Latest Advances in Inverventional Techniques; July 27-30, 2009; Maui, HI.
Hovsepian D.	Embolic Agents: What, Where, When, and How. Annual LAVA: Latest Advances in Inverventional Techniques; July 27-30, 2009; Maui, HI.
Hovsepian D.	Managing Fibroid Expulsion and Other Complications After UFE: Don't Panic! Annual LAVA: Latest Advances in Inverventional Techniques; July 27-30, 2009; Maui, HI.
Hovsepian D.	Pelvic Trauma: IR to the Rescue! Annual LAVA: Latest Advances in Inverventional Techniques; July 27-30, 2009; Maui, HI.
Hovsepian D.	Quality, Safety, and Process Improvement: Three Sides of the Same Coin. Annual LAVA: Latest Advances in Inverventional Techniques; July 27-30, 2009; Maui, HI.
Hwang G.	Glycemic Control in the IR Suite. Annual Workshop at Society of Interventional Radiology; March, 2010; Tampa, FL.
Hwang G.	Liquid Embolics. Annual Workshop at Society of Interventional Radiology; March, 2010; Tampa, FL.
Iagaru A, Mittra ES, Dick DW, Goris ML, Gambhir SS.	Cocktail 18F Fluoride and 18F FDG PET/CT Scan for Evaluation of Malignancy. Annual Congress of the European Association of Nuclear Medicine; October 10-24, 2009; Barcelona, Spain.
Iagaru A, Mittra ES, Dick, DW, Quon A, Gambhir SS.	Prospective Evaluation of 99mTc-MDP Scintigraphy, 18F NaF PET/CT and 18F FDG PET/CT for Detection of Skeletal Metastases. Annual Congress of the European Association of Nuclear Medicine; October 10-24, 2009; Barcelona, Spain.
Ikeda D.	Anatomy, Physiology, & Pathology of the Breast. Annual Symposium on Advances in Breast MRI; October 22-24, 2009; Las Vegas, NV.
Ikeda D.	Biopsies Using Different Imaging Modalities. Asian-Oceanic Congress of Radiology; March 19-21, 2010; Taipei, Taiwan.
Ikeda D.	Breast Cancer Screening with Mammo, US, MRI. Asian-Oceanic Congress of Radiology; March 19-21, 2010; Taipei, Taiwan.

Other Scientific Meeting Presentations

Other Presentations 2010

Ikeda D.	Breast MR Imaging Interpretation Including BI-RADS. UC San Diego Breast Imaging & Interventions Update; October 30-November 1, 2009; Coronado, CA.
Ikeda D.	Breast MRI Interpretation in 2010. Big Sky Radiology conference; January 24-27, 2010; Big Sky, MT.
Ikeda D.	Breast Ultrasound Update. Asian-Oceanic Congress of Radiology; March 19-21, 2010; Taipei, Taiwan.
Ikeda D.	Challening Image-Guided Biopsies. Annual Advances in Breast Imaging and Interventions; March 3-6, 2010; Las Vegas, NV.
Ikeda D.	Correlating Mammo/US/MRI. Annual Advances in Breast Imaging and Interventions; March 3-6, 2010; Las Vegas, NV.
Ikeda D.	Digital Mammography & Tomosynthesis. Annual Advances in Breast Imaging and Interventions; March 3-6, 2010; Las Vegas, NV.
Ikeda D.	Enhancement Characteristics of Cancer on MRI of the Breast and Biopsy Techniques. Annual American Association of Physicists in Medicine (AAPM) Conference; July 28, 2009; Anaheim, CA.
Ikeda D.	Ergonomics for the FFDM Environment. Annual Advances in Breast Imaging and Interventions; March 3-6, 2010; Las Vegas, NV.
Ikeda D.	Extent of Disease. Society of Breast Imaging Biannual meeting; April 27, 2009; Colorado Springs, CO.
Ikeda D.	False Negative Studies on MRI, Mammo, US. Big Sky Radiology conference; January 24-27, 2010; Big Sky, MT.
Ikeda D.	How to Handle Complicated Mammo/US/MRI Cases. Big Sky Radiology conference; January 24-27, 2010; Big Sky, MT.
Ikeda D.	MRI & Digital Mammo Comparison & Correlation. Annual Symposium on Advances in Breast MRI; October 22-24, 2009; Las Vegas, NV.
Ikeda D.	MRI Lexicon Update. Asian-Oceanic Congress of Radiology; March 19-21, 2010; Taipei, Taiwan.
Ikeda D.	MRI Update & Patient Indications. Annual Advances in Breast Imaging and Interventions; March 3-6, 2010; Las Vegas, NV.
Ikeda D.	Multiple Modalities Approaches Breast Lesions. Asian-Oceanic Congress of Radiology; March 19-21, 2010; Taipei, Taiwan.
Ikeda D.	Second Look Sonography after Breast MRI. UC San Diego Breast Imaging & Interventions Update; October 30-November 1, 2009; Coronado, CA.
Ikeda D.	Second Look Sonography after MRI. Annual Symposium on Advances in Breast MRI; October 22-24, 2009; Las Vegas, NV.
Ikeda D.	The Post-Operative Breast. UC San Diego Breast Imaging & Interventions Update; October 30-November 1, 2009; Coronado, CA.
Ikeda D.	Tomosynthesis and FFDM. Big Sky Radiology conference; January 24-27, 2010; Big Sky, MT.
Kamaya A, Gross M, Jeffrey RB.	Sonographic Findings of Thyroid Bed Recurrence. Annual Meeting of the American Roetgen Ray Society; May 2-7, 2010; San Diego, CA.
Kong Y, Yao H, Ren H, Subbian S, Rao J, Cirillo JD.	Application of Reporter-enzyme-fluorescence Imaging to Study of Tuberculosis In Vivo. American Society of Microbiology General Meeting; May 17-21, 2009; Philadelphia, PA.
Kothary N.	Fiducial Implantation for Sterotactic Radiotherapy. Annual Advanced Interventional Management Symposium; New York, NY.
Kothary N.	Image-Guided Radiotherapy vs. Percutaneous Ablation Techniques: Results in Lung and Liver Tumors. Annual Advanced Interventional Management Symposium; New York, NY.

Other Scientific Meeting Presentations

Other Presentations 2010

Kothary N.	Management of Renal Tumors – Transarterial and Percutaneous: The Whole Gamut. Annual Advanced Interventional Management Symposium; New York, NY.
Kurian A, Sigal BM, Plevritis S.	Survival Analysis of Cancer Risk Reduction Strategies for BRCA1/2 Mutation Carriers. National Meeting of the Robert Wood Johnson Foundation; December, 2010; San Diego, CA.
Leung AN.	Adenocarcinoma: Can CT Morphology Predict Prognosis? Annual International Symposium on Multidetector-Row CT; May 19-22, 2009; San Francisco, CA.
Leung AN.	ILD Assessment: Volumetric or Non-Contiguous CT Acquisition? Annual International Symposium on Multidetector-Row CT; May 19-22, 2009; San Francisco, CA.
Leung AN.	Lung Cancer Staging on MDCT: The Essentials. Annual International Symposium on Multidetector-Row CT; May 19-22, 2009; San Francisco, CA.
Levin CS.	Advances in PET and PET/MR. International Symposium on Animal Molecular Imaging; October 10-11, 2009; Taipei, Taiwan.
Levin CS.	Design and Development of an Advaned PET System built from Semiconductor Detectors. Annual American Association of Physicists in Medicine (AAPM) Conference; July 28, 2009; Anaheim, CA.
Liu YI, Kamaya A, Desser TS, Rubin DL.	A Systemic Search for Patterns for Thyroid Nodule Evaluation Using a Bayesian Classifier. Annual Meeting of the American Roetgen Ray Society; May 2-7, 2010; San Diego, CA.
Liu YI, Kamaya A, Desser TS, Rubin DL.	Learning a Bayesian Classifier for Thyroid Nodule Evaluation. Annual Meeting of the American Roetgen Ray Society; May 2-7, 2010; San Diego, CA.
Liu YI, Shin LK, Jeffrey RB, Kamaya A.	Interpatient Variability of Enhancement of Five Abdominal Organis in Triphasic MDCT. Annual Meeting of the American Roetgen Ray Society; May 2-7, 2010; San Diego, CA.
Liu YI, Shin LK, Jeffrey RB, Kamaya A.	What Defines Hepatic "Washout" in Triphasic MDCT? Annual Meeting of the American Roetgen Ray Society; May 2-7, 2010; San Diego, CA.
Mittra ES, Quon A, Gambhir SS, Iagaru A.	Efficacy of 18F-FDG PET/CT for Breast Cancer. Annual Congress of the European Association of Nuclear Medicine; October 10-24, 2009; Barcelona, Spain.
Newman B.	Effective CT Angiography in Cavopulmonary Anastomoses. Annual International Symposium on Multidetector-Row CT; May 19-22, 2009; San Francisco, CA.
Newman B.	The Spectrum of Intrapulmonary Neoplasms in Childhood. Annual International Symposium on Multidetector-Row CT; May 19-22, 2009; San Francisco, CA.
Olcott PD, Peng H, Levin CS.	Cross-strip Capacitive Multiplexing and Electro-optical Coupling for Silicon Photomultiplier Arrays for PET Detectors. “Premier” presentation at the 2009 IEEE Medical Imaging Conference, Orlando FL, October 25-31. Awarded second prize in student paper competition.
Olcott PD, Peng H, Levin CS.	Cross-strip Capacitive Multiplexing and Electro-optical Coupling for Silicon Photomultiplier Arrays for PET Detectors. IEEE Medical Imaging Conference; October 25-31, 2009; Orlando FL.
Peng H, Levin CS.	The Relevance of Peak-to-Valley Ratio and Signal-to-Noise Ratio for Anger-Logic-Based PET Detector Designs. IEEE Medical Imaging Conference; October 25-31, 2009; Orlando FL.
Peng H, Olcott PD, Levin CS.	Preclinical and Clinical PET Detector Design Considerations Using Silicon Photomultipliers. IEEE Medical Imaging Conference; October 25-31, 2009; Orlando FL.
Plevritis S.	Curing Lung Cancer by Early Detection. Annual Scientific Workshop of the Early Detection Research Network; August, 2009; Bethesda, MD.
Plevritis S.	Modeling the Natural History of Cancer. Annual Scientific Meeting of the Society of Medical Decision Making; October, 2009; Holywood, CA.
Rubesova E, Barth RA, Rosenberg J, Brau AC, Vasanawala SS.	3D T1-weighted Fetal MRI. Annual Society for Pediatric Radiology Meeting; April 21-25, 2009; Carlsbad, CA.

Other Scientific Meeting Presentations

Other Presentations 2010

Rubesova E, Vasanawala SS, Rosenberg J, Barth RA.	Single Shot SSFSE Versus Balanced Steady State Imaging: Which Sequence to Choose to Image Fetal Body? Annual Society for Pediatric Radiology Meeting; April 21-25, 2009; Carlsbad, CA.
Segall G.	Dual Time Point: Yes or No? Annual Symposium on PET/CT and Molecular Imaging; February 1-13, 2010; Las Vegas, NV.
Segall G.	PET/CT in the Abdomen and Pelvis. Annual Winter Diagnostic Imaging Update; January 4-8, 2010; Bachelor Gulch, CO.
Segall G.	PET/CT in the Head and Neck. Annual Winter Diagnostic Imaging Update; January 4-8, 2010; Bachelor Gulch, CO.
Segall G.	PET/CT in the Thorax. Annual Winter Diagnostic Imaging Update; January 4-8, 2010; Bachelor Gulch, CO.
Segall G.	PET/CT Slice by Slice: Abdomen and Pelvis. Annual Symposium on PET/CT and Molecular Imaging; February 1-13, 2010; Las Vegas, NV.
Segall G.	Pet/CT State of the Union: The Success of the Past 8 Years and a look to the Future. Annual Symposium on PET/CT and Molecular Imaging; February 1-13, 2010; Las Vegas, NV.
Segall G.	PET/CT: The Good, the Bad, and the Ugly. Annual Winter Diagnostic Imaging Update; January 4-8, 2010; Bachelor Gulch, CO.
Segall G.	Physiology of FDG in the Setting of Radiation Therapy. Annual Symposium on Best Practices in PET/CT; April 2-3, 2009; Sonoma, CA.
Segall G.	Tips on Differentiating the 3 R's in Post-treatment PET/CT: Residual vs. Recurrence vs. Resolution. Annual Symposium on PET/CT and Molecular Imaging; February 1-13, 2010; Las Vegas, NV.
Shin L.	Updates on Imaging of GI Cancers. Annual GI Cancers Symposium; July 31-August 2, 2009; Kohala Coast, HI.
Shin L.	Virtual Colonoscopy. Annual GI Cancers Symposium; July 31-August 2, 2009; Kohala Coast, HI.
Sommer G.	Advanced Processing for MDCT Urography. Annual International Symposium on Multidetector-Row CT; May 19-22, 2009; San Francisco, CA.
Sommer G.	Different Approaches to Acquisition in MDCT Urography. Annual International Symposium on Multidetector-Row CT; May 19-22, 2009; San Francisco, CA.
Sommer G.	Pelvis MR. Annual Current Concepts of Magnetic Resonance Imaging; October 12-15, 2009; Monterey, CA.
Spanoudaki V, Levin CS.	Design and Development of a New PET Detector with Both DoI and ToF Capabilities. IEEE Medical Imaging Conference; October 25-31, 2009; Orlando FL.
Spanoudaki V, Peng H, Olcott PD, Levin CS.	Investigation of Photon Depth of Interaction Issues of a PET Detector Design for Simultaneous PET-MR Brain Imaging. IEEE Medical Imaging Conference; October 25-31, 2009; Orlando FL.
Stevens K.	MRI of the Foot and Ankle: Ligamentous and Tendon Pathology. Annual Winter Diagnostic Imaging Update; January, 2010; Beaver Creek, CO.
Stevens K.	MRI of the Shoulder: Cuff and Labral Pathology. Annual Winter Diagnostic Imaging Update; January, 2010; Beaver Creek, CO.
Stevens K.	MRI of the Wrist and Hand. Annual Winter Diagnostic Imaging Update; January, 2010; Beaver Creek, CO.
Sze D.	Chemoembolization 201: Comparing Methods and Results. Annual Latest Advances in Interventional Techniques; July, 2009; Kaanapali, HI.
Sze D.	Management of Bleeding Conditions: Basics of Embolization. Society of Interventional Radiology Annual Scientific Meeting; March, 2010; Tampa, FL.
Sze D.	Oncology: Primer on Y90. Society of Interventional Radiology Annual Scientific Meeting; March, 2010; Tampa, FL.

Other Scientific Meeting Presentations

Other Presentations 2010

Sze D.	Radioembolization 101: Rationale, Applications, Products. Annual Latest Advances in Interventional Techniques; July, 2009; Kaanapali, HI.
Sze D.	Radioembolization 102: Anatomy, Imaging, Dosimetry. Annual Latest Advances in Interventional Techniques; July, 2009; Kaanapali, HI.
Sze D.	Sinistral Portal Hypertension. Annual Latest Advances in Interventional Techniques; July, 2009; Kaanapali, HI.
Sze DY, Louie JD, Iagaru A, Goris ML.	Survival after 90Y Radioembolization is Predicted by Dose Distribution Scintigraphy. Annual Congress of the European Association of Nuclear Medicine; October 10-24, 2009; Barcelona, Spain.
Vandenbroucke A, Lee J, Spanoudaki V, Lau FW, Reynolds PD, Levin CS.	Temperature and Bias Voltage Studies of a Large Area Position Sensitive Avalanche Photodiode. IEEE Medical Imaging Conference; October 25-31, 2009; Orlando, FL.
Vasanawala C.	Imaging Evaluation of Osseous Neoplasm in Children: Plain Radiographs and Beyond. American Roentgen Ray Society Annual Meeting; April 26-May 1, 2009; Boston, MA.
Vasanawala C.	Volumetric and Functional MR Sequences at 1.5 and 3T. Society of Pediatric Radiology Annual Meeting; April 21-25, 2009; Carlsbad, CA.
Vasanawala SS, Alley MT, Barth RA, Hargreaves BA, Pauly JM, Lustig M.	Faster Pediatric MRI via Compressed Sensing. Society for Pediatric Radiology Meeting; April 21-25, 2009; Carlsbad, CA.
Willmann J.	Imaging of Cystic Pancreatic Lesions. Annual Spring Diagnostic Imaging Update; March 22-26, 2010; Maui, HI.
Willmann J.	Imaging of Cystic Pancreatic Lesions. International Symposium on State-of-the-Art Imaging; July 16, 2009; Taormina, Italy.
Willmann J.	Imaging of Pancreatic Cancer. International Symposium on State-of-the-Art Imaging; July 16, 2009; Taormina, Italy.
Willmann J.	Imaging Pancreatic Cancer. Annual Spring Diagnostic Imaging Update; March 22-26, 2010; Maui, HI.
Willmann J.	Imaging with Liver Specific Contrast Agents: When and How? Annual meeting of the Society of Gastrointestinal Radiology; February 21-26, 2010; Orlando, FL.
Willmann J.	MDCT of Blunt Abdominal Trauma. Annual Spring Diagnostic Imaging Update; March 22-26, 2010; Maui, HI.
Willmann J.	Update on Liver Specific MR Contrast Agents. Annual Spring Diagnostic Imaging Update; March 22-26, 2010; Maui, HI.
Wu A, Rao J, Chen X, Gambhir SS, Barat B, Lepin E, Sirk S, Li J, McCabe K, Gao J, Jang E-S, Chen K, Kim Y-P, Xia Z.	Biological Modification of Quantum Dots for In Vivo Imaging. Annual NCI Alliance for Nannotechnology in Cancer Investigators' Meeting; October 20-22, 2009; Manhattan Beach, CA.
Zaharchuk G.	Advanced Neuroimaging: Problem-solving with Perfusion and Diffusion. Annual Winter Diagnostic Imaging Update; January 4-8, 2010; Beaver Creek, CO.
Zaharchuk G.	Advanced Neuroimaging. Annual Current Concepts of Magnetic Resonance Imaging; October 12-15, 2009; Monterey, CA.
Zaharchuk G.	Advances in the Diagnosis of Dissection: What Is the Best Test? American Heart Association International Stroke Conference (ISC); February, 2010; San Antonio, TX.
Zaharchuk G.	Arterial Spin-Labeling. Annual Current Concepts of Magnetic Resonance Imaging; October 12-15, 2009; Monterey, CA.
Zaharchuk G.	Brain Perfusion Imaging without Contrast Agents: Basics of Arterial Spin Labeling MRI. Annual Winter Diagnostic Imaging Update; January 4-8, 2010; Beaver Creek, CO.
Zaharchuk G.	Comparison of Multidetector CTA and MRI for Evaluating Dissection of the Cervical Arteries. Annual International Symposium on Multidetector-Row CT; May 19-22, 2009; San Francisco, CA.

Published Papers

Other Presentations 2010

Zaharchuk G.	Is CT Brain Perfusion as Useful as MRI in Acute Stroke? Annual International Symposium on Multidetector-Row CT; May 19-22, 2009; San Francisco, CA.
Zaharchuk G.	Modern Acute Stroke Imaging. Annual Winter Diagnostic Imaging Update; January 4-8, 2010; Beaver Creek, CO.
Zaharchuk G.	Vascular Imaging of the Central Nervous System. Annual Current Concepts of Magnetic Resonance Imaging; October 12-15, 2009; Monterey, CA.
Zaharchuk G.	Vascular Imaging of the Central Nervous System. Annual Winter Diagnostic Imaging Update; January 4-8, 2010; Beaver Creek, CO.

Published Papers

Published Papers

Ganguly A, Fieselmann A, Boese J, Rohkohl C, Hornegger J, Fahrig R. Evaluating the Feasibility of C-arm CT for Brain Perfusion Imaging: An In Vitro Study. Proc. SPIE 7625, 76250K.

Barth A. The Brain: Inside Story, Discover Spring 2010: 56-61.

Chan S, Kamaya A. Dermoid cyst. Case-in-Point online teaching file publication. September 3, 2009.

Church DG, Vancil JM, Vasanawala SS. Magnetic Resonance Imaging for Uterine and Vaginal Anomalies. Curr Opin Obstet Gynecol. 2009 Oct;21(5):379-89.

Daniel BL, Hwang G, Kao J, Ikeda DM. Freehand, Non-grid Vacuum Core Biopsies. A Preliminary Analysis of 500 Biopsies. Eur Radiol. 2009;19(Suppl 4): S794-S799.

Daniel BL, Van Den Bosch M, Hargreaves BA, Kao J, Ikeda DM. Small Foci in MR: What Whould We Do? Neglect, Follow, Excise? A Retrospective Analysis of 19 Small Foci Compared with 19 Typical MRI-detected Mammographically Occult Lesions. Eur Radiol. 2009;19(Suppl 4): S799-S802.

Das M, Abdelmaksoud MHK, Loo BW, Kothary N. Alternatives to Surgery for Early Stage Non-small Cell Lung Cancer – Ready for Prime Time? Current Treatment Options in Oncology.

Gao H, Zhu L, Fahrig R. Optimization of System Parameters for Modulator Design in X-ray Scatter Correction Using Primary Modulation. Proc. SPIE 7622, 76222A.

Hahn J, Barnes P. Neuroimaging Advances in Holoprosencephaly: Refining the Spectrum of the Midline Malformation. Am J Med Genet Part C Semin Med Genet. 2010;154C:120-132.

Keller K, Barnes P. Rickets vs. Abuse – The Evidence: Reply. Pediatr Radiol. 2009;39:1130.

Lindsay A, Fischbein N. Adenoid Cystic Carcinoma with Perineural Invasion of the Greater Superficial Petrosal Nerve. ACR case-in-point online teaching file. 2009 Sep.

Mackenzie JD, Vasanawala SS. State-of-the-Art in Pediatric Body and Musculoskeletal Magnetic Resonance Imaging. Semin Ultrasound CT MR. 2010;31:86-99. PMID:20304318.

Narsinh KH, Cao F, Wu JC. Application of Reporter Gene Imaging for Studying Human Embryonic Stem Cells in Living Subjects. Meth Molec Biol. 2009;515:13-32.

Newman B, Cho YA. Left Pulmonary Artery Sling-Anatomy and Imaging. Semin Ultrasound CT MR. 31:158-70.

Rubin DL. Interoperability: Controlled terminology for Reporting and New Emerging Standards in Image Annotation and Mark Up. Appl Radiol. 2009 Dec;38(12):13-7.

Segall GM. PET/CT With and Without Intravenous Contrast: Is there a Standard of Care? SNM PET Center of Excellence Newsletter. 2010;7(1): 1.

Sun N, Longaker MT, Wu JC. Human iPS Cell-based Therapy: Considerations Before Clinical Applications. Cell Cycle. 2010 Mar;9(5):880-5.

Published Papers

Vandenbroucke A, Lee J, Spanoudaki V, Lau FWY, Reynolds PD, Levin CS. Temperature and Bias Voltage Studies of a Large Area Position Sensitive Avalanche Photodiode. Conference Record of the 2009 IEEE Nuclear Science Symposium and Medical Imaging Conference, pp. 3664-3669. Published March 2010.

Wein W, Camus E, John M, Diallo M, Duong C, Al-Ahmad A, Fahrig R, Khamene A, Xu C. Towards Guidance of Electrophysiological Procedures with Real-time 3D Intracardiac Echocardiography Fusion to C-arm CT. Med Image Comput Comput Assist Interv. 2009;12(Pt 1):9-16.

Wilson KD, Huang M, Wu JC. Bioluminescence Reporter Gene Imaging of Human Embryonic Stem Cell Survival, Proliferation, and Fate. Methods in Molecular Biology. 2009;574:87-103. Writing Committee for US Government Interagency Modeling and Analysis Group (IMAG) Report on "The Impact Modeling on Biomedical Research".

Ahn KH, Hargreaves BH, Alley MT, Horst KC, Luxton G, Daniel BL, Hristov D. MRI Guidance for Accelerated Partial Breast Irradiation in Prone Position: Imaging Protocol Design and Evaluation. Int J Radiat Oncol Biol Phys. 2009 Sep 1;75(1):285-93.

Arac A, Lee M, Steinberg GK, Marcellus M, Marks MP. Efficacy of Endovascular Stenting in Dural Sinus Stenosis for the Treatment of Idiopathic Intracranial Hypertension. Neurosurg Focus. 2009 Nov;27(5):E14.

Bailey SL, Sigal BM, Plevritis SK. A Simulation Model Investigating the Impact of Tumor Volume Doubling Time and Mammographic Tumor Detectability on Screening Outcomes in Women Aged 40-49. J Natl Cancer Inst. 2010 Aug 18;102(16):1263-71.

Banovac F, Buckley D, Kuo WT, Lough D, Martin LG. Standards of Practice: Reporting Standards for Endovascular Treatment of Pulmonary Embolism. J Vasc Interv Rad. 2010;21(1):44-53.

Barnes P, Galaznik J, Gardner H, Shuman M. Infant Acute Life-threatening Event – Dysphagic Choking Versus Nonaccidental Injury. Semin Pediatr Neurol. 2010 Mar;17(1):7-11.

Bhatia N, Shah NH, Rubin DL, Chiang AP, Musen MA. Comparing Concept Recognizers for Ontology-Based Indexing: MGREP vs. MetaMap. In: AMIA Summit on Translational Bioinformatics, San Francisco, CA. 2009:12-6.

Blankenberg FG, Levashova Z, Sarkar SK, Pizzonia J, Backer MV, Backer JM. Noninvasive Assessment of Tumor VEGF Receptors in Response to Treatment with Pazopanib: A Molecular Imaging Study. Transl Oncol. 2010;3:56-64. PMID: 20165696.

Blankenberg FG. Apoptosis Imaging: Anti-Cancer Agents in Medicinal Chemistry. Anticancer Agents Med Chem. 2009;9(9):944-51. PMID: 19663787.

Boussel L, Arora S, Rapp J, Rutt B, Huston J, Parker D, Yuan C, Bassiouny H, Saloner D. Atherosclerotic Plaque Progression in Carotid Arteries: Monitoring with High-Spatial-Resolution MR Imaging--Multicenter Trial. Radiology. 2009 Sep;252(3):789-96. Epub 2009 Jun 9.

Burnside ES, Sickles EA, Bassett LW, Rubin DL, Lee CH, Ikeda DM, Mendelson EB, Wilcox PA, Butler PF, D'Orsi CJ. The ACR BI-RADS Experience: Learning from History. J Am Coll Radiol. 2009 Dec;6(12):851-60.

Cao F, Xie X, Gollan T, Zhao L, Narsinh K, Lee RJ, Wu JC. Comparison of Gene Transfer Efficiency in Human Embryonic Stem Cells. Molecular Imaging & Biology. 2010;12:15-24.

Channin DS, Mongkolwat P, Kleper V, Rubin DL. Computing Human Image Annotation. Conf Proc IEEE Eng Med Biol Soc. 2009;2009:7065-8.

Channin DS, Rubin DL. The Annotation and Image Markup Project. Radiology. 2009;253:590-592.

Chen C, Kijowski R, Shapiro L, Tuite M, Davis K, Klaers J, Block W, Reeder S, Gold G. Cartilage Morphology at 3.0T: Assessment of Three-dimensional Magnetic Resonance Imaging Techniques. J Magn Reson Imaging. 2010 Jul;32(1):173-83.

Chen IY, Gheysens O, Ray S, Wang Q, Padmanabhan P, Paulmurugan R, Loening AM, Rodriguez-Porcel M, Willmann JK, Sheikh AY, Nielsen CH, Hoyt G, Contag CH, Robbins RC, Biswal S, Wu JC, Gambhir SS. Indirect Imaging of Cardiac-specific Transgene Expression Using a Bidirectional Two-step Transcriptional Amplification Strategy. Gene Ther. 2010 Jul;17(7):827-38.

Chen J, Butts Pauly K. Optimization of Encoding Gradients for MR-ARFI, MRM, Magn Reson Med. 2010, 63(4):1050-1058.

Chen K, Xie J, Xu H, Behera D, Michalski M, Biswal S, Wang A, Chen X. Triblock Copolymer Coated Iron Oxide Nanoparticle Conjugate for Tumor Integrin Targeting. Biomaterials. 2009 Dec;30(36):6912-9. PMID: 19773081.

Chen MQ, Yu J, Whittington R, Wu JC, Kovacs GT, Giovangrandi L. Modeling Conduction in Host-graft Interactions Between Stem Cell Grafts and Cardiomyocytes. IEEE Eng Med Biol Soc. 2009;2009:6014-7.

Cheng Z, De Jesus OP, Kramer DJ, De A, Webster JM, Gheysens O, Levi J, Namavari M, Wang S, Park JM, Zhang R, Liu H, Lee B, Syud FA, Gambhir SS. 64Cu-labeled Affibody Molecules for Imaging of HER2 Expressing Tumors. Mol Imaging Biol. 2010 Jun;12(3):316-24. PMID: 19779897.

Published Papers

Chennupati SK, Kamaya A, Fisher GA, Ford JM, Kunz P, Itakura H, Welton ML, Shelton A, Van Dam J, Koong AC, Chang DT. Pathological Response after Chemoradiation for T3 Rectal Cancer. Colorectal Dis. 2010 Jul;12(7 online):e24-30.

Choi G, Shin LK, Taylor CA, Cheng CP. In Vivo Deformation of the Human Abdominal Aorta and Common Iliac Arteries with Hip and Knee Flexion: Implications for the Design of Stent-grafts. J Endovasc Ther. 2009 Oct;16(5):531-8.

Choudhury KR, Paik DS, Yi CA, Napel A, Roos J, Rubin GD. Assessing Operating Characteristics Of CAD Algorithms In The Absence Of A Gold Standard. Medical Physics. 2010;37(4):1788-95.

Collins LK, Levin TL, Berdon WE, Cowles RA, Newman B. Rudhe Syndrome: Reversible Right Middle Lobe Emphysema in Infants with Left-to-Right Shunts – A Historical Review. Pediatr Radiol. 2010 May;40(5):762-5.

Colombani M, Ferry M, Toga C, Lacroze V, Rubesova E, Barth RA, Cassart M, Gorincour G. MRI in the Prenatal Diagnosis of Congenital Diarrhea. Ultrasound Obstet Gynecol. 2010 May;35(5):560-5.

D'Souza A, Tseng J, Butts Pauly K, Guccione S, Rosenberg J, Gambhir SS, Glazer G. A Strategy for Blood Biomarker Amplification and Localization Using Ultrasound, Proc Natl Acad Sci U S A. 2009 Oct 6;106(40):17152-7. PMID: 19805109; PMCID: PMC2749842.

De la Zerda A, Bodapati S, Teed R, Schipper M, Keren S, Smith B, Ng J, Gambhir SS. A Comparison between Time Domain and Spectral Imaging Systems for Imaging Quantum Dots in Small Living Animals. Molecular Imaging and Biology, December 10, 2009 Epub.

De la Zerda A, Paulus Y, Teed R, Bodapati S, Dollberg Y, Khuri-Yakub B, Blumenbranz M, Moshfeghi D, Gambhir SS. Photoacoustic Ocular Imaging. Optics Letters. 2010 Feb;35(3):270-2.

Deshmukh S, Rubesova E, Barth R. MR Assessment of Normal Fetal Lung Volumes: A Literature Review. Am J Roentgenol. 2010 Feb;194(2):W212-7.

Deshmukh SD, Willmann JK, Jeffrey RB. Pathways of Extrapancreatic Perineural Invasion by Pancreatic Adenocarcinoma: Evaluation with 3D Volume-rendered MDCT Imaging. Am J Roentgenol. 2010;194: 668-674.

Deshpande N, Needles A, Willmann JK. Molecular Ultrasound Imaging: Current Status and Future Directions. Clin Radiology. 2010 Jul;65(7):567-81.

Deshpande N, Pysz MA, Willmann JK. Molecular Ultrasound Assessment of Tumor Angiogenesis. Angiogenesis. 2010 Jun;13(2):175-88.

Desser TS, Edwards B, Hunt S, Rosenburg J, Purtill MA, Jeffrey RB. The Dangling Diaphragm Sign: Sensitivity and Comparison with Existing CT Signs of Blunt Traumatic Diaphragmatic Rupture. Am Soc Emergency Radio. 2010;17(1):37-44.

Desser TS. Understanding Transient Hepatic Attenuation Differences. Semin Ultrasound CT MR. 2009 Oct;30(5):408-17.

Deuse T, Blankenberg F, Haddad M, Reichenspurner H, Phillips N, Robbins RC, Schrepfer S. Mechanisms Behind Local Immunosuppression Using Inhaled Tacrolimus in Preclinical Models of Lung Transplantation. Am J Respir Cell Mol Biol. 2009 Oct 30 Epub. PMID: 19880819.

Deuse T, Peter C, Fedak PW, Doyle T, Reichenspurner H, Zimmermann WH, Eschenhagen T, Stein W, Wu JC, Robbins RC, Schrepfer S. Hepatocyte Growth Factor or Vascular Endothelial Growth Factor Gene Transfer Maximizes Mesenchymal Stem Cell-based Myocardial Salvage after Acute Myocardial Infarction. Circulation. 2009 Sep 15;120(11 Suppl):S247-54.

Do HM, Fariabi S, Ligon D. Hemi™ Neurovascular Embolization Cover (NEC) Device (NFocus Neuromedical) for the Treatment of Aneurysms in the Rabbit Model. J Neurointerventional Surg. 2009;1:72-3.

Dragulescu-Andrasi A, Liang GL, Rao J. In Vivo Bioluminescence Imaging of Furin Activity in Breast Cancer Cells using Bioluminogenic Substrates. Bioconjug Chem. 2009;20:1660-6.

Ganguly A, Yoon S, Fahrig R. Dose and Detectability for a Cone-beam C-arm CT System Revisited. Medical Physics. Med Phys. 2010 May;37(5):2264-8.

Gao H, Fahrig R, Bennett NR, Sun M, Star-Lack J, Zhu L. Scatter Correction Method for X-ray CT using Primary Modulation: Phantom Studies. Med Phys. 2010 Feb;37(2):934-46.

Gao J, Chen K, Xie R, Xie J, Lee S, Cheng Z, Peng X, Chen X. Ultrasmall Near-infrared Non-cadmium Quantum Dots for In Vivo Tumor Imaging. Small. 2010;6(2):256-61. PMID: 19911392.

Gao J, Chen K, Xie RG, Xie J, Yang YJ, Cheng Z, Peng XG, Chen XY. In Vivo Tumor-targeted Fluorescence Imaging using Near-infrared Non-cadmium Quantum Dots. Bioconjug Chemistry. 2010 APR 21;21(4):604-9. PMID: 20369817.

Gao J, Chen X, Cheng Z. Near-infrared Quantum Dots as Optical Probes for Tumor Imaging. Curr Top Med Chem. 2010;10(12):1147-57. PMID: 20388111.

Published Papers

Published Papers

Gaster R, Hall D, Nielsen C, Osterfeld S, Yu H, Mach K, Wilson R, Murmann B, Liao J, Gambhir SS, Wang S. Matrix-insensitive Protein Assays Push the Limits of Biosensors in Medicine. Nat Med. 2009 Nov;15(11):1327-1332.

Gentles A, Li S, Shachaf C, Shahbaba B, Levy R, Koller D, Plevritis SK. A Gene Module Regulatory Network Analysis of Follicular Lymphoma Transformation. Blood. 2009 Oct 8;114(15):3158-66.

Ghatan CE, Kuo WT, Hofmann LV, Kothary N. Making the Case for Early Medical Student Education in Interventional Radiology: A Survey of 2nd-year Students in a Single U.S. institution. J Vasc Interv Radiol. 2010 Apr;21(4):549-53.

Gold G, Chen C, Koo S, Hargreaves BA, Bangerter N. Recent Advances in MRI of Articular Cartilage. Am J Roentgenol. 2009 Sep;193(3):628-38.

Gonella MC, Fischbein NJ, Lane B, Shuer LM, Greicius MD. Episodic Encephalopathy Due to an Occult Spinal Vascular Malformation Complicated by Superficial Siderosis. Clin Neurol Neurosurg. 2010 Jan;112(1):82-4. PMID: 19857921.

Goris ML, Robinson TE. Sampling Density to Evaluate Quantitative Air Trapping. Pediatr Radiol. 2009;39:2221.

Govaert JA, Swijnenbrug RJ, Schrepfer S, Xie X, van der Bogt K, Hoyt G, Stein W, Ransohoff K, Robbins RC, Wu JC. Poor Functional Recovery after Transplantation of Diabetic Bone Marrow Stem Cells in Ischemic Myocardium. J Heart Lung Transplantation. 2009 Nov;28(11):1158-65.

Grissom W, Kerr A, Holbrook A, Pauly J, Butts Pauly K. Maximum Linear-Phase Spectral-Spatial RF Pulses for Fat-Suppressed PRF-Shift MR Thermometry. Magn Reson Med. 2009 Nov;62(5):1242-50. PMID: 19780177; PMCID: PMC2795148.

Guzman R, Lee M, Achrol A, Bell-Stephens T, Kelly M, Do HM, Marks MP, Steinberg GK. Clinical Outcome after 450 Revascularization Procedures for Moyamoya Disease. J Neurosurg. 2009 Nov; 111(5):927-35.

Hamilton AM, Rogers KA, Belisle AJ, Ronald JA, Rutt BK, Weissleder R, Boughner DR. Early Identification of Aortic Valve Sclerosis using Iron Oxide Enhanced MRI. J Magn Reson Imaging. 2010 Jan;31(1):110-6. PMID: 20027578.

Han M, Beatty PJ, Daniel BL, Hargreaves BA. Independent Slab-Phase Modulation Combined with Parallel Imaging in Bilateral Breast MRI. Magn Reson Med. 2009 Nov;62(5):1221-1231.

Hargreaves BA, Chen W, Lu W, Alley MT, Gold G, Brau ACS, Pauly JM, Butts Pauly K. Accelerated Slice Encoding for Metal Artifact Correction. J Magn Reson Imaging. 2010 Apr;31(4):987-96.

He X, Wang KM, Cheng Z. In Vivo Near-infrared Fluorescence Imaging of Cancer with Nanoparticles-based Probes. Invited review (peer reviewed), WIREs Nanomedicine and Nanobiotechnology. 2010: DOI: 10.1002/wnan.85.

Heilmaier C, Lutz AM, Bolog N, Weishaupt D, Seifert B, Willmann JK. Focal Liver Lesions: Detection and Characterization at Double-Contrast Liver MR Imaging with Ferucarbotran and Gadobutrol versus Single-Contrast Liver MR Imaging. Radiology. 2009 Dec;253(3):724-33.

Ho D, Lin M, Schaenman J, Rosso F, Leung AN, Coutre SE, Sista RR, Montoya JG. Yield of Diagnostic Procedures for Invasive Fungal Infections in Neutropenic Febrile Patients with Chest Computed Tomography (CT) Abnormalities. Mycoses. 2009 Sep 28 [epub ahead of print].

Holbrook A, Santos J, Kaye E, Rieke V, Butts Pauly K. Real-Time MR Thermometry for Monitoring HIFU Ablations of the Liver. MRM. 2010 Feb;63(2):365-73.

Horning SJ, Juweid ME, Schoder H, Wiseman G, McMillan A, Swinnen LJ, Advani R, Gascoyne R, Quon A. Interim Positron Emission Tomography Scans in Diffuse Large B-cell lymphoma: An Independent Expert Nuclear Medicine Evaluation of the Eastern Cooperative Oncology Group E3404 study. Blood. 2010 Jan 28;115(4):775-7; quiz 918.

Hsu A, Hou L, Veeravagu A, Barnes P, Huhn S. Resolution of Syringomyelia after Release of Tethered Cord. Surg Neurol. 2009 Dec;72(6):657-61.

Hsu JJ, Glover GH, Zaharchuk G. Optimizing Saturation-recovery Measurements of the Longitudinal Relaxation Rate Under Time Constraints. Magn Reson Med. 2009 Nov;62(5):1202-10.

Huang M, Chen ZY, Hu S, Jia F, Li Z, Hoyt G, Robbins RC, Kay M, Wu JC. Novel Minicircle Vector for Gene Therapy in Murine Myocardial Infarction. Circulation. 2009 Sep 15;120(11 Suppl):S230-7.

Huang N, Niyama H, Peter C, De A, Natkunam Y, Fleissner F, Li Z, Rollins M, Wu J, Gambhir SS, Cooke J. Embryonic Stem Cell-Derived Endothelial Cells Engraft Into the Ischemic Hindlimb and Restore Perfusion. Arterioscler Throm Vasc Biol. 2010 May;30(5):984-91.

Iagaru A, Mittra E, Goris E, Gambhi SSr. Combined [18F]-FDG and Fluoride Approach in PET/CT Imaging: Is There a Clinical Future? J Nucl Med. 2009 Dec;50(6):1011.

Published Papers

Iagaru A, Mittra E, Yaghoubi S, Dick D, Quon A, Goris M, Gambhir SS. Novel Strategy for a Cocktail [18F] Fluoride and [18F]-FDG PET/CT Scan for Evaluation of Malignancy: Results of the Pilot-Phase Study. J Nucl Med. 2009 Apr;50(4):501-5.

Iagaru A, Mittra ES, Ganjoo K, Knox SJ, Goris ML. 131I-Tositumomab (Bexxar®) vs. 90Y-Ibritumomab (Zevalin®) Therapy of Low-Grade Refractory/Relapsed Non-Hodgkin Lymphoma. Mol Imaging Biol. 2010 Apr;12(2):198-203.

Inlay MA, Bhattacharya D, Sahoo D, Serwold T, Seita J, Karsunky H, Plevritis SK, Dill DL, Weissman IL. Ly6d marks the Earliest Stage of B Cell Specification and Identifies the Branchpoint between B Cell and T Cell Development. Genes and Development. 2009 Oct 15;23(20):2376-81.

Jadvar H, Alavi A, Gambhir SS. [18F] FDG Uptake in Lung, Breast, and Colon Cancers Molecular Biology Correlates and Disease Characterization. J Nucl Med. 2009 Oct;50(11):1820-7.

Jia F, Wilson KD, Sun N, Gupta DM, Huang M, Li Z, Robbins RC, Kay MA, Longaker MT, Wu JC. Minicircle DNA Induces Pluripotency in Adult Human Cells. Nature Methods. 2010;7(3):197-9.

Jiang L, Kimura R, Miao Z, Silverman , Ren G, Liu H, Li P, Gambhir SS, Cochran J, Cheng Z. Evaluation of a (64)Cu-Labeled Cystine-Knot Peptide Based on Agouti-Related Protein for PET of Tumors Expressing Alphavbeta3 Integrin. J Nuc Med. 2010 Feb;51(2):251-8. PMID: 20124048.

Jiang L, Schipper ML, Li P, Cheng Z. 123I Labeled Metaiodobenzylguanidine for Diagnosis of Neuroendocrine Tumors. Reports in Medical Imaging. 2009;2:79-89.

Jimenez-Requena F, Delgado-Bolton R, Fernandez-Perez C, Gambhir SS, Schwimmer J, Perez-Vazquez J, Carreras-Delgado J. Meta-analysis of the Performance of [18F] FDG-PET in Cutaneous Melanoma. Eur J Nuc Med Mol Imaging. 2010 Feb;37(2):284-300.

Kahn CE, Langlotz CP, Burnside ES, Carrino JA, Channin DS, Hovsepian DM, Rubin DL. Towards Best Practices in Radiology Reporting. Radiology. 2009 Sep;252(3):852-6.

Kamaya A, Maturen KE, Tye GA, Liu YI, Parti NN, Desser TS. Hypervascular Liver Lesions. Semin Ultrasound CT MR. 2009 Oct;30(5):387-407.

Kamaya A, Ro K, Benedetti NJ, Chang PL, Desser TS. Imaging and Diagnosis of Postpartum Complications: Sonography and Other Imaging Modalities. Ultrasound Q. 2009 Sep;25(3):151-62.

Kao D, Witteles R, Quon A, Wu J, Gambhir SS, Fowler M. Rosiglitazone Increases Myocardial Glucose Metabolism in Insulin-Resistant Cardiomyopathy. J Am Col Cardiol. 2010 Mar;55(9): 926-7.

Kapinos G, Fischbein NJ, Zaharchuk G, Venkatasubramanian C. Migraine-like headache with Visual Deficit and Perfusion Abnormality on MRI. Neurology. 2010 May 25;74(21):1743-5.

Katz M, Liu C, Schaer M, Parker KJ, Ottet MC, Epps A, Buckmaster CL, Bammer R, Moseley ME, Schatzberg AF, Eliez S, Lyons DM. Prefrontal Plasticity and Stress Inoculation-induced Resilience. Dev Neurosci. 2009;31(4):293-9. PMID: 19546566; PMCID: PMC2820579.

Kaye E, Josan S, Lu A, Rosenberg J, Daniel BL, Butts Pauly K. Consistency of Signal Intensity and T2* in Frozen Ex Vivo Heart Muscle, Kidney and Liver Tissue. J Magn Reson Imaging. 2010 Mar;31(3):719-24. PMID: 20187218; PMCID: PMC2832094.

Kenis H, Zandbergen HR, Hofstra L, Petrov AD, Dumont EA, Blankenberg FG, Haider N, Bitsch N, Gijbels M, Verjans JW, Narula N, Narula J, Reutelingsperger CP. Annexin A5 Uptake in Ischemic Myocardium: Demonstration of Reversible Phosphatidylserine Externalization and Feasibility of Radionuclide Imaging. J Nucl Med. 2010;51:259-67. PMID: 20124049.

Kim JE, Newman B. Evaluation of a Radiation Dose Reduction Strategy for Pediatric Chest CT. Am J Roentgenol. 2010 May;194(5):1188-93.

Kim Y-P, Daniel WL, Xia Z, Xie H, Mirkin CA, Rao J. Gold Nanoparticle-luciferase Conjugates Synthesized via Click Chemistry and Site-specific Protein Ligation: Bioluminescent Nanosensors for Protease Detection. Chemical Communications. 2010;46:76-8.

Kimura R, Miao Z, Cheng Z, Gambhir SS, Cochran J. A Dual-Labeled Knottin Peptide for PET and Near-Infrared Fluorescence Imaging of Integrin Expression in Living Subjects. Bioconjug Chem. 2010 Feb Epub. PMID: 20131753.

Koo S, Giori N, Gold G, Dyrby C, Andriacchi T. Accuracy of Cartilage Thickness Measurement in MRI Changes with Cartilage Thickness: Laser Scanner Based Validation of In Vivo Osteoarthritic Cartilage. J Biomech Eng. 2009 Dec;131(12);1200-04.

Kothary N, Lock L, Sze DY, Hofmann LV. Computed Tomography-guided Percutaneous Needle Biopsy of Pulmonary Nodules: Impact of Nodule Size on Diagnostic Accuracy. Clin Lung Cancer. 2009 Sep;10(5):360-3.

Published Papers

Krishnamurthy G, Krishnamurthy S, Gambhir SS, Rodrigues C, Rosenberg J, Schiepers C, Buxton-Thomas M. Development and Intra-institutional and Inter-institutional Validation of a Comprehensive New Hepatobiliary Software: Part 1 – Liver and Gallbladder Function. Nuc Med Comm. 2009 Dec;30(12): 934-44.

Kuo WT, Gould MK, Louie JD, Rosenberg JK, Sze DY, Hofmann LV. Catheter-directed Therapy for the Treatment of Massive Pulmonary Embolism: Systematic Review and Meta-analysis of Modern Techniques. J Vasc Interv Radiol. 2009 Nov;20(11):1431-40.

Kuo WT, Tong RT, Hwang GL, Louie JD, Lebowitz EA, Sze DY, Hofmann LV. High-risk Retrieval of Adherent and Chronically Implanted IVC Filters: Techniques for Removal and Management of Procedural Thrombotic Complications. J Vasc Interv Radiol. 2009 Dec;20(12):1548-56.

Kurian A, Sigal B, Plevritis SK. A Survival Analysis of Cancer Risk Reduction Strategies for BRCA1/2 Mutation Carriers. J Clin Oncol. 2010 Jan;10;28(2):222-31.

Lazzaro NA, Wright B, Castillo M, Fischbein NJ, Glastonbury CM, Hildenbrand PG, Wiggins RH, Quigley EP, Osborn AG. Artery of Percheron Infarction: Imaging Patterns and Clinical Spectrum. Am J Neuroradiol. 2010 Aug;31(7):1283-9. PMID: 20299438.

Lee DS, Kamaya A, Jeffrey RB. Islet Cell Tumor of the Pancreas: Spectrum of MDCT Findings. A Pictorial Essay. Appl Radiol. 2009;38(11):10-28.

Levashova Z, Backer M, Backer JM, Blankenberg FG. Imaging Vascular Endothelial Growth Factor (VEGF) Receptors in Turpentine-induced Sterile Thigh Abscesses with Radiolabeled Single-chain VEGF. J Nucl Med. 2009 Dec;50(12):2058-63. PMID: 19910439.

Levin YS, Albers MJ, Butler TN, Spielman D, Peehl DM, Kurhanewicz J. Methods for Metabolic Evaluation of Prostate Cancer Cells Using Proton and (13)C HR-MAS Spectroscopy and [3-(13)C] Pyruvate as a Metabolic Substrate. Magn Reson Med. 2009 Nov;62(5):1091-8.

Levy MA, O'Connor MJ, Rubin DL. Semantic Reasoning with Image Annotations for Tumor Assessment. AMIA Annu Symp Proc. 2009 Nov 14;2009:359-363.

Lew C, Alley MT, Spielman DM, Bammer R, Chan FP. Breathheld Autocalibrated Phase-contrast Imaging. J Magn Reson Imaging. 2010 Apr;31(4):1004-14.

Li Z, Wilson K, Smith B, Kraft DL, Jia F, Huang M, Xie X, Robbins R, Gambhir SS, Weissman I, Wu J. Functional and Transcriptional Characterization of Human Embryonic Stem Cell-Derived Endothelial Calls for Treatment of Myocardial Infarction. PLoS One. 2009 Dec 31;4(12):e84443.

Liang G, Ren H, Rao J. A Biocompatible Condensation Reaction for Controlled Assembly of Nanoparticles in Cells. Nat Chem. 2010;2:54-60.

Liu C, Mang SC, Moseley ME. In Vivo Generalized Diffusion Tensor Imaging (GDTI) Using Higher-order Tensors (HOT). Magn Reson Med. 2010 Jan;63(1):243-52. PMID: 19953513; PMCID: PMC2824337.

Liu C, Zhang J, Moseley ME. Auto-calibrated Parallel Imaging Reconstruction for Arbitrary Trajectories using k-space Sparse Matrices (kSPA). IEEE Trans Med Imaging. 2010 Mar;29(3):950-9. PubMed PMID: 20199928.

Liu H, Ren G, Miao Z, Zhang X, Tang X, Han P, Gambhir SS, Cheng Z. Molecular Optical Imaging with Radioactive Probes. PLoS One. 2010 Mar;5(3):E9470. PMID: 20208993.

Liu YI, Kamaya A, Desser TD, Rubin DL. A Controlled Vocabulary to Represent Sonographic Features of the Thyroid and its application in a Bayesian Network to Predict Thyroid Nodule Malignancy. AMIA Summit on Translational Bioinformatics, 2009.

Loening A, Dragulescu-Andrasi A, Gambhir SS. A Red-Shifted Renilla Luciferase for Transient Reporter-Gene Expression. Nature Methods. 2010 Jan;7(1):5-6.

Ma N, Marshall A, Gambhir SS, Rao J. Facile Synthesis, Silanization and Biodistribution of Biocompatible Quantum Dots. Small. 2010 Jul 19;6(14):1520-8.

Mandleblatt J, Cronin K, Bailey S, Berry D, de Koning H, Draisma G, HUnad H, Lee S, Munsell M, Plevritis SK, Ravdin P, Schechter P, Sigal B, Stoto M, Stout N, van Ravestevn Nicolien, Venier J, Zelen M, Feuer EJ. Effects of Mammography Screening under Different Screening Schedules: Model Estimates of Potential Benefits and Harms. Ann Intern Med. 2009 Nov 17;151(10):738-47.

Marsden AL, Reddy VM, Shadden SC, Chan FP, Taylor CA, Feinstein JA. A New Multiparameter Approach to Computational Simulation for Fontan Assessment and Redesign. Cogenit Heart Dis. 2010 Mar 5(2):104-17.

May A, Bhaumik S, Gambhir SS, Zhan C, Yazdanfar S. Whole-Body, Real-Time Preclinical Imaging of Quantum Dot Fluorescence with Time-Gated Detection. J Biomed Optics. 2009 Nov-Dec;14(6):060504.

Mayer D, Yen YF, Tropp J, Pfefferbaum A, Hurd RE, Spielman DM. Application of Subsecond Spiral Chemical Shift Imaging to Real-time Multislice Metabolic Imaging of the Rat In Vivo after Injection of Hyperpolarized 13C1-pyruvate. Magn Reson Med. 2009 Sep;62(3):557-64.

Miao Z, Ren G, Liu H, Jiang L, Cheng Z. Small-Animal PET Imaging of Human Epidermal Growth Factor Receptor 1 Positive Tumor with a 64Cu Labeled Affibody Protein. Bioconjug Chem. 2010 May 19;21(5):947-54.

Published Papers

Miao Z, Ren G, Liu H, Jiang L, Kimura RH, Cochran JR, Gambhir SS, Cheng Z. An Engineered Knottin Peptide Labeled with 18F for PET Imaging of αvβ3 Integrin Expression. Bioconjugate Chemistry. 2009 Dec;20(12):2342-7. PMID: 19908826. [Highlighted by SNM Newsletter, JNM, 2010; 51(1), 18N].

Mittra E, McDougall IR. Cutaneous Graft-versus-host Disease on Tc-99m Leukocyte Scintigraphy. Clin Nucl Med. 2009 Dec;34(12):894-5.

Morris B, Partap S, Yeom K, Gibbs IC, Fisher PG, King A. Cerebrovascular Disease in Childhood Cancer Survivors: A Children's Oncology Group Report. Neurology. 2009 Dec 1;73(22):1906-13.

Newman B, Feinstein JA, Cohen RA, Feingold B, Kreutzer J, Patel H, Chan FP. Congenital Extrahepatic Portosystemic Shunts Associated with Heterotaxy and Polysplenia. Pediatr Radiol. 2010 Jul;40(7):1222-30. PMID 20069288.

Olivot J-M, Mlynash M, Kleinman JT, Straka M, Venkatasubramanian C, Bammer R, Moseley ME, Albers GW, Wijman CAC. Temporal and Spatial Profile of Brain Diffusion-weighted MRI in the First Week after Cardiac Arrest. Stroke. 2010 Aug;41(8):1665-72.

Olivot J, Minynash M, Thijs V, Purushotham A, Kemp S, Lansberg M, Wechsler L, Gold G, Bammer R, Marks M, Albers G. Geography, Structure and Evolution of the Diffusion and Perfusion Lesion in DEFUSE. Stroke 2009 Oct;40(10):3245-51.

Olivot JM, Mylnash M, Thijs VN, Purusshotham A, Kemp S, Lansberg MG, Weschler LR, Gold G, Bammer R, Marks MP, Albers GW. Geography and structure of the penumbra through the eyes of MRI: lesion evolution and infarct prediction. Stroke. 2009;40(10):3245-51.

Pashevich M, Sigal BM, Plevritis SK. A Natural History Model of Metastatic Progression Applied to Lung Cancer. Cancer Causes and Control. 2009 Nov;20(9):1559-69.

Pauly KB, Rieke V, Holbrook AB, Grissom W, Chen J, Kaye E. MR-guidance of HIFU Therapy. Conf Proc IEEE Eng Med Biol Soc. 2009;2009:141-4. PubMed PMID: 19964927.

Peleg M, Rubin DL. Querying Radiology Appropriateness Criteria from a Virtual Medical Record using GELLO. Proc. Workshop on Knowledge Representation for Health-Care: Patient Data, Processes and Guidelines, in conjunction with Artificial Intelligence in Medicine Europe. 2009.

Peng H, Olcott PD, Levin CS. Design Study of a High-resolution Breast-dedicated PET System Built from Cadmium Zinc Telluride Detectors. Phys Med Biol. 2010;55:2761-88.

Vertinsky AT, Rubesova E, Krasnokutsky MV, Bammer S, Rosenberg J, White A, Barnes PD, Bammer R. Performance of PROPELLER Relative to Standard FSE T2-weighted Imaging in Pediatric Brain MRI. Pediatr Radiol. 2009 Oct;39(10):1038-47.

Pham DT, Hura SA, Willman JK, Nino-Murcia M, Jeffrey RB. Pictorial Essay: Evaluation of Periampullary Pathology with CT Volumetric Oblique Coronal Reformations. Am J Roentgenol. 2009 Sep;193(3):786.

Pham DT, Hura SA, Willmann JK, Nino-Murcia M, Jeffrey RB. Evaluation of Periampullary Pathology with CT Volumetric Oblique Coronal Reformations. Am J Roentgenol. 2009 Sep;193(3):W202-8.

Prakash S, Dumoulin SO, Fischbein N, Wandell BA, Liao YJ. Congenital Achiasma and See-saw Nystagmus in VACTERL Syndrome. J Neuroophthalmol. 2010 Mar;30(1):45-8. PMID: 20182207.

PratX G, Levin, CS. Bayesian Reconstruction of Photon Interaction Sequences for High-resolution PET Detectors. Physics in Medicine and Biology. 2009 Sep 7;54(17):5073-94.

Price RO, Jeffrey RB, Vasanawala SS. Appendiceal Hyperemia and/or Distention is Not Always Appendicitis: Appendicitis Mimicry in the Pediatric Population. Clin Imaging. 2009 Sep-Oct;33(5):402-5. PMID: 19712824.

Prümmer M, Hornegger J, Lauritsch G, Wigström L, Girard-Hughes E, Fahrig R. Cardiac C-arm CT: A Unified Framework for Motion Estimation and Dynamic CT. IEEE Trans Med Imaging. 2009 Nov;28(11):1836-49.

Qiu P, Gentles AJ, Plevritis SK. Reducing the Computational Complexity of Information Theoretic Approaches for Reconstructing Gene Regulatory Networks. J Comput Biol. 2010 Feb;17(2):169-76.

Raman P, Raman R, Newman B, Venkatraman R, Raman B, Robinson TE. Development and Validation of Automated 2D-3D Bronchial Airway Matching to Track Changes in Regional Bronchial Morphology Using Serial Low-Dose Chest CT Scans in Children with Chronic Lung Disease. J Digit Imaging. 2009 Sep 15 Epub. PMID: 19756866.

Ren G, Liu Z, Miao Z, Liu H, Jiang L, Subbarayan M, Chin FT, Zhang L, Gambhir SS, Cheng Z. PET of Malignant Melanoma using 18F-labeled Metallopeptides. Journal of Nuclear Medicine. 2009 Nov;50(11):1865-72. PMID: 19837749.

Published Papers

Ren G, Miao Z, Liu H, Jiang L, Limpa-Amara N, Mahmood A,Gambhir SS, Cheng Z. Melanin-targeted Preclinical PET Imaging of Melanoma Metastasis. J Nuc Med. 2009 Oct;50(10):1692-9. PMID: 19759116.

Ren G, Zhang R, Liu Z, Webster J, Miao Z, Gambhir SS, Syud F, Cheng Z. A 2-helix Small Protein Labeled with 68Ga for PET Imaging of HER2 Expressions. J Nucl Med. 2009 Sep;50(9):1492-9. PMID: 19690041.

Ren H, Xiao F, Zhan K, Kim YP, Xie H, Xia Z, Rao J. A Biocompatible Condensation Reaction for Labeling of N-terminal Cysteine on Proteins. Angewandte Chemie International Edition. 2009;48: 9658-62.

Rodriguez-Porcel M, Gheysens O, Paulmurugan R, Chen IY, Peterson KM, Willmann JK, Wu JC, Zhu X, Lerman LO, Gambhir SS. Antioxidants Improve Early survival of Cardiomyoblasts After Transplantation to the Myocardium. Mol Imaging Biol. 2010 Jun;12(3):325-34.

Rogalski EJ, Murphy CM, deToledo-Morrell L, Shah RC, Moseley ME, Bammer R, Stebbins GT. Changes in parahippocampal white matter integrity in amnestic mild cognitive impairment: a diffusion tensor imaging study. Behav Neurol. 2009;21(1):51-61. PMID: 19847045; PMCID: PMC2819387.

Roos JE, Paik DS, Olsen DA, Liu EG, Chow LC, Leung AN, Mindelzun R, Choudhury KR, Naidich DP, Napel S, Rubin GD. Computer-aided detection (CAD) of lung nodules in CT scans: Radiologist performance and reading time with incremental CAD assistance. Eur Radiol. 2010 Mar;20(3):549-57.

Roos JE, Rakshe T, Tran DN, Rosenberg J, Straka M, El-Helw T, Sofilos MC, Napel S, Fleischmann D: Lower Extremity CT Angiography (CTA): Initial Evaluation of a Knowledge-based Centerline Estimation Algorithm for Femoro-popliteal Artery (FPA) Occlusions. Acad Radiol. 2009;16:646-53.

Rubin DL, Mongkolwat P, Channin DS. A Semantic Image Annotation Model to Enable Integrative Translational Research. In: AMIA Summit on Translational Bioinformatics. 2009.

Rubin DL, Supekar K, Mongkolwat P, Kleper V, Channin DS. Annotation and Image Markup: Accessing and Interoperating with the Semantic Content in Medical Imaging. IEEE Intelligent Systems. 2009;24(1):57-65.

Sachs K, Gentles AJ, Youland R, Itani S, Irish J, Nolan GP, Plevritis SK. Characterization of Patient Specific Signaling via Augmentation of Bayesian Networks with Disease and Patient State Nodes. Conf Proc IEEE Eng Med Biol Soc. 2009;6624-7. PMID: 19963681.

Sahoo D, Seita J, Bhattacharya D, Inlay MA, Weissman IL, Plevritis SK, Dill DL. MiDReG: A Method of Mining Developmentally Regulated Genes using Boolean Implications. Proc Natl Acad Sci U S A. 2010 March 30;107(13):5732-7.

Samaniego EA, Stuckert E, Fischbein N, Wijman CA. Crossed Cerebellar Diaschisis in Status Epilepticus. Neurocrit Care. 2010 Feb;12(1):88-90. PMID: 19967565

Schellenberg D, Quon A, Minn AY, Graves EE, Kunz P, Ford JM, Fisher GA, Goodman KA, Koong AC, Chang DT. (18)Fluorodeoxyglucose PET Is Prognostic of Progression-Free and Overall Survival in Locally Advanced Pancreas Cancer Treated With Stereotactic Radiotherapy. Int J Radiat Oncol Biol Phys. 2010 Aug 1;77(5):1420-5.

Schmitz A, van den Bosch MA, Rieke V, Dirbas FM, Butts Pauly K, Mali WP, Daniel BL. 3.0T MR-guided Focused Ultrasound for Pre-operative Localization of Non-palpable Breast Lesions: An Initial Experimental Ex Vivo Study. J Magn Reson Imaging. 2009 Oct;30(4):884-9. PMID: 19787736.

Schroeder AR, Axelrod DM, Silverman NH, Rubesova E, Merkel E, Roth SJ. A Continuous Heparin Infusion Does Not Prevent Catheter-related Thrombosis in Infants Post-cardiac Surgery. Pediatr Crit Care Med. 2010 Jan 22.

Shah NH, Bhatia N, Jonquet C, Rubin DL, Chiang AP, Musen MA. Comparison of Concept Recognizers for Building the Open Biomedical Annotator. BMC Bioinformatics. 2009 Sep 17;10 Suppl 9:S14.

Shahbaba B, Gentles A, Beyene J, Plevritis SK, Greenwood CMT. A Bayesian Nonparametric Method for Model Evaluation: Application to Gene-disease Studies. Journal of Nonparametric Statistics. 2009;21(3):379-96.

Shin DS, Jeffrey RB, Desser TS. Pearls and Pitfalls in Hepatic Ultrasonography. Ultrasound Q. 2010;26(1):17-25.

Shin LK, Fischbein NJ, Kaplan MJ, Jeffrey RB. Metastatic Squamous Cell Carcinoma Presenting as Diffuse and Punctate Cervical Lymph Node Calcifications: Sonographic Features and Utility of Sonographically-guided Fine-needle Aspiration Biopsy. J Ultrasound Med. 2009 Dec; 28(12):1703-7. PMID: 19933485.

Singh M, Spielman D, Adleman N, Alegria D, Howe M, Reiss A, Chang K. Brain Glutamatergic Characteristics of Pediatric Offspring of Parents with Bipolar Disorder. Psychiatry Res. 2010 May 30;182(2):165-71.

Steele JR, Hovsepian DM, Schomer DF. The Joint Commission Practice Performance Evaluation: A Primer for Radiologists. J Am Coll Radiol. 2010 Jun;7(6):425-30.

Published Papers

Steele JR, Wallace MJ, Hovsepian DM, James BC, Kundu S, Miller DL, Rose SC, Sacks D, Shah SS Cardella JF. Guidelines for Establishing a Quality Improvement Program in Interventional Radiology. J Vasc Interv Radiol. 2010 May;21(5):617-25.

Stevens KJ, Crain JM, Akizuki KH, Beaulieu CF. Imaging and Ultrasound-guided Steroid Injection of Internal Oblique Muscle Strains in Baseball Pitchers. Am J Sports Med. 2010 Mar;38(3):581-5.

Stevens KJ. Magnetic Resonance Imaging of the Elbow. J Magn Reson Imaging. 2010 May;31(5):1036-53.

Sun N, Lee A, Wu JC. Long-term Non-invasive Imaging of Embryonic Stem Cells using Reporter Genes. Nat Protoc. 2009;4(8):1192-201.

Sun N, Panetta NJ, Gupta DM, Wilson KD, Lee A, Jia F, Hu S, Cherry AM, Robbins RC, Longaker MT, Wu JC. Feeder-free Derivation of Induced Pluripotent Stem Cells from Adult Human Adipose Stem Cells. Proc Natl Acad Sci U S A. 2009 Sep 15;106(37):15720-5.

Sutter R, Heilmeier C, Lutz AM, Weishaupt D, Seifert B, Willmann JK. MR Angiography with Parallel Acquisition for Assessment of the Visceral Arteries: Comparison with Conventional MR Angiography and 64-detector-row Computed Tomography. Eur Radiol. 2009 Nov;19(11):2679-88.

Swijnenburg RJ, Govaert JA, van der Bogt KE, Pearl JI, Huang M, Stein W, Hoyt G, Vogel H, Contag CH, Robbins RC, Wu JC. Timing of Bone Marrow Cell Delivery has Minimal Effects on Cell Viability and Cardiac Recovery Following Myocardial Infarction. Circulation: Cardiovascular Imaging. 2010;3(1):77-85.

Sze DY, Fleischmann D, Ma AO, Price EA, McConnell MV. Embolization of a Symptomatic Systemic to Pulmonary (right-to-left) Venous Shunt Caused by Fibrosing Mediastinitis and Superior Vena Caval Occlusion. J Vasc Interv Radiol. 2010;21(1):140-3.

Tedesco MM, Terashima M, Blankenberg FG, Levashova Z, Spin JM, Backer MV, Backer JM, Sho M, Sho E, McConnell MV, Dalman RL. Analysis of In Situ and Ex Vivo Vascular Endothelial Growth Factor Receptor Expression during Experimental Aortic Aneurysm Progression. Arterioscler Thromb Vasc Biol. 2009 Oct;29(10):1452-7. PMID: 19574559.

Tognolini A, Louie JD, Hwang GL, Hofmann LV, Sze DY, Kothary N. Utility of C-arm CT in Patients with Hepatocellular Carcinoma Undergoing Transhepatic Arterial Chemoembolization. J Vasc Interv Radiol. 2010 Mar;21(3):339-47.

Tooze JA, Gaussoin SA, Resnick SM, Fischbein NJ, Robinson JG, Bryan RN, An Y, Espeland MA. Women's Health Initiative Memory Study. A Uniform Approach to Modeling Risk Factor Relationships for Ischemic Lesion Prevalence and Extent: The Women's Health Initiative Magnetic Resonance Imaging study. Neuroepidemiology. 2010;34(1):55-62. PMID: 19940514.

Townson JL, Ramadan SS, Simedrea C, Rutt BK, Macdonald IC, Foster PJ, Chambers AF. Three-dimensional Imaging and Quantification of both Solitary Cells and Metastases in Whole Mouse Liver by Magnetic Resonance Imaging. Cancer Res. 2009 Nov 1;69(21):8326-31. PMID: 19843857.

Tu S, Peleg M, Carini S, Bobak M, Rubin DL, Sim I. A Practical Method for Transforming Free-Text Eligibility Criteria into Computable Criteria. AMIA Annu Symp Proc. 2009.

Tuniz F, Soltys SG, Choi CY, Chang SD, Gibbs IC, Fischbein NJ, Adler JR Jr. Multisession Cyberknife Stereotactic Radiosurgery of Large, Benign Cranial Base Tumors: Preliminary Study. Neurosurgery. 2009 Nov;65(5):898-907; discussion 907. PMID: 19834402.

Ueda T, Fleischmann D, Dake MD, Rubin GD, Sze DY. Incomplete Endograft Apposition to the Aortic Arch: Bird-beak Configuration Increases Risk of Endoleak Formation after Thoracic Endovascular Aortic Repair. Radiology. 2010 May;255(2):645-52.

Vaithilingam S, Ma T, Furukawa Y, Wygant I, Zhuang X, De la Zerda A, Oralkan O, Kamaya A, Gambhr SS, Jeffrey RB, Khuri-Yakub B. Three-dimensional Photoacoustic Imaging using a Two-dimensional CMUT Array. IEEE, 56(11): 2411-2419, November, 2009.

Vaithilingam S, Ma TJ, Furukawa Y, Wygant IO, Zhuang X, De La Zerda A, Oralkan O, Kamaya A, Gambhir SS, Jeffrey RB, Khurii-Yakub BT. Three-dimensional Photoacoustic Imaging using a Two-dimensional cMUT array. IEEE Trans Ultrason Ferroelectr Freq Control. 2009 Nov;56(11):2411-9.

Van de Ven S, Lin MC, Daniel BL, Sareen P, Lipson JA, Pal S, Dirbas FM, Ikeda DM. Freehand MRI-guided Preoperative Needle Localization of Breast Lesions after MRI-guided Vacuum-assisted Core Needle Biopsy (VACNB) Without Marker Placement. J Magn Reson Imaging. 2010 Jul;32(1):101-9.

Vandevenne J, Pearle A, Lang P, Butts Pauly K, Bergman G. Clinical Feasibility of a Magnetic Resonance Tracking System to Guide the Position of the Scan Plane during Physiologic Joint Motion. Radiol Med. 2010 Feb;115(1):133-40. PubMed PMID: 20041313.

Vasanawala SS, Iwadate Y, Church DG, Herfkens RJ, Brau ACS. Navigated Abdominal T1 MRI Permits Free-Breathing Image Acquisition with Less Motion Artifacts. Pediatr Radiol. 2010 Mar;40(3)340-4. PMID20066407.

Vasanawala SS. MRI of the Liver – How to Do It. Pediatr Radiol. 2010 Apr;40(4):431-7. PMID: 20225098.

Vertinsky AT, Rubesova E, Krasnokutsky MV, Bammer S, Rosenberg J, White A, Barnes PD, Bammer R. Performance of PROPELLER Relative to Standard FSE T2-weighted Imaging in Pediatric Brain MRI. Pediatr Radiol. 2009 Oct;39(10):1038-47.

Published Papers

Published Papers

Wang B, Sommer FG, Spielman D, Shortliffe LD. Evaluation of Dynamic Constrast-enhanced MRI in Detecting Renal Scarring in a Rat Injury Model. J Magn Reson Imaging. 2010 May;31(5):1132-6.

Wang C, Stebbins GT, Medina DA, Shah RC, Bammer R, Moseley ME, Detoledo-Morrell L. Atrophy and Dysfunction of Parahippocampal White Matter in Mild Alzheimer's Disease. Neurobiol Aging. 2010 Mar 30; Epub. PubMed PMID: 20359781.

Willmann J, Kimura R, Deshpande N, Lutz A, Cochran J, Gambhir SS. Targeted Contrast-Enhanced Ultrasound Imaging of Tumor Angiogenesis with Contrast Microbubbles Conjugated to Integrin-Binding Knottin Peptides. J Nucl Med. 2010 Mar;51(3):433-40.

Willmann JK, Kimura, RH, Deshpande N, Lutz AM, Cochran JR, Gambhir SS. Targeted Contrast-enhanced Ultrasound Imaging of Tumor Angiogenesis with Contrast Microbubbles Conjugated to Integrin-Binding Knottin Peptides. J Nucl Med. 2010 Mar;51(3):433-40.

Won JH, Rosenberg J, Rubin GD, Napel S. Uncluttered Single-Image Visualization of the Abdominal Aortic Vessel Tree: Method and Evaluation. Medical Physics. 2009 Nov;36(11):5245–60.

Wong S, Kupnik M, Watkins R, Butts Pauly K, Khuri-Yakub B. Capacitive Micromachined Ultrasonic Transducers for Therapeutic Applications. IEEE Trans Biomed Eng. 2010 Jan;57(1):114-23. PubMed PMID:19628448.

Wu AS, Do BH, Kim J, Rubin DL. Evaluation of Negation and Uncertainty Detection and its Impact on Precision and Recall in Search. J Digit Imaging. 2009 Nov 10; Epub.

Yen YF, Le Roux P, Mayer D, King R, Spielman D, Tropp J, Butts Pauly K, Pfefferbaum A, Vasanawala S, Hurd R. T(2) Relaxation Times of (13)C Metabolites in a Rat Hepatocellular Carcinoma Model Measured In Vivo using (13)C-MRS of Hyperpolarized [1-(13)C]pyruvate. NMR Biomed. 2010 Feb 19; Epub. PubMed PMID: 20175135.

Yoon S, Pineda AR, Fahrig R. Simultaneous Segmentation and Reconstruction: A Level Set Method Approach for Limited View Computed Tomography. Med Phys. 2010 May;37(5):2329-40.

Yu J, Huang NF, Wilson KD, Velotta JB, Huang M, Li Z, Lee A, Robbins RC, Cooke JP, Wu JC. nAChRs Mediate Human Embryonic Stem Cell-derived Endothelial Cells: Proliferation, Apoptosis, and Angiogenesis. PLoS ONE. 2009 Sep 15;4(9):e7040.

Yuan N, Kane PE, Shelton K, Matel J, Beckel BC, Moss RB. Safety, Tolerability, and Efficacy of High-Frequency Chest Wall Oscillation in Pediatric Patients with Cerbral Palsy and Neuromuscular Diseases: An Exploratory Randomized Controlled Trial. J Child Neurol. 2010 Jul;25(7):815-21.

Zaharchuk G, Bammer R, Straka M, Newbould RD, Rosenberg J, Olivot JM, Mlynash M, Lansberg MG, Schwartz NE, Marks MM, Albers GW, Moseley ME. Improving Dynamic Susceptibility Contrast MRI Measurement of Quantitative Cerebral Blood Flow using Corrections for Partial Volume and Nonlinear Contrast Relaxivity: A Xenon Computed Tomographic Comparative Study. J Magn Reson Imaging. 2009 Oct;30(4):743-52. PMID: 19787719; PMCID: PMC2851938.

Zaharchuk G, Bammer R, Straka M, Shankaranarayan A, Alsop DC, Fischbein NJ, Atlas SW, Moseley ME. Arterial Spin-label Imaging in Patients with Normal Bolus Perfusion-weighted MR Imaging Findings: Pilot Identification of the Borderzone Sign. Radiology. 2009 Sep;252(3):797-807. PMID: 19703858.

Zaharchuk G, Straka M, Marks MP, Albers GW, Moseley ME, Bammer R. Combined arterial spin label and dynamic susceptibility contrast measurement of cerebral blood flow. Magn Reson Med. 2010 Jun;63(6):1548-56.

Zhu L, Wang J, Xie Y, Starman J, Fahrig R, Xing L. A patient set-up protocol based on partially blocked cone-beam CT. Technol Cancer Res Treat. 2010 Apr;9(2):191-8.

Zissen MH, Quon A. Focal fat mimicking multiple hepatic metastases on FDG PET/CT imaging. Eur J Nucl Med Mol Imaging. 2009 Sep;36(9):1527.

Books and Book Chapters

Books and Book Chapters

Binder DK, Sonne DC, Fischbein NJ. Cranial Nerves: Anatomy, Pathology, Imaging. New York: Thieme Medical Publishers, 2010.

Branstetter BF, Rubin DL, Griffin SD, Weiss DL, eds. Practical Imaging Informatics. Society of Imaging Informatics in Medicine, 2009.

Chan C, Gambhir SS. Encyclopedic Reference on Imaging. V. Ntziachristos (Ed.). E-published in 2010 as part of Springer Medicine eBook Collection.

Cho K, Kamaya A, Hahn ST. CO2 with central venous access and venous interventions.
In: Cho K, Hawkins KF, eds. Carbon Dioxide Angiography: Principles, Techniques, and Practices. New York: Informa Healthcare, 2007. pp. 239-252.

Books and Book Chapters

Books and Book Chapters

Deshpande N, Willmann JK. Micro- And Nano-Particle Based Contrast-Enhanced Ultrasound Imaging.
In: Nanoplatform-Based Molecular Imaging. Xiaoyuan Chen (ed.), John Wiley & Sons, New York (2010, in press)

Desser TS, Hann LE. Ultrasound of the liver, biliary tree, and pancreas.
In Jarnagin et al.: Blumgart's Surgery of the Liver, Biliary Tract, & Pancreas, 5th edition, in press.

Fischbein NJ, Lee N. Radiology of Head and Neck Cancer.
In: Leibel S and Phillips T, eds. Textbook of Radiation Oncology, 2nd edition. Philadelphia: Elsevier. Publication expected 2010.

Fischbein NJ, Ong K. Radiology. In: Lalwani A, ed. Current Diagnosis and Treatment in Otolaryngology-Head and Neck Surgery, 3nd edition.
New York: Lange Medical Publishers. Publication expected 2010.

Fleischmann D. Contrast medium administration in Cardiac CT. In: Taylor AJ (editor). Atlas of Cardiovascular Computed Tomography: Expert Consult-Online and Print: Imaging Companion to Braunwald's Heart Disease. Saunders, Philadelphia, ISBN-10: 1416061363

Ha BY, Newman B. Pediatric Emergency Imaging. In: Wang N, Shandro J, Fassl B, Sohoni A editors. Manual of Pediatric Emergency Medicine.
Cambridge: Cambridge University Press. (in press: Feb. 2011).

Ikeda DM. The Requisites: Breast Imaging. 2nd edition. Elsevier, Mosby, Inc. Philadelphia, PA, 2010.

Kim Y-P, Xia Z, Rao J. Multiplexed Detection using Quantum Dots. In: Nanomaterials for Life Sciences Volume 6: Semiconductor Nanomaterials, edited by Challa S.S. R. Kumar. Chapter 4, 147- 175 (2010). (Invited)

Levin CS. Imaging system physics, technology, and methods for visualization and quantification of reporter gene expression in living subjects.
In: Reporter Gene Imaging. Eds. Gambhir and Yaghoubi. Cambridge University Press. (in press, 2010).

Levin CS. Instrumentation and methods to combine small animal PET with other imaging modalities. In: Molecular Imaging: Principles and Practice.
Eds. Gambhir, Weissleder, Ross, and Rehemtulla. BC Decker Inc. (in press, 2010).

Levin CS. Molecular Imaging Instrumentation. In: Molecular Imaging Probes for Cancer Research. Ed. Shawn Chen. World Scientific (in press, 2010).

Liu S, Levi J, Cheng Z. General principles of molecular imaging probe design. Chen X Eds. World Scientific (in press).

Moseley ME. DWI in Cerebral Ischemia: The Early Days. In: Diffusion MRI: Theory, Methods, and Applications. In Press. Elsevier, 2010.

Newman B, Varich LJ. The Term and Preterm Newborn Infant. In: Pediatric Radiology: A Multimodality Pictorial Review,
Daldrup-Link HE and Gooding CA (eds). Cambridge University Press (New York, NY) (in press).

Newman B. Imaging the chest. In: Rudolph's Textbook of Pediatrics, 22nd edition (in press: Jan. 2011)

Nino-Murcia M, Jeffrey RB. Pancreatic Malignancy. In: Husband JE, Reznek RH, ed., Imaging in Oncology, London: Taylor and Francis, 3rd edition. In Press

Paik DS. Visualization. In: Molecular Imaging: Principles and Practice, Weisledder R, Ross BD, Rehemtulla A, Gambhir SS (eds), BC Decker Inc., 2009.

Plevritis SK. Mining Genomic Data for Molecular Imaging Targets. In: Molecular Imaging: Principles and Practice, Editors: Weissleder R, Gambhir SS,
Ross BD, Rehemtulla A, McGraw Hill Publishers, to appear April 2010.

Pysz MA, Willmann JK. Applications of Molecular Small-Animal Imaging in Oncology. In: Multimodality Molecular Imaging of Small Animals: Instrumentation and Applications. H Zaidi (Ed.), Springer, New York. (2010,in press)

Quon A (in press). Breast PET and PET/CT: technical and clinical aspects. In: The Requisites: Breast Imaging. 2nd Edition D. M. Ikeda, Mosby.

Rodriquez-Porcel M, Wu JC, Gambhir SS. Molecular imaging of stem cells. Polak J, Bhatia S, eds. StemBook, 1st ed. 2009

Rubesova E, Varich LJ. Differential Diagnosis in Radiology, Chapter 9-Fetal Imaging; Thieme, 2009

Shapiro L, Gold G. Magnetic Resonance Imaging, submitted for Rheumatology, Hochberg, et al. Elsevier, 2010.

Spanoudaki V, Levin CS. Design considerations of small-animal PET scanners. In: Multimodality Molecular Imaging of Small-Animals: Instrumentation and Applications. Ed. H. Zaidi, Springer (in press, 2010).

Thurmond AS, Hovsepian DM. Tubal Recanalization. In: MEDICAL RADIOLOGY – Diagnostic Imaging, Volume: Radiological Interventions in Obstetrics and Gynecology, Pelage J-P, Ed. Springer-Verlag, Heidelberg, Germany, In press.

Books and Book Chapters

Books and Book Chapters

Weissleder R, Ross B, Rehemtulla A, Gambhir SS. Molecular Imaging: Principles and Practice. People's Medical Publishing House – USA, 2010.

Wu JC, Gambhir SS. Molecular gene of gene expression and cell therapy. In: Zaret BL, Beller GA, eds. Clinical Nuclear Cardiology: State of the Art and Future Directions, 4th ed. St. Louis: Mosby, 2009

Papers Submitted or In Press

Papers Submitted or In Press

Brinton TJ, Wu JC. Current Use of Imaging in Cardiac Stem Cell Clinical Trials. Current Cardiovascular Imaging Reports. 2009;2(1):1-2.

Nguyen P, Wu JC. Importance of Imaging in Studying Cardiac Stem Cells. Imaging in Med. 2010;2(1):1-3.

Segall GM. A Lifer's Reflections on the MOC Exam. ABNM Tracers. 2009;1:2.

Segall GM. Dispelling the Myths about MOC Part IV: Practice Performance Assessment. ABNM Tracers. 2010;1:4.

Segall GM. Part IV Projects in Development. ABNM Tracers. 2009;2:3.

Segall GM. President's report: SNM Working to Prevent the 'Perfect Storm'. SNM PET Center of Excellence Newsletter. 2010;7(1):1.

Segall GM. President's report. SNM PET Center of Excellence Newsletter. 2009;5(4):1.

Segall GM. President's report. SNM PET Center of Excellence Newsletter. 2009;6(3):1.

Wilson KD, Wu JC. The miR-145 Pluripotency Loop in Human Embryonic Stem Cells. Cell Science Reviews. 2009;6(2):51-5.

Ganguly A, Simons J, Schneider A, Keck B, Bennett R, Coogan S, Herfkens RJ, Fahrig R. In Vivo Imaging of Superficial Femoral Artery (SFA) Stents for Deformation Analysis. JVIR March 2010.

Abdelmaksoud MH, Louid JD, Hwang GL, Kothary N, Hofmann LV, Hovsepian DM, Kuo WT, Sze DY. Development of New Hepatico-enteric Collateral Pathways after Hepatic Arterial Skeletonization in Preparation for 90Y Radioembolization. J Vasc Interv Radiol. 2010 Aug 3; Epub.

Akgul CB, Rubin DL, Napel S, Beaulieu C, Greenspan H, Acar B: Content Based Image Retrieval in Radiology: Current Status and Future Directions. J Digital Imaging (in press).

Balchandani P, Pauly J , Spielman DM. Method to Design Adiabatic RF Pulses using the Shinnar Le-Roux Algorithm. Magn Res Med (in press).

Brody JD, Ai WZ, Czerwinski DK, Torchia JT, Levy M, Advani RH, Kim YH, Hoppe RT, Knox SJ, Shin LK, Wapnir I, Tibshirani RJ, Levy R. In Situ Vaccination with a TLR9 Agonist Induces Systemic Lymphoma Regression. J Clin Oncol. 2010 Aug 9; Epub.

Darsaut TE, Darsaut NM, Chang SD, Silverberg GD, Shuer LM, Tian L, Dodd RL, Do HM, Marks MP, Steinberg GK. Predictors of Clinical and Angiographic Outcome Following Surgical or Endovascular Therapy of Very Large and Giant Intracranial Aneurysms. Neurosurgery.

Grissom WA, Lustig M, Holbrook AB, Rieke V, Pauly JM, Butts Pauly K. Reweighted l1 Referenceless PRF Shift Thermometry. MRM (in press).

Grissom WA, Rieke V, Lustig M, Santos J, Pauly JM, McConnell MV, Butts Pauly K. Hybrid Referenceless and Multi-baseline Subtraction Thermometry for Monitoring Thermal Therapies in Moving Organs. Medical Physics (in press).

Hahn J, Barnes P, Clegg N, Stashinko E. Septopreoptic Holoprosencephaly: A Mild Subtype Associated with Midline Craniofacial Anomalies. Am J Neuroradiol. 2010 May 20; Epub.

Hong JC, Yu Y, Rao AK, Dieterich S, Maxim PG, Le QT, Diehn M, Sze DY, Kothary N, Loo BW. High Retention and Safety of Percutaneously Implanted Vascular Embolization Coils as Fiducial Markers for Image-Guided Stereotactic Ablative Radiotherapy of Pulmonary Tumors. Int J Radiat Oncol Biol Phys (in press).

Hristov D, Liu L, Adler JR, Gibbs IC, Moore T, Sarmiento M, Chang SD, Dodd R, Marks M, Do HM. Localization Technique for Frameless Image-guided Robotic Radiosurgery of Arteriovenous Malformations. International Journal of Radiation Oncology, Biology, and Physics (accepted).

Hurd RE, Yen YF, Mayer D, Chen A, Wilson D, Kohler S, Bok R, Vigneron D, Kurhanewicz J, Tropp J, Spielman D, Pfefferbaum A. Metabolic Imaging in the Anesthetized Rat Brain using Hyperpolarized [1-13C] Pyruvate and [1-13C] Ethyl Pyruvate. Magn Reson Med (in press).

Papers Submitted or In Press

Papers Submitted or In Press

Iagaru A, Mittra ES, Quon A, Gambhir SS.
18F FDG PET/CT in Cancers of the Head and Neck: What is the Definition of Whole-Body Scanning? Mol Imaging Biol. 2010

Jang ES, Won JH, Kim YW, Cheng Z, Choy JH.
Dynamic Transition Between Zn-HDS and ZnO; Growth and Dissolving Mechanism of Dumbbell-like ZnO bipod Crystal. CrystEngComm (in press).

Kamaya A, Gross M, Katsu H, Jeffrey RB. Recurrence in the Thyroidectomy Bed: Sonographic Findings. Submitted to AJR, accepted with major revisions.

Kijowski R, Gold G. Routine Three-Dimensional Magnetic Resonance Imaging of Joints. JMRI 2010 in press.

Koch K, Hargreaves BA, Butts Pauly K, Chen W, Gold G, King K.
Technical Review: MR Imaging near Embedded Metal Hardware. J Magn Reson Imaging (in press).

Kothary N, Bartos JB, Hwang GL, Dua R, Hofmann LV. CT-guided Percutaneous Needle Biopsy of Indeterminate Pulmonary Pathology: Efficacy of Obtaining a Diagnostic Sample in Immunocompetent and Immunocompromised Patients. Clin Lung Cancer (in press).

Kuo WT, Hofmann LV. Optimizing Endovascular Therapy for Acute PE: Primum Non Nocere. J Vasc Interv Radiol (in press).

L. Shapiro, E. Starosweicki, G. Gold. Magnetic Resonance Imaging of the Knee: Optimizing 3 Tesla Imaging. Semin Roentgenol (in press).

Lee CI, Tsai EB, Sigal BM, Plevritis SK, Garber AM, Rubin GD. Incidental Extracardiac Findings at Coronary CT: Clinical and Economic Impact. Am J Radiol (in press).

Levashova Z, Backer M, Hamby CV, Pizzonia J, Backer JM, Blankenberg FG. Molecular Imaging of Changes in Vascular Endothelial Growth Factor Receptor Prevalence in Sunitinib-treated Murine Mammary Tumors. J Nucl Med (in Press).

Liu H, Zhang X, Xing B, Han P, Gambhir SS, Cheng Z. Radiation Luminescence Excited Quantum Dots for In Vivo Multiplexed Optical Imaging. Small (in press).

Lutz AM, Willmann JK, Drescher C, Ray P, Cochran FC, Urban N, Gambhir SS. Early Diagnosis of Ovarian Cancer: Is a Solution in Sight? Radiology (in press).

Ma N, Marshall, AF, Rao J. Near-infrared Light Emitting Luciferase via Biominerization. Journal of American Chemical Society. Accepted.

Mansouri MA, Iagaru A. 18F FDG PET/CT Demonstration of Lymphohistiocytic Meningitis. Clin Nucl Med.

Massoud T, Paulmurugan R, Gambhir SS. A Molecularly Engineered Split Reporter for Imaging Protein Protein Interactions with Positron Emission Tomography. Nature Medicine (in press).

Miao Z, Levi J, Cheng Z. Protein Scaffolds Based Molecular Probes for Cancer Molecular Imaging. Amino Acids. 2010 Feb 21; Epub. PMID: 20174842.

Miao Z, Ren G, Liu H, Jiang L, Cheng Z. Cy5.5 labeled Affibody Molecule for Near-infrared Optical Imaging of Epidermal Growth Factor Receptor1 Expression. J Biomed Optics. Oct. 2009 (in press).

Mitra R, Do HM, Alamin T, Cheng I. Facet Pain in Thoracic Compression Fractures. Pain Medicine (accepted).

Mittra E, Goris ML, Iagaru A, Kardan A, Burton L, Berganos R, Chang E, Liu S, Shen B, Chin FT, Chen X, Gambhir SS. First In-man Pharmacokinetic and Dosimetry Studies of [18F]FPPRGD2: A Novel PET Radiopharmaceutical for Imaging αvβ3 Integrin Levels.

Mittra E, Leung A, Iagaru A. Diagnosis Please: Metastatic Pulmonary Artery Sarcoma. Radiology (in press).

Napel S, Beaulieu CF, Rodriguez C, Cui J, Xu J, Gupta A, Korenblum D, Greenspan H, Ma Y, Rubin DL. Automated Retrieval of CT Images of Liver Lesions Based on Image Similarity: Method and Preliminary Results. Radiology (in press).

Napel SA, Beaulieu CF, Rodriguez C, Cui J, Xu J, Gupta A, Greenspan H, Ma Y, Rubin DL, Automated Retrieval of CT Images of Liver Lesions Based on Image Similarity: Method and Preliminary Results. Radiology (in press).

Newbould R, Skare S, Alley M, Gold G, Bammer R. Three Dimensional T1 T2 and Proton Density Mapping with Inversion Recovery Balanced SSFP. Magnetic Resonance Imaging (in press).

Peng H, Levin CS. Recent developments in PET instrumentation. Current Pharmaceutical Biotechnology (in press).

Pu J, Paik DS, Meng X, Roos JE, Rubin GD. Shape Break-and-Repair Strategy and Its Application to Computerized Medical Image Segmentation. IEEE Transactions on Visualization and Computer Graphics (in press).

Papers Submitted or In Press

Papers Submitted or In Press

Pysz MA, Foygel K, Rosenberg J, Gambhir SS, Schneider M, Willmann JK.
Monitoring Anti-Angiogenic Cancer Therapy with Molecular Ultrasound and a New Clinically Translatable Contrast Agent (BR55). Radiology (in press).

Pysz MA, Gambhir SS, Willmann JK. Molecular imaging: Current Status and Emerging Strategies. Clinical Radiology (in press).

Ren G, Pan Y, Cheng Z. Molecular Probes for Malignant Melanoma Imaging. Current Pharmaceutical Biotechnology. 2010 April (in press).

Ren PG, Huang Z, Ma T, Biswal S, Smith RL, Goodman SB. Surveillance of Systemic Trafficking of Macrophages Induced by UHMWPE Particles in Nude Mice by Noninvasive Imaging. J Biomed Mater Res A. 2010 Mar 8;Epub."

Rubin DL, Flanders A, Kim W, Siddiqui KM, Kahn CE. Ontology-Assisted Analysis of Web Queries to Determine the Knowledge Radiologists Seek.
J Digital Imaging. 2010 Mar 31; Epub.

Rubin DL, Napel S.
Imaging Informatics: Toward Capturing and Processing Semantic Information in Radiology Images. 2010 IMIA Yearbook of Medical Informatics. 2010 Mar.

Salehian S, Fischbein NJ. Association of Venous Malformation of the Head and Neck with Meningoencephalocele: Report of 3 Cases.
Am J Neuroradiol. 2010 Apr 1; Epub. PMID: 20360349.

Staroswiecki E, Bangerter NK, Gurney PT, Grafendorfer T, Daniel BL, Gold BE, Hargreaves BA. In-Vivo Sodium Imaging of Human Patellar Cartilage with a 3D Cones Sequence at 3T and 7T. J Magn Reson (in press).

Tan JC, Busque S, Workeneh B, Ho B, Derby G, Blouch K, Sommer FG, Edwards B, Myers B. Effects of Aging on Glomerular Function and Number in Living Kidney Donors. Kidney Int. 2010 May 12; Epub.

Vasanawala SS, Alley MT, Hargreaves BA, Barth RA, Pauly JM, Lustig M. Improved Pediatric MRI via Compressed Sensing. Radiology (In Press).

Wang J, Xie J, Zhou X, Cheng Z, Gu N, Teng G, Hu Q, Zhu F, Chang S, Zhang F, Lu G, Chen X. Ferritin Enhances SPIO Tracking of C6 Rat Glioma Cells by MRI. Molecular Imaging & Biology. 2010 May 4; Epub.

Young P, Brau AC, Iwadate Y, Vasanawala SS, Daniel BL, Herfkens RJ. Respiratory-navigated Free Breathing 3D-spoiled Gradient Echo Sequence for Contrast-enhanced Examination of the Liver: Diagnostic Utility and Comparison with Free Breathing and Breath-hold Conventional Exams. Am J Roentgenol (in press).

Ganguly A, Fieselmann A, Boese J, Rohkohl C, Hornegger J, Fahrig R. Evaluating the feasibility of C-arm CT for Brain Perfusion Imaging: An In Vitro Study. Proc. SPIE 7625, 76250K.

Barth A. The Brain: Inside Story, Discover Spring 2010: 56-61.

Chan S, Kamaya A. Dermoid cyst. Case-in-Point online teaching file publication. September 3, 2009.

Church DG, Vancil JM, Vasanawala SS. Magnetic Resonance Imaging for Uterine and Vaginal Anomalies. Curr Opin Obstet Gynecol. 2009 Oct;21(5):379-89.

Daniel BL, Hwang G, Kao J, Ikeda DM. Freehand, Non-grid Vacuum Core Biopsies: A Preliminary Analysis of 500 Biopsies.
Eur Radiol. 2009;19(Suppl 4): S794-S799.

Daniel BL, Van Den Bosch M, Hargreaves BA, Kao J, Ikeda DM. Small Foci in MR: What should we do? Neglect, Follow, Excise? A Retrospective Analysis of 19 Small Foci Compared with 19 typical MRI-detected Mammographically Occult Lesions. Eur Radiol. 2009;19(Suppl 4): S799-S802.

Das M, Abdelmaksoud MHK, Loo BW, Kothary N.
Alternatives to Surgery for Early Stage Non-small Cell Lung Cancer – Ready for Prime Time? Current Treatment Options in Oncology.

Gao H, Zhu L, Fahrig R.
Optimization of System Parameters for Modulator Design in X-ray Scatter Correction using Primary Modulation. Proc. SPIE 7622, 76222A.

Hahn J, Barnes P. Neuroimaging Advances in Holoprosencephaly: Refining the Spectrum of the Midline Malformation.
Am J Med Genet Part C Semin Med Genet. 2010;154C:120-132.

Keller K, Barnes P. Rickets vs. Abuse – The Evidence: Reply. Pediatr Radiol. 2009;39:1130.

Lindsay A, Fischbein N. Adenoid Cystic Carcinoma with Perineural Invasion of the Greater Superficial Petrosal Nerve.
ACR case-in-point online teaching file. 2009 Sep.

Papers Submitted or In Press

Mackenzie JD, Vasanawala SS. State-of-the-Art in Pediatric Body and Musculoskeletal Magnetic Resonance Imaging.
Semin Ultrasound CT MR. 2010;31:86-99. PMID:20304318

Narsinh KH, Cao F, Wu JC. Application of Reporter Gene Imaging for Studying Human Embryonic Stem Cells in Living Subjects.
Meth Molec Biol. 2009;515:13-32.

Newman B, Cho YA. Left Pulmonary Artery Sling-Anatomy and Imaging. Semin Ultrasound CT MR. 31:158-70.

Rubin DL. Interoperability: Controlled Terminology for Reporting and New Emerging Standards in Image Annotation and Mark Up.
Appl Radiol. 2009 Dec;38(12):13-7.

Segall GM. PET/CT With and Without Intravenous Contrast: Is there a Standard of Care? SNM. PET Center of Excellence Newsletter. 2010;7(1): 1.

Sun N, Longaker MT, Wu JC. Human iPS Cell-based Therapy: Considerations Before Clinical Applications. Cell Cycle. 2010 Mar;9(5):880-5.

Vandenbroucke A, Lee J, Spanoudaki V, Lau FWY, Reynolds PD, Levin CS. Temperature and Bias Voltage Studies of a Large Area Position Sensitive Avalanche Photodiode. Conference Record of the 2009 IEEE Nuclear Science Symposium and Medical Imaging Conference, pp. 3664-3669. Published March 2010."

Wein W, Camus E, John M, Diallo M, Duong C, Al-Ahmad A, Fahrig R, Khamene A, Xu C. Towards Guidance of Electrophysiological Procedures with Real-time 3D Intracardiac Echocardiography Fusion to C-arm CT. Med Image Comput Comput Assist Interv. 2009;12(Pt 1):9-16

Wilson KD, Huang M, Wu JC. Bioluminescence Reporter Gene Imaging of Human Embryonic Stem Cell Survival, Proliferation, and Fate.
Methods in Molecular Biology. 2009;574:87-103. Writing Committee for US Government Interagency Modeling and Analysis Group (IMAG)
Report on "The Impact Modeling on Biomedical Research"

Ahn KH, Hargreaves BH, Alley MT, Horst KC, Luxton G, Daniel BL, Hristov D. MRI Guidance for Accelerated Partial Breast Irradiation in Prone Position: Imaging Protocol Design and Evaluation. Int J Radiat Oncol Biol Phys. 2009 Sep 1;75(1):285-93.

Arac A, Lee M, Steinberg GK, Marcellus M, Marks MP. Efficacy of Endovascular Stenting in Dural Sinus Stenosis for the Treatment of Idiopathic Intracranial Hypertension. Neurosurg Focus. 2009 Nov;27(5):E14.

Bailey SL, Sigal BM, Plevritis SK. A Simulation Model Investigating the Impact of Tumor Volume Doubling Time and Mammographic Tumor Detectability on Screening Outcomes in Women Aged 40-49. J Natl Cancer Inst. 2010 Aug 18;102(16):1263-71.

Banovac F, Buckley D, Kuo WT, Lough D, Martin LG. Standards of Practice: Reporting Standards for Endovascular Treatment of Pulmonary Embolism.
J Vasc Interv Rad. 2010;21(1):44-53.

Barnes P, Galaznik J, Gardner H, Shuman M. Infant Acute Life-threatening Event – Dysphagic Choking Versus Nonaccidental Injury.
Semin Pediatr Neurol. 2010 Mar;17(1):7-11.

Bhatia N, Shah NH, Rubin DL, Chiang AP, Musen MA. Comparing Concept Recognizers for Ontology-Based Indexing: MGREP vs. MetaMap.
In: AMIA Summit on Translational Bioinformatics, San Francisco, CA. 2009:12-6.

Blankenberg FG, Levashova Z, Sarkar SK, Pizzonia J, Backer MV, Backer JM. Noninvasive Assessment of Tumor VEGF Receptors in Response to Treatment with Pazopanib: A Molecular Imaging Study. Transl Oncol. 2010;3:56-64. PMID: 20165696.

Blankenberg FG. Apoptosis Imaging: Anti-Cancer Agents in Medicinal Chemistry. Anticancer Agents Med Chem. 2009;9(9):944-51. PMID: 19663787.

Boussel L, Arora S, Rapp J, Rutt B, Huston J, Parker D, Yuan C, Bassiouny H, Saloner D. Atherosclerotic Plaque Progression in Carotid Arteries: Monitoring with High-Spatial-Resolution MR Imaging--Multicenter Trial. Radiology. 2009 Sep;252(3):789-96. Epub 2009 Jun 9.

Burnside ES, Sickles EA, Bassett LW, Rubin DL, Lee CH, Ikeda DM, Mendelson EB, Wilcox PA. Butler PF, D'Orsi CJ.
The ACR BI-RADS Experience: Learning from History. J Am Coll Radiol.2009 Dec;6(12):851-60.

Cao F, Xie X, Gollan T, Zhao L, Narsinh K, Lee RJ, Wu JC. Comparison of Gene Transfer Efficiency in Human Embryonic Stem Cells.
Molecular Imaging & Biology. 2010;12:15-24.

Channin DS, Mongkolwat P, Kleper V, Rubin DL. Computing Human Image Annotation. Conf Proc IEEE Eng Med Biol Soc. 2009;2009:7065-8.

Channin DS, Rubin DL. The Annotation and Image Markup Project. Radiology. 2009;253:590-592.

Chen C, Kijowski R, Shapiro L, Tuite M, Davis K, Klaers J, Block W, Reeder S, Gold G.
Cartilage Morphology at 3.0T: Assessment of Three-dimensional Magnetic Resonance Imaging Techniques. J Magn Reson Imaging. 2010 Jul;32(1):173-83.

Papers Submitted or In Press

Papers Submitted or In Press

Chen IY, Gheysens O, Ray S, Wang Q, Padmanabhan P, Paulmurugan R, Loening AM, Rodriguez-Porcel M, Willmann JK, Sheikh AY, Nielsen CH, Hoyt G, Contag CH, Robbins RC, Biswal S, Wu JC, Gambhir SS. Indirect Imaging of Cardiac-specific Transgene Expression using a Bidirectional Two-step Transcriptional Amplification Strategy. Gene Ther. 2010 Jul;17(7):827-38.

Chen J, Butts Pauly K. Optimization of Encoding Gradients for MR-ARFI, MRM, Magn Reson Med. 2010, 63(4):1050-1058.

Chen K, Xie J, Xu H, Behera D, Michalski M, Biswal S, Wang A, Chen X. Triblock Copolymer Coated Iron Oxide Nanoparticle Conjugate for Tumor Integrin Targeting. Biomaterials. 2009 Dec;30(36):6912-9. PMID: 19773081.

Chen MQ, Yu J, Whittington R, Wu JC, Kovacs GT, Giovangrandi L. Modeling Conduction in Host-graft Interactions Between Stem Cell Grafts and Cardiomyocytes. IEEE Eng Med Biol Soc. 2009;2009:6014-7.

Cheng Z, De Jesus OP, Kramer DJ, De A, Webster JM, Gheysens O, Levi J, Namavari M, Wang S, Park JM, Zhang R, Liu H, Lee B, Syud FA, Gambhir SS. 64Cu-labeled Affibody Molecules for Imaging of HER2 Expressing Tumors. Mol Imaging Biol. 2010 Jun;12(3):316-24. PMID: 19779897.

Chennupati SK, Kamaya A, Fisher GA, Ford JM, Kunz P, Itakura H, Welton ML, Shelton A, Van Dam J, Koong AC, Chang DT. Pathological Response after Chemoradiation for T3 Rectal Cancer. Colorectal Dis. 2010 Jul;12(7 online):e24-30.

Choi G, Shin LK, Taylor CA, Cheng CP. In Vivo Deformation of the Human Abdominal Aorta and Common Iliac Arteries with Hip and Knee Flexion: Implications for the Design of Stent-grafts. J Endovasc Ther. 2009 Oct;16(5):531-8.

Choudhury KR, Paik DS, Yi CA, Napel A, Roos J, Rubin GD. Assessing Operating Characteristics of CAD Algorithms in the Absence of a Gold Standard. Medical Physics. 2010;37(4):1788-95.

Collins LK, Levin TL, Berdon WE, Cowles RA, Newman B. Rudhe Syndrome: Reversible Right Middle Lobe Emphysema in Infants with Left-to-Right Shunts – A Historical Review. Pediatr Radiol. 2010 May;40(5):762-5.

Colombani M, Ferry M, Toga C, Lacroze V, Rubesova E, Barth RA, Cassart M, Gorincour G. MRI in the Prenatal Diagnosis of Congenital Diarrhea. Ultrasound Obstet Gynecol. 2010 May;35(5):560-5.

D'Souza A, Tseng J, Butts Pauly K, Guccione S, Rosenberg J, Gambhir SS, Glazer G. A Strategy for Blood Biomarker Amplification and Localization Using Ultrasound. Proc Natl Acad Sci U S A. 2009 Oct 6;106(40):17152-7. PMID: 19805109; PMCID: PMC2749842.

De la Zerda A, Bodapati S, Teed R, Schipper M, Keren S, Smith B, Ng J, Gambhir SS. A Comparison between Time Domain and Spectral Imaging Systems for Imaging Quantum Dots in Small Living Animals. Molecular Imaging and Biology, December 10, 2009 Epub.

De la Zerda A, Paulus Y, Teed R, Bodapati S, Dollberg Y, Khuri-Yakub B, Blumenbranz M, Moshfeghi D, Gambhir SS. Photoacoustic Ocular Imaging. Optics Letters. 2010 Feb;35(3):270-2.

Deshmukh S, Rubesova E, Barth R. MR Assessment of Normal Fetal Lung Volumes: A Literature Review. Am J Roentgenol. 2010 Feb;194(2):W212-7.

Deshmukh SD, Willmann JK, Jeffrey RB. Pathways of Extrapancreatic Perineural Invasion by Pancreatic Adenocarcinoma: Evaluation with 3D Volume-rendered MDCT Imaging. Am J Roentgenol. 2010;194: 668-674.

Deshpande N, Needles A, Willmann JK. Molecular Ultrasound Imaging: Current Status and Future Directions. Clin Radiology. 2010 Jul;65(7):567-81.

Deshpande N, Pysz MA, Willmann JK. Molecular Ultrasound Assessment of Tumor Angiogenesis. Angiogenesis. 2010 Jun;13(2):175-88.

Desser TS, Edwards B, Hunt S, Rosenburg J, Purtill MA, Jeffrey RB. The Dangling Diaphragm Sign: Sensitivity and Comparison with Existing CT Signs of Blunt Traumatic Diaphragmatic Rupture. Am Soc Emergency Radio. 2010;17(1):37-44.

Desser TS. Understanding Transient Hepatic Attenuation Differences. Semin Ultrasound CT MR. 2009 Oct;30(5):408-17.

Deuse T, Blankenberg F, Haddad M, Reichenspurner H, Phillips N, Robbins RC, Schrepfer S. Mechanisms Behind Local Immunosuppression Using Inhaled Tacrolimus in Preclinical Models of Lung Transplantation. Am J Respir Cell Mol Biol. 2009 Oct 30 Epub. PMID: 19880819

Deuse T, Peter C, Fedak PW, Doyle T, Reichenspurner H, Zimmermann WH, Eschenhagen T, Stein W, Wu JC, Robbins RC, Schrepfer S. Hepatocyte Growth Factor or Vascular Endothelial Growth Factor Gene Transfer Maximizes Mesenchymal Stem Cell-based Myocardial Salvage after Acute Myocardial Infarction. Circulation. 2009 Sep 15;120(11 Suppl):S247-54.

Do HM, Fariabi S, Ligon D. Hemi™ Neurovascular Embolization Cover (NEC) device (NFocus Neuromedical) for the Treatment of Aneurysms in the Rabbit Model. J Neurointerventional Surg. 2009;1:72-3.

Papers Submitted or In Press

Dragulescu-Andrasi A, Liang GL, Rao J. In Vivo Bioluminescence Imaging of Furin Activity in Breast Cancer Cells using Bioluminogenic Substrates. Bioconjug Chem. 2009;20:1660-6.

Ganguly A, Yoon S, Fahrig R. Dose and Detectability for a Cone-beam C-arm CT System Revisited. Medical Physics. Med Phys. 2010 May;37(5):2264-8.

Gao H, Fahrig R, Bennett NR, Sun M, Star-Lack J, Zhu L. Scatter Correction Method for X-ray CT using Primary Modulation: Phantom Studies. Med Phys. 2010 Feb;37(2):934-46.

Gao J, Chen K, Xie R, Xie J, Lee S, Cheng Z, Peng X, Chen X. Ultrasmall Near-infrared Non-cadmium Quantum Dots for In Vivo Tumor Imaging. Small. 2010;6(2):256-61. PMID: 19911392.

Gao J, Chen K, Xie RG, Xie J, Yang YJ, Cheng Z, Peng XG, Chen XY. In Vivo Tumor-targeted Fluorescence Imaging using Near-infrared Non-cadmium Quantum Dots. Bioconjug Chemistry. 2010 APR 21;21(4):604-9. PMID: 20369817.

Gao J, Chen X, Cheng Z. Near-infrared Quantum Dots as Optical Probes for Tumor Imaging. Curr Top Med Chem. 2010;10(12):1147-57. PMID: 20388111.

Gaster R, Hall D, Nielsen C, Osterfeld S, Yu H, Mach K, Wilson R, Murmann B, Liao J, Gambhir SS, Wang S. Matrix-insensitive Protein Assays Push the Limits of Biosensors in Medicine. Nat Med. 2009 Nov;15(11):1327-1332.

Gentles A, Li S, Shachaf C, Shahbaba B, Levy R, Koller D, Plevritis SK. A Gene Module Regulatory Network Analysis of Follicular Lymphoma Transformation. Blood. 2009 Oct 8;114(15):3158-66.

Ghatan CE, Kuo WT, Hofmann LV, Kothary N. Making the Case for Early Medical Student Education in Interventional Radiology: A Survey of 2nd-year Students in a Single U.S. institution. J Vasc Interv Radiol. 2010 Apr;21(4):549-53.

Gold G, Chen C, Koo S, Hargreaves BA, Bangerter N. Recent Advances in MRI of Articular Cartilage. Am J Roentgenol. 2009 Sep;193(3):628-38.

Gonella MC, Fischbein NJ, Lane B, Shuer LM, Greicius MD. Episodic Encephalopathy due to an Occult Spinal Vascular Malformation Complicated by Superficial Siderosis. Clin Neurol Neurosurg. 2010 Jan;112(1):82-4. PMID: 19857921.

Goris ML, Robinson TE. Sampling Density to Evaluate Quantitative Air Trapping. Pediatr Radiol. 2009;39:2221.

Govaert JA, Swijnenbrug RJ, Schrepfer S, Xie X, van der Bogt K, Hoyt G, Stein W, Ransohoff K, Robbins RC, Wu JC. Poor Functional Recovery after Transplantation of Diabetic Bone Marrow Stem Cells in Ischemic Myocardium. J Heart Lung Transplantation. 2009 Nov;28(11):1158-65.

Grissom W, Kerr A, Holbrook A, Pauly J, Butts Pauly K. Maximum Linear-Phase Spectral-Spatial RF Pulses for Fat-Suppressed PRF-Shift MR Thermometry. Magn Reson Med. 2009 Nov;62(5):1242-50. PMID: 19780177; PMCID: PMC2795148

Guzman R, Lee M, Achrol A, Bell-Stephens T, Kelly M, Do HM, Marks MP, Steinberg GK. Clinical Outcome after 450 Revascularization Procedures for Moyamoya Disease. J Neurosurg. 2009 Nov; 111(5):927-35.

Hamilton AM, Rogers KA, Belisle AJ, Ronald JA, Rutt BK, Weissleder R, Boughner DR. Early Identification of Aortic Valve Sclerosis using Iron Oxide Enhanced MRI. J Magn Reson Imaging. 2010 Jan;31(1):110-6. PMID: 20027578.

Han M, Beatty PJ, Daniel BL, Hargreaves BA. Independent Slab-Phase Modulation Combined with Parallel Imaging in Bilateral Breast MRI. Magn Reson Med. 2009 Nov;62(5):1221-1231.

Hargreaves BA, Chen W, Lu W, Alley MT, Gold G, Brau ACS, Pauly JM, Butts Pauly K. Accelerated Slice Encoding for Metal Artifact Correction. J Magn Reson Imaging. 2010 Apr;31(4):987-96.

He X, Wang KM, Cheng Z. In Vivo Near-infrared Fluorescence Imaging of Cancer with Nanoparticles-based Probes. Invited review (peer reviewed), WIREs Nanomedicine and Nanobiotechnology. 2010: DOI: 10.1002/wnan.85.

Heilmaier C, Lutz AM, Bolog N, Weishaupt D, Seifert B, Willmann JK. Focal Liver Lesions: Detection and Characterization at Double-Contrast Liver MR Imaging with Ferucarbotran and Gadobutrol versus Single-Contrast Liver MR Imaging. Radiology. 2009 Dec;253(3):724-33.

Ho D, Lin M, Schaenman J, Rosso F, Leung AN, Coutre SE, Sista RR, Montoya JG. Yield of Diagnostic Procedures for Invasive Fungal Infections in Neutropenic Febrile Patients with Chest Computed Tomography (CT) Abnormalities. Mycoses. 2009 Sep 28 [epub ahead of print]

Holbrook A, Santos J, Kaye E, Rieke V, Butts Pauly K. Real-Time MR Thermometry for Monitoring HIFU Ablations of the Liver. MRM. 2010 Feb;63(2):365-73.

Horning SJ, Juweid ME, Schoder H, Wiseman G, McMillan A, Swinnen LJ, Advani R, Gascoyne R, Quon A. Interim Positron Emission Tomography Scans in Diffuse Large B-cell Lymphoma: An Independent Expert Nuclear Medicine Evaluation of the Eastern Cooperative Oncology Group E3404 study. Blood. 2010 Jan 28;115(4):775-7; quiz 918.

Papers Submitted or In Press

Papers Submitted or In Press

Hsu A, Hou L, Veeravagu A, Barnes P, Huhn S. Resolution of Syringomyelia after Release of Tethered Cord. Surg Neurol. 2009 Dec;72(6):657-61.

Hsu JJ, Glover GH, Zaharchuk G. Optimizing Saturation-recovery Measurements of the Longitudinal Relaxation Rate under Time Constraints. Magn Reson Med. 2009 Nov;62(5):1202-10.

Huang M, Chen ZY, Hu S, Jia F, Li Z, Hoyt G, Robbins RC, Kay M, Wu JC. Novel Minicircle Vector for Gene Therapy in Murine Myocardial Infarction. Circulation. 2009 Sep 15;120(11 Suppl):S230-7.

Huang N, Niyama H, Peter C, De A, Natkunam Y, Fleissner F, Li Z, Rollins M, Wu J, Gambhir SS, Cooke J. Embryonic Stem Cell-Derived Endothelial Cells Engraft Into the Ischemic Hindlimb and Restore Perfusion. Arterioscler Throm Vasc Biol. 2010 May;30(5):984-91.

Iagaru A, Mittra E, Goris E, Gambhi SSr. Combined [18F]-FDG and Fluoride Approach in PET/CT Imaging: Is There a Clinical Future? J Nucl Med. 2009 Dec;50(6):1011.

Iagaru A, Mittra E, Yaghoubi S, Dick D, Quon A, Goris M, Gambhir SS. Novel Strategy for a Cocktail [18F] Fluoride and [18F]-FDG PET/CT Scan for Evaluation of Malignancy: Results of the Pilot-Phase Study. J Nucl Med. 2009 Apr;50(4):501-5.

Iagaru A, Mittra ES, Ganjoo K, Knox SJ, Goris ML. 131I-Tositumomab (Bexxar®) vs. 90Y-Ibritumomab (Zevalin®) Therapy of Low-Grade Refractory/Relapsed Non-Hodgkin Lymphoma. Mol Imaging Biol. 2010 Apr;12(2):198-203.

Inlay MA, Bhattacharya D, Sahoo D, Serwold T, Seita J, Karsunky H, Plevritis SK, Dill DL, Weissman IL. Ly6d Marks the Earliest Stage of B Cell Specification and Identifies the Branchpoint between B Cell and T Cell Development. Genes and Development. 2009 Oct 15;23(20):2376-81.

Jadvar H, Alavi A, Gambhir SS. [18F] FDG Uptake in Lung, Breast, and Colon Cancers Molecular Biology Correlates and Disease Characterization. J Nucl Med. 2009 Oct;50(11):1820-7.

Jia F, Wilson KD, Sun N, Gupta DM, Huang M, Li Z, Robbins RC, Kay MA, Longaker MT, Wu JC. Minicircle DNA Induces Pluripotency in Adult Human Cells. Nature Methods. 2010;7(3):197-9.

Jiang L, Kimura R, Miao Z, Silverman , Ren G, Liu H, Li P, Gambhir SS, Cochran J, Cheng Z. Evaluation of a (64)Cu-Labeled Cystine-Knot Peptide Based on Agouti-Related Protein for PET of Tumors Expressing Alphavbeta3 Integrin. J Nuc Med. 2010 Feb;51(2):251-8. PMID: 20124048.

Jiang L, Schipper ML, Li P, Cheng Z. 123I Labeled Metaiodobenzylguanidine for Diagnosis of Neuroendocrine Tumors. Reports in Medical Imaging. 2009;2:79-89.

Jimenez-Requena F, Delgado-Bolton R, Fernandez-Perez C, Gambhir SS, Schwimmer J, Perez-Vazquez J, Carreras-Delgado J. Meta-analysis of the Performance of [18F] FDG-PET in Cutaneous Melanoma. Eur J Nuc Med Mol Imaging. 2010 Feb;37(2):284-300.

Kahn CE, Langlotz CP, Burnside ES, Carrino JA, Channin DS, Hovsepian DM, Rubin DL. Towards Best Practices in Radiology Reporting. Radiology. 2009 Sep;252(3):852-6.

Kamaya A, Maturen KE, Tye GA, Liu YI, Parti NN, Desser TS. Hypervascular Liver Lesions. Semin Ultrasound CT MR. 2009 Oct;30(5):387-407.

Kamaya A, Ro K, Benedetti NJ, Chang PL, Desser TS. Imaging and Diagnosis of Postpartum Complications: Sonography and Other Imaging Modalities. Ultrasound Q. 2009 Sep;25(3):151-62.

Kao D, Witteles R, Quon A, Wu J, Gambhir SS, Fowler M. Rosiglitazone Increases Myocardial Glucose Metabolism in Insulin-Resistant Cardiomyopathy. J Am Col Cardiol. 2010 Mar;55(9): 926-7.

Kapinos G, Fischbein NJ, Zaharchuk G, Venkatasubramanian C. Migraine-like Headache with Visual Deficit and Perfusion Abnormality on MRI. Neurology. 2010 May 25;74(21):1743-5.

Katz M, Liu C, Schaer M, Parker KJ, Ottet MC, Epps A, Buckmaster CL, Bammer R, Moseley ME, Schatzberg AF, Eliez S, Lyons DM. Prefrontal Plasticity and Stress Inoculation-induced Resilience. Dev Neurosci. 2009;31(4):293-9. PMID: 19546566; PMCID: PMC2820579.

Kaye E, Josan S, Lu A, Rosenberg J, Daniel BL, Butts Pauly K. Consistency of Signal Intensity and T2* in Frozen Ex Vivo Heart Muscle, Kidney and Liver Tissue. J Magn Reson Imaging. 2010 Mar;31(3):719-24. PMID: 20187218; PMCID: PMC2832094

Kenis H, Zandbergen HR, Hofstra L, Petrov AD, Dumont EA, Blankenberg FG, Haider N, Bitsch N, Gijbels M, Verjans JW, Narula N, Narula J, Reutelingsperger CP. Annexin A5 Uptake in Ischemic Myocardium: Demonstration of Reversible Phosphatidylserine Externalization and Feasibility of Radionuclide Imaging. J Nucl Med. 2010;51:259-67. PMID: 20124049.

Kim JE, Newman B. Evaluation of a radiation dose reduction strategy for pediatric chest CT. Am J Roentgenol. 2010 May;194(5):1188-93.

Papers Submitted or In Press

Kim Y-P, Daniel WL, Xia Z, Xie H, Mirkin CA, Rao J. Gold Nanoparticle-luciferase Conjugates Synthesized via Click Chemistry and Site-specific Protein Ligation: Bioluminescent Nanosensors for Protease Detection. Chemical Communications. 2010;46:76-8.

Kimura R, Miao Z, Cheng Z, Gambhir SS, Cochran J. A Dual-Labeled Knottin Peptide for PET and Near-Infrared Fluorescence Imaging of Integrin Expression in Living Subjects. Bioconjug Chem. 2010 Feb Epub. PMID: 20131753.

Koo S, Giori N, Gold G, Dyrby C, Andriacchi T. Accuracy of Cartilage Thickness Measurement in MRI Changes with Cartilage Thickness: Laser Scanner Based Validation of In Vivo Osteoarthritic Cartilage. J Biomech Eng. 2009 Dec;131(12);1200-04.

Kothary N, Lock L, Sze DY, Hofmann LV. Computed Tomography-guided Percutaneous Needle Biopsy of Pulmonary Nodules: Impact of Nodule Size on Diagnostic Accuracy. Clin Lung Cancer. 2009 Sep;10(5):360-3.

Krishnamurthy G, Krishnamurthy S, Gambhir SS, Rodrigues C, Rosenberg J, Schiepers C, Buxton-Thomas M. Development and Intra-institutional and Inter-institutional Validation of a Comprehensive New Hepatobiliary Software: Part 1 – Liver and Gallbladder Function. Nuc Med Comm. 2009 Dec;30(12): 934-44.

Kuo WT, Gould MK, Louie JD, Rosenberg JK, Sze DY, Hofmann LV. Catheter-directed Therapy for the Treatment of Massive Pulmonary Embolism: Systematic Review and Meta-analysis of Modern Techniques. J Vasc Interv Radiol. 2009 Nov;20(11):1431-40.

Kuo WT, Tong RT, Hwang GL, Louie JD, Lebowitz EA, Sze DY, Hofmann LV. High-risk Retrieval of Adherent and Chronically Implanted IVC Filters: Techniques for Removal and Management of Procedural Thrombotic Complications. J Vasc Interv Radiol. 2009 Dec;20(12):1548-56.

Kurian A, Sigal B, Plevritis SK. A Survival Analysis of Cancer Risk Reduction Strategies for BRCA1/2 Mutation Carriers. J Clin Oncol. 2010 Jan;10;28(2):222-31.

Lazzaro NA, Wright B, Castillo M, Fischbein NJ, Glastonbury CM, Hildenbrand PG, Wiggins RH, Quigley EP, Osborn AG. Artery of Percheron Infarction: Imaging Patterns and Clinical Spectrum. Am J Neuroradiol. 2010 Aug;31(7):1283-9. PMID: 20299438.

Lee DS, Kamaya A, Jeffrey RB. Islet Cell Tumor of the Pancreas: Spectrum of MDCT Findings. A pictorial essay. Appl Radiol. 2009;38(11):10-28.

Levashova Z, Backer M, Backer JM, Blankenberg FG. Imaging Vascular Endothelial Growth Factor (VEGF) Receptors in Turpentine-induced Sterile Thigh Abscesses with Radiolabeled Single-chain VEGF. J Nucl Med. 2009 Dec;50(12):2058-63. PMID: 19910439.

Levin YS, Albers MJ, Butler TN, Spielman D, Peehl DM, Kurhanewicz J. Methods for Metabolic Evaluation of Prostate Cancer Cells using Proton and (13)C HR-MAS Spectroscopy and [3-(13)C] Pyruvate as a Metabolic Substrate. Magn Reson Med. 2009 Nov;62(5):1091-8.

Levy MA, O'Connor MJ, Rubin DL. Semantic Reasoning with Image Annotations for Tumor Assessment. AMIA Annu Symp Proc. 2009 Nov 14;2009:359-363.

Lew C, Alley MT, Spielman DM, Bammer R, Chan FP. Breathheld Autocalibrated Phase-contrast Imaging. J Magn Reson Imaging. 2010 Apr;31(4):1004-14.

Li Z, Wilson K, Smith B, Kraft DL, Jia F, Huang M, Xie X, Robbins R, Gambhir SS, Weissman I, Wu J. Functional and Transcriptional Characterization of Human Embryonic Stem Cell-Derived Endothelial Calls for Treatment of Myocardial Infarction. PLoS One. 2009 Dec 31;4(12):e84443.

Liang G, Ren H, Rao J. A Biocompatible Condensation Reaction for Controlled Assembly of Nanoparticles in Cells. Nat Chem. 2010;2:54-60.

Liu C, Mang SC, Moseley ME. In Vivo Generalized Diffusion Tensor Imaging (GDTI) using Higher-order Tensors (HOT). Magn Reson Med. 2010 Jan;63(1):243-52. PMID: 19953513; PMCID: PMC2824337.

Liu C, Zhang J, Moseley ME. Auto-calibrated Parallel Imaging Reconstruction for Arbitrary Trajectories using k-space Sparse Matrices (kSPA). IEEE Trans Med Imaging. 2010 Mar;29(3):950-9. PubMed PMID: 20199928.

Liu H, Ren G, Miao Z, Zhang X, Tang X, Han P, Gambhir SS, Cheng Z. Molecular Optical Imaging with Radioactive Probes. PLoS One. 2010 Mar;5(3):E9470. PMID: 20208993.

Liu YI, Kamaya A, Desser TD, Rubin DL. A Controlled Vocabulary to Represent Sonographic Features of the Thyroid and its application in a Bayesian Network to Predict Thyroid Nodule Malignancy. AMIA Summit on Translational Bioinformatics, 2009.

Loening A, Dragulescu-Andrasi A, Gambhir SS. A Red-Shifted Renilla Luciferase for Transient Reporter-Gene Expression. Nature Methods. 2010 Jan;7(1):5-6.

Ma N, Marshall A, Gambhir SS, Rao J. Facile Synthesis, Silanization and Biodistribution of Biocompatible Quantum Dots. Small. 2010 Jul 19;6(14):1520-8.

Mandleblatt J, Cronin K, Bailey S, Berry D, de Koning H, Draisma G, HUnad H, Lee S, Munsell M, Plevritis SK, Ravdin P, Schechter P, Sigal B, Stoto M, Stout N, van Ravestevn Nicolien, Venier J, Zelen M, Feuer EJ. Effects of Mammography Screening under Different Screening Schedules: Model Estimates of Potential Benefits and Harms. Ann Intern Med. 2009 Nov 17;151(10):738-47.

Papers Submitted or In Press

Papers Submitted or In Press

Marsden AL, Reddy VM, Shadden SC, Chan FP, Taylor CA, Feinstein JA. A New Multiparameter Approach to Computational Simulation for Fontan Assessment and Redesign. Cogenit Heart Dis. 2010 Mar 5(2):104-17.

May A, Bhaumik S, Gambhir SS, Zhan C, Yazdanfar S. Whole-Body, Real-Time Preclinical Imaging of Quantum Dot Fluorescence with Time-Gated Detection. J Biomed Optics. 2009 Nov-Dec;14(6):060504.

Mayer D, Yen YF, Tropp J, Pfefferbaum A, Hurd RE, Spielman DM. Application of Subsecond Spiral Chemical Shift Imaging to Real-time Multislice Metabolic Imaging of the Rat In Vivo after Injection of Hyperpolarized 13C1-pyruvate. Magn Reson Med. 2009 Sep;62(3):557-64.

Miao Z, Ren G, Liu H, Jiang L, Cheng Z. Small-Animal PET Imaging of Human Epidermal Growth Factor Receptor 1 Positive Tumor with a 64Cu Labeled Affibody Protein. Bioconjug Chem. 2010 May 19;21(5):947-54.

Miao Z, Ren G, Liu H, Jiang L, Kimura RH, Cochran JR, Gambhir SS, Cheng Z. An Engineered Knottin Peptide Labeled with 18F for PET Imaging of αvβ3 Integrin Expression. Bioconjugate Chemistry. 2009 Dec;20(12):2342-7. PMID: 19908826. [Highlighted by SNM Newsletter, JNM, 2010; 51(1), 18N].

Mittra E, McDougall IR. Cutaneous Graft-versus-host Disease on Tc-99m Leukocyte Scintigraphy. Clin Nucl Med. 2009 Dec;34(12):894-5.

Morris B, Partap S, Yeom K, Gibbs IC, Fisher PG, King A. Cerebrovascular Disease in Childhood Cancer Survivors: A Children's Oncology Group Report. Neurology. 2009 Dec 1;73(22):1906-13.

Newman B, Feinstein JA, Cohen RA, Feingold B, Kreutzer J, Patel H, Chan FP. Congenital Extrahepatic Portosystemic Shunts Associated with Heterotaxy and Polysplenia. Pediatr Radiol. 2010 Jul;40(7):1222-30. PMID 20069288.

Olivot J-M, Mlynash M, Kleinman JT, Straka M, Venkatasubramanian C, Bammer R, Moseley ME, Albers GW, Wijman CAC. Temporal and Spatial Profile of Brain Diffusion-weighted MRI in the First Week after Cardiac Arrest. Stroke. 2010 Aug;41(8):1665-72.

Olivot J, Minynash M, Thijs V, Purushotham A, Kemp S, Lansberg M, Wechsler L, Gold G, Bammer R, Marks M, Albers G. Geography, Structure and Evolution of the Diffusion and Perfusion Lesion in DEFUSE. Stroke 2009 Oct;40(10):3245-51.

Olivot JM, Mylnash M, Thijs VN, Purusshotham A, Kemp S, Lansberg MG, Weschler LR, Gold G, Bammer R, Marks MP, Albers GW. Geography and Structure of the Penumbra Through the Eyes of MRI: Lesion Evolution and Infarct Prediction. Stroke. 2009;40(10):3245-51.

Pashevich M, Sigal BM, Plevritis SK. A Natural History Model of Metastatic Progression Applied to Lung Cancer. Cancer Causes and Control. 2009 Nov;20(9):1559-69.

Pauly KB, Rieke V, Holbrook AB, Grissom W, Chen J, Kaye E. MR-guidance of HIFU Therapy. Conf Proc IEEE Eng Med Biol Soc. 2009;2009:141-4. PubMed PMID: 19964927.

Peleg M, Rubin DL. Querying Radiology Appropriateness Criteria from a virtual Medical Record using GELLO. Proc. Workshop on Knowledge Representation for Health-Care: Patient Data, Processes and Guidelines, in conjunction with Artificial Intelligence in Medicine Europe. 2009.

Peng H, Olcott PD, Levin CS. Design Study of a High-resolution Breast-dedicated PET System Built from Cadmium Zinc Telluride Detectors. Phys Med Biol. 2010;55:2761-88.

Vertinsky AT, Rubesova E, Krasnokutsky MV, Bammer S, Rosenberg J, White A, Barnes PD, Bammer R. Performance of PROPELLER Relative to Standard FSE T2-weighted Imaging in Pediatric Brain MRI. Pediatr Radiol. 2009 Oct;39(10):1038-47.

Pham DT, Hura SA, Willman JK, Nino-Murcia M, Jeffrey RB. Pictorial Essay: Evaluation of Periampullary Pathology with CT Volumetric Oblique Coronal Reformations. Am J Roentgenol. 2009 Sep;193(3):786.

Pham DT, Hura SA, Willmann JK, Nino-Murcia M, Jeffrey RB. Evaluation of Periampullary Pathology with CT Volumetric Oblique Coronal Reformations. Am J Roentgenol. 2009 Sep;193(3):W202-8.

Prakash S, Dumoulin SO, Fischbein N, Wandell BA, Liao YJ. Congenital Achiasma and See-saw Nystagmus in VACTERL Syndrome. J Neuroophthalmol. 2010 Mar;30(1):45-8. PMID: 20182207.

PratX G, Levin, CS. Bayesian Reconstruction of Photon Interaction Sequences for High-resolution PET Detectors. Physics in Medicine and Biology. 2009 Sep 7;54(17):5073-94.

Price RO, Jeffrey RB, Vasanawala SS. Appendiceal Hyperemia and/or Distention is Not Always Appendicitis: Appendicitis Mimicry in the Pediatric Population. Clin Imaging. 2009 Sep-Oct;33(5):402-5. PMID: 19712824.

Papers Submitted or In Press

Papers Submitted or In Press

Prümmer M, Hornegger J, Lauritsch G, Wigström L, Girard-Hughes E, Fahrig R. Cardiac C-arm CT: A Unified Framework for Motion Estimation and Dynamic CT. IEEE Trans Med Imaging. 2009 Nov;28(11):1836-49.

Qiu P, Gentles AJ, Plevritis SK. Reducing the Computational Complexity of Information Theoretic Approaches for Reconstructing Gene Regulatory Networks. J Comput Biol. 2010 Feb;17(2):169-76.

Raman P, Raman R, Newman B, Venkatraman R, Raman B, Robinson TE. Development and Validation of Automated 2D-3D Bronchial Airway Matching to Track Changes in Regional Bronchial Morphology Using Serial Low-Dose Chest CT Scans in Children with Chronic Lung Disease. J Digit Imaging. 2009 Sep 15 Epub. PMID: 19756866.

Ren G, Liu Z, Miao Z, Liu H, Jiang L, Subbarayan M, Chin FT, Zhang L, Gambhir SS, Cheng Z. PET of Malignant Melanoma using 18F-labeled Metallopeptides. J of Nuc Med. 2009 Nov;50(11):1865-72. PMID: 19837749.

Ren G, Miao Z, Liu H, Jiang L, Limpa-Amara N, Mahmood A,Gambhir SS, Cheng Z. Melanin-targeted Preclinical PET Imaging of Melanoma Metastasis. J Nuc Med. 2009 Oct;50(10):1692-9. PMID: 19759116.

Ren G, Zhang R, Liu Z, Webster J, Miao Z, Gambhir SS, Syud F, Cheng Z. A 2-helix Small Protein Labeled with 68Ga for PET Imaging of HER2 Expressions. J Nucl Med. 2009 Sep;50(9):1492-9. PMID: 19690041.

Ren H, Xiao F, Zhan K, Kim YP, Xie H, Xia Z, Rao J. A Biocompatible Condensation Reaction for Labeling of N-terminal Cysteine on Proteins. Angewandte Chemie International Edition. 2009;48: 9658-62.

Rodriguez-Porcel M, Gheysens O, Paulmurugan R, Chen IY, Peterson KM, Willmann JK, Wu JC, Zhu X, Lerman LO, Gambhir SS. Antioxidants Improve Early survival of Cardiomyoblasts After Transplantation to the Myocardium. Mol Imaging Biol. 2010 Jun;12(3):325-34.

Rogalski EJ, Murphy CM, deToledo-Morrell L, Shah RC, Moseley ME, Bammer R, Stebbins GT. Changes in Parahippocampal White Matter Integrity in Amnestic Mild Cognitive Impairment: A Diffusion Tensor Imaging Study. Behav Neurol. 2009;21(1):51-61. PMID: 19847045; PMCID: PMC2819387.

Roos JE, Paik DS, Olsen DA, Liu EG, Chow LC, Leung AN, Mindelzun R, Choudhury KR, Naidich DP, Napel S, Rubin GD. Computer-aided Detection (CAD) of Lung Nodules in CT Scans: Radiologist Performance and Reading Time with Incremental CAD Assistance. Eur Radiol. 2010 Mar;20(3):549-57.

Roos JE, Rakshe T, Tran DN, Rosenberg J, Straka M, El-Helw T, Sofilos MC, Napel S, Fleischmann D. Lower Extremity CT Angiography (CTA): Initial Evaluation of a Knowledge-based Centerline Estimation Algorithm for Femoro-popliteal Artery (FPA) Occlusions. Acad Radiol. 2009;16:646-53.

Rubin DL, Mongkolwat P, Channin DS. A Semantic Image Annotation Model to Enable Integrative Translational Research. In: AMIA Summit on Translational Bioinformatics. 2009.

Rubin DL, Supekar K, Mongkolwat P, Kleper V, Channin DS. Annotation and Image Markup: Accessing and Interoperating with the Semantic Content in Medical Imaging. IEEE Intelligent Systems. 2009;24(1):57-65.

Sachs K, Gentles AJ, Youland R, Itani S, Irish J, Nolan GP, Plevritis SK. Characterization of Patient Specific Signaling via Augmentation of Bayesian Networks with Disease and Patient State Nodes. Conf Proc IEEE Eng Med Biol Soc. 2009;6624-7. PMID: 19963681.

Sahoo D, Seita J, Bhattacharya D, Inlay MA, Weissman IL, Plevritis SK, Dill DL. MiDReG: A method of Mining Developmentally Regulated Genes using Boolean Implications. Proc Natl Acad Sci U S A. 2010 March 30;107(13):5732-7.

Samaniego EA, Stuckert E, Fischbein N, Wijman CA. Crossed Cerebellar Diaschisis in Status Epilepticus. Neurocrit Care. 2010 Feb;12(1):88-90. PMID: 19967565.

Schellenberg D, Quon A, Minn AY, Graves EE, Kunz P, Ford JM, Fisher GA, Goodman KA, Koong AC, Chang DT. (18)Fluorodeoxyglucose PET Is Prognostic of Progression-Free and Overall Survival in Locally Advanced Pancreas Cancer Treated With Stereotactic Radiotherapy. Int J Radiat Oncol Biol Phys. 2010 Aug 1;77(5):1420-5.

Schmitz A, van den Bosch MA, Rieke V, Dirbas FM, Butts Pauly K, Mali WP, Daniel BL. 3.0T MR-guided Focused Ultrasound for Pre-operative Localization of Non-palpable Breast Lesions: An Initial Experimental Ex Vivo Study. J Magn Reson Imaging. 2009 Oct;30(4):884-9. PMID: 19787736.

Schroeder AR, Axelrod DM, Silverman NH, Rubesova E, Merkel E, Roth SJ. A Continuous Heparin Infusion does Not Prevent Catheter-related Thrombosis in Infants Post-cardiac Surgery. Pediatr Crit Care Med. 2010 Jan 22.

Shah NH, Bhatia N, Jonquet C, Rubin DL, Chiang AP, Musen MA. Comparison of Concept Recognizers for Building the Open Biomedical Annotator. BMC Bioinformatics. 2009 Sep 17;10 Suppl 9:S14.

Papers Submitted or In Press

Papers Submitted or In Press

Shahbaba B, Gentles A, Beyene J, Plevritis SK, Greenwood CMT.
A Bayesian Nonparametric Method for Model Evaluation: Application to Gene-disease Studies. Journal of Nonparametric Statistics. 2009;21(3):379-96.

Shin DS, Jeffrey RB, Desser TS. Pearls and Pitfalls in Hepatic Ultrasonography. Ultrasound Q. 2010;26(1):17-25.

Shin LK, Fischbein NJ, Kaplan MJ, Jeffrey RB. Metastatic Squamous Cell Carcinoma Presenting as Diffuse and Punctate Cervical Lymph Node Calcifications: Sonographic Features and Utility of Sonographically-guided Fine-needle Aspiration Biopsy. J Ultrasound Med. 2009 Dec; 28(12):1703-7. PMID: 19933485.

Singh M, Spielman D, Adleman N, Alegria D, Howe M, Reiss A, Chang K. Brain Glutamatergic Characteristics of Pediatric Offspring of Parents with Bipolar Disorder. Psychiatry Res. 2010 May 30;182(2):165-71.

Steele JR, Hovsepian DM, Schomer DF. The Joint Commission Practice Performance Evaluation: A Primer for Radiologists.
J Am Coll Radiol. 2010 Jun;7(6):425-30.

Steele JR, Wallace MJ, Hovsepian DM, James BC, Kundu S, Miller DL, Rose SC, Sacks D, Shah SS Cardella JF. Guidelines for Establishing a Quality Improvement Program in Interventional Radiology. J Vasc Interv Radiol. 2010 May;21(5):617-25.

Stevens KJ, Crain JM, Akizuki KH, Beaulieu CF. Imaging and Ultrasound-guided Steroid Injection of Internal Oblique Muscle Strains in Baseball Pitchers. Am J Sports Med. 2010 Mar;38(3):581-5.

Stevens KJ. Magnetic Resonance Imaging of the Elbow. J Magn Reson Imaging. 2010 May;31(5):1036-53.

Sun N, Lee A, Wu JC. Long-term Non-invasive Imaging of Embryonic Stem Cells using Reporter Genes. Nat Protoc. 2009;4(8):1192-201.

Sun N, Panetta NJ, Gupta DM, Wilson KD, Lee A, Jia F, Hu S, Cherry AM, Robbins RC, Longaker MT, Wu JC. Feeder-free Derivation of Induced Pluripotent Stem Cells from Adult Human Adipose Stem Cells. Proc Natl Acad Sci U S A. 2009 Sep 15;106(37):15720-5.

Sutter R, Heilmeier C, Lutz AM, Weishaupt D, Seifert B, Willmann JK. MR Angiography with Parallel Acquisition for Assessment of the Visceral Arteries: Comparison with Conventional MR Angiography and 64-detector-row Computed Tomography. Eur Radiol. 2009 Nov;19(11):2679-88.

Swijnenburg RJ, Govaert JA, van der Bogt KE, Pearl JI, Huang M, Stein W, Hoyt G, Vogel H, Contag CH, Robbins RC, Wu JC. Timing of Bone Marrow Cell Delivery has Minimal Effects on Cell Viability and Cardiac Recovery Following Myocardial Infarction. Circulation: Cardiovascular Imaging. 2010;3(1):77-85.

Sze DY, Fleischmann D, Ma AO, Price EA, McConnell MV. Embolization of a Symptomatic Systemic to Pulmonary (right-to-left) Venous Shunt Caused by Fibrosing Mediastinitis and Superior Vena Caval Occlusion. J Vasc Interv Radiol. 2010;21(1):140-3.

Tedesco MM, Terashima M, Blankenberg FG, Levashova Z, Spin JM, Backer MV, Backer JM, Sho M, Sho E, McConnell MV, Dalman RL.
Analysis of In Situ and Ex Vivo Vascular Endothelial Growth Factor Receptor Expression during Experimental Aortic Aneurysm Progression.
Arterioscler Thromb Vasc Biol. 2009 Oct;29(10):1452-7. PMID: 19574559

Tognolini A, Louie JD, Hwang GL, Hofmann LV, Sze DY, Kothary N. Utility of C-arm CT in Patients with Hepatocellular Carcinoma Undergoing Transhepatic Arterial Chemoembolization. J Vasc Interv Radiol. 2010 Mar;21(3):339-47.

Tooze JA, Gaussoin SA, Resnick SM, Fischbein NJ, Robinson JG, Bryan RN, An Y, Espeland MA. Women's Health Initiative Memory Study.
A Uniform Approach to Modeling Risk Factor Relationships for Ischemic Lesion Prevalence and Extent: The Women's Health Initiative Magnetic Resonance Imaging study. Neuroepidemiology. 2010;34(1):55-62. PMID: 19940514.

Townson JL, Ramadan SS, Simedrea C, Rutt BK, Macdonald IC, Foster PJ, Chambers AF. Three-dimensional Imaging and Quantification of Both Solitary Cells and Metastases in Whole Mouse Liver by Magnetic Resonance Imaging. Cancer Res. 2009 Nov 1;69(21):8326-31. PMID: 19843857.

Tu S, Peleg M, Carini S, Bobak M, Rubin DL, Sim I.
A Practical Method for Transforming Free-Text Eligibility Criteria into Computable Criteria. AMIA Annu Symp Proc. 2009.

Tuniz F, Soltys SG, Choi CY, Chang SD, Gibbs IC, Fischbein NJ, Adler JR Jr. Multisession Cyberknife Stereotactic Radiosurgery of Large, Benign Cranial Base Tumors: Preliminary Study. Neurosurgery. 2009 Nov;65(5):898-907; discussion 907. PMID: 19834402.

Ueda T, Fleischmann D, Dake MD, Rubin GD, Sze DY. Incomplete Endograft Apposition to the Aortic Arch: Bird-beak Configuration Increases Risk of Endoleak Formation after Thoracic Endovascular Aortic Repair. Radiology. 2010 May;255(2):645-52.

Vaithilingam S, Ma TJ, Furukawa Y, Wygant IO, Zhuang X, De La Zerda A, Oralkan O, Kamaya A, Gambhir SS, Jeffrey RB, Khurii-Yakub BT.
Three-dimensional photoacoustic imaging using a two-dimensional cMUT array. IEEE Trans Ultrason Ferroelectr Freq Control. 2009 Nov;56(11):2411-9.

Papers Submitted or In Press

Van de Ven S, Lin MC, Daniel BL, Sareen P, Lipson JA, Pal S, Dirbas FM, Ikeda DM. Freehand MRI-guided Preoperative Needle Localization of Breast Lesions after MRI-guided Vacuum-assisted Core Needle Biopsy (VACNB) without Marker Placement. J Magn Reson Imaging. 2010 Jul;32(1):101-9.

Vandevenne J, Pearle A, Lang P, Butts Pauly K, Bergman G. Clinical Feasibility of a Magnetic Resonance Tracking System to Guide the Position of the Scan Plane during Physiologic Joint Motion. Radiol Med. 2010 Feb;115(1):133-40. PubMed PMID: 20041313.

Vasanawala SS, Iwadate Y, Church DG, Herfkens RJ, Brau ACS. Navigated Abdominal T1 MRI Permits Free-Breathing Image Acquisition with Less Motion Artifacts. Pediatr Radiol. 2010 Mar;40(3)340-4. PMID20066407.

Vasanawala SS. MRI of the Liver – How to Do It. Pediatr Radiol. 2010 Apr;40(4):431-7. PMID: 20225098.

Vertinsky AT, Rubesova E, Krasnokutsky MV, Bammer S, Rosenberg J, White A, Barnes PD, Bammer R. Performance of PROPELLER Relative to Standard FSE T2-weighted Imaging in Pediatric Brain MRI. Pediatr Radiol. 2009 Oct;39(10):1038-47.

Wang B, Sommer FG, Spielman D, Shortliffe LD. Evaluation of Dynamic Constrast-enhanced MRI in Detecting Renal Scarring in a Rat Injury Model. J Magn Reson Imaging. 2010 May;31(5):1132-6.

Wang C, Stebbins GT, Medina DA, Shah RC, Bammer R, Moseley ME, Detoledo-Morrell L. Atrophy and Dysfunction of Parahippocampal White Matter in Mild Alzheimer's Disease. Neurobiol Aging. 2010 Mar 30; Epub. PubMed PMID: 20359781.

Willmann J, Kimura R, Deshpande N, Lutz A, Cochran J, Gambhir SS. Targeted Contrast-Enhanced Ultrasound Imaging of Tumor Angiogenesis with Contrast Microbubbles Conjugated to Integrin-Binding Knottin Peptides. J Nucl Med. 2010 Mar;51(3):433-40.

Willmann JK, Kimura, RH, Deshpande N, Lutz AM, Cochran JR, Gambhir SS. Targeted Contrast-enhanced Ultrasound Imaging of Tumor Angiogenesis with Contrast Microbubbles Conjugated to Integrin-Binding Knottin Peptides. J Nucl Med. 2010 Mar;51(3):433-40.

Won JH, Rosenberg J, Rubin GD, Napel S. Uncluttered Single-Image Visualization of the Abdominal Aortic Vessel Tree: Method and Evaluation. Medical Physics. 2009 Nov;36(11):5245–60.

Wong S, Kupnik M, Watkins R, Butts Pauly K, Khuri-Yakub B. Capacitive Micromachined Ultrasonic Transducers for Therapeutic Applications. IEEE Trans Biomed Eng. 2010 Jan;57(1):114-23. PubMed PMID:19628448.

Wu AS, Do BH, Kim J, Rubin DL. Evaluation of Negation and Uncertainty Detection and its Impact on Precision and Recall in Search.
J Digit Imaging. 2009 Nov 10; Epub.

Yen YF, Le Roux P, Mayer D, King R, Spielman D, Tropp J, Butts Pauly K, Pfefferbaum A, Vasanawala S, Hurd R. T(2) Relaxation Times of (13)C Metabolites in a Rat Hepatocellular Carcinoma Model Measured In Vivo using (13)C-MRS of Hyperpolarized [1-(13)C]pyruvate.
NMR Biomed. 2010 Feb 19; Epub. PubMed PMID: 20175135.

Yoon S, Pineda AR, Fahrig R. Simultaneous Segmentation and Reconstruction: A Level Set Method Approach for Limited View Computed Tomography.
Med Phys. 2010 May;37(5):2329-40.

Yu J, Huang NF, Wilson KD, Velotta JB, Huang M, Li Z, Lee A, Robbins RC, Cooke JP, Wu JC. nAChRs Mediate Human Embryonic Stem Cell-derived Endothelial Cells: Proliferation, Apoptosis, and Angiogenesis. PLoS ONE. 2009 Sep 15;4(9):e7040.

Yuan N, Kane PE, Shelton K, Matel J, Beckel BC, Moss RB. Safety, Tolerability, and Efficacy of High-Frequency Chest Wall Oscillation in Pediatric Patients with Cerbral Palsy and Neuromuscular Diseases: An Exploratory Randomized Controlled Trial. J Child Neurol. 2010 Jul;25(7):815-21.

Zaharchuk G, Bammer R, Straka M, Newbould RD, Rosenberg J, Olivot JM, Mlynash M, Lansberg MG, Schwartz NE, Marks MM, Albers GW, Moseley ME.
Improving Dynamic Susceptibility Contrast MRI Measurement of Quantitative Cerebral Blood Flow using Corrections for Partial Volume and Nonlinear Contrast Relaxivity: A Xenon Computed Tomographic Comparative Study. J Magn Reson Imaging. 2009 Oct;30(4):743-52. PMID: 19787719; PMCID: PMC2851938.

Zaharchuk G, Bammer R, Straka M, Shankaranarayan A, Alsop DC, Fischbein NJ, Atlas SW, Moseley ME. Arterial Spin-label Imaging in Patients with Normal Bolus Perfusion-weighted MR Imaging Findings: Pilot Identification of the Borderzone Sign. Radiology. 2009 Sep;252(3):797-807. PMID: 19703858.

Zaharchuk G, Straka M, Marks MP, Albers GW, Moseley ME, Bammer R. Combined arterial spin label and dynamic susceptibility contrast measurement of cerebral blood flow. Magn Reson Med. 2010 Jun;63(6):1548-56.

Zhu L, Wang J, Xie Y, Starman J, Fahrig R, Xing L. A patient set-up protocol based on partially blocked cone-beam CT. Technol Cancer Res Treat. 2010 Apr;9(2):191-8.

Zissen MH, Quon A. Focal fat mimicking multiple hepatic metastases on FDG PET/CT imaging. Eur J Nucl Med Mol Imaging. 2009 Sep;36(9):1527.

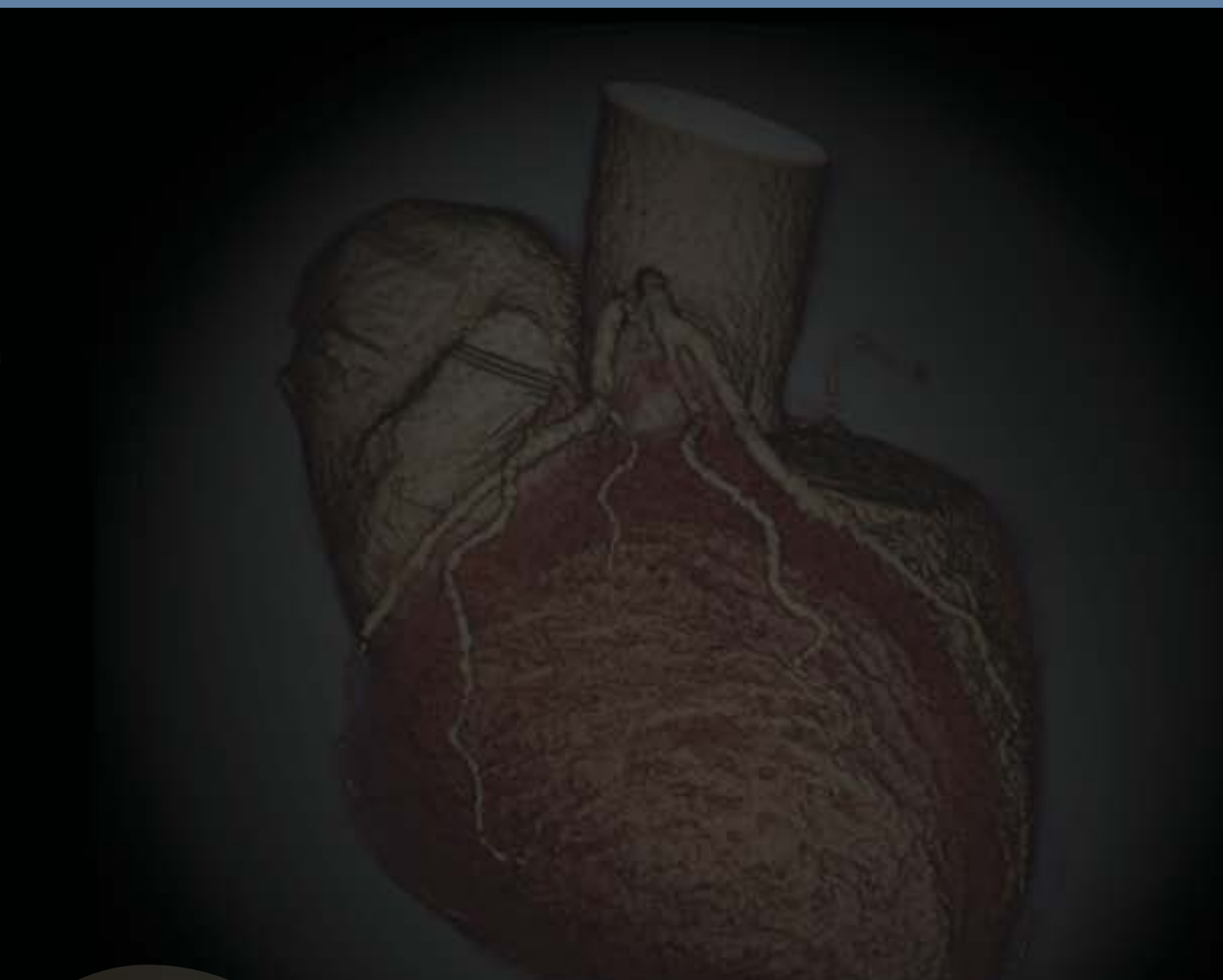

Funding

PI	Type	Title
Roland Bammer, PhD	R01	Improving SENSE MRI for Spiral and Echo-planar Imaging in Stroke
Roland Bammer, PhD	R01 (ARRA)	Novel Acquisition Methods for Diffusion MRI
Roland Bammer, PhD	R21	Real-Time MRI Motion Correction System
Roland Bammer, PhD	R01 (+ARRA supp)	Short Axis EPI for Diffusion Tensor MRI at High Field
Francis Blankenberg, MD	R01 (ARRA)	scVEGF Targeted Radiotherapy of Mammary and Colonic Cancer
Catherine Chang, MS	F32	Temporal Characteristics of Intrinsic Brain Networks Using fMRI
Zhen Cheng, PhD	R21	Quantum Dots for NIR Fluorescence Imaging of Tumor Angiogenesis
Zhen Cheng, PhD	R01	Radiolabeled RGD Peptides for Breast Cancer Imaging and Therapy
Zhen Cheng, PhD	R01 (ARRA)	VEGFR-2 Targeted Imaging
Heike Daldrup-Link, MD	R21*	Novel Imaging Approach to Monitor Chondrogenic Differentiation of IPS Cells
Heike Daldrup-Link, MD	R01	Monitoring of Stem Cell Engraftment in Arthritic Joints with MR Imaging
Bruce Daniel, MD	R01	Techniques for MRI-Guided Cryosurgery of Prostate Cancer
Bruce Daniel, MD	R21*	High Resolution 3D Diffusion-Weighted Breast MRI
Rebecca Fahrig, PhD	S10* (ARRA)	Axiom zeego shared instrument grant
Rebecca Fahrig, PhD	R01 (ARRA)	C-Arm CT for Guidance of Cardiac Interventions
Rebecca Fahrig, PhD	R01*	Dual KV/MV Imaging for Metal Artifact Reduction
Rebecca Fahrig, PhD	R21	Efficient Scatter Correction
Rebecca Fahrig, PhD	R01 (+ARRA supp)	MR-Compatible X-Ray Tube
Rebecca Fahrig, PhD	R21*	Ultrafast Tomosynthesis for Transbronchial Biopsy Guidance
Sam Gambhir, MD, PhD	U54 (+ARRA supp)	Center of Cancer Nanotechnology Excellence Focused on Therapy Response
Sam Gambhir, MD, PhD	R01	Imaging Cytolytic T Cells in Cancer Patients Using PET Reporter Genes/Reporter Probes
Sam Gambhir, MD, PhD	P50**	In Vivo Cellular and Molecular Imaging Center @ Stanford
Sam Gambhir, MD, PhD	R01**	Reporter Imaging of Protein-Protein Interactions
Sam Gambhir, MD, PhD	R25	Stanford Molecular Imaging Scholars (SMIS)
Arundhuti Ganguly, PhD	K99	High Performance CMOS Based X-Ray Detector for C-AM CT Imaging
Gary M. Glazer, MD	T32	Advanced Techniques for Cancer Imaging and Detection
Gary Glover, PhD	P41**	Center for Advanced Magnetic Resonance Technology at Stanford
Garry Gold, MD	R01**	Rapid MRI for Evaluation of Osteoarthritis
Garry Gold, MD	R01	Real-Time MRI and 3D Modeling: Development and Application to Patellofemoral Pain
Brian Hargreaves, PhD	R01 (+ARRA supp)	High-Resolution Whole-Breast MRI at 3.0T
Brian Hargreaves, PhD	R21	Magnetic Resonance Imaging near Metallic Implants

PI	Type	Title
Craig Levin, PhD	R01 (+ARRA supp)	Advanced PET System Dedicated to Breast Cancer Imaging
Craig Levin, PhD	R01	Enhancing Molecular Cancer Imaging with Cadmium Zinc Telluride PET
Michael Moseley, Phd	R01	Microvascular Measures of Perfusion in Stroke Recanalization
Michael Moseley, Phd	S10* (ARRA)	Upgrade of the Stanford GE-Varian Experimental MRI Scanner to the Current Model M
Kim Butts Pauly, PhD	R21*	MRI Methods for Guiding Focused Ultrasound in the Brain
Kim Butts Pauly, PhD	R01	MR-Image Guided Focused Ultrasound for Treatment of Liver and Renal Cancer
Norbert Pelc, ScD	R01 (+ARRA supp)	Inverse Geometry CT for Dose-efficient Volumetric Imaging
Norbert Pelc, ScD	T32*	Predoctoral Training in Biomedical Imaging at Stanford University
Sylvia Plevritis, PhD	R01	Breast Cancer Trend Analysis Using Stochastic Simulation
Sylvia Plevritis, PhD	U01	Computational Modeling of Cancer Biology
Sylvia Plevritis, PhD	U54*	Modeling the Role of Differentiation in Cancer Progression
Jianghong Rao, PhD	R01	QD-BRET nanosensors for protease detection and imaging
Viola Rieke, PhD	K99	MRI-guided Cardiac Focused Ultrasound Ablation
Daniel Rubin, MD	U01*	Computerized Quantitative Imaging Assessment of Tumor Burden
Geoffrey Rubin, MD	R01	Improving Radiologist Detection of Lung Nodules with CAD
Brian Rutt, PhD	S10*	Next Generation 7T MRI Platform Upgrade System
Graham Sommer, MD	R21	MRI - Guided Ultrasonic Ablation of Pancreatic Cancer
Graham Sommer, MD	R01	Precise MRI-Directed Sonic Ablation of Prostate Cancer
Daniel Spielman, PhD	R01	1H MRSI of the Human Brain at 7T
Daniel Spielman, PhD	R01*	Metabolic Imaging of the Cardioprotective Effects of Alcohol and ALDH2 Activators
Shreyas Vasanawala, MD, PhD	R01*	Rapid Robust Pediatric MRI
Juergen Willman, MD	R21	Early Detection of Pancreatic Cancer with Targeted Contrast-enhanced Ultrasound
Joseph Wu, MD, PhD	DP2	09: Inducing Pluripotency with MiRNAs: New Paradigm Shift in Cell Reprogramming
Joseph Wu, MD, PhD	R21 (+ARRA supp)	Biological Insights into Dynamics of Stem Cell Differentiation and Misbehavior
Joseph Wu, MD, PhD	R01*	Integrated Strategies for Novel Treatment of Myocardial Ischemia
Joseph Wu, MD, PhD	R01	Molecular Imaging of Cardiac Stem Cell Therapy
Joseph Wu, MD, PhD	RC1* (ARRA)	Molecular Imaging of Resident Cardiac Stem Cells
Joseph Wu, MD, PhD	R01	Molecular Imaging of Targeted Cardiac Gene Therapy
Joseph Wu, MD, PhD	R33	Nanostructuring and Molecular Imaging of Engineered Cardiovascular Tissues
Joseph Wu, MD, PhD	R01*	Re-Education of the Immune System for hES Cell Tolerance
Gregory Zaharchuk, MD, PhD	R01	Quantifying Collateral Perfusion in Cerebrovascular Disease

NIH Collaborations (Sub-Contracts)

For additional awards, see Awards and Honors pages 24 - 27
* New for 2010
**Longstanding project renewed for another 4-5 years

PI	Type	Title
Xiaoyuan Chen, PhD	Purdue R01	99mPTc-Labeled Cyclic RGD Peptide Tetramers for Breast Cancer Imaging
Sam Gambhir, MD, PhD	UCLA R01	Multimodel Qdot Probes for Bioimaging of Cells and Tumors in Small Animals
Sam Gambhir, MD, PhD	USC*	Multi-Scale Complex Systems Transdisiplinary Analysis of Response to Therapy (MC-START)
Sam Gambhir, MD, PhD	Fred Hutch	Ovarian Cancer Early Detection Using Microbubble Contrast Enhanced Ultrasound (CEUS) Targeting Tumor Associated Angiogenesis
Gary Glover, PhD	UC Irvine	Functional Imaging Research in Schizophrenia Testbed
Garry Gold, MD	UCSF	Data Coordinating Center for Osteoarthritis Initiative
Lawrence Hofmann, MD	Wash U/ Genentech	ATTRACT: Industry Portion
Lawrence Hofmann, MD	Wash U	Pharmacomechanical Catheter-Directed Thrombolysis for Acute DVT-Attract Trial
Daniel Rubin, MD	U Pittsburgh	A Web-Based Portal of Investoried Resources Enabling Clinical and Translational Research Across the CTSA and Beyond
Daniel Rubin, MD	Northwestern	Annotations and Image Markup Project - Phase I and II
Daniel Rubin, MD	Emory Univ	In Silico Research Center
Daniel Rubin, MD	Brigham & Women's	Neuroimaging Analysis Center (NAC)
Daniel Rubin, MD	UCSF*	Ontology-Based Integration of Human Studies Data
Daniel Rubin, MD	U Pittsburgh	The ODIE Toolkit -software for information extraction and biomedical ontology development
Daniel Spielman, MD	U Miami	Partnership for MR Spectroscopic Imaging Data Processing
Daniel Spielman, MD	SRI	Dynamic Metabolic Imaging of Hyperpolarized Substrates
Daniel Spielman, PhD	SRI International	In Vivo Diffusion and Spectroscopic Brain Imaging in Alcoholism
Joseph Wu, MD, PhD	SDSU*	Engineering Cardiac Progenitor Cells to Enhance Myocardial Regeneration

California Supported Research

PI	Type	Title
Qizhen Cao, PhD	UCOP	alpha7-nAChR Targeted Imaging and Therapy of Lung Cancer
Zhen Cheng, PhD	UCOP	Novel Small Proteins for PET Imaging of Breast Cancer
Rebecca Rakow-Penner, MD, PhD	UCOP	Functional Breast MRI with BOLD Contrast
Joseph Wu, MD, PhD	UCOP	Imaging of Novel Stem Cell Therapy Targeting Breast Cancer
Joseph Wu, MD, PhD	CIRM	In Vivo Imaging of Human Embryonic Stem Cell Derivatives and Tumorigenicity

Professional Society & Foundation Supported Research

PI	Type	Title
Scott Atlas, MD	RSNA	Ultra-High Resolution Clinical Imaging of the Human Medial Temporal Lobe with 7T MRI
Zhen Cheng, PhD	Melanoma Rsch Fd	18F Labeled Benzamides for Pre-clinical PET Imaging of Melanoma Metastases
Sam Gambhir, MD, PhD	Ben & Catherine Ivy*	18F PPRGD2 PET/CT and MRI Evaluation of Response to Anti-Angiogenesis Therapy in Recurrent Glioblastoma Multiforme (GBM)
Sam Gambhir, MD, PhD	Doris Duke	Molecular Imaging of Cancer with a Voltage Sensor
Sam Gambhir, MD, PhD	AMI*	Study Drug: Sodium fluoride F18 Injection
Garry Gold, MD	Arthritis Foundation	Sodium MRI of Post-traumatic Arthritis
Benjamin Hackel, PhD	ACS*	Novel High Affinity Protein Scaffolds for Molecular Imaging of Tumors
Shijun Hu, PhD	AHA-California*	Transplantation and Imaging of Novel Cardiac Stem Cell Therapy
Mei Huang, PhD	AHA-California	Novel Non-viral Gene Therapy for Heart Disease
Charles Li, PhD	RSNA	Improved Isotropic 3D FSE Methods for Imaging the Knee
Amelie Lutz, MD	Marsha Rivkin	Early Detection of Ovarian Cancer Using Targeted Microbubble-Enhanced Ultrasound
John Mackenzie, MD	SPR	Evaluation of Pediatric Diseases with Hyperpolarized Carbon-13 Magnetic Resonance Imaging
Sam Mazin, PhD	Ewing Marion Kauffman Fd*	Commercialization of PET-Guided Radiation Therapy
Peter Olcott, MS	SNM	Optically coupled pulse width modulation PET detectors for combined whole body clinical PET/MR systems
Andrew Quon, MD	NCCN	Evaluating Sunitinib Therapy in Renal Cell Carcinoma
Jianghong Rao, PhD	Texas A&M	Development of Fluorgenic Probes for In Vivo Imaging of Tuberculosis
Jianghong Rao, PhD	HFSP	Imaging mRNA in Synaptic Plasticity
Daniel Rubin, MD	ACR	American College of Radiology Imaging Network (ACRIN) Committee Agreement Rubin
Daniel Rubin, MD	RSNA	Enriching the RadLex Ontology to Enable Biomedical Imaging Research in Neuroimaging
Lewis Shin, MD	RSNA	RSNA research seed grant
Shreyas Vasanawala,MD,PhD	ISMRM	Non-Contrast-Enhanced Renal MRA Using Multiple Inversion Recovery
David Wang, MD	RSNA*	Ultrasound - Mediated Suicide gene Therapy with Molecularly Targeted microbubbles in a murine model for tumor angiogenesis
Juergen Willmann, MD	Soc of GI Radiologists	Anti-Angiogenic Treatment Assessment in Abdominal and Pelvic Cancer using Molecular Ultrasound: First Step towards Clinical Translation
Juergen Willmann, MD	Nat. Pancreas Fd	Development of Novel Translatable Molecular Imaging Approach for Early Detection of Pancreatic Cancer
Joseph Wu, MD, PhD	Mallinckrodt, Jr Fd	Innovative Approach for Reprogramming Stem Cells for Regenerative Medicine
Joseph Wu, MD, PhD	BWF	Molecular and Cellular Mechanisms of Cardiac Regeneration
Joseph Wu, MD, PhD	AHA-California	Safety and Efficacy of Novel iPSC Derived Cardiomyocytes
Greg Zaharchuk, MD, PhD	NERF*	Optimizing Arterial Spin Label MRI for the Visualization of Collateral Flow in Moyamoya Disease
Keren Ziv, PhD	Life Science Rsch Fd	Non-Invasive and Real-Time Monitoring of Stem Cells Using Photoacoustic Molecular Imaging in Living Mice

Other Government Supported Research

For additional awards, see Awards and Honors pages 24 - 27

* New for 2010

**Longstanding project renewed for another 4-5 years

PI	Type	Title
Zhen Cheng, PhD	DOD	Msesnchymal Stem Cell as Targeted-delivery Vehicle in Breast Cancer
Zhen Cheng, PhD	DOD*	Peptoid-Based PET Probes for Prostate Cancer Imaging
Brian Hargreaves, PhD	VA	Cartilage Compression Study for VA
Gang Niu, PhD	DOD	*Imaging Heat Shock Protein 90 (Hsp90) Activity in Hormone-Refractory Prostate Cancer
Jianghong Rao, PhD	DOD	Enzyme-triggered Polymerization: a new platform for breast cancer imaging
Jianghong Rao, PhD	DOA	Ribozyme-Mediated Imaging of p53 Expression in Breast Tumor Cells
Arne Vandenbroucke, PhD	DOD*	Commissioning and Characterizing a dedicated high resolution breast PET camera
Adam de la Zerda, PhD	DOD	Early Assessment of Breast Cancer Therapy Responses Using Photoacoustic Molecular Imaging

Industry Supported Research

PI	Type	Title
Sandip Biswal, MD	Kai Pharmaceuticals	Evaluation of the Efficacy of KAI-1678 with Manganese-Enhanced Magnetic Resonance Imaging (MEMRI)
Francis Blankenberg, MD	Genentech, Inc	Choline MRS correlated with Markers of Apoptosis (TUNEL)/biotinylated annexin V & Autopahgy (TYPE II cell death)
Francis Blankenberg, MD	Sibtech, Inc	Targeted Delivery of Lu-177 to tumor vasculature
Francis Blankenberg, MD	Sibtech, Inc*	VEGF-based Targeted Imaging of Tumor Vasculature
Zhen Cheng, PhD	Ocean Nano-Tech, LLC	Iron oxide nanoparticle probes for target specific MR molecular imaging
Rebecca Fahrig, PhD	Siemens Medical Solutions	Cardiac Imaging using C-arm CT: EP registration and perfusion
Rebecca Fahrig, PhD	Siemens Medical Solutions	Perfusion Imaging using C-arm CG: Brain and Liver
Sam Gambhir, MD, PhD	Bayer Corporation*	An Open-label, Non-randomized, Multi-center Study to Optimize Image Assessment and Evaluate the Efficacy and Safety of BAY 94-9172 (ZK 6013443) Positron Emission Tomography (PET) for Detection/Exclusion of Cere
Sam Gambhir, MD, PhD	Schering AG	Collaborative Research Agreement: Project 1: Tumor Lymphangiogenesis Imaging Project 2: PET Imaging of Breast Cancer using Fructose Analogues
Sam Gambhir, MD, PhD	GE Healthcare	Developing Tools for Cell Therapy - specifically cell tracking and quality assurance
Sam Gambhir, MD, PhD	GE Healthcare	Multimodality Molecular Pre-Clinical Imaging
Sam Gambhir, MD, PhD	Schering Plough Rsch Institute	SCH-XXX in Orthotopic U87 Glioblastoma Model
Garry Gold, MD	GE Company	Advanced MR Applications Development
Lawrence Hofmann, MD	Pfizer Pharmaceuticals	A Safety and Efficacy Trial Evaluating the Use of Apixaban for Th e Extended Treatment of Deep Vein Thrombosis and Pulmonary Embolism (CV185057)
Lawrence Hofmann, MD	Pfizer Pharmaceuticals	A Safety and Efficacy Trial Evaluating the Use of Apixaban in the Treatment of Symptomatic Deep Vein Thrombosis and Pulmonary Embolism(CV185056)

Industry Supported Research

For additional awards, see Awards and Honors pages 24 - 27

* New for 2010

**Longstanding project renewed for another 4-5 years

PI	Type	Title
Lawrence Hofmann, MD	OmniSonics Med Tech, Inc	Study of the OmniWave Endovascular System in Subjects with Lower and Upper Extremity Deep Vein Thrombosis: Sonic I Study
Debra Ikeda, MD	ART Advanced Rsch Tech, Inc	SSC-311 Adjunctive Efficacy Study of the SoftScan Optical Breast Imaging System
Debra Ikeda, MD	Spectros	Survey of Optical Measures of Breast Tissue in the Clinic
Nishita Kothary, MD	Siemens Medical Solutions	Clinical Feasibility and Evaluation of RoRo (Rotatinal Mapping); Optimal imaging protocol of HCC undergoing TACE utilizing DynaCT; & Needle Guided Procedures Utilizing DynaCT, Laser Guidance, and 2D3D Registration
Craig Levin, PhD	GE Healthcare	Combined Positron Emission Tomography (PET) Magnetic Resonance (MR) System
Craig Levin, PhD	Philips Healthcare*	GPU-based 3-D List Mode OSEM for ToF PET
Michael Marks, MD	ev3 Neurovascular*	SWIFT-solitaire FR with the intention for thrombectomy study
Sandy Napel, PhD	Kitware, Inc	Automated Bone Removal for Head and Neck CTA using Dual Energy CT
David Paik, PhD	Booz-Allen & Hamilton, Inc	New caBIG Integrated Cancer Research (ICR) Nanotechnology Working Group
Norbert Pelc, ScD	GE Healthcare	Advanced Computed Tomography (CT) Systems and Algorithms
Andrew Quon, MD	Genentech, Inc	Avastin/[18F]-5-fluorouracil PET/CT Imaging Feasibility Project
Daniel Rubin, MD	Booz-Allen & Hamilton, Inc	caBIG Imaging Workspace Participant
Daniel Rubin, MD	Booz-Allen & Hamilton, Inc	caBIG Master Agreement - Subcontract # 95077NBS23
Daniel Rubin, MD	Booz-Allen & Hamilton, Inc	Imaging Workspace in EY2
Geoffrey Rubin, MD	Biosense, Inc	Core Lab for NaviStar ThermCool Catheter for the Radiofrequency Ablation of Paroxysmal Atrial Fibrillation
Virginia Spanoudaki, PhD	AxaGroup	1mm Resolution Position Emission Tomography for Enhanced Molecular Breast Cancer Imaging
Daniel Sze, MD, PhD	WL Gore & Assoc, Inc	A Clinical Study Evaluating the Use of the Thoracic EXCLUDER Endoprostheis in the Treatment of Descending Thoracic Aortic Diseases (SUH#-CVR-01)
Daniel Sze, MD, PhD	WL Gore & Assoc, Inc*	An Evaluation of the GORE Conformable TAG Thoracic Endoprosthesis for the Primary Treatment of Aneurysm of the Descending Thoracic Aorta
Daniel Sze, MD, PhD	WL Gore & Assoc, Inc	Evaluation of the GORE TAG Thoracic Endoprosthesis - 45 mm for the Primary Treatment of Aneurysm of the Descending Thoracic Aorta
Daniel Sze, MD, PhD	WL Gore & Assoc, Inc	Evaluation of the GORE TAG Thoracic Endoprosthesis for the Treatment of Complex Pathology of the Descending Thoracic Aorta
Daniel Sze, MD, PhD	WL Gore & Assoc, Inc	Evaluation of the GORE TAG Thoracic Endoprothesis for Treatment of Descending Thoracic Aneurysms
Daniel Sze, MD, PhD	Cook Foundation	The Zilver PTX Drug Eluding Vascular Stent in the Above the Knee Femoralpopliteal Artery
Daniel Sze, MD, PhD	WL Gore & Assoc, Inc	Treatment IDE for Use of the GORE TAG Thoracic Endoprosthesis in Subjects with Descending Thoracic Aortic Aneurysms Requiring Surgical Repair
Daniel Sze, MD, PhD	Cook Incorporated	Zenith TX2 Thoracic TAA Endovascular Graft

CBIS Seed Funding

The Center for Biomedical Imaging at Stanford (CBIS), directed by Kim Butts-Pauly, PhD, provides educational and networking opportunities for all groups on campus that have an interest in biomedical imaging applications. Through support from the School of Medicine and the Dean's Office, the CBIS Advisory Committee is pleased to announce that out of more than 50 applications, 7 projects were allocated seed funding in 2010. The following projects were selected for their innovative, interdisciplinary, and translational potential. For more details of CBIS and the seed funding program, please see: http://cbis.stanford.edu/about/.

PI	Department	Title
Anita Koshy, MD	Internal Medicine	Using imaging to determine how and why Toxiplasma gondii injects rhoptry proteins it does not invade
Michael Lin, MD, PhD	Pediatrics and Bioengineering	Chemistry-based engineering of autocatalytic fluorescent proteins for whole-animal imaging in the optical window
Andrew Quon, MD	Radiology	18F-Sodium Flouride PET/CT for the pre-surgical evaluation of back pain
Mark Schnitzer, PhD	Applied Physics	Integrated fluorescence microscopes based on CMOS image sensors for teaching digital imaging in the microscopy courses at Stanford University
Colin Carpenter, PhD	Radiation Oncology	Tri-modality Molecular Surgical Guidance Integrated into a Laparoscope
Mark Cutkosky, PhD	Mechanical Engineering	Development and testing of tools with opto-thermal actuation for MRI-guided interventions
Michael Hsieh, MD, PhD	Urology	Single Cell Magnetic Resonance Imaging of Infections Using Bacterial Magnetite

Collaborators Outside of Stanford

We also enjoy many collaborations with foundations, agencies, institutions, and industry for whose support we are indeed thankful. We look forward to continued success in these collaborative endeavors as well.

Advanced Research Technologies (ART), Inc.
American College of Cardiology
American College of Radiology
American Heart Foundation
Angiotech
Axa Group
Bayer Corporation
Biosense, Inc
Booz-Allen & Hamilton, Inc
California Insitute for Regenerative Medicine
Canary Foundation
Cedars Sinai, Los Angeles
Colorado State University—Boulder
Cook Incorporated
Cook Medical Institute, Inc.
Department of Defense
Diversified Diagnostic Products, Inc.
Doris Duke Foundation
Edward Mallinckrodt Jr. Foundation
ev3 Neurovascular
FeRx, Inc.
Fred Hutchinson Cancer Research Center
GE Healthcare
Genentech
InSightec
Kai Pharmaceuticals
Kaufmann Foundation
Kitware, Inc
Life Science Research Foundation
Lucile Packard Foundation
Marsha Rivkin Center for Ovarian Cancer
Melanoma Research Foundation
National Institutes of Health
Ocean NanoTech, LLC
OmniSonics Medical Technologies, Inc
Palo Alto Veterans Administration
Pfizer Pharmaceuticals
Philips Healthcare
Prostate Cancer Foundation
Purdue University
Radiological Society of North America
Richard M. Lucas Cancer Foundation
Riken, Saitama, Japan
Schering AG
Schering Plough Research Institute
Scripps Research Institute
SibTech, Inc
Siemens Corporate Research
Siemens Medical Solutions
Sir Peter & Lady Michael Foundation
Society for Pediatric Radiology
Society of Nuclear Medicine
Spectros Corporation
SRI International
Texas A&M
University of California, Berkeley
University of California, Davis
University of California, Irvine
University of California, Los Angeles
University of California, San Diego
University of California, San Francisco
University of Chicago
University of Miami
University of Pittsburgh
University of Southern California
University of Texas, A & M
University of Texas, Austin
University of Washington
Varian Associates
W.L. Gore and Associates
Wallenberg
Weston Havens Foundation

Collaborating Stanford Departments

We work with almost three hundred faculty, postdoctoral fellows, students, and research staff from across the University. We wish to thank you all for the friendly, productive collaborations that we enjoy all year long. Stanford departments with whom we have long-standing research projects include the following:

Aeronautics and Astronautics
Anesthesia
Applied Physics
Biochemistry
Bioengineering
Bio-X
Cancer Biology
Cancer Center
Cardiothoracic Surgery
Chemistry
Comparative Medicine
Computer Sciences
Developmental Biology
Electrical Engineering
ENT
Freeman Spogli Institute
Genetics
Health Research and Policy
Hematology
Infectious Diseases
Lucile Packard Children's Hospital
Materials Science and Engineering
Mechanical Engineering
Medical Informatics
Medicine
Microbiology and Immunology
Molecular and Cellular Physiology
Neurobiology
Neurology and Neurological Sciences
Neurosurgery
Obstetrics & Gynecology
Oncology
Orthopedics/Orthopedic Surgery
Otolaryngology
Palo Alto VA
Pathology
Pediatrics
Pediatrics/Neonatology
Psychiatry and Behavioral Sciences
Psychology
Radiation Oncology
Stanford Center for Biomedical Ethics
Stroke Center
Surgery